

NC STATE UNIVERSITY

**MURI / ARO
FUNCTIONALLY TAILORED TEXTILES**

FINAL REPORT

**WILLIAM T. KING
COORDINATING PRINCIPAL INVESTIGATOR**

PERIOD: FEBRUARY, 1996-MAY, 2002

U.S. ARMY RESEARCH OFFICE

CONTACT/GRANT NO. DAAH04-96-1-0018

**NORTH CAROLINA STATE UNIVERSITY
COLLEGE OF TEXTILES
RALEIGH, NORTH CAROLINA**

APPROVED FOR PUBLIC RELEASE;

~~RESTRICTED~~



**THE VIEWS, OPINIONS, AND/OR FINDINGS CONTAINED IN THIS REPORT
ARE THOSE OF THE AUTHOR(S) AND SHOULD NOT BE CONSTRUED AS
AN OFFICIAL DEPARTMENT OF THE ARMY POSITION, POLICY, OR
DECISION, UNLESS SO DESIGNATED BY OTHER DOCUMENTATION.**

**Reproduced From
Best Available Copy**

20030227 110

REPORT DOCUMENTATION PAGE

Form Approved
OMB NO. 0704-0188

Public Reporting burden for this collection of information is estimated to average 1 hour per response, including the time for reviewing instructions, searching existing data sources, gathering and maintaining the data needed, and completing and reviewing the collection of information. Send comment regarding this burden estimates or any other aspect of this collection of information, including suggestions for reducing this burden, to Washington Headquarters Services, Directorate for Information Operations and Reports, 1215 Jefferson Davis Highway, Suite 1204, Arlington, VA 22202-4302, and to the Office of Management and Budget, Paperwork Reduction Project (0704-0188,) Washington, DC 20503.

1. AGENCY USE ONLY (Leave Blank)		2. REPORT DATE 15 August, 2002		3. REPORT TYPE AND DATES COVERED FINAL: FEBRUARY, 1996-MAY, 2002	
4. TITLE AND SUBTITLE FUNCTIONALLY TAILORED TEXTILES				5. FUNDING NUMBERS DAAH04-96-1-0018	
6. AUTHOR(S) WILLIAM T. KING, COORDINATING PRINCIPAL INVESTIGATOR					
7. PERFORMING ORGANIZATION NAME(S) AND ADDRESS(ES) NORTH CAROLINA STATE UNIVERSITY COLLEGE OF TEXTILES --BOX 8301 RALEIGH, NC 27695-8301				8. PERFORMING ORGANIZATION REPORT NUMBER	
9. SPONSORING / MONITORING AGENCY NAME(S) AND ADDRESS(ES) U. S. Army Research Office P.O. Box 12211 Research Triangle Park, NC 27709-2211				10. SPONSORING / MONITORING AGENCY REPORT NUMBER 35023-MS-MUR . / 3	
11. SUPPLEMENTARY NOTES The views, opinions and/or findings contained in this report are those of the author(s) and should not be construed as an official Department of the Army position, policy or decision, unless so designated by other documentation.					
12 a. DISTRIBUTION / AVAILABILITY STATEMENT Approved for public release; distribution unlimited.				12 b. DISTRIBUTION CODE	
13. ABSTRACT (Maximum 200 words) Four universities (Drexel University, North Carolina State University, The University of Akron & The University of Pennsylvania) are in collaboration on this basic research. The objective of the program is to improve the survivability of the soldier by functionally tailoring protective clothing that detects and protects against battlefield threats (including chemical/biological agents, fire ballistic, detention, and other threats.) There are four areas of thrust: 1). Fibers and Processing; 2). Polymer Synthesis and Surface Chemistry; 3). Sensors and Smart Materials and 4). Composites. The approach to the research is to bring together Principal Investigators who have worked polymers, fibers, fabrics, and assembly instrumentation systems in a coordinated program. There is further collaboration with ARL, ARO, Natick, US Army SBCCOM, and Industry in this basic research.					
14. SUBJECT TERMS				15. NUMBER OF PAGES	
				16. PRICE CODE	
17. SECURITY CLASSIFICATION OR REPORT UNCLASSIFIED	18. SECURITY CLASSIFICATION ON THIS PAGE UNCLASSIFIED	19. SECURITY CLASSIFICATION OF ABSTRACT UNCLASSIFIED		20. LIMITATION OF ABSTRACT UL	

NSN 7540-01-280-5500

ARO-MURI
FUNCTIONALLY TAILORED TEXTILES
FINAL REPORT (Period: Feb., 1996-May, 2002)

TABLE OF CONTENTS

Section 1--- DREXEL UNIVERSITY

- A) Dr. M.A. El-Sherif—Fiber Optic Sensors for Detection of Biological Threats; Polypyrrole as Conducting Polymer; Development of Chemical Vapor Sensors
- B) Dr. Frank Ko—Modeling of Gradient Composite Armors & Engineered Hybrid nano-fiber yarns

Section 2-- NORTH CAROLINA STATE UNIVERSITY

- A) Dr. Sam Hudson—The Extrusion of Silk-like Protein Fibers
- B) Dr. Alan Tonelli— Inclusion Compounds; Incorporation of additives into Melt-blown & Electro-spun, non-woven webs: Chain-extended crystalline morphology
- C) Dr. T. K. Ghosh
Dr. A. M. Seyam—3-D Fabric Structure Through Melt-blown Technology
- D) Dr. Trevor J. Little
Dr. Benham Pourdeyhimi—Conjugate Bicomponent Fiber Spinning and Characterization—Micro-Fibers
- E) Dr. Mohammed Zikry—Methodologies and Numerical Techniques for new Woven Composites.

Section 3-- THE UNIVERSITY OF AKRON

- A) Dr. William Brittain—Synthesis and Characterization of Novel Block Copolymer Brushes
- B) Dr. Mark Foster—Behavior of Polymer Brush Coatings
- C) Dr. Roderic Quirk—Preparation of Well-defined, Thin Films by Anionic Grafting for use in Chemical Protection and Sensor Applications
- D) Dr. Darrell Reneker—Developing the technology of electro-spining of Polymer nano-fibers, Advances in Stability and Productivity of the Electro-Spinning Process

Section 4-- THE UNIVERSITY OF PENNSYLVANIA

- A) Dr. Alan G. MacDiarmid—Synthesis & Development of a thin film conducting polymer-based optical sensor for detection of low-concentration molecular contaminants such as volatile nerve agents. Report and Presentation by Dr. Wayne E. Jones, Jr, State University of New York at Binghamton.

ARO-MURI
FUNCTIONALLY TAILORED TEXTILES

INDEX
(CROSS REFERENCE TO TABLE OF CONTENTS)

1. FIBERS AND PROCESSING

NORTH CAROLINA STATE UNIVERSITY

- A) Dr. Samuel M. Hudson
- B) Dr. Alan E. Tonelli
- C) Dr. Tushar K. Ghosh
- Dr. Abdelfattah Seyam

UNIVERSITY OF AKRON

- A) Dr. William J. Brittain
- B) Dr. Mark D. Foster
- C) Dr. Roderic P. Quirk
- D) Dr. Darrell H. Reneker

2. POLYMER SYNTHESIS AND SURFACE CHEMISTRY

UNIVERSITY OF AKRON

- A) Dr. William J. Brittain
- B) Dr. Mark D. Foster
- C) Dr. Roderic P. Quirk

UNIVERSITY OF PENNSYLVANIA

- A) Dr. Alan G. MacDiarmid

3. SENSORS AND SMART MATERIALS

DREXEL UNIVERSITY

- A) Dr. Mohammed A. El-Sherif

UNIVERSITY OF AKRON

- B) Dr. Mark D. Foster

4. TEXTILE BASED FABRICS AND COMPOSITES

DREXEL UNIVERSITY

C) Dr. Frank K. Ko

NORTH CAROLINA STATE UNIVERSITY

C. Dr. Tushar K. Ghosh

Dr. Abdelfattah Seyam

D. Dr. Trevor J. Little

Dr. Benham Pourdeyhimi

E. Dr. Mohammed A. Zikry

UNIVERSITY OF AKRON

D. Dr. Darrell H. Reneker

SECTION 1

DREXEL UNIVERSITY

A

**MURI/ARO FUNCTIONALLY TAILORED TEXTILE FABRICS
U.S. ARMY RESEARCH OFFICE CONTRACT/GRANT NO. DAAH 04-96-1-0018**

**The Final Technical Report
On
SENSORS AND SMART FABRICS**

Submitted by:

Dr. M. El-Sherif
Director, Fiber Optics & Photonics Manufacturing Engineering Center
Drexel University
Tel: 215-895-2324
Fax: 215-895-6684
e-mail: elsherif@cbis.ece.drexel.edu,
Website: <http://coe.drexel.edu/FOPMEC>

Research Team

Drexel University (DU)
Prof. M. El-Sherif (PI)
Prof Yen Wei
Jianming Yuan (Received PhD degree in Dec 2000)
Lalitkumar Bansal (Ph.D. Graduate Student Materials Engineering)
Saif El Din Khalil (M.S. Graduate Student Materials Engineering)
Dianne Phelan (Ph.D. Graduate Student Materials Engineering)
Bulent Kose (Ph.D. Graduate Student Electrical Engineering)
Ken Richard (Received M.S. degree in June 2001)

In collaboration with:

University of Pennsylvania (U of P)
Prof. Alan MacDiarmid (PI)

State University of New York at Binghamton (SUNY)
Dr. Wayne E. Jones Jr.
Ben Burton (Ph.D. Graduate Student Chemistry)

June, 2002

Table of Contents

List of Thesis & Publication	i
Abstract	1
PART I: Fiber Optic Sensors for Detection of Biological Threats	3
I.1. Introduction	3
I.2. Experimental Work	5
I.2.1. Processing of polymer thin films	5
I.2.2. Characterization of polymer thin films	5
I.2.3. Processing of fiber optic sensing element	6
I.2.4. Characterization of the modified cladding layer	6
I.2.5. Characterization of the fiber optic sensor	6
I.3. Results and Discussion	7
I.3.1. Optical property of polymer films	7
I.3.2. Morphology of the polymer thin films on both glass slide and optical fiber	7
I.3.3. Optical response of the fiber optic sensors	10
I.3.3.1 Application of Polyaniline	10
I.3.3.2 Application of Polypyrrole	12
I.3.3.2 Detection of DMMP	15
I.3.3.3 Detection of DMMP with doped Polypyrrole	18
I.4. Conclusion on development of biological sensor	21
 Part II: Sol-Gel Optical Fibers for Chemical Sensor Applications	
II.1. Summary	22
II.2. Experimental Procedure	22
II.2.1. Fiber preparation	22
II.2.2. Sol preparation, coating, and drying	23
II.2.3. Sensor preparation	23
II.2.4. Sensor application	23

II.3. Results	24
II.3.1. Sol-gel coating	24
II.3.2. Sensor response	25
II.4. Conclusions on Sol-Gel Optical Fiber Sensors	28
 Part III: Modal Power Distribution Analysis for Sensors Applications	 29
III.1. Objective	29
III.2. Introduction	29
III.3. Theoretical Analysis	30
III.3.1. Light distribution in multimode fibers	30
III.3.2. Formulation of problem	30
III.3.3. Fiber parameters	33
III.3.4. Eigen value equation for step-index fibers	34
III.3.5. Weakly guiding fibers and <i>LP</i> modes	35
III.4. Summary	40
References	41

Thesis

Jianming Yuan, "Polymer Materials as Modified Optical Fiber Cladding for Chemical Sensors" Ph.D Thesis, 2001, Advisor: Mahmoud El-Sherif.

Jianming Yuan "Development of smart structures utilizing chromogenic materials for optical fiber sensors" M.S Thesis, 1997, Advisor: Mahmoud El-Sherif.

Kenneth Scott Richards, "Sol-gel processed optical fibers for sensor applications".M.S. Thesis, 2000, Advisor: Mahmoud El-Sherif.

Publications

M. El-Sherif, M. Li, J. Yuan, D. El-Sherif, A. Rahman, S. Khalil, L. Bansal, M. Abou-iiiana, C. Lee, and J. Fairney, "Smart Textiles With Embedded Opto-Electronic Networks and Sensors – An Overview," International Interactive Textiles for the Warrior Conference, Soldier Biological and Chemical Command, US Army Natick Soldier Center, Boston, Cambridge, 9-11 July, 2002.

Jianming Yuan and Mahmoud El-Sherif, "Fiber Optic Chemical Sensor Using Polyaniline as Modified Cladding Material," IEEE Fiber Optic Sensors, in process, 2002.

L. Bansal, S. Khalil, M. El-Sherif "Fiber Optic Neurotoxin Sensor" IEEE 28th Annual Northeast Bioengineering Conference, pp. 221, 2002.

Jianming Yuan, Mahmoud A. El-Sherif, Alan G. MacDiarmid, and Wayne Jones, "Fiber Optic Chemical Sensors Using Modified Conducting Polymer Cladding., Proc. Of SPIE, vol. 4204 (2001).

Mahmoud El-Sherif and Jianming Yuan, "Smart Fabrics with Embedded Fiber Optic Sensors for Detection of Biological Threats," Intelligent Textiles 2000 Conference, Providence, RI, June 20-21, 2000.

Jianming Yuan, Mahmoud A. El-Sherif, Alan G. MacDiarmid, and Wayne E. Jones Jr., "Fiber Optic Chemical Sensors Using a Modified Sensitive Cladding," SPIE International Symposium on Environmental and Industrial Sensing, Boston, MA, November 5-8, 2000.

Alan G. MacDiarmid, Ian D. Norris, Wayne Jones, Mahmoud A. El-Sherif, Jianming Yuan, Baohua Han, and Frank Ko, Polyaniline Based Chemical Transducers with Sub-micron Dimensions," The Fall American Chemical Society Meeting, Washington, D.C., 2000.

Mahmoud A. El-Sherif and Jianming Yuan, "Fiber Optic Sensors and Smart Fabrics," J. of Intelligent Materials Systems and Structures vol ii no5 pp 325-414, May 2000.

Mahmoud A. El-Sherif and Jianming Yuan, "Fiber Optic Sensors and Smart Fabrics," The Fourth ARO (U.S. Army Research Office) Workshop on Smart Structures, State College, PA, August 16-18, 1999.

J. Yuan, J. Feng, M. El-Sheif and A. G. MacDiarmid, Development of an On-Fiber Chemical Vapor Sensor, OSA Annual Meeting, Baltimore, MD., Oct. 4-9, 1998.

J. Yuan and M. El-Sheif, Development of On-Fiber Optical Sensors Utilizing Chromogenic Materials, SPIE's International Symposium on Intelligent Systems and Advanced Manufacturing, Boston, MA., Nov. 1-6, 1998.

J. Yuan, (Adviser Dr. M. A. El-Sherif), "Development of Smart Structures Utilizing Chromogenic Materials for Optical Fiber Sensors." (M.S. thesis), December, 1997.

El-Sherif, M., (Invited Paper) "Fiber Optic Sensors for Soldiers' Smart Uniforms," Third ARO Workshop on Smart Structures, Virginia Polytechnic and State University, Blacksburg, Virginia, Aug. 27-29, 1997.

ABSTRACT

Progressive research has proven that the Soldier Integrated Protective Ensemble (SIPE) is a smart and very realistic Army Program. It is based on a modular system approach that directs to a fully developed combat system for soldiers' uniforms. Along with the idea of SIPE, the program presents a novel approach based on the development of fiber optic micro-sensors integrated into the soldier's uniform. The fiber optic micro-sensors are capable of sensing chemical and biological hazards in real-time battlefield threats in various environmental conditions. These conditions may include variable temperatures, stresses, electromagnetic fields and chemical environments. The soldier's smart uniform will provide early warnings and feedback information with protective instant reaction against multiple battlefield threats.

In the past five years many results have been reported and published in referred journals, conferences, and M.S and PhD thesis, recording innovations and new developments. In the early years, the project team proved the concept of using regular optical fibers as chemical or environmental sensors integrated into textile structures. Promising results have been presented to enhance a "smart" soldier uniform. This work was conducted in collaboration with the University of Akron (UA), using segmented polyurethane-diacetylene copolymer (SPU) as a thermo chromic material for temperature measurements, and in collaboration with the College of Textiles, NCSU, for the integration of these fiber optic sensors into samples of the soldiers' uniforms.

During the fourth year, the project team successfully developed an optical fiber chemical vapor sensor using polyaniline as the modified cladding material, in collaboration with the University of Pennsylvania (U of P), Dr. Alan MacDiarmid and his group, and Dr. Wyne Jones at State University of New York (SUNY). Novel methodology was also developed for coating the optical fiber with polyaniline as a chemical sensitive agent. In that same year, a feasibility study on using optical fiber clad with sol-gel silica for chemical sensors applications was also constructed with listed advantages. This extensive work was developed in collaboration with Fiber optic Fabrications, Inc., MA (Dr. Bolesh Skutnik's group), provided to us through Dr. Sam Di Vita of the U.S. Army CECOM, Ft. Monmouth, NJ, and Dr. Yen Wei and his group at the Department of Chemistry, Drexel University.

In the fifth year, work was conducted in the application of the developed fiber optic chemical sensor using polypyrrole as the modified cladding material for the detection of an organophosphonate chemical warfare agent simulant, dimethyl methylphosphonate (DMMP). This work was done in collaboration with the University of Pennsylvania (U of P), Dr. Mac Diarmid and his group, and also with the State University of New York Bringhamton, Dr. Wyne Jones and his group. Successful results have been obtained on the processing of polypyrrole in the application form as a sensitive cladding material on optical fibers. It was successfully tested for the detection of DMMP.

The final report is organized in three parts. The first part discusses the use of conducting polymers polyaniline and polypyrrole as sensing material for detection of biological treats. The second part discussed the sol gel optical fibers for chemical sensor

application and the third part discusses the modal power distribution (MPD) analysis for sensor application. The MPD technique is developed by Dr El-Sherif, as a sensitive and inexpensive detection technique for monitoring light intensity distribution in 2D as a measurand of the sensor output.

PART I: Fiber Optic Sensors for Detection of Biological Threats

I.1. Introduction

The fiber optic telecommunication and optoelectric industries evolutions have made dramatic progress in the formation of fiber optic sensors that provide clear advantages over conventional sensors. This aspect has branched into many industries providing capabilities that have not been reached before. In the area of chemical and biological warfare, advanced technological levels have been developed, contributing to the development of novel systems for early warnings and detection of enemy threats. The development of integrated fiber sensors, actuators and feedback control signals into soldiers uniform can present a methodology for sensing and responding to such threats in an efficient and intelligent manner.

The foundation of the developed fiber optic sensors is based on the change of optical power or optical intensity modulation induced within the multimode optical fibers. In the development of the optical fiber chemical sensor, an environmental sensitive material is coated on a small section of the fiber replaces the original cladding. Due to different environmental or chemical changes, the refractive index of the sensitive cladding material will alter and therefore change the light intensity transmitted through the optical fiber. In the past few years, the project team was able to prove the concept of using a modified regular optical fiber as a chemical or environmental sensing element and investigated the probability of integrating them into textile structures [1,2]. The results were encouraging and the development of such sensors integrated into soldiers' uniforms became a reality.

The research was focused on selecting and characterizing available multifunctional materials that are sensitive to different environmental conditions. Two types of materials have been used successfully in the feasibility study to prove the concept of the design and development of the optical fiber sensor. One was segmented polyurethane-diacetylene copolymer (SPU), a thermochromic material, which was synthesized at the University of Akron (AU) [3,4]. The second material was the conducting polyaniline polymer that synthesized at the University of Pennsylvania (U of P) [5,6,7]. The SPU was chosen for temperature measurements application and the polyaniline was chosen for chemical vapor application. Both of these polymers have been

used as the modified sensitive cladding materials for optical fiber sensors systems [8,9,10].

During the fourth year, polyaniline was used as a modified cladding on optical fibers after successfully revealing strong results in a feasibility study providing the concept of the design and development of optical fibers chemical sensors [10]. The polyaniline-modified cladding was used to sense the existence of toxic chemicals vapors such as HCL and ammonia. A methodology was developed for coating the fiber core with polyaniline by using both electronic spinning and in-situ deposition. It was found that for 630nm light source, there is an obvious difference in the light intensity output when exposed between HCL and NH_3 chemical vapors. The change was about 26% and 80% respectively for electronic spinning coated and in-situ deposition coated fibers. Therefore, it was concluded for this case that the sensitivity could be improved by in-situ deposition coating method.

During the fifth year, polypyrrole has been used as a modified cladding to sense chemicals such as hydrazine (reducing agent), hydrogen peroxide (oxidizing agent) & DMMP (dimethyl methylphosphonate). This has been preformed due to the fact that polypyrrole changes its optical properties when switching from oxidized state to a reduced state [10]. The coating was preformed by in-situ deposition and a change of 91% and 28 % in output was reported when the sensor was exposed to hydrazine and hydrogen peroxide respectively, indicating a true responsive optical fiber chemical sensor [11].

For DMMP sensing, in-situ deposition method was used for coating the optical fiber core with two different forms of the polymer, polypyrrole and NDSA doped polypyrrole. In addition, the surface of the fiber's core was also treated before coating to either hydrophilic or hydrophobic and a case study was made to compare the sensitivity of the optical fiber chemical sensor for both cases. The main objective of these experiments was to investigate the response of the optical fiber chemical sensor when exposed to DMMP vapor, using intensity modulation.

The results of these experiments showed a positive response to DMMP vapor. These results varied depending on the surface treatment of the fiber core preformed before, as hydrophilic or hydrophobic, and in-situ deposition time. The sensor components included a light source with a power supply, sensing fiber, photo-detector

and a data acquisition that fed a computerized oscilloscope. To obtain the optimum sensing system, careful in-depth study and research are required to turn the design parameters and required specifications.

I.2. Experimental Work

The experimental work presented in the following has been done in collaboration with Dr. A. G. MacDiarmid and Dr. W. Jones in the University of Pennsylvania. A brief summary of the research and development will be presented in the next five sections. The polymer materials were first processed and characterized to identify the properties of the chemical agent materials. Then the materials were applied to optical fibers, and the morphology and property of sensing components were carefully investigated.

I.2.1. Processing of polymer thin films

Both polyaniline and polypyrrole thin films were formed on the glass slide and silicon wafer substrate by in-situ deposition method. The in-situ deposition method is that the polymer film grows on the substrate during the polymerization of the polymer starting from its monomer solution with oxidant agents. Different deposition times, 7, 10, 20, and 30 minutes, were used for polyaniline films, and 15 and 30 minutes were used for polypyrrole films. To in-situ deposition polyaniline, the solution consists of 2ml of distilled aniline, 1.435g of $(\text{NH}_4)_2\text{S}_2\text{O}_8$ and 200 ml of 1N HCl. To in-situ deposition polypyrrole, the solution consists of 770 mg of pyrrole, 5.0 g of $\text{FeCl}_3 \cdot 6\text{H}_2\text{O}$, 250 ml of 1N HCl, and 200 ml of deionized water.

I.2.2. Characterization of polymer thin films

The films on the glass substrate were used to measure their light absorption in wavelengths from 290 nm to 2600 nm. The refractive indices of the films, which grew on the silicon substrate, were measured by ellipsometry. The morphology of the films was observed by use of a SEM (scanning electron microscope) and an OM (optical microscope). The crystallinity of the films was measured with a X-ray diffractometer.

I.2.3. Processing of fiber optic sensing element

A multimode silica optical fiber with a diameter of 100/140/250 μm in core/cladding/jacket was modified to construct a sensitive region on a small area of the optical fiber. The three step method presented in the previous reports was used. In short, the steps are: (1) removing the jacket, (2) etching the original SiO_2 cladding, and (3) then coating the new sensitive cladding layer. The cladding modification is done on a small section (about 10 mm) of the fiber. In-situ deposition method was used in the recent work to coat polyaniline or polypyrrole on the fiber core.

I.2.4. Characterization of the modified cladding layer

The morphology of the modified cladding layer was observed by SEM (scanning electron microscope), OM (optical microscope), and AFM (atomic force microscope).

I.2.5. Characterization of the fiber optic sensor

After integration of the fiber optic sensing element with light source, photodetector, and other electronic signal processor, the dynamic response of the sensor, when the sensing area was exposed to different vapors, was monitored. The experimental set-up shown in figure1 was used to test the optical fiber response when exposed to different vapours. A further study was carried out on the influence of sensor sensitivity by light excitation condition, which includes the angle, power, and wavelength of the incident light to the optical fiber.

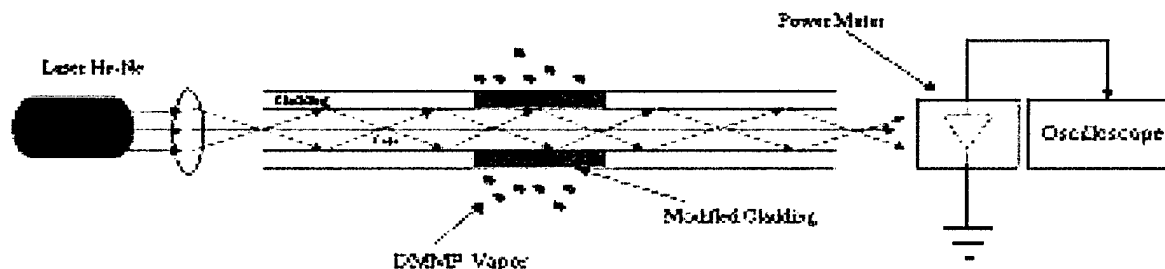


Figure 1. Experimental setup for testing of the optical fiber sensor response.

I.3. Results and Discussion

I.3.1. Optical property of polymer films

For a polyaniline film, the light absorption measurements were done after the film was exposed to HCl and NH₃ vapors, respectively, as shown in Figure 2. The difference of the spectra indicates that HCl and NH₃ vapors induce a different band structure and conformation of the polymer. Therefore, the optical property of the film changes when the film switches from one state (doped by HCl) to another (de-doped by NH₃). The refractive index measurement by ellipsometry shows that the refractive index changed from 2.43 (doped by HCl) to 1.95 (de-doped by NH₃). For a polypyrrole film, the measurements were done before and after the film was exposed to hydrazine (N₂H₄) and hydrogen peroxide (H₂O₂) as shown in Figure 3. The change of the light absorption spectra shows the difference of band structure and conformation of the polymer induced by different chemical vapors. The refractive indices are 1.82 (before exposure to hydrazine) and 1.71 (after exposure to hydrazine).

I.3.2. Morphology of the polymer thin films on both glass slide and optical fiber

The surface morphology of a polyaniline thin film on a glass slide is shown in Figure 4. This film was made by in-situ deposition method. The deposition time is 7 minutes.

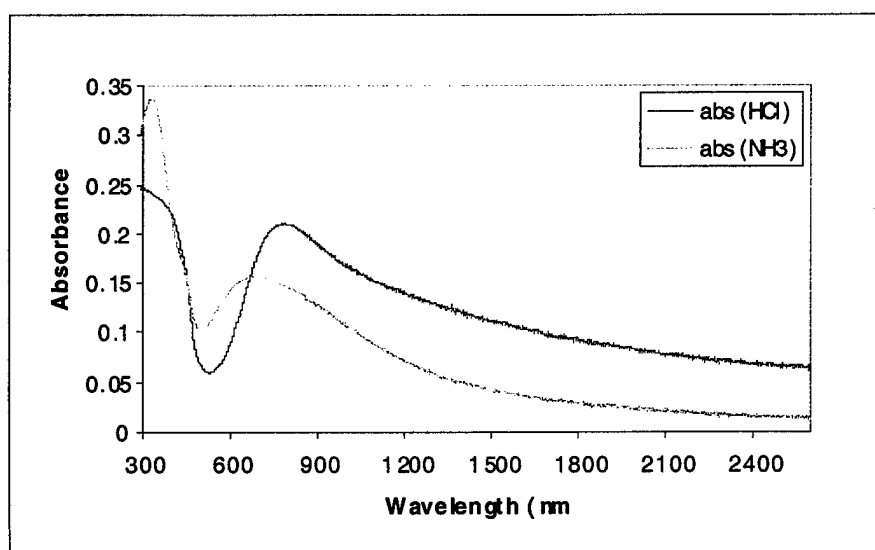


Figure 2. Light absorption spectra of a polyaniline film (deposition time: 7-minute) after exposure to HCl and NH₃ vapors.

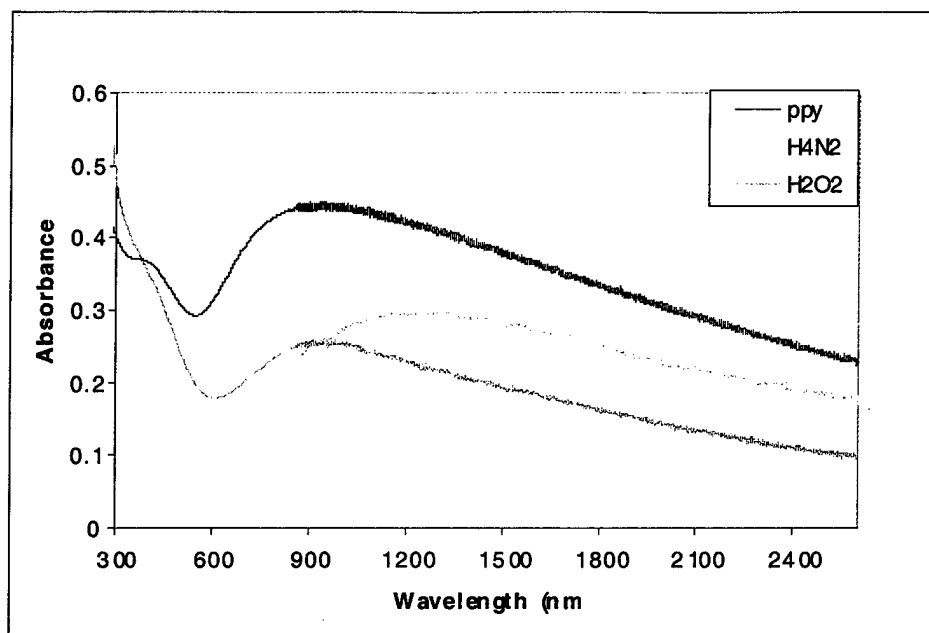


Figure 3. Light absorption spectra of a polypyrrole film (deposition time: 15 mins) before and after exposure to vapors of H_4N_2 (hydrazine) and H_2O_2 (hydrogen peroxide).

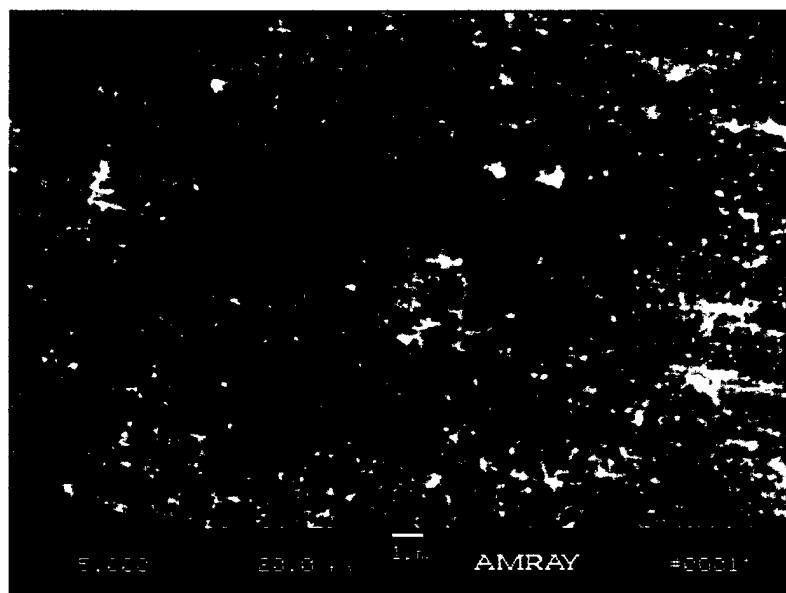


Figure 4. Surface morphology of an in-situ deposited polyaniline thin film.

The following pictures in Figure 5 show the in-situ deposited polyaniline cladding on the optical fiber core. As expected, the polypyrrole cladding layer grew thicker on the fiber during the 30-minute deposition than it did during the 15-minute deposition as shown in Figure 6.

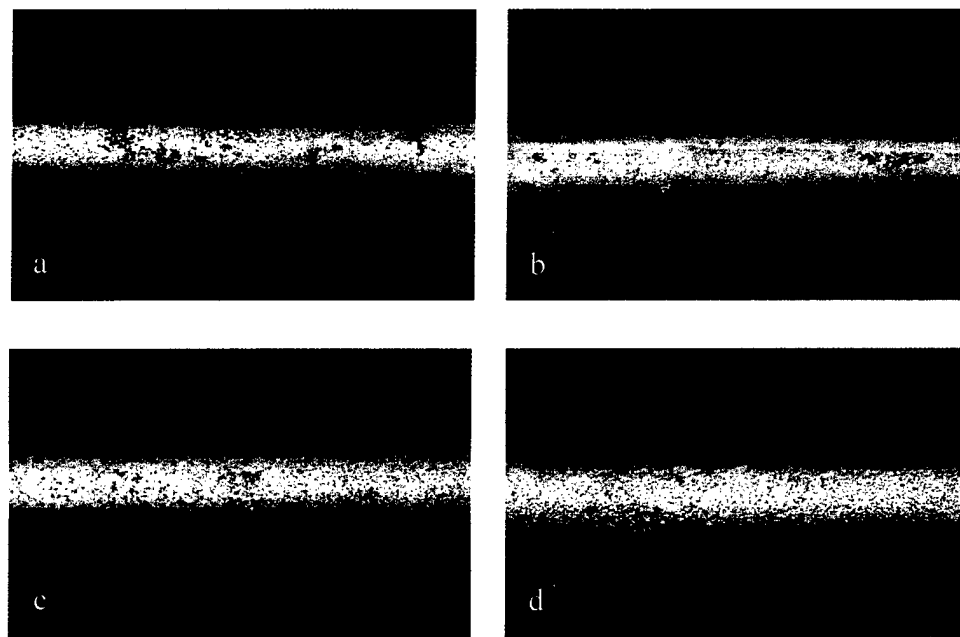


Figure 5. Modified polyaniline cladding layer on the optical fiber by in-situ deposition with different deposition time: (a) 7, (b) 10, (c) 20, and (c) 30 minutes.

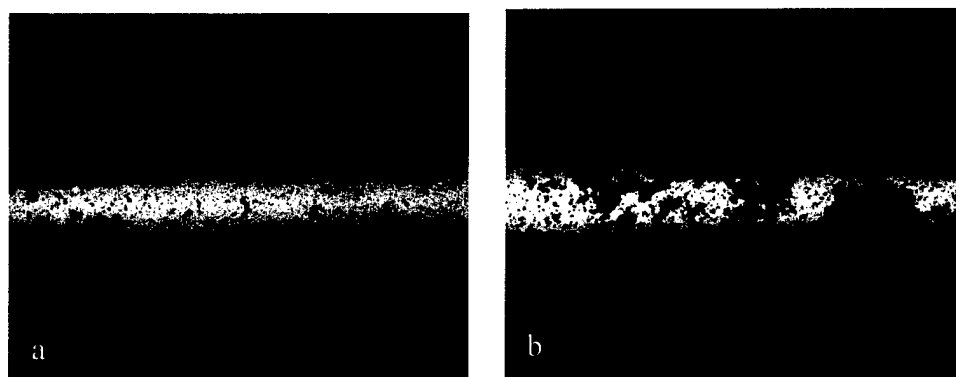


Figure 6. Modified polypyrrole cladding layer on the optical fiber by in-situ deposition with different deposition time: (a) 15 and (b) 30 minutes.

An atomic force microscope was used to show the topography of the polyaniline layer coated on the optical fiber core. The surface roughness is shown in the picture.

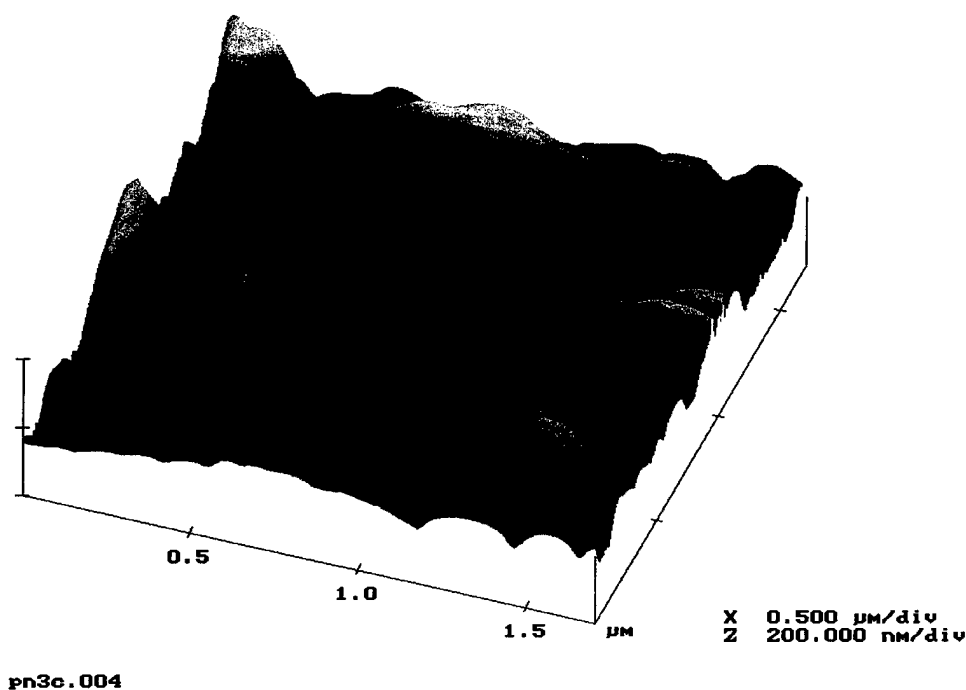


Figure 7. Topography of the polyaniline layer on the optical fiber core.

I.3.3. Optical response of the fiber optic sensors

I.3.3.1 Application of polyaniline

When polyaniline was used as the modified cladding layer, HCl and NH_3 vapors could be detected immediately upon their exposure to the fiber sensing region. It is known that polyaniline can be easily doped by acid (such as HCl) and de-doped by base (such as NH_3). The doping process and de-doping process are reversible. After the polymer is doped, it is stable in the air. It is found that after the de-doping chemical was moved away, the polymer gradually returned to the doped state. The polyaniline was doped after in-situ deposition. When the doped polyaniline is exposed to NH_3 , the polyaniline is de-doped. When the de-doped or partially de-doped polyaniline is exposed to HCl, the polyaniline is doped. The optical property of polyaniline changes from the doped state to the de-doped state, as discussed in section I.3.1. Therefore, when the sensing region of

the optical fiber, which is coated with polyaniline, was exposed to acid vapor (HCl) or base vapor (NH₃), the output intensity of optical signal changed. Figure 8 shows the dynamic change of the sensor when the chemical vapors were exposed to it. The signal response is calculated based on the following equation:

$$\left| \frac{V(\text{air}) - V(\text{chemical})}{V(\text{air})} \right| \quad (1)$$

The response is 50% for NH₃ vapor and 12% for HCl vapor, respectively.

After the NH₃ vapor was moved away for 5 minutes, the polyaniline partially went back to the HCl doped state. This may be the reason for the low response to the HCl vapor. The signal response does not show significant influence by deposition time from 7 to 30 minutes, but the imperfections of the deposited layer (for 10-minute deposition sample in Figure 5) decrease the signal response of the sensor.

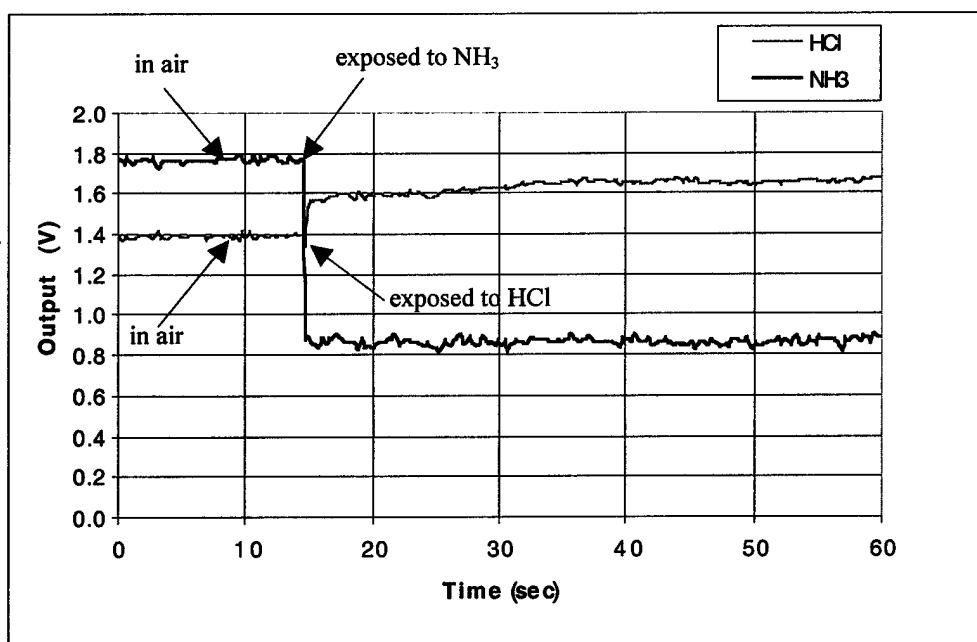


Figure 8. Sensor response to chemical vapors of HCl and NH₃. The sensing fiber was coated with polyaniline using in-situ deposition. The deposition time was 30 minutes.

I.3.3.2 Application of polypyrrole

Polypyrrole was used as the modified cladding layer to detect hydrazine and DMMP vapors. When hydrazine vapor was exposed to the sensing region, the signal response (based on Eq.1) is 91% and 64% for 15 and 30 minute deposited samples, respectively, as shown in Figure 9. The difference of the response may be induced by the thickness, uniformity, and conformation of the polymer layer. After the polypyrrole region was exposed to Hydrazine, it was exposed to hydrogen peroxide vapor and hydrazine vapor again as shown in Figure 10. The output increased by hydrogen peroxide vapor to 23% and decreased by hydrazine vapor to 88%. Each sensor can only be used for a few times, since an irreversible change occurred in polypyrrole after it was exposed to hydrazine.

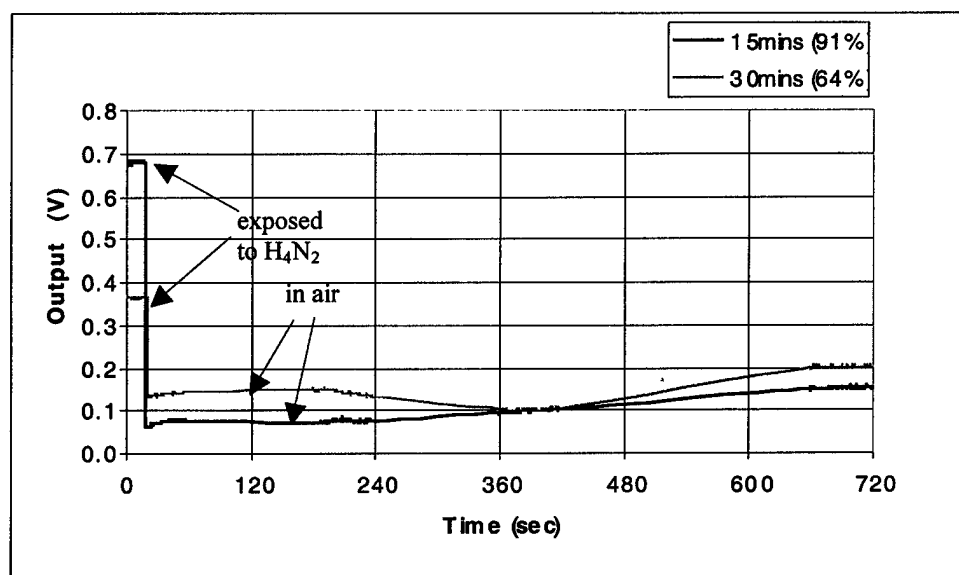


Figure 9. Sensor response to chemical vapor of hydrazine. The sensing fiber was coated polypyrrole by in-situ deposition. The deposition time was 15 and 30 minutes, respectively.

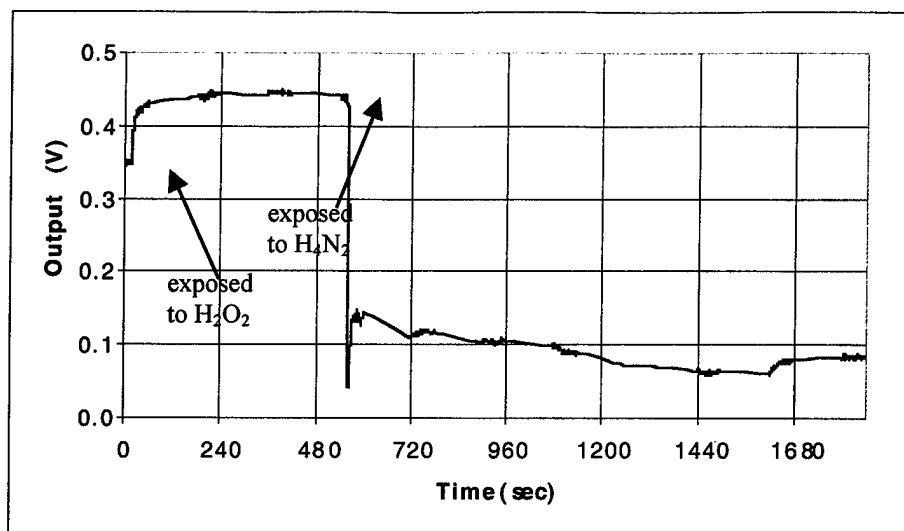


Figure 10. Sensor response to chemical vapors of hydrogen peroxide (H_2O_2) for the second exposure and hydrazine (H_4N_2) for the time exposure an improvement of about 50% in the sensor sensitivity was achieved by using the MPD technique

Based on the results achieved so far, it was clear that polyaniline and polypyrrole can be used as modified cladding to optical fiber sensors. To improve the sensor sensitivity and dynamic range, the MPD technique was applied and tested. Also a short study was conducted on the influence of the light source energy and wavelength on the sensor sensitivity. Therefore, the light excitation condition, which includes incident power, wavelength, and angle, to the optical fiber, was studied preliminarily. A sample was prepared by in-situ deposition with a 15 minute deposition time and tested. The results on the application of the MPD technique were reported in the 4th year ARO report [2] and presented in detail in the Ph.D thesis of J.Yuan[10]. An improvement of about 50% in the sensor sensitivity was achieved by using the MPD technique. For the impact of the light source power it was found that the high power of the incident light to the sensing optical fiber decreases the optical response of the sensor. The percentage change of the output power, between the sensor exposure to HCl and NH_3 vapors, is calculated according to:

$$\left| \frac{P(HCl) - P(NH_3)}{P(HCl)} \right| \quad (2)$$

As shown in Figure 11, when the incident power at wavelength of 770 nm is larger than 10 mW, the percentage change of the power starts to decrease quickly. At a certain high level, the sensor do not work as usual. As an example, when 100 mW power at wavelength of 922 nm was incident to the fiber for a very short time, HCl and NH₃ vapors can not induce the change of the output signal as before. However, when the sensor was tested on the second day, it was found that the sensor was performing in a normal way. This means that the polymer required a certain time to recover after it was exposed to a high power. It was also found that the sensor returned to the same level of sensitivity after the sensing region was doped and de-doped by HCl and NH₃ vapors for several times.

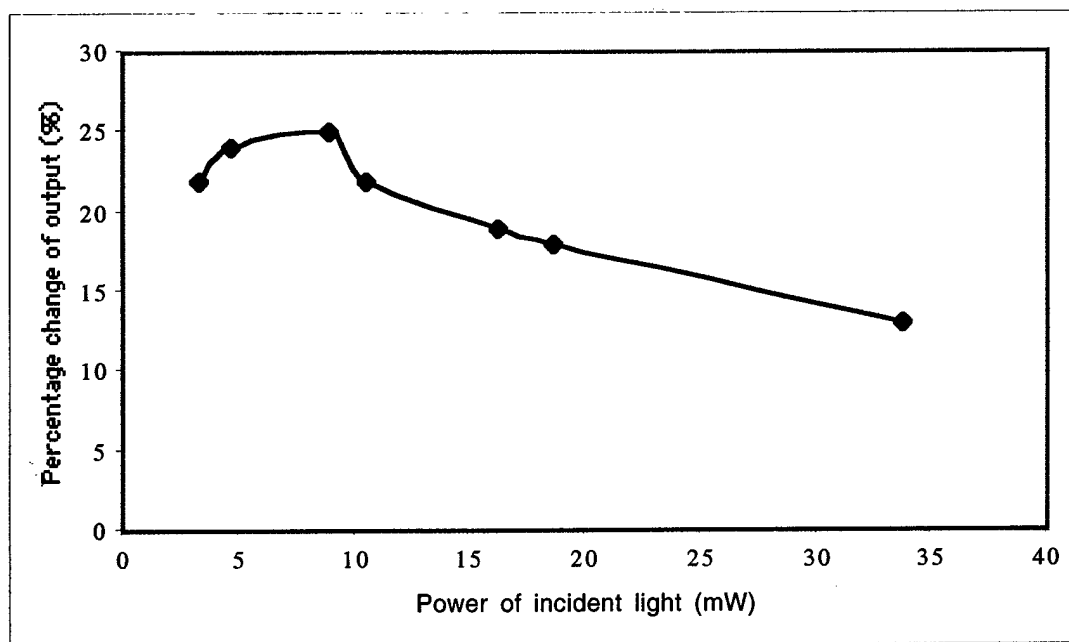


Figure 11. Influence of the incident power on the percentage change of the output power between the sensor exposure to HCl and NH₃ vapors.

The wavelength dependence of the sensor response was reported before. Recently, a tuned laser light source was used in the wavelength range of 768nm to 922 for more investigation. It shows that when the sensing region was exposed to HCl and NH₃ vapors, the sensor response range is from 29% to 19% at wavelength of 860 nm and 800 nm, respectively. Therefore, based on the short study performed, it was clear that the PMD technique can improve the sensor sensitivity, and the incident light power should not

exceed a certain limit. Also the light wavelength has a direct impact on the sensor sensitivity and would be carefully selected.

I.3.3.2 Detection of DMMP

The modified Optical fibers coated with the chemically active polypyrrole, were integrated with a light source (He-Ne laser wavelength 633nm) and a photodetector as shown in figure1. The sensing element was exposed to DMMP (dimethylmethylphosphonate) vapor, which is a mimic to the nerve gas for about 2 minutes. The output intensity was recorded by a power meter, which is connected to an oscilloscope for recording the real time measurement.

Figures12-15 show the waveforms of the test, which show the change in output intensity as the sensing element is exposed to DMMP. The change in output intensity for the optical fibers with no surface treatment is shown in Figures 12 & 13. There is no difference in processing of these two samples. It is seen from the waveforms that there is a step change with a response time of 2 to 4 seconds. The change in the response times can be attributed to the nature of the structure of the film and its porosity. A higher porosity indicates a higher surface area for the reaction with DMMP and hence a faster response. This nature of polypyrrole is shown by the SEM micrograph in Figure 16, the test result on this particular sample is shown in Figure 12.

The output intensity change for the hydrophobic and hydrophilic surface treatment of the optical fibers is shown in Figures 14 & 15 respectively. For the hydrophobic surfaces, it is seen from the waveforms that the change in intensity is gradual instead of a step change as seen in the case of no surface treatment, also the response time is about 7 seconds, which is several seconds higher than the as prepared fibers. For the hydrophilic surfaces no change was observed in the output intensity as seen from the waveform Figure 15.

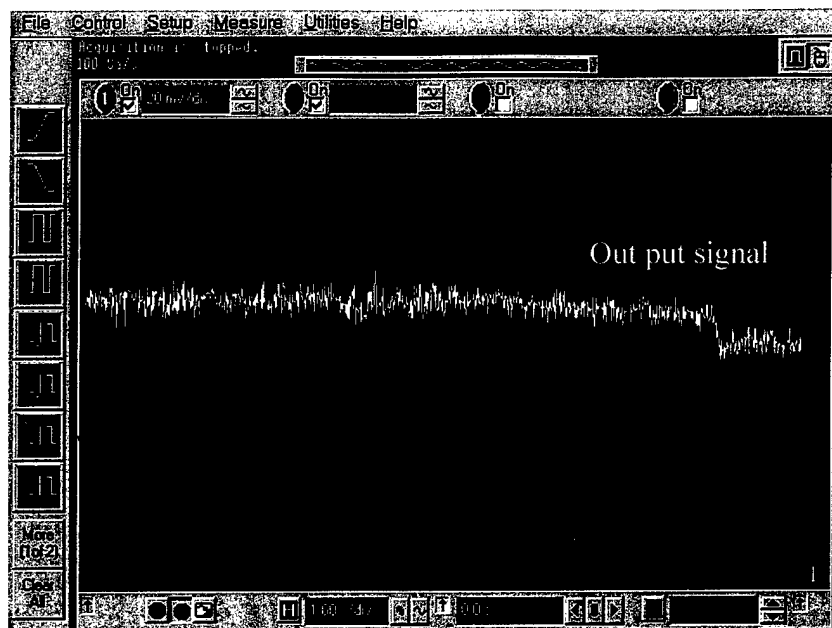


Figure12. Output intensity change for the as-etched fiber with polypyrrole coating

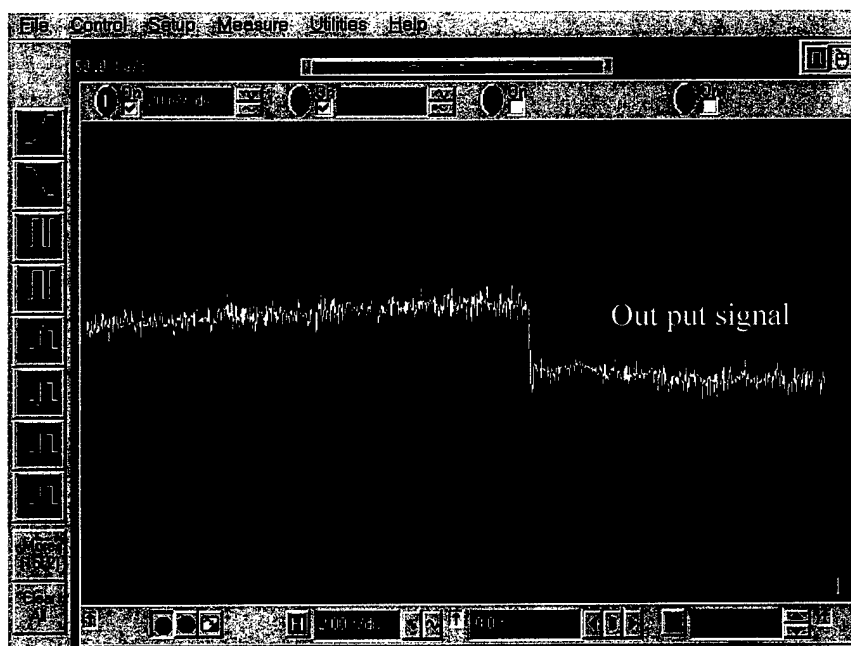


Figure13. Output intensity change for the as-etched fiber with polypyrrole coating, sensor.

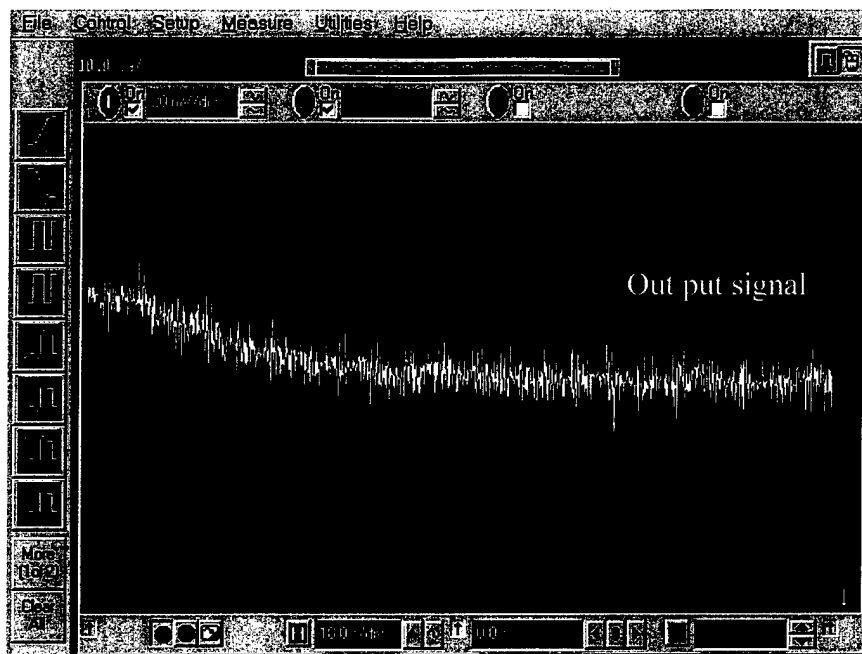


Figure14. Output intensity change for the hydrophobic fiber with polypyrrole coating, sensor.

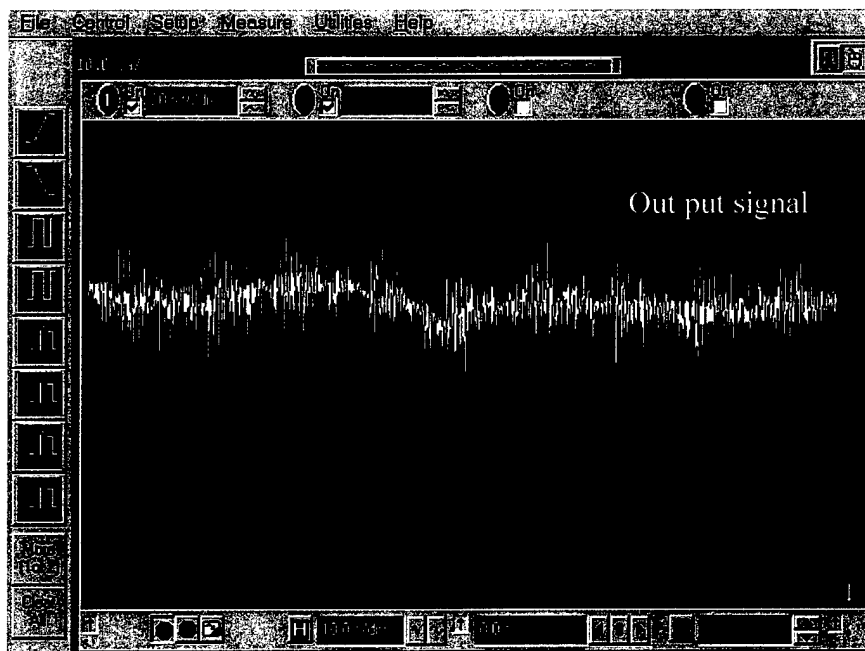


Figure15. Output intensity change for the hydrophilic fiber with polypyrrole coating, sensor.

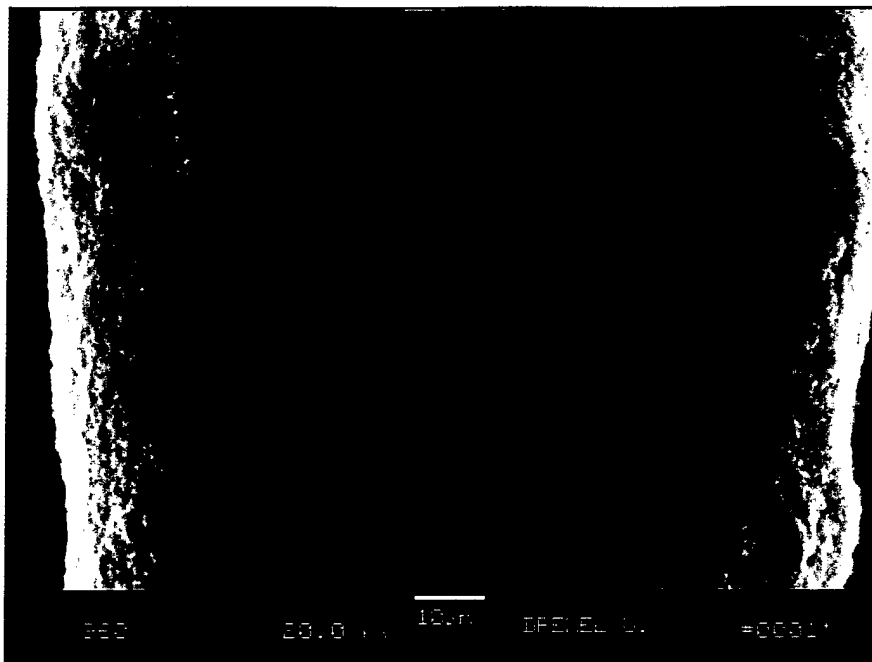


Figure16. SEM micrograph showing the porosity of the polypyrrole structure deposited on the etched section of the optical fiber for 6 minutes.

I.3.3.3 Detection of DMMP with doped Polypyrrole

In order to enhance the detection of DMMP vapor, the modified cladding material, polypyrrole, was doped with Napthalene disulphonic acid (NDSA). It is reported that there is a change in the resistance of polypyrrole thin films doped with NDSA when exposed to DMMP vapor [7]. When the doped polypyrrole thin film was exposed to 28ppm DMMP in dry air there was a drop in the resistance of the thin film as shown in Figure17 [7]. The resistance of the thin film increased after the DMMP vapor was no longer present as seen in the Figure17. It has also been reported that the DMMP interacts electronically with the polypyrrole to increase the amount of free mobile hole charge carriers, which leads to the reported change in resistance [7].

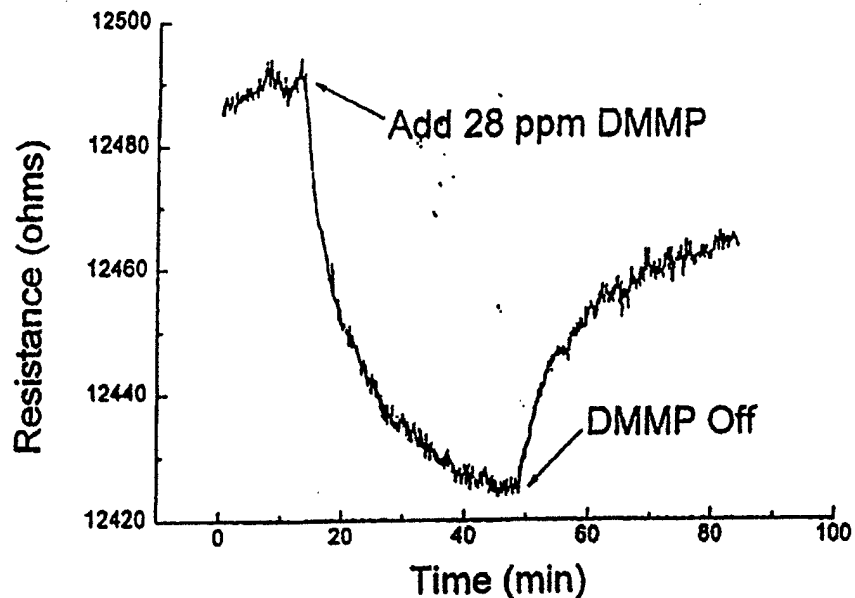


Figure17. Change in the resistance of the NDSA doped polypyrrole thin film exposed to 28ppm of DMMP in dry air [7].

In this experiment, the in-situ deposition of the polypyrrole was used as explained before, the only difference is that 0.1gms of NDSA was added instead of 0.1ml of 1M HCl. In this way polypyrrole was doped at the polymerization stage. The coated optical fiber was connected with a light source and photodetector. The sensor response is shown in Figures 18 & 19.

As compared to the undoped polypyrrole response Figures 12-15, the response obtained for the NDSA doped polypyrrole is 4 to 5 times higher and almost instant as shown in Figure 18. A change of about 80mV was recorded, and for the second exposure a change of about 45mV was recorded. It can be seen from the waveforms that the sensor developed here is reversible, i.e., the power level rises back as soon as the DMMP vapor is removed.

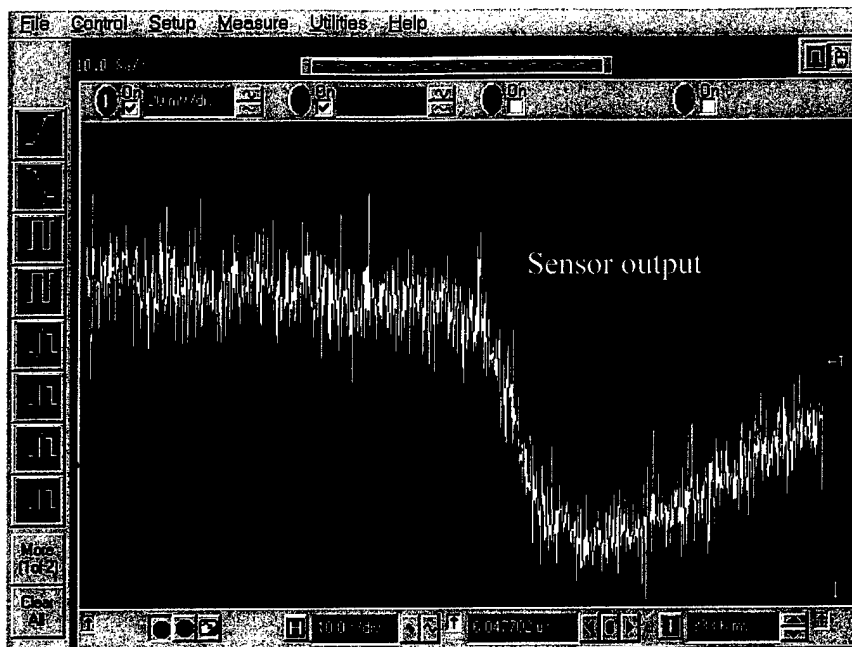


Figure18. Output intensity change for the doped polypyrrole, first cycle.

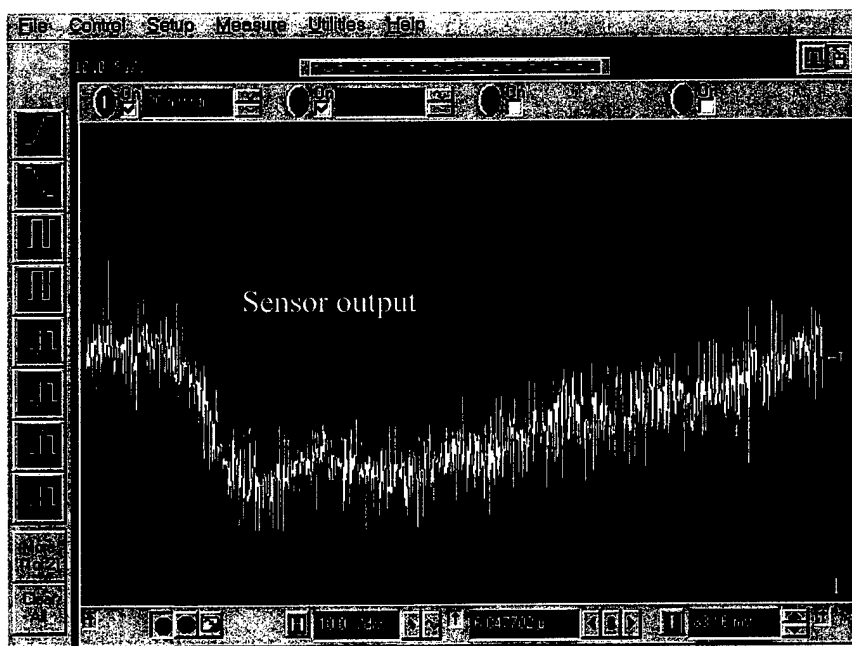


Figure19. Output intensity change for the doped polypyrrole, second cycle.

I.4. Conclusion on the development of a biological sensor

The feasibility study has been successfully completed. The results achieved so far prove that the developed methodology can be applied for the detection of the biological threats in the battlefield. Both polypyrrole and polyaniline were successfully coated on the optical fiber core by in-situ deposition method. For the best response of the fiber optic sensors, the modification process for the cladding must satisfy to get a thin, uniform, non-imperfection cladding layer. The most important criterion to choose the modified cladding material is the change in its optical property by the detected chemical vapor.

A sharp response is achieved for both polyaniline and polypyrrole coated optical fiber sensors to detect chemical vapors of ammonia, hydrogen chloride, and hydrazine. The response time is less than 0.2 seconds, when exposed to DMMP, with a sensor response of 2 to 4 seconds was obtained. For the hydrophobic surfaces a gradual decrease in intensity was recorded when exposed to DMMP, with a response time range from 1 to 7 seconds. The doping of the polypyrrole with NDSA enhanced the sensitivity for DMMP detection, as shown in Figures 18 & 19. As seen from the waveforms, not only the level of the response is much higher but also the process is reversible.

Part II: Sol-Gel Optical Fibers for Chemical Sensor Applications

II.1. Summary

Research conducted on this ARO-MURI project has resulted in the development of several chemical and temperature sensors. These sensors are based on using polymers as a medium for optical signal modulation. These polymers are combined with optical fibers for sensor application. Claddings derived from Sol-Gel processes can be used as substrates for these optically sensitive polymers. During the processing of the silica cladding, the Sol is simply doped with the polymer of choice. Sol-Gel processed silica is also known to be reasonably porous. The pore structure of the claddings can then be tailored using template materials that can be removed with solvent extraction techniques. The porosity in the sol-gel processed silica may lead to increased sensitivity and may also reduce the response time of the sensor. The research conducted in processing sol-gel optical fibers, and on the successful application of these fibers as a chemical sensor is recorded in detail in Mr Ken Richards M.S thesis[12]. The experimental work and results achieved are briefly presented in the next section.

II.2. Experimental Procedure

II.2.1. Fiber preparation.

Several all-silica, step-index 100/125 μm core/clad optical fibers were prepared for coating. The jacket was mechanically stripped, while acetone was used to remove the buffer layer. Next, the surface of the cladding was cleaned with ethanol. To remove the cladding material, a 25% by volume HF acid and distilled water solution was prepared. The fibers were mounted in a well filled with the etching solution and 12.5 μms of silica was removed in approximately 12 minutes. The etched region of the fiber is about 2 cm in length. After etching, all fibers were cleaned in a 25% by volume nitric acid solution at 80°C for two hours and then dried.

II.2.2. Sol preparation, fiber coating, and drying

Several sols were prepared using TMOS and methanol for dilutions. The base sol consisted of TMOS and an additional 10% of phenyl modified TMOS. Separately, a 1% by weight solution of polyaniline in N-methyl-2-pyrrolidone (NMP) was prepared. Next, the base sol was converted into three solutions containing 10, 20, and 30 drops of the polyaniline (panni) solution. After all of the fibers had been cleaned, each was simply dipped into its respective sol solution for approximately 30 seconds. These fibers were placed in cylindrical drying containers and then each container was sealed. All of the fibers were coated and then dried for a minimum of two weeks at room temperature and at a pressure of approximately one atmosphere.

II.2.3. Sensor preparation

Each respective sensor was prepared by mounting the sensing region onto a plastic frame for protection. The end faces of the fibers were prepared by mechanically stripping the jacket material and using acetone to remove the buffer layer. Next, the fibers were carefully cleaned with ethanol and lens paper. The fiber ends were cleaved with an ultrasonic fiber cleaver.

II.2.4. Sensor application

A fiber optic detection system was constructed to demodulate and determine the response time of the sensor and can be seen in Figure 20. The light source is a 4 mW He-Ne Laser operating at 630 nm. To determine the intensity of the sensor output, a simple photodetector was used. A power meter amplifies the photodetector signal and the output of the meter was connected to an oscilloscope. To characterize the response time of the signal, a trigger system was integrated into the oscilloscope system. The trigger consisted of a LED and photodetector that triggered data acquisition when the sensor was exposed to a chemical vapor. When the container that holds the vapor was placed under the sensor, the light beam was broken and the oscilloscope began to collect data. Data was then recorded for the duration of the sensing event. Finally, all data was saved and Microsoft Excel was used to plot and interpret it.

II.3. Results

II.3.1. Sol-Gel silica coating

The scanning electron microscope has been used to evaluate the surface features of all of the coatings applied to optical fibers. Previously, coating thickness ranged from 500 nm to approximately 1000 nm as seen in Figure 21. Since the surface of the core has been treated with a nitric acid bath, all coatings appear to be adhering well. A sample of some of the coatings produced can be seen in Figure 21.

As seen in Figure 21, the coating thickness is approximately 500 nm appears to be continuous, but there are small areas of contamination present. These coatings have not been doped with polyaniline. Images of the doped cladding can be seen in Figure 22. This cladding is continuous, and little or no contamination could be found. The cladding is also about 2.5 μm thick.

The doped claddings that have been produced seem to be more robust than those reported earlier. These claddings are thicker, have better coverage, and seem to be affected less by contamination. One possible explanation for the increased thickness of the cladding is the increased viscosity of the sol solution after the addition of the polyaniline solution. This increase in viscosity may also reduce the effect of contamination on the coating process.

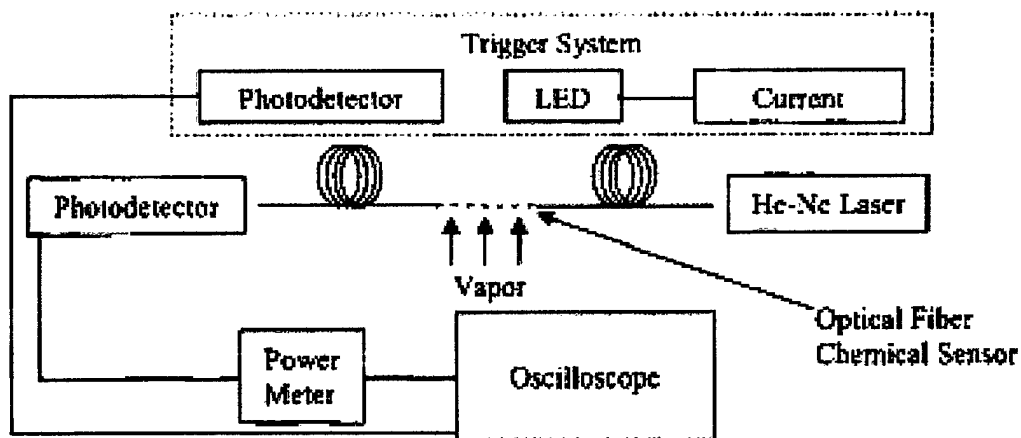


Figure 20 Schematic of signal detection and data acquisition system used to characterize the fiber optic chemical sensor

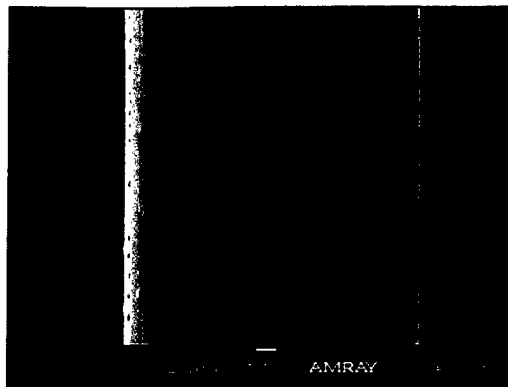
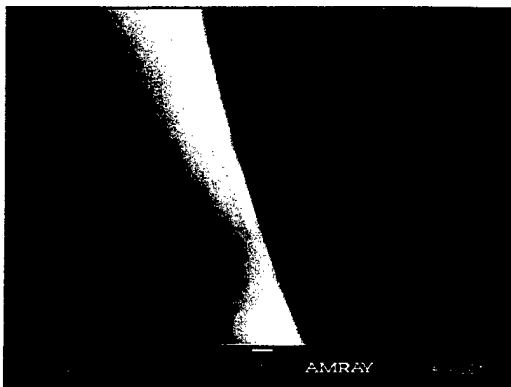


Figure 21. The photo on the left was taken at 5000x with the Scanning Electron Microscope. In this image a cladding of approximately 500nm is shown. The photo on the right is an image of the surface of the cladding taken at 500x. The dark regions are contaminated areas where the cladding did not adhere properly. In both images, the cladding material is not doped with polyaniline.

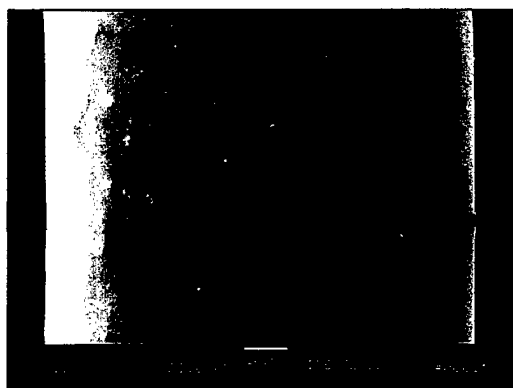


Figure 22. The photo on the left was taken at 1000x with the Scanning Electron Microscope. The cladding material appears to be continuous and there are few surface irregularities. The photo on the right is an image of the cladding taken at 5000x. In both images, the cladding material is doped with polyaniline.

II.3.2. Sensor Response

Several sensors have been tested and some of the data gathered can be seen in Figures 23. When the sensor was exposed to hydrochloric acid, a 15% decrease in total intensity was observed. The response time of the sensor when exposed to the acid appears to be a little more than a second. In Figure 24, the same sensor experienced about a 30% change in total intensity when exposed to ammonium hydroxide. The response time of this reaction

was also about one second. This sensor also has a polyaniline concentration of approximately 0.2% by weight (this assumes that all of the solvent has evaporated). The thickness of the cladding is also about 2.5 μm .

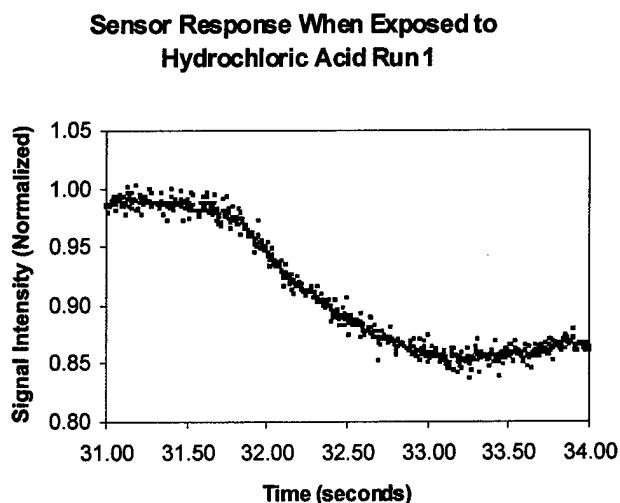


Figure 23. The plot above represents the intensity response when the optical fiber chemical sensor is exposed to ammonium hydroxide. This sensor has approximately 0.2% by weight of polyaniline in the cladding. The magnitude of the response is less than 15% over a 1 second duration.

Another set of fibers was coated with about 0.1% by weight of polyaniline in the cladding. The response of the sensor can be seen in Figure 25. These response measurements were recorded with a trigger system in place. The trigger helps in recording the actual time the sensor was exposed to the chemical vapors. This will help better approximate the response time of the sensor. Figure 25 shows a decrease in normalized intensity that is less than 20% when the sensor is exposed to hydrochloric acid. The duration of the intensity change is about 1 second.

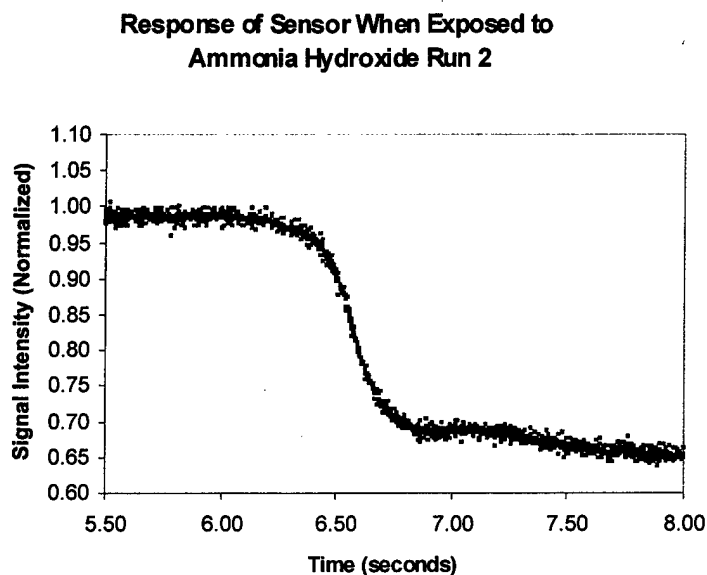


Figure 24. The plot above represents the intensity response when the optical fiber chemical sensor is exposed to ammonium hydroxide. This sensor has approximately 0.2% by weight of polyaniline in the cladding. The magnitude of the response is about 30% over a 1 second duration.

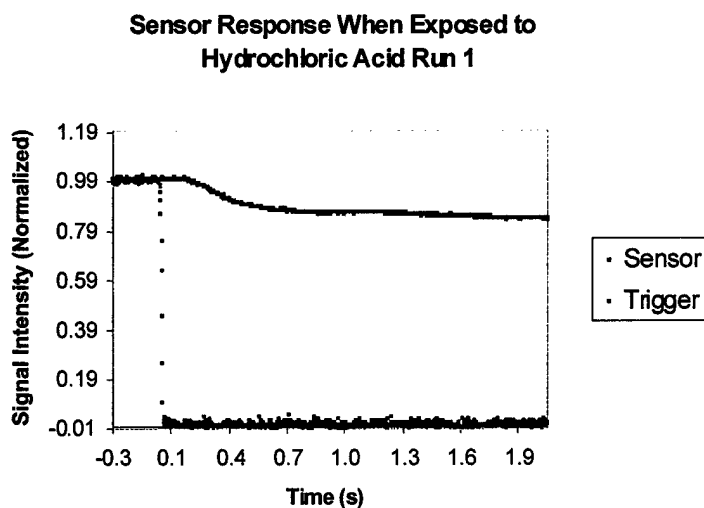


Figure 25. The plot above represents the intensity response when the optical fiber chemical sensor is exposed to ammonium hydroxide. This sensor has approximately 0.1% by weight of polyaniline in the cladding. The magnitude of the response is less than 20% over a 2 second duration.

Sensor Response When Exposed to Ammonium Hydroxide Run 2

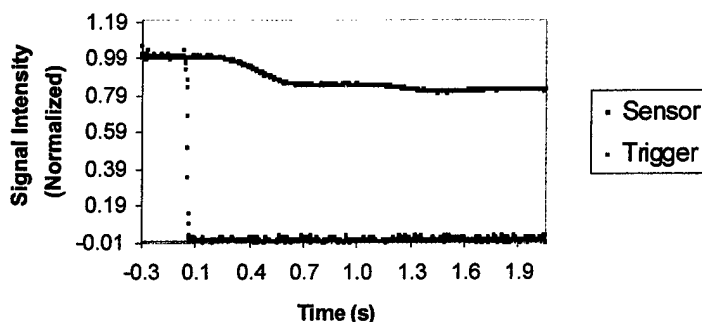


Figure 26. The plot above represents the intensity response when the optical fiber chemical sensor is exposed to ammonium hydroxide. This sensor has approximately 0.1% by weight of polyaniline in the cladding. The magnitude of the response is less than 20% over a 2 second duration.

Figure 26 shows the response of the same sensor when it has been exposed to ammonium hydroxide. Again, the decrease in normalized intensity is less than 20% over a period of about one second. Also, the thickness of the cladding of this sensor is about 3 μm .

From the past four figures we can surmise that response of the sensor can be controlled by the concentration of polyaniline in the cladding. The sensor response will also be affected by the thickness of the cladding.

II.4. Conclusions on Sol-Gel Optical Fiber Sensors.

Several sensors have been successfully developed that incorporate polyaniline into a Sol-Gel processed cladding. This doped cladding appears to adhere well to the core of the optical fiber, and response curves have shown changes of up to 30% in total intensity. Even though the response of these sensors appears to be simple, the behavior of this materials system is still not fully understood. Many more sensors, however, have been characterized in an attempt to explain the above-mentioned phenomena. The study of the dependence of sensor response as a function of dopant concentration and cladding thickness is presented in detail in Mr. Ken Richards MS thesis [12].

Part III: Modal Power Distribution Analysis for Sensors Applications

III.1. Objective

The objective of this research is to develop inexpensive and relatively simple fiber optic sensors with multimode fibers. Modal power distribution in multimode optical fibers is proposed for various sensors applications. This research comprises two major parts. The first part involves theoretical analysis and modeling of excitation, modal power distribution and far-field radiation. The second part involves the experimental verification of the developed model.

III.2. Introduction

Fiber optic sensors have been studied and developed extensively. The existing technologies include intensity modulation, phase modulation, polarization modulation and frequency modulation (fiber Bragg gratings: FBG). The phase modulation technique is the most sensitive method among these. The next most sensitive technique is polarization modulation. In general both techniques require complicated and expensive system equipment. Sensors of these types are suitable for applications that require high sensitivity but do not have size constraints on the actual sensor.

Fiber Bragg grating sensors are very sensitive, but they are also usually complicated and expensive. Similar to phase modulation and polarization modulation techniques, FBGs are also used for various sensing applications that require high precision measurements. Simple and inexpensive sensors can be built by using intensity modulation technique. However, total intensity modulation is not very sensitive. Thus there is a need for another technique that could lead to the development of sensors with a reasonable level of sensitivity, which are also inexpensive and compact.

Modal Power Distribution (MPD) in multimode fibers is a reasonably sensitive and inexpensive sensing method that has many applications. MPD is based on modal

coupling and modal power redistribution among the guided and leaky orthogonal modes in a multimode fiber. Light distribution in multimode fibers is analyzed and characterized by using geometric and wave optic methods. When fiber parameters (refractive index, core diameter, etc.) are modified by ambient effects, the light distribution among the orthogonal modes will change. Optical power redistribution can be analyzed and correlated with the perturbation by scanning the far field pattern of the fiber. This technique is thus proposed as a simple and inexpensive method for sensors applications.

III.3. Theoretical Analysis

III.3.1. Light distribution in multimode fibers

The general solution of a wave equation inside an optical fiber clad dielectric waveguide is accomplished through the separation of variables method. With the assumption of cylindrical symmetry and homogeneous material properties, the Helmholtz equation is solved, and the result is ordinary and modified Bessel functions as transverse field distributions. Through the application of boundary conditions at the core-cladding boundary, eigenvalue equations are found. Mode solutions present guided orthogonal modes that can propagate down the fiber. [13]

III.3.2. Formulation of problem

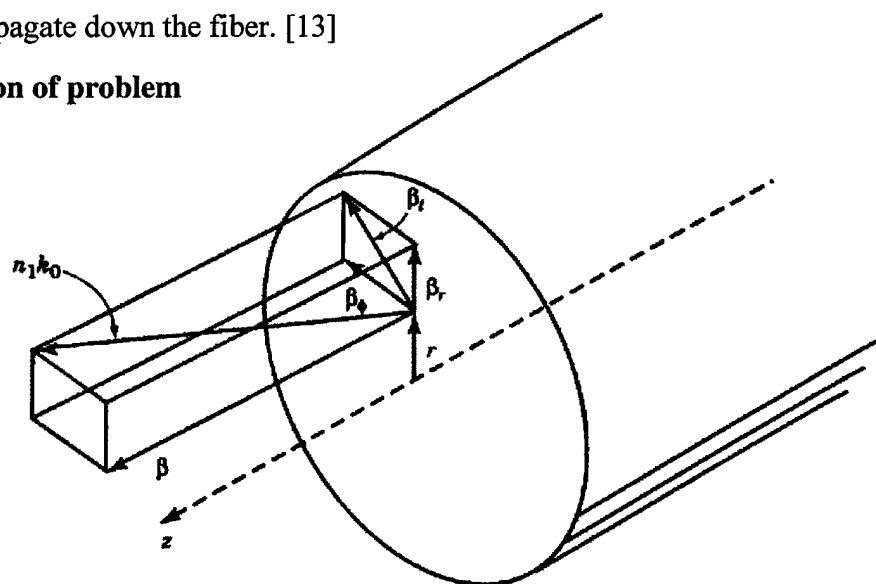


Figure 27. Components of wave-number β corresponding to a particular mode in a general skew ray [13].

Electric and magnetic field components can be written as follows, if we assume harmonic solutions with optical frequency ω and if we use complex phasor notation

$$\begin{aligned} E &= E_0(r, \phi) \exp(-j\beta z) \\ H &= H_0(r, \phi) \exp(-j\beta z) \end{aligned}$$

where E_0 and H_0 are electrical and magnetic field vectors with transverse dependence and the field is assumed to travel along the direction z with a propagation constant β . The Helmholtz equation is written for the core and the cladding regions for the z -component of the fields as:

$$\begin{aligned} \nabla_t^2 E_{z1} + (n_{core}^2 k_0^2 - \beta^2) E_{z1} &= 0 & r \leq a \\ \nabla_t^2 E_{z2} + (n_{clad}^2 k_0^2 - \beta^2) E_{z2} &= 0 & r \geq a \end{aligned}$$

E_{z1} and E_{z2} are the z -components of electric field inside the core and the cladding regions respectively and k_0 is the free-space wave-number.

After the transverse wave-number in core and cladding regions is defined as

$$\beta_{t1}^2 = (n_{core}^2 k_0^2 - \beta^2) \quad \beta_{t2}^2 = (n_{clad}^2 k_0^2 - \beta^2)$$

The Helmholtz equation for the z -component becomes

$$\frac{\partial^2 E_z}{\partial r^2} + \frac{1}{r} \frac{\partial E_z}{\partial r} + \frac{1}{r^2} \frac{\partial^2 E_z}{\partial \phi^2} + \beta_t^2 = 0$$

The following solution is suggested by using the separation of variables method.

$$E_z = \sum_i R_i(r) \phi_i(\varphi) \exp(-j\beta_i z)$$

E_z is a summation over all orthogonal mode solutions.

After taking derivatives with respect to r and ϕ , the following equation is found

$$\frac{r^2}{R} \frac{d^2 R}{dr^2} + \frac{r}{R} \frac{dR}{dr} + r^2 \beta_i^2 = -\frac{1}{\phi} \frac{d^2 \phi}{d\varphi^2}$$

It is reduced to the following form by further separating r and ϕ components

$$\frac{d^2 \phi}{d\varphi^2} + q^2 \phi = 0 \quad \frac{d^2 R}{dr^2} + \frac{1}{r} \frac{dR}{dr} + (\beta_i^2 - \frac{q^2}{r^2}) R = 0$$

Finally, the solution to this differential equation appears in this form

$$\phi(\varphi) = \begin{cases} \cos(q\varphi + \alpha) \\ \sin(q\varphi + \alpha) \end{cases} \quad R(r) = \begin{cases} AJ_q(\beta_i r) + A'N_q(\beta_i r) & \beta_i \text{ real} \\ CK_q(|\beta_i| r) + C'I_q(|\beta_i| r) & \beta_i \text{ imaginary} \end{cases}$$

Determining whether to use sine or cosine is a matter of choosing a particular orientation for the field, since there is a cylindrical symmetry. Therefore, α does not affect the solution; it only represents the rotation of the symmetry axis.

The z-component of the magnetic field, H_z is solved in the same manner. The two field solutions are given below:

$$E_z = \begin{cases} AJ_q(ur/a)\sin(q\phi)\exp(-j\beta z) & r \leq a \\ CK_q(wr/a)\sin(q\phi)\exp(-j\beta z) & r \geq a \end{cases}$$

$$H_z = \begin{cases} BJ_q(ur/a)\cos(q\phi)\exp(-j\beta z) & r \leq a \\ DK_q(wr/a)\cos(q\phi)\exp(-j\beta z) & r \geq a \end{cases}$$

III.3.3. Fiber Parameters

Fiber structural parameters, which are essential in terms of sensors applications are given below:

V-number: $V^2 = u^2 + w^2 = a^2 k_0^2 (n_{core}^2 - n_{clad}^2) = a^2 2\pi / \lambda^2 (n_{core}^2 - n_{clad}^2)$

Normalized propagation constant: $u = a \sqrt{n_{core}^2 k_0^2 - \beta^2}$

Normalized attenuation constant: $w = a \sqrt{\beta^2 - n_{clad}^2 k_0^2}$

Propagation constant: $\beta = \sqrt{n_{core}^2 \left(\frac{2\pi}{\lambda_0}\right)^2 - \left(\frac{u}{a}\right)^2}$

With the assumption of infinite cladding, the core radius, index of refraction in the core and the cladding and optical frequency are important fiber parameters that can be

controlled or perturbed to create a correlation between applied perturbations and output ring pattern. Using weakly guiding assumption and boundary conditions, eigenvalue equations are formed to find propagation constants (β) of modes.

III.3.4. Eigenvalue Equation for Step-index Fibers

The general form of the eigenvalue equation is given below:

$$\left(\frac{J'_q(u)}{uJ_q(u)} + \frac{K'_q(w)}{wK_q(w)} \right) \left(\frac{n_{core}^2}{n_{clad}^2} \frac{J'_q(u)}{uJ_q(u)} + \frac{K'_q(w)}{wK_q(w)} \right) = q^2 \left(\frac{1}{u^2} + \frac{1}{w^2} \right) \left(\frac{n_{core}^2}{n_{clad}^2} \frac{1}{u^2} + \frac{1}{w^2} \right)$$

Above equation is reduced to the following simpler form by using weakly guidance approximation: $n_{core} \approx n_{clad}$

$$\frac{J'_q(u)}{uJ_q(u)} + \frac{K'_q(w)}{wK_q(w)} = \pm \left(\frac{1}{u^2} + \frac{1}{w^2} \right)$$

The *TE* and *TM* mode solutions exist in optical fibers,. Moreover, hybrid modes which are named as *EH* and *HE* modes exist as well. Degenerate modes with same propagation constant can be added together fieldwise among these four types of mode solutions. The resulting field distribution is linearly polarized and designated as *LP_{lm}*.

Eigenvalue equations for *TE_{0m}*, *TM_{0m}*, *HE_{qm}*, *EH_{qm}* and *LP_{lm}* modes:

$$TE_{0m}, TM_{0m}: \quad u \frac{J_0(u)}{J_1(u)} = -w \frac{K_0(w)}{K_1(w)}$$

$$HE_{qm}: \quad u \frac{J_q(u)}{J_{q-1}(u)} = w \frac{K_q(w)}{K_{q-1}(w)}$$

$$EH_{qm}: \quad u \frac{J_q(u)}{J_{q+1}(u)} = -w \frac{K_q(w)}{K_{q+1}(w)}$$

$$LP_{lm}: \quad u \frac{J_{l-1}(u)}{J_l(u)} = -w \frac{K_{l-1}(w)}{K_l(w)}$$

A computer program has been developed to solve the eigenvalue equations numerically for linearly polarized modes. Field solutions can be found up to a constant for x-polarized or y-polarized electric field.

III.3.5. Weakly Guiding Fibers and *LP* Modes

For the weakly guiding fibers, the combination of *TE*, *TM*, *HE* and *EH* modes forms degenerate *LP* modes. Solving the last equation above for normalized propagation constant u , normalized propagation constant β can be calculated for every LP_{lm} mode. Given the assumption that electric field is linearly polarized, an *x-polarized* or *y-*

polarized field can be assumed. The transverse intensity distribution of the field inside and outside of the fiber for propagating modes can be calculated.

For an x-polarized electric field, field distribution will be as follows:

LP_{0m}

$$E_{LP_{0m}} = E_0 J_0\left(\frac{ur}{a}\right) \quad r \leq a$$

$$E_{LP_{0m}} = E_0 \frac{J_0(u)}{K_0(w)} K_0\left(\frac{wr}{a}\right) \quad r \geq a$$

LP_{1m}

$$E_{LP_{1m}} = 2E_0 J_1\left(\frac{ur}{a}\right) \sin \phi \quad r \leq a$$

$$E_{LP_{1m}} = 2E_0 \frac{J_1(u)}{K_1(w)} K_1\left(\frac{wr}{a}\right) \sin \phi \quad r \geq a$$

LP_{lm}

$$E_{LP_{lm}} = 2E_0 J_l\left(\frac{ur}{a}\right) \sin(l\phi) \quad r \leq a$$

$$E_{LP_{lm}} = 2E_0 \frac{J_l(u)}{K_l(w)} K_l\left(\frac{wr}{a}\right) \sin(l\phi) \quad r \geq a$$

where E_0 is the magnitude of the field given by $j\beta Aa/u$. Here, A is the unknown constant coming from excitation conditions. Therefore, we can interpret E_0 as a constant of magnitude for the electric field.

Intensity distribution is calculated as the following:

$$I_{lm} = I_0 J_l^2\left(\frac{ur}{a}\right) \sin^2(l\phi) \quad r \leq a$$

$$I_{lm} = I_0 \left(\frac{J_l(u)}{K_l(w)} \right)^2 K_l^2 \left(\frac{wr}{a} \right) \sin^2(l\phi) \quad r \geq a$$

Here also I_0 is the constant magnitude which is related to the input conditions through $A \beta$ and u .

The following figures (Figs 28 & 29) are two dimensional images that are created by use of the intensity distribution formula given above. The plot data is created by using the program to solve eigenvalue equations, and Matlab is used to plot the images. Figure 29 shows the far field pattern redistribution induced by a small change in the refractive index of the clad material (0.005). This simulates the proposed biological sensors, where the modified clad material is sensitive to the environmental condition. Changing the environmental condition will result in variation of the material refractive index.

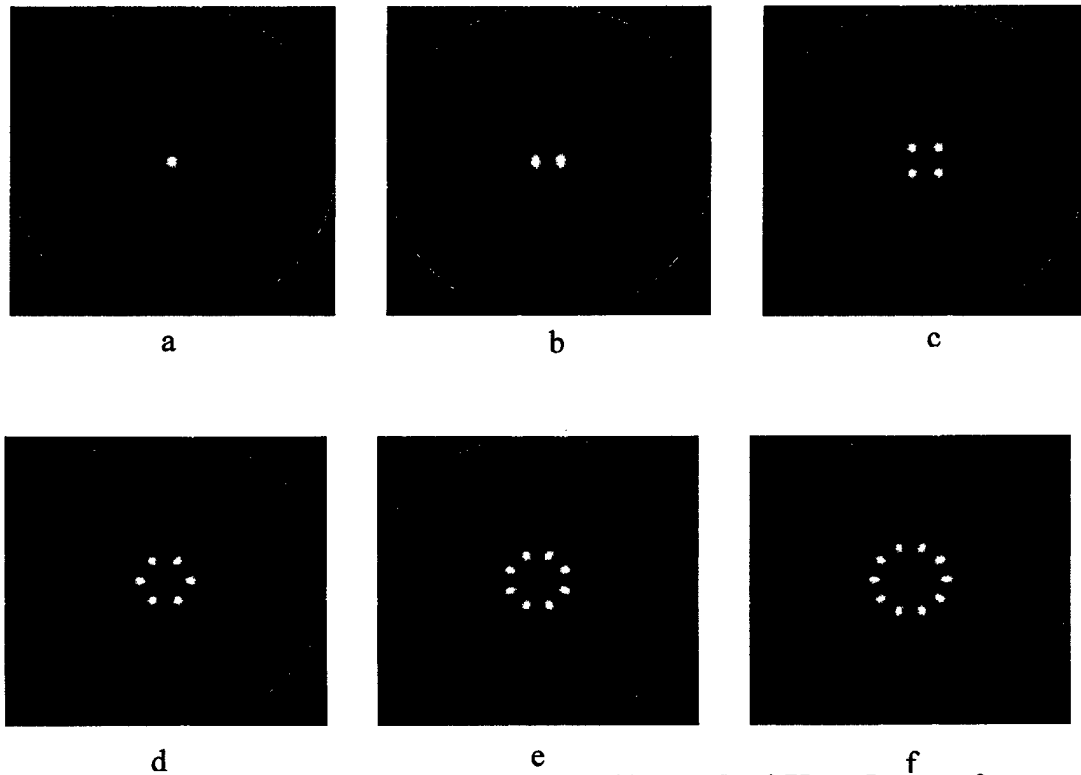


Figure 28. Field intensity profiles for LP_{lm} modes with $a = 20 \mu\text{m}$ and $l = 0.75 \mu\text{m}$. Images a-f correspond to LP_{0m} - LP_{5m} respectively.

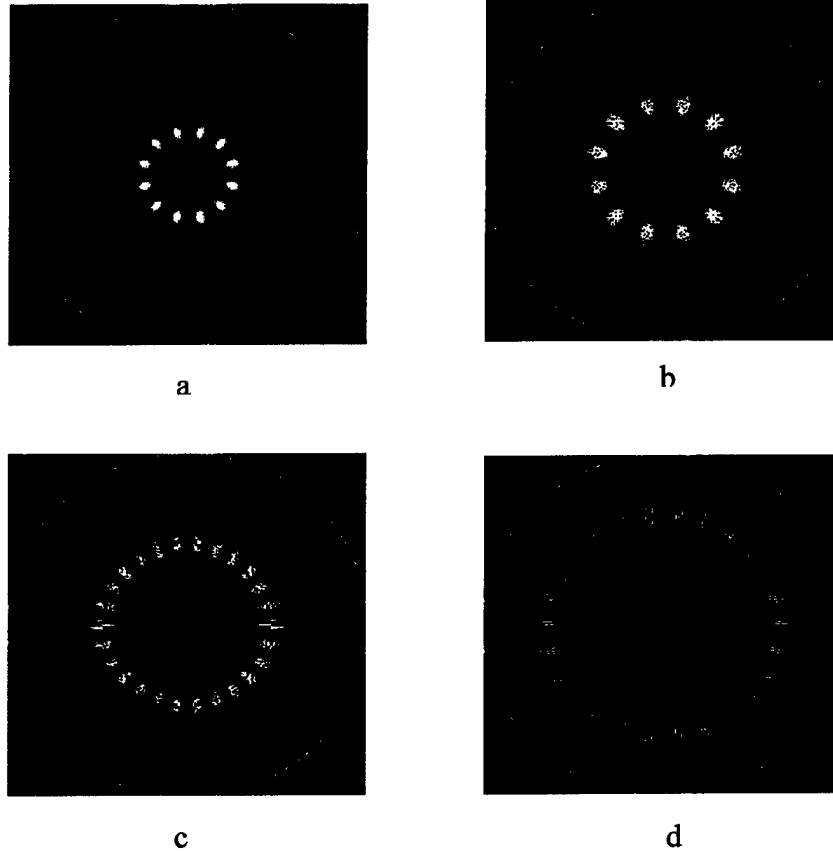


Figure 29. (a). $l = 6$, $n_{clad} = 1.45$, (b). $l = 6$, $n_{clad} = 1.455$

(c). $l = 13$, $n_{clad} = 1.45$, (d). $l = 13$, $n_{clad} = 1.455$

$n_{core} = 1.46$

The MPD technique is based on the selective excitation of higher order modes and the creation of a ring pattern at the far field of the fiber. Using an LED light source, with a narrow band of frequencies, the overlapping pattern will result in a ring shape.

Experimental observation and verification of the method is done in the past work on MPD [14, 15]. Figure 30 shows the far field pattern variation with respect to changing fiber conditions. Here, transverse stress loading causes the change in refractive index and

results in modal power redistribution. Also in [15], some simulations are carried out that shows that the theory matches with the experimental work.

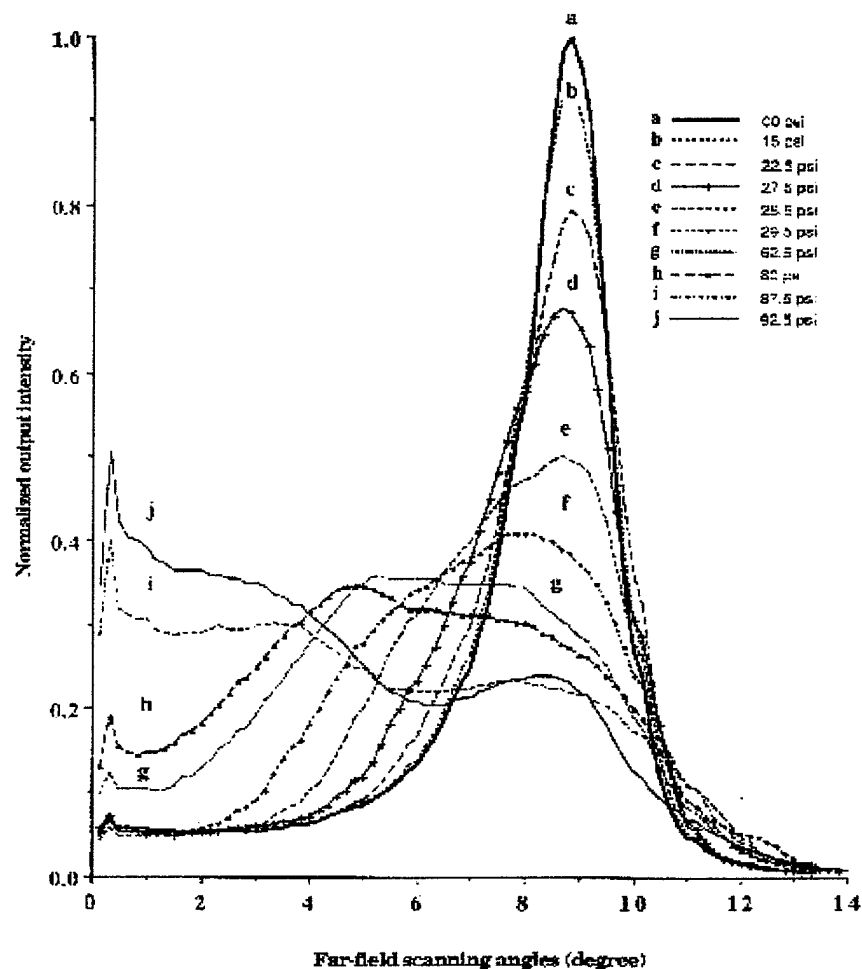


Figure 30. Normalized intensity profile of far-field pattern versus scanning angle for enhanced samples at different stress levels.

III.4. Summary

The present work aims at a thorough analysis of selective excitation in multimode fibers, modal coupling analysis based on [14] and [15] and far field pattern analysis and modeling for the purpose of being able to design a sensor using MPD technique. The developed model will be verified experimentally. Therefore, developing an experimental procedure for selective excitation is also an essential part of this study which needs to be addressed.

Reference

- [1] M. El-Sherif, "Fiber Optic Sensors for Soldiers' Smart Uniforms," Third ARO Workshop on Smart Structures, Virginia Polytechnic and State University, Blacksburg, Virginia, Aug. 27-29, 1997.
- [2] M. El-Sherif, Jianming Yuan, Fuzhang Zhao and Xiangyang Wang, "Annual Report of MURI/ARO (Multi-Disciplinary University Research Initiative-Army Research Office) Functionally Tailored Fibers and Fabrics," ARO Research DAAH 04-96-1-0018, 1997, 1998, 1999, 2000.
- [3] M. F. Rubber, "Polyurethane-Diacetylene Elastomers: A New Class of Optically Active Materials," ACS Polym. Materls. Sci. and Eng. Preprints, Vol. 53, 683-688, 1985.
- [4] M. F. Rubber, "Novel Optical Properties of Polyurethane-Diacetylene Segmented Copolymer," Vol. 54, 665-669, 1996.
- [5] A. G. MacDiarmid, "Polyaniline and Polypyrrole: Where are they headed?," Synthetic Metals, 84, 27-34, 1997.
- [6] A. G. MacDiarmid, W. J. Zhang, J. Feng, F. Huang and B. R. Hsieh, "Application of Thin Films of Conjugated Oligomers and polymers in Electronic Devices," Polymer preprints, 339 (1), 82, 1998
- [7] G. E. Collins and L. J. Buckley, "Conductive Polymer-Coated Fabrics for Chemical Sensing", Synthetic Metals, 78, 93-101, 1996.
- [8] J. Yuan, J. Feng, M. El-Sherif and A. G. MacDiarmid, "Development of an on Fiber Chemical Vapor Sensor," OSA Annual Meeting, Baltimore, MD., Oct. 4-9, 1998.
- [9] Jiangming Yuan and Mahmoud El-Sherif, "Development of On-Fiber Optical Sensors Utilizing Chromogenic Materials," SPIE International Symposium on Industrial and Environmental Monitors and Biosensors, Boston, MA, USA, Nov. 2-5, 1998.
- [10] Jianming Yuan, "Polymer Materials as Modified Optical Fiber Cladding for Chemical Sensors" Ph.D Thesis, 2001, Advisor: Mahmoud El-Sherif.
- [11] Mahmoud A. El-Sherif and Jianming Yuan, "Fourth Year Technical report on sensors and smart fabrics", US Army Research Office, DAAH 04-96-1-0018, 2000.

- [12] Kenneth Scott Richards, "Sol-gel processed optical fibers for sensor applications".M.S. Thesis, 2000, Advisor: Mahmoud El-Sherif.
- [13] John A.Buck, *Fundamentals of Optical Fibers*, New York: John Wiley & Sons, 1995
- [14] M. A. El-Sherif, "On-fiber active devices," Ph.D Thesis, Drexel University, June 1987.
- [15] J. Radhakrishnan, "Real time characterization of composite materials using fiber optic techniques", Ph.D Thesis, Drexel University, June 1996

FUNCTIONALLY TAILORED FIBERS AND FABRIC RESEARCH
FINAL REPORT
ON
TASK 3.1 ADVANCED TEXTILE BASED COMPOSITE MATERIALS
TASK 3.6.B. TEXTILE MANUFACTURING

BY

FRANK K. KO
AND
ANTONIOS ZAVALIANGOS

AND
GRADUATE STUDENTS
AFAF EL-AUFY
ASHRAF A. ALI
HOA LAM
JOVAN JOVICIC
JUN CHANG
SAKINA KHAN
WENDY HAN

CONTRIBUTING FACULTY ASSOCIATES
DR. AMOTZ GESHURY
DR. RYSZARD LEC
DR. ANDREW FERTALA

U.S. ARMY RESEARCH OFFICE

DAAH 04-96-1-0018

DEPARTMENT OF MATERIALS ENGINEERING
FIBROUS MATERIALS RESEARCH CENTER
DREXEL UNIVERSITY

DECEMBER 2001

APPROVED FOR PUBLIC RELEASE

DISTRIBUTION UNLIMITED

THE VIEWS, OPINIONS AND/OR FINDINGS CONTAINED IN THIS REPORT ARE THOSE OF THE AUTHORS AND SHOULD NOT BE CONSTRUED AS AN OFFICIAL DEPARTMENT OF THE ARMY POSITION, POLICY OR DECISION, UNLESS SO DESIGNATED BY OTHER DOCUMENTATION.

Executive Summary

This final report describes the research performed on gradient composite armor and on nanofibers and nanofibrous structures. Two faculty members and seven graduate students participated in the program with a strong and fruitful interaction with research colleagues at NC State, Akron and the University of Pennsylvania. Research in gradient composites continues on a two-prong approach focusing on empirical and numerical modeling with significant progress made in fiber architecture modeling. Major progress has been made in nanofibers and nanofibrous structures through a fundamental study of the effect of molecular conformation on the diameter of the fibers by electrospinning; rotary-electrospinning of oriented yarns; and wet-electrospinning of fiber coils. Nanofibers have been shown to be an effective means to deliver multifunctionality through the demonstration of conducting nanofibers, bioactive fibers and carbon nanotube reinforced nanocomposites.

Gradient Composite Armor - Based on the studies of ballistic group, the critical design parameters were identified for the gradient composite system. These parameters are the material properties of the ceramic sphere facing and that of the composite backing, the density of the backing and facing materials, and their geometry (thickness ratio). It was found that the modified Florence model provides a reasonable relationship between the ballistic limit V_{50} and the design parameters. In order to explore a broader region of design feasibility, a Response Surface Methodology (RSM) was used with virtual experimental data generated by the Florence model. The RSM can be used effectively to generate contour diagrams showing the optimum combination of design parameters for the responses of interest. For example, the responses, ballistic limit V_{50} and areal density A_d can be generated with the Florence Model with appropriate experimental design. The ballistic limit and areal density for various types of ceramic sphere and geometric combinations can be obtained by the response surface analysis. With the RSM established, one can now ask the question of whether the current state of the art material can effectively meet the ballistic limit and areal density requirements of the Army. One can further investigate what material property goals we should set for future armor development.

Complementing the empirical modeling work, our research has been focused on the improvement of the geometric details of the elements for finite element analysis of the gradient composite. The design of such materials includes a plethora of parameters. In order to develop precise methodology for optimization the gradient design composite armors, an improved understanding of the relative significance of the design parameters must be developed. One way to study the relative significance of these parameters is through computational modeling. Computational limitations impose compromises in the modeling of both geometry and material behavior. Of particular interest are geometric effects, such as the uniformity of penetration resistance, the optimization of packing geometry (in terms of fraction, arrangement, size distribution etc.), baseline comparisons with monolithic ceramic facing, and later on the optimization of multiple layers. To this end separate models are required for the individual phases. Two types of models are discussed: (a) an approximate

fiber/epoxy two-phase model for the backing, and (b) a damage-based, rate-dependent model for the ceramic spheres embedded in the epoxy. The development of a library of fiber architectures based on the unit cell has been initiated, which opens the possibility of the structural optimization along with simulation of the high velocity impact phenomena of advanced composites. An ability to transfer energy rapidly away from the point of impact is the most desirable quality for ballistic efficiency. Since the target, in this case the armor, is composed of various material systems, stress pulses incident to an interface will have components transmitted and reflected waves depending on the mechanical impedance, areal density and speed of wave. Thus, our additional interest was based on the investigation of various mechanisms of impact energy transfer in order to explore the possibility of developing new defeat strategies by examining mutual influence of the facing ceramic spheres, the backing material and its fiber architecture.

Nanofiber Technology - The incorporation of nanofibers into textile structures provides an effective means for increasing the surface area per unit mass of textile materials. The goal of preparing such carbon nanotube containing composite can lead towards versatile applications including military application, battery and memory storage devices, safe affordable space travel etc. The high surface area will greatly enhance the capability of clothing to protect against chemical warfare agents by absorbing the agent and/or deactivating the absorbed molecules. By proper use of polymers such as conductive polymer, a large family of electronic devices can be developed for the detection of chemical/bio/mechanical stimuli. These nanofibers can be formed directly into nonwoven fabrics or converted into a linear assembly (yarn) by air, fluid or various means of mechanical entanglement as well as wrapping onto another yarn. Since all life is carbon based, and carbon nanotubes are solely made of carbon with same scale size as DNA, the molecule of life, and the application of CNT composite in the field of biomedical science also unlimited, such as, artificial organs and drug delivery device. By creating the nanofibers in linear assemblies, we can also create nanofiber based hierarchical structures similar to biological tissues. Therefore these nanofibrous structure can be used effectively for scaffolds for cell adhesion and proliferation in tissue engineering.

Studies in nanofibers were carried out on a scientific and engineering level. Scientifically, we dedicated to understand the conditions under which nanoscale (diameter < 100 nm) polymeric fibers and composites can be produced. Polymer chain conformation in solution plays an important role in the electrospinning of nano-scale fibers. Under the same processing conditions, the morphology of electro-spun fibers is affected by the degree of chain entanglement, which is related to a dimensionless Berry Number. Using Poly(lactic acid) of different molecular weight, the experimental correlation between fiber diameter and Berry Number is obtained. It was shown that Berry number could be used as an index for fiber formation and to establish the processing window for nanoscale fibers. In addition, multifunctionality of the nanofibrous structures were demonstrated through collaborative work with Professor MacDiarmid's group at the University of Pennsylvania, by polymer blending of Polyaniline with various polymers to form electrically conducting or electronic nanofibers.

On the engineering level, two processes were investigated to create nanofiber linear assemblies by “Rotary Dry electrospinning” and “Wet Electrospinning”. Factorial experiments were designed and response surface analysis was carried out to optimize the processing parameters. In the Rotary Dry electrospinning process, a 3^3 factorial experiment was carried out on Polyethylene Oxide (PEO) polymer to study the effect of the electrospinning processing parameters on the physical & mechanical properties of the nanofibrous assemblies. The nanofibrous assemblies were characterized by SEM observations and tensile stress-strain testing. Additional experiments were done to orient these fibers onto the rotating disk & collecting them into yarn. It was found that, for the PEO nanofibrous structures, uniform diameter & areal density could be achieved by proper control of charge density, spinneret distance & of spinneret diameter. In the “Wet Electrospinning” process, polyacrylonitrile (PAN) solution with a 7%wt. Concentration was spun into a water bath. By SEM observations, the diameter of the produced fiber was found to be ranging from 50nm-500nm. On the basis of these measurements, the optimum height and charge density were determined. Additional experiments were carried out to study the ability to collect oriented fibers into a linear assembly and the formation of a new family of self assembled coiled structures.

By the demonstration of functionally tailored nanofibrous structures via electronic nanofibers, bioactive nanofibers, carbon nanotube composites, and nanofiber based bio/chemical/mechanical sensors this study provides a foundation for the creation of nanoscale fibers and fibrous assemblies which are essential for the manufacturing of next generation composites, scaffolds in tissue engineering and for the design and production of chem/bio protective materials.

TABLE OF CONTENTS

A. Statement of the Problem Studied	7
1. Modeling of Gradient Composite Armors	7
2. Engineered Hybrid Nanofiber Yarns	9
B. Summary of the Important Results	10
1. Optimization of the performance of gradient composite armor	10
1.1 The Software Package of Response Surface Analysis	12
1.2 Gradient Design Composite Armor	13
2. Numerical Modeling of Impact Behavior of Gradient Design Composites	25
3. Nanofiber linear assemblies. Processing, Structure, and Properties	31
3.1 Rotary Electrospinning	32
3.2 Electro-Spinning with Liquid (Wet) Assist Take-up	38
3.3 Multifunction Tailoring through Nanofiber Technology	55
3.3.1 Electroactive Nanofibers and Fibrous Assemblies	55
3.3.2 Bioactive Nanofibers and Fibrous Assemblies	56
3.3.3 Ultrasensitive Sensors from Nanofiber Films	57
3.3.4 Carbon Nanofibers and Nanocomposites	59
3.3.5 The Effect of Molecular Conformation of Poly(L-lactic acid) in Chloroform Solution on the Morphology of Electrospun Nanofibers	71
C. List of Publications and Technical Reports	72
D. List of Participating Scientific Personnel	74
E. Report of Inventions	74

- A. Comparison of the Low and High Velocity Impact Response of Kevlar Fiber-Reinforced Epoxy Composites
- B. Modeling of the Ballistic Behavior of the Gradient Design Composite Armor
- C. Optimization of Performance of Gradient Composite Armor
- D. Modeling and Simulation of Impact Behavior of Gradient Composites
- E. Electrostatic Fabrication of Ultrafine Conducting Fibers: Polyaniline/Polyethylene Blends
- F. Polyaniline Based Chemical Transducers with Sub-micron Dimensions
- G. Electrostatically-Generated Nanofibers of Electronic Polymers
- H. The Effect of Molecular Conformation of Poly (L-lactic acid) in Chloroform Solution on the Morphology of Electrospun Nanofibers
- I. On the Structure and Properties of Nano-Fibers & Nano-Fibrous Assemblies
- J. Numerical Modeling and Analysis of Dynamic Behavior of Gradient Design Composites
- K. A Novel Polymer Nanofiber Interface for Chemical Sensor Applications
- L. Fiber Architecture Based Computer Modeling of Textile Composites
- M. The effect of processing parameters on the morphology of electro-spun PAN fibers
- N. Three Dimensional Fibrous Scaffolds for Tissue Engineering
- O. Integrated Design for Manufacturing of Composite Helmets
- P. Carbon Nanotube Reinforced Nanocomposites by the Electrospinning Process

A Statement of the Problem Studied

1. Modeling of Gradient Composite Armors

The unique advantage of composite material is their ability to tailor their properties to the structural or materials system of which they are intended. On the other hand, many structural components have to meet service conditions and, hence, required materials performance, which vary with location within the component. This consideration founds basics for development of a special class of composite materials, that are functionally graded-*Gradient Design Composites* (GDC).

In order to defeat higher velocity threats and address the need for lighter weight and more complex shape structures, the concept of introducing a harden phase in the spherical form or Gradient Design Composite (GDC) was applied to novel armor structure. The system consists of a harden component with ceramic spheres for destroying the projectile tip and creating a greater surface area to contact between the facing layer and the backing composite plate which is for maximizing strength and energy absorption.

The application of gradient design concept in armors offers possibilities in the reduction of weight and cost without significant reduction of ballistic resistance. Experimental results of composite backed plates consisting of layers of ceramic spheres embedded in epoxy showed that a ballistic limit of 3,000 ft/sec. can be achieved without weight penalty comparing to solid ceramic tiles. In addition to capable of deforming the projectile the ceramic sphere facing also provided additional defeat mechanism as well as the feasibility for conformable armor manufacturing. It is evident that the complexity of the modern light armor construction has increased many fold and so did its structural analysis. To complement and perhaps guide the necessary experimental evaluation of such system, it is essential to develop a computational methodology that may lead us to an improved understanding of the relative significance of the various design parameters. The associated computational complexity in terms of both geometry and material models is the key difficulty of this approach.

The characteristic of our approach is that it considers each material separately. From the computer simulation point of view, the introduction of discrete models for the study of textile composites offers the advantage of using different and more detailed description of material properties for both matrix and fibers, with a more accurate description of the geometry. In this way, more elaborate (and more realistic) failure criteria can be introduced. Using the higher-order discretization it is possible to explore the effects of fiber architecture on the dynamic properties of these composites.

The primary focus area of the research program has been concentrated on modeling, establishing constitutive relations for the component materials and study of damage mechanism relative to the GDC composites. A fiber architecture based model has been developed that can account for the contribution of matrix and fibers to energy absorption.

Important factor that influences armor penetration resistance is using of obliquity between the projectile and armor to enhance performance. Another consideration for system integration is back face deformation, or the deflection of the armor material on the back surface. Even though the armor may defeat a threat projectile, the back face deformation can cause other damage, for example, blunt force trauma to a person wearing an armored vest or a helmet.

Guided by experimental observations, a modified Florence model was used to generate contour diagrams for a large family of high performance fiber reinforced backing composites and selected ceramic sphere facings according to the Response Surface methodology (RSM). It was determined that boron carbide provides the best combination of weight and hardness advantages. However, backing composite plate plays a significant role in the overall ballistic performance of the armor. A combination of high fiber strength and toughness is essential to achieve the Army After Next (AAN) specific V_{50} requirements. The RSM study showed that state-of-the-art synthetic fibers fail to meet the AAN goals. Accordingly, before a new super fiber such as the spider silk are available, we must rely on innovative design of the material combination and architecture of facing material and backing composite structures. Preliminary evidence obtained by high speed camera observation of damage mechanisms and by numerical simulation appears to support the notion that the ceramic spheres in the face plate is capable of redirecting the projectile to assume an oblique angle.

This 5 Year program has been focused on the ballistic limit of gradient composite armor system under certain constrain of area density, the development of software package of response surface analysis, and the development of a library of fiber architectures based on the unit cell.

The use of honeycomb and Spectra shield in gradient design composite panel for ballistic protection to improve impact resistance is very promising. The new honeycomb design concept provides excellent conformability, larger surface for bonding to the backing layers, flexibility in designing arising from the ability in manufacturing from various types of fabric, ability to produce different cell sizes, and continuous manufacturing resulting in cost effectiveness.

2. Engineered Hybrid Nanofiber Yarns

The aim of the hybrid yarn project was to combine electrospun specialty polymers with high strength core yarn through an air-vortex/fluid entanglement spinning system. The nanofiber component provides a means to introduce multi-functions while the core yarn provides strength and facilitate processing into textile and garment structures. The nanofiber yarn spinning system consists of an electrospinning (ES) unit and a take-up device. These components are interconnected and they operate as a unit. The nanofiber spun from the ES unit is fed into the vortex tube to form air-twisted pure nano-yarn or air-wrapped yarn with a core yarn already positioned in the vortex tube. As the nano-yarn and hybrid yarns are formed, the take-up system will wind the yarn at an appropriate speed to control the yarn linear density and surface geometry. A multitude of ES jets may be employed to regulate the deposition rate and tailored the yarn geometry. The availability of this unit is essential for our parametric study of the optimum processing parameters for the hybrid yarn.

While Professor Reneker's group focus on ES processing from the polymer and fiber science point of view, the work at Drexel focus on the processing mechanics, structural geometry and structural mechanics of linear nanofibrous assemblies. Our work were complemented each other to create a prototype nano-yarn manufacturing system and generate meaningful engineering data such that the benefit of nano-yarn and hybrid yarns can be fully exploited. In addition, the multifunctionality of the nanofibrous structures were demonstrated through collaborative work

with Professor MacDiarmid's group at the University of Pennsylvania, by polymer blending of Polyaniline with various polymers to form electrically conducting or electronic nanofibers. The key challenges in this program were to produce nanoscale fibers with diameters consistently below 100 nm at significantly higher strength. These nanofibers must be oriented and assembled into linear fibrous assemblies for the hierarchical construction of higher level 2-D and 3-D nanofiber based structures. The fibers and yarns were characterized by SEM imaging; linear density measurement; fiber crystallinity determination; voluminosity and surface area measurement by mercury porosimetry measurement; fiber helix angle in yarn; and tensile stress strain testing. Response surface analysis was carried out to establish the optimum processing conditions for the nanofibers and nanofibrous assemblies.

Functionally tailored nanofibrous structures were demonstrated via electronic nanofibers, bioactive nanofibers, carbon nanotube composites, and nanofiber based bio/chemical/mechanical sensors.

B. Summary of the Important Results

1. Optimization of the Performance of Gradient Composite Armor

Project Team:

Professor Frank Ko and Ph.D. students Hoa Lam and Jun Chang and Natick Collaborator John Song

Based on the studies carried out in the past few years, Response Surface Methodology (RSM) combined with virtual experimental data generated by the modified Florence model was proved to show the optimum combination of design parameters for the responses of Gradient Composite Armor (GDC). With the RSM established, one can now ask the question of whether the current state of the art material can effectively meet the ballistic limit and areal density requirements of the Army. In order to explore the ballistic limit of GDC, the state-of-the-art materials systems were studied (which include the advanced engineering fibers current available, the cutting-edge structure ceramic, and the resin), as shown in Table 1. It is found that state-of-the-art materials fail to meet the specific ballistic requirements. Spider silk appears to be the most promising fiber for high performance body armor. New Mechanism for defeating the threat is recommended before a super materials system is available.

Table 1. Fiber Property Requirements for AAN Armor Systems.

Fiber	Current Properties					Target Properties		Improvement Needed (X)
	Density (kg/m ³)	Strength (GPa)	Strain (%)	S.S.E (GPa)	Modulus (GPa)	Strength (GPa)	S.S.E (GPa)	
Spider Silk	1098	1.75	26	0.455	34	2.34	0.608	1.34
PBO	1540	5.8	3.5	0.2146	270	24.86	0.92	4.28
Nylon (HT)	1140	0.986	15	0.148	5.5	4.7	0.70	4.77
S Glass	2480	4.59	5.5	0.253	85.5	24.74	1.36	5.39
Spectra 1000	970	3	3.4	0.102	172	18.85	0.64	6.28
KM2	1440	3.28	4	0.1312	43	21.4	0.856	6.52
Kevlar 29	1450	2.8	3.6	0.1008	45	23.67	0.852	8.45
E Glass	2540	3.45	4.8	0.1656	72.4	36.12	1.734	10.47
PEN	1380	1.21	4	0.0484	40	36.18	1.447	29.9
AS4	1800	3.58	1.54	0.0089	588	417.5	1.041	116.6

1. S.S.E : Specific Strain Energy 2. Assume strain remain constant 3. Boron Carbide facing

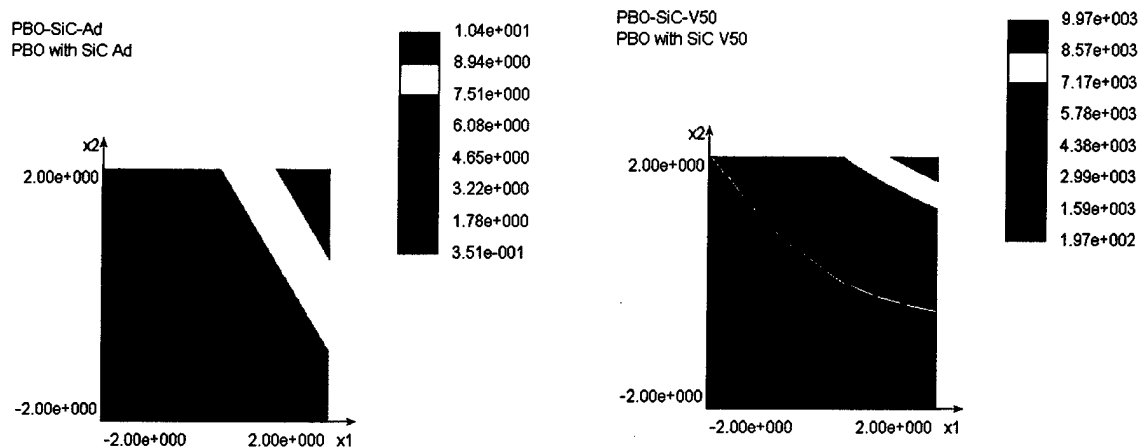


Fig.1 Response Surface of PBO / B₄C Composite.

1.1 The Software Package of Response Surface Analysis

The current analysis works are done by using several software packages (MAPLE, MICROSOFT EXCEL, EXCEL SOLVER, etc.) and through few separate steps. Lots of manual work of data input and transfer as well as function expression are required. And the image quality of response surface contour is not satisfied. Therefore it is necessary to incorporate all these steps into single software and make it using friendly. Software programmed by Microsoft VISUAL BASIC 6.0 and Microsoft Access was developed. This software includes the following features:

- A database where the materials properties of advanced fiber, ceramic, resin and projectiles are stored in.
- Computer aided experimental design and variance analysis
- Experimental data virtually generated by modified Florence model
- Automatic response approximation (polynomial approximation)
- Response surface contour plotting
- Report on analytical results

1.2 Gradient Design Composite Armor

With the design tools established through empirical modeling and numerical modeling, we can now more conveniently assess various design concepts and optimize the design.

In the earlier study, ceramic spheres were added on top of the Spectra shield backing panel to absorb the impact energy. With this technique it was difficult to control the distribution/arrangement of ceramic spheres across the surface of the backing panel. For better distribution and control of the spheres across the surface, commercially available honeycomb structures such as aluminum, glass and carbon fiber reinforced plastic was used as illustrated in Figure 2. A combination of flexible Spectra shield layer and honeycomb allows the preform to be conformed into contour surface prior to the addition of resin and molding.

In order to examine the possibility for toughness enhancement and material cost reduction, the concept of hybrid sandwich structure is explored. The hybrid sandwich structure consists of Spectra Shield skins with PEN Shield core structure.

1.2.1 Traditional Honeycomb Structures

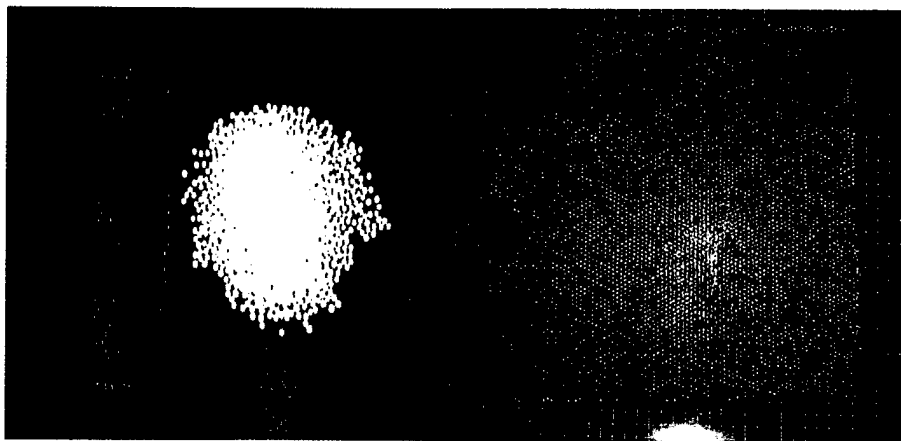
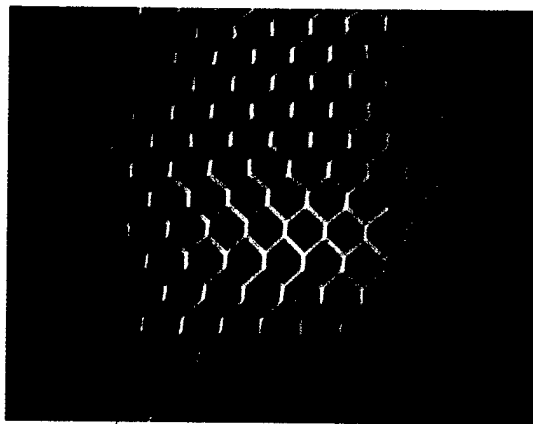


Fig 2. Gradient design composite panel, with conventional honeycomb structure for better distribution of ceramic spheres across the surface.

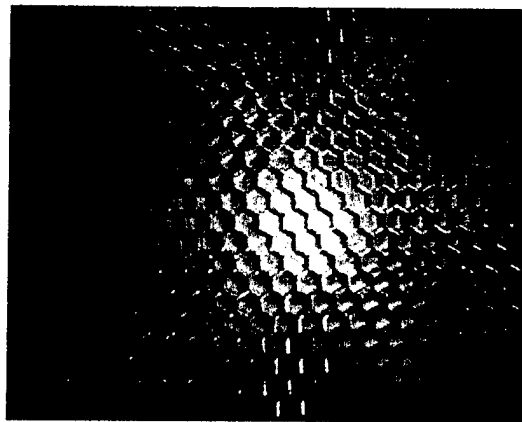
Traditional honeycomb structures (Fig.3), either aluminum, carbon fibers, or glass fibers are manufactured by spot welding or adhesive bonding of strips of materials at predetermined locations. Honeycomb structure is formed by pulling apart the welded strips. This conventional technique required a 3-step process:

- 1) Manufacturing of the designated material in appropriated width and thickness;
- 2) Stacking and welding/bonding of the strips;
- 3) Opening of the strips into final structure.

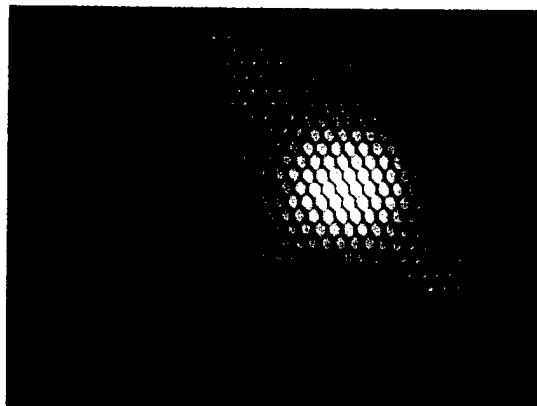
In the case of fiber honeycomb, the strips are manufactured from continuous, unidirectional fiber, which provides adequate properties in a specific direction. The strips materials are normally impregnated in an epoxy matrix.



(a)



(b)



(c)



(d)

Fig.3 Conventional honeycomb structure: (a) and (b) are aluminum; (c) and (d) are glass fiber reinforced plastic.

An example of aluminum honeycomb filled with a layer of ceramic spheres is presented on Fig.4. As can be seen from, the surface available for bonding to the backing panel is very minimal.

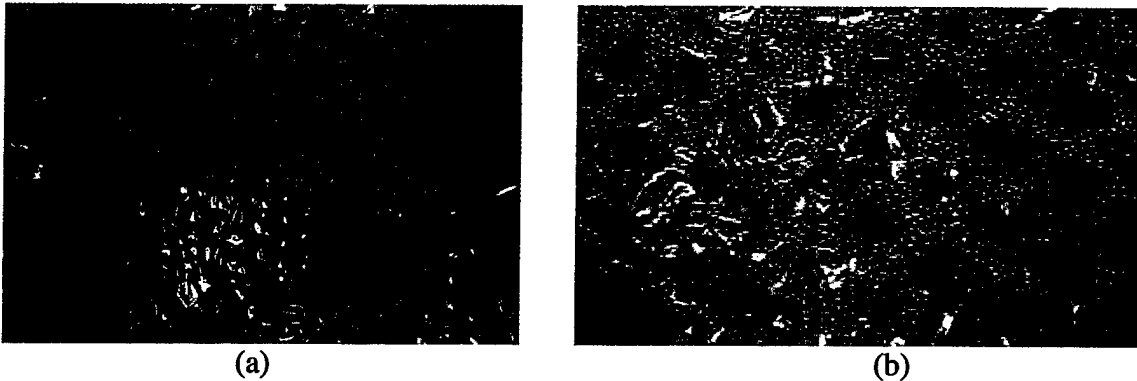


Fig.4 Aluminum honeycomb filled ceramic spheres, showing uniform distribution of spheres in a layer. (a) 0.25" diameter spheres; (b) 0.5" diameter spheres plus smaller ones to fill the remaining cell space.

In addition, commercially available honeycombs are limited to certain cell sizes. There is a certain degree of flexibility associated with the existing honeycomb structures; however, the flexibility can significantly improved by constructing the structure from dried fabric.

1.2.2 New Honeycomb Design

A new honeycomb design has recently been studied and shown enormous improvement in many aspects. The newly design structures provides more surface area for bonding to the backing panel as illustrated in Figure 5.

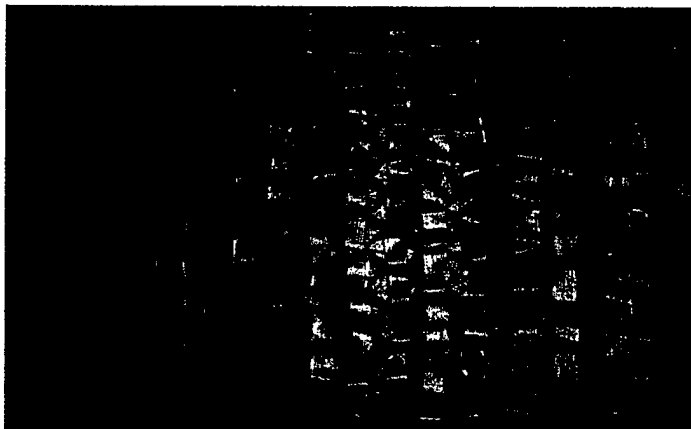


Fig.5 New honeycomb design fabricated from Spectra fabric (0°/ 90°).

This structure is very much similar to the traditional design, except the addition of more surface area through the introduction of bands across the individual cells. Since the structure is constructed from dried fabric, the degree of flexibility is much greater, providing excellent conformability over contour surfaces.

In addition to the mentioned advantages, honeycomb can be fabricated from any commercially available fabrics such as non-woven, woven, knitted, and braided fabrics of any materials depending on the application. For example, Spectra fabric provides high toughness and lightweight, while carbon fabric provides high strength, stiffness and also lightweight. Oriented fabric can also be used to provide reinforcement in specific direction as shown in Figure 6, where triaxially woven carbon fabric is used to fabricate the honeycomb structure to hold 0.5" diameter ceramic spheres. Whereas Figure 7 demonstrates a filled honeycomb constructed from laminated Spectra fabric (0°, 90°).

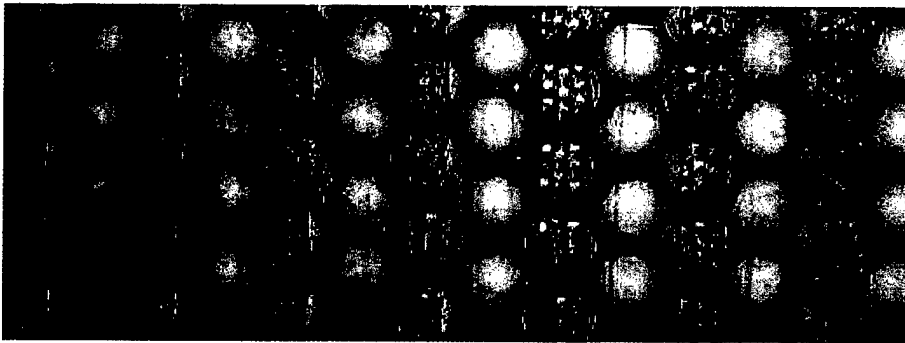


Fig.6 Honeycomb fabricated from triaxially woven carbon fiber fabric, filled with 0.5" diameter ceramic spheres.

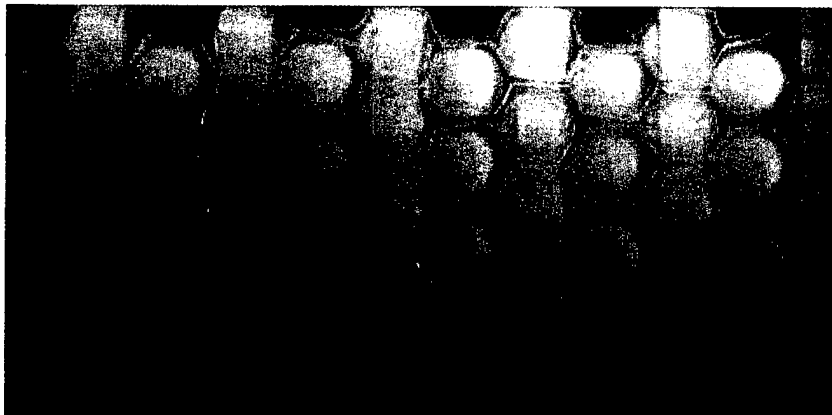
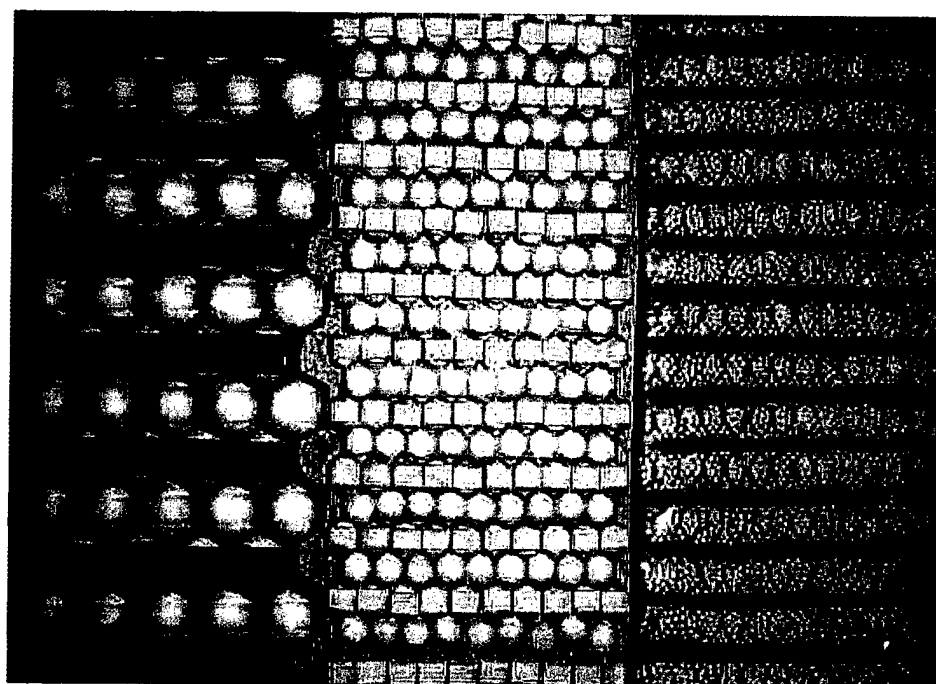


Fig.7 Honeycomb manufactured from laminated Spectra fabric (0°/90°), filled with 0.5" ceramic spheres.

The cell can be designed to accept any diameter sphere from 0.125" and higher. Obviously, spheres less than 0.125" diameter can also be used. Instead of having one sphere per cell, each cell is now occupied by multiple spheres when smaller spheres. Figure 8 shows honeycomb with various cell sizes. With this new design concept, the honeycomb is fabricated by punching a series of rectangles out of the fabric and then fold in both directions to form cells. The cell or rectangle dimension is related to the diameter of the sphere; therefore, it can easily be designed to hold any given diameter filler.



(a) 0.5" diameter

(b) 0.25" diameter

(c) less than 0.125" diameter

Fig.8 Honeycombs with various cell sizes.

1.2.3 Sandwich structure

In the past, laminated pure Spectra Shield layers were used as composite backing panel. Although the Spectra Shield backing has been shown to provide adequate protection when sufficient layers are used, they are expensive and they are often in short supply. The availability of Polyethylene Naphthalate (PEN) shield – a strong fiber produced by Honeywell (AlliedSignal), offers new design options. Although PEN fibers are not as strong as the Spectra Shield, it is a much tougher fiber and less expensive than Spectra Shield, at less than 30% of the cost. Accordingly, the challenge is to design an optimum sandwich structure consisting of the Spectra Shield skin with a PEN shield core to provide equivalent energy absorption and penetration resistant capability.

Three different combinations of Spectra and PEN layers are used to form the sandwich structure. Fig.9 is the schematic diagram of the single sandwich panel. The layer fractions of Spectra shield are chosen as 0.25, 0.5 and 0.75. The total number of layers of sandwich structure is fixed to 108 layers.

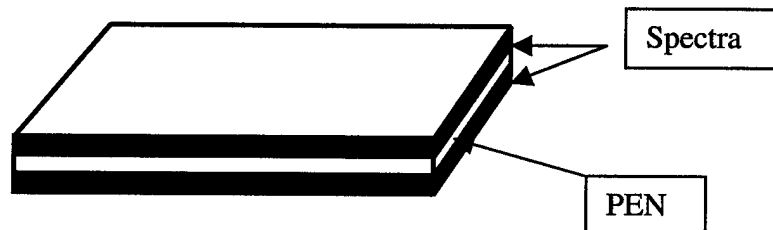


Fig.9 The schematic diagram of the single sandwich panel.

Another sandwich structure is multiple fine sandwich structure (Fig.10), in which the composite backing panel is made of many sandwich layer and every sandwich consists of the Spectra and PEN layers. The layer fraction of Spectra layers is chosen as 0.75 so that the layer fraction of Spectra layers is still as same as that in single sandwich panel. The total layers of sandwich composite panel are fixed to 108 layers.

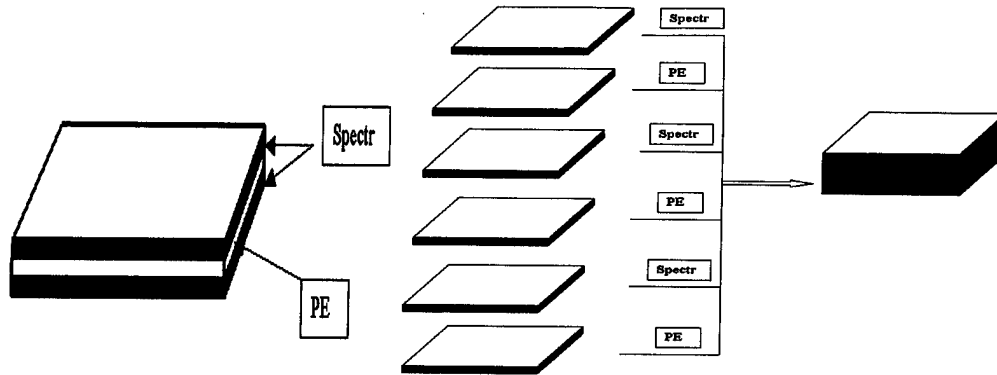


Fig.10 Schematic diagram of the sandwich panel.

1.2.4 Processing of composite backing panel

Hot pressing is used to laminate the sandwich composite panel. And Fig.11 is the processing diagram of the sandwich composite panel.

- The prepreg Spectra and PEN fabrics are cut to required shape.
- The Spectra and PEN layers are stacked carefully to form sandwich structure.
- The Sandwich panel is laminated by hot pressing.

The conditions of sample preparation and process are listed in Table.2

Table 2 The summary of sample preparation and process.

	Single sandwich			Multiple sandwich		
Ratio (Spec/PEN)	25:7	50:5	75:2	25:7	50:5	75:5
	5	0	5	5	0	0
Layers (Spectra)	27	54	81	27	54	81
Dimension (in)	12 x 12					
Process	Hot press					

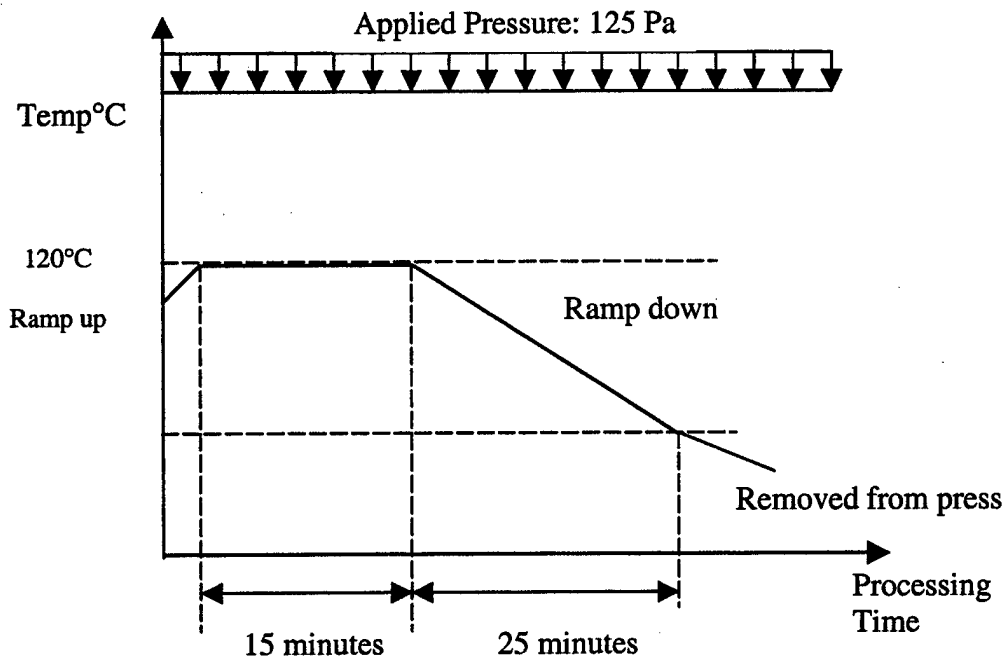


Fig.11 The diagram of processing of composite panel.

1.2.5 Design of the face panel

It is now well recognized that after impact, a conical fracture pattern developed at the impact zone, propagating towards the ceramic-backing plate interface. Also, tensile fracture develops at the interface as the result of the reflection of the initial compressive wave as a tensile one. Later, a conical zone of fully fragmented material develops in front of the projectile and, as a consequence of the interaction between the projectile and the ceramic powder, projectile erosion occurs. The energy consumed in the fracture of the ceramic tile is very small compared with the energy of the impact; the development of a zone of fractured material ahead of the penetrator seems to be of the greatest importance in defeating the projectile.

The face panel destroys the projectile shape, reduce the projectile velocity and spread the impact energy over a wider area on the backing panel. More experiments are needed to allow further examination the effects of the ceramic sphere type, sphere size and the arrangement of ceramic sphere.

The effect of ceramic type

Because of the area density requirement, the lighter ceramic sphere seems to be a good choice. Table 3 lists some promising candidates that can be used as ceramic sphere.

Table 3 Properties of ceramic materials.

Materials	Density (g/cm ³)	Modulus (GPa)	Hardness (kg/mm ²)
Aluminum Oxide	3.40	227	1800
Boron Carbide	2.48	440	2790
Silicon Carbide	3.2	440	2700
Boron Carbide & Silicon Carbide	2.60	340	2750

The dimensional effect of ceramic sphere

Three different radiuses of ceramic sphere, $0.5r$, $1r$ and $2r$ (r is the radius of projectile) are chosen to study the dimensional effect of ceramic sphere. For 7.62 NATO projectile, the radius equals to 3.6mm. So the radius of chosen ceramic sphere is 1.8mm, 3.6mm and 7.2mm, respectively.

The arrangement of ceramic sphere

For one-layer ceramic panel, it was made of ceramic sphere in honeycomb structure as shown as following:

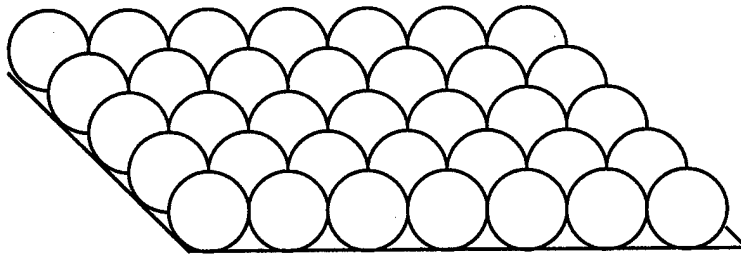


Fig.12 Schematic diagram of one layer face panel.

For two-layer face panel, the structure of every layer is as same as the one-layer face panel where ceramic spheres are close packed in honeycomb (Fig.13).

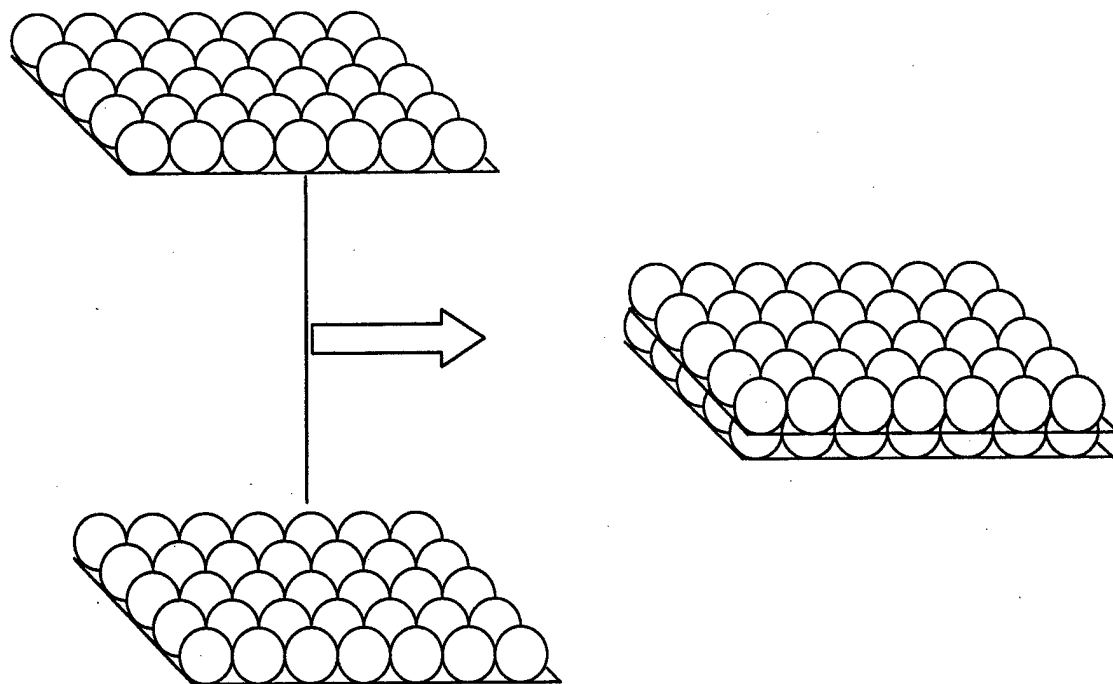


Fig.13 Schematic diagram of two layers face panel.

1.2.6 Testing

Indentation

Indentation test has been done on the Instron 1127-instrumented tester with a 0.5-inch diameter indenter. The indentation load vs. displacement has been characterized for each sample.

Drop weight impact test

Drop-weight impact test was performed on each sample. The impact load vs. time and impact energy vs. time responses has been characterized for each sample. All the impact tests was performed on a Dynatup model 8140 instrumented impact tester in conjunction with a Dynatup model 730-I data acquisition system driven by a PC. Fig.14 shows the schematic diagram for the impact tester.

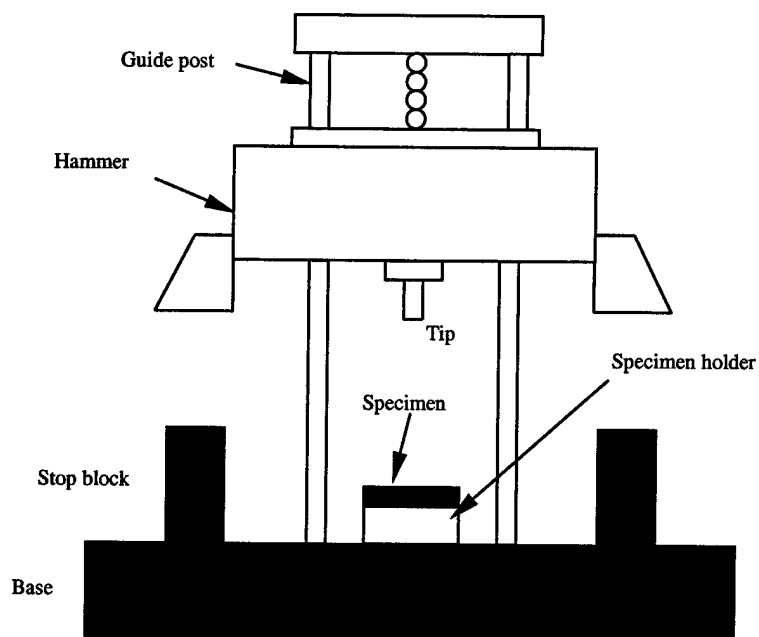


Fig.14 Schematic diagram for the impact tester.

Ballistic test

Ballistic testing was performed at Natick using projectiles from a rifle or a light gas gun. Kinetic energy absorption during ballistic penetration was measured using the high-speed impact apparatus located at the Army Research Laboratory. Ballistic resistance tests were conducted in accordance with Military Standard MIL-STD-662E, V50 Ballistic Test for Armor. The impact points were at minimum distance of 1½ inch from each other. The samples were rigidly mounted with the area of impact normal to the lines of fire.

1.2.7 Finite Element Modeling

The objective of Finite Element modeling of armor is to complement the experimental components of this phase of design, and to obtain a thorough understanding of deformation, energy absorption mechanisms and failure of armors.

- Modeling the indentation by using Ansys commercial software and compare results with experimental data.
- Modeling the drop weight impact test by using Ansys and compare with the experimental results.

2. Numerical Modeling of Impact Behavior of Gradient Design Composites

Project Team:

Professors Frank. Ko, and Antonios Zavaliangos and Ph.D. student Jovan Jovicic.

Experiments with lightweight armor systems are essential to improve the understanding of the penetration mechanisms. Unfortunately, the complexity and briefness of the impact event make instrumentation and measurements very difficult, and experiment becomes expensive and time consuming. On the other hand, with such complex designs the number of independent parameters is very large. To complement and perhaps guide the necessary experimental evaluation of such system, it is essential to develop a computational methodology that may lead us to an improved understanding of the relative significance of the various design parameters. The key difficulty of this approach is the associated computational complexity in terms of both geometry and material models.

The focus of this phase of the study was in the numerical assessment of energies, stresses and deformation and velocity histories of the different Gradient Design Composite systems in the event of impact.

For Gradient Design Composite model, consisting of ceramic spheres facing and polymer matrix composite backing, influence of various micro structural variables of both projectile and target on the target ballistic performance have been explored (Fig. 15).

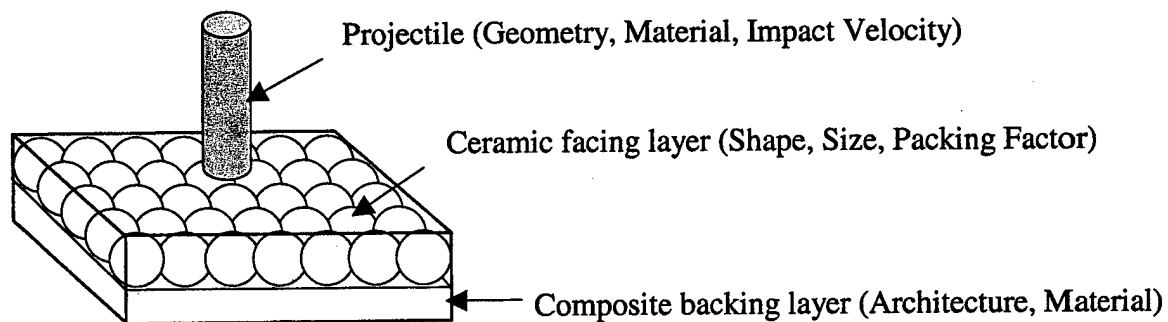


Fig.15 Various variables influence the energy absorption characteristics of GDC material.

The most important characteristics of the backing composite plate is type of the fibers and resins used, the way fibers are arranged and the fiber/matrix interface bond strength.

In the case of ceramic facing, energy absorption characteristics depends on both material properties and geometry of the ceramic particles in the facing layer of the GDC material: their shape, size and way of packing.

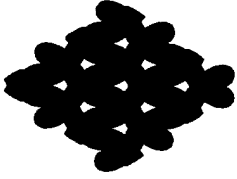
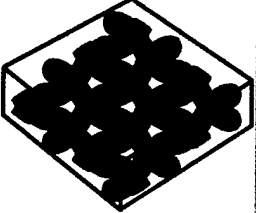
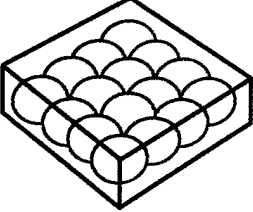
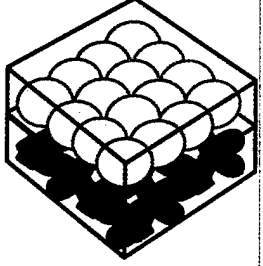
Model type	Solid model (Hexahedral elements)	Velocity range [m/s]	Model description	
			Geometry	Materials
Textile perform		10-100	Full geometry <ul style="list-style-type: none"> • Woven • Braided • Knitted • Orthogonal 	<ul style="list-style-type: none"> • Elastic-plastic • Strain rate effect • Orthotropic vs. isotropic
Polymer Matrix Composite		100-300	<ul style="list-style-type: none"> • Full geometry • Hexahedral elements • Volume fraction 	<ul style="list-style-type: none"> • Elastic-plastic • Strain rate effect • Orthotropic preform • Isotropic matrix
Ceramic facing layer		100-500	Monolithic vs. Spherical	<ul style="list-style-type: none"> • Brittle vs. • Elastic-plastic with brittle failure
Gradient Design Composite		500-2000 > 2000	Hexahedral elements	<ul style="list-style-type: none"> • Elastic-plastic • EOS

Fig.16 Developed FE models, their characteristics, and domains of application.

It is evident that the complexity of the GDC constructions has increased many folds and so did its structural analysis. Figure 16 presents developed models and problems that have been addressed during this phase of the project.

The geometry is the first step in understanding any composite structure, and the model presented here allows one to look at the 3D nature of a textile composites structure in those cases where simple models prove inadequate.

The characteristic of our approach is that it considers each material separately (Fig.17). From the computer simulation point of view, the introduction of discrete models for the study of textile composites offers the advantage of using different and more detailed description of material properties for both matrix and fibers, with a more accurate description of the geometry. In this way, more elaborate (and more realistic) failure criteria can be introduced and the effects of fiber architecture on both static, and dynamic properties of these composites can be explored.

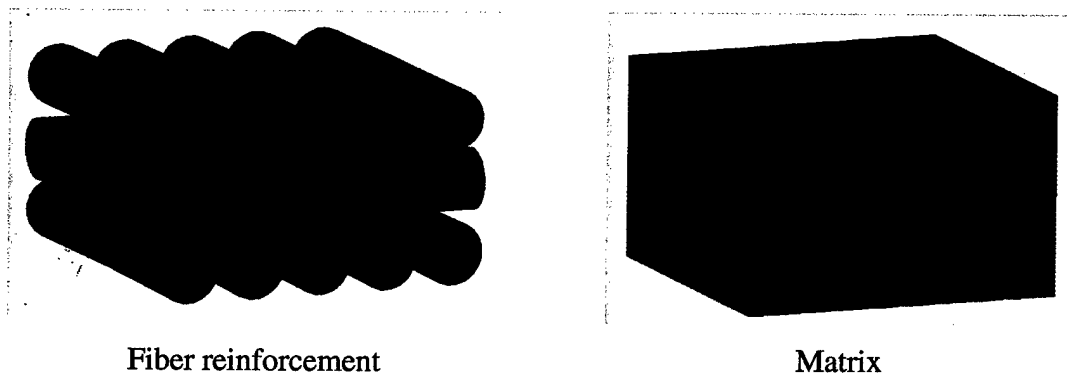


Fig.17 3D FE model of a typical 0°/90° textile composite unit cell.

Procedures written in MAPLE are used to model the textile. The model is linked with user subroutines to ABAQUS-Explicit finite element code (version 6.2, Hibbitt, Karlsson & Sorensen, INC., Rhode Island, 2001), to simulate the structural behavior of textile composites, and assess the effect of materials selection and fiber architecture on their mechanical properties.

This model is capable of representing different material volumes and material properties to approximate the volume fraction and fiber orientation distribution resulting from preforming and textile formation processes.

Developed algorithm is able to create true 3D fiber architecture-based unit cell models of textile preforms, and to produce adequate meshing of increasing detail using solid brick elements.

The main advantage of our approach is that different architectures, mesh densities, boundary and load conditions of a textile and its RVE-s are functions of only few parameters that can be easily controlled and changed.

The present analysis, based on the representative volume element (RVE), of textile composites, allows prediction of the engineering constants of the constituents, as well as the detailed material model description within the RVE.

The developed code can be used to generate an input file for any commercial FE computer software.

The development of a library of fiber architectures based on the unit cell has been initiated (Fig.18), which opens the possibility of the structural optimization along with simulation of the high velocity impact phenomena of advanced composites. Using this approach it is possible to include more information for the textile composite such as the overall architecture as well as particular geometric characteristics such as crimp etc.

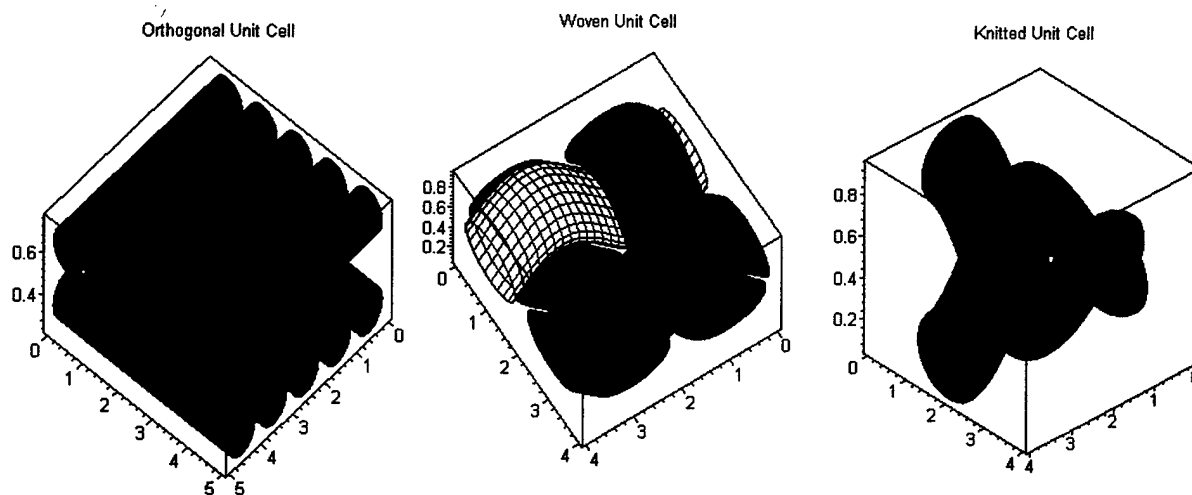


Fig.18 Computer-based modeling of the textile reinforced composite structure.

Effect of impact velocity on residual velocity time history for textile composites with different fabric architectures was investigated, giving target behavior for a range of velocities from 10m/s up to 1000m/s. This type of case study is attractive for various applications: from drop-weight test simulation up to modeling of ballistic impact on composite structure.

Residual velocity and back-plane displacement time history were evaluated as a function of different impact site and the projectile incident angle. Changing the direction of a projectile, by its deflection on the particulate ceramic facing, gives the additional effect to the energy absorption increase.

The effect of the ceramic facing size on the projectile residual velocity and displacement of the backing plate was investigated, and it was found that projectile impact between two spheres, and smaller facing size compared to projectile size, lower residual velocity and back-plane displacement.

The projectile shape, material and initial or striking velocity are also important factors that influence outcome of the impact phenomenon.

Two types of used material models are discussed: fiber/epoxy viscoelastic rate-dependent model for backing, and damage-based model for brittle ceramic facing.

Addition of the strain rate effect on Spectra fabric modulus in numerical simulations, showed better target ballistic performance and necessity of using dynamic material properties in moderate to high velocity impact simulations. However, the study of the dynamic properties is not complete by simply changing the modulus. The reduction of strain to failure with strain rate is equally important and has to be included in the further analyses.

Residual velocity time history was evaluated for both, plain woven and unidirectional ($0^\circ/90^\circ$) textile composite target with two types of facing layers. Ballistic resistance of gradient design composite with facing layer of ceramic spheres embedded in epoxy is showed to be comparable to that of solid ceramic tile. It is shown that mutual contribution of both, textile architecture and

ceramic facing layer influences ballistic performance of specific armor structure. Better penetration resistance is predicted for orthogonal composite backing, which is able to absorb and disperse ballistic energy immediately, compared to woven fabric which crossover points probably serve as barriers to fast and efficient energy transfer. In the same time, the spherical ceramic facing seems to be good alternative to traditional monolithic ceramic plates, since simulations show comparable ballistic resistance.

It can be concluded that ceramic spheres can be used effectively to replace the conventional ceramic tiles to reduce weight and cost without sacrificing its ballistic effectiveness.

The issue of optimization of the energy absorption mechanism is also addressed. The influence of material impedance mismatch on stress wave propagation is examined and as a result, the selected combination of the facing/backing plate materials is proposed according to their ability to transfer the impact energy as fast as it is possible from the impact site.

3. Nanofiber Linear Assemblies. Processing, Structure, and Properties

Project team: Professors Frank K. Ko, Darrell Reneker (Akron University), and Ph.D. student Afaf El-Aufy

In this study, we investigated two approaches to create nanofiber linear assemblies by “Rotary Dry electrospinning” (3.1), and “Wet Electrospinning” (3.2). Factorial experiments were designed and response surface analysis were carried out to optimize the processing parameters. In the Rotary Dry electrospinning process, a 3^3 factorial experiment was carried out on Polyethylene Oxide (PEO) polymer to study the effect of the electrospinning processing parameters on the physical & mechanical properties of the nanofibrous assemblies. The nanofibrous assemblies were characterized by SEM observations and tensile stress-strain testing. Additional experiments were done to orient these fibers onto the rotating disk & collecting them into yarn. It was found that, for the PEO nanofibrous structures, uniform diameter & areal density could be achieved by proper control of charge density, spinneret distance & of spinneret diameter. In the “Wet Electrospinning” process, polyacrylonitrile (PAN) solution with a 7%wt. concentration was spun into a water bath. By SEM observations, the diameter of the produced fiber was found to be ranging from 50nm-500nm. On the basis of these measurements, the optimum height and charge density were determined. Additional experiments were carried out to study the ability to collect oriented fibers into a linear assembly.

In addition to the research being carried out on high damage resistant composites and the processing of nanofibrous assemblies, enormous amount of exploratory research have also been carried out through fruitful collaboration among the various partners in the MURI program (3.3). In summary, this study provides a foundation for the creation of nanoscale fibrous assemblies, which is essential for the manufacturing of scaffolds in tissue engineering and for the design and production of chem/bio protective materials.

3.1 Rotary Electrospinning

The incorporation of nanofibers into textile structures provides an effective means for increasing the surface area per unit mass of textile materials. The high surface area will greatly enhance the capability of clothing to protect against chemical warfare agents, by absorbing the agent and if the surface is properly treated, deactivating the absorbed molecules. By proper use of polymers such as conductive polymer, a large family of electronic devices can be developed for the detection of chemical/bio/mechanical stimuli. In addition to the formation of nonwoven nanofiber assemblies the nanofibers were converted directly into a yarn by air, fluid or various means of mechanical entanglement as well as wrapping onto textile fibers and yarn assemblies.

Table 4. The following material material-process-structure combination have been investigated:

Materials	Process	Structures	Properties
PAN Nylon 6 PEO PLAGA PAN Polycarbonate	Electrospinning Collection (air vortex, fluid,mechanical) Alignment Attenuation Twisting	Homogeneous Hybrid Core spun	Linear density SEM Porosity Pore surface Tensile

A factorial experiment was carried out on PLAGA polymers to study the effect of the electrospinning processing parameters on the physical and mechanical properties of the nanofibrous assemblies. The nanofibrous assemblies were characterized by SEM observations, mercury poresymetry, and tensile stress-strain testing. In addition, Nylon 6 and Polyacrylonitril (PAN) linear nanofibrous assemblies were characterized by physical and mechanical measurements.

It was found that, for the PLAGA nanofibrous structures, uniform fiber diameter and areal density could be achieved by proper control of polymer viscosity and charge density. Nanofiber webs with areal density ranging from 15 to 35 g/m² (0.5 – 1.0 oz./sq.yd) were fabricated. These nanofibrous assemblies are characterized by high porosity, from 85 to 95%, having pore areas ranging from 20 to 100 m²/gm., which is two to three (order of magnitude greater than that of microfibrinous structures and sintered sphere structures. The mechanical properties of these

nanofibrous structures are characterized by high elongation at break, from 70-120% and low strength, from 15 – 25 MPa.

In linear assemblies, nanofibrous yarns with linear density ranging from 6 to 40 deniers have been fabricated. With fiber diameters on the order of 200 to 400 nm, these nanoyarns are characterized by a large number of fibers in the yarn cross-section, close to 0.5 million fibers! Similar to the nanofiber webs, the nanofibrous yarns have a high breaking elongation of over 70% at a significantly higher strength of 40MPa, due to the increase in fiber cohesion as a result of twist insertion. The nanofibrous yarns were subjected to the braiding demonstrating the processability of the nanofibrous materials and consequently, the potential of incorporating multifunction; into various structures of interest to the Army.

The objectives for our research are to:

- Understand the electrospinning process.
- Create nanofiber based structures
- Develop new properties, function.

The following figures demonstrate the ES process to spin aligned fibrous assemblies with a good orientation, Figure 19 shows a schematic of the ES process showing the Taylor cone and the coiled polymer jet which could be aligned into oriented fibrous yarn by increasing the speed of the Rotary disk. SEM photo (Figure 20), clarify the polymer jet behavior to make coils instead of straight fibers. Figure 21 and 22 illustrate the Rotary disk system to align fibers into yarn form.

The parameters controlling the electrospinning; using the Rotary disk system, were studied by applying the Response surface technique (RS). The RS technique combines these parameters as shown in Figure 23. It is clear that to get finer diameters of the nanofibers the diameters or the pipette should be within 1.2-1.4 mm, lowering the height of the spinneret, and achieving the saddle point of the radial distance. Figures 24-25 shows the progress in producing the oriented linear assemblies. At first the nanofibers were random then by using the correct combination of parameters we got oriented nanofibers within the twisted yarn.

By studying the mechanical properties of the nanofibers collected into yarn and nonwoven web, Figure 26-27 shows the high elongation at break with relatively low strength.

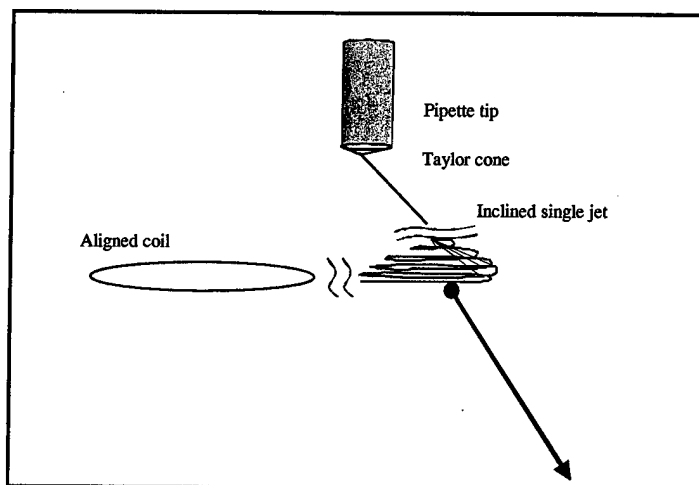


Fig. 19 Schematic diagram of electrospinning process.

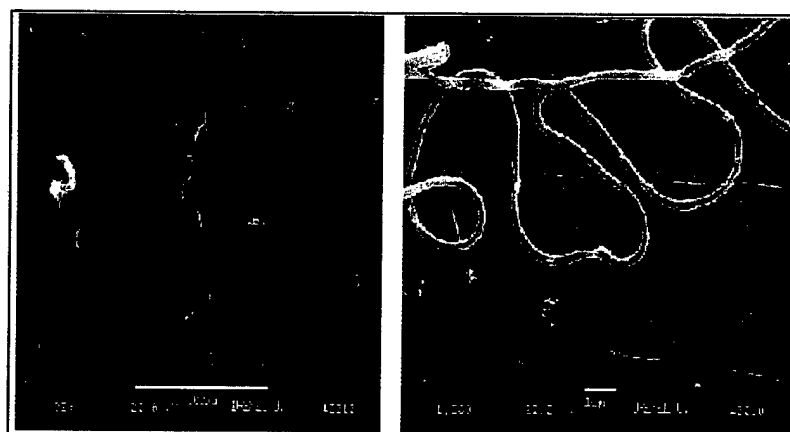


Fig.20 SEM pictures of straight and coiled fibers.

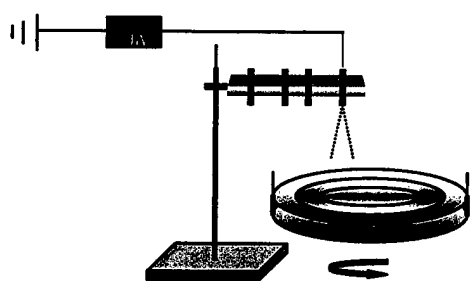


Fig. 21



Fig. 22

Alignment of nanofibers by electrospinning onto rotating disk.

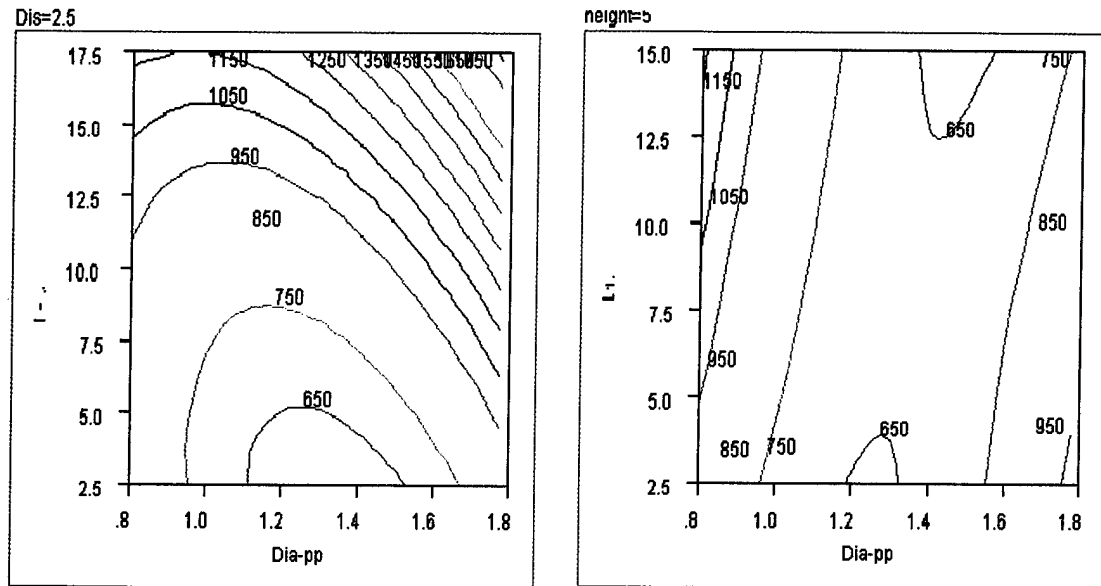


Fig.23 Response Surface diagrams.

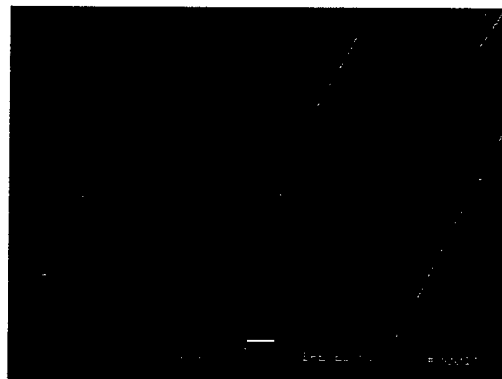


Fig.24 SEM of the relative oriented nanofibers within the yarn.

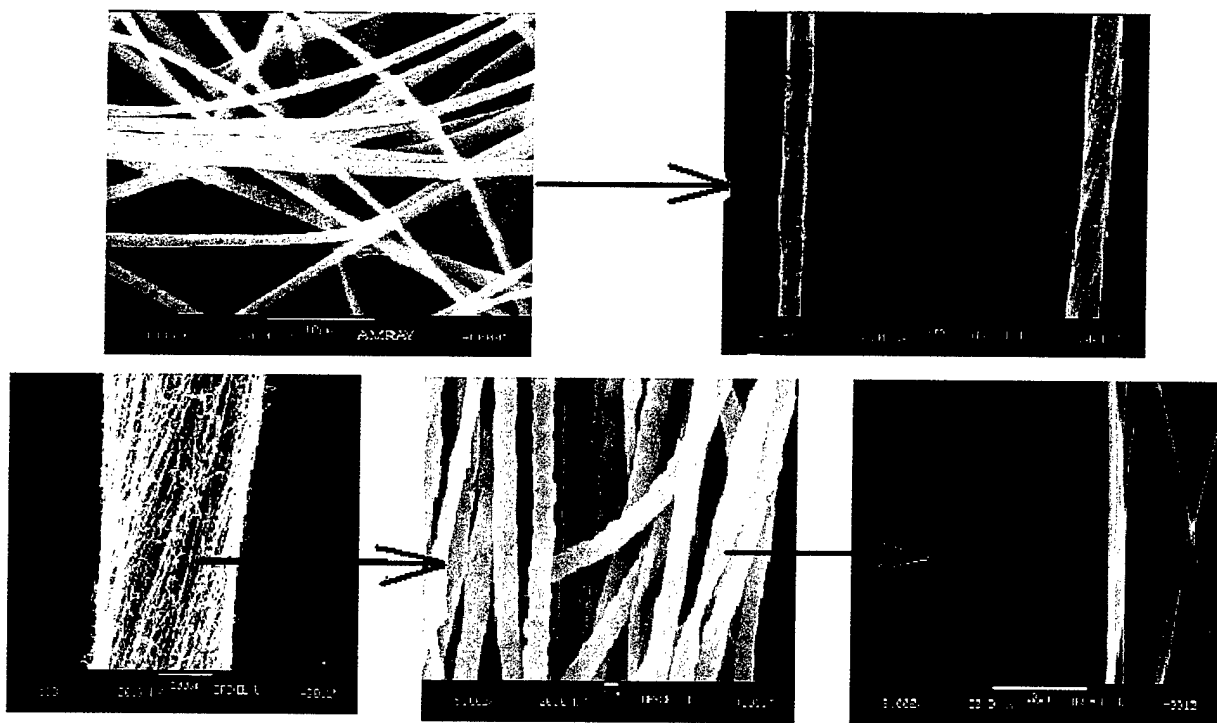


Fig.25 SEM of the relative oriented nanofibers within the yarn.

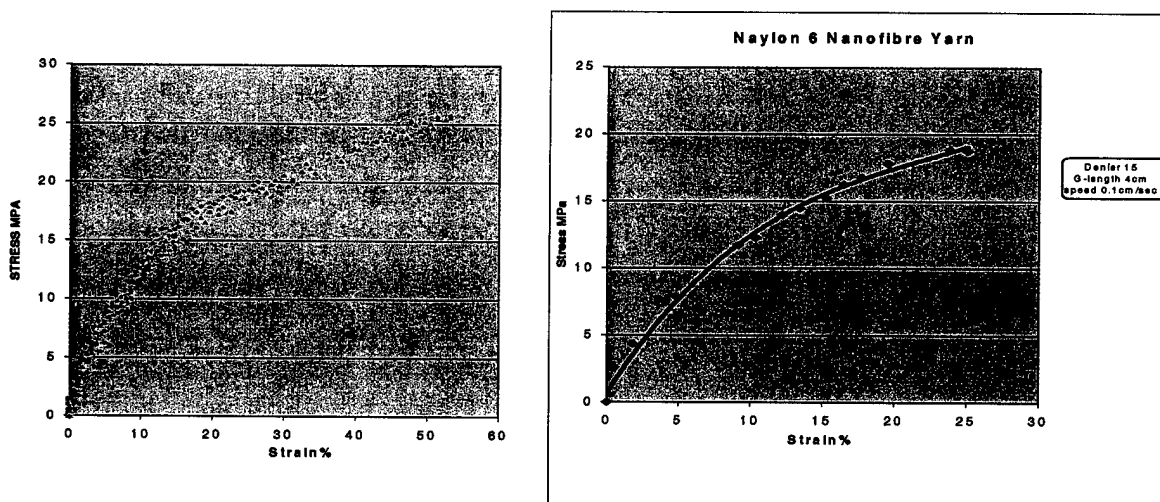


Fig.26 Stress-Strain behavior of Nanofiber yarn.

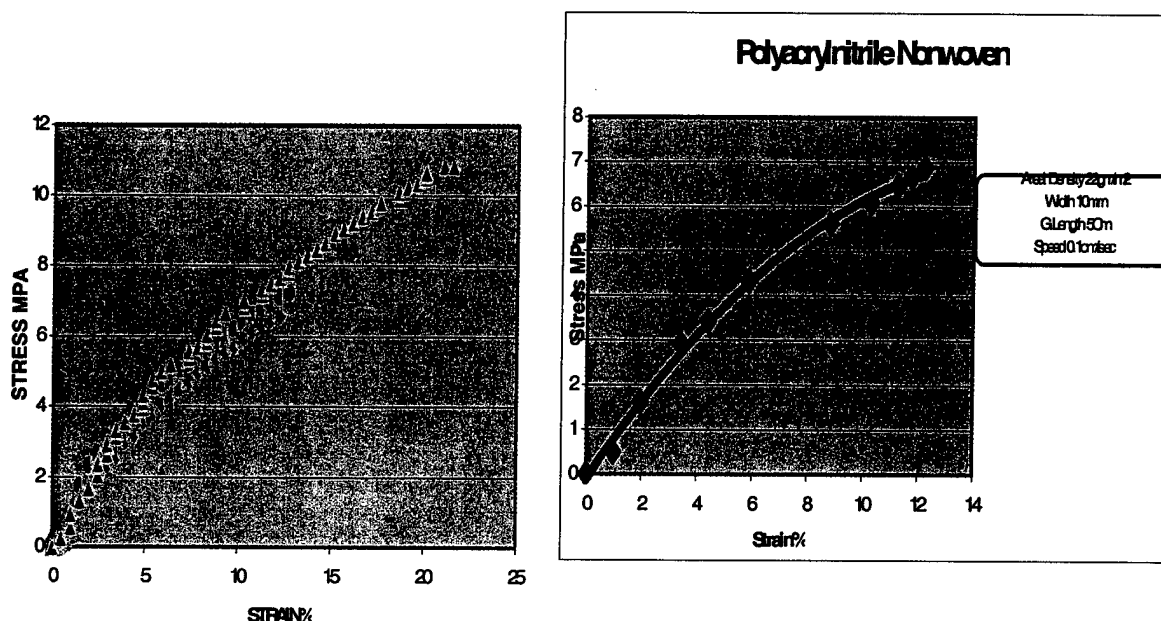


Fig.27 Stress-Strain Behavior of PAN Nonwoven.

In summary

- Nanofiber webs with areal density ranging from 15-100 g/m² were fabricated.
Uniform fiber diameter and areal density could be achieved by proper control of polymer viscosity and charge density.
- These nanofibrous assemblies are characterized by high porosity, from 85-95% having pore areas ranging from 20-100 m²/gm. which is two to three order of magnitude greater than that of microfibrinous structures and sintered sphere structures.
- The mechanical properties of these nanofibrous structures are characterized by high elongation at break, from 70-120% and low strength, from 1-25MPa.
- The nanofibrous yarns were subjected to the braiding demonstrating the processability of the nanofibrous materials and consequently, the potential of incorporating multifunction into various structures of interest to the Army.

3.2 Electro-Spinning with Liquid (Wet) Assist Take-up

Project team: Professors Frank K. Ko, and Ph.D. student Ashraf Ali

Objectives:

- 1- Understand the wet-electro-spinning
- 2- Create nanofiber based structures

Advantages:

The advantages of electrospun non-woven fiber mats for filter applications make these materials excellent candidates for soldier's protective clothing.

A major problem with current protective clothing is that barrier materials designed to keep warfare agents out also prevent the evaporation of perspiration. One method to address this problem is to use nanoporous fluoro-polymer membranes "easily made by wet-electro-spinning technique", which wick perspiration away from the body. However, these membranes are expensive. By using wet-electro-spinning technique, which provides non-woven fabrics with large specific surface area and small pore size, it should be possible to produce fabrics with properties similar to these fluoro-polymer membranes at a much cheaper cost.

Definition:

Wet-electro-spinning is a laboratory technique to produce nanofiber by spinning electrostatic charged polymeric solutions into a grounded wet coagulating bath as shown in Figure 28.

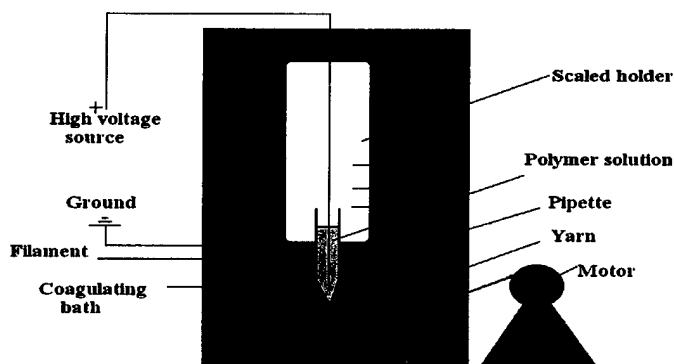


Fig.28 Laboratory station for wet-electro-spinning continuous nanofiber.

Parameters Affecting Wet-Electro-Spinning:

Viscosity of the polymer, μ

Surface tension, γ

Pipette diameter, d

Flow rate, Q

Collector area, A

Inclination angle, θ

Height, H

Charge density, E/H

Parameters selected to be studied first:

-PAN (Polyacrylonitrile) with 7%wt concentration dissolved in N,N-Dimethylformamide.

-Height, H . 10-80 mm

-Charge density, E/H 2.5-20

Results and Discussions:

Effect of Height on Morphology:

As we can see from Figure 29, by changing the spinning height we can get the optimum spinning conditions which is characterized by the most uniform fiber diameter distribution and the minimum average fiber diameter.

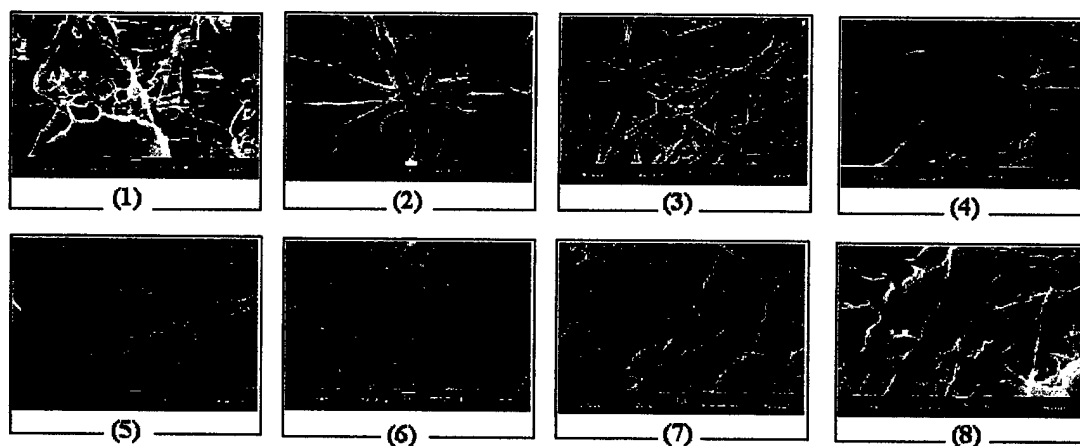


Fig.29 The Effect of height and charge density on the morphology.

Table 5 The Effect of height and charge density on the morphology.

Sample#	1	2	3	4	5	6	7	8
H (mm)	10	20	30	40	50	60	70	80
E (KV)	20	20	20	20	20	20	20	20

Fiber Diameter Distribution:

The fiber diameters have been measured by using SEM Pictures at each height & charge density. A special method invented to be able to measure the fiber diameter distribution across the SEM pictures as shown in Figure 30.

The optimum conditions are given by $H = 50$ mm and $E/H = 0.4$ KV/mm as shown in Figure 31 and Figure 32.

The optimum average fiber diameter required by the wet-electro-spinning process for PAN is 250 nm and the smallest measured fiber diameter was 50 nm.

A predicted relationship between the fiber diameter and the charge density has been developed as follows:

$$d_f = 28.4(E / H)^2 - 301.9(E / H) + 1199.6$$

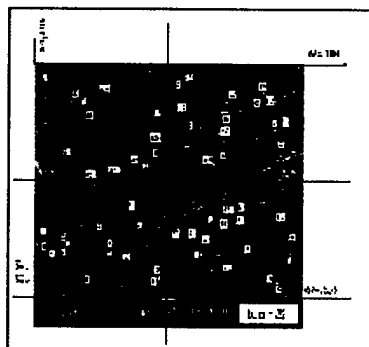


Fig. 30

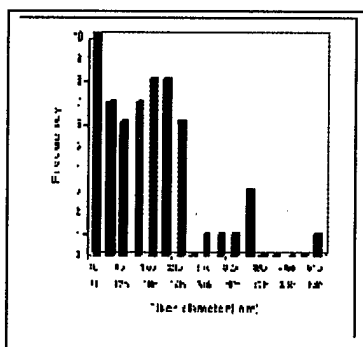


Fig. 31

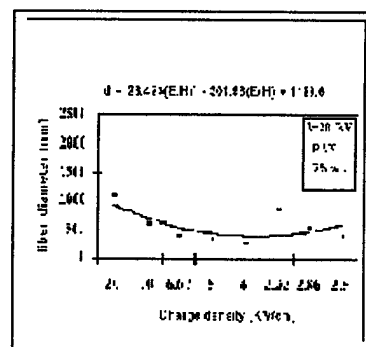


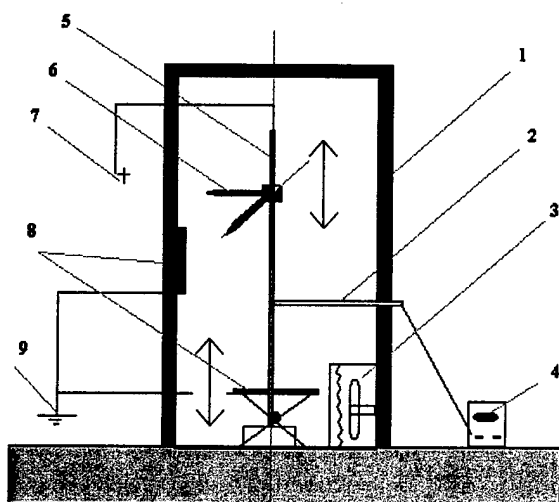
Fig. 32

From this point it is obvious that the idea of producing 100 nm fiber diameters can not be achieved by using the previous wet-spinning station or processing parameters so a new parameters should add to achieve that goal.

In the new work we have two main objectives to achieve:

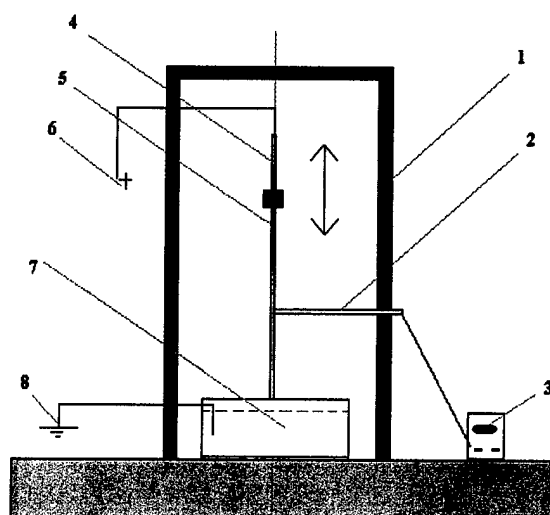
- 1- Producing 100 nm and describe the electrospinning condition for that.
- 2- Producing a continuous yarn of nanofiber diameters.

The following two stations have been prepared two achieve the first goal as shown in the following figures:



- 1- Station environmental control box
- 2- Thermocouple
- 3- Heating fan
- 4- Digital thermometer
- 5- Stand
- 6- Glass pipette
- 7- High voltage source
- 8- Metal screen
- 9- Ground

Fig. 33 Dry Electro-Spinning Station



- 1- Station environmental control box
- 2- Thermocouple
- 3- Digital thermometer
- 4- Stand
- 5- Glass pipette
- 6- High voltage source
- 7- Water bath
- 8- Ground

Fig. 34 Wet Electro-Spinning Station

According to the survey the most important parameters that may affect the electro-spinning process are the distance between spinneret and target, polymer concentration, Berry number, viscosity, surface tension, electric volt density, atmosphere condition, pipette diameter, and the collector type.

Some of these parameters have been selected in our PAN system as follows:

- 1- Concentration; c by weight% (6, 9 & 12)
- 2- Height; H in cm (10, 15 & 20)
- 3- Charge density; E/H in KV/cm (1, 1.5 & 2)
- 4- Solvent type; bp in $^{\circ}\text{C}$ (153, 171 & 189)
- 5- Environmental temperature; T in $^{\circ}\text{C}$ (23, 35 & 47)
- 6- Spinning angle; θ in degree (0, 45 & 90)
- 7- Wet vs. dry collectors

Fibers of Polyacrylonitrile (PAN) are the precursor of 90% of the produced carbon fibers. It is generally thought that the better the degree of molecular orientation in the original PAN fiber, the better the mechanical properties, in particular the modulus of the resultant fibers.

The electro-spinning technique, a method for making very small diameter fibers, was applied under different processing conditions to achieve fiber diameter within the nanometer range. Concentrations of the PAN in DMF, height, environmental temperature, spinning angle, solvent boiling point and wet vs. dry collectors have been studied. The resulting fiber diameters were examined using SEM. The results showed an important role of the assigned processing parameters in the diameter of the produced fiber. By varying the above parameters, 100 nm PAN fiber diameter has been achieved.

Till now and up to our knowledge there is no continuously yarns produced by using the electro spinning technique for any of the electro spun polymer solutions, which give a limitation of using these small produced fibers in the textile applications.

This work states the first step to produce a continuously electro spun yarns by using the PAN polymer solution.

The Effect of Processing Parameters On the Morphology Of Electro-Spun PAN Fibers

1) Concentration effect on PAN fiber formation

As shown in Figure 35 the SEM picture divided into four equal regions then same amount of measured fibers took from each quarter. The fiber distribution took bimodal shape as it can be seen from Fig. 36.

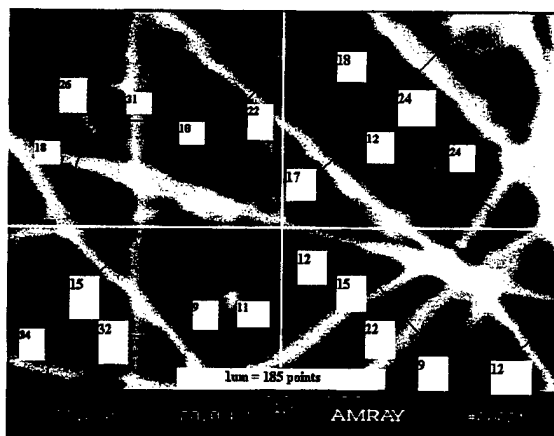


Fig.35 SEM picture for PAN + DMF C=6%, H= 15 cm, and E/H=1.5 KV/cm.

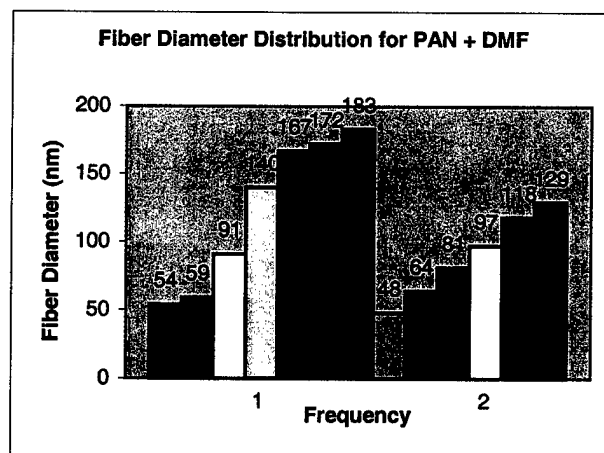


Fig.36 Fiber Diameter Distribution

As shown in Figure 37 and Figure 38, the relationship made between the fiber diameter and the concentration in PAN polymer solutions by using two different solvents the results show that the fiber diameter decreases as the polymer concentration decreases which has a good agreement with the all other electro-spun polymer solutions in the literatures.

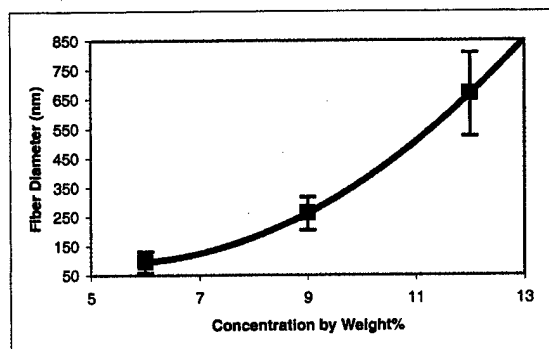


Fig.37 Effect of Concentration on Fiber Diameter for PAN and DMF System.

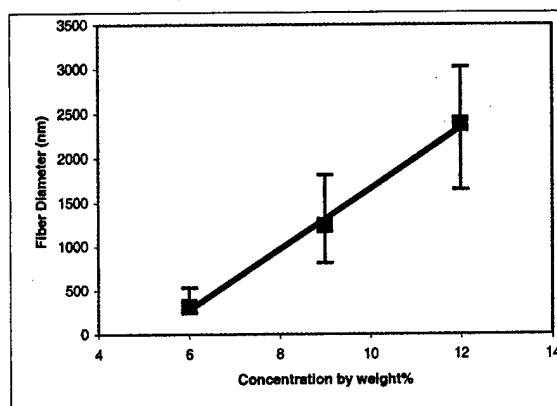


Fig.38 Effect of Concentration on Fiber Diameter for PAN and DMSO System.

Also from the figures it can empirically conclude that the governing equation for the PAN and DMF system is a parabolic relation that for a 15 cm height and 1.5 KV/cm charge density and can given as follows:

$$d_f (\text{nm}) = 13.2 (c\%)^2 - 142.3(c\%) + 473.8$$

On the other hand for the PAN and DMSO system the relation is linear and following the same trend and it governed by the following equation at 15 cm height and 1.5 KV/cm charge density:

$$d_f (\text{nm}) = 344.39 (c\%) - 1783.7$$

These results can easily explained from the effect of the evaporation amount of solvent from the same jet diameter in each case.

prove some kind of relationship between the degree of entanglement inside the polymer solution and the fiber diameter distribution.

As the amount of solvent increases inside the jet the produced fiber diameters will decrease.

Also we can conclude from the figures that: as the concentration increases the fiber distribution or in another words, the standard deviation increases which can be explained from the effect of Berry number and the degree of entanglement inside the polymer solution as can be seen by compare the values of the standard deviation in both figures.

To prove this correlation let us first measure the intrinsic viscosity of PAN + DMF and PAN + DMSO systems then calculate the values of Be# at two different concentrations.

As shown in Figures (39 & 40) for PAN + DMF and PAN + DMSO systems the measured intrinsic viscosity = 1.1142 and 1.766 respectively and the calculated Be# values, which is the product of the concentration in the intrinsic viscosity, for the first at 9% & 12% concentrations and the second at 6% & 9% concentrations are almost equal (10.03 g/dl & 13.40 g/dl for the first and 10.60 g/dl & 15.90 for the second respectively).

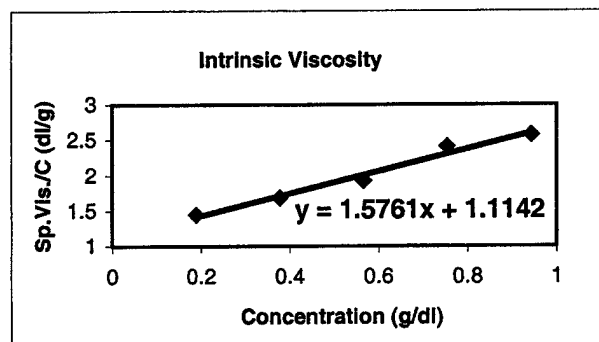


Fig.39 Intrinsic Viscosity of PAN + DMF System

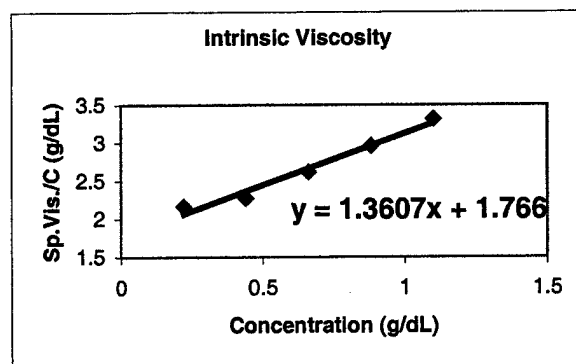


Fig.40 Intrinsic Viscosity of PAN + DMSO System

On the other hand the calculated standard deviation values are 56.92 & 262.3 for the first and 92.27 & 366.7 for the second respectively, which approve some kind of relationship between the degree of entanglement inside the polymer solution and the fiber diameter distribution.

2) Height effect on PAN fiber formation

It is shown that in Figure 41 as the height increases the fiber diameter distribution increases; the governing equation for the average fiber diameter is parabolic and shows an increase in the fiber diameter as the height increases is as follows:

$$d_f \text{ (nm)} = 2.646H^2 - 56.57H + 515.5$$

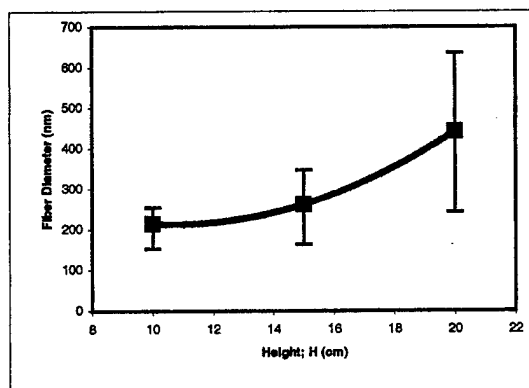


Fig.41 Effect of Height on Fiber Diameter For PAN + DMF System.

From the figure, we can say that there is no significant effect of the height from 10 to 15 cm on the fiber diameter but there is a significant effect on the fiber distribution. At heights in excess of 15 cm, there is a significant effect on fiber diameter and distribution.

In this experiment we kept the charge density in each case equal to 1.5 KV/cm and concentration of 9% in each case.

Theoretically speaking, any one expect to get smaller fiber diameter by increasing the height due to the longer path that the jet will travel till it hits the target which is completely in the opposite side for our results so, the only explanation up to our knowledge we can introduce is the change in the flow rate due to changing of the height which may be the only left logic reason.

3) Charge density effect on PAN fiber formation

As shown in Figure 42 the effect of the charge density on the fiber diameter distribution is very clear and the distribution increases as E/H increases. That is can be explained from the effect of the charge density on the size of the hanged droplet. When E/H reach 1 KV/cm the electric field is sufficient to over comes the surface tension of the hanged polymer solution droplet and forming a Taylor cone size related to the size of the droplet. Eventually the size of the droplet is smaller than the size of the pipette diameter. As the charge density increases from 1 to 1.5 KV/cm for same height the hanged droplet disappeared and the Taylor cone formed at the tip of the pipette which is larger in diameter than that one formed from the hanged droplet, for more prove see reference [8], so the formed fibers in this case are larger in diameter than the previous one, further more if the charge density increases to 2 KV/cm the jet comes out also from the orifice of the pipette not only that but splitting into many jets which is the parameter reduced the fiber diameter from case two to three.

The effect of the charge density on the average fiber diameter can be described by the following parabolic relation:

$$d_f(\text{nm}) = -641.6(E/H)^2 + 2074.8(E/H) - 715.2$$

This relation describes the effect of the charge density on the fiber diameter and distribution for 9% concentration and a 15 cm height.

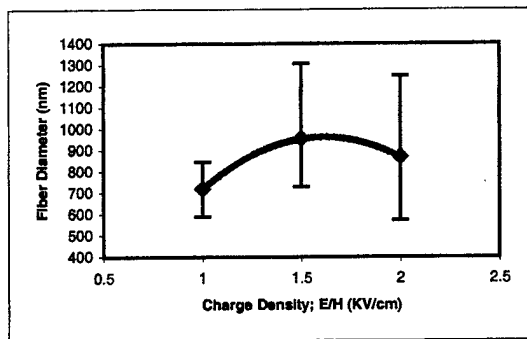


Fig.42 Effect of Charge Density on Fiber Diameter for PAN + (50%DMF + 50%DMSO) System.

4) Solvent effect on PAN fiber formation

In this experiment the effect of the solvent; which can be described here by its effect on the intrinsic viscosity of the polymer solution at same concentration was studied. PAN with 100%DMF, PAN with 50%DMF+50%DMSO, and PAN with 100% DMSO were prepared at 9% concentration and spun at 15 cm height with charge density of 1.5 KV/cm in room temperature. The SEM results can be seen in Figure 43.

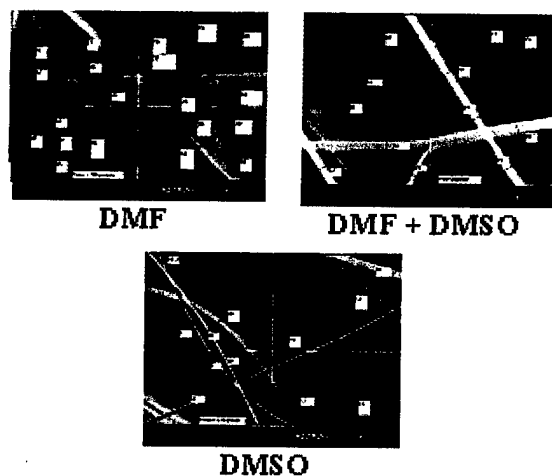


Fig.43 SEM results for different solvents.

The effect of the solvent on the fiber diameter and its distribution can be seen in figure 44.

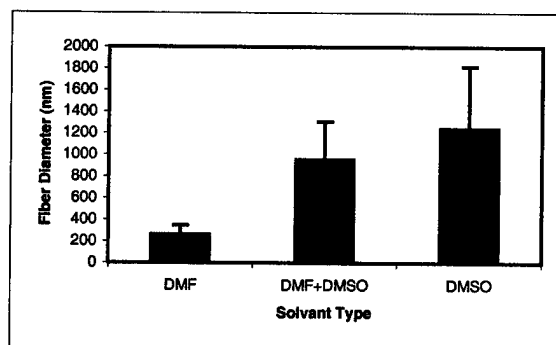


Fig.44 Effect of solvent Type on Fiber Diameter.

As can be seen from the figure, the intrinsic viscosity of the PAN + solvent system increases the fiber diameter and distribution also the rate of evaporation of the solvent is a restricted parameter by its boiling point and as the boiling point increases the evaporation rate and amount within the same height decreases then the fiber diameter increases.

5) Environmental temperature effect on PAN fiber formation:

From the previous experiment, it can be concluded that if the rate of evaporation of the solvent is increased the fiber diameter and its distribution will decrease. Therefore the following experiment will be conducted using the same spinning conditions, $H = 15$ cm, $C = 9\%$ wt., $E/H = 1.5$ KV/cm, and changing the temperature inside the station. The net results can be seen in the following figure.

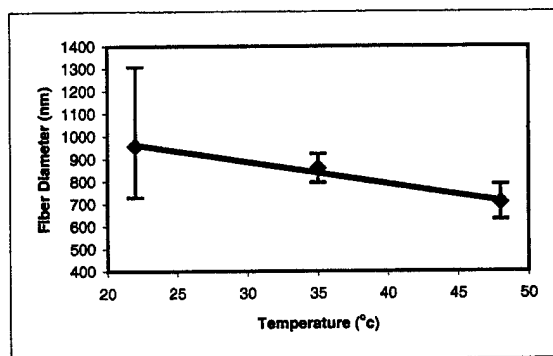


Fig.45 Effect of Environmental Temperature in the Fiber Diameter of PAN + (50%DMF + 50%DMSO)

Also from the Figure 45 it can be concluded that the effect of the temperature is linear and is describable by the following equation:

$$d_f (\text{nm}) = -9.6019(T) + 1173.9$$

6) Spinning angle effect on PAN fiber formation

In some of the low concentration solutions it is necessary to tilt the pipette at an angle to avoid droplets interfering with the collected fibers. This experiment was conducted to study the effect of the spinning angle on the fiber formation under the following conditions:

$$H = 15 \text{ cm, } E/H = 1.5 \text{ KV/cm, and } C = 9\%.$$

The results can be shown in the following figure.

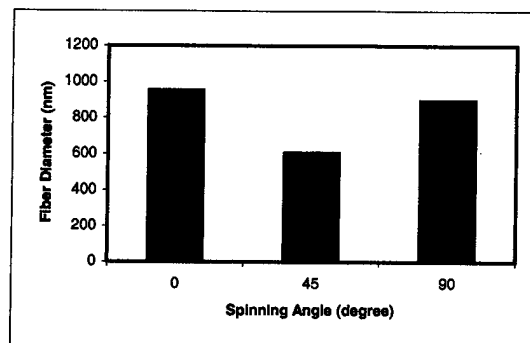


Fig.46 Effect of Spinning Angle on Fiber Diameter for PAN + (DMF 50% + DMSO 50%).

From the figure it can be concluded that a 45-degree angle may help in reducing the fiber diameter.

This can be explained since a longer path must be traveled by the jet under the tilted angle more than the directed one.

7) *Wet vs. dry effect on PAN fiber formation*

It was thought that by removing all of the solvent inside the ejected jet before it completely dried the fiber diameter would be reduced; therefore the following experiment was conducted.

Figure 47 shows the SEM pictures in the wet and dry spinning conditions.

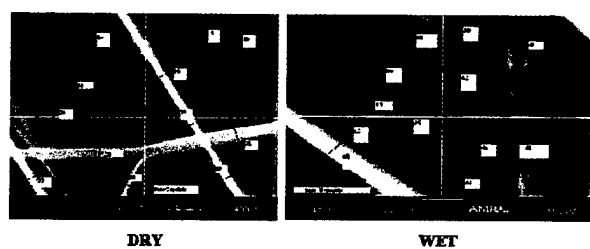


Fig.47 SEM Results for Different Collector Types.

As can be seen from Figure 48, the diameters of the fibers spun in water are much lower than that spun onto the metal screen. Also it can be seen that there is improvement in the fiber distribution from dry to wet spinning. The spinning conditions for both are: $H = 15\text{cm}$, $E/H = 1.5\text{KV/cm}$, and $C = 9\%$.

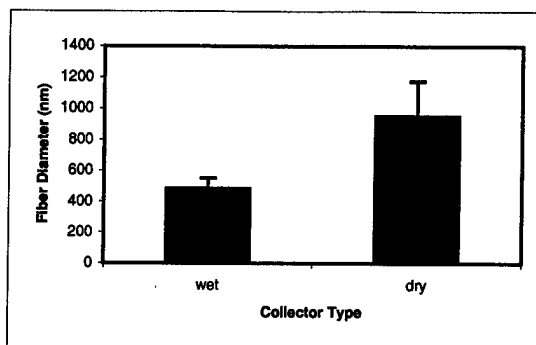


Fig.48 Effect of Dry vs. Wet Spinning for PAN + (DMF 50% + DMSO 50%)

Continuously Electro spun PAN Yarn: Phenomenon description and Yarn Properties

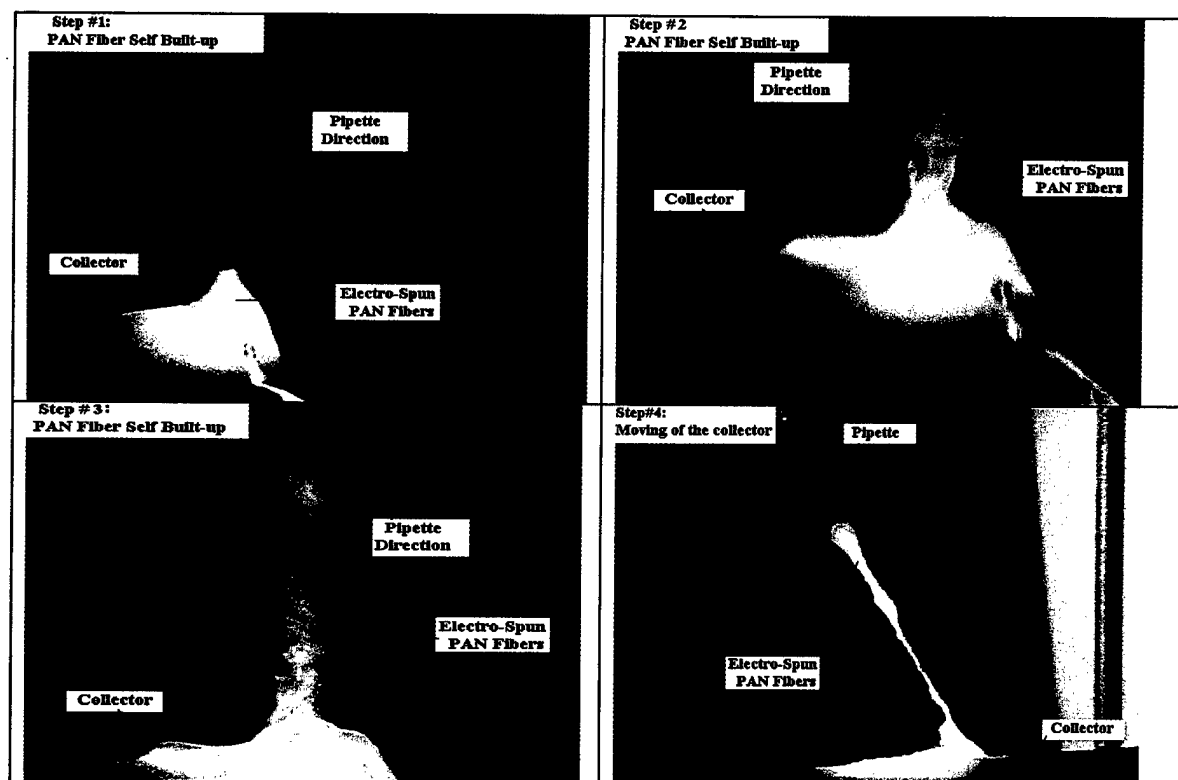


Fig.49 Life Pictures for the Continuous Electro-Spun Yarn with Stationary Collector.

Take-up system:

From Figure 49 the idea of producing continuous Electro-spun nano-fiber PAN yarns can be started and the parameters should be taking into consideration will be:

- 1- Height (H)
- 2- Charge (E; + vs. -) its sign and values

- 3- Concentration (C% wt.)
- 4- Solvent (DMF vs. DMSO)
- 5- Spinning angle (θ)
- 6- Spinneret diameters and materials (d and glass vs. metal)
- 7- Take-up linear speed (v)
- 8- Polymer solution volume (V)

An experimental set up system has been designed to study the previous parameters and there effects on the continuous producing yarn phenomenon.

Figure 50 shows the take-up system set up used to get the working window of the yarn formation phenomenon. Also it shows sequences of pictures taking during the take-up process and after it done.

As shown in Figure 50 the produced yarn recollected in a glass tube and specimens out of it were taken to study its properties. Some of these properties have been compared with the regular produced random pattern PAN nano-fiber.

The results of the working window for the phenomenon can be stated generally as in the following table.

Table 6 Working window for the continuous yarn phenomenon.

Height; H (cm)	Charge; (kV) & + vs. -	C% wt.	Solvent DMF vs. DMSO	Spinning angle; θ (degree)	Spinneret diameter and material	Take-up linear speed; v (m/sec)	Polymer solution volume; V (ml)
6-12 cm	15-25 & both work	5-8 DMF with low and high Mw 5-7 DMSO with low and high Mw	Both work with low and high Mw	From 0-90 all work	0.9 mm glass 0.6 & 0.8 mm steel needles	Less or equal 0.025	0.1ml and up

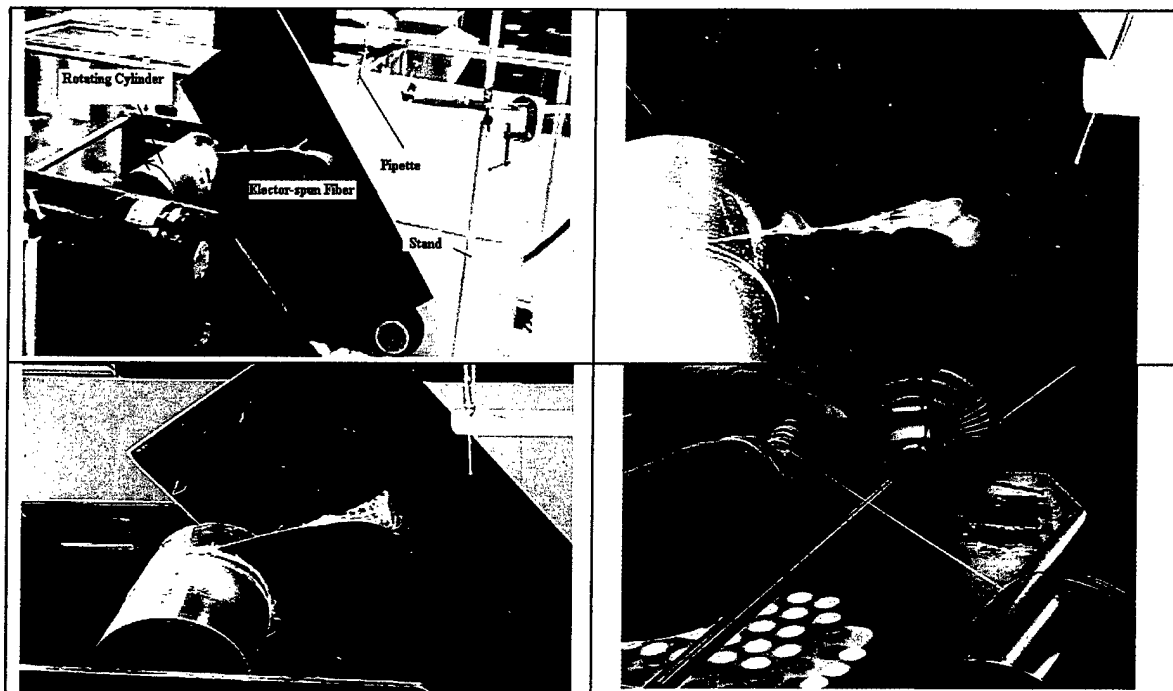


Fig.50 Life Pictures for the Continuous Electro-Spun Yarn with Rotating Collector.

Yarn Specifications:

1) X-Ray Diffraction

The most important characteristic that the textile engineer tries to establish in the producing fiber is the orientation and the crystal lenity.

In the following experiment the comparison between two samples, the first one is the random pattern electro spun PAN sample and the second one is the continuously produced electro spun yarn, has been conducted by using the X-ray diffraction.

As shown in Figure 51, both samples gave a peak at approximately $2\theta = 18^\circ$ also as we can see in the figure the yarn sample gives narrower peak than the random pattern one which indicates that the produced yarn has more crystal lenity and the fibers are more aligned.

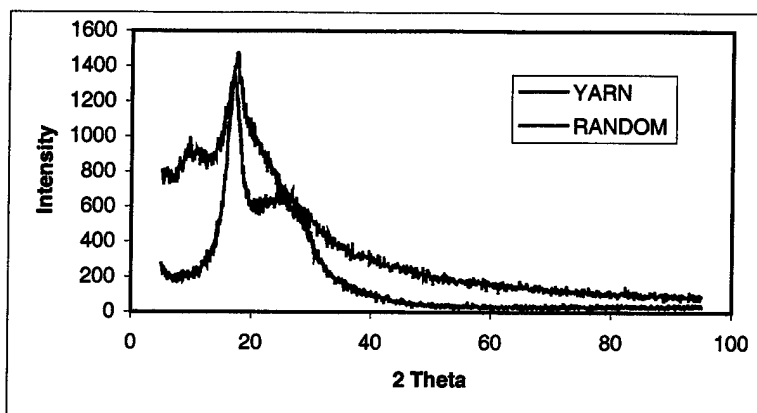


Fig.51 X-Ray Diffraction for Both Yarn and Random Pattern fibers.

2) Mechanical Properties:

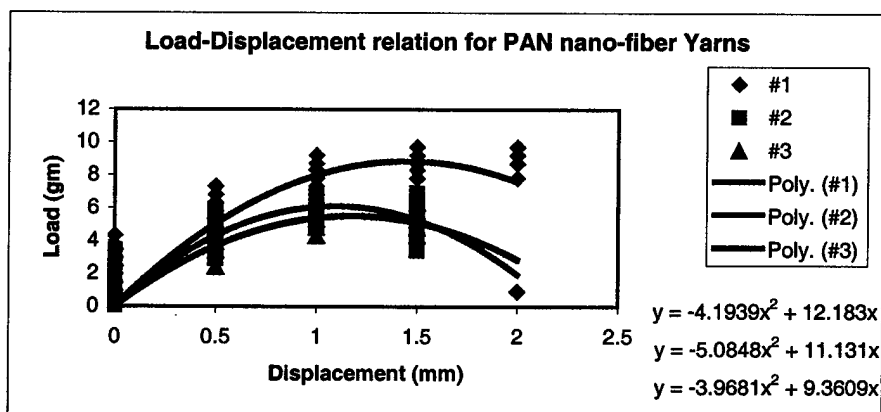


Fig. 52 Load-Displacement relationship for the produced yarn.

From Figure 52 and after the weighting of the samples the average results for the three samples are as follows:

Yarn Properties:

Yarn average denier = 61 denier

Average maximum load = 7.63gm

Average maximum strength = 11.24MPa

Average yield strength = 9.54MPa

Average Modulus = 0.48GPa

Fiber Properties:

The fiber properties can be calculated from the governing equation in the mechanics of the in plan random fiber.

Average fiber strength = 38MPa

Average fiber modulus = 1.91GPa

3.3 Multifunction Tailoring through Nanofiber Technology

In addition to the research being carried out on high damage resistant composites and the processing of nanofibrous assemblies, enormous amount of exploratory research have also been carried out through fruitful collaboration among the various partners in the MURI program. The most significant are our collaboration with Professor Alan MacDiarmid at the University of Pennsylvania and Professor Reneker at the University of Akron as well as with several other colleagues at Drexel University. These collaborative researches have significant implications for the next generations of multifunctional, intelligent fibrous structures. These exploratory research activities are organized into four general areas:

3.3.1 Electroactive Nanofibers and Fibrous Assemblies (with Professor Alan MacDiarmid)

Electrically conducting blends of PAn.HCSA in a variety of different conventional polymers such as PEO, polystyrene, polyacrylonitrile, etc. have been produced. For example, ~ 20 wt% blends of PAn.HCSA in polystyrene (Mw 114,200) are obtained by electrospinning a chloroform solution; fiber diameter characteristics: average, 85.8 nm; maximum, 100.0 nm; minimum 72.0 nm. These fibers are sufficiently electrically conductive that their SEMs may be recorded without the necessity of applying a gold coating.

Current/voltage (I/V) curves are given in for a single 419 nm diameter fiber (Fiber 1) of a blend of 50 wt% PAn.HCSA and polyethylene oxide collected on a silicon wafer coated with a thin layer of SiO₂. Two gold electrodes separated by 60.3 μ m are deposited on the fiber after its

deposition on the substrate. The conductivity (two probe) of the electrospun fiber (diameter 419-600 nm) is $\sim 10^{-1}$ S/cm. Non-linear I/V curves may be obtained from some polyaniline samples, possibly caused by the presence of defect sites induced by imperfections or impurities in the polyaniline. Such imperfections are expected to be more apparent in thin fibers since there are fewer molecular pathways by which charge carriers can by-pass the defect sites.

3.3.2 Bioactive Nanofibers and Fibrous Assemblies (with Professor Andrew Fertala and Professor Cato Laurencin)

Nanofibrillar three-dimensional matrices were prepared from mixtures of poly(L-lactic acid) and poly(β -CBZ-lysine) by the electrostatic spinning process. The matrices were coated with genetically engineered recombinant collagen II variants and used as a support for chondrocyte attachment and spreading. It was found that there is a significant difference in the morphology of cells grown as a mono-layer on the surface of a plastic dish and the cells cultured in the three-dimensional gels or scaffolds. For example, as analyzed by transmission electron microscopy of a mouse cartilage, the average diameter of chondrocytes is 10 μ m, whereas the same chondrocytes seeded onto two-dimensional planes have a diameter of about 40 μ m. To study how the different collagen II regions promote migration of chondrocytes through three-dimensional matrices, nanofibrillar materials coated with collagen II variants were fabricated and used in the migration assays. The cells were seeded onto matrices and, after 48 hrs of culture, examined by scanning electron microscopy. Cells seeded onto matrices coated with full-length collagen and -D3 collagen migrated into the openings of the matrices. Similar behavior was characterized with cells seeded onto matrices coated with -D1 or -D2 collagen II variants. In contrast, the chondrocytes seeded onto matrices coated with -D4 collagen or bovine serum albumin had a tendency to form clusters and remain on the surface of the nanofibrous material. The bioactive nanofibers have been shown to provide favorable surfaces for cell adhesion and mechanical compliance for cell migration.

3.3.3 Ultrasensitive Sensors from Nanofiber Films (with Professor Ryszard Lec)

The feasibility of using thin polymeric films made of nanofibers as ultrahigh sensitive (UHS) piezoelectric gas sensor interface has been carried out. Thin films made of nanofibers have surface area approximately one to two orders of the magnitude larger than continuous films, and hence their potential gas sensitivities. The studied nanofibers were made of Poly-Lactic Acid-Co-Glycolic Acid (PLAGA) polymers with the diameters ranging from 50 to 500 nanometers. The films were deposited on the gold surface of piezoelectric resonant sensors using electrospinning techniques. Different physical and chemical properties of the films and their relation to the various deposition conditions were determined. The UHS sensor application in the medical, pharmaceutical, chemical and environmental industries were determined.

The UHS sensor operates based on mass changes due to the physico-chemical processes between nanofiber and gas molecules, UHS sensor can detect the presence of the gas. These changes influence electrical sensor properties, such as the transfer function, the resonant frequency or the resonant amplitude and can be directly related to the gas concentration. The following illustrate the sensor and nanofiber film deposited on the gold surface of piezoelectric resonant sensors.

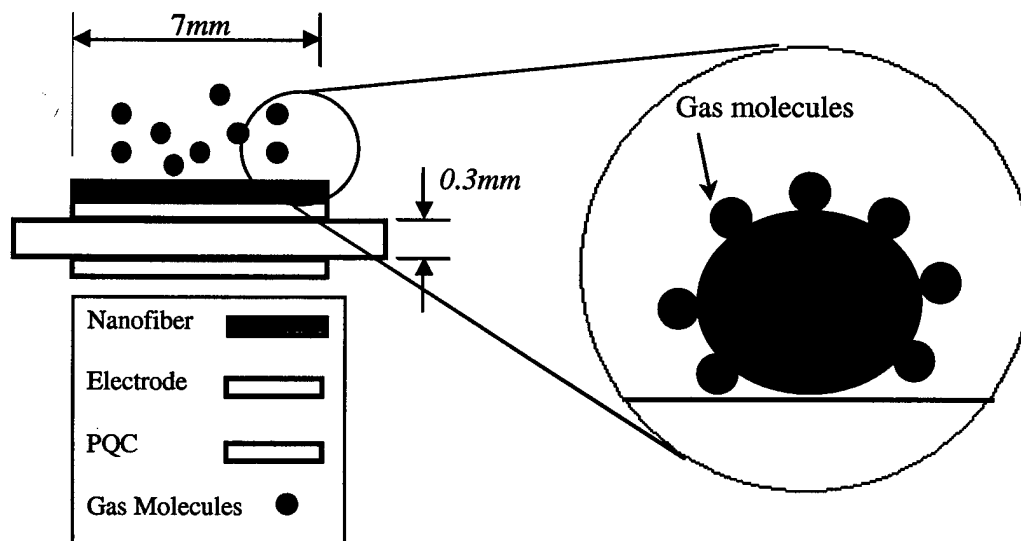


Fig.53



Prototype UHS sensor
($f_r = 10\text{MHz}$)

Fig.54

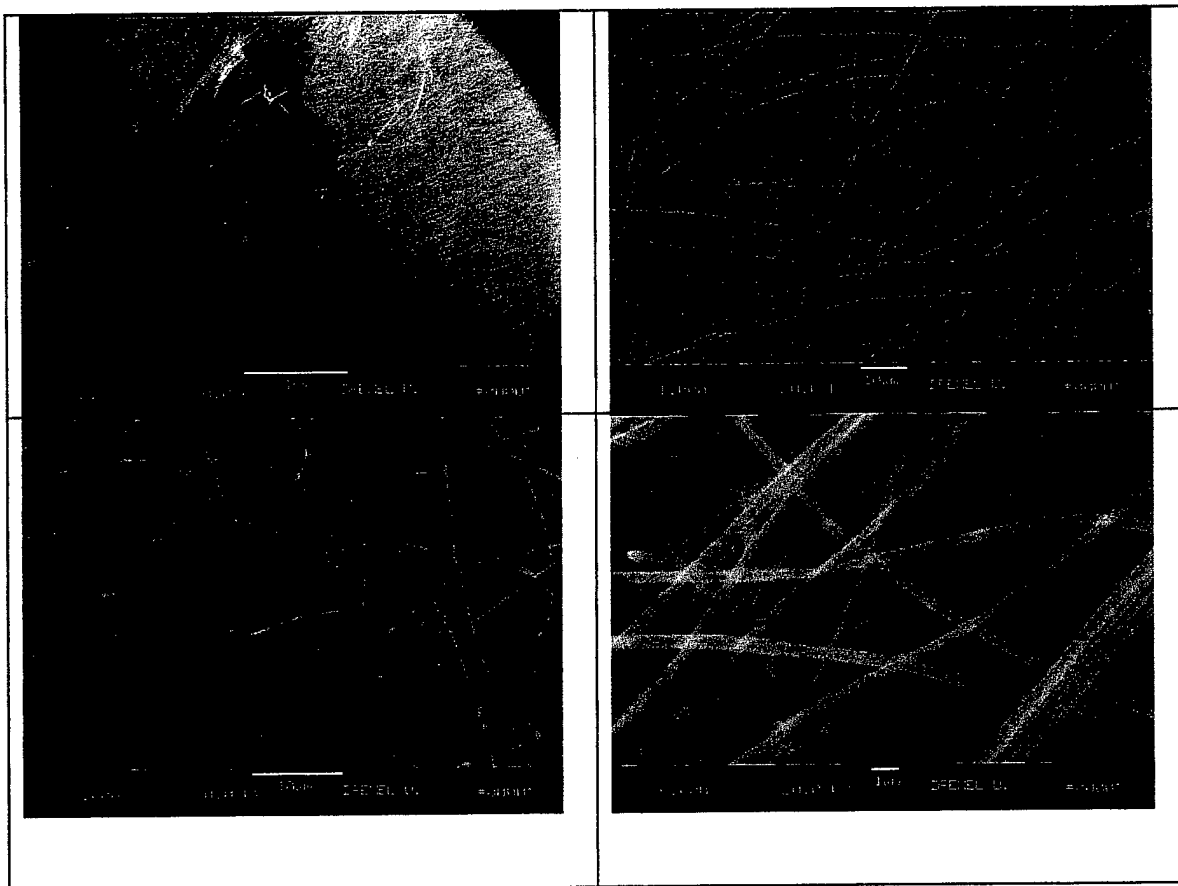


Fig.55

3.3.4 Carbon Nanofibers and Nanocomposites (with Professor Yury Gogotsi, Professor Christopher Li, and Professor Guoliang Yang)

Polyacrylonitrile fibers produced by electrospinning may be thermally converted to carbon nanofibers with some shrinkage. We have similarly converted a polyacrylonitrile fiber (diameter 750 nm) to a carbon fiber by first heating at 200°C in air for 20 minutes followed by heating at 800°C for 2 hours under nitrogen. A current/voltage curve was obtained for a 600 nm diameter carbon fiber. The controlled conversion of organic electrospun polymer fibers presents interesting opportunities for the fabrication of a variety of carbon nanofibers. These ultrafine fibers may also serve as a precursor for ceramic fibers. In addition, carbon nanotube and SiC ceramic particles have been co-electrospun with a polymer matrix to form nanocomposite fibrils.

Purified single wall nanotubes were used to process polymer fiber mat containing carbon nanotubes. Carbon nanotubes were mixed with the polymer solution by sonication. The continuous flow and the electromagnetic field produced by the opposite charge of the source and collecting plate during electrospinning help the alignment of the nanotubes, which is necessary to achieve maximum conductivity. The nanoscale of the polymer fibers also help to align the polymer fibers in a well-organized way than filtered or casted polymer films. With wrapping of the highly self-adhesive nanotubes, and using proper nanotube/polymer concentration under certain voltage of electrospinning nanotube/polymer composite was successfully produced.

Characterizations of the composite were done as follows:

Transmission electron microscopy:

Transmission Electron microscopy was performed to confirm the presence of nanotubes in polymer fibers. The images (mgf.180666) showed polymer fibers are holding a large number of nanotubes. The nanotubes appear to be embedded into the fiber surface. Figure 56 shows a polyacrylonitrile fiber with a diameter of 132.5 nanometer holding 10 to 12 tubular structures around its periphery per unit length. The tubes are closely packed and look like entanglement with each other. The diameters of the nanotubes were measured 16 to 20 nanometers.

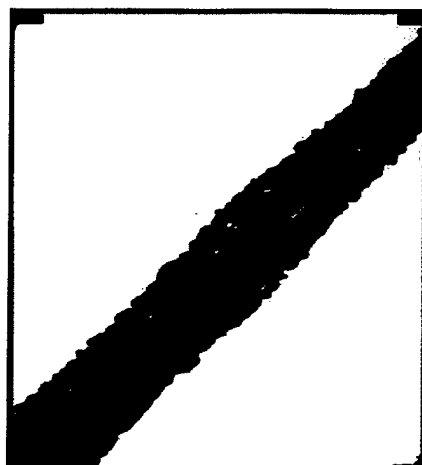


Fig.56 TEM of CNT polymer fiber.

Atomic Force Microscopy:

Tapping mode atomic force microscopy was performed for the nanotube containing polymer fibers and compared with the AFM of polymer fibers without nanotubes. Significant difference was found between the two samples. Figure 57 shows polymer fiber spun with nanotubes (scan size: 3.030) with diameters from 600 nanometers to one micron, appeared to be covered with closely packed patch like structures with diameters ranging from 105 to 154 nanometers.

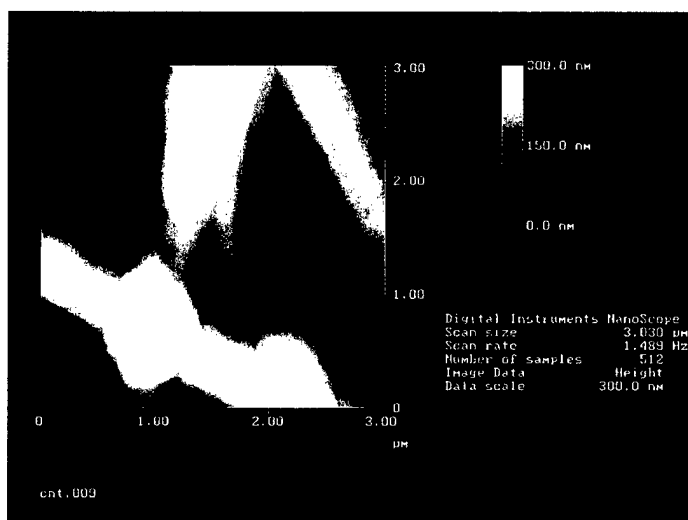


Fig.57 AFM of CNT-PAN fiber.

On the other hand, in Figure 58 (scan size 2.943 μm) the PAN fibers without nanotubes showed no such covered structure rather they appeared to be very smooth continuous fibers.

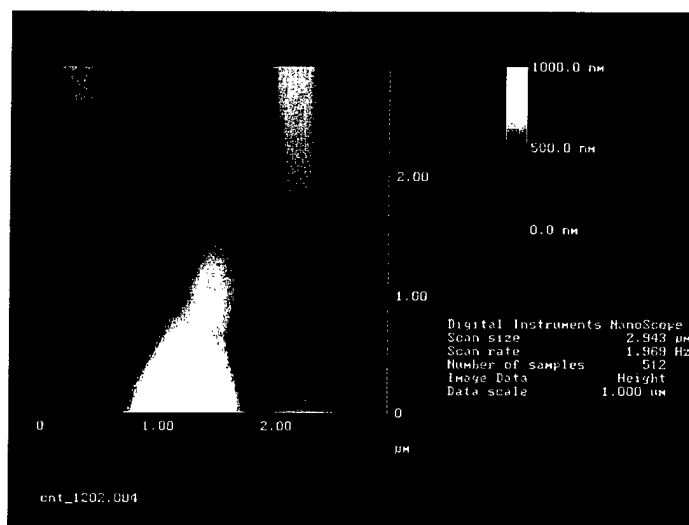


Figure 58: AFM of PAN fibers.

X-Ray Diffraction Study:

Comparative x-ray diffraction of polymer fibers with and without nanotubes was performed and the polymer fiber mat with nanotubes showed more crystallinity than the one without nanotubes.

Raman Electron Microscopy:

This characterization indicated the presence of nanotubes in the polymer fiber mat.

The co-electrospinning process introduced as a means to align and carry the CNT in the form of nanocomposite fibrils; thus form the precursor for linear, planar and 3D fiber assemblies for macrocomposites. A hierarchical fiber architecture based design methodology is offered in this part of the project, to account for the contribution of these nanocomposite fibril building blocks over the entire structure length scales from the CNT level to the macrostructural level. Preliminary experimental results showed that key to realization of the potential of CNT is to overcome the challenges in dispersing and aligning the CNT in the polymer matrices.

Carbon nanotubes (CNTs) are seamless graphene tubule structures with nanometer-size diameters and high aspect ratios. This new class of one-dimensional material is shown to have exceptional mechanical, thermal and novel electronic properties. The elastic moduli of the CNTs are in the range of 1-5 TPa and fracture strains of 1 to 30%, both are about a factor of ~100 better than those of the commercial carbon fibers which typically have 0.1-0.5 TPa elastic moduli and 0.1-2% fracture strains. The factor of 100 enhancement in strength implies that, for the same performance, replacing the commercial carbon fibers with CNTs will lead to significant reduction in the volume and weight of the structural composites currently used in space applications.

Based on a recent NASA study by Harris et. al using micromechanics computation, as shown in Table 7, it was concluded that an order of magnitude increase in specific modulus can be achieved with CNT composites. However, it was also recognized that it would be significantly more challenging in the conversion of CNT to useful structures.

Table 7. Properties of SWNT and their Composites

Properties	Aluminum 2219-T87	IM7/8552 Quasi-isotropic Composite	CNT/Polymer Quasi-isotropic Composite (1)	CNT SWNT Crystal
Tensile strength (GPa)	0.46	1.3	2.5	180
Tensile Modulus (GPa)	73	58	240	1200
Rupture Elongation(%)	10	1.6	6	15
Density (g/cc)	2.83	1.59	0.98	1.2
Specific Strength	0.16	0.80	2.5	170
Specific Modulus	26	36	240	1000
Thermal Conductivity (W/mK)	121	5	5	5000
Manufacturability (2)	9	6-9	1	1

(1) based on 60% fiber volume fraction in a quasi-isotropic laminate, with strength at 1% strain

(2) manufacturability rating, in the range of 0 to 10, with 10 being the best.

In addition to potential applications as high performance fibers, carbon nanotubes are shown to have promising materials properties for applications as hydrogen storage materials, high energy capacity battery electrodes, and cold-cathode electron emitters. Depending on their chiralities and

diameters, CNTs can be either semiconducting or metallic. The electrical conductivity of the metallic CNTs is (6000 S/cm) significantly higher than the best commercial carbon fibers. Because of their high degree of graphitization, CNTs are expected to have higher thermal conductivity than the best carbon fibers (2000 W/m-K).

Despite their promises, most of the current studies are limited to the physics and chemistry of individual CNTs. There is limited knowledge on the properties of macroscopic materials comprising CNTs as the basic building blocks for macroscopic structures. It is still not clear whether the superb properties observed at the individual molecular level can be utilized in the macroscopic structures. For example, most of the studies on nanotube - polymer composites have been on electron microscopy investigation of deformation of the individual CNTs embedded in polymeric matrices. No significant enhancement in the mechanical strength has been achieved in nanotube-polymer composites, presumably due to the weak interface between CNTs and composites. In order to realize the exciting potential of CNT, there is a need for processing methodologies and robust manufacturing technology to convert the CNT to macroscopic structures. To assure proper translation of the properties of CNT to the structural level, an integrated design for manufacturing methodology reflecting the hierarchical structural geometry must be available. Accordingly, it is the objective of this paper to introduce a concept that converts CNT into nano scale filamentous composites by the co-electrospinning process. Using these CNT composite filaments as building blocks, a framework for hierarchical design for manufacturing will be presented.

The Concept of CNT Nanocomposite Fibrils

It is well known that the translation of reinforcement properties to the composite depends on the alignment or orientation θ , of the reinforcement for a given volume fraction of the reinforcement, V_f , with θ and V_f functions of fiber architecture as illustrated in Figure 59. It shows the range of obtainable elastic moduli for various composites normalized by the fiber modulus E_f , versus the appropriate fiber volume for the fiber architecture indicated.

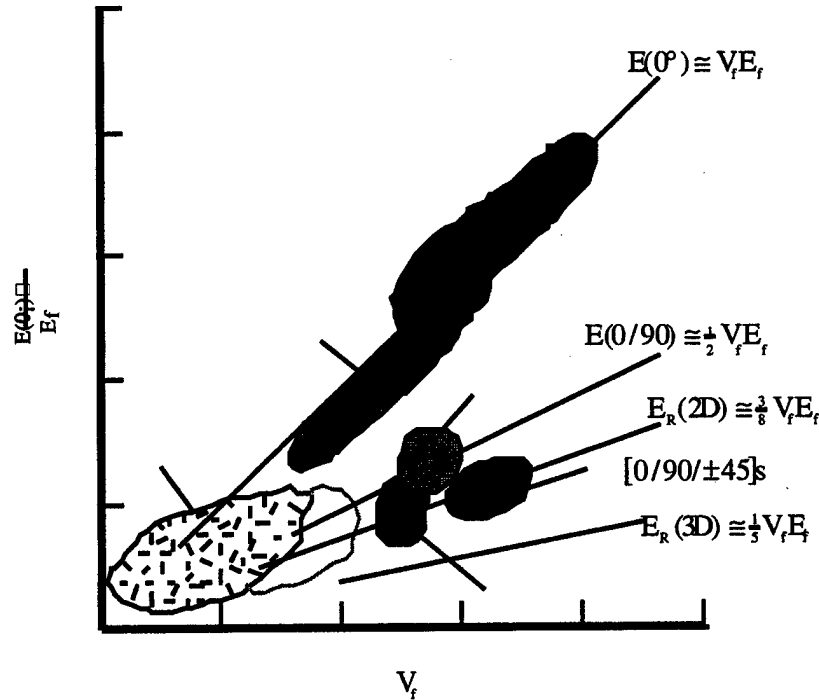


Fig.59 Effect of fiber architecture on material property translation in fiber reinforced composites

CNTs are expected to have highly anisotropic mechanical, thermal, and electrical properties. To measure and utilize these anisotropic properties, many attempts have been made to fabricate materials with controllable degree of CNT alignment. These methods include:

- A. mechanical stretching - nanotubes can be aligned inside polymeric matrices by mechanical stretching and developed procedures to determine the direction and the degree of alignment;
- B. roll-cast- membranes CNTs embedded in thermoplastic matrices by solution cast and produced composites with uniaxially aligned SWNTs by mechanical shearing;
- C. magnetic alignment - thick film of SWNT and ropes are aligned by filtration/deposition from suspension in strong magnetic fields.

A new method, the co-electrospinning method, is demonstrated in this study by spinning mixtures of CNT and polymer solution to form aligned nanocomposite fibrils by the electrospinning process. Electrospinning is an electrostatic induced self-assembly process wherein ultrafine fibers down to the nanoscale are produced. In the electrospinning process, a high voltage electric

field is generated between an oppositely charged polymer fluid contained in a glass syringe with a capillary tip and a metallic collection screen. Once the voltage reaches a critical value, the charge overcomes the surface tension of the suspended polymer with cone formed on the capillary tip of the syringe (spinneret or glass pipette) and a jet of ultrafine fibers is produced. As the charged polymer jets are spun, the solvent quickly evaporates and the fibrils are accumulated on the surface of the collecting screen. This results in a nonwoven mesh of nano to micron scale fibers. A nanoscale fiber is called a fibril. Varying the charge density, polymer solution concentration and the duration of electrospinning can control the fiber diameter and mesh thickness. A schematic illustration and an example of a composite formed by the process are shown in Figure 60a. The concept of CNT nanocomposites (CNTNC) can be illustrated in Figure 60b, showing the orientation of the CNT in a polymer matrix through the electrospinning process by flow and charge induced orientation as well as confinement of the CNT in a nanocomposite filament.

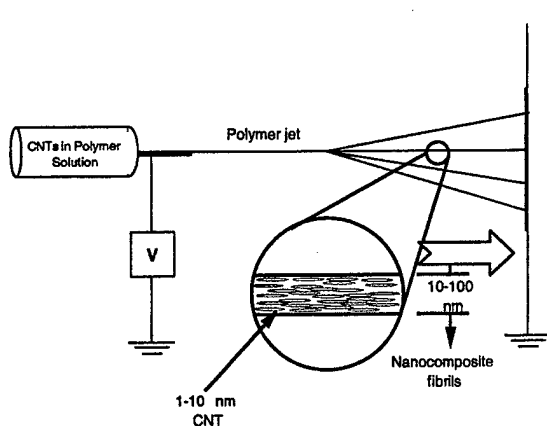


Figure 60a Co-electrospinning of CNT

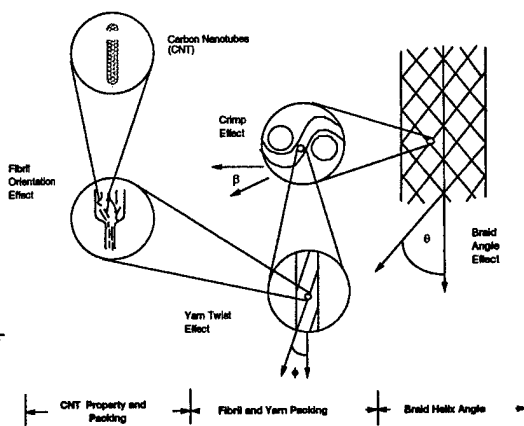


Figure 60b. Concept of CNTC

The nanofibril composite can also be subsequently deposited as a spunbonded nanofibril mat for subsequent processing into composites or for use as a nonwoven mat (Figure 65). Alternately, by proper manipulation, the CNTNC filaments can be aligned as a flat composite filament bundle or twisted to further enhance handling and/or tailoring of properties in higher order textile preforms for structural composites. As shown in Figure 60b, by twisting the nanocomposite fibrils, off-axis angular orientation may be introduced to the nanocomposite filament in order to tailor the composite filament modulus.

Modeling of CNTNC

Geometric Properties of CNTNC

The translation of properties to macrostructures begins with a consideration of the packing of the CNT. Depending on the nature of the CNT packing, the volume fraction of CNT can range from .75 to .90 for open, square and close packing as shown in Figure 61.

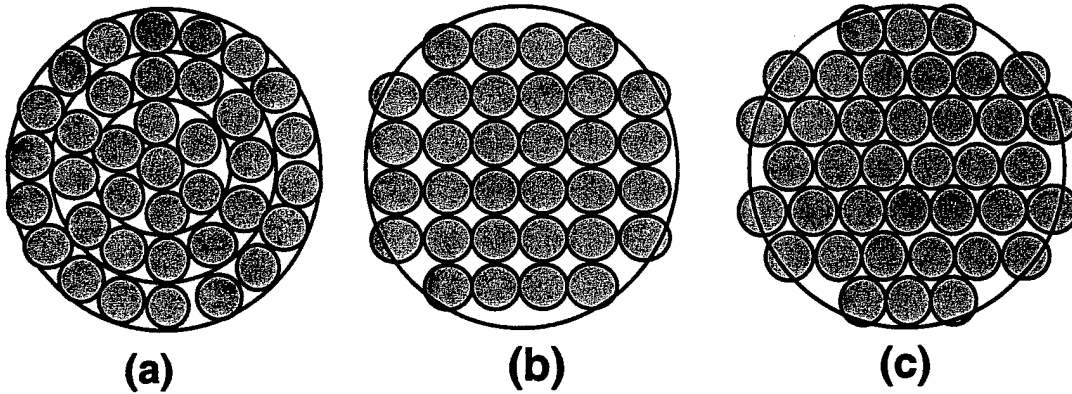


Fig.61 Idealized fibrillar packings:
(a) open packing; (b) square packing; (c) close packing.

A twisted bundle of fibrils is called a yarn wherein the fibrils are no longer aligned to the yarn axis. Instead, the fibrils assume helixial geometry in the yarn, as shown in Figure 62a. For fibril yarn composites, fiber volume fraction is equivalent to its fiber packing fraction, and related to fibril helix angle, θ , fibril diameter, d , and number of twist per unit length, T , by equation (1):

$$V_f = \left[d + \frac{\tan \theta}{\pi T} \right]^{-2} \quad (1)$$

For a 12K yarn with 100 nm diameter fibrils, the relationship between fibril volume fraction, fibril orientation (surface helix angle), and twist level can be established as shown in Figure 62b. Clearly, for a given twist inserted to the fibril bundle, fibril volume fraction decreases as fibril orientation angle increases.

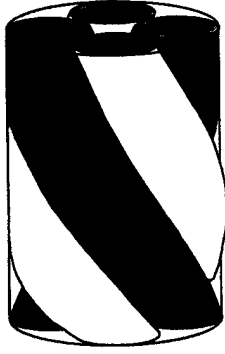


Figure 62a. Geometry of twisted yarn

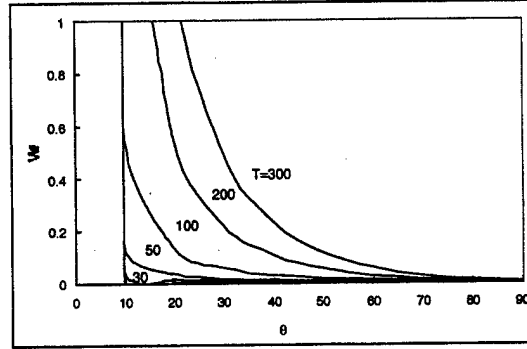


Figure 62b. Relationship of fibril volume fraction to fibril orientation at various twist levels.

Mechanical Properties of CNTNC

As shown in Figure 60b, a macrocomposite consists of several structural levels at multiple length scales. Starting from the CNT level, one may predict the macrocomposite properties using micromechanics models such as the Fabric Geometry Model (FGM). Conversely, one may also test the macrocomposites and back out the CNT properties. The mechanical properties of the nanocomposite fibril, as a first approximation, may be modeled as a short fiber composite with CNT playing the role of a short fiber that has a high aspect ratio. For an aligned CNT fibril assembly of CNT of length l , the longitudinal modulus is given by:

$$E_{\text{fibril}} = \eta_l E_{\text{cnt}} v_{\text{cnt}} + E_m (1 - v_{\text{cnt}}) \quad (2)$$

where, v_{cnt} is the volume fraction of the CNT, E_{cnt} is the longitudinal modulus of the CNT and E_m is the modulus of the matrix material. η_l is an efficiency parameter and is given by:

$$\eta_l = 1 - \frac{\tanh(\frac{1}{2}\beta l)}{\frac{1}{2}\beta l} \quad (3)$$

l is the length of the CNT and θ is given by:

$$\beta = \sqrt{\frac{8G_m}{E_{\text{cnt}} d^2 \ln \frac{2R}{d}}} \quad (4)$$

G_m is the shear modulus of the matrix, d is the fibril diameter and $2R$ is the inter-fibril spacing.

For a twisted assembly of the nanocomposite fibrils embedded in a resin matrix that we will call yarn composite, with fibril orientation of ϕ , The modulus of the yarn composite can be related to the modulus of CNT by equation (5):

$$E_{\text{fibril}} = \eta E_{\text{cnt}} v_{\text{cnt}} \cos^4 \phi + E_m (1 - v_{\text{cnt}}) \quad (5)$$

By taking the packing density of CNT and fibrils into consideration, using the CNT properties shown in Table 8 the tensile modulus of the composite fibril and yarn can be plotted as a function of CNT and fibril orientation respectively in Figures 63a and 63b:

Table 8 CNT and Polymer Matrix Properties

CNT	
Elasticity, E_{cnt}	1 TPa
Length, l	1000 nm
Diameter, d	1 nm
Matrix	
Elasticity, E_m	3.5 GPa

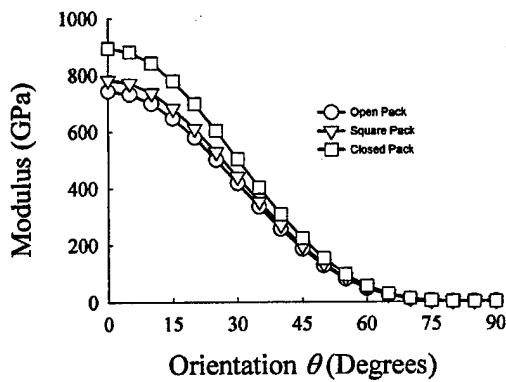


Figure 63a. Longitudinal modulus of the fibril as a function of orientation of the CNT

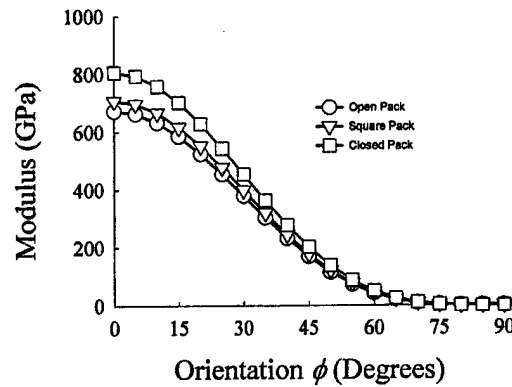


Figure 63b. Longitudinal modulus of the yarn composite as a function of orientation of the fibril

For a close packed CNT fibril, it can be seen in Figures 63a and 63b that the tensile moduli for the fibril and composite yarn are 895 and 807 GPa respectively. Assume a 60% fibril volume fraction as in most of the structural composites the moduli of the unidirectional composite and quasi isotropic composite consisting of the CNT fibrils are 538 and 203 GPa respectively. This agrees well with the prediction by Harris et.al. showing a more than three fold increase in modulus compared to aluminum and high modulus carbon fiber reinforced composites. For a spun bonded mat with randomly oriented CNT with 30% fibril fraction, the estimated tensile modulus is 100 GPa!

Fabrication of CNTNC by Co-electrospinning

To demonstrate the co-electrospun CNTNC concept, SWNT bundles were synthesized by ablating a graphite target containing Ni/Co metal catalysts (0.3 atm% each) using a 1064nm Nd:YAG laser in a Ar-filled furnace at 1150°C. The raw SWNT are shown in Figure 64a. The raw material was refluxed in 20% H₂O₂ solution at 100°C for 6 hours then filtered and rinsed well with methyl alcohol assisted by ultrasonication after the ultrasonication in the CS₂ and methyl alcohol 1:1 mixture for 2 hours. After well dried in the air, the sample was annealed in 6.3×10^{-6} Torr vacuum at 200°C for 4 hours and then at 1000°C for 1 hour. The purified material is shown in Figure 64b.

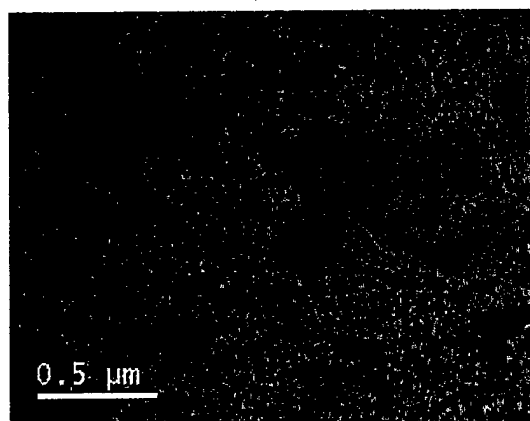


Figure 64a. Raw SWNT materials

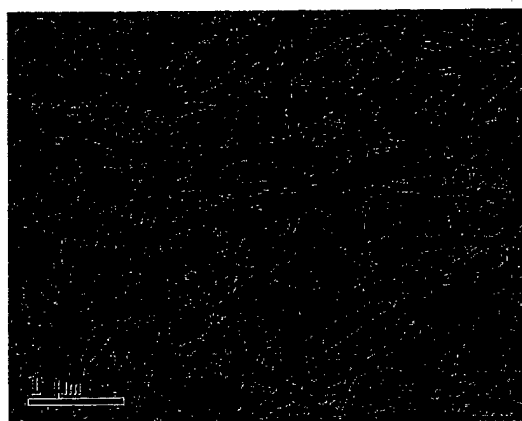


Figure 64b. Purified SWNT material

The CNT were dispersed in polyethylene oxide (PEO) with an appropriate surfactant so that the CNT are distributed uniformly in the polymer solution for subsequent formation of the CNT composite fibrils by the electrospinning process. The PEO/CNT systems were processed in two solvents, chloroform and water. A 95:5 mixtures by weight of PEO and CNT were mixed with 3% by weight solvent concentration of chloroform and water respectively.

Electrospinning for the PEO/CNT/Chloroform and PEO/CNT/water system were carried out with an electric field strength of 3.0 and 0.75 KV/cm. The nominal spinneret diameter was 1 mm. In the case of water base system, a 0.11 weight % of Polystyrene Sulfuric Acid was added to further disperse the CNT. The CNT fibrils are shown in Figures 65a and 65b using chloroform and water as solvent respectively. In Figures 66a the straight fibril and stretched coil fibrils are shown. Figure 66b is a close-up of the fibril showing the tendency of the CNT to cluster along the length

of the fibril indicating that better dispersion of the CNT is required in order to produce fine fibrils with well aligned CNT.

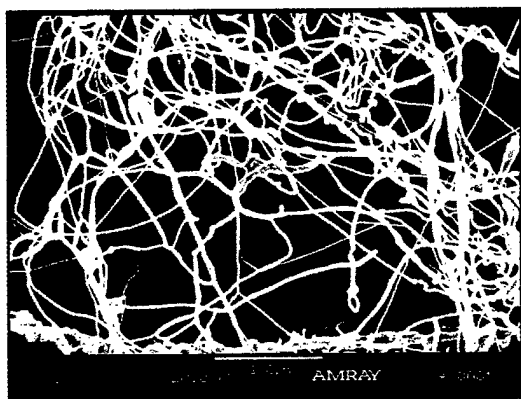


Figure 65a. Fibril mat of PEO co-spun with CNT from Chloroform solution

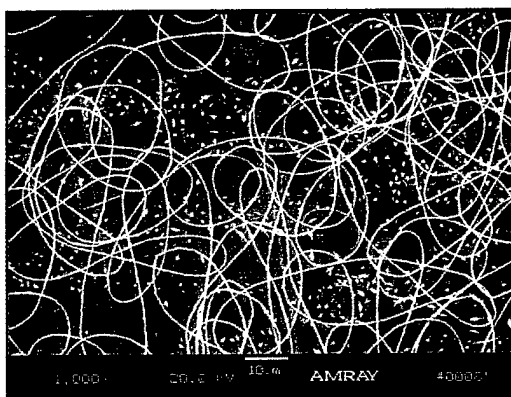


Figure 65b: Fibril mat of PEO co-spun with CNT from water solution 2,000x



Figure 66a. Oriented and coil fibril of PEO co-spun with CNT (using Chloroform as solvent) 100x

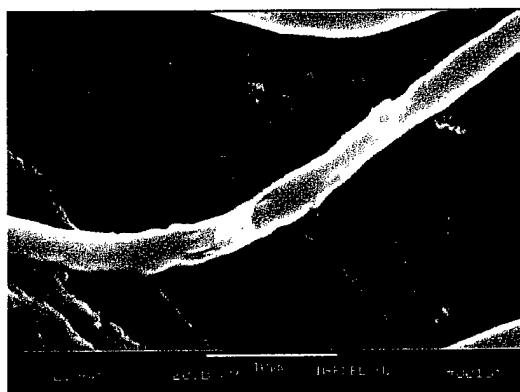


Figure 66b. Single fibril of PEO co-spun with CNT (using Chloroform as solvent) 2,960x showing clusters of CNT in the fibril

It must be noted that the simple model that we employed in this study is based on traditional composite micro mechanics. Many of the unique features of the CNT such as the transverse properties; the interfacial characteristics; the unusually high elongation at break have not been considered. What is the failure behavior of the CNT composite? How does CNT react with metal, ceramic and carbon matrix? How does the “nano effect “ of the CNT interact with the macro scale structures? Thus, there is plenty of challenging processing and analytical problems ahead as well as ample opportunities to uncover the exciting properties of CNT based composites.

3.3.5 The Effect of Molecular Conformation of Poly(L-lactic acid) in Chloroform Solution on the Morphology of Electrospun Nanofibers (paper presented at Fiber Society Meeting 2001)

Electrospinning is a unique process that produces continuous polymer fibers with diameters ranging over several orders of magnitude, from the micrometer range typical of conventional fibers, down to the nanometer range. Non-woven textiles composed of electrospun fibers have a large specific surface area and small pore size compared to commercial textiles, making them excellent candidates for use in filtration and membrane applications. In addition, the possibility of manipulating them into three-dimensional structures during deposition has implicated their use in biomedical applications such as scaffoldings for tissue growth. Biodegradable aliphatic polyesters like poly(lactic acid) (PLA) are of particular interest for tissue engineering. This is largely due to their biocompatibility and to their resorbability through natural pathways.

While the process of electrospinning has been known for over half a century, current understanding of the process and those parameters, which influence the properties of the fibers produced from it, is very limited. This contribution is dedicated to the influence of polymer molecular conformation in solution, described by a dimensionless Berry number (Be), on electrospinning of Poly(L-lactic acid)/Chloroform system:

$$Be = [\eta]c$$

Where $[\eta]$ is the intrinsic viscosity of the polymer ($[\eta]$ =the ratio of specific viscosity to concentration at infinite dilution) and c is the concentration of the solution.

It has been found that the degree of entanglement of polymer chains in solution can be described by Be . When the polymer is in a very dilute solution, polymer molecules are so far apart in the solution that individual molecules rarely touch each other and Be is less than unity. When the polymer concentration is increased, at some overlap concentration the individual molecules interact, from many contacts, and therefore become entangled; Be is then greater than unity.

In this work, we have compared and evaluated systematically the effects of Berry number on the morphology of electrospun nanofibers of two different molecular weights.

C. List of Publications and Technical Reports

Ko, F., Sun, W., Zavaliangos, A., Jovicic, J., El-Shiekh, A., and Song, J.: "Integrated Design for Manufacturing of Composite Helmets", Symposium on "The Design and Integration of Helmet Systems", December 2-5, 1997, Framingham, Massachusetts.

Jovan Jovicic, Antonios Zavaliangos and Frank Ko: Modeling of the Ballistic Behavior of Gradient Design Composite Armor", *Symposium on Recent Developments in the Study of Impacts on Composite Materials*. ASME 1999 Mechanics and Materials Conference, Blacksburg, VA, June 27-30, 1999.

Frank K. Ko, Jun Chang and John Song "Optimization of Performance of Gradient Composite Armor" *12TH International Conference on Composite Materials*, 5th-9th July 1999 Paris France.

Frank K. Ko, Jun Chang and John Song "Optimization of Performance of gradient Composite Armor", *NIDA*, Orlando, Florida, August, 1999.

Ian D. Norris, Manal Shaker, Frank K. Ko and Alan g. MacDiarmid: "Electrospinnig of Ultrafine Fibers from Polyaniline/Polyethylene Oxide Blends. *Synthetic Metals*, Elsevier Science. Vol. 114 (2000), 109-114.

Ko, F.K., and Laurencin, C.T.: Three Dimensional Fibrous Scaffolds for Tissue Engineering", Book of Abstracts, *Fifth International Conference on Frontiers of Polymers and Advanced Materials and NATO Advanced Research Workshop on Polymers and Composites for Special Applications*, Poznan, Poland, June 21-25, 1999.

M.Shaker, F.Ko, and J.Song: "Comparison of the Low and High Velocity Impact Response of Kevlar Fiber-Reinforced Epoxy Composites". *Journal of Composite Technology and Research*. Vol. 21, n4. October 1999.

Jovan Jovicic, Antonios Zavaliangos, and Frank Ko, "Modeling of the Ballistic Behavior of Gradient Design Composite Armor", *Special issue of Composite Part A: Applied Science and Manufacturing*. Elsevier Science. Vol.31 (8), pp.773-784. August 2000.

Jovan Jovicic, Antonios Zavaliangos, and Frank Ko: "Modeling and Simulation of Impact Behavior of Gradient Composites". *The 32nd International SAMPE Technical Conference*. Boston, November 5 - 9, 2000.

Jovan Jovicic, Antonios Zavaliangos, and Frank Ko: "Fiber Architecture Based Computer modeling of the Composites". Poster Presentation on the *Fifth International Conference on Textile Composites (TEXCOMP 5)*, Katholieke Universiteit Leuven, Belgium, September 18-20, 2000.

Sun Jong Kwoun, Ryszard Lec, Frank Ko, and Baohua Han: "A Novel Polymer Nanofiber Interface for Chemical Sensor Applications". *2000 IEEE/EIA International Frequency Control Symposium and Exhibition*.

A.G. MacDiarmid, I.D. Norris, W.E. Jones, M. A. El-Sherif, J. Yuan, B. Hua and F.K. Ko: "Polyaniline Based Chemical Transducers with Sub-micron Dimensions," Polymer Preprints, ACS Meeting Abstracts, Washington, D.C., September, 2000.

Baohua Han, Kinnari Chandriani, Alan MacDiarmid and Frank Ko: "The Effect of Molecular Conformation of Poly(L-lactic acid) in Chloroform Solution on the Morphology of Electrospun Nanofibers". *To be published*.

Afaf EL-Aufy, and Frank Ko: "On the Structure and Properties of Nano-Fibers & Nano-Fonrous Assemblies". To be submitted for publication to *Textile Research Journal*.

Ashraf A. Ali, Amotz J. Geshury and Frank K. Ko, "The effect of processing parameters on the morphology of electro-spun PAN fibers" 2001. To be submitted for publication to *Polymer Journal*.

Jovan Jovicic, Antonios Zavaliangos, and Frank Ko: "Numerical Modeling and Analysis of Dynamic Behavior of Gradient Design Composites". Presented on the 13th. *International Conference on Composite Materials (ICCM-13)*. Beijing China, June 25-29, 2001.

Frank Ko, Wendy Han, Anisur Rahman, Hideo Shimoda, and Otto Zhou: "Carbon Nanotube Reinforced Nanocomposites by the Electrospinning Process". *Presented at the University of Akron, October 20, 2001*.

D. List of Participating Scientific Personnel Showing any Advanced Degrees earned by them while Employed on the Project

Dr. Jenny Yu, currently working with Goodyear, Tire and Rubber Company.

E. Report of Inventions

1. Ko and MacDiarmid et al.: U.S. patent Application entitled "Ultrafine Conductive Polymeric Fibers and Fibrous Structures and Methods for Producing and Using These Fibers and Fibrous Structures".
2. Patent disclosure: Akron University/Drexel University, Reneker, D. and Ko, Frank et al.: Process for making from nanofibers, for wrapping nanofibers onto a textile fiber on a textile yarn, and for incorporating nanofibers into braided, woven, or other textiles.

Appendix-Publications

Presented at the National Defense Industrial Association Seminar on "The Design and Integration of Helmet Systems", Framingham MA, December 2-5, 1997

INTEGRATED DESIGN FOR MANUFACTURING OF COMPOSITE HELMETS

Frank K. Ko¹, Wei Sun², Antonios Zavaliangos¹, Jovan Jovicic¹, Aly El-Shiekh³,
and John Song⁴

1. Department of Materials Engineering, Drexel University
2. Department of Mechanical Engineering, Drexel University
3. School of Textiles, N.C. State University
4. U.S. Army Natick RDEC

Abstract

This paper reports the progress made in the Multidisciplinary University Research Initiative (MURI) sponsored by the US Army Research Office. In this program, new reinforcement concepts were developed and evaluated for personnel protection against ballistic threats. In order to facilitate the translation of design concepts into production reality, an integrated design for manufacturing (IDM) framework was established. This paper describes specifically the use of CAD/CAE/CAM in a concurrent engineering environment to design and fabricate the composite helmet system. To address the problems associated with the laborious hand lay-up process currently being used for composite helmet manufacturing, 3-D braided Kevlar, Spectra and Hybrid of Kevlar/Spectra preforms were designed and fabricated for compression molding and resin transfer molding. The composite material properties of the 3-D braided preforms were generated with the Fabric Geometry Model (FGM) for structural analysis. Finite element analysis and simulation were used to assess the effect of fiber architecture on the performance of the composite helmets. Tooling and mold making were accomplished through CAD solid model and rapid Prototyping. Composite helmets were fabricated for testing and verification of structural analysis.

1. Introduction

In order to enhance the survivability of soldiers in the battlefield as well as during peacekeeping missions, there is a need for a significant improvement in penetration resistant; impact energy dissipation, and damage containment capability for the next generation of "light armor systems". The success of developing the next generation high performance lightweight armor systems, which include helmet, body armor and other protective gears, hinges on our ability to translate creative material design concepts into cost effective manufacturable products in a timely manner.

Because of their capability to conform to complex shapes, the possibility of fiber architecture tailoring and the potential to reduce manufacturing cost, textile composites have attracted renewed interest in the recent years. Studies at Drexel University over the past decade has generated a considerable body of knowledge [1-8] on damage tolerant

advanced textile based composite materials including polymer matrix composites (PMC) [2, 3, 6], metal matrix composites (MMC) [1, 5] and ceramic matrix composites (CMC) [4, 7, 8]. Invariably, these studies showed that fiber architecture plays a significant role in the damage tolerance characteristics of composites via the mechanism of structural toughening. For example, one early work on 3-D braided glass, nylon and Kevlar fiber reinforced epoxy composites showed multiple hit capability of 3-D composites having V_{50} as high as 3,000 ft/sec.¹ This study also showed the dependency of ballistic performance of the composites on fiber packing density (fiber volume fraction) as shown in Figure 1.

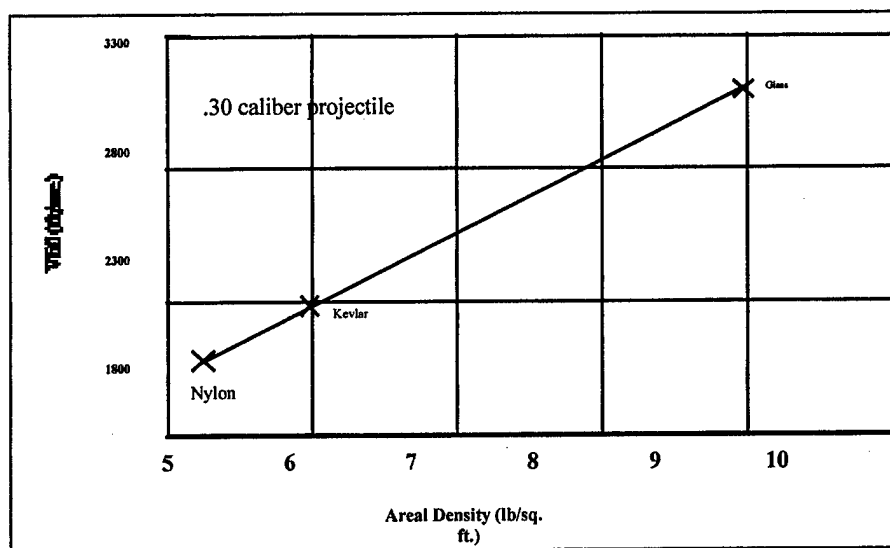


Figure 1. Penetration Resistance of 3-D Braided Polymer Matrix Composites

Subsequent work at Drexel demonstrated the potential of material and geometric hybrid to improve the concomitant properties of stiffness and toughness of polymer, metal and ceramic matrix composites [9]. This series of experiments demonstrated the role of the 3-D fiber network in providing structural toughening while a second phase can be introduced to increase strength and stiffness in a synergistic manner.

Encouraged by these early results, a collaborative study was initiated in 1993 with researchers in the Army Natick RDEC to investigate the feasibility of 3-D composites for lightweight body armor. This study confirms the importance of fiber packing density and fiber orientation effect, which are related to fiber interlacing density and fiber symmetry. In order to defeat higher velocity threats and address the need for lighter weight and more complex shape structures the concept of introducing a harden phase in the spherical form or the Gradient Density Composite (GDC) was developed. It was demonstrated [11-13], as shown in Figure 2, that the ceramic spheres can be used effectively to replace the conventional ceramic tiles to reduce weight and cost without sacrificing its ballistic

¹ Unpublished study sponsored by GM

effectiveness. With proper selection of the composite backing material, thickness, a V_{50} of over 1,000 m/s was achieved using a 7.62 x 39 mm AK-47 type projectile.

Considering the attractive ballistic performance obtained with the ceramic sphere harden composite armor plates, it is of interest to explore the feasibility of using the GDC for complex shape armors such as the helmet. Accordingly, the aim of our current ARO Multidisciplinary University Research Initiative (MURI) study is to demonstrate, using the helmet as an example, the feasibility of superimposing a harden surface with high symmetry strong and tough fibrous network to produce light weight, complex shape armor systems which are capable of defeating high velocity projectiles to the 1,000 meter/second level.

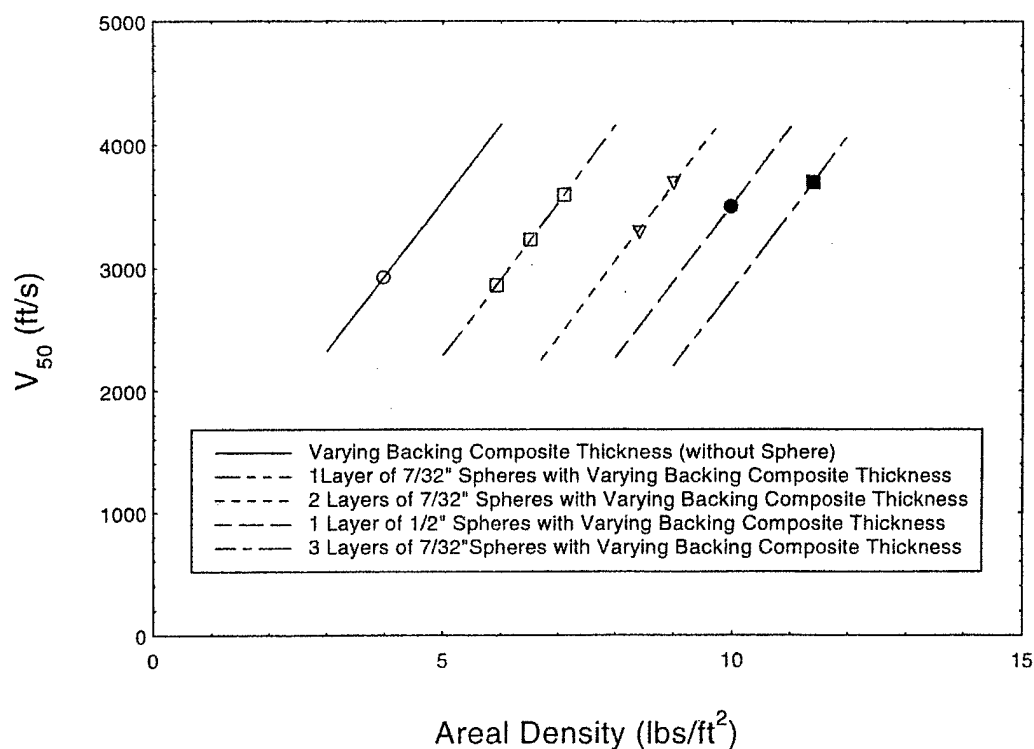


Figure 2. Gradient Density Composite Using Ceramic Spheres

2. Integrated Design for Manufacturing

In order to realize the full potential of the gradient density composites (GDC) for armor, an integrated design for manufacturing (IDM) approach was employed in this study. By integrating performance requirements, processing and manufacturing considerations from the conceptual stage, it is envisaged that the path from concept to product reality will be shortened. Various computer-aided technologies such as CAD/CAM, finite element analysis and simulation, and rapid prototyping and manufacturing have been adopted throughout the project. Based on the design criteria for the helmet (e.g. weight and

penetration resistance), as illustrated in the flow diagram shown in Figure 3, many tasks in the development of the composite helmet are performed in a parallel, concurrent manner. For example, CAD design modeling during reverse engineering goes hand in hand with the tooling and composite processing. Likewise, the mechanisitic structural analysis must be carried out taking the preform process parameters into consideration because they dictate the micro-geometry of the unit cell.

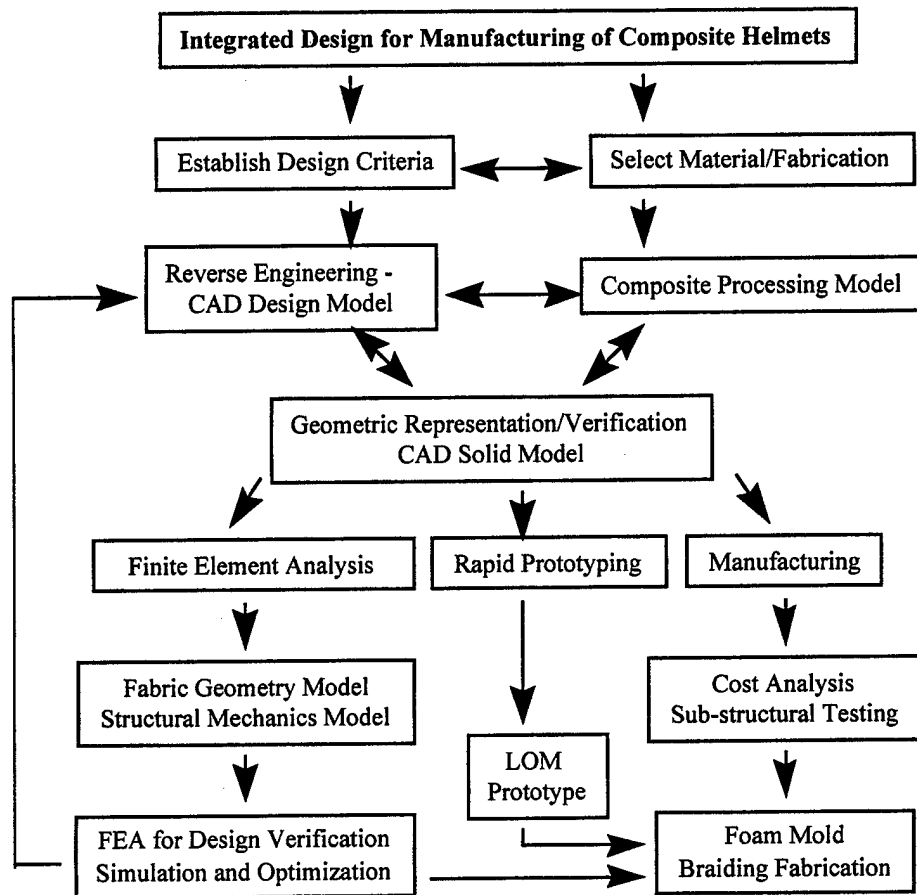


Figure 3. An Integrated Design for Manufacturing of 3-D Fabric Composite Helmets

Within this integrated design for manufacturing framework, the design criteria and an appropriate material and manufacturing processing are defined and selected in the initial design phase. The design and manufacturing were integrated concurrently through reverse engineering to obtain design representation and simulation of helmet structural performance by considering the impact of the design criteria on material selection, fabrication system and manufacturing cost.

In order to maintain the current helmet geometry currently in use, a reverse engineering approach was used to develop the helmet design model. Coordinate Measurement

Machine (CMM) was used to measure the existing helmet profile. The measured coordinate points were converted to IGES format and imported to I-DEAS software to form a surface model before creating a helmet solid model (Figure 4 and 5). The color rendered CAD solid model provides a visualized design representation for verification of the proposed design structure and geometric configuration. The solid model also provides an effective digitized prototype to communicate with manufacturing engineers to select composite processing system. In addition, the solid model also serves as a central repository that integrates engineering design, analysis, finite element simulation, and rapid prototyping in a concurrent engineering environment.

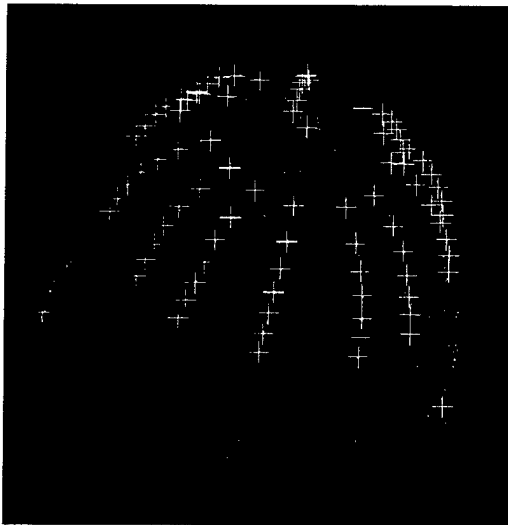


Figure 4. IGES Points
for Surface Model



Figure 5. Solid Model

After the design configuration and the corresponding manufacturing processing were established, the CAD solid model was used to perform finite element analyses for the composite helmet. The design and analysis of the composite helmet requires knowledge of the properties of fiber, matrix, and their geometric arrangement in the braided composite structure. The different geometry of fiber architecture resulting from a particular fabrication technique dictates the fiber orientation and fiber volume fraction, and also strongly influences the integrity, performance, and the manufacturability of the helmet structure. A fabric geometry model, which combines textile engineering methodology and modified lamination theory [8,10], has been adopted to predict the mechanical behavior of composite helmets.

3. Material Concept Development

An examination of the literature indicates that the use of materials of different hardness to produce dual hardness armor dates back to the fourteenth century and the same concept has been used with some success in the past two decades [14]. The dual hardness concepts take advantage of the ability of the hard layer to break up or slow down the projectile, whereas the softer steel backing layer will absorb the remaining impact energy.

This dual hardness concept was also implemented successfully with hard ceramic tile on a softer organic composite backing. As the demand for mobility and flexible manufacturing increases, there is a strong need for lighter, tougher and more manufacturable armor materials. The steel and monolithic ceramic armors in service today can no longer meet this demand because they are too heavy, difficult to produce economically or both.

Building on our successful demonstration of structural toughness capability of 3-D fiber architecture and the use of ceramic spheres to replace ceramic tile, a design concept for creating an armor structure concept with gradient hardness and toughness is proposed. This concept can be realized by the placement of various concentrations (density) of harden substrates in the form of spheres and platelets. In the GDC, the fiber reinforced composites include a 3-D fully integrated fibrous network and multilayer integrated fibrous network as well as a combination of both layered and 3-D fiber architecture. Schematic diagrams of the GDC are shown in Figure 6.

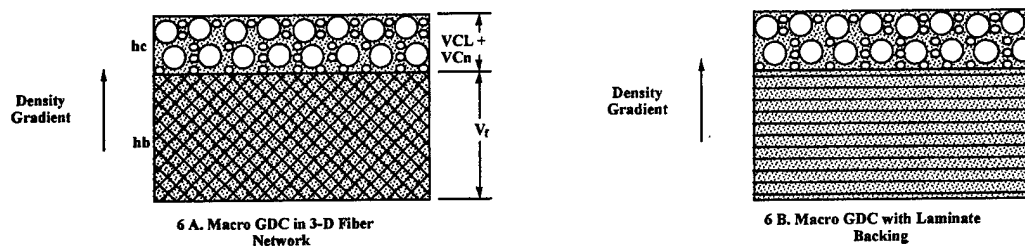


Figure 6. Schematic Representation of the Gradient Density Composite

Complementing the ability of the hardened component in destroying the projectile, the fibrous network will perform the functions of energy dissipation and damage containment.

4. Fiber Architecture Modeling

The engineering design and analysis of a 3-D fabric composite structural component requires the knowledge of not only the properties of fiber, matrix and fiber-matrix interface, but also the geometric arrangement of the fabric reinforcement. The geometry of fiber architecture resulting from a particular fabrication technique dictates the fiber orientation and fiber volume fraction, and will strongly influence the integrity and performance of the composite structure, as well as the processability of the composite system. Likewise, from a structural analyst' point of view, it is important that the mechanical behavior of these 3-D fabric composite systems can be determined based on their fiber architecture and the properties of constituents. For this purpose, a Fabric Geometry Model, which combines textile engineering methodology and a modified lamination theory, has been developed to characterize the fabric composites [10]. Through geometric modeling [15], the engineering parameters θ , and V_f can be expressed in terms of processing parameters as shown in Figure 7.

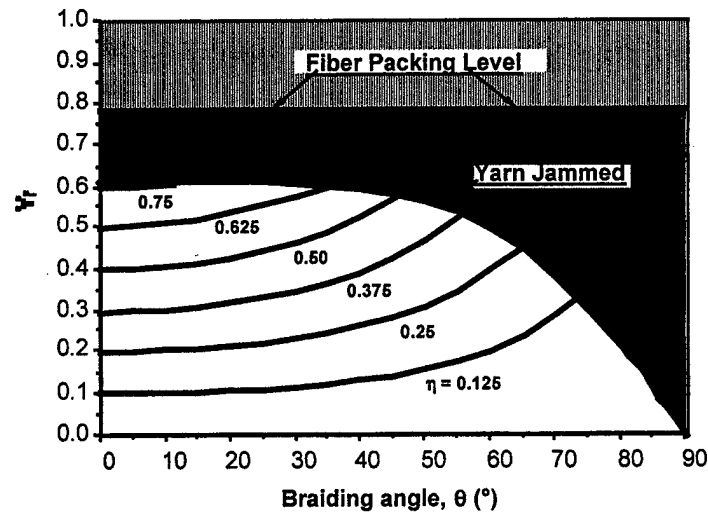


Figure 7. Relationship of fiber volume fraction to braiding angle for various tightness factors

Once the fabric geometry is quantified, the results can be used together with the fiber and matrix properties to predict the mechanical properties of a fabric composite system through a modified lamination theory. Fabric Geometry Model begins with the unit geometry identified with the process window. Through proper coordinate transformation coupled with knowledge of the composite properties of the yarn elements in the unit cell the total elastic stiffness matrix, $[C^c]$, of the composite panel can be obtained by the equation

$$[C^c] = \sum_i k_i [C^i]$$

where k_i is the fractional volume of the i^{th} yarn system [1].

5. Finite Element Modeling

The finite element analysis was performed to simulate the structural behavior of helmets. This model is capable of representing different material volumes and material properties to approximate the volume fraction and fiber orientation distribution resulting from preforming and composite formation processes. The seamless integration of advanced CAD/CAE provided an effective tool for design and structural optimization, and to guide the optimization of fiber architecture design in the braided composites.

The simulation of high velocity impact and penetration processes into non-isotropic fiber reinforced materials is important in the design process of both protective systems and of the composite materials used in these structures. Such analysis may help to understand the complex dynamic interactions between structural components undergoing large

deformations and nonlinear material behavior including failure, de-lamination, erosion, etc.

In order to simulate the dynamic behavior of the composite materials, the constitutive equations must cover the elastic regime, the material failure, and the behavior of the partially or completely failed material. These equations then may be integrated in a Finite Element code suitable for impact/contact problem. Typically it is done using nonlinear LaGrange codes with explicit time integration. The modeling in this study was performed using ABAQUS-EXPLICIT computer code.

Specifically, the oblique impact of a spherical projectile onto a spherical armor surface was considered at a velocity of 1,000 m/s. The projectile was assumed to have a diameter of 7.62mm and it is rigid, with a mass corresponding to a uniform material, which has a density of 18,630kg/m³. The helmet was further assumed to have a thickness of 8mm. Due to symmetry, only half of a helmet was modeled, using appropriate symmetry boundary conditions in the x-z plane. The Model has 63,350 nodes (over 316,000 degrees of freedom) with 12,240 3-D solid elements and 48,960 rod elements (Fig.8). Continuum elements represent the behavior of polymer matrix and rod elements represent the behavior of the fiber. In the discrete models the element representing the polymer matrix occupies a larger volume than in reality. Therefore, a procedure for the selection of equivalent material properties was established relating fiber cross section area, A_f , fiber volume fraction, V_f , braiding angle θ ; and the unit cell width, W by the following equation:

$$A_f = (V_f/8)W^2 \sin\theta \tan\theta$$

The equivalent properties modulus, density and failure stress of the matrix are calculated respectively by the following relationships: $E_{m(eq.)} = (1-V_f)E_m$; $\rho_{m(eq.)} = (1-V_f)\rho_m$; and $\sigma_{fail.(eq.)} = (1-V_f)\sigma_{fail.}$

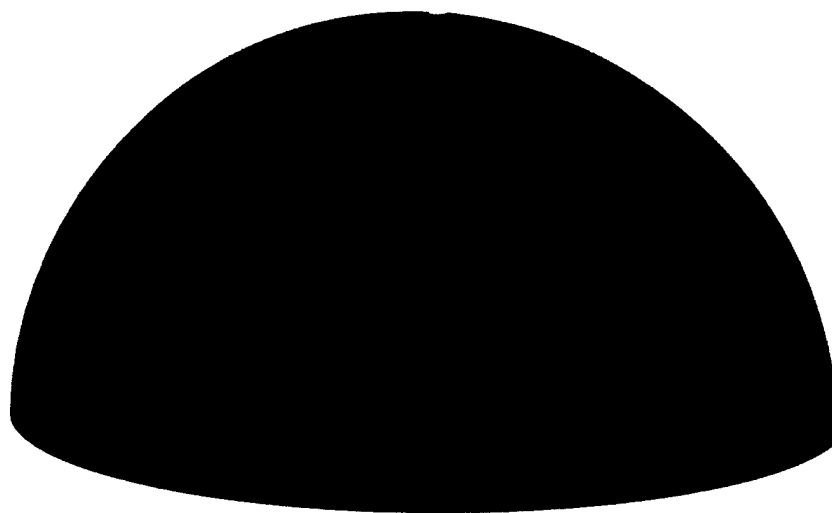


Fig.8 3-D Finite element model

Two cases were considered in the FEM modeling. In the first case, a four-layer 3-D braided Spectra fibers reinforced epoxy helmet, was analyzed with a fiber volume fraction of 60%. In the second model the surface layer of the four layer 3-D braided structure was replaced with a ceramic layer. It is of interest to note the mass difference of these helmet systems, which varying from 1.04 kg for the pure Spectra composite; 1.6 kg for Spectra composite consisting of one, 2 mm thick ceramic layer; and 2.15 kg for the Spectra composite consisting of two ceramic layers.

It has to be highlighted that only static material properties were used in these calculations.

Material	E [GPa]	ν	ρ [kg/m ³]	σ_y [MPa]	ϵ_y	ϵ_f
Epoxy	5	0.3	1800	50	0.1	0.4
Spectra	268	0.4	970	3000	0.027	0.07

In the study of the conditions that lead to fracture, the calculated results should correctly describe the plasticity behavior of the material prior to fracture. In this case it was assumed that fracture occurred when the material is in a plastic state, i.e. ductile fracture. Brittle fracture, on that way can be considered a limiting case of ductile fracture if fracture occurs after very little plastic flow.

In the analysis of the 3-D braided composite the variation of fiber orientation in the helmet was considered. Although there is a continuous variation of fiber orientation from the top to the bottom of the composite preform, the fiber orientations were grouped into three zones from top to bottom at 38° 53°, 72 °, respectively. Numerical analysis was performed accordingly for three different projectile impact angles. Using this analysis the effect of fiber volume fraction (60% vs. 90%) and material properties (Spectra vs. hybrid of composite with ceramic) were examined by simulation, comparison of residual velocity, and specific absorbed kinetic energy of the various helmet systems.

Figures 9 and 10 show the residual velocity and specific absorbed kinetic energy (per unit of target mass) of a projectile respectively, as a function of time for different samples and impact (braiding) angles.

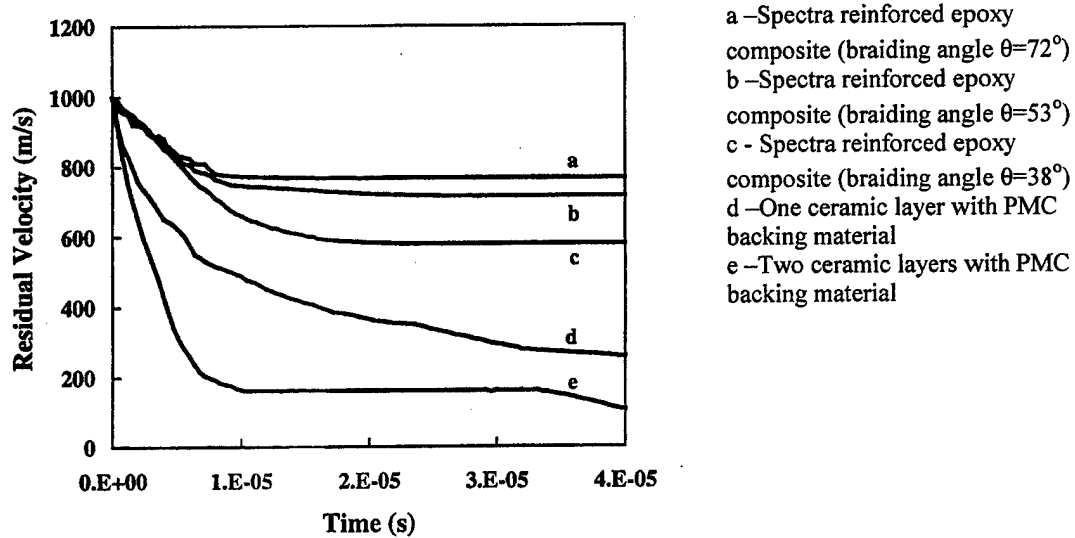


Fig.9 Residual projectile velocity as a function of time.

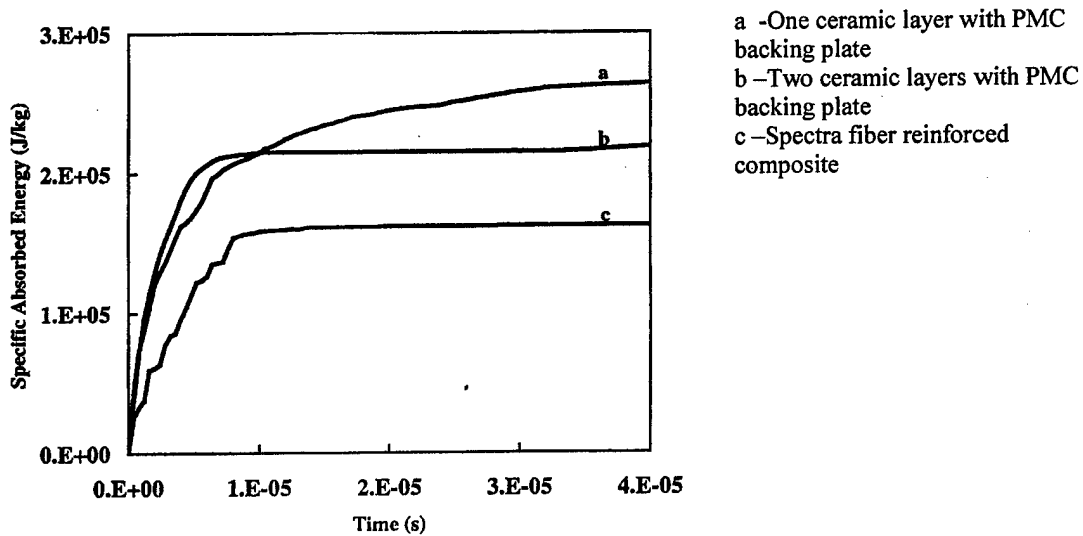


Fig.10 Specific absorbed energy as a function of time.

It can be seen that the projectile was completely stopped with the hybrid (ceramic/composite) helmet, whereas penetration occurred in the pure composite helmets. It was shown, however, that energy absorption increases as braiding angle decreases. As

shown in Figure 11, energy absorption can also be improved with the increase of fiber volume fraction.

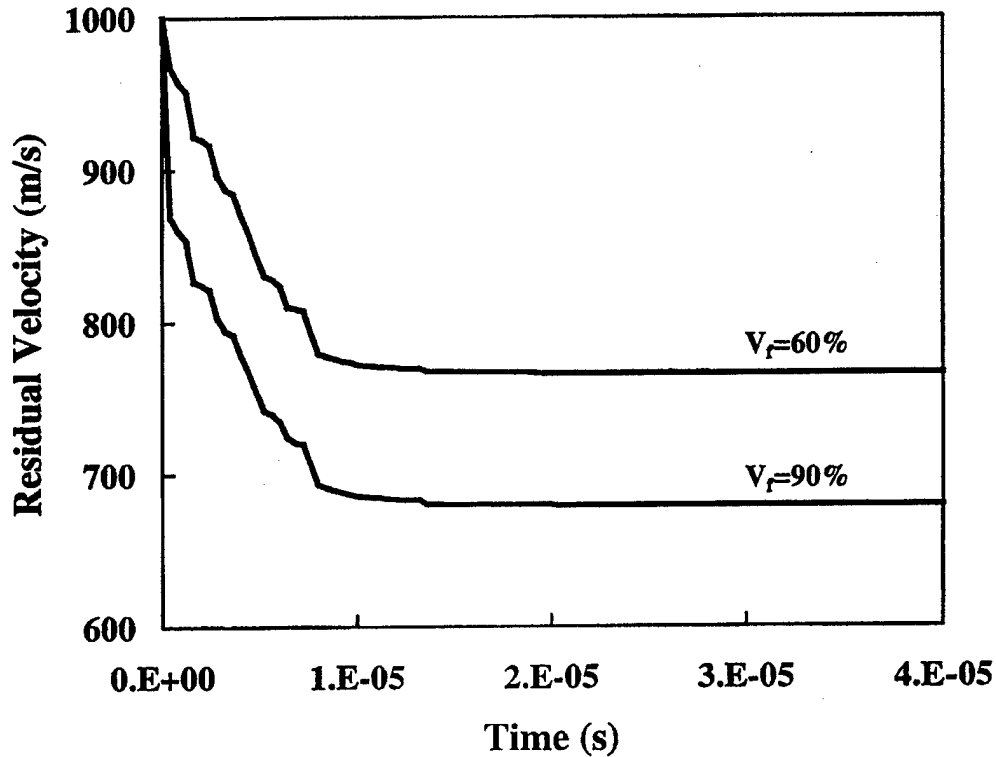


Fig.11 Effect of fiber volume fraction.

Figure 12 presents Von Mises stresses in Spectra fibers 40 μ sec after impact. The projectile has exited the model and is moving as a rigid body. The mechanism of defeat for the ceramic/composite hybrid differs from that of the pure composite helmet. The initial part of the penetration resistance-time curve of the ceramic/composite corresponds to the crushing of ceramic and the effect of mutual influence of composite components. By increasing the proportion of the ceramic surface layer in the hybrid ceramic with composite backing, it is shown that a high velocity projectile (1,000 m/sec velocity) can be defeated.

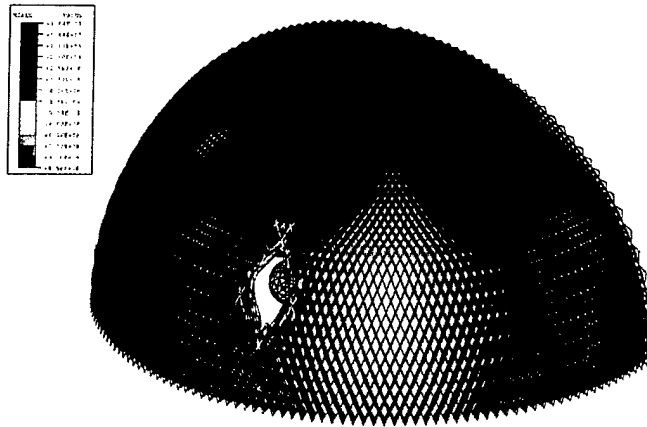


Fig.12a. Von Mises stress in the fabric reinforcement phase of the composites

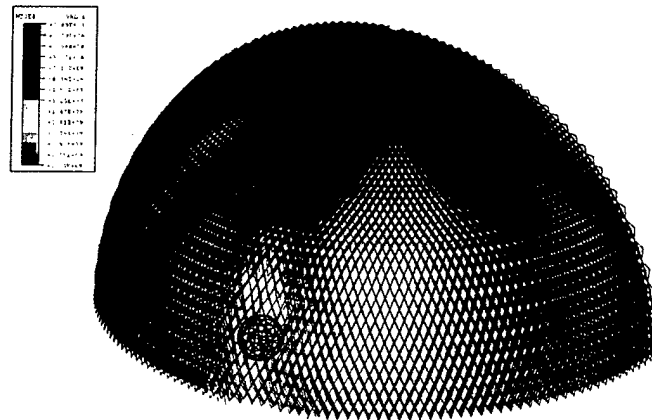


Fig. 12b. Von Mises stress in the fabric reinforcement phase of the composite with ceramic facing

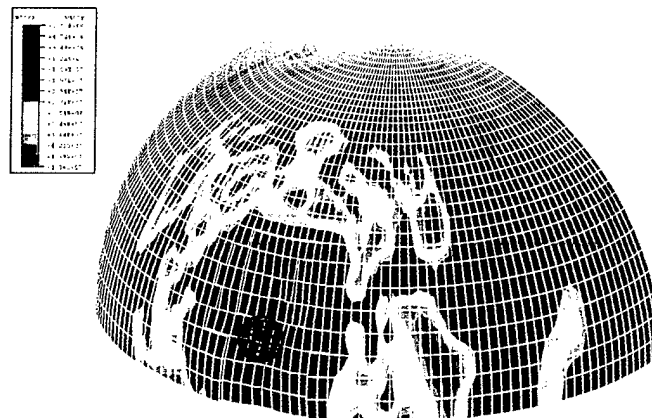


Fig. 12c. Von Mises stress in the matrix phase of the composite with ceramic facing

It should be noted that the current analysis provides only a rough first approximation of the penetrative mechanics of braided composites. Several refinements should be made when using the unit cell model. First, further improvement of the detail description of the unit cell requires a larger number of elements. Second, the assignment of local properties and the restriction of using element that have geometry associated with their properties (since they represent the unit cell) render the use of automatic mesh generation practically impossible. In addition, the dimensions of the unit cell are relatively small. As a result, the total number of elements required to model a realistic helmet could number in the hundreds of thousands.

One solution to this problem is the use of a model which is locally detailed (i.e. based on the detailed description of the unit cell) around the impact site and for the rest of the structure utilizes a simple homogenized model for properties. In this way the maximum information is obtained exactly where it is needed.

Another refinement of the model to be made is the use of dynamic material properties in the model (i.e. strain rate dependent material parameters) instead of the static material properties, as was done in the present analysis.

6 Prototyping and Fabrication

With the helmet solid model the STL output files can be generated and sent to prototyping shop for fabrication of a pattern. The LOM or SLA prototyping technique can be used to build the helmet pattern. The prototype or pattern will be used to verify the design and for the fabrication of a composite mold, as well as serving as a mandrel for net shape braiding of the helmet preform on a 3-D braiding machine as shown in Figures 13. The braided preforms were then placed in the composite mold for compression or resin transfer molding. Figure 14 shows the braided composite helmets produced with ceramic sphere hardened surface.

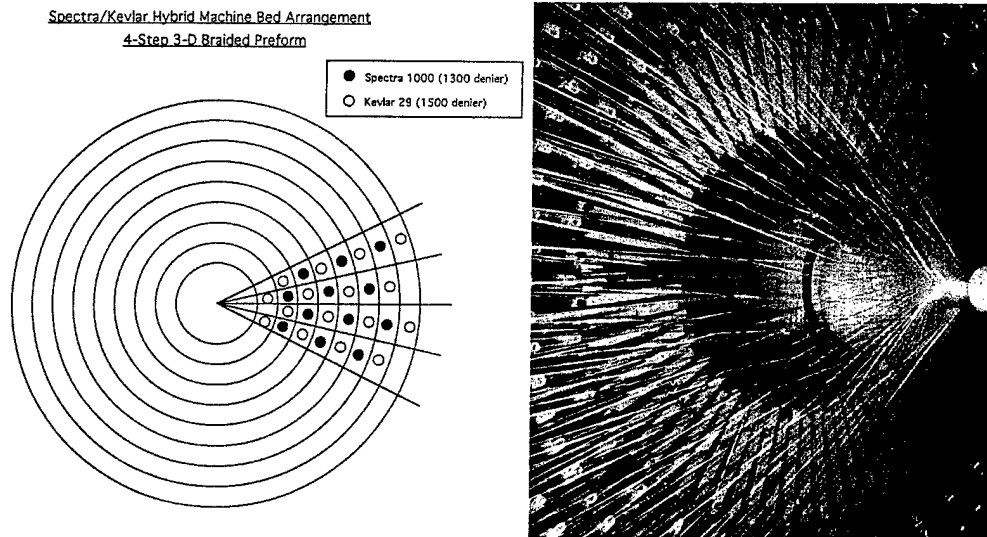


Figure 13. Net shape braiding of the helmet preform.

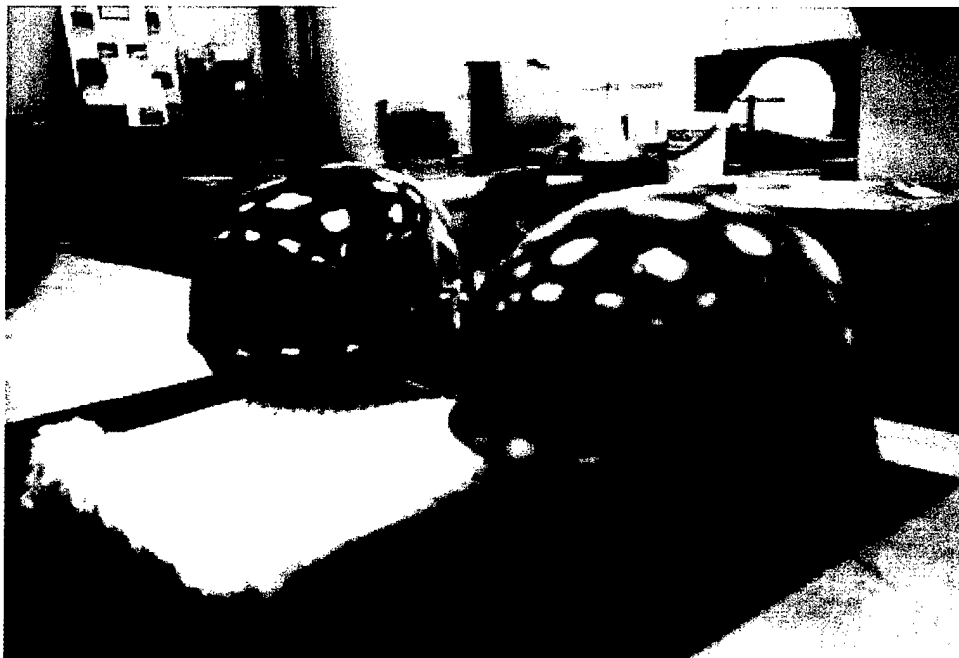


Figure 14. Braided Composite Helmets

7. Summary

Building on the Gradient Density Composite (GDC) Concept, an Integrated Design for Manufacturing (IDM) framework has been established for the design and manufacturing of high performance helmets. By incorporation of the fiber architecture based model -the FGM into FEM structural modeling, the coupling effect of microstructure and macrostructure were considered through out the design and manufacturing phase therefore allowing the tailoring of reinforcement architecture and fine tuning of the processing parameters in a concurrent manner.

The simulated ballistic response of the modeled 3-D braided composite systems with and without ceramic facing showed that a helmet system capable of defeating 1,000 m/sec. projectiles can be produced at a fraction of the weight of the steel helmets. The CAD design process was demonstrated through reverse engineering by copying the existing army helmet geometry. 3-D braided composite helmets with and without ceramic sphere facing were produced.

When the composites are properly characterized through ballistic testing to verify the models, the hybrid composite system can be further optimized. With the potential simplification of composite fabrication processes the use of the 3-D braiding net shape manufacturing process may prove to be an attractive alternative to the current way of making laminated helmets.

Acknowledgments

The authors gratefully acknowledge the funding from the Army Research Office for this study under the Multidisciplinary University Research Initiative on Functionally Tailored Fibers and Fabric Research with Dr. Edward Chen as program monitor.

References

1. F. K. Ko, "Three Dimensional Fabric for Composites," Textile Structural Composites, Chou, T.W. and Ko, F. K., editors, *Elsevier*, New York, 1989.
2. F. K. Ko, and D. Hartman, "Impact Behavior of 2-D and 3-D Glass/Epoxy Composites", *SAMPE J.*, Vol. 22, No. 4, July/August 1986, pp. 26- 30.
3. J.Z. Yu, C. Lei and F. K. Ko, "Impact Responses of Gradient Designed Textile Structural Composite under Low and High Impact Velocities," ANTEC, 1994.
4. F.K. Ko, "Preform Architecture for Ceramic Matrix Composites," *Ceramic Bulletin*, February 1989.
5. F.K. Ko, "Development of High Damage Tolerant Net Shaped Composites Through Textile Structural Design", *Proceedings of ICCM V, Fifth International Conference on Composite Materials*, W.C. Harrigan, et al, eds. The Metallurgical Society, 1985, pp. 1201-1210.
6. F.K. Ko, H. Chu and E. Ying, "Damage tolerance of 3-D Braided Commingled Carbon/PEEK Composites", *Advanced Composites: The Latest Developments, Proceedings of 2nd Conference, ASM International*, Metals Park, OH 1986, pp. 75-88.
7. F.K. Ko, P. Fang, M. Koczak and G. Layden, "Toughening of SiC/LAS III Ceramic Composites by Hybrid 3-D Architecture", *Proceedings of ICCM VIII*, Beijing, China, August 1989.
8. T.M. Tan, C.M. Pastore and F. K. Ko, "Engineering Design of Tough Ceramic Matrix Composites for Turbine Components", *Transactions of ASME*, Paper No. 89-GT-294, 1989
9. F.K. Ko.: "Advanced Textile Structural Composites," *1st US/Mexico Bilateral Symposium*, September 24-27, 1991
10. F.K. Ko.: C.M. Pastore, C. Lei, D.M.. Whyte "A Fabric Geometry Model for 3-D Braid Reinforced Composites", in *Proc. of 1987 Int. SAMPE Metals Conf.*, Covina CA 1988.
11. 5. F. Ko, C. Lei, A. Rahman, M. Shaker, A. Zavaliangos, J. Z. Yu and J. Song, "Viscoelastic Properties of Advanced Polymer Composites for Ballistic Protective Application: *Technical Report/ NATICK/TR-94/035* (1993).
12. J. Z. Yu and F. Ko, "The Effect of Fiber Orientation on the Dynamic Mechanical Behavior of Kevlar Fiber Reinforced Composites," *Proceedings of ICCM-10*, Vol.10, Canada, (1995).
13. J.W.Song, A. Geshury, and F. K. Ko., "Behavior of Gradient Designed Composite under ballistic Impact", *Proceedings of Vol. II , ICCM-11*, Australia. (1997)

14. R. C. Laible, "Ballistic Materials and Penetration Mechanics", *Elsevier Scientific Publishing Company*, Amsterdam, Volume 5, pp. 239, 1980.
15. F.K. Ko and G.W. Du, "Processing of Textile Preforms", in Chapter 5., pp 157-205, *Advanced Composites Manufacturing*, T. G. Gutowski, editor, John Wiley & Sons, New York, 1997.

Optimization of the Performance of Gradient Composite Armor

Frank K. Ko and Jun Chang

*Department of Materials Engineering, Drexel University
Philadelphia, PA19104, USA*

SUMMARY: Gradient Design Composite (GDC) was developed at Drexel University by a combination of material and geometry hybrid. Response Surface Analysis(RSA) methodology is used to optimize the specific ballistic limits of the GDC. The modified Florence's Model was used to generate virtual experimental results under a factorial design of experiment. Using this model a wide range of combinations of factors can be examined for a given objective function. The response surfaces generated in this study will provide guidance for the selection of optimum combination of design parameters for high performance composite armors.

KEYWORDS: Response Surface Analysis (RSA), Gradient Design Composite (GDC), Ballistic limit, Optimization, Composite armors

INTRODUCTION

As the velocity of impact and the nature of the impactor changes, as in the case of a very high velocity projectile (~3000ft/s), a ceramic plate is often added to the surface of the polymer composite. Lots of works have been done to understand the performance of ceramic composite armors. It is now well recognized that after impact, a conical fracture pattern develops at the impact zone, propagating towards a ceramic-backing plate interface. Also tensile fracture develops at the interface at the results of interflexion of the initial compress wave. Later a conical zone of fully fragmented materials developed in front of the projectile and, as a consequence of the interaction between the projectile and the ceramic powder, projectile erosion occurs. Although as previously mentioned, the energy consumed in the fracture of the ceramic tile is very small compared with the energy of impact, the development of a zone of fractured material ahead of the penetrator seems to be of the greatest importance in defeating the projectile. Florence[1] developed a model for estimating the ballistic limit of ceramic armors, based on the assumptions that armor piercing projectiles are first shattered or blunted by the hard

ceramic, and the load is then spread over large area. The composite backing deforms to absorb the remaining kinetic energy of the projectile. The ballistic limit was estimated using

$$V = \left(\frac{\epsilon_c S}{0.91 f(a) M_p} \right)^{\frac{1}{2}} \quad (1)$$

Where M_p is the projectile mass
 a_p is projectile radius (for 7.62 NATO projectile, the radius is 3.81mm)
 $a = a_p + 2h_c$
 h_c is the thickness of ceramic plate
 h_b is the thickness of the backing composite plate
 $S = UTS * h_b$
 UTS is ultimate tensile strength of backing plate,
 ϵ_c is breaking strain of backing plate
 d_c is the density of ceramic
 d_b is the density of backing plate
 $f(a) = M_p / (M_p + (h_c d_c + h_b d_b) \pi a^2) \pi a$

Current small arms protective body armor systems used in the US. Army frequently consist of a ceramic face backed by fiber reinforced composite. In the interest of improving the ballistic resistance of composite armors, a Gradient Design Composite (GDC) was developed at Drexel University by a combination of material and geometry hybrid[2]. The GDC is a design concept wherein the material system consists of a harden component, an energy dissipation component and a damage containment which are organized according to a gradient of varying functions. Ceramic spheres of various sizes are embedded in a matrix of appropriate rigidity to form a face component. The backing plate is composed of fiber reinforced composite with various levels of structural integration. By proper selection of material systems and design of fiber architecture, it has been shown that a high level of damage containment can be achieved as demonstrated in the compression after impact test[3].

In past few years, a considerable research has been directed to the study of GDC [4]. It was found that modified Florence model with several simplifying assumptions provides a good prediction regarding the ballistic velocities at the experimental design stage. A novel experimental design, in which Florence model is used as a virtual experimental generator to provide the experimental data, is thus developed in this paper to exploit the GDC to its fullness and examine the performance limit of the State-of-the-Art material system.

For the GDC system, a major concern in the experimental design stage is how to achieve an optimum selection of the system parameters, such as the thickness ratio h_c/h_b (h_c is the thickness of ceramic facing plate, h_b is the thickness of composite backing plate), so that the GDC system will process the desired materials characteristics and meet given specification. As a powerful and mature design tool, the Response Surface Analysis

(RSA) methodology [5] is used to optimize the specific ballistic limits of the GDC. The response surface methodology is a collection of mathematical and statistical techniques that are useful for the modeling and analysis of problems in which a response of interest is influenced by several variables and the objective is to optimize the response. It is assumed that a system involves some response which depends on the input variables. The relationship between response and variables sometimes is very complicated. The success of the RSM depends on the approximation of the relationship by a low order polynomial in some of the independent variables. The polynomial coefficients are estimated by the least square procedure to minimize the root-mean-square (rms) error. In this case the response is a linear function of the coefficient, and the least square fit requires the solution of a linear system of the equations, with the process called *linear regression*. The response surface can be reduced to canonical form, and the nature of the stationary point can be determined so that the optimal conditions can be found.

In this paper, response surface analysis methodology fits quadratic polynomial to the experimental data generated by Florence model, using least square procedure. The design optimization process then can employ the simple fitted function.

EXPERIMENTAL DESIGN

In order to optimize the ballistic properties of the ceramic armored composite, the first step is to decide the variables and response. Here the ballistic limit V and the areal density of whole composite panel are considered as responses. Experimental results show that the ballistic limit is the function of sphere size and the ratio of ceramic and composite layers. It can also be found from the Florence Model that the ballistic limit is affected by the arrangement and type of ceramic spheres, and the arrangement and type of backing composite. Simply, three independent variables, the layers of Spectra fabrics, the ratio of ceramic sphere and backing composite plate, and the density of ceramic sphere, are considered.

Table1. Properties of ceramic materials

Materials	Density (g/cm ³)	Modulus (GPa)	Hardness (Kg/mm ²)
Aluminum Oxide	3.4	227	1800
Boron Carbide	2.48	440	2790
Silicon Carbide	3.20	370	2700
Boron Carbide & Silicon Carbide	2.60	340	2750

The Second step is the design for fitting second order model. In this paper, the central composite design was selected. Box and Wilson have devised a workable alternative to the 3^k factorial system through the development of the class of the composite designs. The composite design are first order factorial designs augmented by additional points to allow estimation of the coefficients of a second order surface. The central composite designs is the 2^k factorial (the two levels of each variable coded to the usual $-1, +1$) augmented by the following: For $k > 2$, the number of experimental points needed in central composite design are considerable less than the number required by a 3^k factorial

design. The composite design can achieve a great saving in the number of the experimental runs required when the number of factors is large. According to the theory of Response Surface Methodology, for quadratic polynomial response surface with 3 independent variables, there should be 15 experiments in order to optimize the ballistic limit.

Table 2. The experimental design

Factors		Levels				
Coded variables	Actual variables	-2	-1	0	1	2
X_1	No. of layers	105	115	125	135	145
X_2	Ratio of h_c/h_b	0.4	0.5	0.6	0.7	0.8
X_3	Ceramic density	2.48	2.71	2.94	3.27	3.6

Variables: thickness of backing composite panel (h_b): from 105 layers to 145 layers
thickness ratio of ceramic plate and polymer panel (h_c/h_b): from 0.4 to 0.8
the density of ceramic sphere (d_c): from 2.48g/cm^3 to 3.4g/cm^3

The coded variables are:

$$\begin{aligned} X_1 &= (h_b - 125)/10 \\ X_2 &= 10(h_c/h_b - 0.6) \\ X_3 &= (d_c - 2.94)/0.23 \end{aligned}$$

The third step is to collect the experimental data. In this paper, the Florence's Mode I was used as a *virtual experimental generator* to produce the virtual experimental results of ballistic limit. The area density A_d was calculated as the following equation:

$$A_d = d_c \times h_c + d_b \times h_b \quad (2)$$

Where d_c , d_b are the density of ceramic sphere and backing composite panel, respectively
 h_c , h_b are the thickness of these two panels, respectively.

Next, the surface response of ballistic limit and area density is calculated by using the least square procedure. Maple Software package was used to obtain the quadratic polynomial and to plot the contour of surface response.

Finally, the optimum operation conditions is determined. The optimization was performed using a generalized reduced gradient optimizer available in Microsoft EXCEL

RESULTS

The virtual experimental results of ballistic limit V_{50} generated by Florence model and area density A_d calculated by using Equation 2 are shown in Table3. Spectra 1000 laminated composite was chosen as the backing plate (density: 1000kg/m^3 , Spectra® 1000 fiber breaking strain of 3.4% and Spectra® 1000 fiber tensile strength 3.0×10^9 Pa were used in calculation).

Table.3 The response of experiment design

	X1	X2	X3	V ₅₀ (ft/s)	Area Density (lb/ft ²)
1	-1	-1	-1	3534.3	8.070
2	-1	-1	1	4092.4	9.474
3	-1	1	-1	3852.3	9.928
4	-1	1	1	4470.3	11.655
5	1	-1	-1	3672.6	8.859
6	1	-1	1	4256.8	10.3944
7	1	1	-1	4029.3	11.03
8	1	1	1	4680.4	12.95
9	0	0	0	3734	8.649
10	2	0	0	4682.3	11.94
11	-2	0	0	3691.3	8.1055
12	0	2	0	4432.4	12.486
13	0	-2	0	3901.7	9.2678
14	0	0	2	4248.4	11.32
15	0	0	-2	4078.7	10.296

The quadratic polynomial responses surface of ballistic limit V_{50} and area density of A_d as shown below are calculated .And the contour of ballistic limit and area density were plotted by using Maple software at fixed density of ceramic sphere of $2.64/\text{g}/\text{cm}^3$

$$V_{50} = 4078.8 + 301.8x_1 + 184.9x_2 + 86.5x_3 - 2x_1^2 - 4.2x_2^2 - 9x_3^2 + 15.8x_1x_2 + 7.4x_1x_3 + 10.6x_2x_3$$

$$A_d = 10.2967 + 0.8233x_1 + 1.095x_2 + 0.5134x_3 - 0.0005x_1^2 - 0.0001x_2^2 - 0.0006x_3^2 + 0.0879x_1x_2 + 0.0413x_1x_3 + 0.0855x_2x_3$$

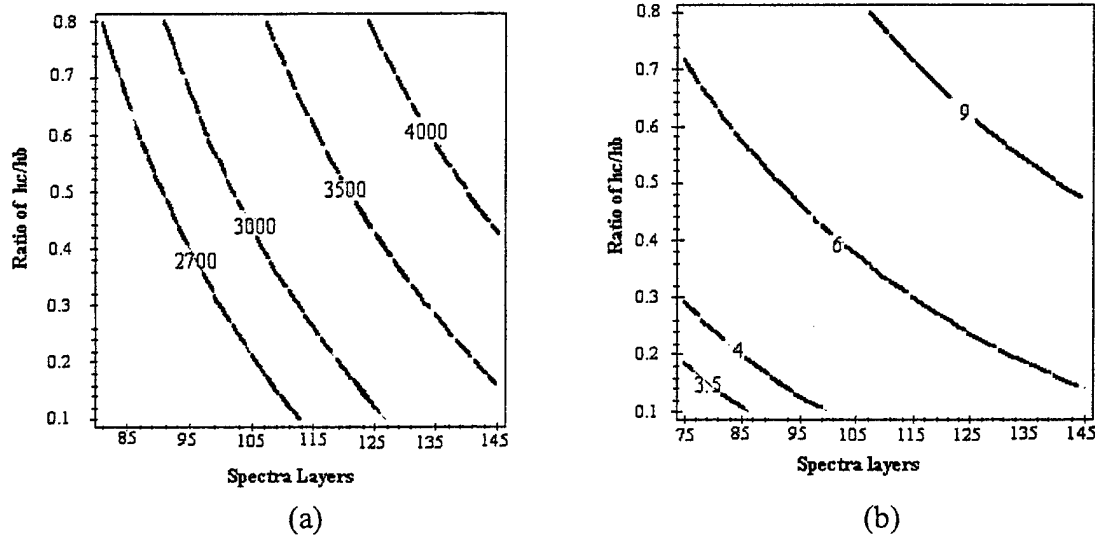


Fig.1 The response contour of GDC

(a). The response of ballistic limit

(b). The response of area density

From the quadratic polynomial of ballistic limit, the stationary point was calculated by canonical analysis

$$\begin{aligned} X_1 &= 13.56 \\ X_2 &= 17.38 \\ X_3 &= 11.0 \end{aligned}$$

Which are far beyond the design region (from -2, to 2). In other words, there is no stationary point in the region we are interested in.

Table 4. Optimum Design obtained using response surface

Ballistic limit (ft/s)	2582
Area Density (4lb/ft ²)*	4
Spectra layers	106
Diameter of ceramic sphere (in)	0.066
The density of ceramic (g/cm ³)	2.64

* Constraint condition

The optimization was performed using a generalized reduced gradient optimizer available in Microsoft EXCEL. The optimum design obtained, subject to the constraints of area density (Area density is less than 4 lb/ft²) is shown in table 4

It is found from the above analysis that it is very hard to meet the required criteria using Florence model, which also means it is impossible to only use the ceramic plate as the face panel of ceramic armored composite. This is why the concept of ceramic sphere in honeycomb structure is introduced. And thus the modification of Florence model is necessary.

DISCUSSION

From the above analysis, it is impossible to meet the required criteria, which requires that the ballistic limit is more than 2700ft/s while the area density is less than 4 lb/ft², Some kinds of improvement would be considered.

a). The improvement of material properties of backing composite layers

Table 5 lists the properties of state-of-art materials we currently used in backing panel. It is shown that the specific energy absorption ability (which equals to $UTS * \epsilon_c / d_b$) of the Spectra 1000 is the best among these currently used materials. The experimental results indicate that it is impossible to reach the specific criteria by using current material. A new question should be answered, what kind of material properties are needed to meet the specific criteria? From Florence model, it is found that the ballistic limit increases with the energy absorption ability of the backing composite layers. If a new fiber with better absorption ability can be found, or the energy absorption ability of Spectra fiber can be improved, the ballistic limit can be raised without the change of area density.

Table 5. The properties of state-of-art materials

material	Density (kg/m ³)	Ultimate tensile strength (GPa)	Broken strain (%)
Spectra 1000	1000	3	3.4
Kevlar 29	1450	2.8	4.1
PEN	1380	1.21	4
Graphite(AS4)	1800	3.58	1.54
E Glass	2540	3.45	4.8
Polypropylene	910	0.638	14

Besides the three variables use above, the fourth variable ξ_4 , which is equals to the product of ultimate tensile strength and breaking strain of backing plate, is introduced.

$$\xi_4 = s \times \varepsilon_c$$

For Spectra[®] 1000 fiber, $\xi_4 = 3 \times 10^9 \times 3.4\% = 1.02 \times 10^8$. If we assume the improved absorption ability can reach 2.04×10^8 , the coded variable

$$x_4 = [(\xi_4 \times 10^{-8}) - 1.53] / 0.255$$

According to the theory of Response Surface Methodology, for quadratic polynomial response surface with 4 independent variables, there should be 25 experiments in order to get the optimization of the ballistic limit

Table 6. The experimental design with improved backing composite

Factors		Levels				
Coded variables	Actual variables	-2	-1	0	1	2
X_1	No. of layers	105	115	125	135	145
X_2	Ratio of h_c/h_b	0.4	0.5	0.6	0.7	0.8
X_3	Ceramic density	2.48	2.71	2.94	3.27	3.6
X_4	Energy absorption ability ($\times 10^8$)	1.02	1.275	1.53	1.785	2.04

The experiment results are obtained by using Florence Model. The responses V_{50} and A_d are calculated. The optimum conditions can be found by using Microsoft Excel Solver.

Table 7. Optimum Design obtained using response surface

Ballistic limit (ft/s)	2716
Area Density (4lb/ft ²)*	4
Spectra layers	104
Diameter of ceramic sphere (in)	0.059
Density of ceramic (g/cm ³)	3.4
Ultimate strength ($\times 10^9$ Pa) [†]	3.3

* Constraint condition

† As the upper limit

It is interesting that a small improvement in backing composite (10% increase of energy absorption ability, which is the product of ultimate strength and breaking strain) can improve the ballistic limit without increasing the area density. It provides a potential way to meet the specific criteria of GDC.

b). The introduction of ceramic sphere

With the introduction of ceramic sphere, the ceramic plate is replaced with ceramic composite panel in which ceramic sphere are the reinforcement and the epoxy as the matrix. Thus the area density of GDC composite can be decreased at a slight reduction of the ballistic limit. The area density of composite is:

$$A_d = (d_c v_{fc} + d_e v_{fe}) h_c + d_b h_b$$

Where d_c : the density of ceramic sphere

v_{fc} : the volume fraction of ceramic sphere in surface composite. ($\pi/6$)

d_e : the density of epoxy (1.22 g/cm^3)

v_{fe} : the volume fraction of epoxy ($1 - \pi/6$)

h_c : the thickness of ceramic sphere (which is assumed as the diameter of ceramic sphere)

Also the parameter $f(a)$ in Florence model should be modified as:

$$f(a) = M_p / (M_p + (h_c(d_c v_{fc} + d_e v_{fe}) + h_b d_b) \pi a^2) \pi a$$

Here we assume that the other parameters in Florence Model are not changed with the introduction of ceramic sphere.

By using the same experimental design in table 2, the responses were calculated by the modified Florence model.

The responses V_{50} and A_d as shown below are calculated. The optimum conditions can be found by using Microsoft Excel Solver.

Table 8. Optimum Design obtained using response surface

Ballistic limit (ft/s)	3330	3053
Area Density (4lb/ft ²)*	4	3.5
Spectra layers	110	97
Diameter of ceramic sphere (in)	0.063	0.055
Density of ceramic (g/cm ³)	3.4	3.4

* Constraint condition

Table 9 lists all optimum conditions to reach the specific requirements:

Table 9 . The comparison of optimum results of three experimental designs

	Spectra layers@	Ratio of h_c/h_b @	Density of ceramic @ (g/cm^3)	Ultimate strength@ ($\times 10^9 \text{ Pa}$)	V_{50} (ft/s)	A_d (lb/ft ²)
Exp#1	106	0.1	2.645	fixed	2582	4
Exp#2	104	0.1	3.4	3.3	2716	4
	93	0.1	3.4	4.12	2769	3.5
Exp#3	110	0.1	3.4	fixed	3330	4
	97	0.1	3.4	Fixed	3053	3.5

@: the optimum conditions

*: the constraint condition

FUTURE WORK

Obviously more tests need to be done. There are only three variables, the layers of Spectra fabrics, the ratio of ceramic sphere and backing composite plate, and the density of ceramic sphere, are considered in the analysis above. In reality, there are other variables, such as the geometry of backing composite plate, the structure of ceramic sphere and so on, affecting the response surface. And also the economic consideration should be another response. In our design the ceramic layer is made of ceramic sphere in honeymoon structure and the conical fracture pattern is changed with the geometry of ceramic sphere.

CONCLUSION

The RSA can be used effectively to generate contour diagrams showing the optimum combination of design parameters for the response of interest. In this study, the response, ballistic limit V_{50} and area density A_d can be generated with the Florence's Model according to the experimental design. The ballistic limit and area density for various types of ceramic sphere and geometric combinations can be obtained by the response surface analysis. It is found that the current material system can not meet the specific requirement of ballistic limit with the certain constraint of area density. The search for better material and improvement of structural design are needed.

REFERENCES

1. Box, G.E.P. and K.B. Wilson. *On the Experimental Attainment of Optimum Condition*. J.Roy. Statist. Soc., B13,1, 1951
2. Ko, F.K., Yu, J.Z., And Song, J.W., "Characterization of Multifunctional Composite Armor", *Proceedings of the America Society for Composite*, Atlanta, GA. October 8, 1996

3. Ko, F.K., *Three dimensional Fabrics for Composite in Textile Structural Composites*, edited by Chou, T.W. and Ko, F.K., pp129-171, Elsevier Science Publishers B.V., Amsterdam, 1989
4. Ko, F.K., Geshury, A. And Song, J.W., "Behavior of gradient Designed Composites under ballistic Impact". *Proceedings, ICCM11*, Gold Coast, Australia, 1997
5. Florence, A.L., "Interaction of Projectile and Composite Armor", Part II, *Stanford research Institute Report*, AMMRG-CR-69-15, 1969

Acknowledgements

This study is supported by the USA Army Research Office under the Multidisciplinary University Research Initiative (MURI) with Dr. Iqbal Ahmads as the program monitor.

Electrostatic fabrication of ultrafine conducting fibers: polyaniline/polyethylene oxide blends

Ian D. Norris^a, Manal M. Shaker^b, Frank K. Ko^b, Alan G. MacDiarmid^{a,*}

^a Department of Chemistry, University of Pennsylvania, Philadelphia, PA 19104, USA

^b Fibrous Materials Research Center, Department of Materials Engineering, Drexel University Philadelphia, PA 19104, USA

Received 7 December 1999; received in revised form 8 February 2000; accepted 10 February 2000

Abstract

Ultrafine fibers of polyaniline doped with camphorsulfonic acid (PAn.HCSA) blended with polyethylene oxide (PEO) were prepared by a non-mechanical, electrostatic spinning (“electrospinning”) technique. The morphology and fiber diameter of electrospun polyaniline blend fibers revealed that both the PEO and the PAn.HCSA/PEO blend fibers had a diameter ranging between 950 nm and 2.1 μm , with a generally uniform thickness along the fiber. The UV–visible spectra of these electrospun fibers were similar to those for cast films produced from the same solutions. As expected, the conductivity of the non-woven fiber mat, as measured by the four-point probe method, was slightly lower than that of a cast film, due to the high porosity of the non-woven mat. The rate for the vapor phase de-doping/re-doping of the electrospun fibers is at least one order of magnitude faster than for cast films, stressing the enormous effect an increase in the surface-to-volume ratio, accomplished by electrospinning the material into fibers, can have on the selected chemical properties of polyaniline blends. © 2000 Elsevier Science S.A. All rights reserved.

Keywords: Electrostatic fabrication; Ultrafine conducting fibers; Polyaniline/polyethylene oxide blends; Electrospinning

1. Introduction

Electrostatic generation of ultrafine fibers (“electrospinning”) has been known since the 1930s [1]. This technique has been recently rediscovered for applications such as high performance filters [2,3] and for scaffolds in tissue engineering [2,4] that utilize the unique characteristics of the high surface area ($\sim 10^3 \text{ m}^2/\text{g}$) provided by the fibers. In this non-mechanical, electrostatic technique, a high electric field is generated between a polymer fluid contained in a glass syringe with a capillary tip and a metallic collection screen. When the voltage reaches a critical value, the charge overcomes the surface tension of the deformed drop of the suspended polymer solution formed on the tip of the syringe, and a jet is produced. The electrically charged jet undergoes a series of electrically induced bending instabilities during its passage to the collection screen that results in the hyper-stretching of the jet. This stretching process is accompanied by the rapid evaporation of the solvent molecules that reduces the diameter of the jet, in a cone-shaped volume called the

“envelope cone”. The dry fibers are accumulated on the surface of the collection screen resulting in a non-woven mesh of nano to micron diameter fibers. The process can be adjusted to control the fiber diameter by varying the charge density and polymer solution concentration, while the duration of electrospinning controls the thickness of fiber deposition [5]. A schematic drawing of the electrospinning process is shown in Fig. 1.

Considering the well-known fact that the rate of electrochemical reactions is proportional to the surface area of the electrode, we are interested in exploiting the high surface to volume ratio of electrospun fibers to develop porous polyaniline electrodes. Reneker and Chun [5] have reported that polyaniline fibers can be successfully electrospun from sulfuric acid into a coagulation bath. Another way of producing electrically conductive nanofibers is, as reported by Chun et al. [6], by the pyrolysis of electrospun polyacrylonitrile nanofibers into carbon nanofibers. However, the conductivity value of neither the electrospun polyaniline nor the carbon nanofibers was reported.

In this paper, we describe a novel technique for the production of ultrafine electrically conducting fibers to form a non-woven mat using a polyaniline/polyethylene

* Corresponding author.

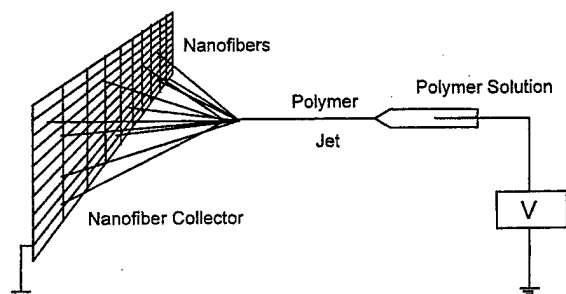


Fig. 1. Schematic of the electrospinning process.

oxide (PEO) blend dissolved in chloroform. A unique characteristic of these polyaniline blend fibers is their electroactive nature (i.e. their electronic, magnetic, optical and associated properties which respond to external influences).

2. Experimental

2.1. Materials

PEO (M_w 900,000 Da) and 10-camphorsulfonic acid (HCSA) and chloroform were purchased from Aldrich; the emeraldine base (M_w 120,000 Da) was supplied by Neste Oy. These chemicals were used without further purification.

2.2. Solution preparation

Various polymer blend solutions were prepared with the concentration of polyaniline doped with HCSA (PAn.HCSA) ranging from 0.5 to 2 wt.% and the concentration of PEO ranging from 2 to 4 wt.%. By varying the ratio of polyaniline to PEO, the concentration of doped polyaniline in the PEO matrix varied between 11 and 50 wt.%. These polymer blend solutions were prepared by first dissolving the exact amount of HCSA required to fully dope the emeraldine base in chloroform. The emeraldine base was slowly added to the chloroform solution with vigorous stirring at room temperature. This solution was allowed to stir for 2 h and subsequently filtered using a No. 42 Whatman filter paper to remove any particulate matter. The PEO was then slowly added to the doped polyaniline solution over a period of 1 h with magnetic stirring to obtain a homogeneous solution.

2.3. Electrospinning experiments

The electrospinning apparatus, as shown in Fig. 1, used a variable high voltage power supply purchased from Gamma High Voltage Research. The glass pipette used in these experiments had a capillary tip diameter of 1.2 mm, and the pipette was tilted at approximately 5° from hori-

zontal so that a small drop was maintained at the capillary tip due to the surface tension of the solution. Alternatively, to produce larger quantities of electrospun fibers, the glass pipette in the above set-up was replaced by a 5-ml glass syringe with a Becton Dickinson 18 hypodermic needle. The tip of the needle was filed to produce a flat tip. A positive potential was applied to the polymer blend solution, by inserting a copper wire into the glass pipette or by attaching the lead to the high voltage power supply directly to the outside of the hypodermic needle. The collection screen was a 10 × 10 cm copper plate placed 25 cm horizontally from the tip of the pipette as the grounded counter electrode. The potential difference between the pipette and the counter electrode used to electrospin the polymer solution was 25 kV (electrical field strength, 1 kV/cm).

2.4. Characterization of electrospun fibers

The fiber diameter and polymer morphology of the electrospun PAn.HCSA/PEO fibers were determined using scanning electron microscopy (SEM). A small section of the non-woven mat was placed on the SEM sample holder and sputter-coated with gold (Denton Desk-1 Sputter Coater). An Amray 3000 SEM using an accelerating voltage of 20 kV was employed to take the SEM photographs.

The conductivity of the electrospun PAn.HCSA/PEO fibers and the cast film on a microscope glass slide was measured using the four-point probe method [7]. The thickness of the non-woven fiber mat and the cast films were measured using a digital micrometer (Mitutoyo) with a resolution of 1 μm. The current was applied between the outer electrodes using a Princeton Analytical Research 363 potentiostat/galvanostat and the resulting potential drop between the inner electrodes was measured with a Keithley 169 multimeter.

The polymer conformation of the electrospun fibers was determined using UV-visible spectroscopy by inserting a microscope glass slide into the path of the polymer jet in front of the copper target for 30 s. The UV-visible spectra of these fibers were measured between 300 and 1100 nm using a Perkin-Elmer Lambda 9 UV-visible-NIR spectrometer. As a comparison between the polymer blend in the solid state and electrospun fibers, the same polymer blend solution was used for electrospinning and also for casting a film onto a microscope glass slide.

3. Results and discussion

3.1. Fiber formation and morphology of electrospun PAn.HCSA/PEO fibers

Without the addition of PEO to PAn.HCSA dissolved in chloroform, no fiber formation occurred, as the viscosity

and surface tension of the solution were not high enough to maintain a stable drop at the end of the capillary tip. Adding more doped polyaniline could not increase the viscosity of the polymer solution, as PAn.HCSA has a very low solubility in chloroform. A stable drop at the end of the capillary tip was achieved once 2 wt.% PEO was added to the solution.

Before any PAn.HCSA/PEO electrospun fibers were produced, PEO was electrospun from chloroform at concentrations between 2 and 4 wt.% to examine the influence of adding polyaniline to the blend on the morphology of the fibers produced. As the potential difference between the capillary tip and the copper plate counter electrode was gradually increased, the polymer solution drop at the end of the capillary tip elongated from a hemispherical shape into a cone shape, that is often referred to as a Taylor cone [5]. Further increasing the applied potential resulted in a jet being initiated near the end of the capillary tip.

The morphology and fiber diameter of the PEO electrospun fibers produced was examined using SEM. For example, the SEM micrograph of the electrospun fibers from a 4 wt.% PEO solution dissolved in chloroform, shown in Fig. 2, revealed that the diameter of the PEO fibers in the

non-woven mat ranged from 950 nm to 2.1 μm , with an average fiber diameter of 1.6 μm . The individual electrospun PEO fibers appear to be randomly distributed in the non-woven mat, and the fibers generally had a slightly varied thickness along the fiber but without the presence of any beads [8]. Although a systematic study to determine the optimal electrical field and concentration for these PEO electrospun fibers with regard to fiber diameter was not completed, it appeared that the thickness of the electrospun PEO fibers was relatively independent of the concentration of the PEO dissolved in chloroform electrospun under these conditions.

The fiber diameter and morphology indicated that the PEO fibers produced were not nanofibers; however, these results are essentially identical to those obtained by Jaeger et al. [9,10] who have extensively studied the electrospinning of PEO fibers from both chloroform and aqueous solutions. They noted that although PEO fibers electrospun from chloroform had larger fiber diameters (1–2 μm) with a uniform thickness, this solvent eliminated the “beads on a string” morphology [9] sometimes found in thinner PEO fibers (200–800 nm) electrospun from aqueous solutions.

Based on these results, we subsequently investigated various ratios of polyaniline and PEO dissolved in chloroform to produce electrospun fibers. The polyaniline in the blend investigated ranged between 11 wt.% (0.5 wt.% PAn.HCSA and 4 wt.% PEO) and 50 wt.% (2 wt.% PAn.HCSA and 2 wt.% PEO). These limits were based on the solubility of PAn.HCSA in chloroform and the minimum concentration of PEO to maintain a stable jet. The experimental conditions successfully used to produce PEO fibers described previously were also used to electrospin the polyaniline/PEO blend fibers. More importantly, the addition of PAn.HCSA to the PEO dissolved in chloroform did not appear to hinder the electrospinning process. As was observed for the electrospinning of PEO fibers from chloroform, the jet was initiated at the end of the capillary tip.

The fiber diameter morphology of the polymer blend electrospun fibers was again examined using SEM. Based on the SEM micrographs for the different PAn.HCSA/PEO blend fibers investigated, these fibers showed a similar fiber diameter and morphology to the PEO fibers described above. For example, the SEM micrograph of the non-woven mat of electrospun fibers from a 2 wt.% PAn.HCSA/2 wt.% PEO solution, shown in Fig. 3, revealed that the fibers in the non-woven mat ranged between 950 nm and 1.9 μm (average fiber diameter, 1.6 μm) with a generally uniform thickness along the fiber. Again the electrospun fibers were distributed randomly in the non-woven mat. From the SEM micrographs of all the different polyaniline/PEO blends electrospun at an electrical field strength of 1 kV/cm, it appears that the addition of PAn.HCSA to the PEO solution has little effect on the diameter of the electrospun fiber. The PAn.HCSA/PEO electrospun fibers produced showed no evidence of any birefringence, thus

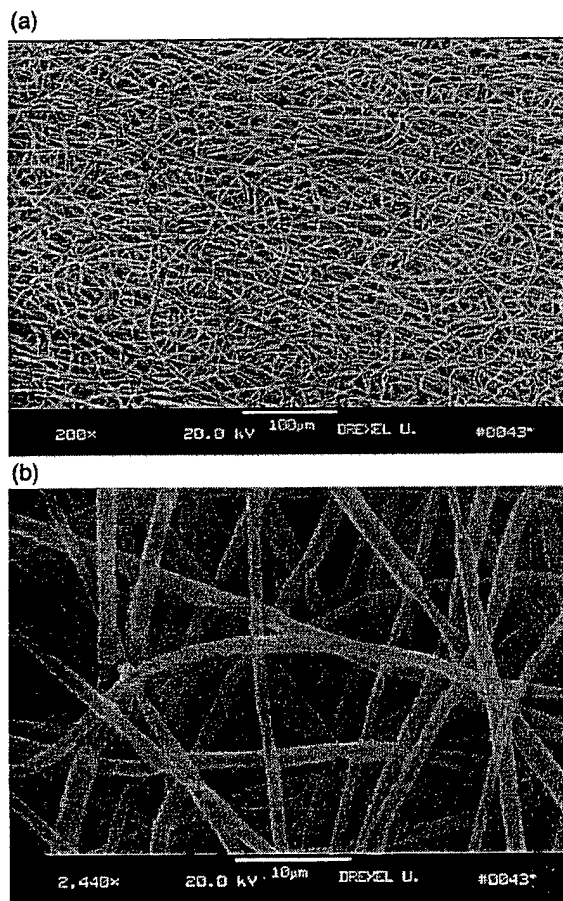


Fig. 2. SEM micrographs of the electrospun fibers from a 4 wt.% PEO solution dissolved in chloroform at 25 kV at (a) 200 and (b) 2440 magnification.

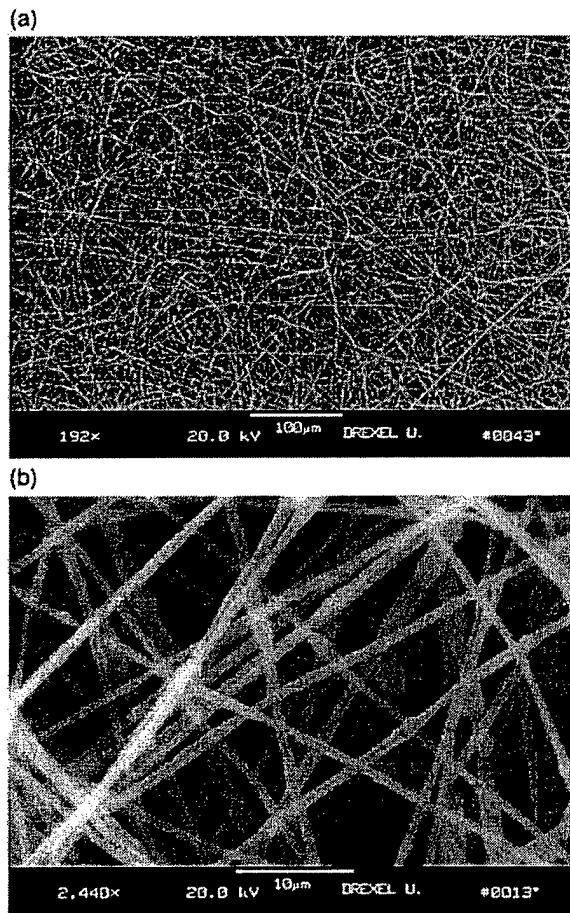


Fig. 3. SEM micrographs of the electrospun fibers from a 2 wt.% PAn.HCSA/2 wt.% PEO solution dissolved in chloroform at 25 kV at (a) 192 and (b) 2440 magnification.

indicating that the polymer chains in the fiber were not oriented with respect to the fiber axis.

3.2. Conductivity of PAn.HCSA/PEO blend films and fibers

Fig. 4 shows the room-temperature conductivity of the PAn.HCSA/PEO electrospun fibers and cast films at various ratios of polyaniline and PEO in the blend. This graph clearly demonstrates that the conductivity of the electrospun fibers in the non-woven mat is significantly lower than that for a cast film at the same polyaniline concentration. This is not an unexpected result as the four-point probe method measures the volume resistivity from which the conductivity can then be calculated and not that of an individual fiber. It must be noted that obtaining the conductivity of the non-woven mat was considerably more difficult than measuring the conductivity of the cast film due to the difficulty in obtaining an accurate thickness measurement on the highly compressible non-woven mat using the micrometer. As can be seen from the SEM micrographs of the electrospun fibers (Fig. 3), the non-woven mat is highly porous and therefore the “fill factor” of the polyaniline fibers is less than that of a cast film. However, it is reasonable to expect that the conductivity of an individual electrospun fiber will be higher than that of the non-woven mat and in fact should be approximately equal to the conductivity of the cast film.

The experimental results for the conductivity of the cast film show similar trends to that observed by Sixou et al. [11] who have extensively studied the conductivity of films cast from NMP solutions of polyaniline doped with trifluo-

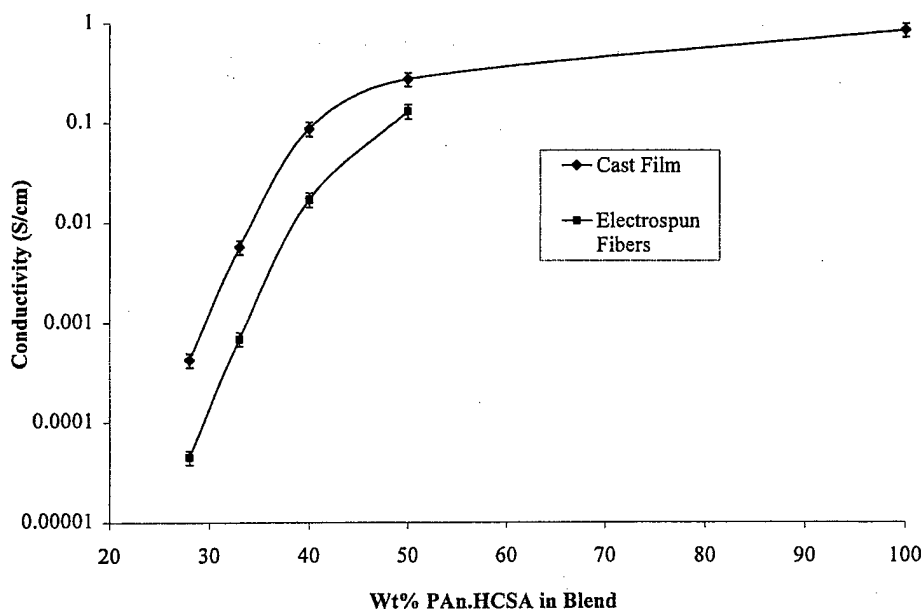


Fig. 4. Electrical conductivity of the PAn.HCSA/PEO blend electrospun fibers and cast films prepared from the same solution.

romethane sulfonimide acid and blended with PEO. Their results suggest that for doped polyaniline blended with PEO, the percolation threshold is approximately 4%, which is significantly higher than the percolation threshold for blends of polyaniline doped with HCSA and poly(methyl methacrylate) (PMMA) or nylon (in both cases less than 1%) prepared from *m*-cresol solvent [12,13]. Although not calculated in the present study, the percolation threshold for the PAn.HCSA/PEO blend is qualitatively consistent with the above study [11]. It is also significantly higher than that of PAn.HCSA blended with PMMA or nylon, which suggests that PAn.HCSA produces a more entangled network in these polymers than in PEO.

3.3. Spectroscopic characterization of PAn.HCSA/PEO blend films and fibers

The UV–visible spectra of different PAn.HCSA/PEO blend films cast onto a glass slide from chloroform after the solution was stirred for 24 h are shown in Fig. 5. The absorption spectra for the different blends show three absorption bands in the visible region, which are consistent with the emeraldine salt form of polyaniline. Both PEO and HCSA have absorption bands only at wavelengths shorter than 300 nm. The position of the two lower wavelength absorption bands at 352 and 430 nm (assigned as the benzenoid/quinoid π – π^* transition and a low wavelength polaron band, respectively) did not change significantly with the concentration of polyaniline in the blend [14]. However, as the concentration of PEO in the blend increased, the position of the high wavelength localized polaron band shifted to lower wavelengths. The position of this band blue-shifted from 793 nm for the pure PAn.HCSA film to 763 nm for the 33 wt.% PAn.HCSA/PEO blend (2 wt.% PAn.HCSA/4 wt.% PEO).

Recently, Zheng et al. [15] have shown that when emeraldine base is doped with HCSA in chloroform to

form a 2-wt.% solution of polymer and dopant, the high wavelength localized polaron band of the PAn.HCSA initially formed, gradually shifts from 730 to 800 nm over 72 h. This shift in the position of the localized polaron band is believed to arise from the slow de-aggregation of the polyaniline chains in solution. With stirring, the aggregated/cross-linked emeraldine base chains [16] gradually becomes disentangled after protonation with HCSA, resulting in a slow conformational change of the polyaniline backbone. This conformational change causes an increase in the conjugation length for the polymer chains, and hence the observed red shift of the localized polaron band. The position of the localized polaron band for the pure PAn.HCSA film is in excellent agreement for the position of this band as determined by Zheng et al. [15] for a film cast from chloroform after 24 h of stirring. However, the red shift of the localized polaron band, as the concentration of PEO in solution is decreased is due to the polyaniline chains becoming entangled with the PEO chains in solution, thus inhibiting the rate of de-aggregation of the polyaniline chains in solution.

MacDiarmid and Epstein [17,18] have proposed that polyaniline can exist in two distinct conformations: the crystalline “extended coil” (highly conducting) conformation and the amorphous “compact coil” (less conducting) conformation. As the above cast films exhibited an intense, well-defined localized polaron band between 760 and 790 nm and no significant near-infrared absorption, this indicates a “compact coil” conformation for the polyaniline chains, which is consistent with the low conductivity observed for the polyaniline/PEO blends.

The UV–visible spectra of different PAn.HCSA/PEO blend fibers electrospun onto a glass slide that was placed just in front of the copper target showed an essentially identical spectra to the cast films prepared from the same solutions (Fig. 5). Both the cast films and the electrospun fibers were prepared after 24 h of stirring, so the position of the absorption bands of the electrospun fibers are directly comparable to those observed in the cast film. The spectra for the electrospun fibers shows a π – π^* transition at 352 nm and a low wavelength polaron band at 420 nm, which are again independent of the PEO concentration. However, as was observed for the cast film, the position of the localized polaron band varied between 766 nm for the 2 wt.% PAn.HCSA/4 wt.% PEO electrospun non-woven mat and 785 nm for the 2 wt.% PAn.HCSA/2 wt.% PEO electrospun non-woven mat.

Absorption spectra of the polyaniline blend electrospun fibers were consistent with those of polyaniline in the emeraldine salt oxidation state and no other absorption bands were observed in the visible region, indicating that the high voltage used in this electrostatic process did not result in any over-oxidation of the polyaniline chains. Over-oxidation causes the degradation of the polyaniline backbone that results in inferior electronic and mechanical properties for the polymer [19].

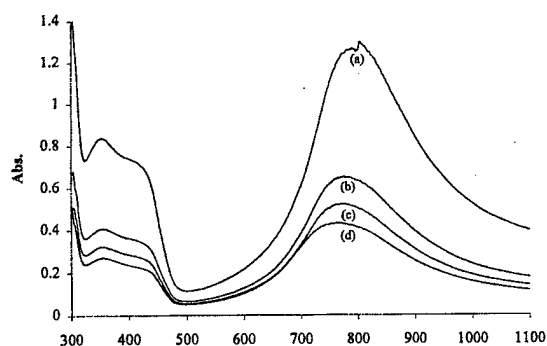


Fig. 5. UV–visible spectra of PAn.HCSA/PEO films cast from chloroform at various PEO concentrations for (a) 2 wt.% PAn.HCSA (pure PAn.HCSA), (b) 2 wt.% PAn.HCSA/2 wt.% PEO, (c) 2 wt.% PAn.HCSA/3 wt.% PEO and (d) 2 wt.% PAn.HCSA/4 wt.% PEO.

3.4. De-doping of electrospun PAn.HCSA / PEO fibers

De-doping of the electrospun PAn.HCSA/PEO fibers could not be achieved by suspending the non-woven mat in 1.0 M ammonium hydroxide aqueous solution since the water dissolved the PEO and caused the fibrous network in the non-woven mat to break apart. Instead, de-doping of the electrospun PAn.HCSA/PEO fibers (11–50 wt.% PAn.HCSA) was achieved by suspending the non-woven mat above the vapor of concentrated aqueous ammonium hydroxide solution. Within 3 s of exposing the non-woven mat to the ammonia vapor, the green non-woven fiber mat turned to blue, indicating that the emeraldine salt in the blend fibers was converted to emeraldine base. Attempts to characterize the emeraldine base/PEO blend fibers by both SEM and UV–visible spectroscopy were unsuccessful, as after the non-woven mat was removed from the ammonia source, the polyaniline in the non-woven mat turned back to the original green color of the as-spun mat. This indicated that emeraldine base in the blend was completely converted back to the conducting emeraldine salt form of polyaniline. The time for this spontaneous re-doping process depended on the ratio of polyaniline to PEO and varied between 3 s for the non-woven mat containing 11 wt.% PAn.HCSA and 7 s for the non-woven mat containing 50 wt.% PAn.HCSA. This extremely high rate of de-doping and spontaneous re-doping occurs at a very much faster rate than for films cast from the same solutions, which occurs on the minute time-scale. This presumably arises from a faster diffusion rate of ammonia vapor into and out of the polyaniline blend fibers, thus stressing the enormous effect an increase in the surface-to-volume ratio accomplished by the ultrafine fibers can have on selected chemical properties of a specific polymer.

4. Conclusions

Conducting ultrafine fibers with diameters less than 2 μm have been successfully produced using the electrospinning process by the blending of the conducting polymer, polyaniline, and PEO, in a wide range of blending ratios. By controlling the ratio of polyaniline to PEO in the blend, fibers having a desired conductivity (comparable to that of PAn.HCSA/PEO cast films) were produced.

The importance of the high surface to volume ratio provided by the electrospun fibers was evident from the at

least one order of magnitude increase in the rate of the vapor phase de-doping and at least two orders of magnitude in the rate of spontaneous re-doping, compared to the cast film.

The successful demonstration of the feasibility of producing electrically conducting blends of polyaniline and PEO in ultrafine fiber form has opened up new functional opportunities for electronic polymers in their doped (metallic) forms.

Acknowledgements

This work was financed jointly by the Office of Naval Research and the Army Research Office under the Multidisciplinary University Research Institute (MURI) program. The authors are grateful to Mr. Wan-Ju Li for his useful discussions and assistance at the beginning of this project.

References

- [1] A. Formhals, US Patent #1,975,504, 1934.
- [2] J. Doshi, D.H. Reneker, *J. Electrostat.* 35 (1995) 151.
- [3] P.W. Gibson, H.L. Schreuder-Gibson, D. Riven, *AIChE J.* 45 (1999) 190.
- [4] F.K. Ko, C.T. Laurencin, M.D. Borden, D.H. Reneker, The dynamics of cell–fiber architecture interaction, in: *Proceedings, Annual Meeting, Biomaterials Research Society, San Diego, April, 1998.*
- [5] D.H. Reneker, I. Chun, *Nanotechnology* 7 (1996) 216.
- [6] I. Chun, D.H. Reneker, H. Fong, X. Fang, J. Deitzel, N.B. Tan, K. Kearns, *J. Adv. Mater.* 31 (1996) 36.
- [7] ASTM Designation: D4496-87, 453.
- [8] H. Fong, I. Chun, D.H. Reneker, *Polymer* 40 (1999) 4585.
- [9] R. Jaeger, M.M. Bergshoeff, C.M.I. Batlle, H. Schonherr, G.J. Vancso, *Macromol. Symp.* 127 (1998) 141.
- [10] R. Jaeger, H. Schonherr, G.J. Vancso, *Macromolecules* 29 (1996) 7634.
- [11] B. Sixou, J.P. Travers, C. Barthet, M. Guglielmi, *Phys. Rev. B* 56 (1997) 4604.
- [12] Y. Cao, P. Smith, A.J. Heeger, *Synth. Met.* 55–57 (1993) 3514.
- [13] C.O. Yoon, M. Reghu, D. Moses, A.J. Heeger, Y. Cao, *Synth. Met.* 63 (1994) 47.
- [14] S. Stafstrom, J.L. Bredas, A.J. Epstein, H.S. Woo, D.B. Tanner, W.S. Huang, A.G. MacDiarmid, *Phys. Rev. Lett.* 59 (1987) 1464.
- [15] W. Zheng, Y. Min, A.G. MacDiarmid, M. Angelopoulos, Y.H. Liao, A.J. Epstein, *Synth. Met.* 84 (1997) 109.
- [16] M. Angelopoulos, Y.-H. Liao, B. Furman, T. Graham, *Macromolecules* 29 (1996) 3046.
- [17] A.G. MacDiarmid, A.J. Epstein, *Synth. Met.* 65 (1994) 103.
- [18] A.G. MacDiarmid, A.J. Epstein, *Synth. Met.* 69 (1995) 82.
- [19] P.J.S. Foot, R. Simon, *Phys. D Appl. Phys.* 22 (1989) 1598.

Presented at Fifth International Conference on Frontiers of Polymers and Advanced Materials and NATO Advanced Research Workshop on Polymers and Composites for Special Applications, Poznan, Poland, June 21-25, 1999.

Three Dimensional Fibrous Scaffolds for Tissue Engineering

Frank K. Ko Ph.D and Cato T. Laurencin, M.D. Ph.D
Drexel University, Philadelphia., PA. USA

ABSTRACT

The architecture of an engineered scaffold is an important consideration in the design of a synthetic tissue replacement. A hierarchical fiber scale design methodology has been employed in our laboratory ranging from microscale nonwoven to 3-D integrated fiber bundles in orthopaedic tissue engineering applications. Using the bioresorbable copolymer, poly(D,L-lactide-co-glycolide) [PLGA], we have fabricated a microfiber non-woven mesh and a 3-dimensional braided structure. These structures were examined by SEM in an *in vitro* cell culture environment. Matrices were seeded with osteoblasts from neonatal rat calvaria to determine the effect of scaffold architecture on cellular morphology and proliferation. SEM analysis of the microfiber matrix indicated a highly porous, structure resulting from the random arrangement of the microfibers. The 3-D braided matrix was shown to have a organized fibrous structure resulting from the 3-D braiding process. Examination of the attachment and proliferation of cells on the matrices revealed that cell morphology and proliferation patterns were dependent on cell type and matrix geometry. SEM analysis also indicated that cells responded dynamically to changes in structure due to the onset of degradation.

Introduction

Tissue Engineering was identified by the U.S. National Science Foundation some ten years ago as an emerging area of national importance and established the following definition: [1]

"Tissue engineering is the application of principles and methods of engineering and the life sciences toward the fundamental understanding of structure/function relationships in normal and pathological mammalian tissues and the development of biological substitutes to restore, maintain or improve functions"

Fueled by the exciting progress made in biotechnology in recent years, Tissue Engineering is quickly becoming a method of choice for the development of implants in surgery. It is expected that Tissue Engineering will become a viable option in the health care industry and it is anticipated to be on the verge of breaking into a rapid growth mode in the next decade. For example, in orthopaedic reconstruction, surgeons often replace damaged tissue resulting from

trauma, pathological degeneration, or congenital deformity with autogenous grafts [1.] Reconstructive surgery is based upon the principle of replacing these types of defective tissues with viable, functioning alternatives. The grafting of bone in skeletal reconstruction has become a common task of the orthopaedic surgeon with over 863,200 grafting procedures performed each year in the U. S. For cartilage replacement, there are over 1,000,000 procedures of various types performed each year and for ligament repairs, there are approximately 90,000 procedures performed per year [1.] Currently, autografts [2,3] (tissue taken from the patient) and allografts [4-6] (tissue taken from a cadaver) are the most common replacement sources for the treatment of musculoskeletal problems. In repair of anterior cruciate ligament injuries, a segment of the patellar tendon has been frequently used.[3] For cartilage and bone repair, transplantation of autogenous grafts has been the current treatment of choice. Unfortunately, these gold standards possess certain disadvantages. For any type of autogenous tissue, the key limitations are donor site morbidity where the remaining tissue at the harvest site is damaged by removal of the graft, and the limited amount of tissue available for harvesting. The use of allograft attempts to alleviate these problems. However, this type of graft is often rejected by the host body due to an immune response to the tissue. Allografts are also capable of transmitting disease. Although a thorough screening process eliminates most of the disease carrying tissue, this method is not 100% effective.[4] As a result of the limitations with conventional reconstructive graft materials, surgeons have looked to the field of tissue engineering for synthetic alternatives.[1,6-12]

As articulated succinctly by Professors Vacanti and Mikos, [13] the key challenges in Tissue Engineering are the synthesis of new cell adhesion-specific materials and development of fabrication methods to produce reproducible three-dimensional synthetic or natural biodegradable polymer scaffolds with tailored properties. These properties include porosity, pore size distribution, and connectivity, mechanical properties for load-bearing applications, and rate of degradation. In this paper, we introduce the large family of three-dimensional fiber architectures as well as the range of fiber size scale available for tissue engineering. The importance of structural size scale of the basic fiber building blocks was examined through controlled experiments by observing the cell-fiber architecture interaction.

Hierarchical Fiber Architecture Design

It is well known that biological tissues consist of well organized hierarchical fibrous structures ranging from nano to μm scale. (Fig. 1).[14] The successful regeneration of biological tissue and organs calls for the development of fibrous structures with fiber architectures conducive to cell deposition and cell proliferation. Of particular interest in Tissue Engineering is the creation of reproducible and biocompatible 3-D scaffold for cell ingrowth resulting in bio-matrix composites for various tissues repair and replacement.

THREE DIMENSIONAL FIBROUS SCAFFOLDS FOR TISSUE ENGINEERING

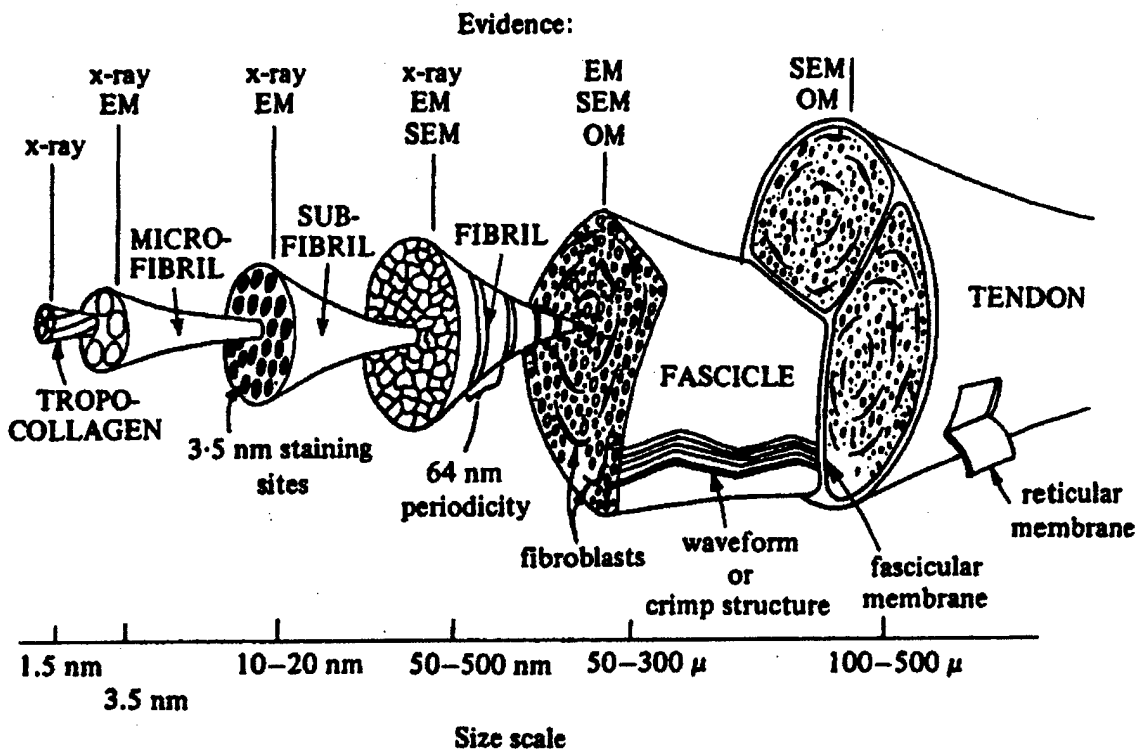


FIGURE. 1 Hierarchical Fiber Architecture of Tendons [14]

There is a large family of fiber architectures available for surgical implants (Figure 2), [15]. The design and selection of these fiber architectures for tissue engineering can be carried out on the fiber level and structural level resulting in a wide range of dimensional scale, fiber tortuosity and fabric porosity as characterized by the fiber volume fraction-orientation map .

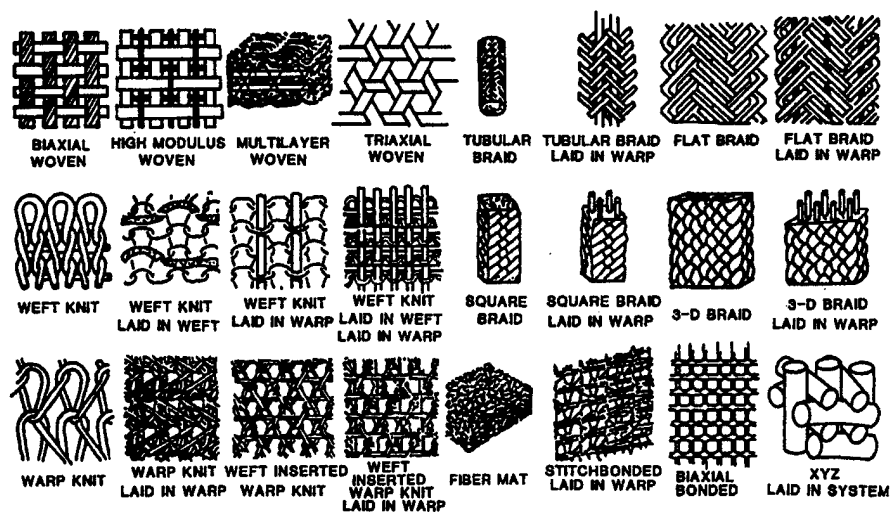


FIGURE. 2 Fiber Architecture for Surgical Implants

Since the 1950's, many of the textile structures illustrated in Figure 2 have been used for surgical implants with considerable success. Some of the structures and their respective applications are summarized in Table I. These fibrous structures are mostly from non-absorbable polymers consisting of fibers larger than 10 μm in diameter, although some microfibers are increasingly being used. Unfortunately, these fibers are developed primarily for clothing rather than for medical applications.

TABLE I. Textile Structures for Surgical Implants [16]

Application	Material	Structure	
		Yarn	Fabric
Arteries	Polyester Dacron 56 Teflon	Textured	Weft/warp knit Straight tube bifurcation Plain woven Straight tube, nonwoven
Tendon	Polyester Dacron 56 Kevlar	Low twist filament	Plain woven narrow tape coated with silicon rubber
Hernia Repair	Polypropylene	Monofilament	Tricot jersey knit
Esophagus	Regenerated collagen	Multifilament	Plain weave
Heart Valve	Polyester Dacron 56	Multifilament	Plain weave Knit
Patches	Polyester Dacron 56	Textured	Knitted velour
Sutures	Polyester Nylon Regen. collagen Silk	Monofilament Multifilament	Braid Woven tapes
Ligament	Polyester Teflon Polyethylene	Multifilament	Braid
Bone and Joints	Carbon in Thermoset or Thermoplastic Matrix	Multifilament	Woven Braid

In order to take into consideration of the three dimensional and nanofibrous nature of biological tissue we have developed an integrated hierarchical design methodology for the manufacturing of scaffolds for tissue engineering. A schematic of the hierarchical structural design of a braided structure is shown in Figure 3.

THREE DIMENSIONAL FIBROUS SCAFFOLDS FOR TISSUE ENGINEERING

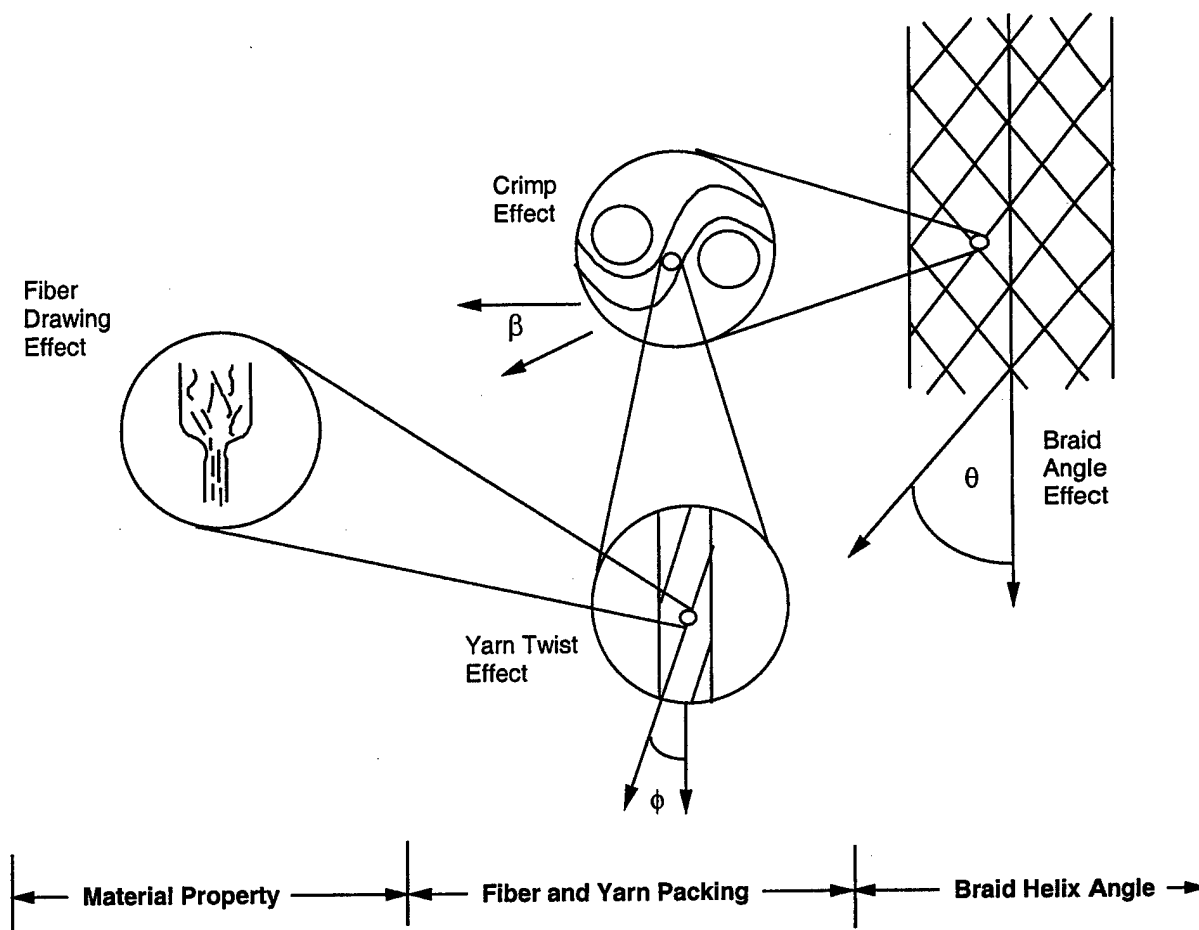


FIGURE 3. Structural Hierarchy of Fibrous Assemblies

In order to investigate the geometry and size scale effect, a nanofibrous structure and a 3-D braided structure were used for this preliminary demonstration of the design concept. The ultrafine fibers in the nano to micro scale were produced by an electrospinning technique[17,18,19]. In the electrospinning process an electric field is generated between an oppositely charged polymer fluid and a collection screen, the electrode. A polymer solution is added to a glass syringe with a capillary tip. An electrode is placed in the solution with another connection made to a metal screen. As the power is increased, the charged polymer solution is attracted to the screen. Once the voltage reaches a critical value, the charge overcomes the surface tension of the polymer cone formed on the capillary tip of the syringe and a jet of ultrafine fibers is produced. As the charged fibers are splayed, the solvent quickly evaporates and the fibers are accumulated randomly on the surface of the collection screen. This results in a nonwoven mesh of nano to micron scale fibers. A schematic drawing of the electrospinning process is shown in Figure 4.

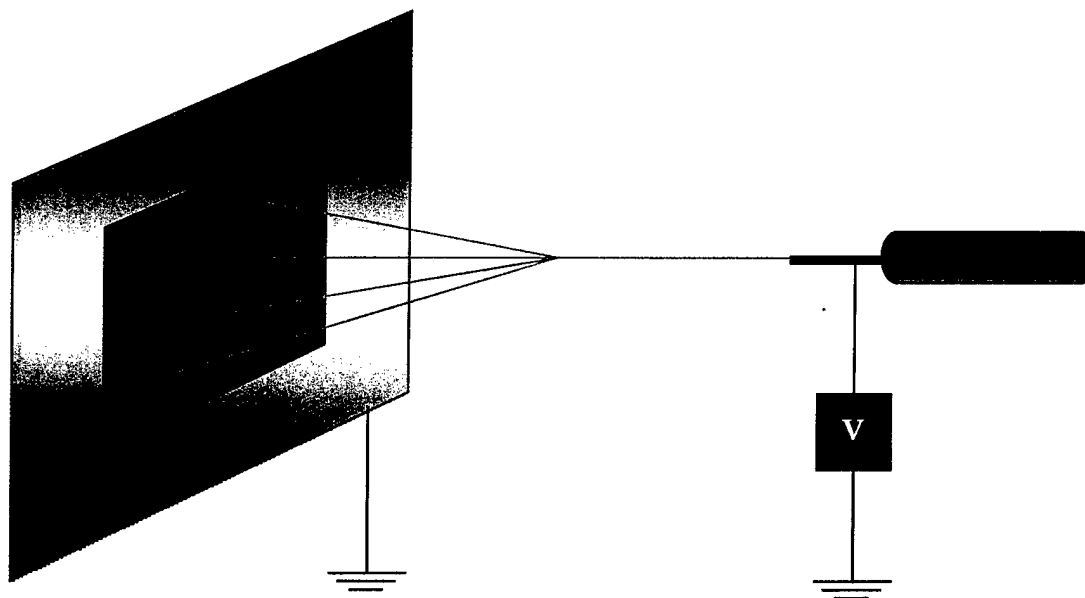


FIGURE 4. Schematic of the Electrospinning Process

The 3-dimensional braid consists of PLAGA yarns. This 3-D scaffold was formed by a braiding technique also known as the 4-step braiding process which uses alternative track and column motion to create a 3-dimension interconnected fibrous assembly. [19] A schematic drawing of the 4-step braiding equipment in circular and rectangular configurations is shown in Figure 5. along with the net shape 3-D structures that have been created with the 3-D braiding process [20].

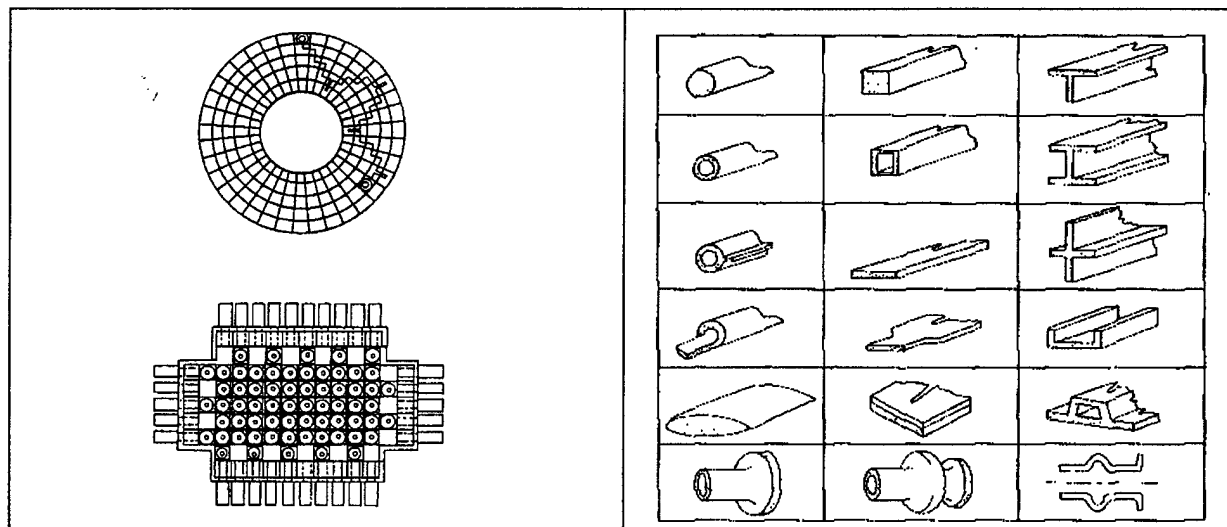


FIGURE 5. 3-D Braiding Equipment and Net Shaped Structures

THREE DIMENSIONAL FIBROUS SCAFFOLDS FOR TISSUE ENGINEERING

Movement of the carriers within the tracks is used to create vertical columns in the 3-D structure. Alternating rows and columns of the carriers in the braiding lattice are shifted to create the 3-D braid. The geometric parameters which determine the shape and fiber architecture of 3-D braids includes braiding angle distribution, yarn volume fraction, number of carriers, and braiding yarn width. This highly versatile system allows the freedoms for the direct formation of a variety of 3-D braided scaffolds with different architecture, geometrical shapes and mechanical properties.

EXPERIMENTAL

To demonstrate our hierarchical design concept, experiments were carried out using osteoblasts isolated from neonatal rat calvaria and grown to confluence in Ham's F-12 medium (GIBCO), supplemented with 12% Sigma fetal bovine on PLAGA sintered spheres, 3-D braided 20 mm filament bundles and nanofibrils. Four matrices were fabricated for the cell culture experiments. These matrices include (1.) 150 - 300 mm PLAGA sintered spheres. (2.) Unidirectional bundles of 20 mm filaments (3.) 3-D braided structure consisting of 20 bundles of 20 mm filaments. (4.) Nonwoven consisting of nanofibrils. The porosity of the microsphere structure, the nanofibrous specimens and the 3-D braided structures were characterized by mercury porosimetry measurement to characterize their pore size distributions. Cells were seeded on the UV sterilized PLAGA matrices at a density of 100,000 cells/sq. cm. The osteoblasts were cultured on the matrices for duration ranging from one day to 21 days. They were prepared according to established procedures by fixing in glutaraldehyde and dehydrated through a series of ethanol dilution. The seeded cells were labeled with [^3H]-thymidine and the thymidine were measured at 1,3,7,10, and 11 day interval.

OBSERVATIONS

Pore Size Distribution

The pore size and distribution were characterized using a Micrometrics Autopore III porosimeter. As shown in Figure 6, a bimodal distribution of pores was observed for the 3-D braided structures showing the existence of large interstitial pores on the order of 250 μm . and interfiber pores having a diameter on the order of 30 μm . On the other extreme, as shown in Figure 7, the nanofiber structures show a predominant concentration of pores with an average pore size of 14 μm . The pore surface of the nanofibrous structures was 0.823 m^2/g , an order of magnitude greater than that in the 3-D braided structure at 0.0045 m^2/g . The sintered spheres show a single mode pore diameter distribution over the range of 200-600 μm as shown in Figure 8, depending on the sphere diameter.

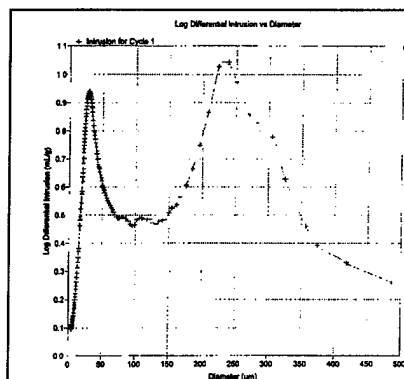


FIGURE 6. Pore Size Distribution of Braided Structure

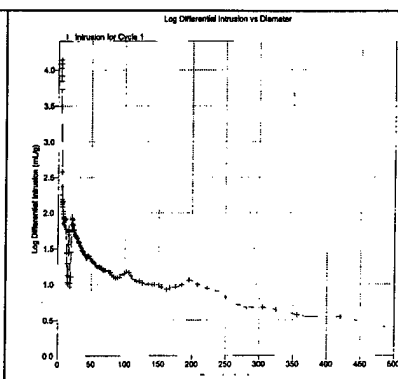


FIGURE 7. Pore Size Distribution of Nanofibrous Structure

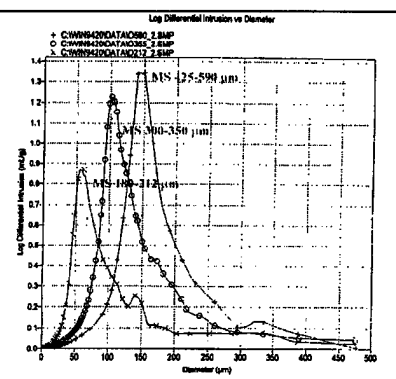


FIGURE 8. Pore Size Distribution of Sintered Spheres

Cell Proliferation

Cell proliferation was quantitatively measured by uptake of radio labeled methyl [^3H] thymidine (Sigma - St. Louis, MO). During the last 6 hours of cell incubation, 10 μCi of [^3H] thymidine was added to each sample well. Incubation was terminated by removal of the radioactive media. Cells were fixed to the matrices by soaking in methanol for 10 minutes. Samples were then rinsed twice with Hank's Balanced Salt Solution (HBSS). Uptake of [^3H] thymidine into cellular DNA was assessed by dissolution of the material in 2N perchloric acid. Uptake was measured using a EC&G-Wallac 1027 Beta scintillation counter.

The cell proliferation, as shown in Figure 9, is expressed in terms of the amount of [^3H] -thymidine uptake as a function of time. It can be seen that there is a consistent increase of cell population with time. The nanofibrous structure demonstrated the most proliferate cell growth whereas the tightly woven 3-D braided structure showed the least proliferation. On the other hand, the cell growth in fused microsphere structure is between that of the 3-D braid and the nanofibrous structures showing a surprising drop after the 10th day.

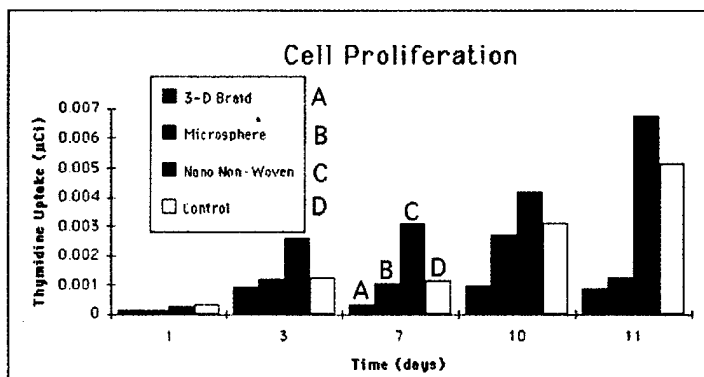


FIGURE 9. Cell Proliferation of Fibrous Scaffolding

THREE DIMENSIONAL FIBROUS SCAFFOLDS FOR TISSUE ENGINEERING

Cell-Scaffold Architecture Interaction

Experimental results show that cell growth pattern is related to the relative dimensions between of the components in the scaffold and that of the cells. Scanning electron microscopy pictures were taken from the cell-matrix systems which were prepared in a series of Freon 113 dilution (25%, 50%, 75%, and 100%). The SEM samples were sputter coated with gold (Denton Desk-1 Sputter Coater). An Amray 3000 SEM using an accelerating voltage of 20 kV was employed to take the SEM photographs shown in Figures 10. It can be seen that, in responding to the large spheres wherein the cells are more than 10X smaller than the spheres (Figure 10.a), the cells tend to spread over the surface of the sphere before connecting to the adjacent spheres and eventually forming an interconnected cellular network. In the case of 20 μ m filaments in unidirectional bundles and 3-D braid (Figure 10.b) wherein the cells are about the same order of magnitude in dimension, the cell-matrix reaction appear to be similar. The cells tend to slide off the matrix at the moment of seeding. Those cells remain on the surface of the substrates the cells tend to grow around the filaments and bridge onto the adjacent filaments along the length. The most intensive cell deposition was seen in the nanofibril nonwoven structure (Figure 10.c.) wherein the cells are more than an order of magnitude larger than the individual fibrils. Extensive cell spreading was observed along the length of the fibrils and through the thickness.

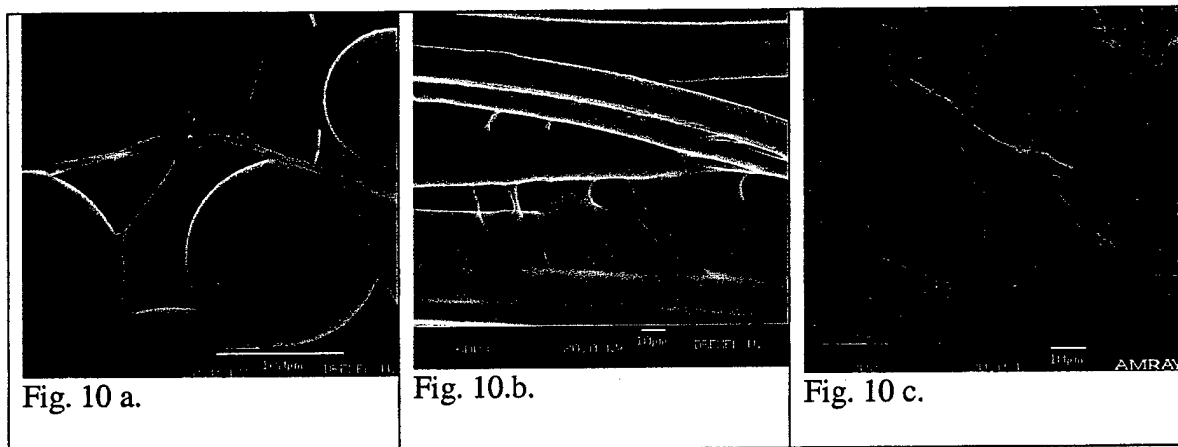


Figure 10. Cell-fiber Architecture Interaction

Summary and Conclusions

This study has shown that fiber based scaffolds are capable of supporting cell attachment and proliferation. The use of fiber technology in tissue engineering holds several advantages over a number of non-fibrous 3-D structures. Mainly, the ability to impart high levels of structural organization to the matrix may allow for precise control of matrix structure. The 3-D braided and nonwoven matrices demonstrate a range of 3-D fiber architectures one can design and produce. The braided matrix consisted of highly organized PLAGA yarns woven into a 3-D

structure. Although the nonwoven matrix was the result of randomly oriented microfibers, the structure was highly uniform. Both the 4-step 3-D braiding technique and the electrospinning process are promising fabrication methods showing high levels of versatility. The use of hierarchical fiber architecture based design includes the following advantages: 1) the ability to tailor a broad spectrum of substrates with a wide range of mechanical properties, and 2) the ability to create structures capable of supporting cell proliferation as well as the micro-diffusion of nutrients throughout the structure. The ability to manufacture a variety of different matrices and to maintain precise control over matrix fabrication are extremely important factors in the design of a tissue engineered scaffold. Based on the results of this preliminary study, we feel that fiber based scaffolds show promise as replacements for orthopaedic tissues as well as for a broad range of biological tissues such as skin, arteries, muscles etc.

ACKNOWLEDGMENTS

This study was supported in part by the following grants: NIH Grant 5 F31 GM18905-02, NIH Grant AR46117 and NSF Presidential Grant BES9553162/BES981782. The assistance provided by Roger Li, Mark Borden, James Cooper and Mitch Marmel in the preparation of this paper is appreciated.

REFERENCES

1. Skalak, R., Fox, C.F. and Fung, Y.C. Preface, in *Tissue Engineering*, Skalak, R., Fox, C.F. editors, Proceedings of NSF workshop on Tissue Engineering, Granlibakken, Lake tahoe, California, Feb. 26-29, 1988.
2. R. Langer, and J.P. Vacanti. *Science*. 260, 920 (1993).
3. O.H. Friedman, J.M. Sherman, et al. *Clin. Ortho.* 196, 9, (1985).
4. G.E. Jackson, R. Windler, and T.M. Simon. *Amer. J. Sports Med.* 18, 1, (1990).
5. A.R. Gadzag, J.M. Lane, D. Glaser, R.A. Forster. *J. Amer. Acad. Ortho. Surg.* 3, 1 (1995).
6. M. Shino, S. Inoue, et al. *J. Bone and Joint Surg.* 70B, 556 (1988).
7. D.W. Jackson, J.T. Heinrich, M. Timothy, and M.S. Simon. *Arthroscopy* 10, 442, (1994).
8. M.A. Attawia, J.E. Devin, and C.T. Laurencin. *J. Biomed. Mater. Res.* 29, 843 (1995).
9. C.N. Cornell. *Tech. in Orthop.* 7, 55 (1992).
10. D.W. Jackson, Ed. *The Anterior Cruciate Ligament: Current and Future Concepts*. (Raven Press: New York; 1993).
11. C.B. Frank, S.L.-Y. Woo, T. Andriacchi, et al. *Injury and Repair of the Musculoskeletal Soft Tissues*. edited by S.L.Y. Woo, and J.A. Buckwalter. (American Academy of Orthopaedic Surgeons, Park Ridge, 1988), p. 45.
12. R.P. Lanza, R. Langer, and W.L. Chick, Eds, *Principles of Tissue Engineering*. (R.G. Landes Company and Academic Press, Inc.; 1997).
13. Vacanti, C.A. and Mikos, A.G., Letter from the Editors, *Tissue Engineering*, Vol. 1, Number 1., 1995

THREE DIMENSIONAL FIBROUS SCAFFOLDS FOR TISSUE ENGINEERING

14. Kastelic, J., Galeski, A., and Baer, E., "Structure and Function of Mammalian Tendon," *Journal of Connective Tissue Research*, 6, 1978, pp.11-23
15. Ko, F.K., "Preform Architecture for Ceramic Matrix Composites," Ceramic Bulletin, February, 1989.
16. Ko, F. K., "Medical Applications for Textile Structures," *Textile Asia*, April, 1997.
17. Formhals, A., US Patent 1,975,504 (1934)
18. Ko, F K., Laurencin, C. T., Borden, M.D and Reneker, D., "The Dynamics of Cell-Fiber Architecture Interaction," *Proceedings, Annual Meeting, Biomaterials Research Society*, San Diego, April, 1998.
19. J. Doshi and D. Reneker. *J. of Electrostatics*. 35, 151 (1995).
20. Ko, F. K., "Three Dimensional Fabrics for Composites" in *Textile Structural Composites*. Edited by T.W. Chou and F.K. Ko (Elsevier, Amsterdam, 1989).

Comparison of the Low and High Velocity Impact Response of Kevlar Fiber-Reinforced Epoxy Composites

REFERENCES: Shaker, M., Ko, F., and Song, J., "Comparison of the Low and High Velocity Impact Response of Kevlar-Fiber Reinforced Epoxy Composites," *Journal of Composites Technology and Research*, JCTRER, Vol. 21, No. 4, October 1999, pp. 224-229.

ABSTRACT: Failure mechanisms of basket weave and 3-D braided Kevlar-fabric reinforced epoxy composites under low and high velocity impacts have been studied. The purpose of this study is to examine the initiation and development of damage under these two widely differing loading conditions on 2-D and 3-D structure fabric composites. The critical evaluation of post-damage composite panels was conducted using a combination of high magnification photography, optical microscopy, and scanning electron microscopy (SEM). The first objective, quantification, has been realized in principle with regards to laminated composites, and it has been demonstrated that dispersive failure occurs in these composites. The second objective in this work established the relationship between kinetic energy absorbed and the damage tolerance of interleaved composites as assessed by the impact tests. High velocity impact loading by a small projectile is generally more detrimental to the integrity of a composite structure than low velocity dropweight impact loading.

KEYWORDS: Kevlar-fabric reinforced epoxy, impact test, low velocity, high velocity, 3-D braid, basket weave

Many researchers have studied impact failure mechanisms, and much effort has been concentrated on studying low velocity impact failure mechanisms. The failure mechanisms of composites have become of great academic and practical interest [1-5]. However, the failure mechanisms of composites are still poorly understood, possibly because of the complex structures of these materials. With the increasing use of advanced composite material in both civil and military structural applications, attention is currently being centered on assessing their response to localized impact loading. The impact threat may take many forms, ranging from a dropped tool traveling at perhaps three or four meters per second to small arms fire traveling at many hundreds of meters per second. In these two extremes the response of the structural component is likely to be completely different. Under conditions of low velocity impact loading, where the time of contact between the projectile and target are relatively

long, the whole structure responds, enabling kinetic energy to be accommodated at points well away from the point of impact [6]. Here, the geometrical configuration of the target is likely to be important since it will determine its energy-absorbing capability. Indeed, Broutman and Rotem [7] have shown that increasing the length of a glass-fiber reinforced composite beam increases its low velocity impact response. Conversely, high velocity impact loading by a light projectile tends to induce a more localized form of target response, resulting in the dissipation of energy over a comparatively small region [8]. Clearly, these two distinct forms of impact loading will create differing levels of damage with differing consequences on the subsequent load-carrying capability of the structure.

The work presented here examines the low and high velocity impact response of basket weave and 3-D braided structures of Kevlar fabric reinforced epoxy composite and assessed the relative severity of these two loading conditions. Information obtained from optical micrographs and a scanning electron microscope (SEM) was used to examine the initiation and development of impact damage in these composites and was then used to investigate the influence of target geometry on impact response.

Experimental and Sample Preparation

Ballistics Impact Testing

Ballistic impact testing was performed using the high-speed impact apparatus located at the Army Research Laboratory, Aberdeen Proving Grounds, MD. The tests were conducted in accordance with Military Standard MIL-STD-662E, V50 Ballistic Test for Armor [9]. The fragment-simulating projectile was the .22 caliber type 2 conforming to MIL-P-46593, weighing 17 grains. The impact points were a minimum distance of 3.81 cm (1.5 in.) from each other. The samples were rigidly mounted with the area of impact normal to the lines of fire.

Testing Conditions:

- Type of projectile: Fragment simulating projectile
- Weight of FSP: 17 grains (1.1 g)
- Shape of FSP: Cylinder with chiseled head
- Diameter of FSP: 5.59 mm
- L/D of FSP: 1.0
- FSP Material: Steel
- Modulus of FSP: 200 GPa
- V50 of Actual Helmet: 2150 ft/sec (656 m/sec)
- Density of Steel: 7.8 g/cm³

¹ Drexel University, Department of Materials Engineering, Philadelphia, PA 19104.

² U.S. Army Natick Research, Development, and Engineering Center, Fiber and Polymer Science Division, Science and Technology Directorate, Natick, MA 01760.

Assuming that the projectile mass is constant during the penetration of the target, the kinetic energy (KE) absorbed by the target is:

$$KE = 1/2 m (V_s^2 - V_r^2) \quad (1)$$

where m is the projectile mass (kg), and V_s and V_r are striking and residual velocities (m/s), respectively.

Drop Weight Impact Testing

Low velocity impact tests were performed on a Dynatup model 8140 instrument impact tester in conjunction with a Dynatup model 730-1 data acquisition system [10]. Under normal testing conditions, the striking energy should be greater than needed in order to penetrate the tough samples, while not exceeding the load cell capabilities. Through testing, it was found that the following is a suitable combination for the samples in this study:

- Drop Weight: 295 kg (606 lb)
- Tup Diameter: 1.27 mm (0.5 in.)
- Velocity: 3.1 m/s (10.18 ft/s)
- Impact Energy: 1332 J (982.36 ft-lb)

Microscopy

An optical microscope was employed to evaluate the internal features of composites. In addition, optical microscopy was used to observe morphological changes to the fibers. The surface features of these composites were viewed using scanning electron microscopy (SEM JOEL model JSM-35CF), which provided a three-dimensional perspective of both fibers and yarns.

Results and Discussion

The kinetic energy absorbed by four different types of fabric structure reinforced composites during drop-weight impact and ballistic impact is shown in Fig. 2.

As it can be seen, in all cases, kinetic energies absorbed under ballistic impact (high velocity impact) were considerably lower than those under drop-weight impact (low velocity impact). Furthermore, it is clear that the most dramatic differences were observed in 3-D structure composites (3-D braided and multi-axial warp knit (MWK)). In fact, kinetic energy absorbed by these composites under low-velocity impact were more than twice of the kinetic energy absorbed under high-velocity impact.

In the case of 2-D structure composites (basket and triaxial), the basket weave composite shows higher energy absorption over the triaxial weave composite under both low and high-velocity impact loading.

For detailed failure behavior of the different structures, the basket weave composite and the 3-D braided composite were chosen as representations of 2-D and 3-D structure, respectively.

1. Comparison of the Low and High Velocity Impact Response of Basket Weave Kevlar Fiber-Reinforced Epoxy

For conditions of low velocity impact loading, the size and shape of the target determines its energy-absorbing capability and, therefore, its impact response. High velocity impact loading by a fast moving projectile induces a localized form of target response, and the level of damage incurred does not, therefore, appear to be governed by the areal size of the component.

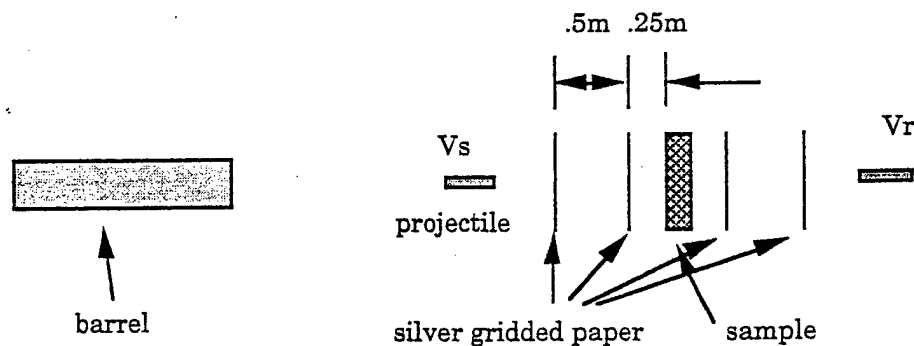


FIG. 1—Schematic of ballistic test setup.

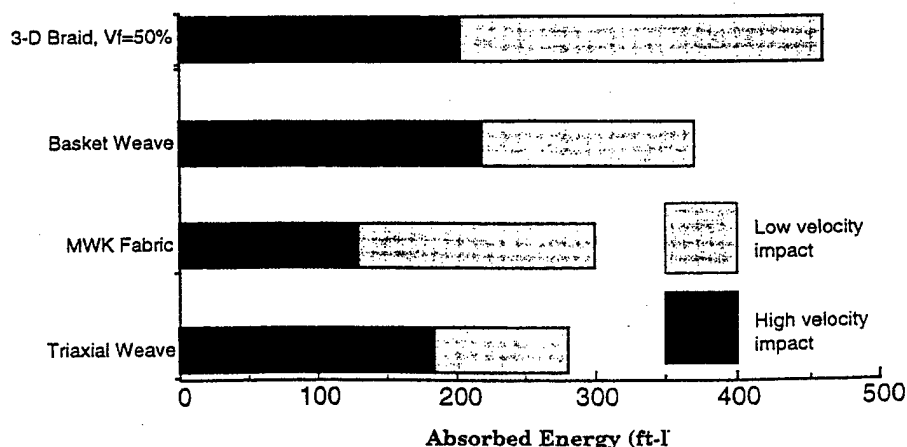


FIG. 2—Kinetic energy under drop-weight and ballistic impact testing.

Fracture Surface Observation

A side view of the basket weave ($V_f = 50\%$) composite in low velocity impact is shown in Fig. 3. When sufficient energy to crack the matrix was applied (Fig. 3), delamination and fiber fracture was extensive throughout the thickness of the laminate, spreading to points well away from the point of impact. Here, the penetrating action of the impact tended to shear the fibers to the direction of impact, resulting in formation of a frustrum-shaped fracture zone. Initiation and development damage in this laminate is detailed in optical micrographs (Figs. 4 and 5).

Damage development in the laminate plies after high velocity impact loading is shown in Fig. 6. When sufficient energy to crack the matrix was applied, delamination extended well away from the point of impact, and damage on both the upper and lower surfaces of the target was clearly visible. Complete target perforation occurred at high velocity (this being somewhat higher than that measured for drop-weight loading) and again resulted in the formation of the characteristic conically shaped shear zone around the point of impact (Figs. 7, 8, and 9).

High-velocity impact loading induces a localized form of target response (Fig. 6) where most of the energy is dissipated over a small zone immediate to the point of impact. Conversely, low velocity impact loading generates an overall mode of target response whereby energy can be dissipated at points well away from the

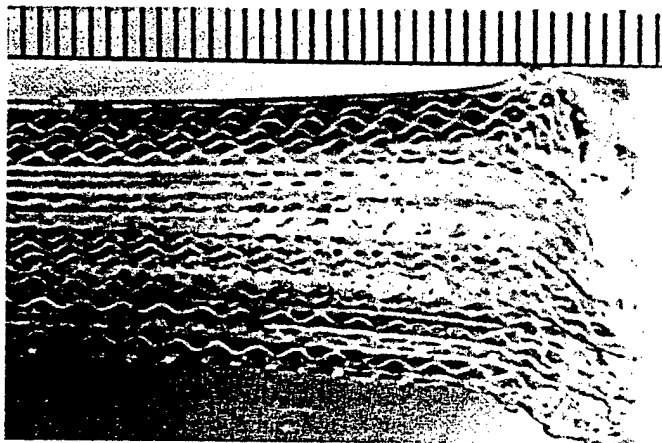


FIG. 3—Side view of fracture surface of low velocity impact.

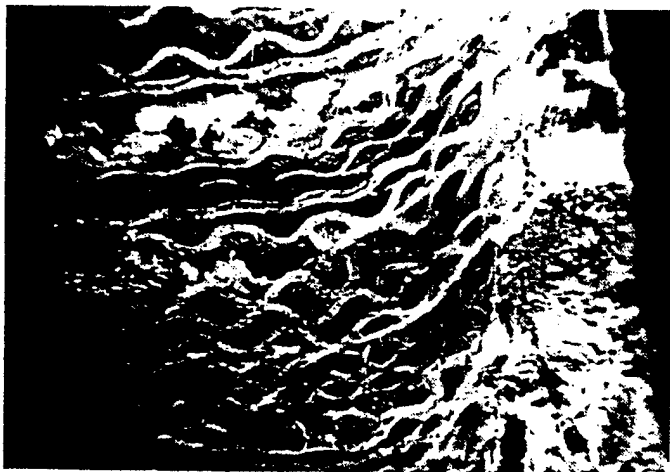


FIG. 4—Optical microscope photo side of low velocity impact.

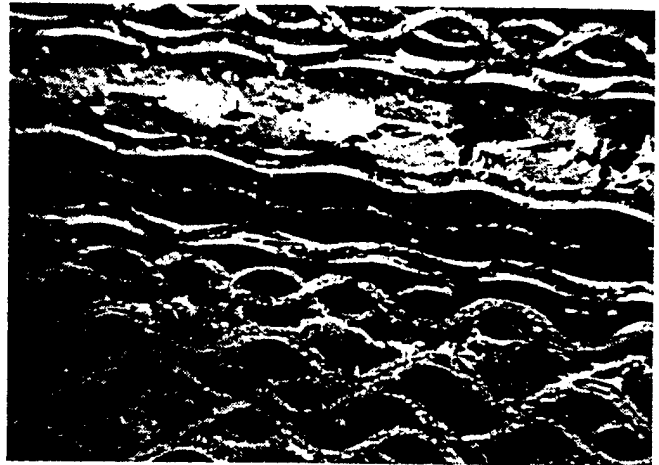


FIG. 5—Optical microscope photo side of low velocity impact.

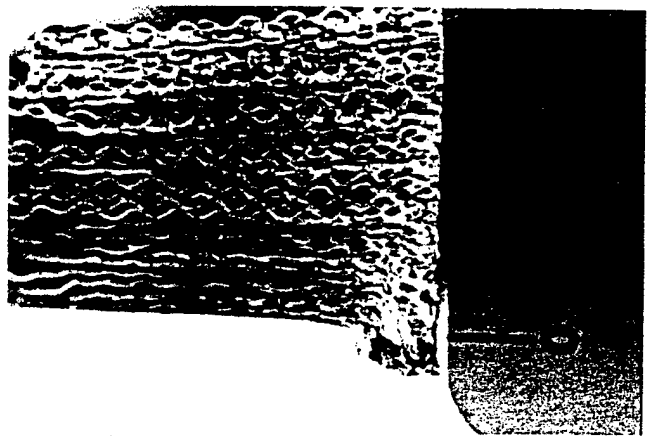


FIG. 6—Side view of fracture surface of high velocity impact.

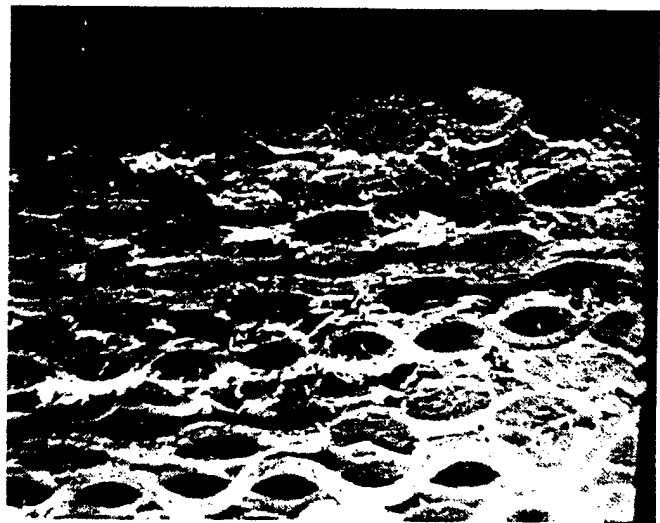


FIG. 7—Optical microscope photo side of high velocity impact.

point of contact (Fig. 3). These phenomena are clear in SEM photos of the impact area for high and low velocity impact (Figs. 10 and 11).

In the case of high velocity impact loading, the level of delamination was significantly greater. Clearly, under these conditions of

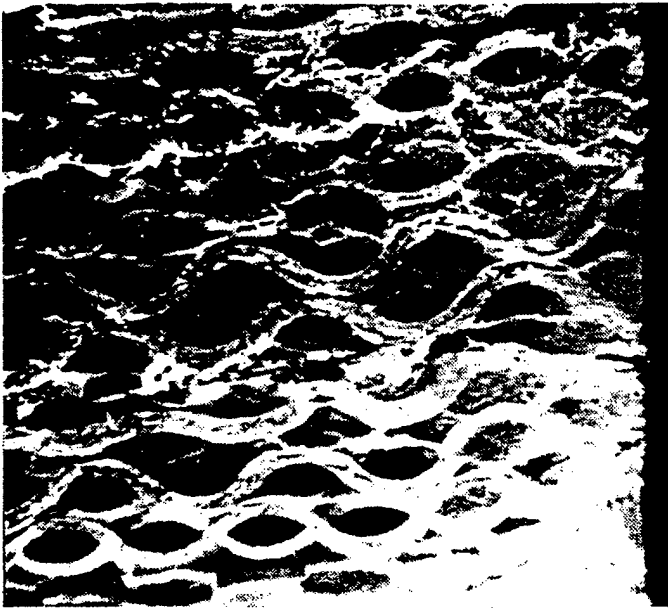


FIG. 8—Optical microscope photo side of high velocity impact.

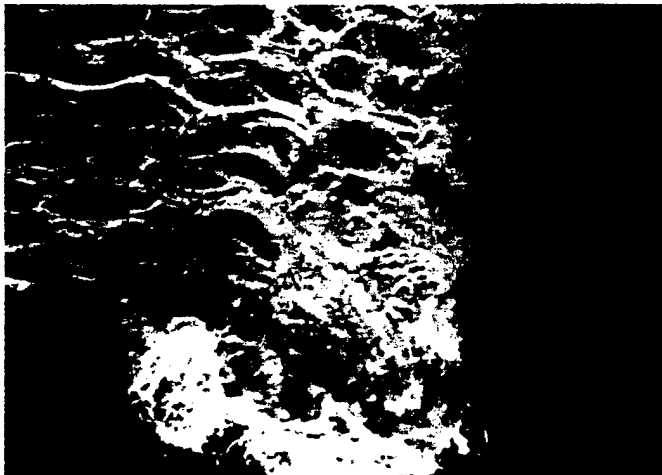


FIG. 9—Optical microscope photo side of high velocity impact.

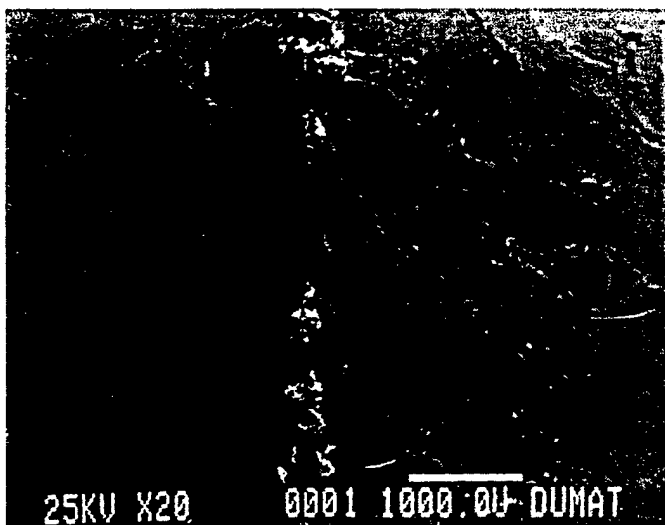


FIG. 10—SEM photo for impact area at high velocity impact.

high velocity impact loading more energy was dissipated in creating these zones of interlaminar fracture. Previous photos clearly show that high velocity impact represents a more severe form of loading condition.

2. Comparison of the Low and High Velocity Impact Response of 3-D Braided Kevlar Fiber Reinforced Epoxy

Fracture surface observation: The side view of the 3-D braided composite in low and high velocity impact are shown in Figs. 12 and 13, respectively.

At low velocity, the penetrating action of the impactor tended to shear the fiber to direction of impact, resulting in the formation of a frustrum-shaped fracture zone (Fig. 12). However, at high velocity impact, complete target perforation occurred, this being somewhat higher than that measured for drop weight loading, and again resulted in formation of the characteristic conically shaped shear zone around the point of impact cup—cone fractures can be seen at both sides of the sample (Fig. 13).

The matrix is shown in Figs. 14 and 15 cracking along the braiding yarn path near the penetration entrance. This clearly shows that high velocity represents a more severe form of loading condition. The same phenomena can be seen in Figs. 16 and 17, showing the bottom of the sample at low and high velocity impact. An examination of the bottom of the high velocity impact sample (Fig. 17)



FIG. 11—SEM photo for impact area at low velocity impact.



FIG. 12—Side view of fracture surface of low velocity impact.

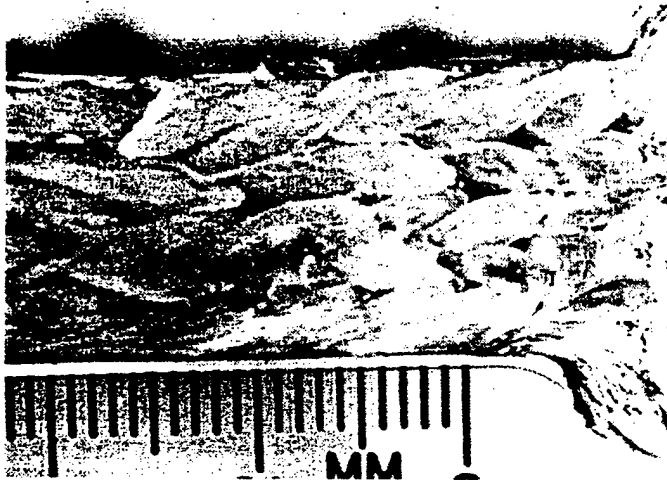


FIG. 13—Side view of fracture surface of high velocity impact.

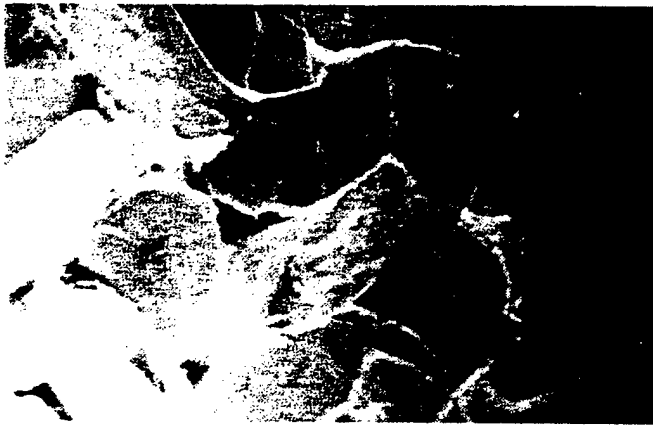


FIG. 14—Optical microscope photos of the center of high velocity impact.



FIG. 15—Optical microscope photos of the center of low velocity impact.



FIG. 16—Bottom of the sample at low velocity impact.

shows that the cracks grew along the matrix fiber and are more severe than those produced under low impact.

SEM photos for the impact area reveal that the impact area (Fig. 18) of a high velocity impact is very small when compared to a low velocity impact (Fig. 19). Some similarities apparently do exist between processes of damage development under low and high velocity impact conditions. In both cases initial failure occurred at the lower surface of target, probably as a result of a locally high flexural stress field. Furthermore, the shear zones observed at the perforation thresholds were remarkably similar considering the enormous difference in impact strain rates.

In Figs. 18 and 19, SEM photos illustrate how the cracks in the matrix grew along the fiber (near the circumference of each fiber bundle) and were retarded by the fiber under low and high velocity impact are same.

Conclusion

Impact tests on a number of Kevlar fiber-reinforced epoxy composites indicate that the low and high impact responses of a composite structure may vary considerably. Under low-velocity impact loading (where the energy absorbing capability of the structure is important), structural geometry determines the target's impact response. Conversely, under conditions of high velocity impact loading (where the projectile generates a localized form of target re-

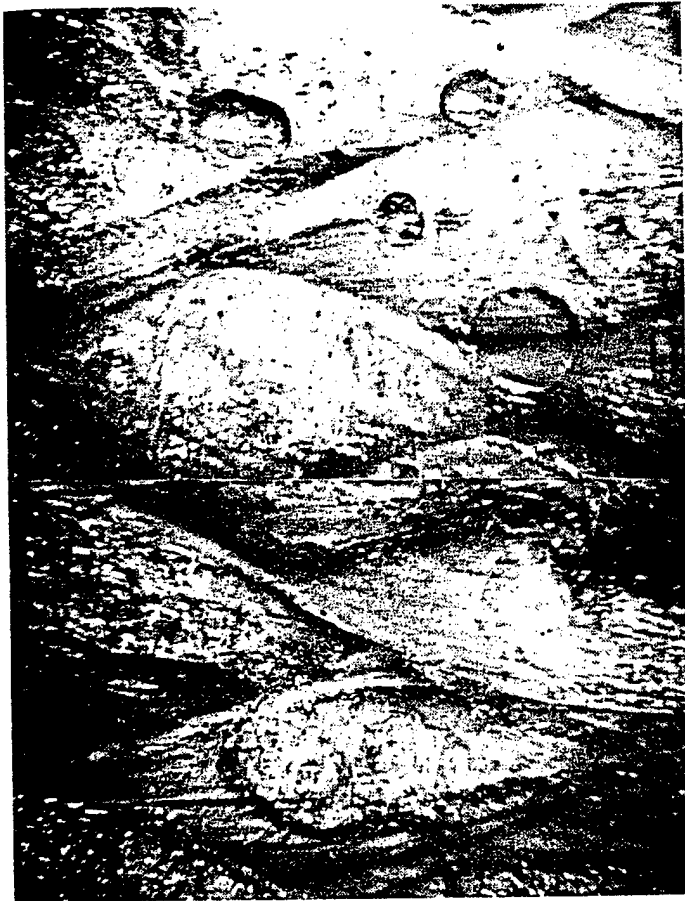


FIG. 17—Bottom of the sample under high velocity impact.

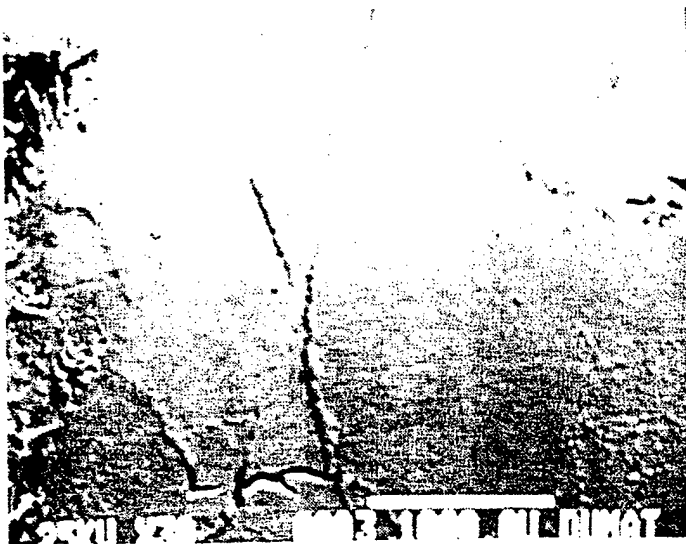


FIG. 18—SEM photo for side view at high velocity impact.

sponse), geometrical parameters such as the width and length of the target appear to have very little effect on impact response. Consequently, ballistic impact loading tends to produce greater levels of damage.

High velocity impact loading by a small projectile is generally more detrimental to the integrity of a composite structure than low velocity drop-weight impact loading at the impact point.

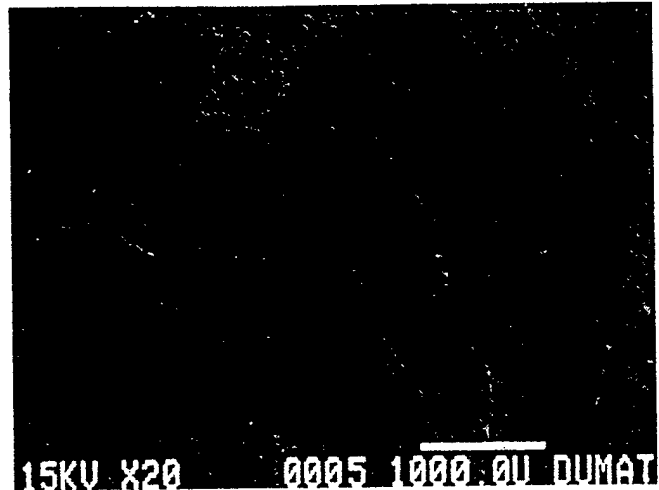


FIG. 19—SEM photo for side view at low velocity impact.

Acknowledgment

The authors gratefully acknowledge the financial support for the project from the U.S. Army Natick Research, Development and Engineering Center, Natick Massachusetts.

References

- [1] Smith, J. C., Fenstermaker C. A. and Shouse, P. J. "Stress-Strain Relationships in Yarns Subjected to Rapid Impact Loading," *Textile Research Journal*, November 1963.
- [2] Cruse T. A., and Stout, M. G., "Fractographic Study of Graphite-Epoxy Laminated Fracture Specimens," *Journal of Composite Materials*, Vol. 7, 1973, pp. 272-76.
- [3] Jang, B. Z., Lieu, Y. K., Chang Y. S., and Hwang, L. R., "Cryogenic Failure Mechanisms of Fiber-Epoxy Composites for Energy Applications," *Polymer Composites*, Vol. 8, No. 3, 1987.
- [4] Purslow, D. "Fractography of Fiber-Reinforced Thermoplastics. Part 3 Tensile, Compressive and Flexural Failures," *Composites Vol. 19*, No. 5, September 1988.
- [5] Birger, S., Moshonov A., and Kenig, S., "The Effects of Thermal and Hygrothermal Ageing on the Failure Mechanisms of Graphite-Fabric Epoxy Composites Subject to Flexural Loading," *Composites*, Vol. 20, No. 4, July 1989.
- [6] Cantwell, W. J. and Morton, J., "Comparison of the Low and High Velocity Impact Response of CFRP," *Composites*, Vol. 20, 1989, pp. 545-551.
- [7] Broutman, L. J. and Rotem, A., "Impact Strength and Toughness of Fiber Composite Materials," *ASTM STP 568*, 1975, pp. 114-133.
- [8] Cantwell, W. J., "The Influence of Target Geometry on the High Velocity Impact Response of CFRP," *Composite Structures*, Vol. 10, 1988, pp. 247-265.
- [9] Ko, F. K. and Hartman, D., "Impact Behavior of D and 3-D Glass/Epoxy Composites," *SAMPE Journal*, July/August, 1986.
- [10] Dynatup General Research Corp., GRC 730 Operator's Manual.

Modeling of the ballistic behavior of gradient design composite armors

J. Jovicic*, A. Zavaliangos, F. Ko

Department of Materials Engineering, Drexel University, 31st & Chestnut St., Philadelphia, PA 19104, USA

Received 30 August 1999; received in revised form 19 October 1999; accepted 3 January 2000

Abstract

The application of gradient design concept in armors offers possibilities in the reduction of weight and cost without significant reduction of ballistic resistance. Experimental results of composite backed plates consisting of layers of ceramic spheres embedded in epoxy showed that a ballistic limit of 3000 ft/s (1000 m/s) can be achieved, as shown in Fig. 1, without weight penalty compared to solid ceramic tiles. The ceramic sphere facing also provides the feasibility for flexible armor manufacturing. The design of such materials includes a plethora of parameters. In order to develop a precise methodology for the optimization of gradient design composite armors, an improved understanding of the relative significance of the design parameters must be developed. One way to study the relative significance of these parameters is through computational modeling. Computational limitations impose compromises in the modeling of both geometry and material behavior. Two types of models are discussed: (a) an approximate fiber/epoxy two-phase model for the backing; and (b) a damage-based, rate-dependent model for the ceramic spheres embedded in the epoxy. The development of a library of fiber architectures based on the unit cell has been initiated, which will open the possibility of the structural optimization along with simulation of the high velocity impact phenomena of advanced composites. © 2000 Elsevier Science Ltd. All rights reserved.

Keywords: Gradient design composites; A. Fabrics/textiles

1. Introduction

The next generation peacekeeping forces and law enforcement officers are under increasing ballistic threats. The development of the light armor materials systems, which would have a significant improvement in penetration resistance, impact energy dissipation, and damage containment, is of great importance in designing of body armors, helmets, and protection against projectile threats in structures such as helicopters, tanks and aircraft.

An understanding of the fundamental dynamic response of the material/structural geometry interaction is essential to the development and assessment of new armor systems. Accordingly, the aim of our current study is to demonstrate the feasibility of superimposing a hardened surface with a high symmetry, strong and tough fibrous network to produce highly conformable, high impact resistant armor systems. The finite element (FE) analysis was performed to simulate the structural behavior of composite armors, and assess the effect of materials selection and fiber architecture.

2. Background

The high velocity impact of a projectile with a solid target results in an extremely complex mechanical (and not only mechanical) process that has been examined for the past 200 years. A complete description of this problem would involve considerations of all phases in the theory of continuum mechanics. This includes the compressible fluid flow, dynamics of elasticity and plasticity, but also other behavior such as melting and solidification, vaporization and condensation, and kinetics of phase change [14]. As a consequence, certain simplification is needed for tackling the problems. Several models have been proposed for various stages of the impact process [1,2,20].

At the present time, there are three reasonably distinct directions for these investigations [17,20]:

- derivation of empirical formulas based on extensive testing;
- development of relatively “simple” models of the perforation process and applying the relevant equations of motion and material behavior; and
- full numerical solutions based on solving all the governing equations over a spatial grid at successive time increments.

* Corresponding author. Tel.: +1-215-895-2327; fax: +1-215-895-6760.

E-mail address: jovan@drexel.edu (J. Jovicic).

Since the general objective of this work is to address the computational modeling of the impact process involving brittle and ductile solids, current approaches to the subject will be briefly reviewed and discussed in the following section.

2.1. Numerical solution

Classical continuum mechanics attempts to describe the dynamics of a continuous media with a set of differential equations established through the application of the principles of conservation of mass, momentum, and energy from a macroscopic point of view. An equation of state relates the density (or volume) and internal energy (or temperature) of the material, with pressure. A constitutive relation describes the particular nature of the material by relating the stress in the material with the amount of distortion (strain) required to produce this stress. The constitutive relation may include work hardening, strain rate effects, thermal softening, etc.

The differential equations relate material density ρ , velocity v_i , specific total energy e , the stress tensor σ_{ij} , and external body forces per unit mass f_i , where subscripts represent standard tensorial notation. Two fundamental descriptions of the kinematic deformation of continuous media exist: the Eulerian (spatial), and Lagrangian (material) description. The conservation equations for the two descriptions are:

account for the resistance to hydrostatic compression. The increase in internal energy due to thermodynamically non-reversible processes (e.g. plastic work, shock loading), and phase transitions (both solid–solid as well as melting and vaporization) is expressed as:

$$P = P(\rho, E). \quad (5)$$

Secondly, a constitutive model is required to account for strength effects. In general, it permits the stress to be a function of strain ϵ_{ij} , strain rate $\dot{\epsilon}_{ij}$ (both in loading and unloading, i.e. stress relaxation), internal energy E (thermal softening), and damage D :

$$\sigma_{ij} = f(\epsilon_{ij}, \dot{\epsilon}_{ij}, E, D). \quad (6)$$

Of course, before a solution can be obtained, appropriate boundary and initial conditions must also be prescribed.

Essential to the development of the constitutive equations is information on the dynamic properties of the material system under study.

The establishment of these properties for metals is itself a challenging task; for composites this task is further complicated by the directional dependence of the properties due to the anisotropy of the material system.

3. Approach

The design of an armor system to resist projectile perforation requires: the armor to be as thick as possible; high bulk and

Principles of:	Lagrangian	Eulerian
Conservation of Mass	$D\rho/Dt + \rho(\partial v_i/\partial x_i) = 0$	$\partial\rho/\partial t + (\partial/\partial x_i)(\rho v_i) = 0$
Conservation of Momentum	$Dv_i/Dt = f_i + 1/\rho(\partial\sigma_{ij}/\partial x_j)$	$\partial v_i/\partial t + v_j\partial v_i/\partial x_j = f_i + 1/\rho(\partial\sigma_{ij}/\partial x_j)$
Conservation of Energy	$De/Dt = f_i v_i + 1/\rho(\partial/\partial x_j)(\sigma_{ij} v_i)$	$\partial e/\partial t + v_i(\partial e/\partial x_i) = f_i v_i + 1/\rho(\partial/\partial x_j)(\sigma_{ij} v_i)$

The differences between the two sets of equations are inherent in the definition of the total time derivative D/Dt :

$$D/Dt = \partial/\partial t + v_i(\partial/\partial x_i). \quad (1)$$

The specific total energy is the sum of specific kinetic energy and specific internal energy E :

$$e = 1/2(v_i v_i) + E. \quad (2)$$

The equation that describes conservation of energy is often rewritten in terms of the specific internal energy:

$$\text{Lagrangian: } DE/Dt = P/\rho^2(D\rho/Dt) + 1/\rho(s_{ij}\dot{\epsilon}_{ij}) \quad (3)$$

$$\text{Eulerian: } \quad (4)$$

$$\partial E/\partial t + v_i\partial E/\partial x_i = P/\rho^2(\partial\rho/\partial t + v_i\partial\rho/\partial x_i) + 1/\rho(s_{ij}\dot{\epsilon}_{ij})$$

where s_{ij} and $\dot{\epsilon}_{ij}$ are the stress deviators and strain rates, respectively, and P the hydrostatic pressure.

Two more expressions are required to complete the set of equations. Firstly, an equation of state is necessary to

shear modulus; high yield stress, to maintain the resistance to deformation at high stress levels, resistance to fracture when large tensile stresses occur.

When the total weight must be considered, no one material satisfies all requirements because the total areal density of the target must be minimized. This has led to the development of composite armors in which a ceramic-face plate is backed by a material that can resist failure from tensile stresses. The use of materials of different hardness to produce dual hardness armor, take advantage of the ability of the hard, ceramic layer, to break up or slow down the projectile; whereas the softer organic composite backing layer will absorb the remaining impact energy.

Due to their high impact resistance and low density, fabric armors are usually employed for personal protection, and considerable research has been directed to the study of the ballistic behavior of laminated, woven, and braided fabric [12].

In order to defeat higher velocity threats and address the

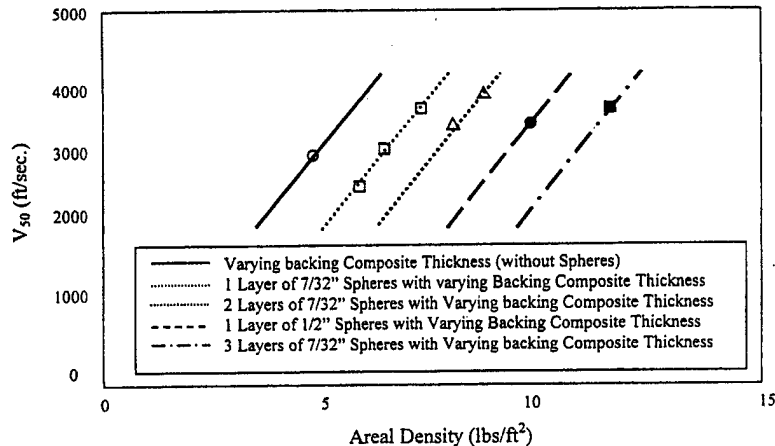


Fig. 1. Gradient density composite using ceramic spheres.

need for lighter weight and more complex shape structures, the concept of introducing a harden phase in the spherical form or Gradient Design Composite (GDC) was developed [18]. The system consists of a hardened component with ceramic spheres for destroying the projectile tip and creating a greater surface area to contact between the facing layer and the backing composite plate which is for maximizing strength and energy absorption.

Experimental results of a two layer composite armor consists of an aluminum oxide ceramic sphere layer bonded by epoxy and an orthogonal $[0^\circ/90^\circ]$ Spectra Shield composite backing, showed that a ballistic limit of 3000 ft/s (1000 m/s), can be achieved [18]. Fig. 1 shows predicted v_{50} values, calculated from the analytical model developed by Florence [10], as a function of the areal density of the experimental panels. Ballistic limit or v_{50} , for the specific projectile–target pair, is defined as the minimum impact velocity for perforation, or the maximum impact velocity for which the residual velocity is zero. In Fig. 1, the lines are the predicted values as varying the thickness of backing composite plate and thickness of sphere face. Data points in the figure are predicted values of actual panels examined

in the study [18]. The projectile used for the testing was a 7.62 mm \times 39 mm AK-47 type projectile.

Fig. 2 shows the damaged areas of front and backing panel. Authors also report [18] on the destruction and deformed shape of the projectile and the panel after ballistic testing. Breakage of ceramic spheres was also observed, but the damage was not as severe as it might be observed on shattering of solid tiles to very small pieces, which is usually observed in ballistic impact on ceramic armor.

The conclusion from this experimental work was that ceramic sphere facing provides the feasibility for flexible armor manufacturing without sacrificing its ballistic effectiveness.

4. Numerical analysis of composite armor

Contrary to the analysis of a high velocity impact on materials such as steel or aluminum, the simulation of high velocity impact and penetration processes into non-isotropic fiber reinforced material is a more difficult research task. Such analysis may help to understand the complex dynamic interactions between structural components undergoing large deformations and nonlinear material behavior including failure, de-lamination, erosion, etc. In order to simulate the dynamic behavior of composite materials, the constitutive equations must cover the elastic regime, the material failure, and the behavior of the partially or completely failed material.

First numerical simulations were performed on a flat target and then on a three-dimensional (3D) curved plate [13], using a concept of a simplified unit cell that captures the major features of the underlying microstructure and composition in the material (Fig. 3). Continuum elements represent the behavior of polymer matrix and rod elements represent the behavior of the fiber. It has to be highlighted that periodicity of loading in this case was not obtained.

It was predicted [13], that the projectile was completely

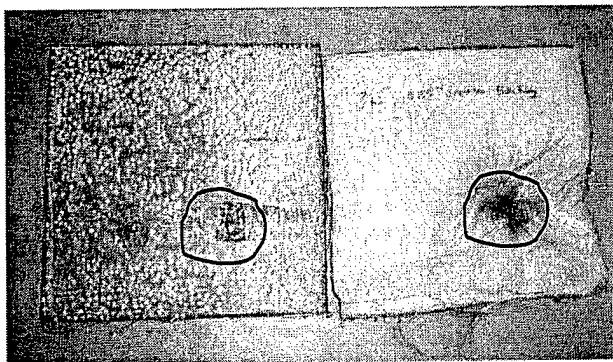


Fig. 2. Damaged areas on the facing and backing layers of panel after ballistic impact.

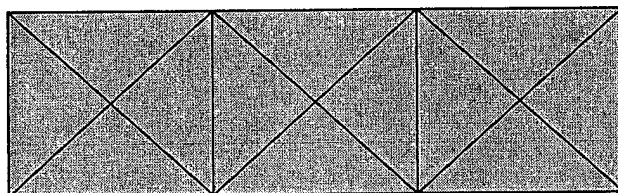


Fig. 3. Polymer-reinforced textile composite.

stopped with the hybrid (ceramic/composite) armor model (Fig. 4), whereas penetration occurred in the pure 3D braided composite targets. It was also shown that energy absorption increases as braiding angle decreases.

Although being just preliminary analyses, these numerical simulations [13] raised important ideas for further research. The first issue was to increase geometric detail in the unit cell (3D solid elements for fibers). Using this approach it is possible to include more information for the textile composite such as overall architecture as well as particular geometric characteristics such as crimp, etc. Using the higher-order discretization it is possible to explore the effects of fiber architecture on the properties of these composites. In addition, using separate models for the fiber and matrix will allow for more complex models for both materials that can include rate dependence in the modulus of the fiber and matrix behavior.

Computational limitations impose compromises in the modeling of both geometry and material behavior. Two types of models have to be addressed: (a) an approximate fiber/epoxy two-phase model for backing; and (b) a damage-based, rate dependent model for the ceramic spheres embedded in the epoxy.

5. Material model selection

In this work we are interested in providing guidelines for the evaluation of polymer–ceramic composites as substitutes of monolithic ceramic facings of textile composites (Fig. 4). The main advantages of such armor structures are

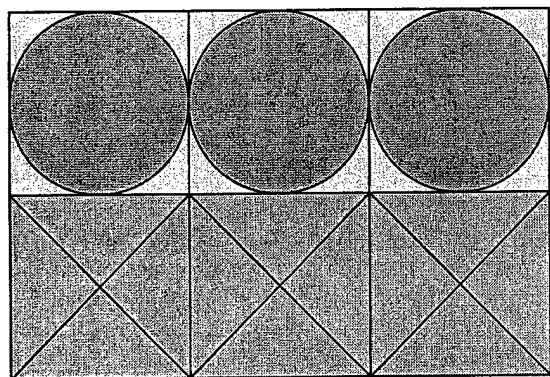


Fig. 4. Polymer-reinforced composite with ceramic spheres.

low weight and the ability to manufacture complex and flexible shapes.

In the modeling of the polymer/ceramic facing system, of particular interest are geometric effects, such as the uniformity of penetration resistance, the optimization of packing geometry (in terms of fraction, arrangement, size distribution, etc.), baseline comparisons with monolithic ceramic facing, and later on the optimization of multiple layers. To this end separate models are required for the individual phases.

5.1. Introduction of failure models

It is well known that the absorption of energy in ballistic situations depends strongly on the evolution of damage in the target and the resulting progressive degradation of its properties during its interaction with the projectile. For this reason, any computational simulation of impact phenomena must integrate in a rational way the dominant damage mechanisms in the target (and occasionally in the projectile). There are three ways that damage can be integrated in a FE simulation:

- *Ductile/Brittle Interfaces* [5,6]. In this case the connectivity of the elements is allowed to change during impact, via a force–displacement law for element boundaries that includes a separation criterion based on maximum force, displacement or other criteria that combine both forces and displacements. Such models are useful in modeling fragmentation, and usually allow no interactions between elements after they have been separated. Such models preserve kinetic energy, and special formulations are required to give consistent, mesh-independent fracture behavior. Best applications suitable for these models are the studies of fragmentation and post-impact debris.
- *Element Elimination* [4,5,16,19]. In these models, failure is considered to occur at the element level, on the basis of strain, stress or combined stress–strain criteria. After the failure condition is satisfied in a particular element, the element is “eliminated” from the model, in other words, the element no longer participates in the subsequent analysis. This is a key disadvantage of this approach when the failed material is contained in the impact area and participates in the damage resistance even after the initial failure (comminution).
- *Distributed Damage* [8,9,11]. In order to represent quantitatively the effects of the intermediate stages of damage development, models with distributed damage are used.

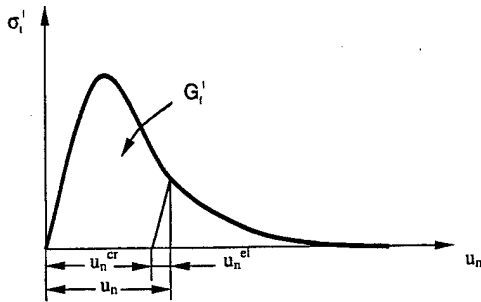


Fig. 5. Mode I fracture energy based cracking behavior.

The variables assigned to damage may have a physical or phenomenological interpretation. An evolution equation for damage is necessary to complete the model and must be integrated together with the equilibrium equations. The representation of non-monotonic damage evolution is possible, to represent cases where the external loading—e.g. large compressive hydrostatic pressure, etc. can result in damage healing (partial closure of a previously open crack). Distributed damage models provide great flexibility in the description of the physical phenomena associated with damage. They tend, however, to be relatively complex. As a result their validation is not straightforward, particularly because the evaluation of the material parameters can be at best not straightforward.

For simplicity we have selected an element failure model for the polymeric constituent. The role of the polymer backing plate is to transmit load before local failure. After failure, it is postulated that its contribution to impact resistance is negligible. On the other hand, we chose to work on a distributed damage model for the ceramic [9,13].

5.2. A cracking model for ceramic facing

This section describes the cracking constitutive model for brittle materials used for ceramic facing. This is a “smeared” model in the sense that damage is considered to be homogeneous within an element—even if the length of individual cracks is much smaller than the element size. It is a “fixed orthogonal crack model”, because it considers damage to be described by micro-cracks oriented along mutually perpendicular planes. These cracks are considered to develop in the undamaged material when a maximum principal stress criterion is satisfied. The direction of the maximum principal stress at that time defines the normal to plane, along which the micro-cracks appear. Subsequent cracks may develop along the same plane or two other planes normal to the initial crack plane. The coordinate system defined by the cracks may rotate due to rigid rotation of the elements. Cracks are considered to be irreversible, in the sense that once generated, they will always be there. There is the possibility, however, of partial closure of a previously open crack due to compressive forces normal

to its plane. The basis of the model is the work of Hilleborg [11] and Crisfield [5], and its “plasticity-like” theory is briefly described below.

5.2.1. Strain rate decomposition

The total macroscopic strain is partitioned into an elastic part and a crack-induced part:

$$d\epsilon = d\epsilon^{el} + d\epsilon^{cr}. \quad (7)$$

The elastic part of the model requires the description of elastic response to be dependent on damage.

Given a system of cracks, a geometric relation between the stress with respect to the global coordinates and the stress in local coordinates (defined by the crack directions) is:

$$t = T^T \sigma \quad (8)$$

where T is the rotation matrix between the global coordinates system and the crack directions. The global stress-strain relation is given by:

$$d\sigma = E(d\epsilon - T d\epsilon^{cr}). \quad (9)$$

A consistency condition is employed for the development of crack-induced strains, based on the local stresses with respect to the crack system

$$C = C(t, \sigma^{I,II}) = 0 \quad (10)$$

where t is a stress tensor expressed in the local crack system and $\sigma^{I,II}$ represents a tension softening model (Mode I fracture) in the case of the direct components of stress and shear softening/retention model (Mode II fracture) in the case of the shear components of stress (material properties).

The consistency condition can be written for a plane of cracks for open and closed cracks as follows:

$$\text{Open crack : } C_{nn} = t_{nn} - \sigma_i^I(\epsilon_{nn}^{cr}) = 0 \quad (11)$$

where $\sigma_i^I(\epsilon_{nn}^{cr})$ is the tension softening evolution, and

$$\text{Closed crack : } C_{nn} = t_{nn} - \sigma_C^I(\max \epsilon_{nn}^{cr}) = 0 \quad (12)$$

where $\sigma_C^I(\max \epsilon_{nn}^{cr})$ is the crack closing/reopening evolution, which depends on the maximum crack opening strain.

In simpler words, for an open crack system, the maximum stress that can be carried in the direction normal to the crack depends on the current crack induced strain (which implicitly represents a crack size). For a crack that is temporarily closed (e.g. due to the application of compressive stress normal to it), the maximum allowed tensile stress depends on the maximum tensile strain attained over the time history of the crack.

5.2.2. Mode I behavior

The model describes the post-cracking behavior of the material on the basis of the brittle fracture concept of Hilleborg [11]. The fracture energy required to form a unit area of crack is considered to be a material property

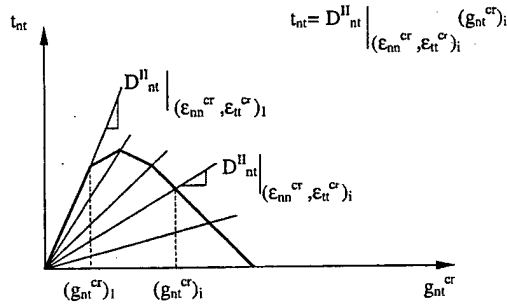


Fig. 6. Crack opening dependent shear retention (total) model.

and can be computed from measuring the tensile stress (σ_t^I) as a function of the crack opening displacement:

$$G_f^I = \int \sigma_t^I du_n. \quad (13)$$

Here, u_n^{cr} is the displacement across the crack and u_n^{el} the elastic part of the displacement. In other words, the fracture energy is the total area under the curve in Fig. 5. The material behavior is defined by the maximum stress under tension σ_{max} and the maximum displacement under tension, as well as by the shape of the curve.

In addition a length scale is introduced by assuming that the strain induced by cracking is given by:

$$du_n^{cr} = h d\epsilon_{nn}^{cr}.$$

It is important to note that the length h must be defined appropriately. In ABAQUS implementation, h is computed from the dimensions of the elements. This introduces a mesh-sensitivity in the results. Further ideas on the elimination of this mesh sensitivity are being considered.

5.2.3. Mode II behavior

Mode II behavior, i.e. crack extension due to non-normal stresses with respect to the crack, is only considered in this model in the post-cracking regime. In other words, crack initiation can only be caused by tensile principal stresses while normal and shear stresses with respect to the crack can cause crack extension. This model defines the total shear stress as a function of the total shear strain (shear direction

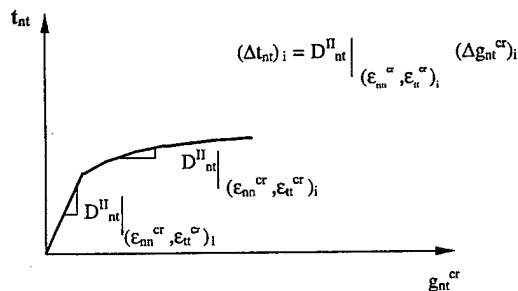


Fig. 7. Crack opening dependent shear retention (incremental) model.

nt is used as an example):

$$t_{nt} = D_{nt}^{II}(\epsilon_{nn}^{cr}, \epsilon_{tt}^{cr}) g_{nt}^{cr} \quad (14)$$

$D_{nt}^{II}(\epsilon_{nn}^{cr}, \epsilon_{tt}^{cr})$ is a stiffness which depends on crack opening and may be expressed as:

$$D_{nt}^{II} = \alpha(\epsilon_{nn}^{cr}, \epsilon_{tt}^{cr}) G \quad (15)$$

where G is the undamaged shear modulus; and $\alpha(\epsilon_{nn}^{cr}, \epsilon_{tt}^{cr})$ is the damage function. A commonly used mathematical form for this dependence when there is only one crack, associated with direction n , is the power law:

$$\alpha = (1 - \epsilon_{nn}^{cr}/\epsilon_{nn}^{cr_{max}})^p / \{1 - (1 - \epsilon_{nn}^{cr}/\epsilon_{nn}^{cr_{max}})^p\} \quad (16)$$

which is determined by the damage state via ϵ_{nn}^{cr} . Here p and $\epsilon_{nn}^{cr_{max}}$ are material parameters.

This total stress–strain shear retention model differs from the traditional shear retention models in which the stress–strain relations are written in incremental form:

$$\Delta t_{nt} = D_{nt}^{II}(\epsilon_{nn}^{cr}, \epsilon_{tt}^{cr}) \Delta g_{nt}^{cr} \quad (17)$$

where $D_{nt}^{II}(\epsilon_{nn}^{cr}, \epsilon_{tt}^{cr})$ is an incremental stiffness which depends on crack opening.

The difference between the total and incremental formulations is best illustrated by considering the shear response of the two models in the case when a crack is simultaneously opening and shearing (see Fig. 6 for the total model, and Fig. 7 for the incremental model). In the total approach, it is obvious that, the shear stress tends to zero as the cracks open and shears, while, in the incremental model, the shear stress tends to a finite value. This may explain rather stiff responses that are usually obtained with the conventional shear retention models.

5.3. Element failure model for polymer matrix composite

The ductile failure model, used for the polymer matrix composite, provides simple failure criteria, which are designed to allow the stable removal of elements from the mesh as a result of tearing or opening of the structure. The failure model is based upon the value of the equivalent plastic strain. When the equivalent plastic strain at a

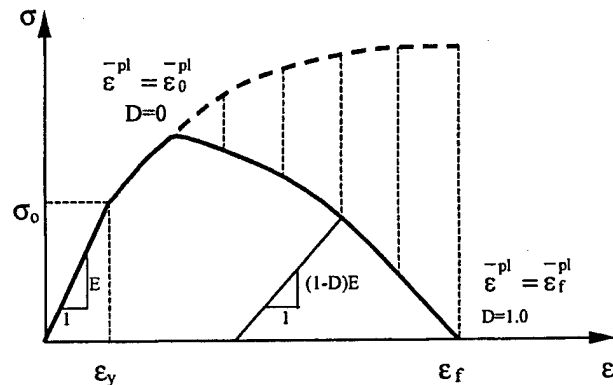


Fig. 8. Stress–strain curve using the ductile mode.

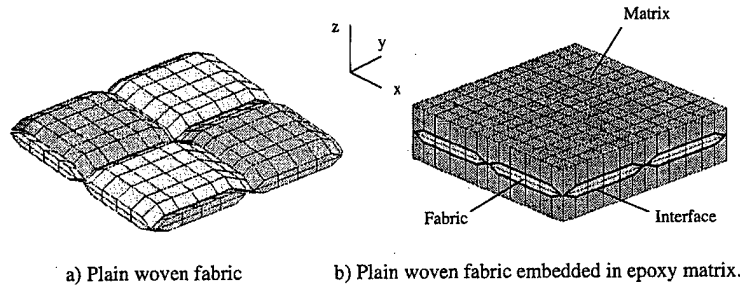


Fig. 9. Unit cell model of a plain weave composite: (a) plain woven fabric; and (b) plain woven fabric embedded in epoxy matrix.

material point reaches the value defined as the plastic failure strain, ϵ_f^{pl} , the material point is failed. If all of the material points in the element fail, the element loses its ability to resist any further load and, hence, it is removed from the mesh.

The ductile failure model is based on a damaged Von Mises plasticity theory with isotropic hardening. The damage manifests itself in two forms: degradation of the yield stress with damage and damaged elasticity.

Fig. 8 illustrates the deviatoric stress/strain behavior of the material model. The solid curve represents the actual stress while the dashed curve represents undamaged behavior, that is, only elasto-plasticity.

Until the initial yield stress, σ_0 , is reached, the material behaves as elastic. Plastic strain then occurs following the conventional Von Mises plasticity theory. If the strain continues to increase, damage will increase from zero, when the plastic strain is less than or equal to the offset plastic strain, ϵ_0^{pl} , to a value of one when the plastic strain reaches the plastic failure strain, ϵ_f^{pl} . At that time the corresponding total strain is ϵ_f .

The damage (D), is calculated from the equivalent plastic strain as

$$D = (\bar{\epsilon}^{pl} - \bar{\epsilon}_0^{pl}) / (\bar{\epsilon}_f^{pl} - \bar{\epsilon}_0^{pl}) \quad (18)$$

where $\bar{\epsilon}^{pl}$ is the current equivalent plastic strain experienced

by the material. The equivalent plastic strain is defined as:

$$\bar{\epsilon}^{pl} = \int_0^t \sqrt{(2/3) \dot{\epsilon}^{pl} : \dot{\epsilon}^{pl}} dt \quad (19)$$

where $\dot{\epsilon}^{pl}$ is the plastic strain rate tensor.

The material's elastic response is based on damaged elasticity. The damaged elastic moduli are given by:

$$G_D = (1 - D)G, \quad (20)$$

$$K_D = (1 - D)K \quad (21)$$

where G_D is the damaged shear modulus and K_D the damaged bulk modulus. The unloading path along the damaged modulus is shown in Fig. 13.

The damaged plastic yield surface is defined as

$$\sigma_y = (1 - D)\sigma_y(\bar{\epsilon}^{pl}). \quad (22)$$

The yield surface shrinks to a single point in stress space when the damage reaches a value of one. Due to the damaged elasticity, the model becomes nonlinear in terms of the equivalent plastic strain. Therefore, the decomposition of a strain into its elastic and plastic parts is history dependent.

6. Three-dimensional finite element model of a woven unit cell

A set of 3D FE analysis was carried out to evaluate the stiffness constants for a developed plain woven, textile composite unit cell. Fig. 9 shows a FE mesh of the plain weave composite considered in this work. The interface between the matrix and woven fabric is modeled separately, so the issue of interface contribution in the energy absorption of textile composites in the ductile interface model can be attacked also. In this case, it is assumed that interface material has the same properties as an epoxy matrix.

This mesh has 272 solid elements (eight noded bricks) and 591 nodes. Both normal and shear loading were considered for computing normal and shear moduli. Six FE cases were run for the same model of a unit cell, corresponding to the six individual strain vectors (ϵ_x , ϵ_y , ϵ_z , γ_{xy} , γ_{yz} , γ_{xz}). The relevant boundary conditions for each case are obtained using the linear strain-displacement

Table 1
Boundary conditions

Case	Strain vector	Boundary conditions
A	$\epsilon_x = 0.0001$	$\partial x _{x=l_x} = 0.001l_x$; $\partial x _{x=0} = 0$; $\partial y _{x=0} = 0$; $\partial y _{x=l_x} = 0$; $\partial z _{x=0} = 0$; $\partial z _{x=l_x} = 0$
B	$\epsilon_y = 0.0001$	$\partial x _{x=l_x} = 0$; $\partial x _{x=0} = 0$; $\partial y _{x=0} = 0$; $\partial y _{x=l_x} = 0.001l_y$; $\partial z _{x=0} = 0$; $\partial z _{x=l_x} = 0$
C	$\epsilon_z = 0.0001$	$\partial x _{x=l_x} = 0$; $\partial x _{x=0} = 0$; $\partial y _{x=0} = 0$; $\partial y _{x=l_x} = 0$; $\partial z _{x=0} = 0.001l_z$; $\partial z _{x=l_x} = 0$
D	$\gamma_{xy} = 0.0001$	$\partial x _{x=l_x} = 0.0005l_y$; $\partial x _{x=0} = 0$; $\partial y _{x=0} = 0$; $\partial y _{x=l_x} = 0.0005l_x$; $\partial z _{x=0} = 0$; $\partial z _{x=l_x} = 0$
E	$\gamma_{yz} = 0.0001$	$\partial x _{x=l_x} = 0$; $\partial x _{x=0} = 0$; $\partial y _{x=0} = 0$; $\partial z _{x=0} = 0$; $\partial y _{x=l_x} = 0.0005l_z$; $\partial z _{x=l_x} = 0.0005l_y$
F	$\gamma_{xz} = 0.0001$	$\partial x _{x=l_x} = 0.0005l_z$; $\partial x _{x=0} = 0$; $\partial y _{x=0} = 0$; $\partial y _{x=l_x} = 0$; $\partial z _{x=0} = 0$; $\partial z _{x=l_x} = 0.0005l_x$

Table 2
Engineering elastic constants of composite material constituents

Material	Property									
	ρ (kg/m ³)	E_1 (GPa)	E_2 (GPa)	E_3 (GPa)	ν_{12}	ν_{23}	ν_{13}	G_{12} (GPa)	G_{23} (GPa)	G_{13} (GPa)
Epoxy	1200	3.45	3.45	3.45	0.35	0.35	0.35	1.3	1.3	1.3
Spectra	970	268	4.72	4.72	0.4	0.4	0.4	36	34	34

Table 3
The engineering elastic constants

	E_1 (GPa)	E_2 (GPa)	E_3 (GPa)	ν_{12}	ν_{13}	ν_{23}	G_{12} (GPa)	G_{23} (GPa)	G_{13} (GPa)
M1	46	46	7.1	0.025	0.265	0.265	18.75	6.5	6.5
M2	48.5	48.5	7.5	0.027	0.272	0.272	20	6.8	6.8
M3	52	52	8	0.028	0.29	0.29	23	7.3	7.3
M4	52.1	52.1	8.1	0.028	0.292	0.292	23.2	7.31	7.31

relationships listed in Table 1, where l_x , l_y , and l_z are lengths of a unit cell in the x -, y -, and z -direction, respectively.

The FE mesh was generated using both, ALGOR and ABAQUS computer codes. The resulting nodal forces due to the applied displacements are computed and by dividing them by the cross-sectional area the average stresses are computed. The effective modulus is computed by dividing this average stress by the applied strain. Computing the average strain in the transverse direction and dividing it by the applied strain also computes Poisson's ratios [3]. The engineering elastic constants of composite material constituents are given in Table 2.

In order to explore convergence of the results, four unit cells with different mesh densities were modeled (respectively: M2, 1067 nodes and 840 elements; M3, 1547 nodes and 1248 elements; and M4, 2123 nodes and 1726 elements), and the results are presented in Table 3. The analysis in this part of the work was limited to linear elastic analysis.

In the absence of the appropriate experimental results, to

validate the present numerical model, comparison is carried out using data available in the literature. The constituent material properties and the unit cell geometries for the examples are listed in Table 4.

Table 5 compares the developed FE model (M4) of the unit cell with available literature results. In both cases the engineering constants obtained from presented numerical model were in good agreement with available results.

7. Impact modeling

7.1. Two-dimensional impact simulation

In order to evaluate the baseline performance of the model, the impact on a 2D ceramic plate was simulated (Fig. 10). The figure shows the damaged state associated with cracks that are open in different directions. Note that although the primary loading is compressive, local shear stresses result in large tensile principal stresses, which

Table 4
Properties of constituent materials

Dasgupta et al. [7]; unit cell size: $1.68 \times 1.68 \times 0.228$ mm ³ ; volume fraction: $V_f = 0.26$	Glass fiber	$E_1 = 58.61$ GPa, $E_2 = E_3 = 14.49$ GPa, $G_{12} = 5.38$ GPa, $\nu_{12} = 0.25$, $\nu_{23} = \nu_{13} = 0.247$
	Epoxy matrix	$E = 3.45$ GPa, $\nu = 0.37$
Naik [15]; unit cell size: $2.82 \times 2.82 \times 0.255$ mm ³ ; volume fraction: $V_f = 0.64$	Graphite fiber	$E_1 = 144.8$ GPa, $E_2 = E_3 = 11.73$ GPa, $G_{12} = 5.52$ GPa, $\nu_{12} = 0.23$, $\nu_{23} = \nu_{13} = 0.3$
	Epoxy matrix	$E = 3.45$ GPa, $\nu = 0.35$

Table 5
Comparison of continuum properties

	E_1, E_2 (GPa)	E_3 (GPa)	G_{13}, G_{23} (GPa)	G_{12} (GPa)	ν_{13}, ν_{23}	ν_{12}
Dasgupta et al. [7]	14.38	6.25	1.94	3.94	0.463	0.167
FEM (M4)	12.81	6.14	1.84	3.15	0.441	0.182
Naik [15]	64.38	11.49	5.64	4.87	0.396	0.027
FEM (M4)	57.61	10.88	4.61	4.75	0.375	0.048

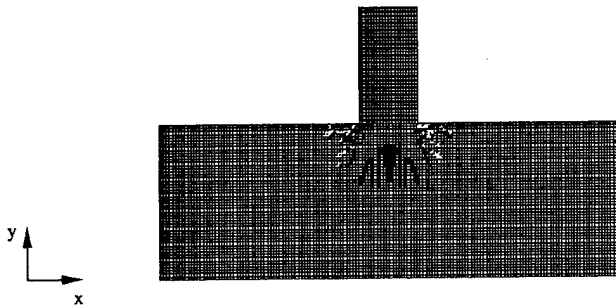


Fig. 10. Simulated impact on the monolithic ceramic plate.

open the cracks. Further crack opening can be obtained due to all stresses.

A cylindrical projectile, with a diameter of 7.62 mm, was modeled as a deformable, elastic plastic steel material. The impact velocity is assumed to be 1000 m/s.

In the case of the GDC model, consisting of ceramic spheres facing and polymer matrix composite backing, two different impact simulations have been considered: one with the axis of penetration going through the center of the ceramic sphere (both orthogonal and oblique), and one between two adjacent spheres. Fig. 11 represents the time history of the backing plate deformation as a function of impact site. Results show that both, side impact and oblique impact lower displacement of a backing plate. It was also found that projectile impact between two spheres gives lower deformation of a backing plate.

The time history of the residual velocity as a function of impact site is presented in Fig. 12. Oblique and side impact again show better impact resistance compared to central impact, lowering projectile residual velocity.

The reason that side impact gives better penetration resistance in terms of lower residual velocity is probably because

of the fact that impact loading is evenly distributed on two spheres, which as a result, spreads impact energy on the larger area of a backing plate.

The effect of the ceramic facing size on the projectile residual velocity was investigated (see Fig. 13, where R_p is projectile size and R_f is ceramic facing size). It was found that lowering ceramic facing size ($R_p > R_f$), for the same projectile, results in lower projectile residual velocity.

Work can be further extended to the investigation of relative size and packing factor effect (e.g. R_f/R_p) on the target ballistic resistance.

At this time, the presented observations are not experimentally validated.

7.2. Three-dimensional impact simulations

The central impact of a spherical projectile onto a polymer matrix composite plate is considered (Fig. 14). The rigid projectile was assumed to have a diameter of 7.62 mm, with a mass corresponding to a uniform material, which has a density of $18,630 \text{ kg/m}^3$. The plate is further assumed to have thickness of 3 mm. The model has 2592 matrix elements, 5184 interface elements, and 3456 woven fabric elements, which makes total number of 11,232 3D solid elements with 12,987 nodes.

High-velocity impact response is dominated by stress wave propagation through the material, in which the structure does not have time to respond, which is leading to very localized damage [1,13,18].

Two different simulations were performed in terms of the prescribed boundary conditions. In the first model, boundary conditions were free and in the second one the target had constrained edges; and the results showed no effect of the boundary conditions on the target ballistic performance in this case. It can be concluded that boundary conditions can

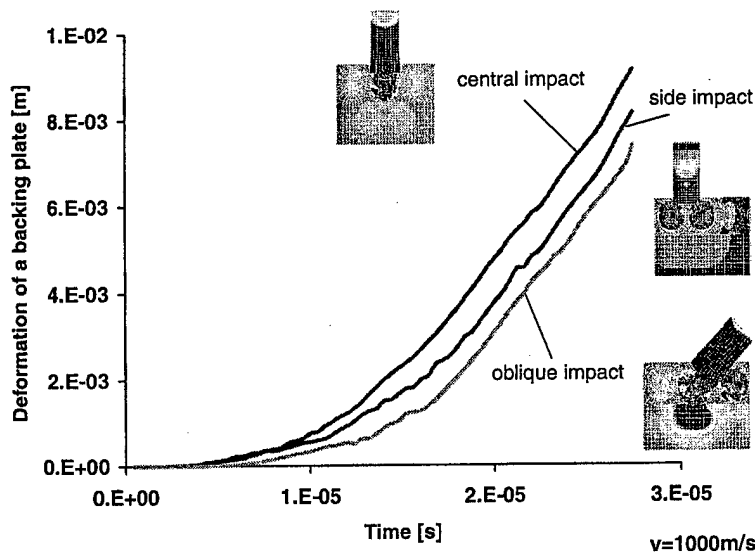


Fig. 11. Influence of the impact site on backing plate deformation.

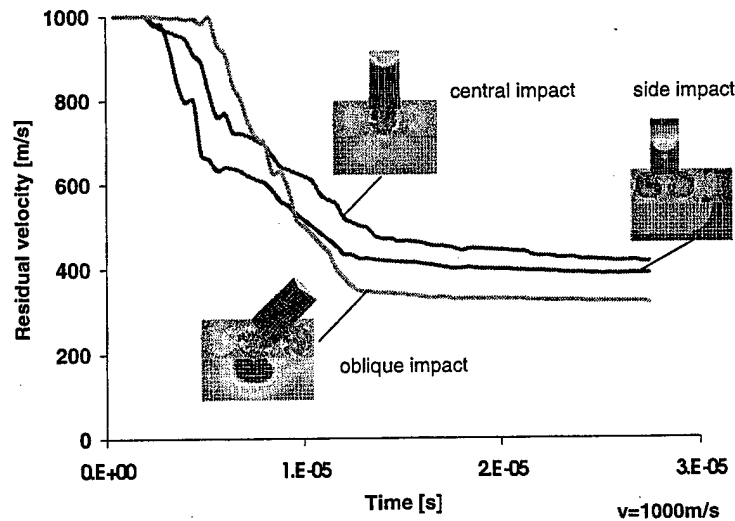


Fig. 12. Residual velocity as a function of time for a different impact site.

be ignored, because the impact event is over before the stress waves have reached the edge of the structure [13].

Fig. 15 presents Von Mises stresses in Spectra fabric after different times of impact. Stress wave propagation is the result of a specific woven pattern employed in the fabric model.

After the impact of $40 \mu\text{s}$ the projectile has perforated the target and it is moving as a rigid body (see Fig. 16). Fig. 17 represents Von Mises stress distribution in the epoxy resin after impact of $40 \mu\text{s}$.

In order to achieve higher penetration resistance, both experimental results and these simulations show necessity for harder, facing layer, which would first shatter or blunt the armor piercing projectile, and then spread the load over a larger area. The composite backing would, in that case deform to absorb the remaining kinetic energy of the projectile.

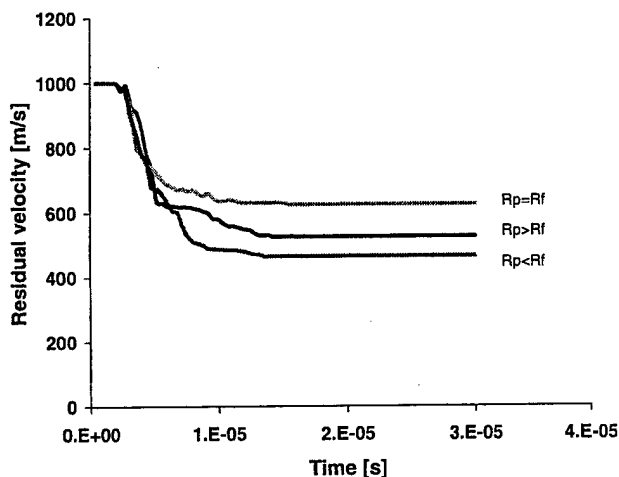


Fig. 13. Effect of ceramic facing size on residual velocity.

8. Conclusions

The application of gradient design concept in armors offers possibilities in the reduction of weight and cost without significant reduction of ballistic resistance. Experimental results of composite backed plates consisting of layers of ceramic spheres embedded in epoxy showed that a ballistic limit of 1000 m/s (3000 ft/s) can be achieved without weight penalty compared to solid ceramic tiles.

In order to develop a precise methodology for optimizing the gradient design composite armors, an improved understanding of the relative significance of the design parameters must be developed. One way to study the relative significance of these parameters is through computational modeling. Computational limitations impose compromises in the modeling of both geometry and material behavior. Two types of models are discussed: (a) an approximate fiber/epoxy two-phase model for the backing; and (b) a damage-based, model for the ceramic spheres embedded in the epoxy.

For the GDC model, consisting of ceramic spheres facing and polymer matrix composite backing, two different

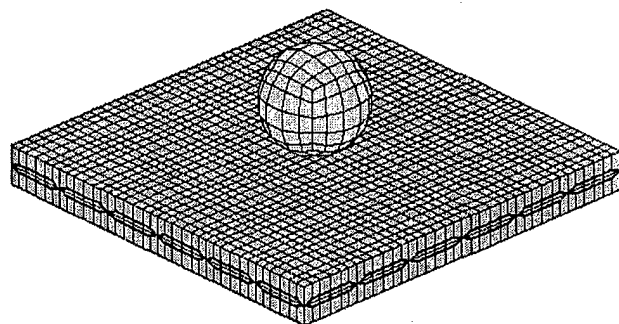


Fig. 14. 3D model of a composite armor under impact.

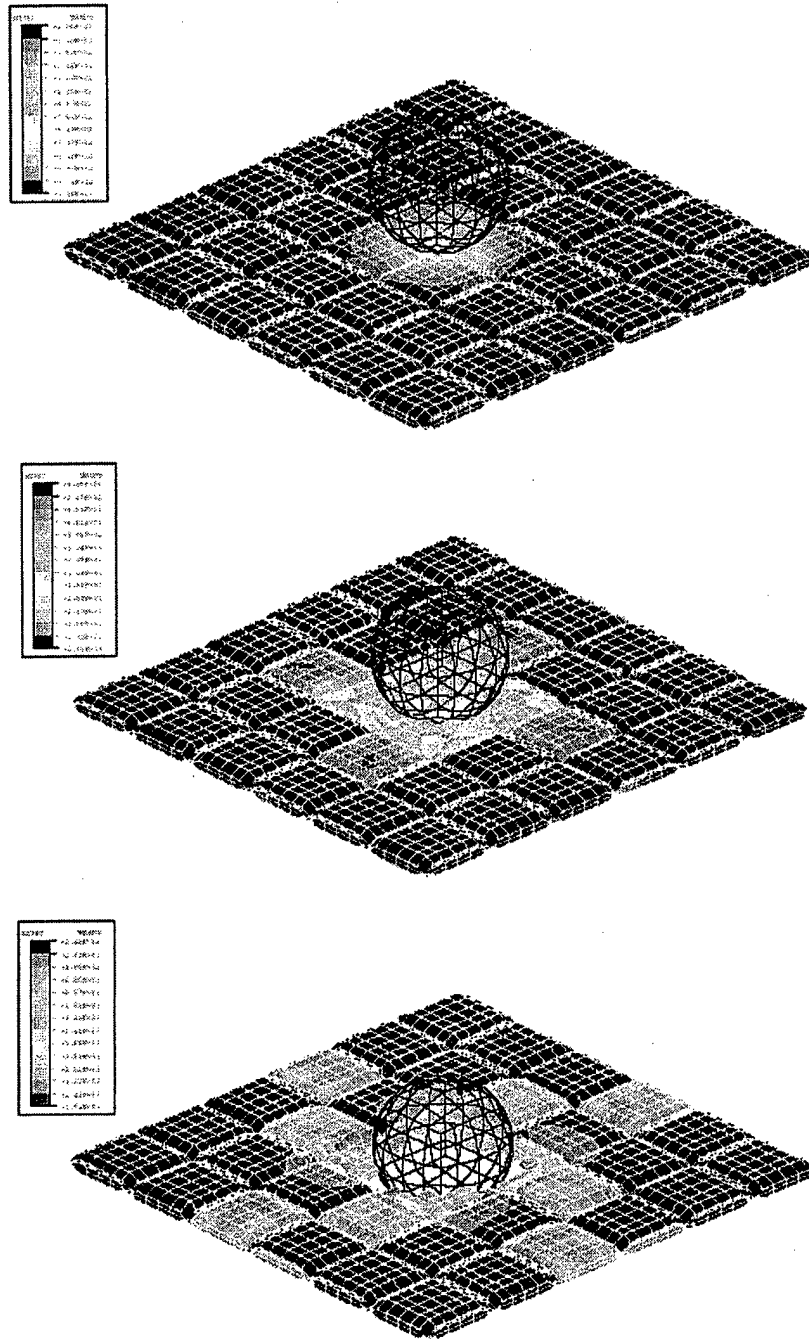


Fig. 15. Von Mises stress in the fabric reinforcement phase of the composite: (a) after impact of $t = 8 \mu\text{s}$; (b) after impact of $t = 20 \mu\text{s}$; and (c) after impact of $t = 40 \mu\text{s}$.

impact simulations have been considered: one with the axis of penetration going through the center of the ceramic sphere (both orthogonal and oblique), and one between two adjacent spheres.

Residual velocity and back-plane displacement time history were evaluated as a function of different impact site and the projectile incident angle. Results show better penetration resistance in the case of oblique impact compared to normal impact.

The effect of the ceramic facing size on the projectile residual velocity and displacement of the backing plate was investigated, and it was found that projectile impact between two spheres, and smaller facing size compared to projectile size, lower residual velocity and back-plane displacement.

The development of a library of fiber architectures based on the unit cell has been initiated, which will open the possibility of the structural optimization along with

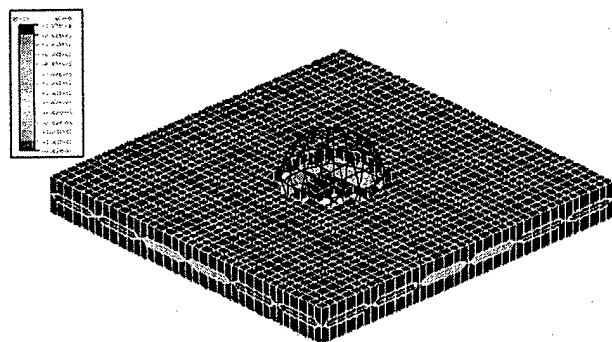


Fig. 16. 3D model of a composite plate after impact of $t = 40 \mu s$.

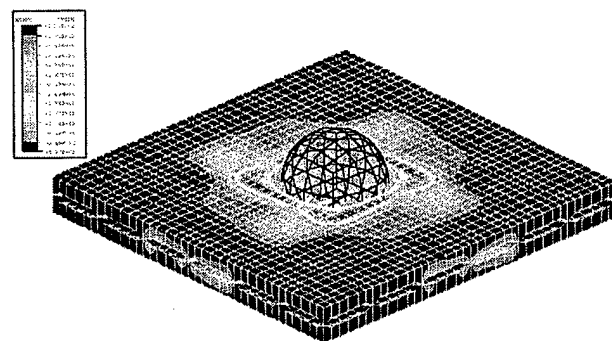


Fig. 17. Von Mises stress in the epoxy resin after impact of $t = 40 \mu s$.

simulation of the high velocity impact phenomena of advanced composites. Using this approach it will be possible to include more information for the textile composite such as the overall architecture as well as particular geometric characteristics such as crimp, etc.

Successful completion of these tasks will facilitate the engineering design of the next generation of multifunctional armors. Accordingly, a library of fiber architectures (orthogonal, woven, braided, knitted), based on the unit cell will be available for structural optimization along with simulation of the high velocity impact phenomena of advanced composites.

Acknowledgements

This work is supported by the US Army Research Office under the Multidisciplinary University Research Initiative on Functionally Tailored Textile Fabrics.

References

- [1] Anderson C, Bodner S. Ballistic impact: the status of analytical and numerical modeling. *Int J Impact Engng* 1988;7(1):9–35.
- [2] Backman M, Goldsmith W. The mechanics of penetration of projectiles into targets. *Int J Engng Sci* 1978;16:1–99.
- [3] Chamis CC. Simplified composite micromechanics equations for hygral, thermal, and mechanical properties. *SAMPE Quarterly* 1984;April:14–23.
- [4] Cortes R, Navarro C, Martinez A, Rodriguez J, Sanchez-Galvez V. Numerical modeling of normal impact on ceramic composite armors. *Int J Impact Engng* 1992;12:639–51.
- [5] Crisfield MA. Snap-through and snap back response in concrete structures and the dangers of under-integration. *Int J Numer Meth Engng* 1986;22:751–67.
- [6] Curran DR, Seaman L, Cooper T, Shockey DA. Micromechanical model for comminution and granular flow of brittle material under high strain rate application to penetration of ceramic targets. *Int J Impact Engng* 1993;13:53–83.
- [7] Dasgupta A, Bhandarkar S, Pecht M, Barkar D. Thermo-elastic properties of woven-fabric composites using homogenization techniques. In: *Proceedings of the American Society for Composites, Fifth Technical Conference, Lansing, MI. Technomic: Lancaster, PA, 1990. p. 1001–110.*
- [8] Graham RA. Solids under high-pressure shock compression. New York: Springer, 1993.
- [9] Graham RA, editor. High-pressure shock compression of solids II. New York: Springer, 1995.
- [10] Florence AL. Interaction of projectile and composite armor, Part II. Stanford Research Institute Report, AMMRG-CR-69-15, 1969.
- [11] Hilleborg A, Modeer M, Petersson P. Analysis of crack formation and crack growth in concrete by means of fracture mechanics and finite elements. *Cement Concrete Res* 1976;6:773–82.
- [12] Ko FK. Three dimensional fabric for composites. In: Chou TW, Ko FK, editors. *Textile structural composites*. New York: Elsevier, 1989.
- [13] Ko FK, Sun W, Zavaliangos A, Jovicic J, El-Shiekh A, Song J. Integrated design for manufacturing of composite helmets. The design and integration of helmet systems. US Army Natick Symposium, Framingham, MA, 1997.
- [14] Meyers MA. *Dynamic behavior of materials*. New York: Wiley, 1994.
- [15] Naik RA. Analysis of woven and braided fabric reinforced composites. NASA CR-194930, National Aeronautics and Space Administration, Washington, DC, 1994.
- [16] Ruiz C. Overview of impact properties of monolithic ceramics. *Int J Fracture Mech* 1985;29:101.
- [17] Sedgwick RT, et al. Numerical investigations in penetration mechanics. *Int J Engng Sci* 1978;16:859–69.
- [18] Song JW, Geshury A, Ko FK. Behavior of gradient designed composites under ballistic impact. *Proceedings of the 11th International Conference on Composite Materials, Goald Coast, Australia, July 14–18, 1997.*
- [19] Woodward RL, et al. A study of fragmentation in the ballistic impact of ceramic. *Int J Impact Engng* 1994;15:605–18.
- [20] Zukas JA. *Impact dynamics*. New York: Wiley, 1982.

MODELING AND SIMULATION OF IMPACT BEHAVIOR OF GRADIENT COMPOSITES*

Jovan Jovicic, Antonios Zavaliangos, and Frank Ko
Department of Materials Engineering, Drexel University
31 st. & Chestnut St. Philadelphia PA 19104

ABSTRACT

In order to understand the dynamic response of the material/structural geometry interaction in gradient composite armor systems, three-dimensional finite element analysis is performed to simulate the structural behavior of the multi-component composite armors. Ballistic resistance is studied for a developed plain woven composite plate model, with and without ceramic facing layer, for impacting velocities ranging between 10m/s-1000m/s. Materials properties and geometry effects are explored.

KEYWORDS: Gradient Design Composites, Textile Composites, Ballistic Impact, Finite Element Modeling

1. INTRODUCTION

The general objective of this work is to address the computational modeling of the impact process involving textile composite and Gradient Design Composite (GDC) materials. Possible applications of these kind of materials, would be the development of the light armor materials systems: body armors, helmets, and protection against projectile threats in structures such as helicopters, tanks and aircrafts, which would have a significant improvement in penetration resistance, impact energy dissipation, and damage containment. Due to their high impact resistance and low density, fabric composite armors are usually employed for personal protection, and considerable research has been directed to the study of the ballistic behavior of laminated, woven, and braided fabrics [2,3,4].

With such complex designs the number of independent parameters is very large. To complement and perhaps guide the necessary experimental evaluation of such system, it is essential to develop a computational methodology that may lead us to an improved understanding of the relative significance of the various design parameters. The key difficulty of this approach is the associated computational complexity in terms of both geometry and material models.

*Supported by the US Army Research Office under the Multidisciplinary University Research Initiative on Functionally Tailored Textile Fabrics.

In the work reported here, we probe the ability to analyze the ballistic impact on complex structures, such as plane woven composite model, with and without ceramic facing layer. The characteristic of our approach is that we consider each material separately. From the computer simulation point of view, the introduction of simple discrete models for the study of textile composites offers the advantage of using different and more detailed description of material properties for both matrix and fibers, with a more accurate description of the geometry. In this way, more elaborate (and more realistic) failure criteria can be introduced. Using the higher-order discretization it is possible to explore the effects of fiber architecture on the properties of these composites. On the other hand, small physical length scale dictates the level of discretization and the computation expense of the simulation is heavy.

2. BACKGROUND AND OBJECTIVES

The unique advantage of composite material is their ability to tailor their properties to the structural or materials system of which they are intended. On the other hand, many structural components have to meet service conditions and, hence, required materials performance, which vary with location within the component. This consideration founds basics for development of a special class of composite materials, that are functionally graded-*Gradient Design Composites* (GDC). Rather than developing new materials with higher stiffness, it might be more advantageous to create structures using the optimal placement of components.

The performance of a fiber-matrix composite depends on orientation, length, shape, and composition of the fibers; mechanical properties of the matrix; and integrity of the bond between fibers and matrix. In order to achieve higher penetration resistance, both experimental results [3], and numerical simulations [2], show necessity for harder, facing layer, which would first shatter or blunt armor piercing projectile, and then spread the load over a larger area. The composite backing would, in that case deforms to absorb the remaining kinetic energy of the projectile.

In order to defeat higher velocity threats and address the need for lighter weight and more complex shape structures, the concept of introducing a harden phase in the spherical form or Gradient Design Composite (GDC) was developed [3]. The system consists of a harden component with ceramic spheres for destroying the projectile tip and creating a greater surface area to contact between the facing layer and the backing composite plate which is for maximizing strength and energy absorption, (Fig.1).

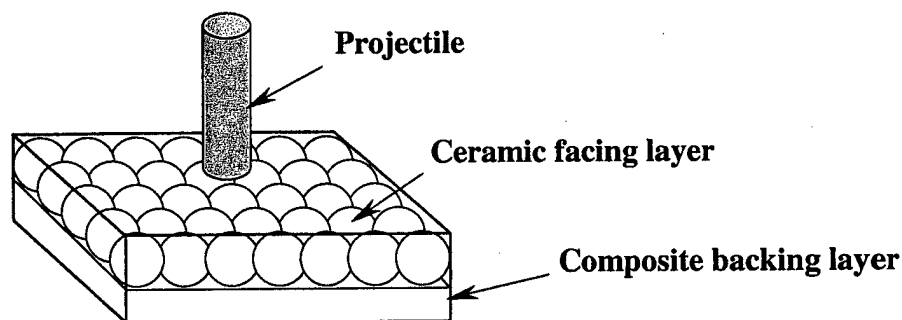


Fig.1 Gradient Design Composite material concept.

Changing the direction of a projectile, by its deflection on the particulate ceramic facing, gives the additional effect to the energy absorption increase.

Our objectives in this work are the following:

- To evaluate an ability to simulate complex material systems such as the Gradient Design Composites using finite element analysis.
- To attribute significance to the various design parameters such as material property, fiber and overall composite architecture, and more specifically,
- To evaluate the difference in performance between a full ceramic facing versus a set of ceramic spheres embedded in light epoxy.

It is important to note, that the results presented below may be influenced by the level of discretization, which is often coarse in order to limit the CPU time of the simulations to bellow one hour, on a modern (733MHz) personal computer. An effort to understand the effect of mesh density on the results is underway.

3. NUMERICAL MODELING

A set of three-dimensional finite element analyses (using ABAQUS-EXPLICIT computer code), was carried out to evaluate the impact resistance for a developed plain woven composite plate (Fig.2), with and without ceramic facing layer. Due to symmetry, only one quarter of the model is considered with appropriate boundary conditions. The interface between the matrix and woven fabric is modeled separately, so the issue of interface contribution in the energy absorption of textile composites in the ductile interface model can be attacked also. In this case, it is assumed that interface material has the same properties as an epoxy matrix.

The developed model for polymer matrix composite plate has 2592 matrix elements, 5184 interface elements, and 3456 fabric elements, which makes total number of 11232 3D-solid elements with 12987 nodes, while ceramic facing layer has 15900 3D-solid elements with 21042 nodes. A cylindrical projectile, with a diameter of 7.62mm, was modeled as a deformable, elastic plastic steel material. The impact velocities are assumed to be in the range of 10m/s to 1000m/s. The backing plate is further assumed to have thickness of 6mm, and ceramic facing thickness of 8mm. Volume fraction of backing polymer matrix composite was 50%.

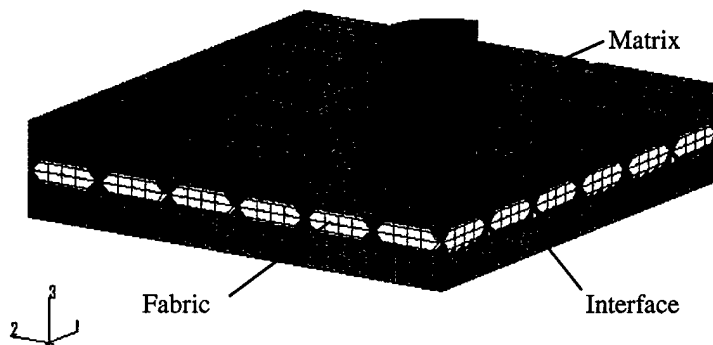


Fig.2 Plane woven composite model.

Two different simulations were performed in the terms of prescribed boundary conditions. In the first set of models, boundary conditions were free and in the second one target had constrained edges.

Another set of simulations is performed in order to explore effect of different ceramic facing geometries (monolithic ceramic tile versus layer of spheres embedded in epoxy), on the ballistic resistance of armor model. Figure 3 represents GDC model with spherical ceramic facing.

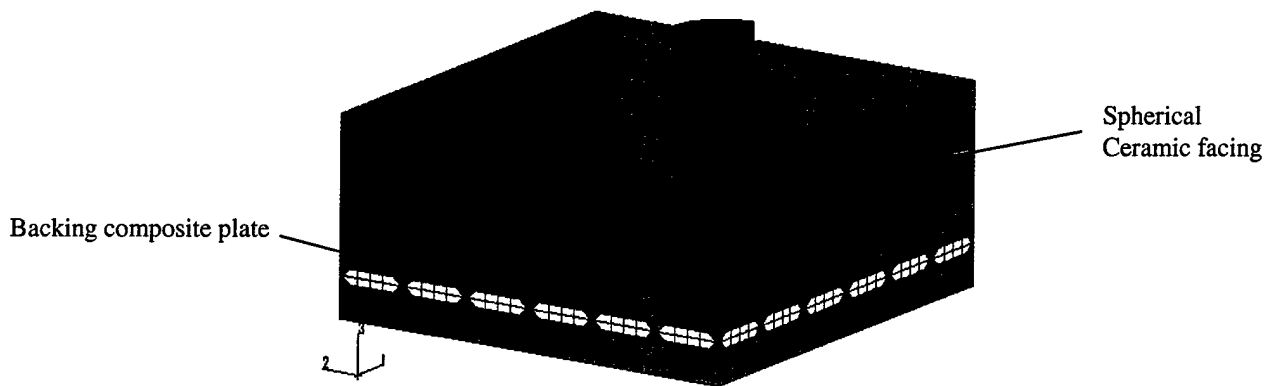


Fig.3 GDC model with spherical ceramic facing.

4. MATERIAL MODELS

Contrary to the analysis of a high velocity impact on materials such as steel or aluminum, the simulation of high velocity impact and penetration processes into non-isotropic fiber reinforced material is a more challenging research task. However, such analysis is needed in order to understand the complex dynamic interactions between structural components undergoing large deformations and nonlinear material behavior including failure, de-lamination, erosion, etc.

In order to simulate the dynamic behavior of composite materials, the constitutive equations must cover the elastic regime, the material failure, and the behavior of the partially or completely failed material.

From the computer simulation point of view, the introduction of simple discrete models for the study of textile composites offers the advantage of introduction of different material properties for both matrix and fibers, as far as possibility of more accurate description of the geometry. Further, more elaborate (and more realistic) failure criteria can be introduced.

Using the higher-order discretization it is possible to explore the effects of fiber architecture on the properties of these composites. In addition using separate models for the fiber and matrix will allow for more complex models for both materials that can include rate dependence in the modulus of the fiber and matrix behavior.

4.1 The Failure Models

The absorption of energy under both low and high velocity impacts depends strongly on the evolution of damage in the target and the resulting progressive degradation of its properties during its interaction with the projectile. For this reason, any computational simulation of impact phenomena must integrate in a rational way the dominant damage mechanisms in the target (and occasionally in the projectile). There are three ways that damage can be integrated in a finite element simulation:

- Ductile/Brittle Interfaces: In this case the connectivity of the elements is allowed to change during impact, via a force-displacement law for element boundaries that includes a separation criterion based on maximum force, displacement or other criteria that combine both forces and displacements. Such models are useful in modeling fragmentation, and usually allow no interactions between elements after they have been separated. Such models preserve kinetic energy, and special formulations are required to give consistent, mesh-independent fracture behavior. Best applications suitable for these models are the studies of fragmentation and post-impact debris.
- Element Elimination : In these models, failure is considered to occur at the element level, on the basis of strain, stress or combined stress-strain criteria. After the failure condition is satisfied in a particular element, the element is "eliminated" from the model, in other words, the element no longer participates in the subsequent analysis. This is a key disadvantage of this approach when failed material is contained in the impact area and participates in the damage resistance even after the initial failure (comminution).
- Distributed Damage : In order to represent quantitatively the effects of the intermediate stages of damage development, models with distributed damage are used. The variables assigned to damage may have a physical or phenomenological interpretation. An evolution equation for damage is necessary to complete the model and must be integrated together with the equilibrium equations. The representation of non-monotonic damage evolution is possible, to represent cases where the external loading – e.g., large compressive hydrostatic pressure etc. can result in damage healing (partial closure of a previously open crack). Distributed damage models provide great flexibility in the description of the physical phenomena associated with damage. They tend, however, to be relatively complex. As a result their validation is not straightforward, particularly because the evaluation of the material parameters can be at best not straightforward.

For simplicity we have selected an element failure model for the polymeric constituent. The role of the polymer backing plate is to transmit load before local failure. After failure, it is postulated that its contribution to impact resistance is negligible. On the other hand, we chose to work on a distributed damage model for the ceramic.

4.2 A Cracking Model for Ceramic Facing

This section describes the cracking constitutive model for brittle materials used for ceramic facing. This is a "smeared" model in the sense that damage is considered to be homogeneous within an element - even if the length of individual cracks is much smaller than the element size. It is a "fixed orthogonal crack model", because it considers damage to be described by micro-cracks oriented along mutually perpendicular planes. These cracks are considered to develop in

the undamaged material when a maximum principal stress criterion is satisfied. The direction of the maximum principal stress at that time defines the normal to plane, which along which the micro-cracks appear. Subsequent cracks may develop along the same plane or two other planes normal to the initial crack plane. The coordinate system defined by the cracks may rotate due to rigid rotation of the elements. Cracks are considered to be irreversible, in the sense that once generated, they will always be there. There is the possibility, however, of partial closure of a previously open crack due to compressive forces normal to its plane. The basis of the model is the work of Hilleborg and Crisfield, and its "plasticity-like" theory [1].

The elastic properties of a brittle material, used in the simulations are $E=350\text{GPa}$, $\nu=0.2$, and the cracking failure parameters: cracking failure stress, 2.5GPa , direct cracking failure strain, 0.036 , and the Mode I fracture energy 120N/m . The mass density is 4000kg/m^3 .

4.3 Element Failure Model for Polymer Matrix Composite

The ductile failure model, used for both fabric and matrix phase of polymer matrix composite, provides simple failure criteria, which are designed to allow the stable removal of elements from the mesh as a result of tearing or opening of the structure. The failure model is based upon the value of the equivalent plastic strain. When the equivalent plastic strain at a material point reaches the value defined as the plastic failure strain, ϵ_f^p , the material point is failed. If all of the material points in the element fail, the element loses its ability to resist any further load and, hence, it is removed from the mesh.

The ductile failure model is based on a damaged Von Mises plasticity theory with isotropic hardening. The damage manifests itself in two forms: degradation of the yield stress with damage and damaged elasticity.

The engineering elastic constants of backing composite material constituents are given in the T1.

Property	ρ [kg/m ³]	E_1 [GPa]	E_2 [GPa]	E_3 [GPa]	ν_{12}	ν_{23}	ν_{13}	G_{12} [GPa]	G_{23} [GPa]	G_{13} [GPa]
Material										
Epoxy	1200	3.45	3.45	3.45	0.35	0.35	0.35	1.3	1.3	1.3
Spectra	970	268	4.72	4.72	0.4	0.4	0.4	36	36	36

T1. Engineering elastic constants of composite material constituents.

When a viscoelastic material is subjected to high strain rates, such as a ballistic event, the material displays considerable stiffness, which is similar to the behavior of polymeric materials at low temperatures. The damping behavior in the amorphous regions in a viscoelastic material appears negligible at high strain rates. Upon ballistic impact, material's ability to elongate is reduced and the amount of energy absorbed depends on its stiffness. However, it has to be highlighted that the study of the dynamic properties is not complete by simply changing the modulus. The reduction of strain to failure with strain rate is equally important. Thus, it can be said that increasing the modulus only, offers a very biased view of the problem.

The introduction of fully dynamic material model is planned in the future, based on available experimental results.

Table 2 shows Spectra modulus for different rates of strain.

Strain rate (min^{-1})	10	500	1,000	5,000	10,000
E [GPa]	101	130	145	221	268

T2. Spectra fiber modulus strain rate dependency.

5. RESULTS AND DISCUSSION

The most important characteristic of protective ballistic system is its ability to slow down and stop the projectile. The best way to estimate armor penetration resistance is to measure residual velocity of a projectile. Another consideration for system integration is back face deformation, or the deflection of the armor material on the back surface. Even though the armor may defeat a threat projectile, the back face deformation can cause other damage, for example, blunt force trauma to a person wearing an armored vest or a helmet.

The effect of boundary conditions was investigated for both moderate and high impact velocities. Generally, the boundary conditions depend on, projectile size, its initial velocity, and target geometry and thickness. In this case, where velocity was 250m/s, impact resistance of a target depends on boundary conditions as it is shown in the Fig.4. However, the simulations showed no effect of the boundary conditions, on the target ballistic performance, in the case of impact velocity of 1000m/s. It is apparent during ballistic event that the localized material response in the vicinity of the applied load becomes primary important whereas the overall geometric configuration of the structure becomes secondary.

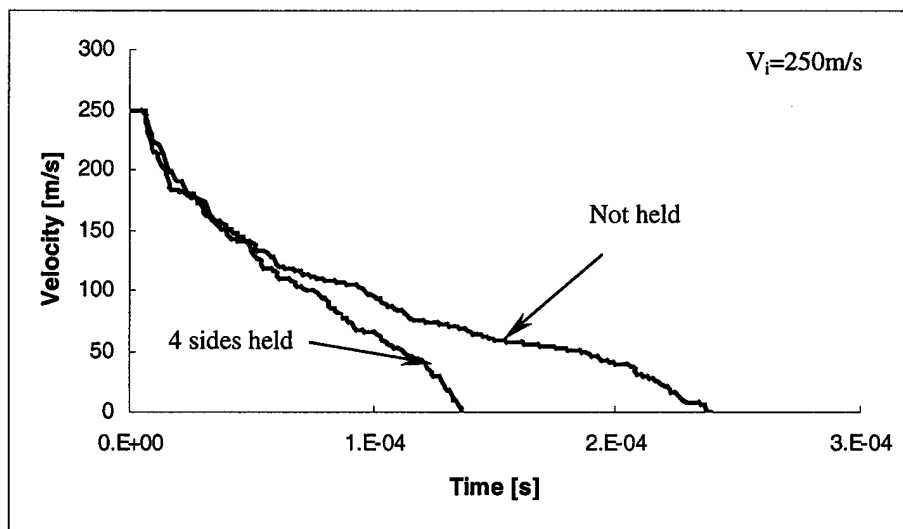


Fig.4 Boundary condition effect on textile fabric ballistic resistance.

It can be concluded, that boundary conditions for high velocity impact, in this case can be ignored, because the impact event is over before the stress waves have reached the edge of the structure [2].

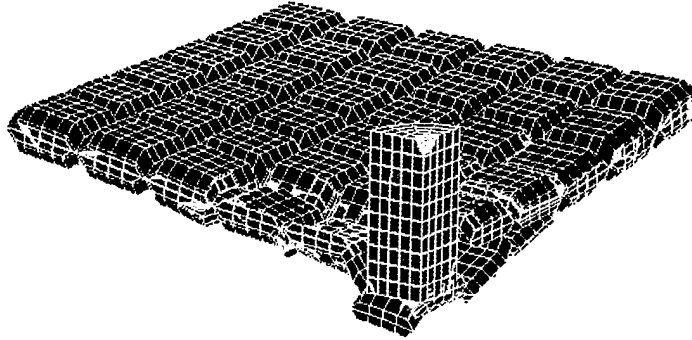


Fig.5 Yarn breakage during the impact, in the fabric phase of the structure.

Three impact numerical simulations with initial velocities of 10m/s, 100m/s, and 1000m/s, on a plane woven Spectra composite plate, were performed using, in the first case static, and in the second, strain rate dependent modulus, listed in the Table 2. These velocities are of interest because each of them is related to different dynamic event in the engineering practice [4]. For instance, bird strike on an airplane structure occurs at velocity of 10m/s. Small-arm projectiles have velocities in the range of hundred meters per second, while velocities of an armor piercing bullets are in the range of 1000m/s.

Results are showing better penetration resistance (lower residual velocity of the penetrator), in the case where strain rate dependent modulus were used (Fig.6). Strain rate effect is more evident for higher velocity impact simulation, however, in the case of the highest impact velocity (1000m/s), the difference is not noticed mainly because of the lack of data for such high strain rate event.

Introduced strain rate effect increases the Young's modulus of the fabric, which attributes to better penetration resistance on two ways. Firstly, material becomes more stiff, and secondly, since modulus is directly proportional to the velocity of the deformation (both elastic and plastic) in the material:

$$c=(E/\rho)^{1/2}$$

the deformation waves are traveling faster in the plane normal to impact, spreading the load over a larger area away of the impact site.

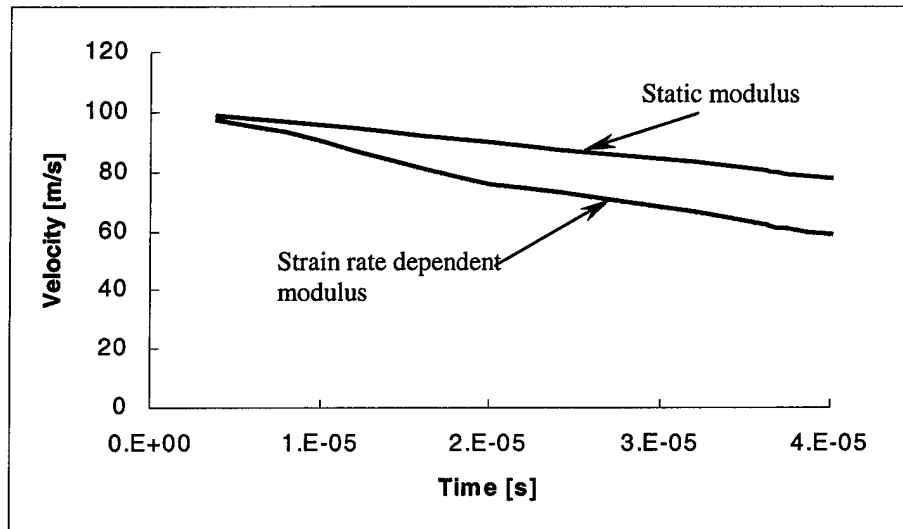


Fig.6 Effect of an introduction of dynamic modulus on target ballistic performance.

Effect of impact velocity on residual velocity time history for a woven fabric model was investigated (Fig.7). This kind of study is useful because it gives target behavior for a range of velocities. At low velocities (bird strike, drop-weight test), impactor would bounce back from the target, just elastically deformed it, while for a moderate and high velocities in the range of hundreds meters per second, ballistic limit of a given structure (V_{50}), can be determined.

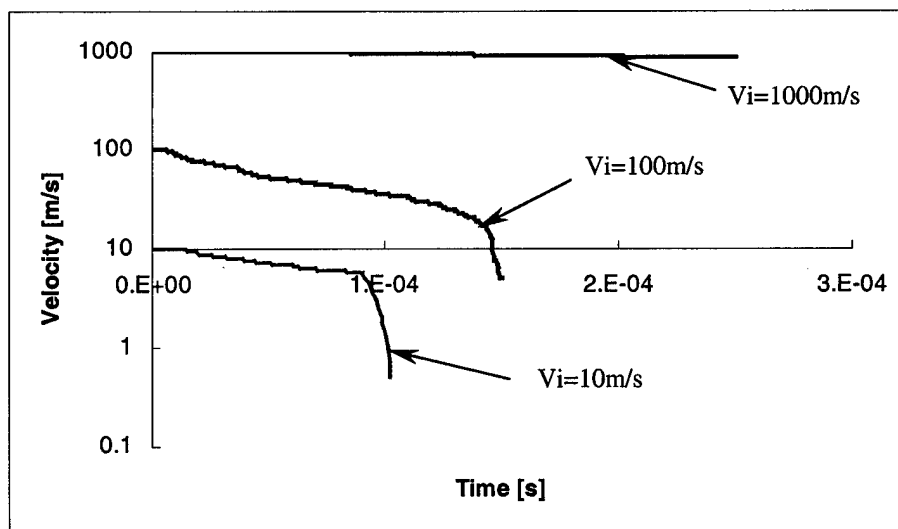


Fig.7 Effect of impact velocity on velocity time history for a woven fabric model.

Figure 8, gives relative absorbed energy of impact for a 10m/s, 100m/s, and 1000m/s initial velocities. It can be noticed that absorbed impact energy by the textile fabric structure, even in the case of 1000m/s is not negligible.

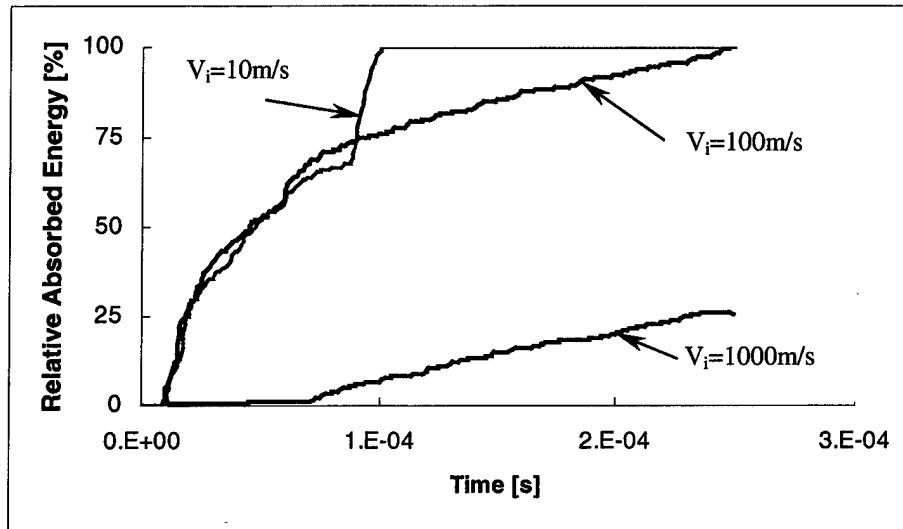


Fig.8 Effect of initial velocity on relative absorbed energy during the impact.

Difference between ballistic resistances of various composite models is presented on Fig.9. It is shown that application of Gradient Design Composite material offers high impact resistance comparable to the traditional textile composite material.

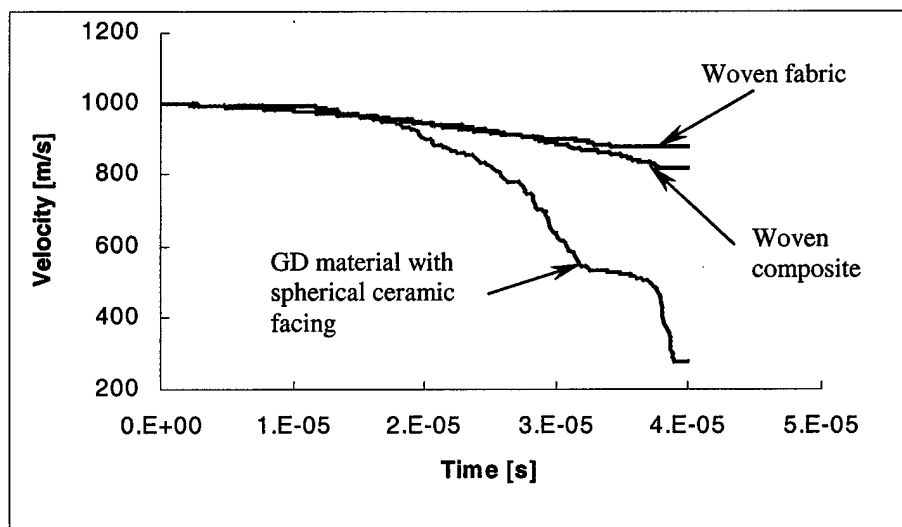


Fig.9 Velocity as a function of time for different composite models.

Finally, the effect of different ceramic facing layer structure, on the residual velocity is examined for the same, woven fabric backing plate, (Fig.10). Ballistic resistance of spherical ceramic-faced gradient design material is showed to be comparable to that of target system with a monolithic ceramic layer, with a significantly less mass of a spherical ceramic facing armor system.

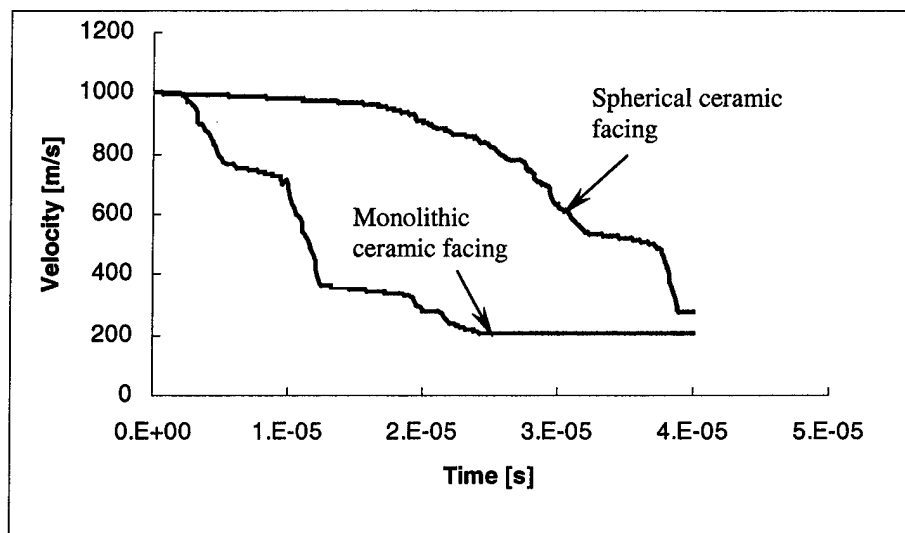


Fig.10 Effect of ceramic facing layer on velocity time history.

6. CONCLUSIONS

Simulations of the ballistic impact response of developed plain woven composite plate model, for impacting velocities ranging between 10m/s-1000m/s with and without ceramic facing layer are presented.

Two types of used material models are discussed: fiber/epoxy viscoelastic rate-dependent model for backing, and damage-based model for brittle ceramic facing.

Addition of the strain rate effect on Spectra fabric modulus in numerical simulations, showed better target ballistic performance and necessity of using dynamic material properties in moderate to high velocity impact simulations. However, the study of the dynamic properties is not complete by simply changing the modulus. The reduction of strain to failure with strain rate is equally important and has to be included in the further analyses.

Residual velocity time history was evaluated for the plain woven textile composite target with two types of facing layers. Ballistic resistance of gradient design composite with facing layer of ceramic spheres embedded in epoxy is showed to be comparable to that of solid ceramic tile. It can be concluded that ceramic spheres can be used effectively to replace the conventional ceramic tiles to reduce weight and cost without sacrificing its ballistic effectiveness.

Effect of impact velocity on residual velocity time history for a woven fabric model was investigated, giving target behavior for a range of velocities from 10m/s up to 1000m/s. This type of case study is attractive for various applications: from drop-weight test simulation up to modeling of ballistic impact on composite structure.

7. LITERATURE

- [1] Hilleborg A, Modeer M, Petersson P., Cement and Concrete Research, Vol.6, pp. 773-782, (1976).
- [2] Jovicic, J., Zavaliangos, A. and Ko, F., Special issue of Composite Part A: Applied Science and Manufacturing, Elsevier Science. Vol.31 (8), pp.773-784. August 2000.
- [3] Song JW, Geshury A, and Ko F., Proceedings, Eleventh International Conference on Composite Materials, Gold Coast, Australia, July 14-18, (1997).
- [4] Zukas, Impact Dynamics. John Wiley & Sons, New York, 1982.

Presented on the *Fifth International Conference on Textile Composites (TEXCOMP 5)*,
Katholieke Universiteit Leuven, Belgium, September 18-20, 2000.

FIBER ARCHITECTURE BASED COMPUTER MODELING OF TEXTILE COMPOSITES*

Jovan Jovicic, Frank Ko and Antonios Zavaliangos

Department of Materials Engineering
DREXEL UNIVERSITY

Philadelphia, USA



**Supported by the US Army Research Office under the Multidisciplinary
University Research Initiative on Functionally Tailored Textile Fabrics*

1. INTRODUCTION

Textile Composites



```
graph LR; A[Textile Composites] --> B[Applications]; B --> C[Engineering Design Tools];
```

Applications

- Building infrastructure
- Automotive
- Marine structures
- Aircraft and aerospace
- Biomedical

Engineering Design Tools

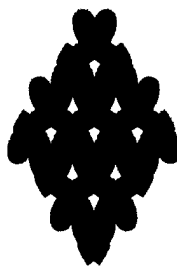
- Analytical
- Experimental
- Numerical

2. OBJECTIVES

Finite Element Modeling

Material model selection

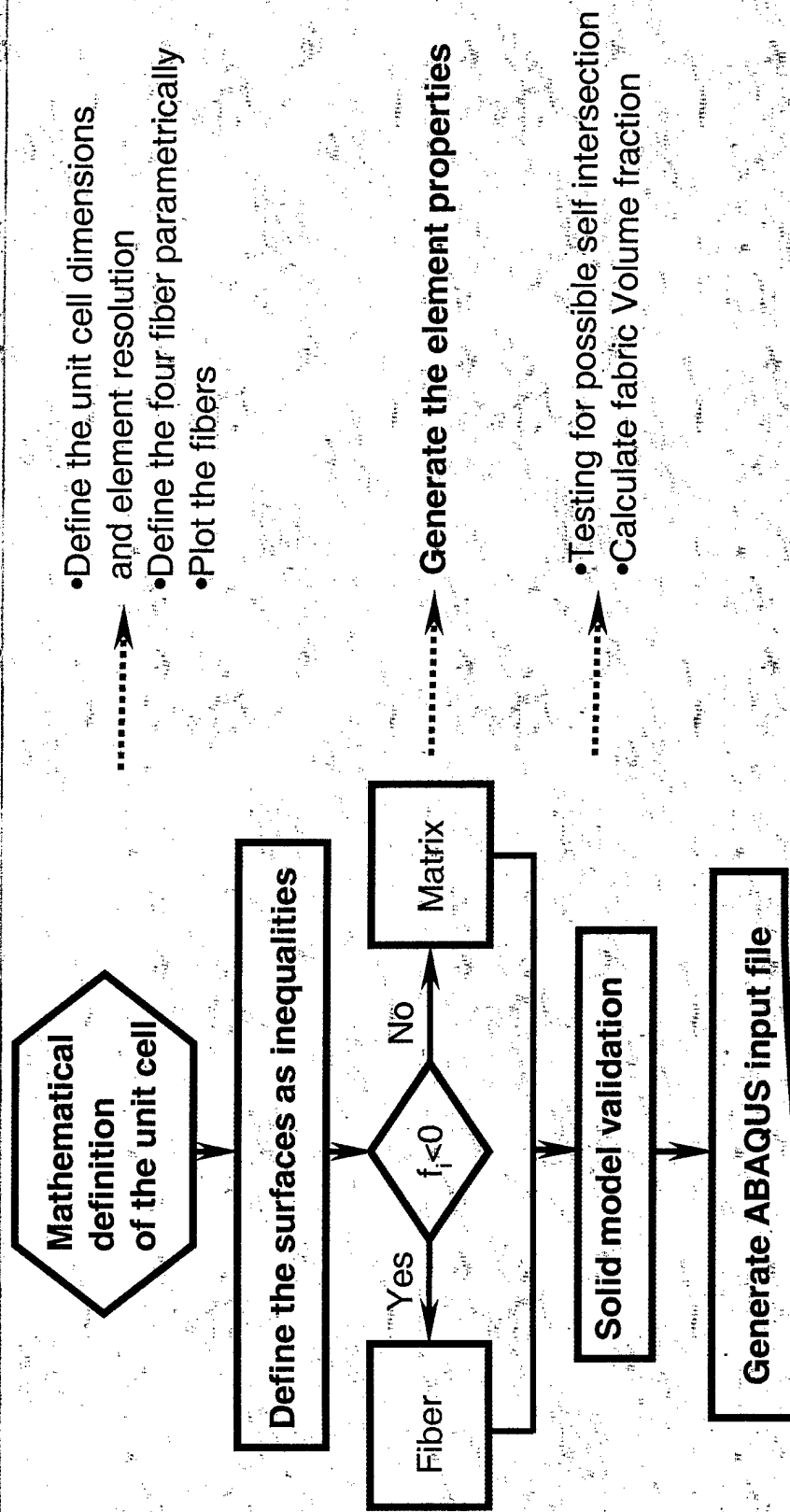
Detailed geometry description



3. APPROACH

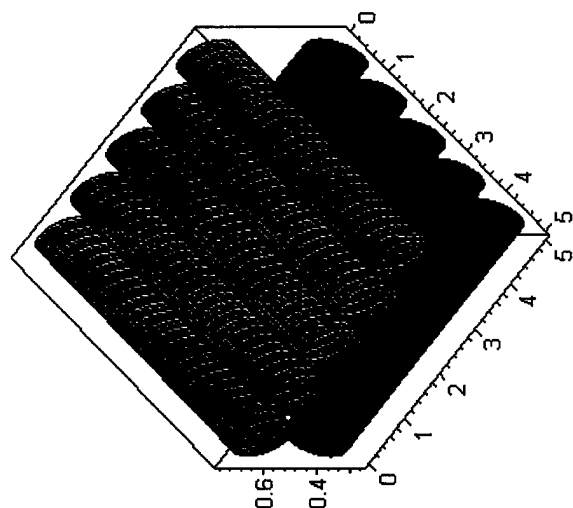
- In-house, ABAQUS-EXPLICIT based, MAPLE computer code is used to simulate the structural behavior of textile composite, and assess the effect of materials selection and fiber architecture.
- Developed algorithm is able to create true 3D fiber architecture-based unit cell models of textile composite preforms, and to produce adequate meshing or increasing detail using solid brick elements for both matrix and fibers.
- Geometry of a unit cell, cross-sectional shapes and the "centerline architecture of a fabric preform are parametrically defined.

ALGORITHM OF A MAPLE CODE

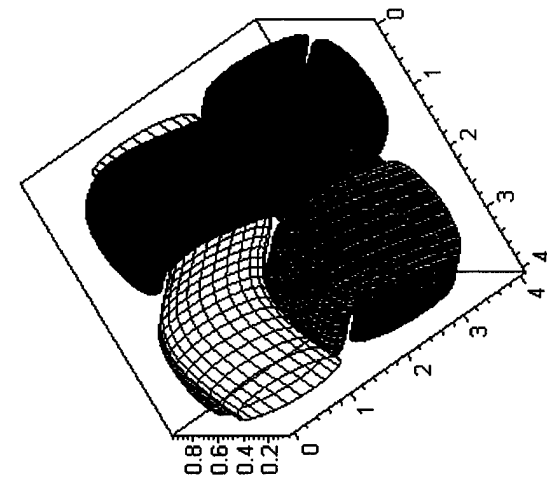


4. COMPUTER-BASED MODELING OF THE TEXTILE REINFORCED COMPOSITE STRUCTURE

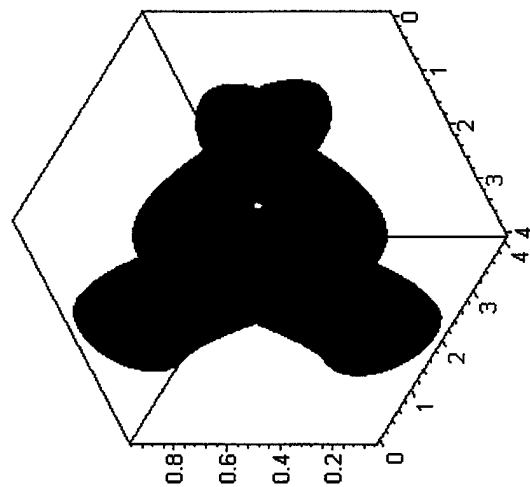
Orthogonal Unit Cell



Woven Unit Cell



Knitted Unit Cell

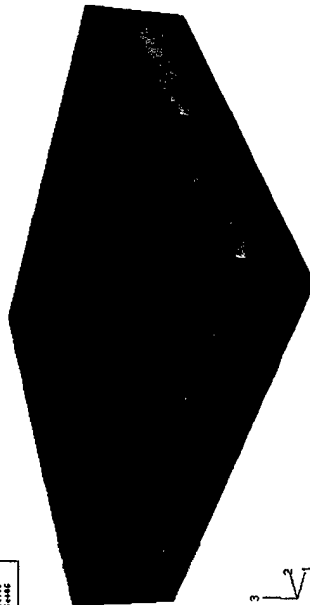
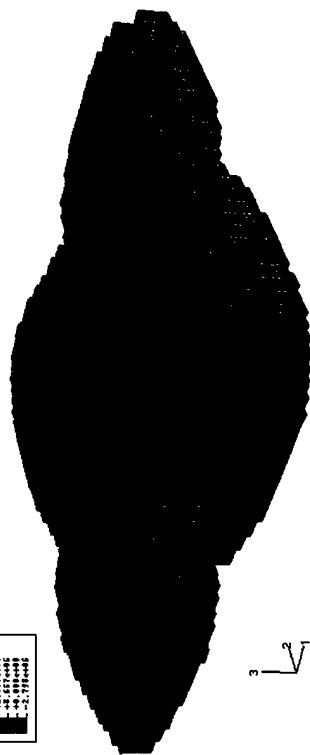
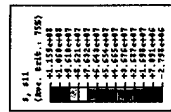
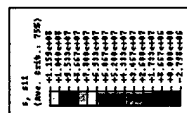


5. MECHANICAL PROPERTIES OF A REPRESENTATIVE UNIT CELL

Property	ρ [kg/m ³]	E1 [GPa]	E2 [GPa]	E3 [GPa]	ν_{12}	ν_{23}	ν_{13}	G_{12} [GPa]	G_{23} [GPa]	G_{13} [GPa]
Material										
Epoxy	1200	3.45	3.45	3.45	0.35	0.35	0.35	1.3	1.3	1.3
Spectra	970	268	4.72	4.72	0.4	0.4	0.4	36	36	36

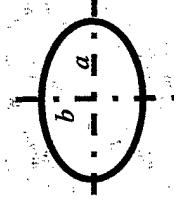
Engineering elastic constants of composite material constituents

6. WOVEN UNIT CELL FE MODEL UNDER UNIAXIAL TENSION



Maximal principal stress in the textile composite unit cell model

7. PARAMETRIC STUDY



Yarn cross-section

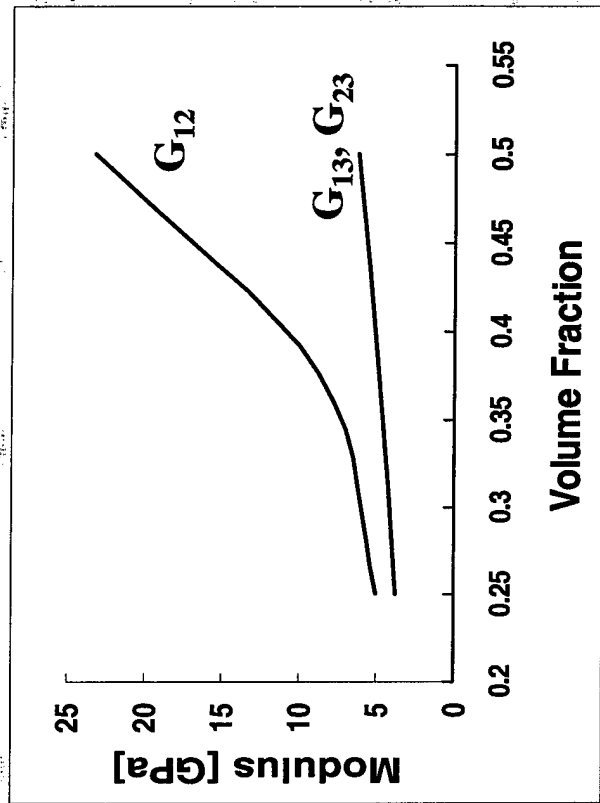
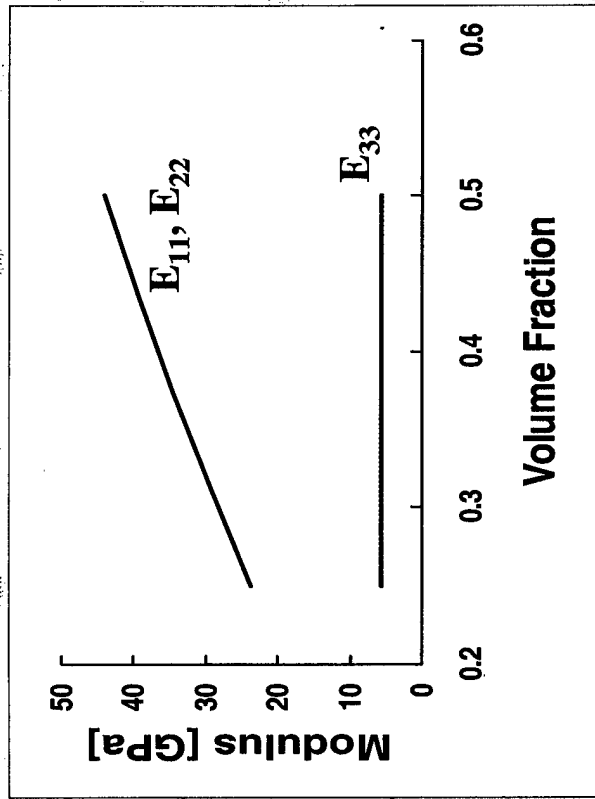


Fabric architecture

■ **Flattening factor- $f=a/b$**

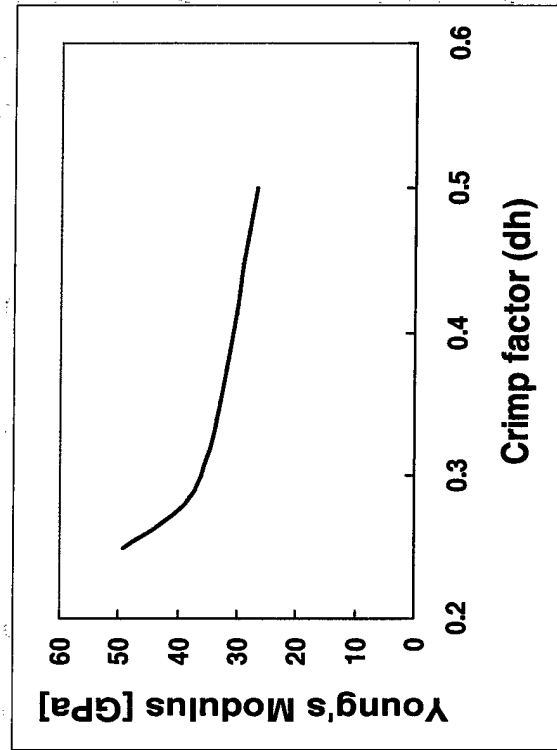
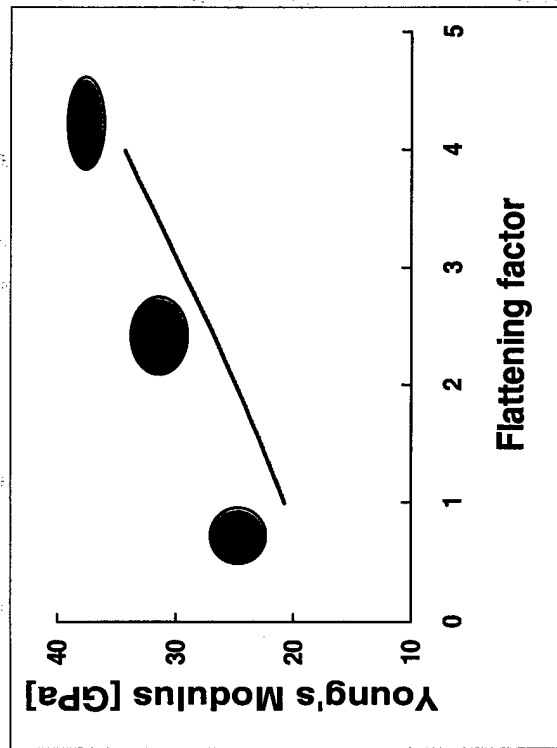
■ **Crimp factor- dh**

8. ELASTIC PROPERTIES AS A FUNCTION OF FABRIC VOLUME FRACTION



Influence of fabric Volume fraction on composite mechanical properties

ELASTIC PROPERTIES AS A FUNCTION OF YARN CROSS-SECTION AND FABRIC ARCHITECTURE



9. DISCUSSION

Yarn shape, yarn orientation and fabric volume fraction are demonstrated to influence the elastic moduli.

It was found that Young's moduli (E_{11} , E_{22}) are strong functions of fabric volume fraction, while E_{33} is not, which shows tailoring capabilities of this class of composites.

It is shown that Young's modulus decreases with increasing of fabric crimp.

It was also found that the flatter the yarn cross-section the higher the resistance to tension of the composite in the reinforced plane, because flattening of a yarn decrease the distance between them.

10. CONCLUSIONS

The geometry is the first step in understanding any composite structure, and the model presented in this work allows one to look at the three dimensional nature of a textile composites structure in those cases where simple models prove inadequate.

Although more costly in terms of computational resources, the present analysis, based on the representative volume element (RVE), of a textile composites, allows prediction of the engineering constants of the constituents, as well as the detailed material model description within the RVE.

The main advantage of our approach is that different architectures, mesh densities, boundary and load conditions of a textile composites and its RVE-s are functions of only few parameters that can be easily controlled and changed.

The developed code can be used to generate an input file for any commercial FE compute software.

11. FUTURE WORK

- Generate a family of unit cells (orthogonal, woven, braided, knitted) in order to explore the role of architecture and interface cohesion in the mechanical behavior of textile composite structure.
- Successfully completion of presented algorithm will facilitate the engineering design of the next generation of multifunctional textile composites.
- Accordingly, a library of fiber architectures based on the unit cell will enable the structural optimization along with simulation of mechanical response of advanced composites.

12. REFERENCES

- Chou, T.W. and F.K. Ko, ed's. *Textile Structural Composites*, Elsevier, 1989.
- Glaessgen, E., Pastore, C., Griffin, H. and Birger, A. *Geometrical and Finite Element Modeling of Textile Composites*. Composites Part B, 1995.
- Liao, T. Adanur, S. *A Novel Approach to Three-Dimensional Modeling of Interlaced Fabric Structures*. Textile Research Journal, 1998, 68 No. 11 pp. 841-847.
- Paumelle, P., Hassim, A. and Lene, F., *Composites with Woven Reinforcements: Calculation and Parametric Analysis of the Properties of the Homogeneous Equivalent*. La Recherche Aerospatiale, 1, 1990.
- Peirce, F.T. *The Geometry of Cloth Structure*. Textile Research Journal, December 1976.

A Novel Polymer Nanofiber Interface for Chemical and Biochemical Sensor Applications

S. J. Kwoun, R. M. Lec, B. Han* and F. K. Ko*

The School of Biomedical Engineering, Science and Health System, Drexel University, Philadelphia, PA, USA, sunkwoun@biomed.drexel.edu; rlec@coe.drexel.edu

* Department of Materials Engineering, Drexel University, Philadelphia, PA, USA, baohuah@hotmail.com; fko@coe.drexel.edu

ABSTRACT

Polymer thin films are used extensively as a chemically sensing medium in variety types of acoustic sensors. It is well known that the sensitivity of a sensing film is proportional to the surface area of the film per unit mass. In our research we have studied the feasibility of using thin polymeric films made of nanofibers (NFs) as novel sensor interface. Thin NF films have surface area approximately one to two orders of the magnitude larger than continuous films. The NF films made of Poly-Lactic Acid-Co-Glycolic Acid (PLAGA) polymers were studied with Thickness-Shear Mode (TSM) resonator operating at 10 MHz. The response of the NF sensor to gaseous and liquid media under various ambient conditions was studied in details.

Keywords: Nanofiber; Piezoelectric Sensors, Quartz Crystal Microbalance; TSM; Chemical Sensor

1 INTRODUCTION

A considerable attention has been given to different interfaces for chemical and biomedical sensors; metal oxides films for gas sensors, polymer films for gas and liquid phase sensors, biologically active films such as antigens, enzymes, DNA, cells, etc., for biomedical sensors [1,2]. Since the properties of the interface influence significantly the sensor performance (sensitivity, selectivity, time response, aging) [3,4], several advanced techniques such as RF & DC sputtering, electron beam, Langmuir-Blodgett, spinning, and sol-gel have been used for fabrication of thin sensing film. All these techniques make continuous films that have relatively low sensing surface area. In this paper we propose to use a NF thin film produced with electrospinning technique as a new sensing interface.

It is well known fact that the sensitivity of the sensing film is proportional to the surface area of the film per unit mass. Thin film made of NFs has surface area approximately one to two orders of the magnitude larger than continuous films [5]. Poly-Lactic Acid-Co-Glycolic Acid (PLAGA) polymer NF with the diameter about 500 nm were deposited on the gold surface of AT-cut TSM quartz crystal operating at the resonant frequency of 10 MHz. The response of the NF sensor to gaseous and liquid

media under various ambient conditions was studied in details and acoustic and viscoelastic properties of NF thin films were measured.

2 EXPERIMENT

2.1 Preparation of NF Thin Film

Electrospinning technique was used to fabricate thin NF films [6]. In our case, the applied voltage was 15,000 volts DC and the distance between the target TSM sensor and the tip of the micronozzle was maintained all the time at 20 cm [7]. NF films were deposited on one surface of AT-cut TSM disk-shaped quartz crystals of the diameter of 13 mm having 5 mm circular electrodes (Fig. 1a). The 5% PLAGA in DMF (Dimethyl formamide) solution was applied to fabricated NF films at several different deposition times equal to 15, 30, 45, 90, and 120 seconds.

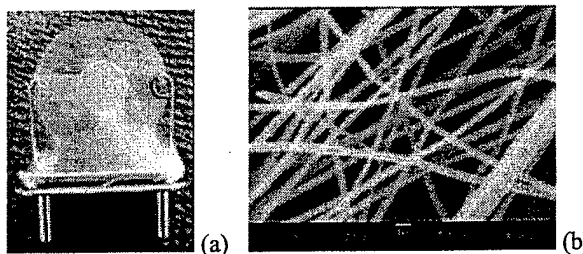


Figure 1. Photograph of the TSM sensor with deposited NF film (a) and the SEM picture of the NF film at 6000X magnification (b).

2.2 Measurement Systems

Initially NF films were characterized using SEM microscope, which provided data on their size, structure and thickness (Fig. 1b). HP 4395A network / spectrum / impedance analyzer based measurement system was used to measure electrical characteristics of the NF sensors. The amplitude and phase components of the scattering parameter S_{21} were measured as a function of the frequency, and based on it the resonant frequency and amplitude of the sensor were determined. A Precision Mechanical Convection Oven, Model STM 80 was utilized for measuring temperature behavior of the sensor in the

temperature range from 25°C up to 100°C. The influence of the air pressure on the sensor response was studied using a high vacuum Kurt Lesker system, Model SuperSystem I/II. An in-house developed gas delivery system was utilized for to study of the sensitivity of the NF film to benzene gas, and a custom-made liquid delivery system was used for study of the sensor response to different liquid loadings.

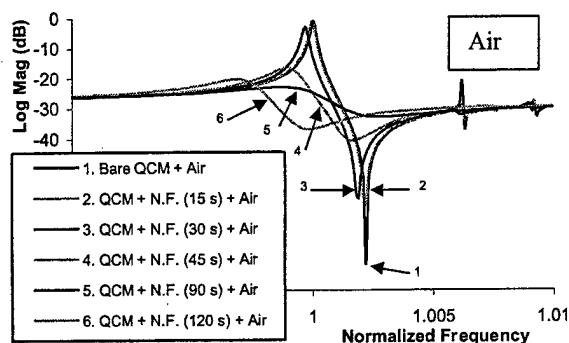


Figure 2. The S_{21} amplitude, α , characteristics, of the NF sensors in air as a function of frequency for five different deposition times.

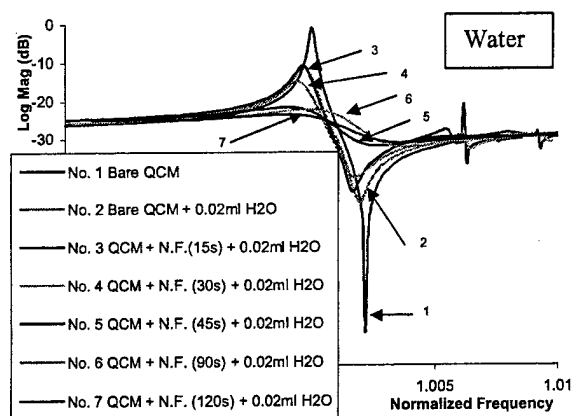


Figure 3. The S_{21} amplitude, α , characteristics of NF sensor with Newtonian liquid loading as a function of the deposition time.

3. RESULT AND DISCUSSION

3.1 Response of NF Sensor in Air and Vacuum

The changes in the resonant frequency, f_r , attenuation, α , frequency shift, Δf , and attenuation shift, $\Delta\alpha$, due to acoustic loading of NF film are presented in Figure 2 and 3. The presented S_{21} characteristics show the response of the TSM transducer loaded with the NF films of different thickness, which corresponds to different deposition times equal to 15, 30, 45, 60, 90, and 120 seconds. In Figure 2 and 3 the NF film are exposed to air, and water

correspondingly. The NF sensors evidence the response, which is typical for viscoelastic loading (Figure 2, 3). The resonant frequency decreases and the attenuation increases. Due to the whole 3-D structures of NFs and the NF mesh, the mechanism of the interaction between the shear wave generated by the TSM resonator and the NF film is different in comparison to a continuous polymer film. The propagation of the shear waves through the NF film depends on the viscoelastic properties of single NF, internal fiber bonding, the NF structure and the effective thickness of the NF film.

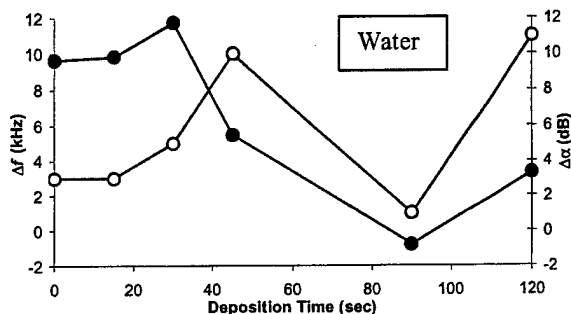
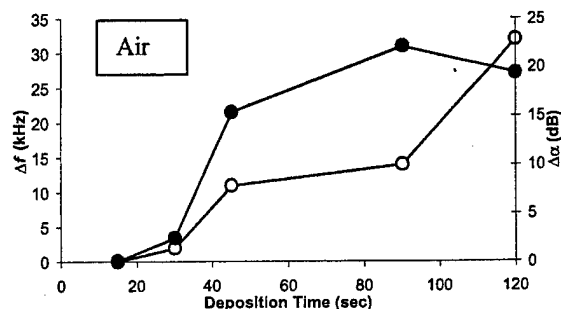


Figure 4. Resonant frequency shift Δf and attenuation $\Delta\alpha$ of NF sensors in air (upper) and with Newtonian liquid loading (lower) for five films fabricated at different deposition times (corresponding to different NF film thickness).

From the Figure 2-4 it can be seen that the NF film corresponding to 90 second deposition time exhibits resonant behavior. This effect could be the case when the acoustic resonant features of the film having the thickness about half of the wavelength. The 90 seconds deposition time NF sensor showed relatively small Δf in air and with Newtonian liquid loading. The attenuation factor at that thickness is smaller with water in comparison to air loading. This phenomenon can be described as the coupled resonant systems between TSM resonator and NF film [8].

Because of the mesh structure of the NF film, the question of the influence of a trapped air on the sensor response was studied. The NF sensor was placed inside a high vacuum chamber to test the effect of the ambient air. The air pressure was slowly decreased from 760 Torr to

10^{-6} Torr and the resonant frequency, attenuation and phase at the resonant frequency were measured.

As one can notice from Figure 5 there is clear changes in both attenuation and phase between the pressure at 760 Torr and less than 10^{-3} Torr. This shows that the ambient air pressure is affecting the response of the NF film.

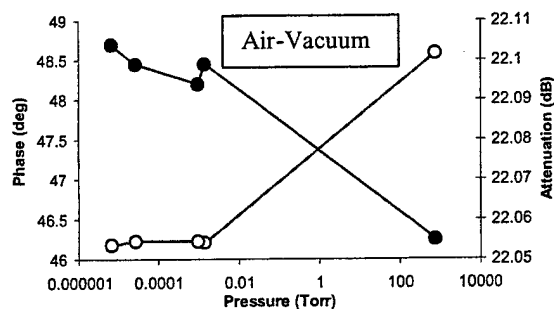


Figure 5. Attenuation (?) and phase (?) changes of NF sensor under different pressure

3.2 Influence of Temperature on NF Sensor Response.

Since the mechanical losses in the NF sensor were relatively large, we studied the influence of the temperature cycling treatment on the NF sensor behavior. Figure 6 shows response of a bare TSM resonator as a function of temperature, and Figure 7 presents the temperature dependence of the sensor with 120 seconds NF film. The results show typical polymer thin film interacting with TSM resonator. NF film shows dramatic shift in mechanical resonant frequency and attenuation at around its glassy transition temperature, T_g , 52°C. However, at about 100°C the resonant frequency returned back to the value closed to that at room temperature, but the attenuation factor was large and clearly growing. After cooling the sensor back to room temperature, both the resonant frequency and the attenuation returned to the initial values, which were held before the experiment. In this experiment we expected that the heat treatment would have an impact on the sensor room temperature operating parameters, however, the results showed that the impact was almost negligible.

3.3 Response of NF Sensor to Benzene

A preliminary study of the sensitivity of NF film for gas sensor applications was performed with benzene gas. Benzene gas does not chemically react with PLAGA film, so only physical sorption was detected by the NF sensor. The NF sensor with 120 seconds film deposition time was tested with benzene gas. Figure 8 shows the attenuation and phase response of the NF sensor. Right after the benzene injection, the responses of both the S_{21} attenuation and phase were detected. From the phase track in Figure 8 one can notice the mass loading mechanism in NF film by decreasing in phase after benzene injection. After 30

minutes from the injection the phase stopped the decreasing and the response was stable over several minutes.

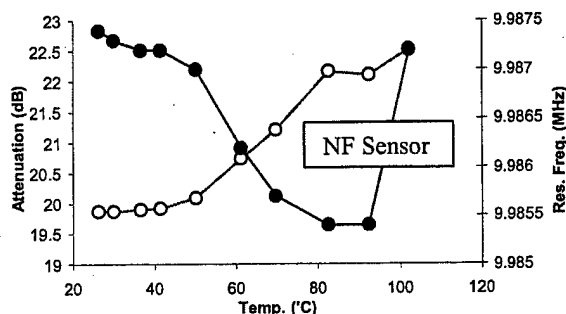


Figure 6. Response of NF sensor to different temperature. (? : resonant frequency and ? : attenuation)

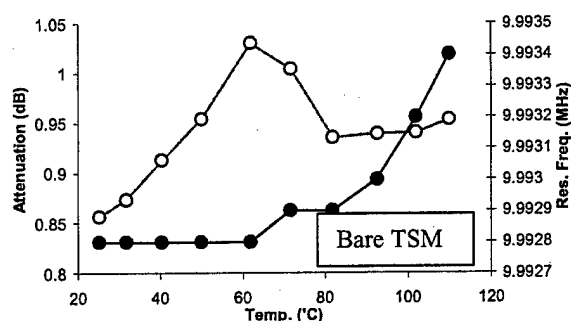


Figure 7. Response of bare TSM resonator to different temperature. (? : resonant frequency and ? : attenuation)

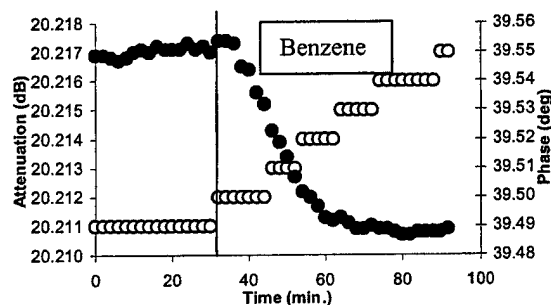


Figure 8. NF sensor response to Benzene injection. (? : phase, ? : attenuation and vertical line: injection time)

3.4 Response of NF Sensors to Hydrophobic and Hydrophilic Liquid Loading

This experiment explains an important issue about different interactions of NF film with hydrophobic and hydrophilic liquids. PLAGA polymer exhibits moderate hydrophobic properties with respect to water and moderate hydrophilic properties with respect to propanol. The presented S_{21} response of the NF sensor shows clearly that the NF film responded very differently to these two different liquids (Figure 9). We observed during the experiment that water was rather "sitting" on the nanofiber film, but propanol

immediately penetrated the film and directly loaded the surface of the TSM resonator. Also, it is interestingly to notice, that the NF sensitivity to water loading was very small, because the response of the sensor to air and water loading was almost the same.

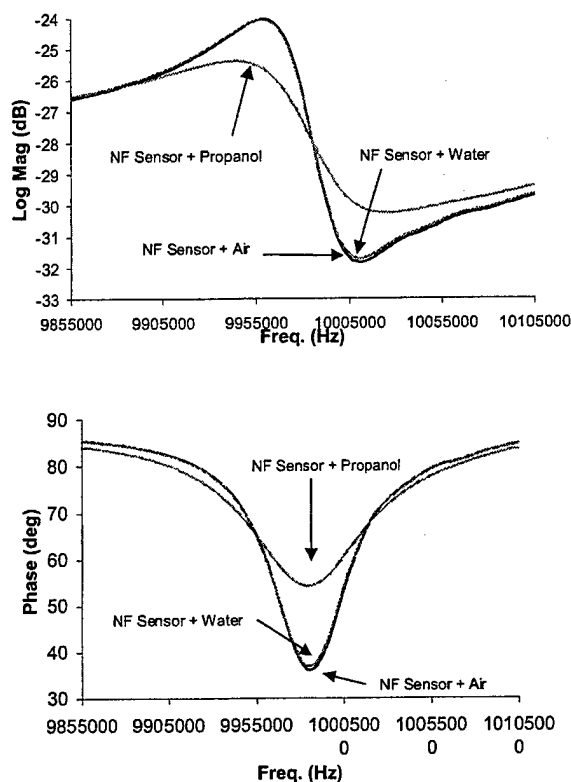


Figure 9. NF Sensor S_{21} response to hydrophobic (water) and hydrophilic (propanol) loads. [Amplitude (upper) and phase (lower) responses].

4 CONCLUSIONS

The results describing the properties of TSM resonator coated with NF thin film operating under different ambient conditions are presented. NF sensors were tested in air and vacuum, with hydrophobic and hydrophilic liquids. Also, the sensor was exposed to benzene gas and the influence of temperature was examined.

The geometrical arrangement of the PLAGA NF film has a 3-D mesh structure that is totally different than continuous polymer film. However, NF sensor exhibited quite high strong viscoelastic characteristics, which on macroscopic scale was similar to viscous loading. The NF film also strongly responded at glassy transition temperature with the changes in both amplitude and frequency. Also, the NF film exhibited some dependence on the pressure of air. When the NF sensors were exposed to benzene gas it showed a strong resonant frequency shift due to additional mass from benzene gas molecules.

Among these responses of NF sensor, the most interesting result was the different response of NF sensor to hydrophilic and hydrophobic liquid loading. Even the areal density of water is larger than one of propanol, NF sensors showed more loading from propanol. This effect is very unique and presents a very advantageous feature of NF films as a chemical or biochemical sensing interface.

Future work will be focus on the intrinsic properties of NF film. As a sensing film, the density and thickness are very critical to evaluate the performance of the NF film. However, in contrary to continuous polymer films, it is very difficult to determine the density and thickness of the NF films. Therefore, new approaches which could measure exactly density and thickness of the NF film will be developed. Also, applications for biological and biochemical sensors will be explored.

REFERENCES

- [1] Taylor, R.F., and Schultz, J.S., *Handbook of Chemical and Biological Sensors*, IOP Publishing Ltd., Bristol and Philadelphia, 1996.
- [2] Falconer, R.S., Lec, R.M., Vetelino, J.F., and Xu, Z., "Optimization of a SAW Metal Oxide Semiconductor Gas Sensor," *IEEE Ultrasonic Symposium*, 1989.
- [3] Janata, J., and Huber, R.J., *Solid State Chemical Sensors*, Academic Press, Inc., Orlando, 1985.
- [4] Xu, Z., Vetelino, J.F., Lec, R.M., and Parker, D.C., "Electrical Properties of Tungsten Trioxide Films," *Journal of Vacuum Science and Technology*, 1990.
- [5] Ko, F.K., and Laurencin, C.T., "Three Dimensional Fibrous Scaffolds for Tissue Engineering," *Proceedings, Fifth International Conference on Frontiers of Polymers and Advanced Materials*, NATO Advanced Research Workshop, Poland, June 23, 1999.
- [6] Jaeger, R., Bergshoeff, M.M., Batlle, C.M., Schonherr, H., and Vancso, G.J., "Electrospinning of Ultra-Thin Polymer Fibers," *Macromol. Symp.* Vol. 127, 1998.
- [7] S. J. Kwoun, R. M. Lec, B. Han, and F. K. Ko, *IEEE/EIA International Frequency Control Symposium and Exhibition 2000*, 52-57.
- [8] Ballantine, D.S., White, R.M., Martin, S.J., Ricco, A.J., Zellers, E.T., Frye, G.C., and Wohltjen, H., *Acoustic Wave Sensors: Theory, Design, and Physico-Chemical Applications*, Academic Press, Chestnut Hill, 1997.

Draft/to be published in Polymer
**The Effect of Molecular Conformation of Poly(L-lactic acid) in
Chloroform Solution on the Morphology of Electrospun Nanofibers**

Baohua Han, Kinnari Chandriani, Alan MacDiarmid* and Frank Ko

Department of Materials Engineering
Drexel University, Philadelphia, PA 19104

*Chemistry Department
University of Pennsylvania, Philadelphia, PA 19104

1. Introduction:

Electrospinning is a unique process that produces continuous polymer fibers with diameters ranging over several orders of magnitude, from the micrometer range typical of conventional fibers, down to the nanometer range. Non-woven textiles composed of electrospun fibers have a large specific surface area and small pore size compared to commercial textiles, making them excellent candidates for use in filtration and membrane applications [1]. In addition, the possibility of manipulating them into three-dimensional structures during deposition has implicated their use in biomedical applications such as scaffoldings for tissue growth [2]. Biodegradable aliphatic polyesters like poly(lactic acid) (PLA) are of particular interest for tissue engineering [3]. This is largely due to their biocompatibility and to their resorbability through natural pathways [4].

While the process of electrospinning has been known for over half a century, current understanding of the process and those parameters, which influence the properties of the fibers produced from it, is very limited. This contribution is dedicated to the influence of polymer molecular conformation in solution, described by a dimensionless Berry number (Be) [5, 6], on electrospinning of Poly(L-lactic acid)/Chloroform system:

$$Be = [\eta]c$$

Where $[\eta]$ is the intrinsic viscosity of the polymer ($[\eta]$ =the ratio of specific viscosity to concentration at infinite dilution) and c is the concentration of the solution.

It has been found that the degree of entanglement of polymer chains in solution can be described by Be [6]. When the polymer is in a very dilute solution, polymer molecules are so far apart in the solution that individual molecules rarely touch each other and Be is less than unity. When the polymer concentration is increased, at some overlap concentration the individual molecules interact, from many contacts, and therefore become entangled; Be is then greater than unity.

In this work, we have compared and evaluated systematically the effects of Berry number on the morphology of electrospun nanofibers of two different molecular weights.

2. Experimental:

Poly(L-lactic acid) (PLA) (Mw 200,000 and 300,000) was supplied by Polysciences Inc.; Chloroform was purchased from Aldrich and used as received. Various polymer solutions were prepared for electrospinning with the concentration ranging from 1 to 15g/dL.

Viscosity measurements of dilute PLA solutions (0.05-1g/dL) in Chloroform were carried out using Cannon-Fenske Routine Viscometer (ASTM D 445) at 22°C. Intrinsic viscosities of two different molecular weights were obtained as the reduced viscosities extrapolated to zero concentration.

The electrospinning apparatus (Fig. 1) consisted of a 20 cc glass syringe, a metal needle with a capillary tip diameter of 0.8 mm, a flat piece of Aluminum foil (10x10cm) as the collection target and a variable high voltage power supply. A positive potential was applied to the polymer solution by attaching the metal needle to the voltage source. The collection target was placed 20cm horizontally from the tip of the needle as the grounded counter electrode. The potential difference between the solution and the counter electrode used to electrospin the polymer solution was 20kv (electrical field strength, 1kv/cm). The deposition of nanofiber took place in air at room temperature.

The morphology of the electrospun nanofibers was observed with AMRAY 1830 Scanning Electron Microscope. Using the saved SEM images, diameter distributions were obtained using the Paint program (Fig. 2).

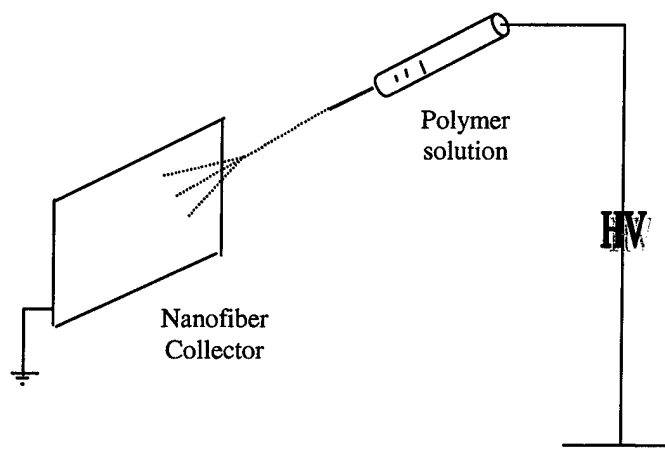


Figure 1. Setup used for electrospinning of PLA

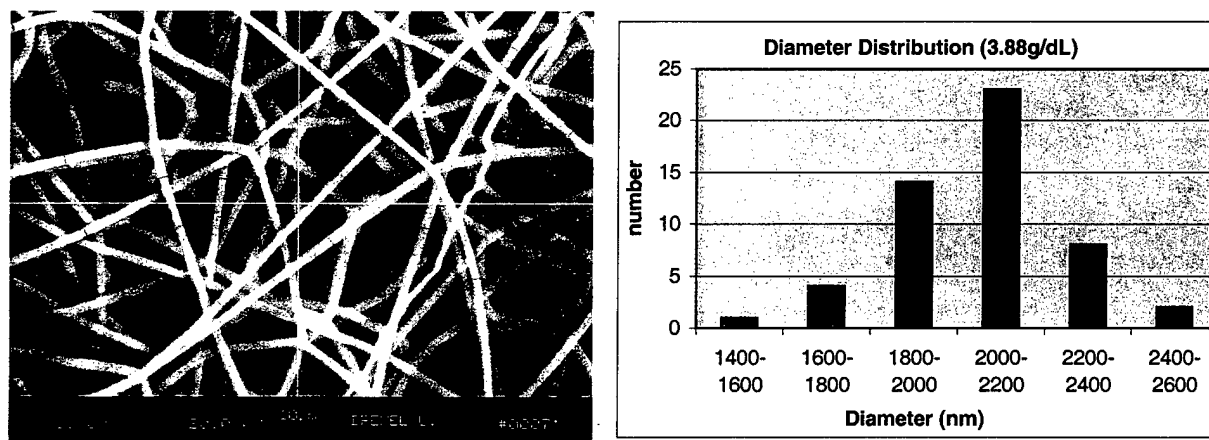


Figure 2. Diameter measurements and Diameter distribution graph (3.88g/dL, Mw=300,000)

3.Results and Discussion:

Two series of solutions were prepared for the study: (1) PLA (Mw=200,000) with Chloroform, concentrations ranging from 3.00g/dL to 15.00g/dL; (2) PLA (Mw=300,000) with Chloroform, concentrations ranging from 1.00g/dL to 5.00g/dL. The morphology of electrospun fibers from these two series is shown in Figure 3 and 4.

Figure 3 shows the representative SEM images of fibers for PLA (Mw=200,000) solutions with a range of concentrations. Generally, the results showed a dependent relationship between concentration and average fiber diameter: the higher the concentration, the larger the fiber diameter (Figure 5). In addition, the uniformity of the fibers changed with concentration. At very low concentrations of PLA, beads and beaded fibers were formed due to the capillary breakup of the electrospinning jets by surface tension [7]. At higher concentrations (>5.00g/dL), fibers were present without any beads. However, there seemed to be two layers of fibers: the upper layers had relatively thicker fibers and the background layers had much thinner ones.

Figure 4 shows a similar relationship between concentration and fiber morphology. At very low concentrations, spherical to spindle-like beads were formed. At higher concentrations, uniform fibers with consistent sizes were present. Lastly, the “two-layers” phenomena appeared at a concentration of 4.81 g/dL.

3.1. AFD vs. Concentration

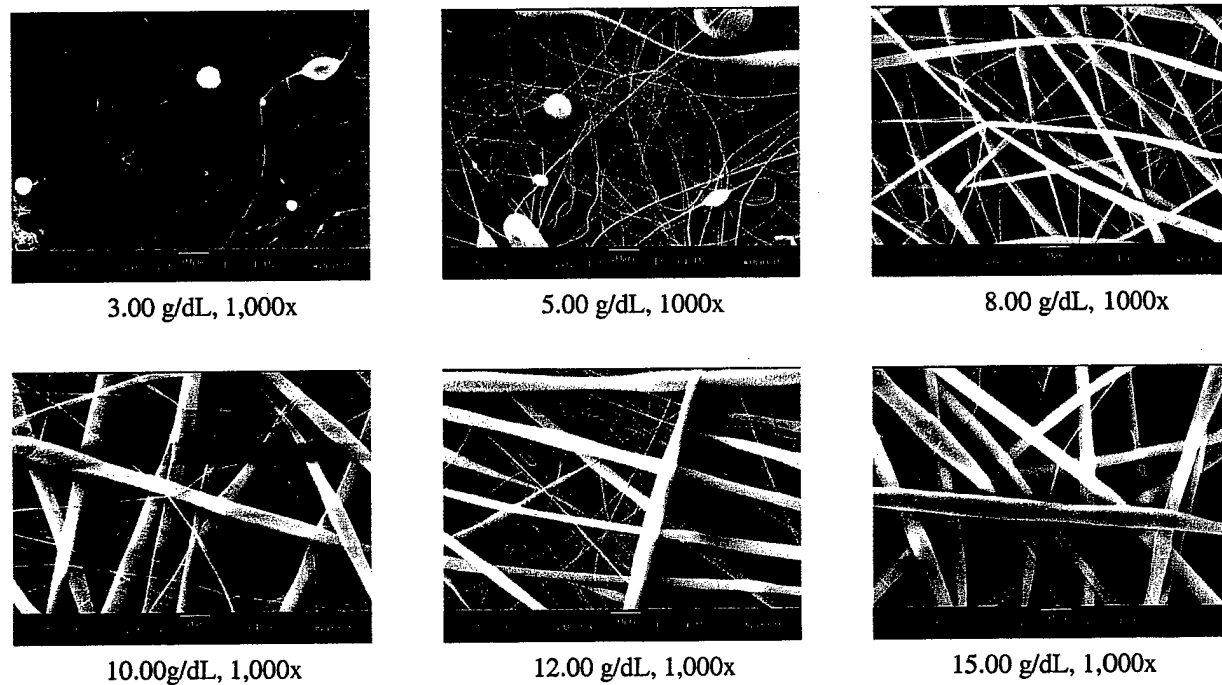


Figure 3. SEM micrographs of electrospun nanofibers of PLA (Mw=200,000)

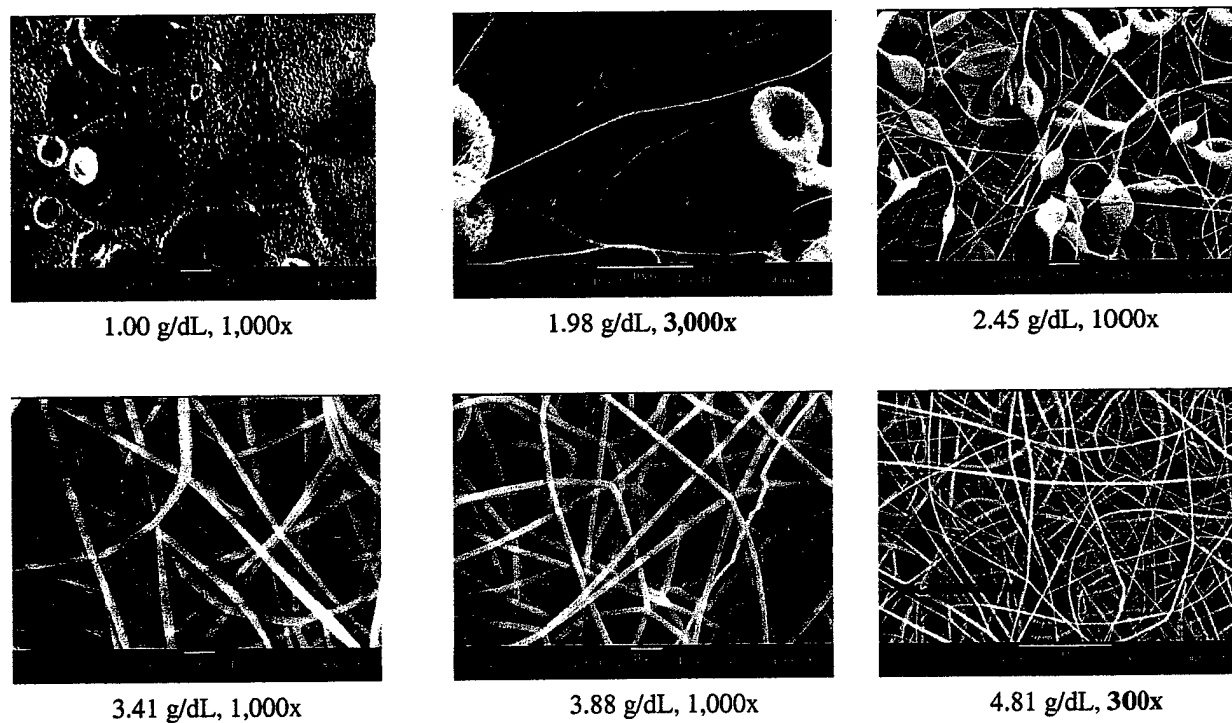


Figure 4. SEM micrographs of electrospun nanofibers of PLA (Mw=300,000)

The relationships between concentration and Average Fiber Diameter (AFD) were plotted in figure 5. Although two series of solutions covered different ranges of concentrations (3-15g/dL vs. 1-5g/dL), the AFD turned out to cover the same range: from ~100nm to ~2500nm. Therefore, for polymers of different molecular weight, different levels of concentrations are required to obtain a certain level of fiber diameter.

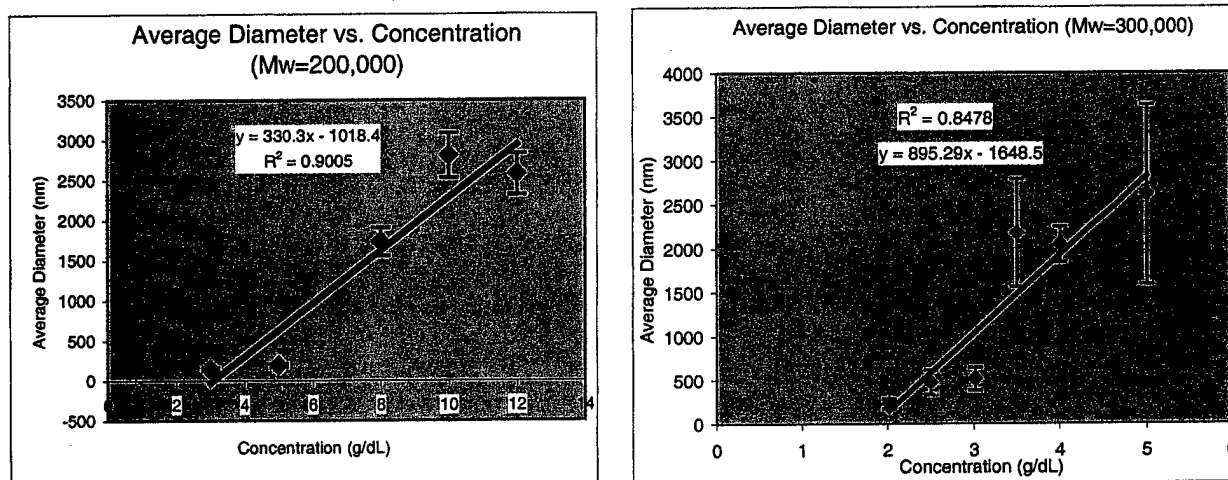


Figure 5. Fiber diameter increases with increasing concentrations

3.2. AFD vs. Chain Conformation

A polymer molecule in solution is not a stationary piece of string, but instead is a constantly coiling and uncoiling chain whose conformation in space is ever changing. In a very dilute solution the individual molecules can be considered as acting independently. Each molecule can be pictured as a string of beads with a tendency to coil in upon itself to form a spherical cloud of chain segments having radial symmetry. As the concentration increases, one polymer chain becomes surrounded by segments of all its neighboring polymer chains, which form a series of barriers to motion so that single polymer molecules no longer diffuse separately, but drag along neighbors. The degree of chain entanglement in solution can be described by Berry Number (Be), which normalizes the effects of both molecular weight and concentration: increasing concentration leads to increased inter-molecular entanglement while increased molecular weight contributes to both inter- and intra-molecular entanglement.

The intrinsic viscosities of the PLA polymers with Mw=200,000 and 300,000 were measured as 0.3595 dL/g and 1.3256 dL/g (22°C, Chloroform), respectively. The Berry Numbers for each solution were obtained as the intrinsic viscosity multiplied by concentration.

Figure 6 shows the relationship between fiber diameter and Berry Number. There are four regions on this graph: (I) $Be < 1$, polymer is in a very diluted solution and individual chains barely touch each other, apparently it is almost impossible to form fibers by electrospinning of such solution, since there is not enough chain entanglement to form a continuous fiber, and the effect of surface tension will make the extended conformation of a single molecule unstable. (II) $1 < Be < 3$, AFD increase slowly with Be from ~100nm to ~500nm. In this region the degree of entanglement is good enough for fiber formation. The coiled macromolecules of the dissolved polymer are transformed by the elongational flow of the jet into orientated, entangled networks that persist as the fiber solidifies. Also in this region beads are likely to form due to surface tension. (III) $3 < Be < 4$, AFD increases steeply with Be from ~1700nm to ~2800nm. In this region the chain entanglement becomes serious enough to contribute heavily to the viscosity; in order to separate the network of coils, the entangled polymer chains must first disentangle, which requires a large effort from the driving force of electrospinning. (IV) $Be > 4$: the relationship between AFD and Be is unpredictable again. The degree of chain entanglement becomes too high to affect the fiber diameter. In this case other processing parameters, such as electric field strength, become dominant factors over fiber diameter.

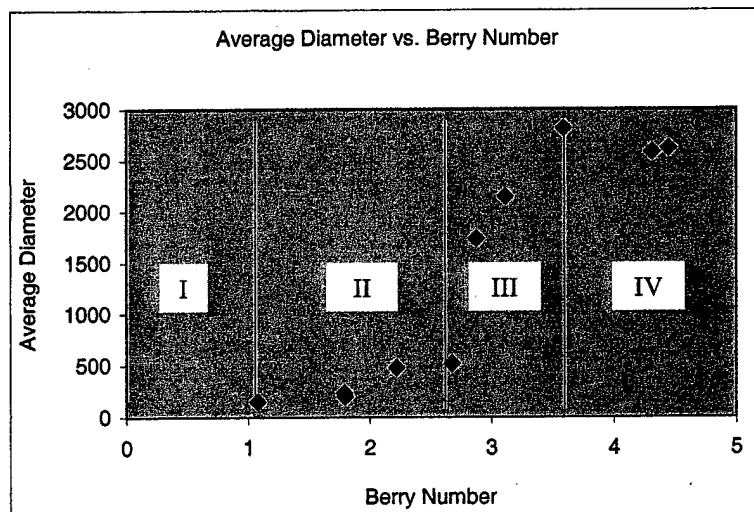


Figure 6. Average Diameter vs. Berry Number: 3 regions

4. Conclusions

Polymer chain conformation in solution plays an important role in the electrospinning of nano-scale fibers. Under the same processing conditions, the morphology of electro-spun fibers is affected by the degree of chain entanglement, which is related to a dimensionless Berry Number. Using Poly(lactic acid) of different molecular weight, the experimental correlation between fiber diameter and Berry Number is obtained. The result shows that in order to get certain average fiber diameter, there are appropriate regions of Berry Number to fall in. In addition, a subnet fiber structure is presented with lower AFD in the range of about 100nm-500nm. This phenomena seems to be unique for Poly(lactic acid) and has been reported by M. Bognitzki et al. [8].

References:

- [1] Gibson PW, Shreuder-Gibson HL, Rivin D. *AIChE Journal* 1999, 45, 190
- [2] Buchko CJ, Chen LC, Shen Y, Martin DC. *Polymer* 1999, 40, 7397
- [3] Langer R, Vacanty JP. *Science* 1993, 260, 920
- [4] Vert M, Chabot F, Leray J, Christel P. *Makromol. Chem. Suppl.* 1981, 5, 30
- [5] Hager BL, Berry GC. *Journal of Polymer Science, Polymer Physics Edition* 1982, 20, 911
- [6] Feng J. *Poly-anilines: Synthesis, Characterization and Applications*. Ph. D. Dissertation in Chemistry, University of Pennsylvania, 1999
- [7] Fong H, Chun I, Reneker DH. *Polymer* 1999, 40, 4585
- [8] Bognitzki M, Frese T, Wendorff JH, Greiner A. *Proceedings of the American Chemical Society Division of Polymeric Materials: Science and Engineering*. March 26-30, 2000, 82, 115

ON THE STRUCTURE AND PROPERTIES OF NANO-FIBERS & NANO-FIBROUS ASSEMBLIES

Afaf El-Aufy and Frank Ko

Abstract

Electrospinning is a process that produces polymer fibers with diameters in the range of micron to nanometers. While most of the previous researches the polymer was electrospun into a non-woven sheets, in this work we are trying to collect the fibers into a linear assembly. Our work will focus on creating a prototype nano-yarn manufacturing system and generate meaningful engineering data such that the benefit of nano-yarn & hybrid yarns can be fully exploited. The key challenges in this research are to produce nanoscale fibers with diameters consistently below 100nm at significantly higher strength. These nanofibers must be oriented & assembled into linear fibrous assemblies for the hierarchical construction of higher level 2-D and 3-D nanofiber based structures. In the prototype system; which is named the Rotary Dry electrospinning process, a 3^3 factorial experiment & a Response Surface analysis were carried out on Polyethylene Oxide (PEO) polymer to establish the optimum processing conditions for the nanofibers and nanofibrous assemblies.

Introduction

Electro-spinning is a unique process in that it is able to produce ultra-thin fibers ranging from nanometers to few micrometers.

Electro-spinning is a simple process, occurs when the electrical forces at the surface of a polymer solution or melt overcome the surface tension and cause an electrically charged jet of polymer hit the surface of a grounded target. The jet; as shown in figure (1), splays into finer jets before it reaches the target, dries, and transforms into small fibers.

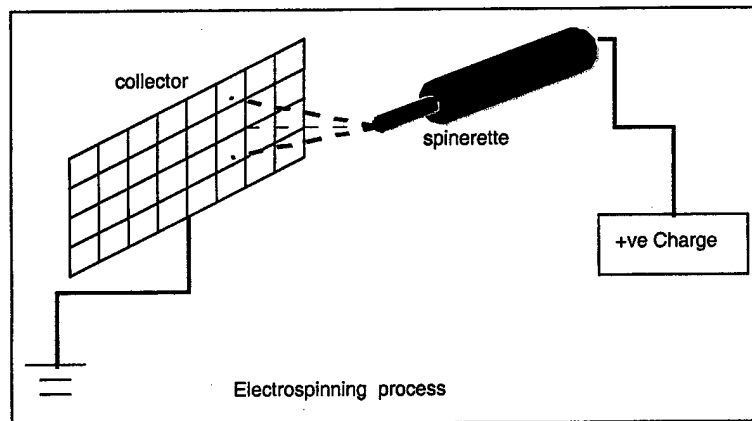


Figure (1) the electro-spinning process

The electro-spinning process has been known for a long time. Threads of molten sealing wax, were formed by using a high electric field in the early 20th century ⁽¹⁾. The electro-spinning process was first patented by Formhals⁽²⁾ in 1934 and succeeded to make fine polymer fibers.

Many researchers study the electro-spinning phenomenon and nanofibres production. They introduced different aspects (trends) that serve this field:

Technology trend

An electrostatic fountain was invented by Vonnegut and Neubauer⁽³⁾ and they mentioned that when the spray of droplets was illuminated with a beam of parallel white light, colors were seen. Taylor ⁽⁴⁾ studied the disintegration of water drops in an electric field . He demonstrated that a drop elongates and a cone, which has semi angles close to 49.3° forms at each end.

In 1971, Baumgarten ⁽⁵⁾ produced acrylic micro-fibers by using electrical forces. The fibers diameters were in range from 0.05 to 1.1 microns. He gave a good idea that there is a relation ships between fiber diameter, jet length, solution viscosity, solution feed rate & surrounding gas. Larrondo & Manely⁽⁶⁾ moved a forward step by making continuous fibers of polyethylene & polypropylene using electric fields as the driving force. Doshi & Renker⁽⁷⁾ used electro-spinning to make fibers of water soluble poly(ethylene oxide) with diameters of 0.05 to 5 microns. Srinivasan & Renker⁽⁸⁾ electrospun nanofibers from a liquid crystal solution of poly(P-phenylene terephthalamide) in sulfuric acid. Chun & Reneker⁽⁹⁾ produced polyester nanofibers from solution, from the melt in air& from the melt in vacuum. Doshi & Reneker⁽¹⁰⁾ described electro-spinning conditions, fiber morphology & some possible application of electrospun fibers made from several polymers. The diameters of these fibers were in the range of 0.05 to 5 microns. Kim & Reneker⁽¹¹⁾ made a nanofiber reinforced epoxy composite using a fabric composed of partially aligned nanofibers. Chun & Reneker ⁽¹²⁾ also electrospun carbon nanofibers from both polyacrylonitrile & mesophase pitch. The diameters of the carbon nanofibers were in the range from 100 nanometers to a few microns. Jaeger & Bergshoef ⁽¹³⁾ also used electro-spinning technique to spin ultra-thin fibers from several polymer/solvent systems. The diameter of the electrospun fibers ranged from 16nm to 2 μ m . They used chloroform

with the PEO to avoid the “beads on a string” phenomenon. Gibson & Rivin ⁽¹⁴⁾ studied the transport properties of electrospun nanofibers mats & they mentioned that the electrospun layers present minimal impedance to moisture vapor diffusion required for evaporative cooling.

Fong & Renker ⁽¹⁵⁾ electrospun nanofibers of a commercial styrene-butadiene-styrene tri-block copolymer, from solution & collected them either as a nonwoven elastomeric fabric on a layer of graphite that was evaporated onto a glass microscope slide. The resulting nanofibers were elastic, birefringent, & most had diameters around 100nm. They observed separated phases of styrene & butadiene blocks. The single-phase domains were irregular in shape but elongated along the axis of the fibers. Kim & Reneker ⁽¹⁶⁾ made nanofibers of aromatic heterocyclic PBI polymer by an electro-spinning process and collect them into nonwoven sheet of 20*100 cm² in size. They tried to improve the strength by treating the fiber sheet with sulfuric acid & then washed dried & heated.

Modeling trend

In 1978 Hendricks ⁽¹⁷⁾ studied the charge distribution & the forces on an electrically driven jet. He presented a numerical solution of the charge distribution based on the measurement of the jet profile & the jet current.

Spivak & Reneker ⁽¹⁸⁾ formulated a general 3-dimensional electro-hydrodynamic model of a weakly conductive viscous jet accelerated by an external electric field taking into account inertial, hydrostatic, viscous, electric and surface tension forces.

Fong & Reneker ⁽¹⁹⁾ analyzed the reasons for the instability of electrospun of polymer jet & they explained it using a mathematical model. The 3-dimensional paths of continuous jets were calculated, both in the nearly straight region where the instability grew slowly & in the region where the bending dominated the path of the jet.

Warner & Rutledge ⁽²⁰⁾ summarized the electro-spinning parameters controlling the process and they gave a quantitative modeling of the electro-spinning process with some trials to make some oriented fibers.

Application Trend

Renker ⁽²¹⁾ demonstrates the uses of polymer nanofibers. He described the production, characterization, & the identification of the useful properties of nanofibers. The

engineering of fibrous structures, which are thinner than the diameter of a typical textile fiber, is introduced.

Fang & Reneker ⁽²²⁾ used the electrospinning technique to spin DNA fibers. The electrospun DNA fibers had diameters around 50 to 80 nanometers. Bead-like structures were observed on many of the fibers.

Buchko & Chen ⁽²³⁾ create biocompatible thin films by electro-spinning for use in implantable devices. They found that the morphology of the thin films to depend on process parameters including solution concentration, applied electric field strength, deposition distance, & deposition time.

The nanofibers produced by electro-spinning are collected into a nonwoven web form. The nonwoven web, containing very fine fibers, generally has poor orientation and likely poor mechanical properties. The study here represents a way of collecting the fibers into linear assemblies; yarn form, trying to improve the mechanical properties & gives a good image of the yarn morphology & physical properties.

Experimental Part

- **Sample preparation**

PEO (MW 900,000 g/mole) was obtained from Aldrich & was used without further modification or purification. We prepared PEO solution with concentration of 3wt%, in chloroform (99.8%). The solution was very gently stirred for 10:15 hr. at room temperature using a magnetic stirrer in order to obtain a homogeneous solution.

- **Rotary Dry Electrospinning Device**

In order to spin the polymer solution into aligned nanofibers, we established the "Rotary Dry Electrospinning Device".

As shown in figure(2), the device is consisting of :-

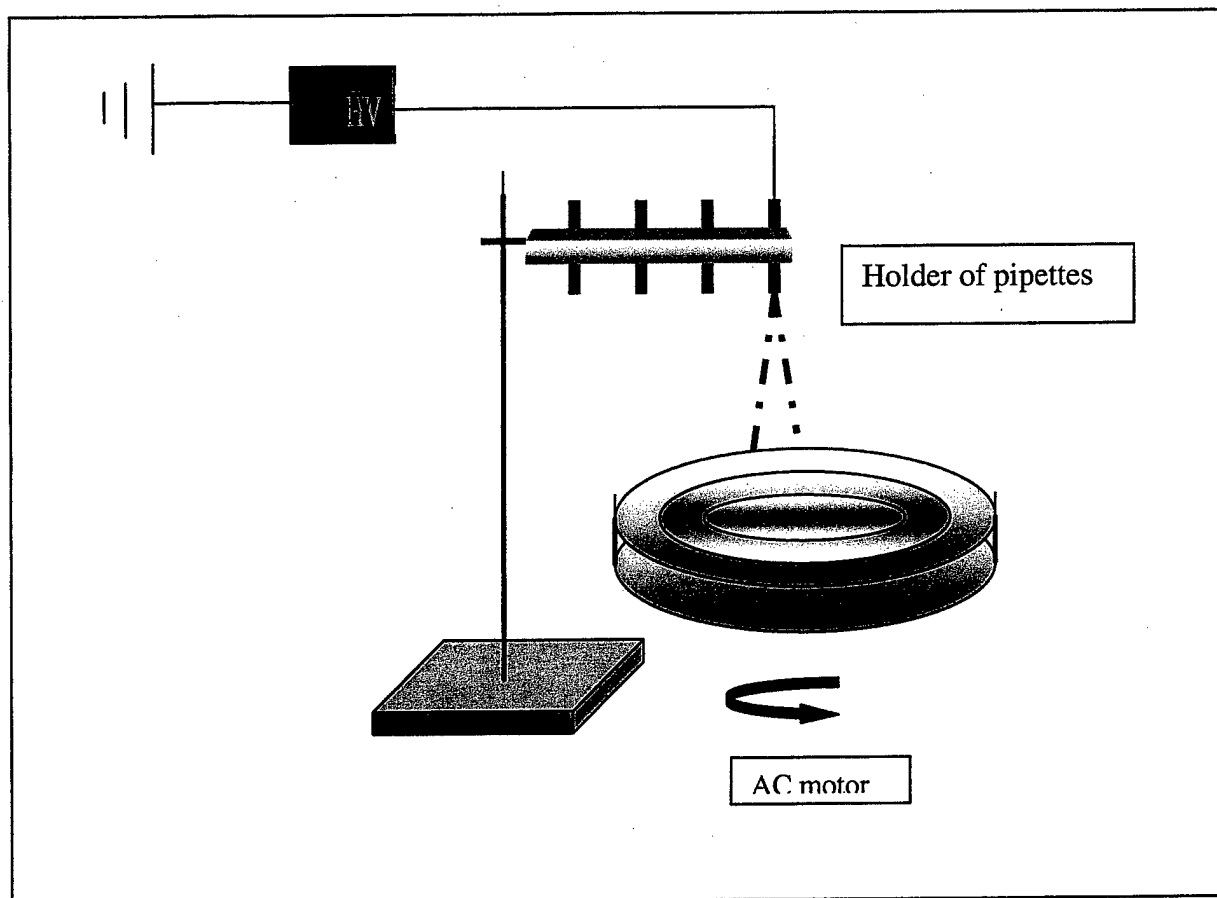


Figure (2)

A rotary disk driven through AC Motor (1/15 HP, 1550 RPM, 60 HZ, 115 V & 2.8 A) with a regulator to apply different variable speeds. The disk is covered with aluminum foil, to work as fiber collector, and connected to the negative terminal of an electrical supply as grounded electrode.

A holder is placed above the disk holding a frame with multiple holes to enable using different numbers of spinnerets (glass capillary pipettes). The pipettes are connected to the positive terminal of the electrical supply through a copper wire inserted inside the polymer solution.

The holder can move upward & downward to change the height of spinning & can rotate around its axis to change the spinning angle. All of these parts are covered with a Plexiglas box to control the influence of the outside environment.

- **The Electrospinning Process**

When the electrical field is applied between the spinneret (pipette) and the rotary disk (grounded electrode), the drop at the tip of the pipette is deformed into conical shape, called the "Taylor cone" ⁽⁴⁾. At a threshold value of the voltage, the electrostatic forces acting on the surface of the cone overcome the surface tension of the drop, and a jet is ejected from the cone. For certain polymer-solvent system a "splaying" of the jet into finer filaments can be observed. Then the jet hit the rotating disk into a coil shape and the speed of the rotating disk works to stretch the coils into aligned rings, as shown in Figure (3) . The shape of jet in the distance between the Taylor cone and the hitting of the disk is still ambiguous and need more theoretical studies. When the solvent is evaporated, the dry fibers in ring shape can be collected into linear strand to form a nonfibrous yarn.

- **Parameters Studied**

In our study, we fixed the angle of spinning at 90^0 (vertical position) to spin vertically and the speed of rotation to 55% of 1500 R.P.M. and the voltage at 30Kv.

We changed other parameters and use them into different combinations to study their influence on the electro-spinning process.

- The diameter of the pipettes, we select 3 different diameters : $D = 0.9, 1.3,$ and 1.7mm
- The height of spinning of $H = 10, 25, 40$ cm which reflects the charge density from 3 : 0.75 Kv/cm .
- The radical distance of spinning, the distance from the center of rotating disk to the center of pipette position which was: $R = 2, 5.25, 8.5$ in

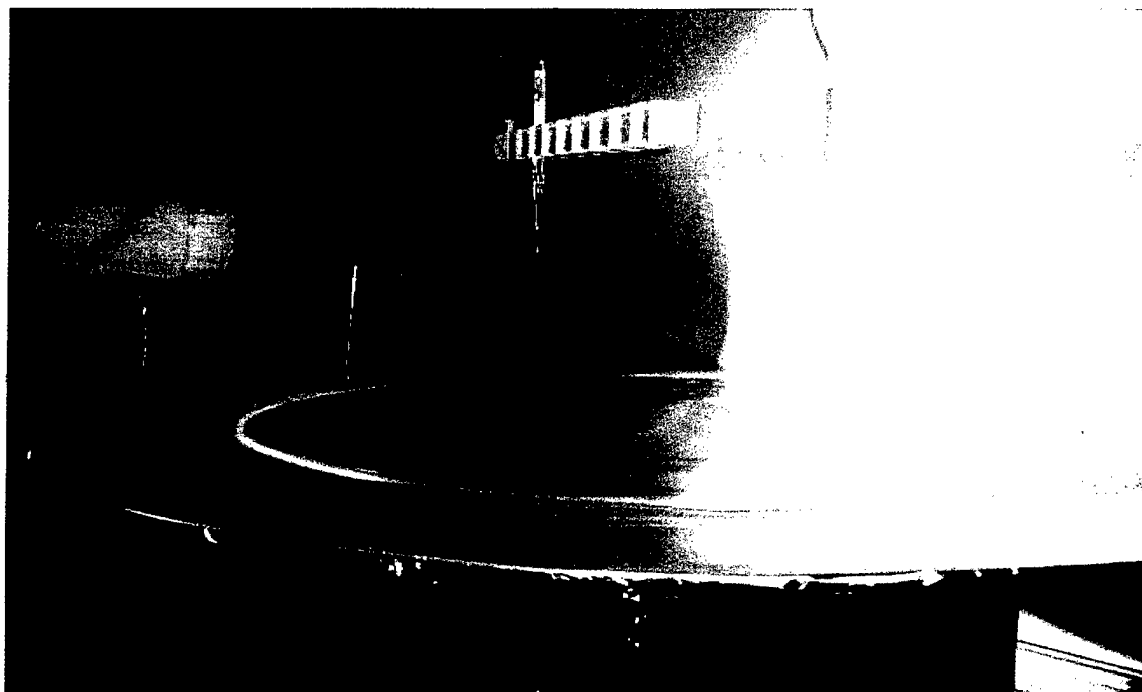


Figure (3)

Results and Discussion

Many other researchers studied the nanofibers & electrospun them into nonwoven web. The objectives of our research here are to understand the electrospinning process, create linear assemblies of nanofibers, study the morphology of the nanofibers and determine the parameters controlling this process.

Nanofiber morphology : Processing

The following figures demonstrate the electrospinning process to spin aligned fibrous assemblies with good orientation. Figure (4) shows a schematic of the electrospinning process showing the Taylor cone and the coiled polymer jet which could be aligned into oriented fibrous yarn by increasing the speed of the Rotary disk. The SEM image clarifies the polymer jet behavior to make coils instead of straight fibers. By adjusting the controlling parameters; e.g. height, pipette diameter, a well defined oriented fibers could be collected and twisted into a yarn.

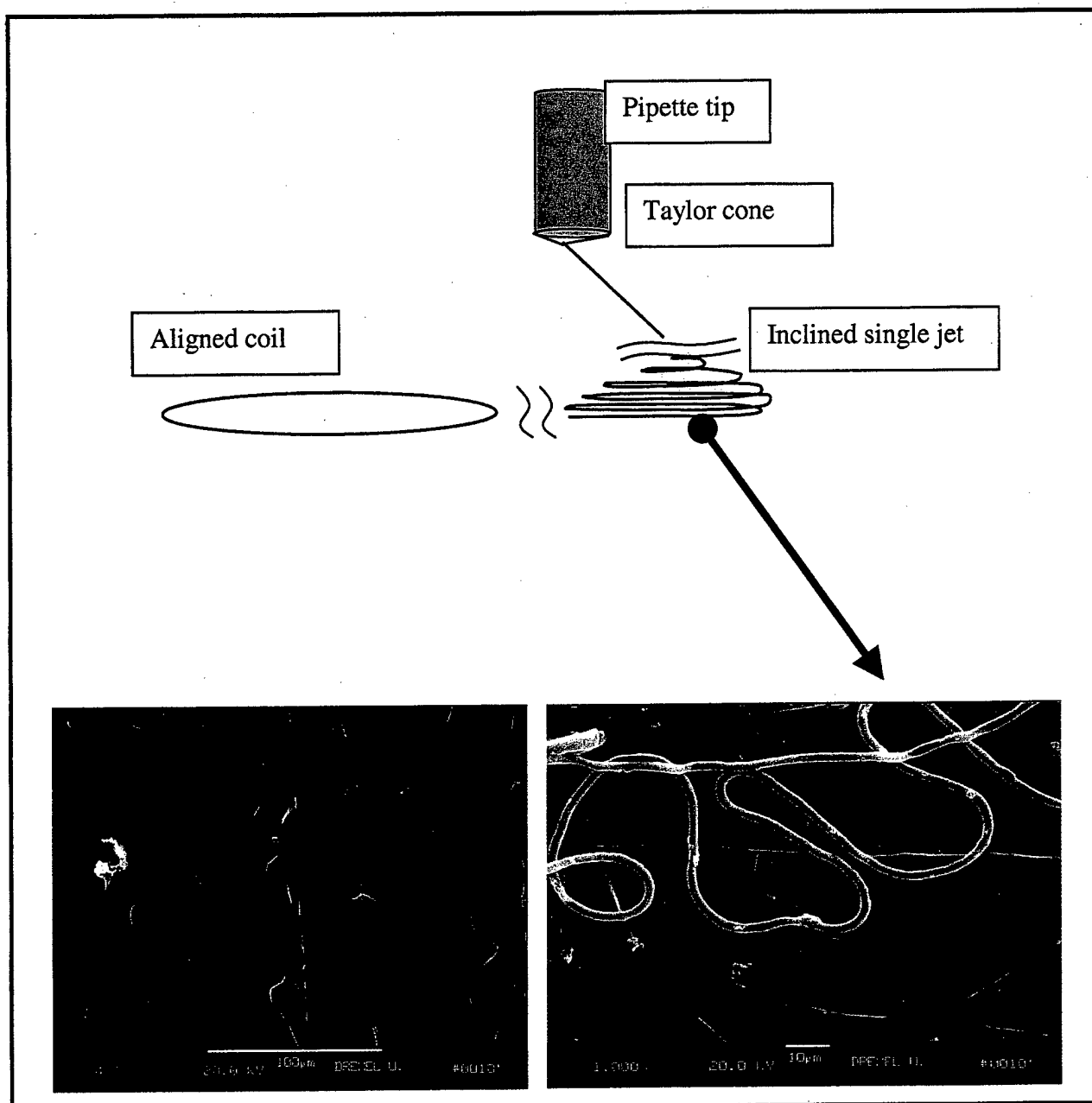


Figure (4)

Nanofiber morphology : Response surface analysis:

As shown in the previous part, the nanofibers are electro-spun in the form of curly and entangled fibers. Our interest here is to study the parameters that help to orient and align these fibers. A 3^3 factorial experiment was carried on the polyethylene oxide (PEO) polymer to study the effect of the electro-spinning processing parameters on the morphology and orientation of the nanofibrous assemblies. Consequently , a response surface analysis was carried out to determine the optimum processing conditions for the

nanofibers and nanofibrous assemblies. The factors affecting the process with the different levels are shown in the following designed matrix.

Factors	Levels		
	-1.0	0.0	+1.0
Diameter of pipette	0.9	1.3	1.7
Height of spinneret	4	10	16
Radial distance of spinneret	4	9	14

The detected response parameter was the diameter of the fiber. The fiber diameter was measured by using SEM technique. By measuring the diameters of 8:12 random fibers for each sample, the average fiber diameter was calculated. By feeding the whole data of the experiments to the RS program, the following results were obtained;

1. The best pipette diameter is the middle value ;1.3 mm, with slight increasing to 1.4:1.5 mm as the radial distance increased (as shown in fig 5 &6)

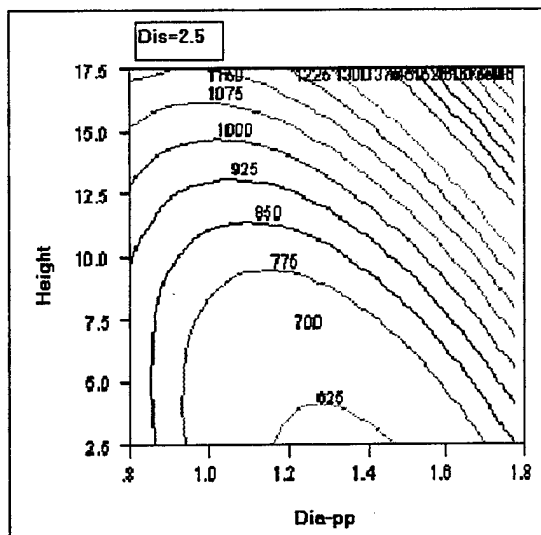
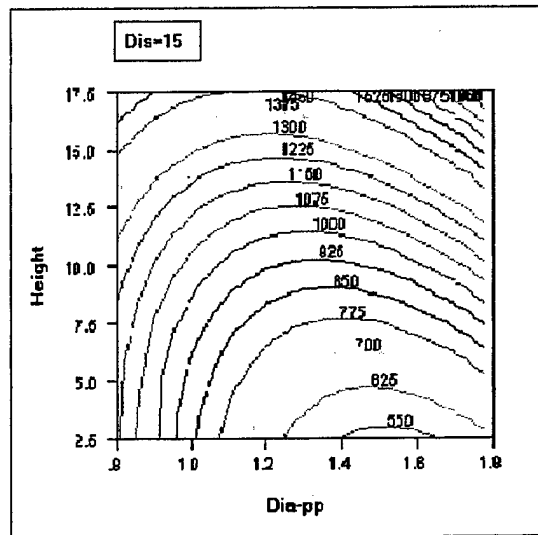


Figure (5)



Figure(6)

2. The lower is the height of spinning tip, the finer is the electrospun fibers.

3. By decreasing the radial distance & lowering the height of spinneret , the electrospun fibers become finer as illustrated in figure(7). This effect is enhanced by reaching the middle value of pipette diameter (1.2:1.4) as shown in fig(8). If we go further higher pipette diameters, the fibers would become coarse.

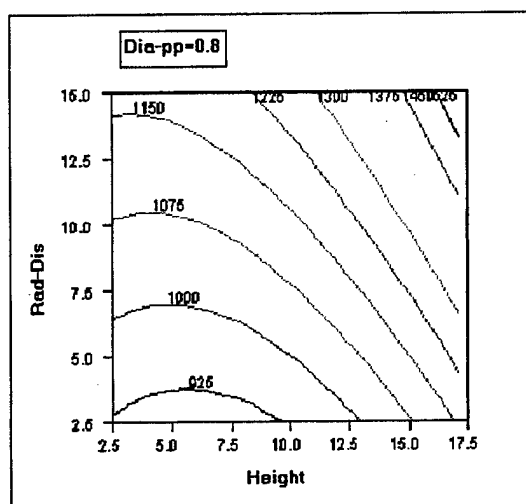


Figure (7)

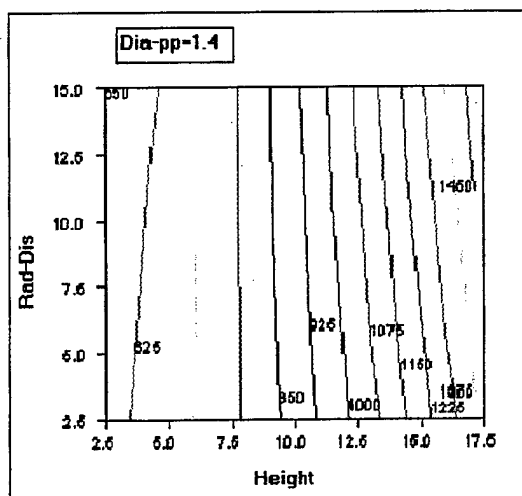


Figure (8)

4. Figure (9) shows that we have a saddle point for the fiber diameter by decreasing the radial distance and optimize the pipette diameter.

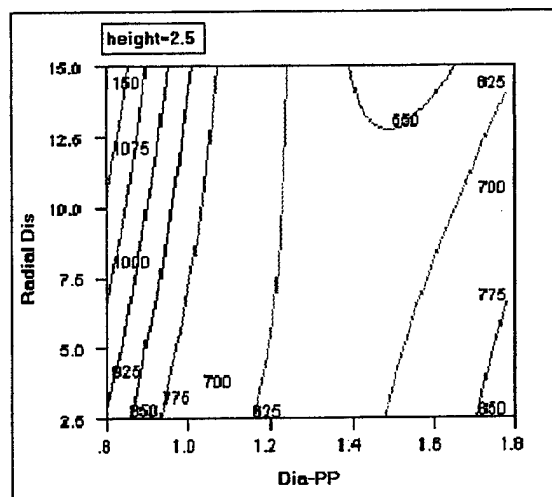


Figure (9)

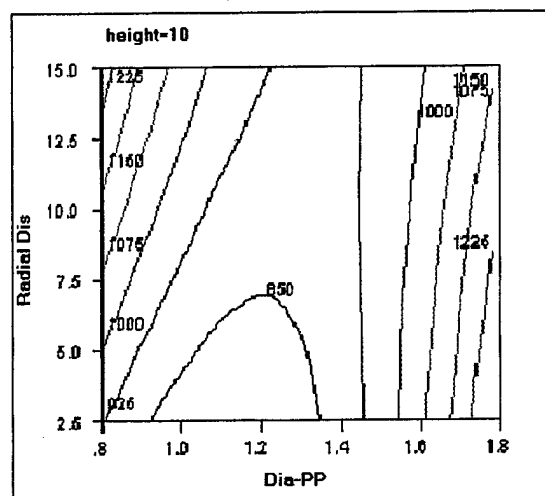


Figure (10)

5. The following equation gives the relation between the fiber diameter and the optimized parameters of electro-spinning process.

$$D_f = 1.28d_p + 0.169H - R_d$$

Where

D_f fiber diameter

D_p Pipette diameter

H Height of spinneret

R_d radial distance of spinneret.

6. The Fs test shows that the most significant parameter is the pipette diameter, then the height of the spinneret and after that is the radial distance of the spinneret.

Nanofiber morphology : SEM

Several experiments were carried out and by using the response surface results; we pass through different stages of collecting the fibers. The first stage was collecting the fibers into non-woven web as a random form. The second stage was by using the rotary dry disk, the fibers were electro-spun onto the rotating disk forming concentric rings. Easily the fibers were twisted into fibrous assembly form (yarn). The third stage was applying the optimum conditions to orient and align the nano-fibers into the yarn.

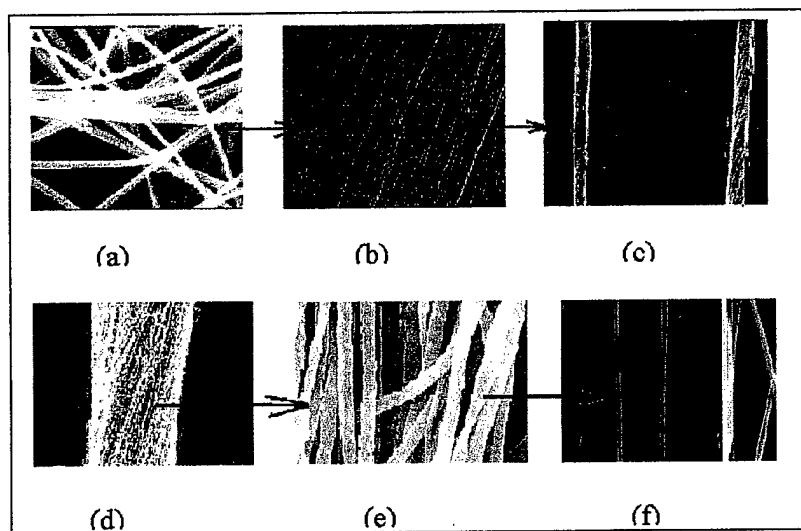


Figure (10) Scanning electron micrographs of nano-fibers electro-spun yarn

Scanning electron micrographs were applied during the all stages through the whole research. As shown in figure(10-a) , the randomness of fibers at the first stage and after that figure (10-b,e,f) shows how the fibers are oriented and aligned within the yarn figure(10-c,d). We are counting on this orientation to improve the mechanical behavior, which is our research interest in the following step.

Every sample of the 33 experiments was tested on the SEM PC to calculate the fiber's diameter. Each image was divided into 4 parts and from each quarter, a three readings were recorded. The whole 12 readings for the 33 electro-spun fibers were plotted to demonstrate the diameter distributions. Figure (11) illustrates the fiber diameter versus the number of fibers. The fibers' diameters vary from 100 nanometer to 4.8 microns with an average of 500:700 nanometer.

Diameter Distribution

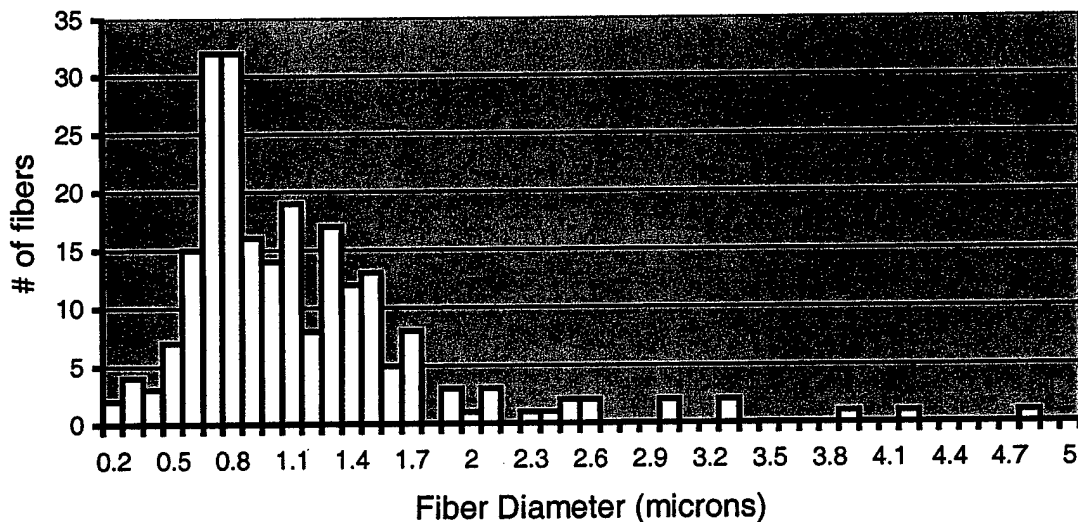


Figure (11)

Conclusions

Our work focused on the alignment and orientation of nano-fibers into linear assemblies. In this research, a new device; to align & orient the nano-firbers into linear assemblies, was established. This device was named a Dry Rotary Disk.

The effects of processing parameters on the morphology of individual electro-spun PEO nano-fibers have been explored. The Response Surface Methodology technique was used to establish a 3^3 factorial experiments & to optimize the electro-spinning processing parameters. We have found that, increasing the rotating speed enhances the alignment of curly nanofibers. Also, we have found that, the orientation and morphology of the nano-fibers produced were influenced strongly by parameters such as H; height of spinneret (charge density), R_d ; radial distance, and d_p ; the pipette diameter. The pipette diameter is the most significant factor to achieve better orientation and finer fibers, coming after that the height and then the radial distance of the spinneret. The RSM gives us an equation governing these parameters.

$$D_f = 1.28d_p + 0.169H - R_d$$

Contour plots showed a saddle point of the fiber diameter by optimize the pipette diameter, lowering the height of spinneret and decreasing the radial distance of spinneret. The diameter size distribution plot behaves as Chi-Square mode with minimum fiber diameter of 100 nm and 500:700 nm average range.

Our future work will focus on the mechanical properties of nano-fibrous yarn and reduction of the fiber diameter.

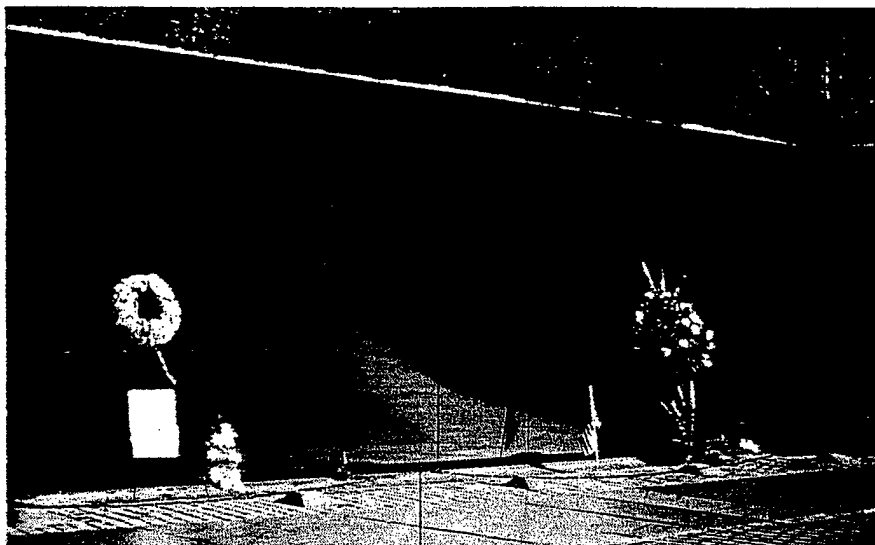
Reference:

- 1) Zeleny, J., Physical Review, X (1), 1 (1917).
- 2) U.S. Pat, 1,975,504 (Oct. 2, 1934) A, Formhals.
- 3) Vonnegut, B. and Neubauer, R.L., Journal of Colloid Science, 7, 616 (1952).
- 4) Taylor, G., Proceedings of the Royal Society of London Series A, 280, 383 (1964).
- 5) Baumgarten, P.K., Journal of Colloid and Interface Science, 36, 71, (1971).
- 6) Larrondo L. and St. J. Manley, R., Journal of Polymer Science, Polymer Physics Edition, 19, 933 (1981).
- 7) Doshi, J. and Reneker, D.H., Proceedings of IEEE Industry Applications Society Meeting Part 3, 3 (1993).
- 8) Srinivasan, G. and Renker, D.H. Polymer International, 36, 195 (1995).

- 9) Chun, I. and Reneker, D.H., "Fine Fibers spun by Electrospinning Process from Polymer Solutions and Polymer Melts in Air and Vacuum: Characterization of Structure and Morphology on Electrospun Fibers and Developing a New Process Model," Dissertation, The University of Akron, (1995).
- 10) Doshi, J. and Reneker, D.H., *Journal of Electrostatics*, 35 (1995) 151-160.
- 11) Kim, J. and Reneker, D.H., "Improved Mechanical Properties of Composites Using Ultrafine Electrospun Fibers," Dissertation, The University of Akron, (1997).
- 12) Chun, I. and Reneker, D.H., *Journal of Advanced Materials*, 31, no.1, (1999).
- 13) Jaeger, R. and Bergshoeff, M., *Macromol, Symp.* 127, 141-150 (1998).
- 14) Gibson, P. and Rivin, D., *AIChE Journal*, 45, no. 1, (1999).
- 15) Fong, H. and Reneker, D.H., *Journal of Polymer Science, Polymer Physics Edition*, (1999).
- 16) Kim, J. and Reneker, D.H., *Polymer Engineering and Science*, 39, no. 5, (1999).
- 17) Hendricks, C. and Horning, D., *J. Appl. Phys.*, 50, no.4, (1979).
- 18) Spivak, A. and Reneker, D. H., NSF grant No DMI-9523022.
- 19) Fong, H. and Reneker, D. H., *Journal of Applied Physics*, 87, no.9, (2000).
- 20) Warner, S. and Rutledge, G., *National Textile Center Annual Report*, (1998).
- 21) Reneker, D.H., "Nanofibers for Engineered Textiles", The University of Akron.
- 22) Fang, X. and Reneker, D. H., "DNA fibers by Electrospinning", University of Akron, (1996).
- 23) Buchko, C. and Chen, L., *Polymer* 40 (1999) 7397-7407.



POLYMERIC MATERIALS: SCIENCE AND ENGINEERING



VOLUME 83



FALL MEETING
AUGUST 20-24, 2000
WASHINGTON, D.C.

PROCEEDINGS OF THE AMERICAN CHEMICAL SOCIETY
DIVISION OF POLYMERIC MATERIALS: SCIENCE AND ENGINEERING

©2000 American Chemical Society

Polyaniline Based Chemical Transducers with Sub-micron Dimensions

Alan G. MacDiarmid and Ian D. Norris
Department of Chemistry
University of Pennsylvania
Philadelphia, PA 19104

Wayne E. Jones Jr.
Chemistry Department and Institute for Materials Research
State University of New York at Binghamton
Binghamton, NY 13902

Mahmoud A. El-Sherif, Jianming Yuan, Baohua Han and Frank K. Ko
Department of Materials Engineering
Drexel University
Philadelphia, PA 19104

Introduction

It is well established that conducting polymers such as polyaniline [1] and polypyrrole [2] show considerable potential for the detection of gaseous analytes in air. A variety of devices have been constructed using conducting polymers and thin films on, for example, inter-digited electrodes where changes in resistance were the basis for signal transduction [3]. We have been investigating new methods for the application of conducting polymers in fiber optic sensor devices. One set of studies are directed to investigating the cladding of optical fibers with sub-micron thick films of polyaniline which change upon reaction with acidic, basic, oxidative, and reductive vapors. This chemical interaction results in: (1) a change in the refractive index, and (2) a change in the optical absorption spectrum, of the polymer film. Both of these changes modify the intensity of the light transmitted through the optical fiber as a result of changes in the refractive index and interactions with the evanescent field respectively [4].

The surface-to-volume ratio is also of great significance in the well-established area of chemically modified conducting polymer electrodes for biological and chemical sensors. It is envisaged that a method of increasing the effective surface area of these conducting polymer sensors will offer the opportunity for improved sensitivity over an expanded range. We have also been investigating the production of conducting polymer nanofibers by a simple, electrostatic, non-mechanical ("electrospinning") technique to give a mat of random (meters long) fibers [5]. This technique produces fibers with the unique characteristic of the high surface area ($\sim 10^3 \text{ m}^2/\text{gm}$) provided by the nanofibers.

During the preparation of these sub-micron transduction material fabrication methodologies, the response, both electronic and optical, has been observed as a function of time. The rapidity of the response is greatly decreased by reducing the thickness of the solid thin films of the conducting polymer. In each case, the surface to volume ratio of the sensor materials has been increased resulting in an emphasis of the surface properties of the polymer.

Experimental

Materials

All chemicals were purchased from Aldrich and used without further purification unless noted. Aniline and pyrrole were distilled under nitrogen prior to use and stored in the dark at -10°C . Emeraldine base for the electrospinning experiments was purchased from Neste Oy Co. and used as received.

Optical Fiber Cladding

Optical fibers from General Fiber Optics Corp. were etched with aqueous HF solution (30%) to remove the cladding and expose the optical core [6]. Polyaniline in its emeraldine salt oxidation state was deposited directly on the optical core from HCl solution using an in-situ deposition method that has been described previously [7]. Deposition times were varied from 3 minutes to 30 minutes. Glass slides (Fisher) were cleaned using a "piranha" solution and used for control experiments along with each optical fiber sample.

Nanofiber Production

Various polymer blend solutions dissolved in chloroform were prepared with the concentration of polyaniline doped with HCSA (PAN.HCSA) ranging from 0.5 to 2 wt% and the concentration of PEO ranging from 2 to 4 wt%. By varying the ratio of polyaniline to polyethylene oxide, the concentration of doped polyaniline in the polyethylene oxide matrix varied between 11 wt% and 50 wt%. Nanofibers were prepared by generating a high electrical field (1 kV/cm) between the polymer blend solution contained in a glass syringe with a capillary tip and a metallic collection screen. As the electrical potential is increased beyond a critical value, the charged polymer solution overcomes the surface tension of the liquid and a jet of ultrafine fibers is produced. The solvent quickly evaporates and the dry fibers are accumulated on the surface of the collection screen.

Nanofibers of conventional polymers can serve as excellent substrates for the in-situ deposition of a thin conducting polymer layer. For example, we have prepared polyacrylonitrile nanofibers ($\sim 400 \text{ nm}$ in diameter) in air from 10 wt% polyacrylonitrile solution dissolved dimethyl formamide solutions at an electrical field strength of 1 kV/cm. These nanofibers were subsequently coated with a cohesive layer of polypyrrole doped with Cl^- by in-situ deposition from an aqueous polymerizing solution of pyrrole by a previously reported method [8].

Results and Discussion

Optical Fiber Sensors

Recently we have demonstrated the use of in-situ deposition methods for preparing thin, 20-30 nm thick films of conducting polymers on glass slides [7]. We have extended this method to the deposition of polyaniline on glass optical fibers in which the protective cladding first had been removed by aqueous HF solution. The resulting in-situ deposited polyaniline films were found to undergo small reversible changes in the optical spectrum (Figures 1) accompanied by large changes in surface resistivity, R_s , upon exposure to HCl or NH_3 vapor. This observation is consistent with previous reports on the polyaniline system in which the emeraldine base form is switched to the emeraldine salt form of the polymer by gaseous HCl [9]. We have also shown that the emeraldine base form will react with the reducing agent hydrazine to form the leucoemeraldine state [10].

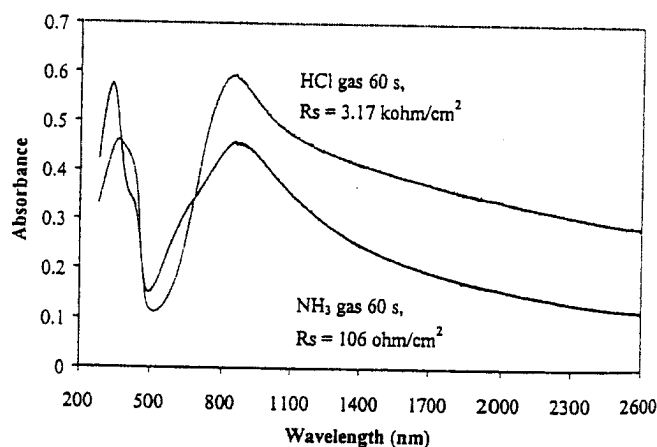


Figure 1. UV-visible spectra of in-situ deposited polyaniline film following exposure to HCl or NH_3 vapors for 60 s.

The change in the resistance of the sample was determined by either 4-probe or 2-probe measurements. The time response observed for either the resistance or absorption changes that occurred when NH_3 or HCl vapor was exposed to the film was found to be < 4 seconds, as shown in Figure 2. Following exposure to basic vapors, the films spontaneously reverted from the emeraldine base form back to the emeraldine salt if left in air. Experiments on spin coated films on glass slides undergo similar changes, however the changes occur on a time scale of minutes.

Optical microscopy demonstrated that the in-situ deposition method successfully deposited a uniform polyaniline film on the exposed core of the optical fibers. The influence of the polymer cladding on optical fibers was monitored as the total intensity of light through the fiber at 630 nm from a

to switch by as much as 80% upon exposure of the emeraldine salt form of the polymer to basic vapors [11]. By monitoring the change in light throughput as a function of excitation wavelength, the optimum excitation conditions could be established. It was observed that this optimum wavelength did not correspond to the maximum change in the optical absorption spectrum of the polymer, Figure 1. This result suggests that it is the combination of the absorption of the polymer and the change in refractive index that led to the observed optical fiber response.

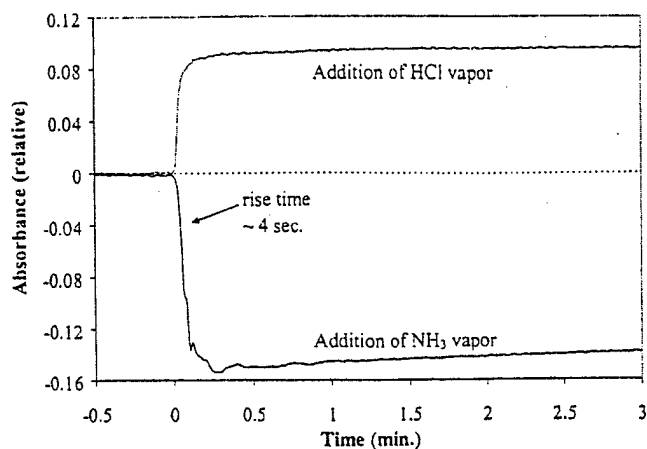


Figure 2. Time-resolved change in the optical absorption spectrum at 1300 nm following exposure to HCl or NH₃ vapors.

Nanofiber Sensors

Given the interest in increased surface to volume ratios for traditional resistance-based conducting polymer chemical sensors, new methods of preparing sub-micron diameter fibers of conducting polymers have been investigated. Electrospinning has been known for over 60 years, but has only recently become of interest for the preparation of nanometer sized polymer structures [5]. Nanofibers of conventional organic polymers, as well as electroactive organic polymers and their blends have already been produced. For example, we have prepared conducting nanofibers from a mixture of polyaniline doped with camphorsulfonic acid (PAN.HCSA) and polyethylene oxide (PEO) in chloroform [12].

The enhanced performance in a high surface to volume ratio material is clearly demonstrated in the rate of de-doping of these polyaniline blend nanofibers with NH₃ vapor as compared to a cast film. De-doping of the electrospun PAN.HCSA/PEO fibers (11-50 wt% PAN.HCSA) was achieved by suspending the non-woven fibrous mat above the vapor of concentrated aqueous ammonium hydroxide solution. Within 3 seconds of exposing the non-woven mat to the ammonia vapor, the green non-woven fiber mat turned to blue indicating that the emeraldine salt in the blend fibers was converted to emeraldine base. After the non-woven mat was removed from the ammonia source, the polyaniline in the non-woven mat spontaneous turned back to the original green color of the as-spun mat. This de-doping and spontaneous re-doping occurs at an extremely fast rate relative to films cast from the same solutions, similar to the rapid response of the 20 nm thick films on optical fibers. This presumably arises from a faster diffusion rate of ammonia vapor into and out of the polyaniline blend fibers. This result highlights the enormous effect of an increase in the surface-to-volume ratio accomplished by the nanofibers can have on the properties of conducting polymers.

Given the poor solubility of many conducting polymers, a method to prepare nanofibers of insoluble conducting polymers is important for the extension of the electrospinning technology for sensor development. Traditional woven textiles have previously been coated by polypyrrole doped with a variety of anions using in-situ deposition from aqueous solutions [8]. These conducting polypyrrole coated textiles have been found to show gas sensing capabilities for a variety of vapors including ammonia, HCl, NO₂, and the chemical warfare stimulant, dimethyl methylphosphonate (DMMP) [2,13]. We have used the same in-situ deposition technique to coat polypyrrole on polyacrylonitrile fibers as shown in Figure 3. The average diameter of the polyacrylonitrile fibers was ~ 400 nm with a ~25 nm coating of polypyrrole.

surface to volume ratio over previous techniques of producing conducting polymer based textile sensors. When incorporated into a sensor device, this should lead to an enhancement of the surface electronic properties and enhanced signal response times without sacrificing the sensitivity of the material [2].

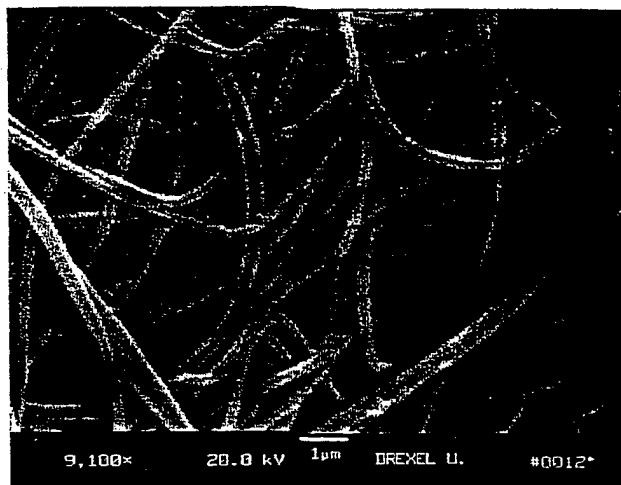


Figure 3. SEM image of electrospun polyacrylonitrile fibers that are coated by in-situ deposition by polypyrrole doped with Cl⁻.

Conclusions

The applications of two different methods for the preparation of sub-micron dimension conducting polymer materials are described. Both in-situ deposition onto optical fibers and the preparation of conducting polymer nanofibers have been found to have enhanced response times relative to spin coated solutions. The increased surface area emphasizes the importance of surface response as compared to bulk diffusion.

Acknowledgements

This work was financed jointly by the Office of Naval Research and the Army Research Office under the Multidisciplinary University Research Institute (MURI) program.

References

1. A.G. MacDiarmid, F. Huang, J. Feng, "Doped Polymer Light Emitting Devices and Sensors for Volatile Organic Compounds" in *Semiconducting Polymers - Applications, Properties and Synthesis*, (1999) B.R. Hsieh and Y. Wei Editors, American Chemical Society.
2. G.E. Collins GE and L.J. Buckley, *Synthetic Metals*, **78(2)** (1996) 93.
3. J.N. Barisci, C. Conn and G.G. Wallace, *Trends in Polymer Science*, **4** (1997) 307.
4. M. A. El-Sherif, *IEEE Trans. On Instrumentation and Measurements*, April (1989) 595.
5. D. H. Reneker and I. Chun, *Nanotechnology*, **7** (1996) 216.
6. M. A. El-Sherif, US Patent, #5,060,307, (1991).
7. Z. Huang, P.-C. Wang, A.G. MacDiarmid, Y. Xia, and G. Whitesides, *Langmuir*, **13(24)** (1997) 6480.
8. R.V. Gregory, W.C. Kimbrell and H.H. Kuhn, *Synthetic Metals*, **28(1-2)** (1989) C823.
9. A. J. Epstein, J. M. Ginder, F. Zuo, R. W. Bigelow, H.-S. Woo, D. B. Tanner, A. F. Richter, W.-S. Huang and A. G. MacDiarmid, *Synthetic Metals*, **18** (1987) 303.
10. C.H. Hsu, P. M. Peacock, R.B. Flippen, S.K. Manohar, A. G. MacDiarmid, *Synthetic Metals*, **60(3)** (1993) 233.
11. M. A. El-Sherif and J. Yuan, *Journal of Intelligent Material Systems and Structures*, (2000), in press.
12. I.D. Norris, M.M. Shaker, F.K. Ko, A.G. MacDiarmid, *Synthetic Metals*, (2000) in press.
13. D. Kincal, A. Kumar, A.D. Child and J.R. Reynolds, *Synthetic Metals*, **92(1)** (1998) 53.

The Effect of Processing Parameters On the Morphology Of Electro-Spun PAN Fibers

Ashraf A. Ali, Amotz J. Geshury and Frank K. Ko

Fibrous Materials Research Center, Materials Engineering Department, Drexel University, USA, 2001

Abstract:

Fibers of Polyacrylonitrile (PAN) are the precursor of 90% of the produced carbon fibers. It is generally thought that the better the degree of molecular orientation in the original PAN fiber, the better the mechanical properties, in particular the modulus of the resultant fibers.

The electro-spinning technique, a method for making very small diameter fibers, was applied under different processing conditions to achieve fiber diameter within the nanometer range. Concentrations of the PAN in DMF, height, environmental temperature, spinning angle, solvent boiling point and wet vs. dry collectors have been studied. The resulting fiber diameters were examined using SEM. The results showed an important role of the assigned processing parameters in the diameter of the produced fiber. By varying the above parameters, 100 nm PAN fiber diameter has been achieved.

Introduction:

Polyacrylonitrile (PAN) is widely commercialized as acrylic fiber, and it is also used as the starting materials for high performance carbon fiber [1].

It is generally thought that the better the degree of molecular orientation in the original PAN fiber, the better the mechanical properties, in particular the modulus, of the resultant fibers.

Electro-spinning is a unique process in that it is able to produce polymer fibers with diameters ranging over several orders of magnitude, from the micrometer range typical of conventional fibers down to the nanometer range [2].

In the electro-spinning process a high electric field is applied to a hanging droplet of polymer solution contained in a capillary tube. When the applied electric field overcomes surface tension a charged jet of the solution is ejected. Fibers are formed upon removal of the solvent by either two ways the evaporation of the solvent through the distance between the spinneret and the collector or by dissolving the solvent inside the coagulating bath [3].

Interest in the electro-spinning process has increased in recent years [4-11]. Most of the literature on electro-spinning has explored the types of polymer solvent systems from which fibers can be produced. A few studies have also addressed the processing/property relationships in electro-spun polymer fibers [12]. A few processing parameters considered have included solution concentration, viscosity effect, tip-to-target distance and Berry number. Baumgarten has also correlated spinning atmosphere with the occurrence of the jet-splaying phenomenon in PAN system [13].

The present study is an attempt to characterize the electro-spinning process as well as the influence of its processing parameters in the produced fiber from PAN polymer solutions and to answer the question at which condition PAN fibers be produced below 100 nm? Also using the work in this paper as a preliminary result to start a series of research projects in the area of producing carbon fibers in a random and continuous shape by electro-spinning PAN polymer solution.

Experimental Work:

1-Materials:

Polymer: PAN polymer from Scientific polymer product SP² Catalog # 134 with 150000 molecular weight.

Solvent: Two types of solvent from Aldrich

DMF Catalog # 31,993-7 with boiling point = 153°C

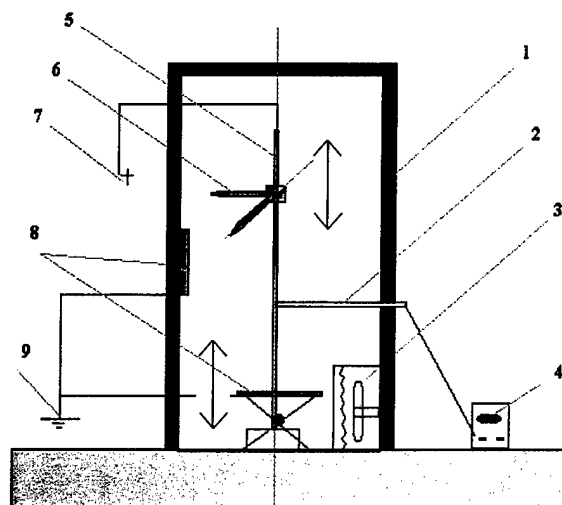
DMSO Catalog # 47,126-7 with boiling point = 189°C

Preparations of polymer solutions were made by weight % by using magnetic shaker under 60°C for 20 min.

2-Electro-spinning system:

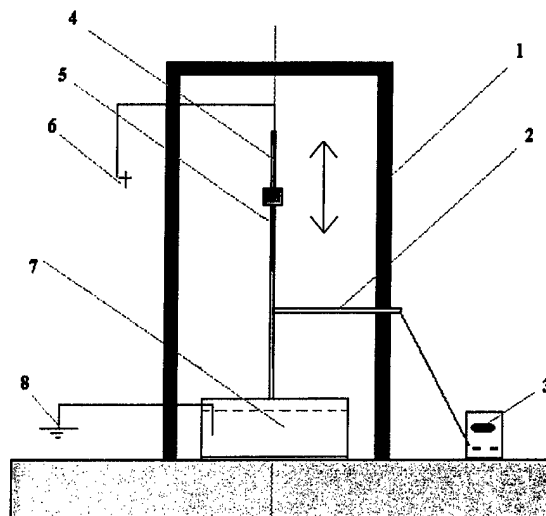
Spinneret: Glass pipette 0.9 mm diameter and 3cm³ total volume.

Stations: Figure (1) and (2) show the description of the two stations used in our experiments.



- 1- Station environmental control box
- 2- Thermocouple
- 3- Heating fan
- 4- Digital thermometer
- 5- Stand
- 6- Glass pipette
- 7- High voltage source
- 8- Metal screen
- 9- Ground

Fig. (1): Dry Electro-Spinning Station



- 1- Station environmental control box
- 2- Thermocouple
- 3- Digital thermometer
- 4- Stand
- 5- Glass pipette
- 6- High voltage source
- 7- Water bath
- 8- Ground

Fig. (2): Wet Electro-Spinning Station

3-Processing Parameters:

According to the survey the most important parameters that may affect the electro-spinning process are the distance between spinneret and target, polymer concentration, Berry number, viscosity, surface tension, electric volt density, atmosphere condition, pipette diameter, and the collector type.

Some of these parameters have been selected in our PAN system as follows;

- 1- Concentration; c by weight% (6, 9 & 12)
- 2- Height; H in cm (10, 15 & 20)
- 3- Charge density; E/H in KV/cm (1, 1.5 & 2)
- 4- Solvent type; bp in °C (153, 171 & 189)
- 5- Environmental temperature; T in °C (23, 35 & 47)
- 6- Spinning angle; θ in degree (0, 45 & 90)
- 7- Wet vs. dry collectors

Figure (3) describes the assigned parameters studied in this paper. The figure shows the idea of studying one parameter per each experiment and for the important parameters we increased the number of experiments by using the square focus idea that shown in the same figure.

4-Characterization:

Morphological observation made by using SEM (describe it). The samples were coated by using a sputter machine (describe it) for 90 sec; According to the sputter machine catalog the expected coating thickness under the used conditions = 10-20 nm.

Each of the SEM pictures has been divided into four equal regions then same amount of measured fibers took from each quarter. By using Paintbrush software the diameters were measured precisely by correlating the number of the points that used by the software to the giving measured distance from the SEM in each picture.

decreases which has a good agreement with the all

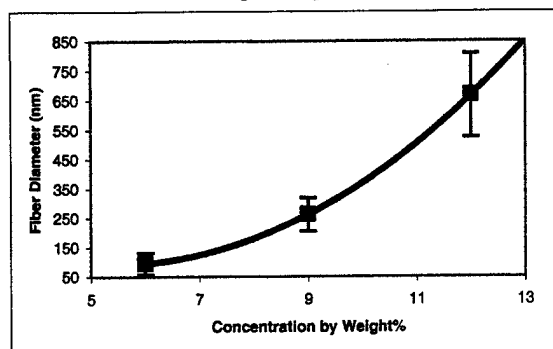


Fig. (6): Effect of Concentration on Fiber Diameter for PAN and DMF System

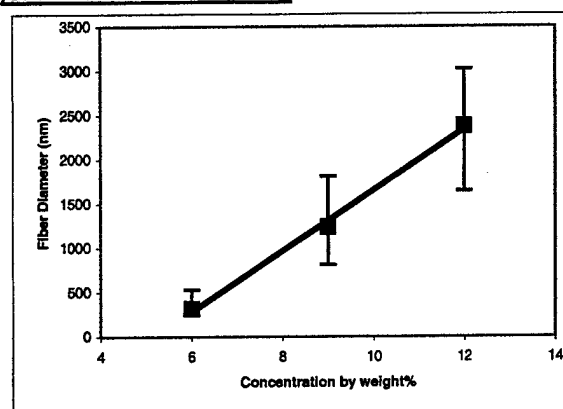


Fig. (7): Effect of Concentration on Fiber Diameter for PAN and DMSO System

As the amount of solvent increases inside the jet the produced fiber diameters will decrease.

Also we can conclude from the figures that; as the concentration increases the fiber distribution or in another words, the standard deviation increases which can be explained from the effect of Berry number and the degree of entanglement inside the polymer solution as can be seen by compare the values of the standard deviation in both figures.

To prove this correlation let us first measure the intrinsic viscosity of PAN + DMF and PAN + DMSO systems then calculate the values of Be# at two different concentrations.

As shown in figures (8 & 9) for PAN + DMF and PAN + DMSO systems the measured intrinsic viscosity = 1.1142 and 1.766 respectively and the calculated Be# values, which is the product of the concentration in the intrinsic viscosity, for the first at 9% & 12% concentrations and the second at 6% & 9% concentrations are almost equal (10.03 g/dl & 13.40 g/dl for the first and 10.60 g/dl & 15.90 for the second respectively).

On the other hand the calculated standard deviation values are 56.92 & 262.3 for the first and 92.27 & 366.7 for the second respectively which

diameter in each case.

prove some kind of relationship between the degree of entanglement inside the polymer solution and the fiber diameter distribution.

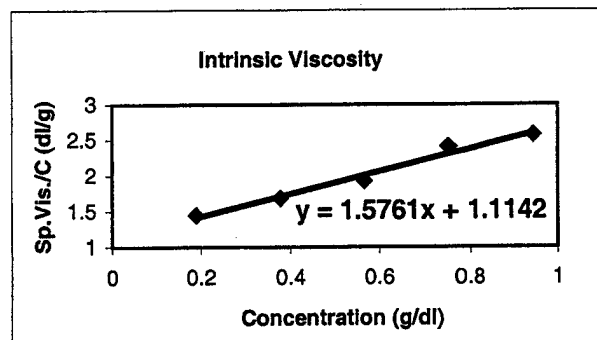


Fig. (8): Intrinsic Viscosity of PAN + DMF System

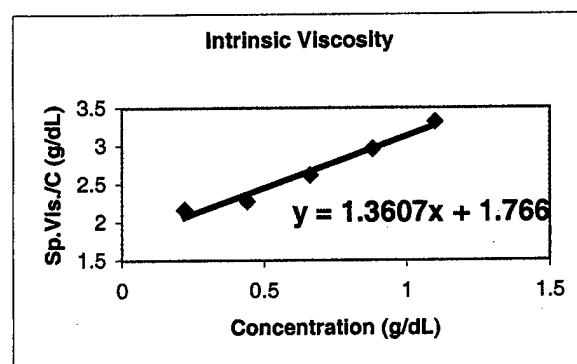


Fig. (9): Intrinsic Viscosity of PAN + DMSO System

2-Height effect on PAN fiber formation:

It is shown that in figure (10) as the height increases the fiber diameter distribution increases; the governing equation for the average fiber diameter is parabolic and shows an increase in the fiber diameter as the height increases is as follows:

$$d_f \text{ (nm)} = 2.646H^2 - 56.57H + 515.5$$

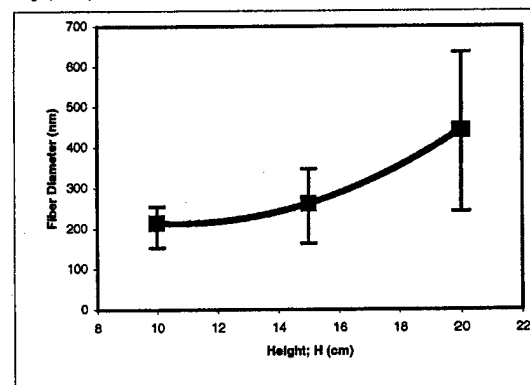


Fig. (10): Effect of Height on Fiber Diameter For PAN + DMF System

From the figure, we can say that there is no

92.27 & 366.7 for the second respectively, which fiber diameter but there is a significant effect on the fiber distribution. At heights in excess of 15 cm, there is a significant effect on fiber diameter and distribution.

In this experiment we kept the charge density in each case equal to 1.5 KV/cm and concentration of 9% in each case.

Theoretically speaking any one expect to get smaller fiber diameter by increasing the height due to the longer path that the jet will travel till it hits the target which is completely in the opposite side for our results so, the only explanation up to our knowledge we can introduce is the change in the flow rate due to changing of the height which may be the only left logic reason.

3-Charge density effect on PAN fiber formation:

As shown in figure (11) the effect of the charge density on the fiber diameter distribution is very clear and the distribution increases as E/H increases. That is can be explained from the effect of the charge density on the size of the hanged droplet. When E/H reach 1 KV/cm the electric field is sufficient to over comes the surface tension of the hanged polymer solution droplet and forming a Taylor cone size related to the size of the droplet. Eventually the size of the droplet is smaller than the size of the pipette diameter. As the charge density increases from 1 to 1.5 KV/cm for same height the hanged droplet disappeared and the Taylor cone formed at the tip of the pipette which is larger in diameter than that one formed from the hanged droplet, for more prove see reference [8], so the formed fibers in this case are larger in diameter than the previous one, further more if the charge density increases to 2 KV/cm the jet comes out also from the orifice of the pipette not only that but splitting into many jets which is the parameter reduced the fiber diameter from case two to three.

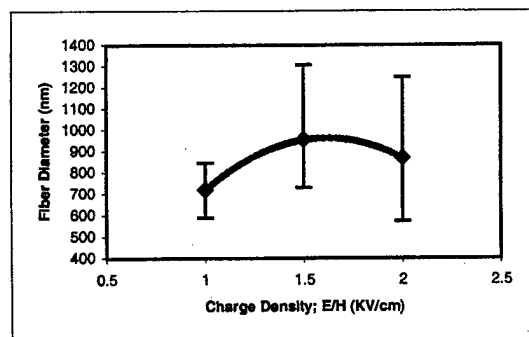


Fig. (11): Effect of Charge Density on Fiber Diameter for PAN + (50%DMF + 50%DMSO) System

The effect of the charge density on the average fiber diameter can be described by the following.

significant effect of the height from 10 to 15 cm on the parabolic relation:

$$d_f(\text{nm}) = -641.6(E/H)^2 + 2074.8(E/H) - 715.2$$

This relation describes the effect of the charge density on the fiber diameter and distribution for 9% concentration and a 15 cm height.

4-Solvent effect on PAN fiber formation:

In this experiment the effect of the solvent; which can be described here by its effect on the intrinsic viscosity of the polymer solution at same concentration was studied. PAN with 100%DMF, PAN with 50%DMF+50%DMSO, and PAN with 100% DMSO were prepared at 9% concentration and spun at 15 cm height with charge density of 1.5 KV/cm in room temperature. The SEM results can be seen in figure (12).

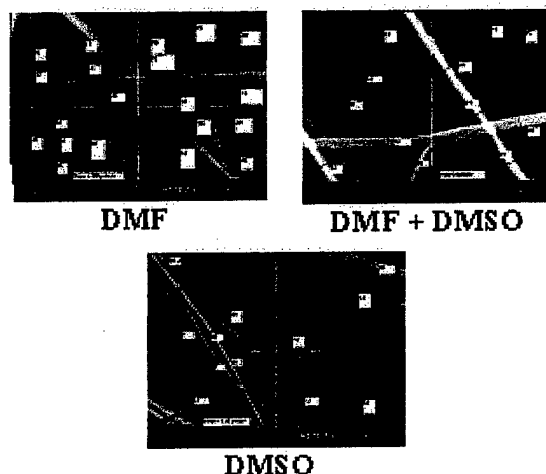


Fig. (12): SEM results for different solvents.

The effect of the solvent on the fiber diameter and its distribution can be seen in figure (13).

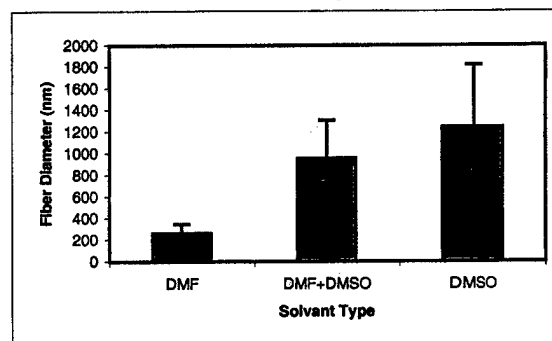


Fig. (13): Effect of solvent Type on Fiber Diameter

As can be seen from the figure, the intrinsic viscosity of the PAN + solvent system increases the fiber diameter and distribution also the rate of evaporation of the solvent is a restricted parameter by its boiling point and as the boiling point increases the evaporation rate and amount within the same height decreases then the fiber

fiber diameter can be described by the following.

5-Environmental temperature effect on PAN fiber formation:

From the previous experiment, it can be concluded that if the rate of evaporation of the solvent is increased the fiber diameter and its distribution will decrease. Therefore the following experiment will be conducted using the same spinning conditions, $H = 15$ cm, $C = 9\%$ wt., $E/H = 1.5$ KV/cm, and changing the temperature inside the station. The net results can be seen in the following figure.

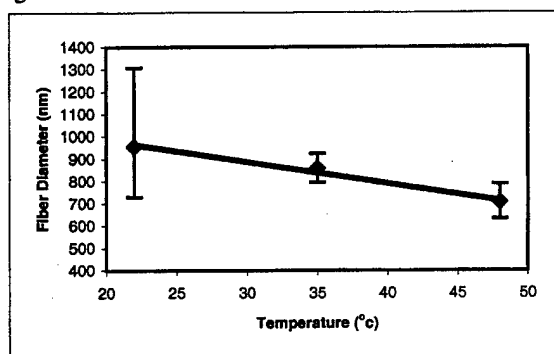


Fig. (14): Effect of Environmental Temperature in the Fiber Diameter of PAN + (50%DMF + 50%DMSO)

Also from the figure it can be concluded that the effect of the temperature is linear and is describable by the following equation:

$$d_f(\text{nm}) = -9.6019(T) + 1173.9$$

6-Spinning angle effect on PAN fiber formation:

In some of the low concentration solutions it is necessary to tilt the pipette at an angle to avoid droplets interfering with the collected fibers. This experiment was conducted to study the effect of the spinning angle on the fiber formation under the following conditions:

$H = 15$ cm, $E/H = 1.5$ KV/cm, and $C = 9\%$. The results can be shown in the following figure.

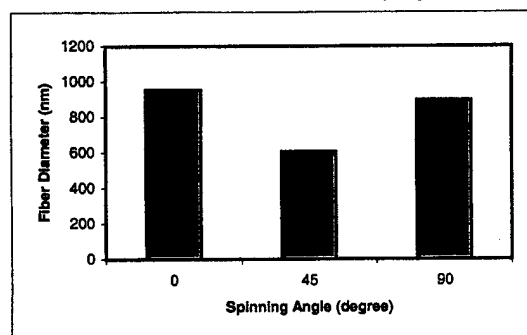


Fig. (15): Effect of Spinning Angle on Fiber Diameter for PAN + (DMF 50% + DMSO 50%)

diameter increases.

From the figure it can be concluded that a 45-degree angle may help in reducing the fiber diameter. This can be explained since a longer path must be traveled by the jet under the tilted angle more than the directed one.

7-Wet vs. dry effect on PAN fiber formation:

It was thought that by removing all of the solvent inside the ejected jet before it completely dried the fiber diameter would be reduced; therefore the following experiment was conducted.

Figure (16) shows the SEM pictures in the wet and dry spinning conditions.

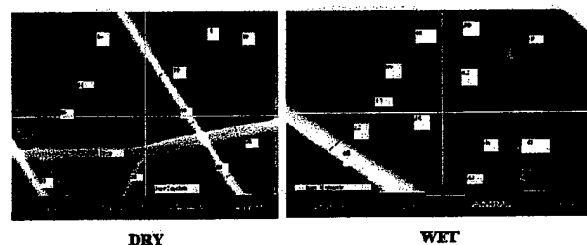


Fig. (16): SEM Results for Different Collector Types

As can be seen from figure (17), the diameters of the fibers spun in water are much lower than that spun onto the metal screen. Also it can be seen that there is improvement in the fiber distribution from dry to wet spinning. The spinning conditions for both are: $H = 15$ cm, $E/H = 1.5$ KV/cm, and $C = 9\%$.

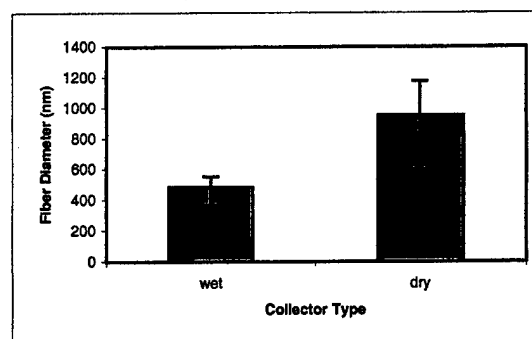


Fig. (17): Effect of Dry vs. Wet Spinning for PAN + (DMF 50% + DMSO 50%)

Conclusions:

- 1- A 100 nm PAN fiber diameter can be produced under the following conditions: 6% Wt. Concentration in DMF solvent, 1.5 to 2 KV/cm charge density, 10X10 cm target size, 15 to 20 cm height, 0.9 mm pipette diameter and in 35°C environmental temperature.
- 2- As the height, the concentration and the solvent boiling point reduced within the prescribed range the produced diameter and its distribution can be reduced.
- 3- As the environmental temperature increased the fiber diameter and its distribution decreased.
- 4- Berry number has a quantitative effect on the diameter distribution and only a qualitative effect on the fiber diameter.
- 5- Any extra charges than the required to start the spinning has a bad effect on the produced fiber diameter distribution.
- 6- By using 45° spinning angle the produced fiber diameter can be reduced under the same other spinning conditions.
- 7- Spinning inside a solution may help to reduce the fiber diameter and its distribution.

References:

- [1] E.Fitzer and M.Heine, "Carbon fiber manufacture and surface treatment" chapter 3 in, A.R.Bunsell, "Fiber reinforcements for composite materials" Elsevier Science Publishing Company Inc., pp. 73-148,1988.
- [2] S.B. Warner, A. Buer, S.C. Ugbolue, G.C.Rutledge, M.Y. Shin, "A fundamental investigation of the formation and properties of electrospun fibers", National textile center annual report, pp. 83-90,November 1998.
- [3]Gokul Srinivasan and Darrell H. Reneker,"Structure and morphology of small diameter electrospun aramid fibers", polymer international36 (1995) 195-201.
- [4]P.W. Gibson, H.L. Schreuder-Gibson and D. Rivin, " Electrospun fiber mats: Transport properties", AIChE Journal, January 1999 Vol. 45, No. 1.
- [5] Jayesh Doshi and Darrell H. Reneker, " Electrospinning process and applications of electrospun fibers", Journal of Electrostatics 35 (1995) 151-160.
- [6] Darrell H. Reneker and Iksoo Chun, " Nanometre diameter fibers of polymer, produced by electrospinning", Nanotechnology 7 (1996) 216-223.
- [7] Raimund Jaeger, Michel M. Bergshoeff, Cristina Martin I Batlle, Holger Schonherr and G. Julius Vancso, " Electrospinning of ultra-thin polymer fibers", Macromol. Symp. 127, 141-150 (1998).
- [8] Christopher J. Buchko, Loui C. Chen, Yu shen and David C. Martin, " Processing and microstructural characterization of porous biocompatible protein polymer thin films", polymer 40 (1999) 7397-7407.
- [9] Jong-Sang Kim and Darrell H. Reneker, " Polybenzimidazole nanofiber produced by electrospinning", Polymer Engineering and Science, May 1999, Vol. 39, No. 5.
- [10] Darrell H. Reneker, Alexander L. Yarin, Hao Fong and Sureeporn Koombhongse, " Bending instability of electrically charged liquid jets of polymer solutions in electrospinning", Journal of Applied Physics, Volume 87, No. 9, 2000.
- [11] J.M. Deitzel, J.D. Kleinmeyer, J.K. Hirvonen, N.C. Beck Tan, " Controlled deposition of electrospun Poly(ethylene oxide) fibers, Polymer 42 (2001) 8163-8170.
- [12] J.M. Deitzel, J.D. Kleinmeyer, D. Harris, N.C. Beck Tan, " The effect of processing variables on the morphology of electrospun nanofibers textiles", polymer 42 (2001) 261-272.
- [13] Peter K. Baumgarten, "Electrostatic spinning of Acrylic microfibers", Journal of Colloid and Interface Science, Vol. 36, No. 1, May 1971.

*Presented at The ICCM-13 (Thirteen International Conference on Composite Materials).
Beijing China, June 25 -29, 2001.*

NUMERICAL MODELING AND ANALYSIS OF DYNAMIC BEHAVIOR OF GRADIENT DESIGN COMPOSITES

Jovan Jovicic, Antonios Zavalangos, and Frank Ko

*Department of Materials Engineering, Drexel University
31 st. & Market St. Philadelphia PA 19104 USA*

ABSTRACT: The paper gives some numerical results of ballistic resistance studied for a developed plain woven and orthogonal ($0^\circ/90^\circ$) composite plate models, with and without ceramic facing (Gradient Design Composite). The difference in performance between a full ceramic facing versus a set of ceramic spheres embedded in light epoxy is evaluated. Materials properties and geometry effects are explored. Possible applications include body armors, helmets, and protection against projectile threats in structures such as helicopters, tanks and aircrafts.

KEYWORDS: Textile Composites, Gradient Design, Numerical Modeling.

INTRODUCTION

The main objective of this work is to address the computational modeling of the impact performance of textile based composite and Gradient Design Composite (GDC) materials. Possible applications of these kind of materials, would be the development of the light armor materials systems: body armors, helmets, and protection against projectile threats in structures such as helicopters, tanks and aircrafts, which would have a significant improvement in penetration resistance, impact energy dissipation, and damage containment. Due to their high impact resistance and low density, fabric composite armors are usually employed for personal protection, and considerable research has been directed to the study of the ballistic behavior of laminated, woven, and braided fabrics [1,5].

It is evident that the complexity of the modern light armor construction has increased many fold and so did its structural analysis. To complement and perhaps guide the necessary experimental evaluation of such system, it is essential to develop a computational methodology that may lead us to an improved understanding of the relative significance of the various design parameters. The associated computational complexity in terms of both geometry and material models is the key difficulty of this approach.

This work explores the ability to analyze the ballistic impact on complex structures, such as plane woven and orthogonal composites, with and without ceramic facing layer. Additional goal was to evaluate the difference in performance between a full ceramic facing versus a set of ceramic spheres embedded in light epoxy.

The characteristic of presented approach is that it considers each material separately. From the computer simulation point of view, the introduction of discrete models for the study of textile composites offers the advantage of using different and more detailed description of material properties for both matrix and fibers, with a more accurate description of the geometry. In this way, more elaborate (and more realistic) failure criteria can be introduced and the effects of fiber architecture on the dynamic properties of these composites can be explored.

BACKGROUND AND OBJECTIVES

The unique advantage of composite material is their ability to tailor their properties to the structural or materials system of which they are intended. On the other hand, many structural components have to meet service conditions and, hence, required materials performance, which vary with location within the component. This consideration founds basics for development of a special class of composite materials, that are functionally graded-*Gradient Design Composites* (GDC). Rather than developing new materials with higher stiffness, it might be more advantageous to create structures using the optimal placement of components.

The performance of a fiber-matrix composite depends on orientation, length, shape, and composition of the fibers; mechanical properties of the matrix; and integrity of the bond between fibers and matrix. In order to achieve higher penetration resistance, both experimental results [5], and numerical simulations [1], show necessity for harder, facing layer, which would first shatter or blunt armor piercing projectile, and than spread the load over a larger area. The composite backing would, in that case deforms to absorb the remaining kinetic energy of the projectile.

In order to defeat higher velocity threats and address the need for lighter weight and more complex shape structures, the concept of introducing a harden phase in the spherical form or Gradient Design Composite (GDC) was developed [5]. The system consists of a harden component with ceramic spheres for destroying the projectile tip and creating a greater surface area to contact between the facing layer and the backing composite plate which is for maximizing strength and energy absorption, (Fig.1).

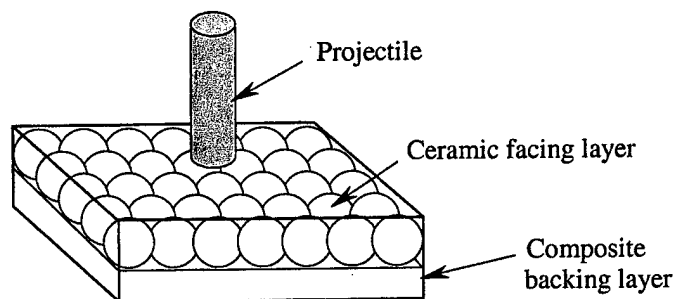


Fig.1 Gradient Design Composite material concept.

Changing the direction of a projectile, by its deflection on the particulate ceramic facing, gives the additional effect to the energy absorption increase.

Main objectives of this work are: to evaluate an ability to simulate complex material systems such as the Gradient Design Composites using finite element analysis; to attribute significance to the various design parameters such as material property, textile and overall composite architecture, and to evaluate the difference in performance between a full ceramic facing versus a set of ceramic spheres embedded in light epoxy.

It is important to note, that the results presented below may be influenced by the level of discretization, which is often coarse in order to limit the CPU time of the simulations to bellow one hour, on a modern (733MHz) personal computer. An effort to understand the effect of mesh density on the results is underway.

IMPACT MODELING

A set of 3D FE simulations (using ABAQUS-Explicit computer code) were carried out to evaluate the impact resistance for a developed plain woven and orthogonal ($0^\circ/90^\circ$) composite plates (Fig.2), with the same volume fraction of 50%, with and without ceramic facing layer. Models of a plain woven fabric and orthogonal composite structure are shown in details.

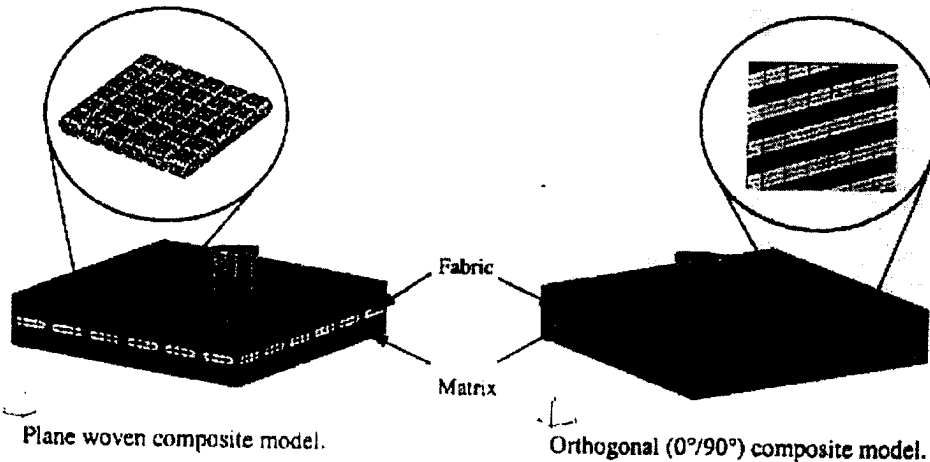


Fig.2 FE models of different fabric architecture.

In order to explore effect of different ceramic facing geometries on the ballistic resistance of armor model, monolithic ceramic tile versus layer of spheres embedded in epoxy, were considered. Figure 3 represents GDC model with spherical ceramic facing.

ABAQUS-Explicit utilizes an explicit time integration scheme designed specifically to model nonlinear dynamic problems. It also has the ability to reduce the stiffness of elements that reach user defined, failure criterion.

Due to symmetry, only one quarter of the model is considered with appropriate boundary conditions. The model consisted of 38962 eight-node hexahedral, reduced integration elements and 42548 nodes. Specifically, the projectile, the ceramic facing and the backing plate used 262, 9000 and 29700 elements, respectively. A cylindrical projectile with a diameter of 7.62mm, was modeled as a deformable, elastic plastic steel material. The dimension of a model is 28mm x 28mm and backing plate is assumed to have thickness of 6mm, and ceramic facing thickness of 8mm.

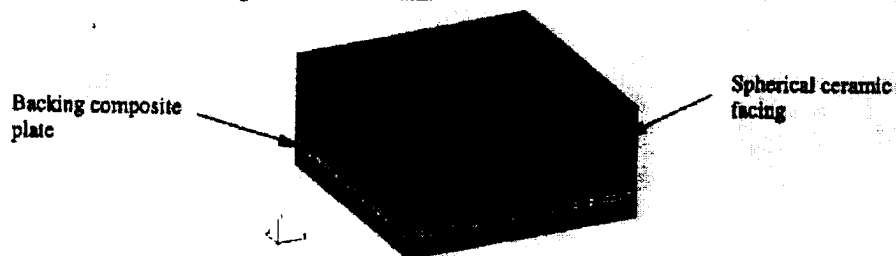


Fig.3 GDC model with spherical ceramic facing.

The impact velocities are assumed to be in the range of 250m/s to 1000m/s. An initial velocity was imparted on all nodes of the projectile to simulate the incident velocity. Contact was defined between the outer surface of the projectile and the nodes in the target. The termination time, for the FE runs of GDC models, was set at 100 μ s. This particular value is arrived at after several iterations and after analysing the maximum displacement and kinetic energy distributions of the projectile, which were leveled off at around 80 μ s.

MATERIAL MODELS

Contrary to the analysis of a high velocity impact on materials such as steel or aluminum, the simulation of high velocity impact and penetration processes into non-isotropic fiber reinforced material is a more challenging research task. However, such analysis is needed in order to understand the complex dynamic interactions between structural components undergoing large deformations and nonlinear material behavior including failure, delamination, erosion, etc.

In order to simulate the dynamic behavior of composite materials, the constitutive equations must cover the elastic regime, the material failure, and the behavior of the partially or completely failed material.

From the computer simulation point of view, the introduction of simple discrete models for the study of textile composites offers the advantage of introduction of different material properties for both matrix and fibers, as far as possibility of more accurate description of the geometry. Further, more elaborate (and more realistic) failure criteria can be introduced.

Using the higher-order discretization it is possible to explore the effects of fiber architecture on the properties of these composites. In addition using separate models for the fiber and matrix will allow for more complex models for both materials that can include rate dependence in the modulus of the fiber and matrix behavior.

The absorption of energy under both low and high velocity impacts depends strongly on the evolution of damage in the target and the resulting progressive degradation of its properties during its interaction with the projectile. For this reason, any computational simulation of impact phenomena must integrate in a rational way the dominant damage mechanisms in the target (and occasionally in the projectile).

T1. Material properties used in impact models

	Steel	Alumina	Epoxy	Spectra
Density (kg/m ³)	7800	3900	1200	970
Modulus (GPa)	210	350	4.5	268
Poisson's ratio	0.3	0.22	0.35	0.4
Plasticity σ (MPa), ϵ_p	1500, 0.00 1800, 0.10	2400, 0.00	50	3000, 0.00
Tensile strength (MPa)	/	360	/	/
Strain to failure	1.0	/	0.4	0.07

Material properties used for steel, alumina and polymer matrix composite, consisted of spectra fabric embedded in epoxy matrix, are shown in Table 1.

Alumina was modeled to fail at a tensile stress of 360MPa. At this value of stress, the material underwent brittle failure.

The ductile failure model, used for both fabric and matrix phase of polymer matrix composite, provides simple failure criteria, which are designed to allow the stable removal of elements from the mesh as a result of tearing or opening of the structure. The failure model is based upon the value of the equivalent plastic strain. When the equivalent plastic strain at a material point reaches the value defined as the plastic failure strain, ϵ_p^f , the material point is failed. If

all of the material points in the element fail, the element loses its ability to resist any further load and, hence, it is removed from the mesh.

The ductile failure model is based on a damaged Von Mises plasticity theory with isotropic hardening. The damage manifests itself in two forms: degradation of the yield stress with damage and damaged elasticity. In the case of epoxy, it was assumed that fracture occurred when the material is in plastic state, i.e. ductile fracture. Brittle fracture of spectra fibers, on that way, was considered as a limiting case of ductile fracture where fracture occurs after very little plastic flow.

Due to very limited experimental results available in (at least, open) literature, for this simulations, viscoelasticity of spectra polymer fabric is introduced in stepwise manner. Static Young's moduli are used but elevated according to specific strain rate. Table 2 shows Spectra modulus for different rates of strain [2].

T2. Spectra fiber modulus strain rate dependency.

Strain rate (min^{-1})	10	500	1,000	5,000	10,000
E [GPa]	101	130	145	221	268

Based on some experimental results [3,4], during the impact, alumina below the projectile crushed and consolidate. To model this behavior, as it is suggested in [3], a limited number of alumina elements directly below projectile were not allowed to fail in tension, (Fig.4). The addition of this "fail-free" zone, greatly improved the stability of solution and has solved convergence problems, due to mesh distortion.

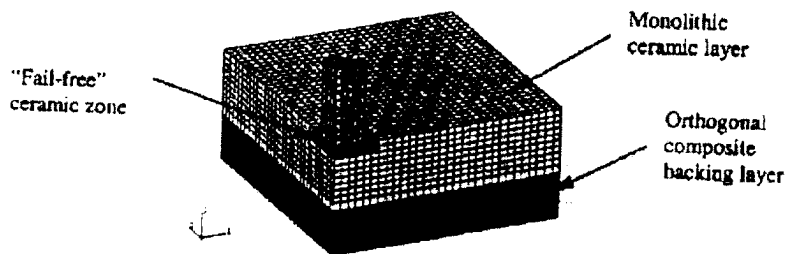


Fig.4 Fail-free zone in ceramic layer under the projectile.

The displacement of the projectile tip and center point of the back plate surface, as a measure of the penetration depth and blunt trauma effect, respectively, were tracked throughout the solution. The velocity of the projectile as well as time history of the energy, for the model constituents, is also recorded.

RESULTS AND DISCUSSION

In order to explore effects of textile architecture on the armor impact performance, first set of simulations was performed on both plain woven and orthogonal ($0^\circ/90^\circ$) polymer matrix composite models, for the impact velocity of 250m/s.

From Fig. 5, that shows velocity time history for different textile architectures, it is clear that fabric geometry plays important role in the textile composite impact resistance. While woven

composite model is completely perforated for a given impact velocity, projectile was stopped by the orthogonal composite.

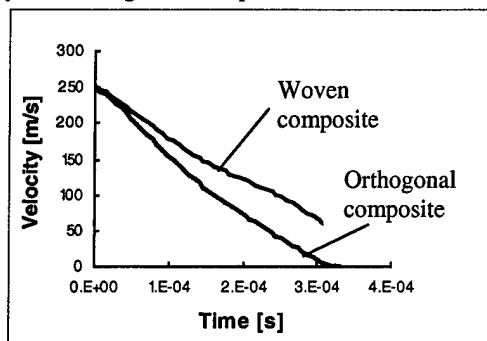


Fig.5 Effect of composite fabric architecture on velocity time history.

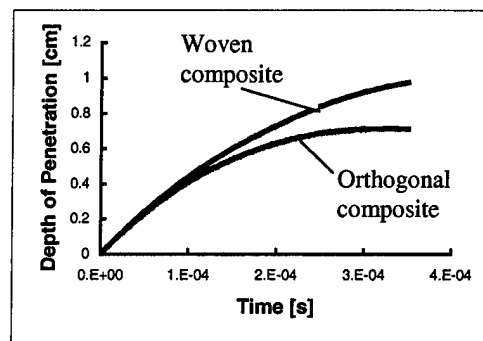


Fig.6 Depth of penetration as a function of composite fabric architecture.

The similar effect of the textile architecture on the ballistic effectiveness is shown on Fig.6, where penetration depth is given as a function of time.

Described behavior is shown on Fig.7 and Fig.8 for initial and final stage of simulation.

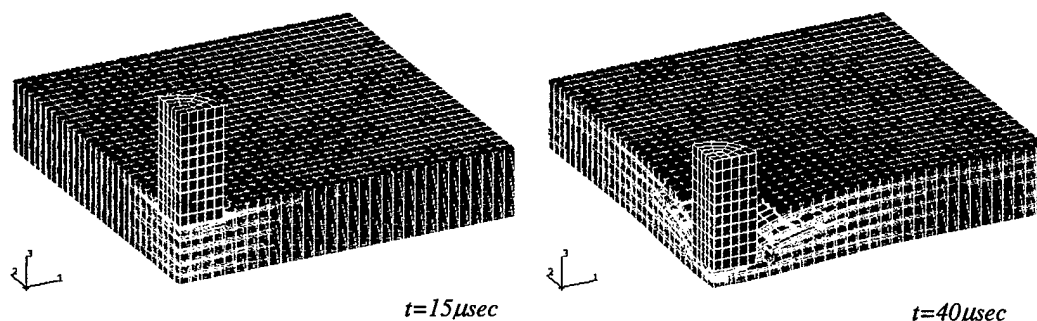


Fig.7 Von Mises stress distribution in the orthogonal composite model during the impact.

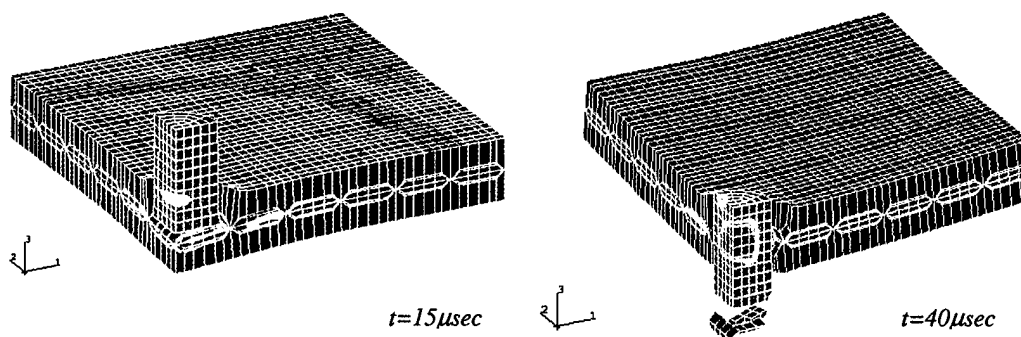


Fig. 8 Von Mises stress distribution in the plane woven composite model during the impact.

Since the target is composed of various material systems, stress pulses incident to an interface will have components transmitted and reflected waves depending on the mechanical impedance, areal density and speed of wave [6]. At the moment of impact (within 10μsec), a very high stress develops at the impact point. As a result, fiber breakage is expected. As time passes, the highest stress moves away from the impact site. Impact simulations have showed potential of layered, orthogonal fabric structure to absorb and transfer impact energy faster

than woven textile composite, lowering on that way stresses and deformations at the impact site.

In the case of Gradient Design Composite, ballistic resistance of four different models were evaluated, under two different impact velocities, 500m/s and 1000m/s, namely:

- *wcmf*-woven composite backing with monolithic ceramic facing,
- *wcsf*-woven composite backing with spherical ceramic facing,
- *ocmf*-orthogonal composite backing with monolithic ceramic facing, and
- *ocsf*-orthogonal composite backing with spherical ceramic facing.

The most important characteristic of protective ballistic system is its ability to slow down and stop the projectile. The best way to estimate armor penetration resistance is to measure residual velocity of a projectile. Another consideration for system integration is back face deformation, or the deflection of the armor material on the back surface. Even though the armor may defeat a threat projectile, the back face deformation can cause other damage, for example, blunt force trauma to a person wearing an armored vest or a helmet.

Figure 9 shows effects of both fabric architecture (woven vs. orthogonal), and ceramic facing (monolithic vs. the set of discrete spheres), on velocity time history for two impact velocities.

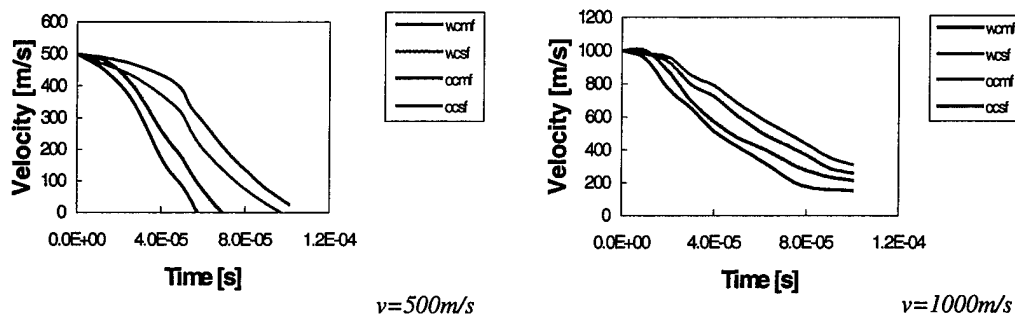


Fig. 9 Effect of composite fabric architecture and ceramic facing on velocity time history.

Better penetration resistance is predicted for orthogonal composite backing, which is able to absorb and disperse ballistic energy immediately, compared to woven fabric which crossover points probably serve as barriers to fast and efficient energy transfer. In the same time, the spherical ceramic facing seems to be good alternative to traditional monolithic ceramic plates, since simulations show comparable ballistic resistance.

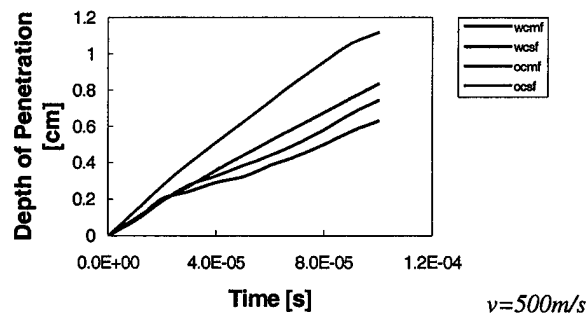


Fig. 10 Depth of penetration as a function of time for different models.

After impact, the kinetic energy of the projectile is imparted to the armor, and as the projectile penetrates the target, the kinetic energy will be reduced while the internal energy of the system will increase. Distributions of these energies (KE-kinetic energy; SE-recoverable strain energy; PD-energy dissipated by rate-independent and rate-dependent plastic

deformation), for different parts of a system (c-ceramic facing; r-rod-like projectile), and two impact velocities, with respect to time, are shown in Fig. 11. Kinetic energy dissipation is an indication that the velocity of the projectile is being slowed down as it ploughs through the armor.

The total energy balance for the model (ET) is seen to remain almost constant during the analysis, as it should.

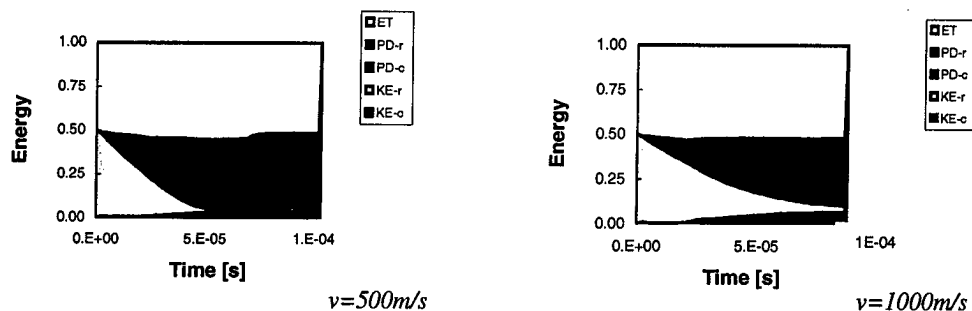


Fig. 11 Energy time history for orthogonal composite with monolithic ceramic facing.

Absorbed projectile impact energy is mainly transformed into kinetic (KE) and plastic energy dissipated in the target (PD) and deformation of rod-like projectile (PD-r), as it is shown on Fig.12. Due to crimped structure, woven preform absorbs more recoverable strain energy (SE), than orthogonal one.

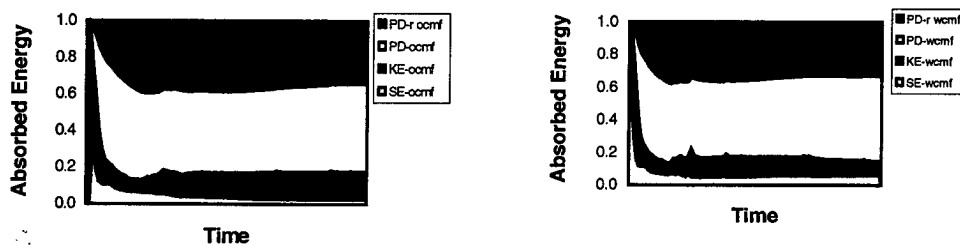


Fig. 12 The influence of textile architecture on energy time history ($v=1000\text{m/s}$).

Figure 13 represents relative distribution of the projectile kinetic energy in the different parts of target structure (E_c -total energy dissipated in ceramic facing; E_t , E_m -total energy absorbed by textile and matrix respectively), and the projectile (E_r), as a function of ceramic facing.

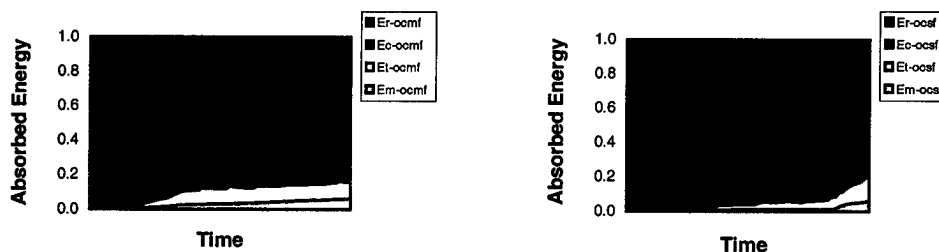


Fig. 13 The influence of ceramic facing on energy time history ($v=1000\text{m/s}$).

Considerably energy absorption capabilities of spherical ceramic facing are shown, comparable to that of solid ceramic tile.

One of the important effects in the ballistic event is the role of projectile deformation. In the presented simulations is observed that the projectile deforms significantly during the first part of penetration within the ceramic layer.

The slowing down and the deformation of a projectile can be visualized in Fig.14.

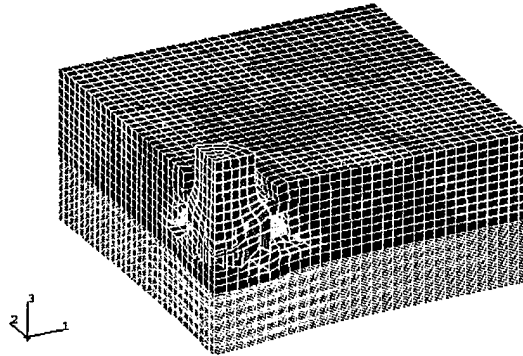


Fig.14 Von Mises stress distribution during the penetration of GDC.

CONCLUSION

The focus of the study is in the numerical assesment of energies, stresses and deformations and velocity histories of the different Gradien Design Composite systems in the event of an impact.

The developed FE tool shows to be capable to simulate structural behavior of textile composite, and to assess the effect of materials selection and fiber architecture.

Results are showing better penetration resistance of orthogonal ($0^{\circ}/90^{\circ}$) textile composites compared to woven composite.

It is shown that mutual contribution of both, textile architecture and ceramic facing layer influences ballistic performance of specific armor structure.

Ballistic resistance of GDC with facing layer of ceramic spheres embedded in epoxy is showed to be comparable to that of solid ceramic tile.

As a result of presented simulations, it can be said that ceramic spheres can be used effectively to replace the conventional ceramic tiles to reduce weight and cost without sacrificing its ballistic effectiveness.

ACKNOWLEDGEMENTS

The authors would like to thank the US Army Research Office (ARO) to support this work under the Multidisciplinary University Research Initiative (MURI), on Functionally Tailored Textile Fabrics.

REFERENCES

1. Jovicic, J., Zavaliangos, A. and Ko, F., *Special issue of Composite Part A: Applied Science and Manufacturing, Elsevier Science*. 2000;31:773-784.
2. Prevorsek, D.C., et al.: "Strain Rate Effects in Ultrastrong Polyethylene Fibers and Composites". *Journal of Applied Polymer Science*. 1991;47:45-66.
3. Roeder, B., Sun, C.T.: "Dynamic Penetration of Alumina/Aluminum Laminates: Experiment and Modeling". *International Journal of Impact Engineering*, 2000;25:169-185.
4. Sherman, D.: "Impact Failure Mechanisms in Alumina Tiles on Finite Thickness Support and the Effect of Confinement". *International Journal of Impact Engineering*, 2000;24:313-328.
5. Song JW, Geshury A, and Ko FK.: "Behavior of Gradient Designed Composites Under Ballistic Impact". Proceedings, *Eleventh International Conference on Composite Materials*, Gold Coast, Australia, July 14-18, 1997.
6. Zukas: "Impact Dynamics". *John Wiley & Sons*, New York, 1982.

Presented by Professor Ko at the University of Akron, OH, on October 20, 2001

Carbon Nanotube Reinforced Nanocomposites by the Electrospinning Process

**Frank K. Ko, Wendy B. Han and Anisur Rahman,
Drexel University, Philadelphia, PA, 19104; and
Hideo Shimoda and Otto Zhou,
University of North Carolina, Chapel Hill, NC 27599**

ABSTRACT

Recent studies showed that on the molecular level, CNT possess many unique characteristics that promise to revolutionize the world of structural materials resulting in significant impact on our capability to build lighter, smaller and higher performance structures for aerospace and many other industrial applications. When the CNT are aligned, micromechanical studies showed an order of magnitude increase in mechanical properties comparing to the state of the art carbon fiber reinforced composites. The co-electrospinning process is introduced as a means to align and carry the CNT in the form of nanocomposite fibrils; thus forming the precursor for linear, planar and 3D fiber assemblies for macrocomposites. A hierarchical fiber architecture based design methodology is offered in this paper to account for the contribution of these nanocomposite fibril building blocks over the entire structure length scales from the CNT level to the macrostructural level. Preliminary experimental results showed that key to realization of the potential of CNT is to overcome the challenges in dispersing and aligning the CNT in the polymer matrices

INTRODUCTION

Carbon nanotubes (CNTs) [1] are seamless graphene tubule structures with nanometer-size diameters and high aspect ratios. This new class of one-dimensional material is shown to have exceptional mechanical, thermal and novel electronic properties. The elastic moduli of the CNTs are in the range of 1-5 TPa [2-4] and fracture strains of 1 to 30%, both are about a factor of ~100 better than those of the commercial carbon fibers which typically have 0.1-0.5 TPa elastic moduli and 0.1-2% fracture strains [5]. The factor of 100 enhancement in strength implies that, for the same performance, replacing the commercial carbon fibers with CNTs will lead to significant reduction in the volume and weight of the structural composites currently used in space applications.

Based on a recent NASA study by Harris et. al using micromechanics computation [6], as shown in Table 1., it was concluded that an order of magnitude increase in specific modulus can be achieved with CNT composites. However, it was also recognized that it would be significantly more challenging in the conversion of CNT to useful structures.

Table 1. Properties of SWNT and their Composites [6]

Properties	Aluminum 2219-T87	IM7/8552 Quasi- isotropic Composite	CNT/Polymer Quasi- isotropic Composite (1)	CNT SWNT Crystal
Tensile strength (GPa)	0.46	1.3	2.5	180
Tensile Modulus (GPa)	73	58	240	1200
Rupture Elongation(%)	10	1.6	6	15
Density (g/cc)	2.83	1.59	0.98	1.2
Specific Strength	0.16	0.80	2.5	170
Specific Modulus	26	36	240	1000
Thermal Conductivity (W/mK)	121	5	5	5000
Manufacturability (2)	9	6-9	1	1

(1) based on 60% fiber volume fraction in a quasi-isotropic laminate, with strength at 1% strain

(2) manufacturability rating, in the range of 0 to 10, with 10 being the best.

In addition to potential applications as high performance fibers, carbon nanotubes are shown to have promising materials properties for applications as hydrogen storage materials [7-9] high energy capacity battery electrodes [10], and cold-cathode electron emitters [11,12]. Depending on their chiralities and diameters, CNTs can be either semiconducting or metallic [13]. The electrical conductivity of the metallic CNTs is (6000 S/cm) significantly higher than the best commercial carbon fibers. Because of their high degree of graphitization, CNTs are expected to have higher thermal conductivity than the best carbon fibers (2000 W/m-K).

Despite their promises, most of the current studies are limited to the physics and chemistry of individual CNTs. There is limited knowledge on the properties of macroscopic materials comprising CNTs as the basic building blocks for macroscopic structures. It is still not clear whether the superb properties observed at the individual molecular level can be utilized in the macroscopic structures. For example, most of the studies on nanotube - polymer composites have been on electron microscopy investigation of deformation of the individual CNTs embedded in polymeric matrices [13-15]. No significant enhancement in the mechanical

strength has been achieved in nanotube-polymer composites [16], presumably due to the weak interface between CNTs and composites. In order to realize the exciting potential of CNT, there is a need for processing methodologies and robust manufacturing technology to convert the CNT to macroscopic structures. To assure proper translation of the properties of CNT to the structural level, an integrated design for manufacturing methodology reflecting the hierarchical structural geometry must be available. Accordingly, it is the objective of this paper to introduce a concept that converts CNT into nano scale filamentous composites by the co-electrospinning process. Using this CNT composite filaments as building blocks, a framework for hierarchical design for manufacturing will be presented.

THE CONCEPT OF CNT NANOCOMPOSITE FIBRILS

It is well known that the translation of reinforcement properties to the composite depends on the alignment or orientation θ , of the reinforcement for a given volume fraction of the reinforcement, V_f , with θ and V_f functions of fiber architecture as illustrated in Figure 1. [17]. Figure 1 shows the range of obtainable elastic moduli for various composites normalized by the fiber modulus E_f , versus the appropriate fiber volume for the fiber architecture indicated.

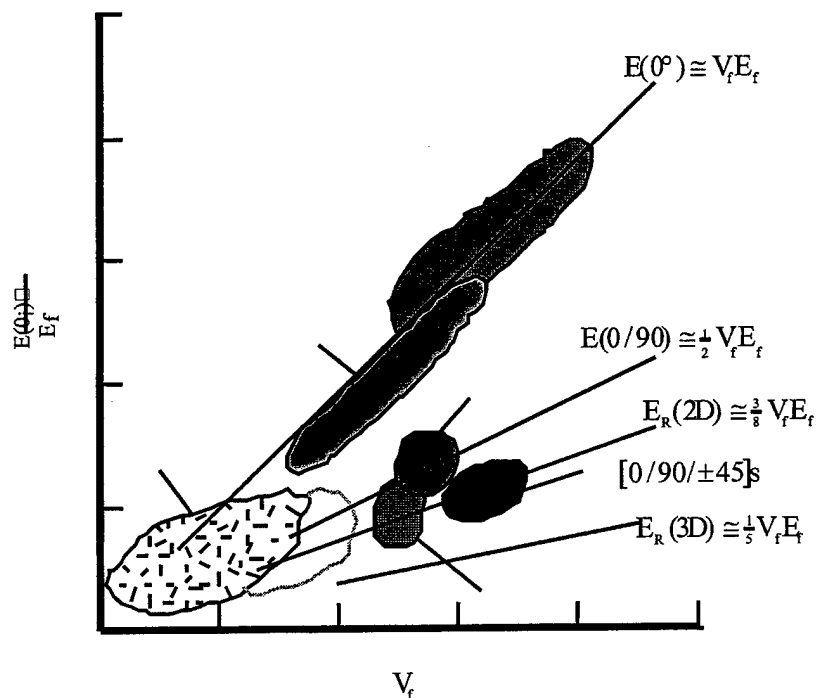


Figure 1. Effect of fiber architecture on material property translation in fiber reinforced composites

CNTs are expected to have highly anisotropic mechanical, thermal, and electrical properties. To measure and utilize these anisotropic properties, many attempts have been made to fabricate materials with controllable degree of CNT alignment. These methods include:

- [1] mechanical stretching - nanotubes can be aligned inside polymeric matrices by mechanical stretching and developed procedures to determine the direction and the degree of alignment [18];
- [2] roll-cast- membranes CNTs embedded in thermoplastic matrices by solution cast and produced composites with uniaxially aligned SWNTs by mechanical shearing [16,18];
- [3] magnetic alignment - thick film of SWNT and ropes are aligned by filtration/deposition from suspension in strong magnetic fields. [19];

A new method, the co-electrospinning method, is demonstrated in this study by spinning mixtures of CNT and polymer solution to form aligned nanocomposite fibrils by the electrospinning process. Electrospinning is an electrostatic induced self-assembly process wherein ultrafine fibers down to the nanoscale are produced. In the electrospinning process, a high voltage electric field is generated between an oppositely charged polymer fluid contained in a glass syringe with a capillary tip and a metallic collection screen. Once the voltage reaches a critical value, the charge overcomes the surface tension of the suspended polymer with cone formed on the capillary tip of the syringe (spinneret or glass pipette) and a jet of ultrafine fibers is produced. As the charged polymer jets are spun, the solvent quickly evaporates and the fibrils are accumulated on the surface of the collecting screen. This results in a nonwoven mesh of nano to micron scale fibers. A nanoscale fiber is called a fibril. Varying the charge density, polymer solution concentration and the duration of electrospinning can control the fiber diameter and mesh thickness. A schematic illustration and an example of a composite formed by the process are shown in Figure 2a. The concept of CNT nanocomposites (CNTNC) can be illustrated in Figure 2b, showing the orientation of the CNT in a polymer matrix through the electrospinning process by flow and charge induced orientation as well as confinement of the CNT in a nanocomposite filament [20,21].

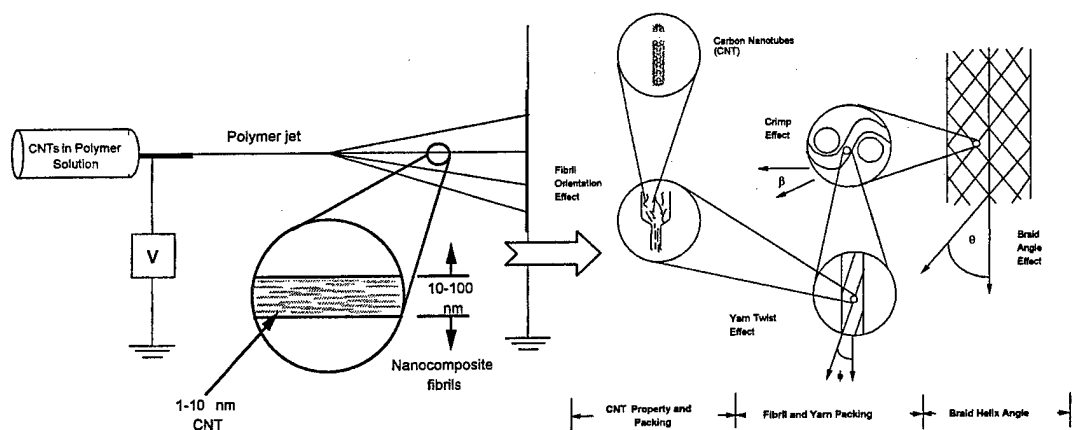


Figure 2a Co-electrospinning of CNT

Figure 2b. Concept of CNTC

The nanofibril composite can also be subsequently deposited as a spunbonded nanofibril mat for subsequent processing into composites or for use as a nonwoven mat (Figure 7). Alternately, by proper manipulation, the CNTNC filaments can be

aligned as a flat composite filament bundle or twisted to further enhance handling and/or tailoring of properties in higher order textile preforms for structural composites. As shown in Figure 2b, by twisting the nanocomposite fibrils, off-axis angular orientation may be introduced to the nanocomposite filament in order to tailor the composite filament modulus.

MODELING OF CNTNC

Geometric Properties of CNTNC

The translation of properties to macrostructures begins with a consideration of the packing of the CNT. Depending on the nature of the CNT packing, the volume fraction of CNT can range from .75 to .90 for open, square and close packing as shown in Figure 3.

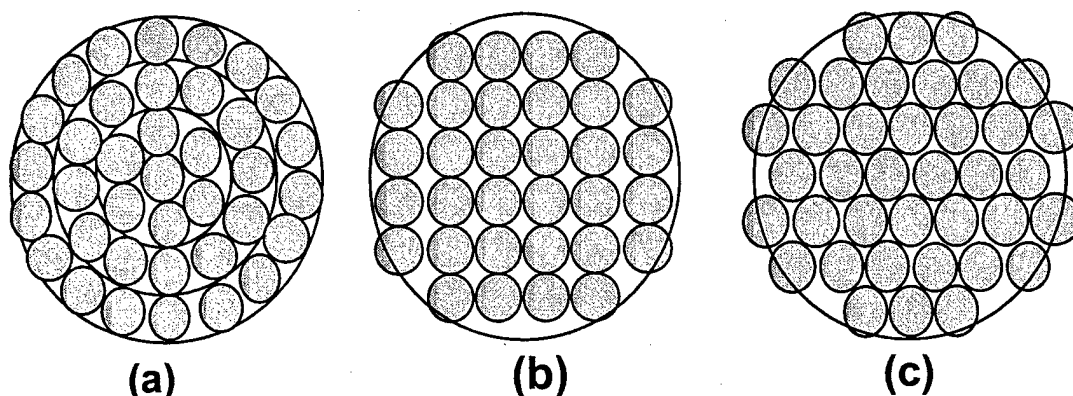


Figure 3 Idealized fibrillar packings:
(a) open packing; (b) square packing; (c) close packing.

A twisted bundle of fibrils is called a yarn wherein the fibrils are no longer aligned to the yarn axis. Instead, the fibrils assume helixial geometry in the yarn, as shown in Figure 4a. For fibril yarn composites, fiber volume fraction is equivalent to its fiber packing fraction, and related to fibril helix angle, θ , fibril diameter, d , and number of twist per unit length, T , by equation (1) :

$$V_f = \left[d + \frac{\tan \theta}{\pi d T} \right]^{-2} \quad (1)$$

For a 12K yarn with 100 nm diameter fibrils, the relationship between fibril volume fraction, fibril orientation (surface helix angle), and twist level can be established as shown in Figure 4b. Clearly, for a given twist inserted to the fibril bundle, fibril volume fraction decreases as fibril orientation angle increases.

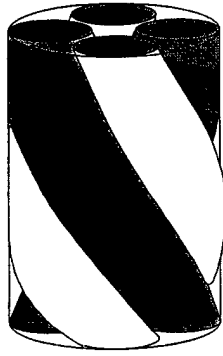


Figure 4a. Geometry of twisted yarn

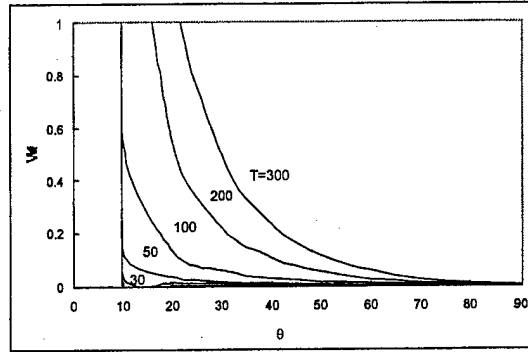


Figure 4b. Relationship of fibril volume fraction to fibril orientation at various twist levels.

Mechanical Properties of CNTNC

As shown in Figure 2b, a macrocomposite consists of several structural levels at multiple length scales. Starting from the CNT level, one may predict the macrocomposite properties using micromechanics models such as the Fabric Geometry Model (FGM) [22]. Conversely, one may also test the macrocomposites and back out the CNT properties. The mechanical properties of the nanocomposite fibril, as a first approximation, may be modeled as a short fiber composite with CNT playing the role of a short fiber that has a high aspect ratio. For an aligned CNT fibril assembly of CNT of length l , the longitudinal modulus is given by: [23]

$$E_{\text{fibril}} = \eta_l E_{\text{cnt}} v_{\text{cnt}} + E_m (1 - v_{\text{cnt}}) \quad (2)$$

where, v_{cnt} is the volume fraction of the CNT, E_{cnt} is the longitudinal modulus of the CNT and E_m is the modulus of the matrix material. η_l is an efficiency parameter and is given by:

$$\eta_l = 1 - \frac{\tanh(\frac{1}{2} \beta l)}{\frac{1}{2} \beta l} \quad (3)$$

l is the length of the CNT and θ is given by:

$$\beta = \sqrt{\frac{8G_m}{E_{\text{cnt}} d^2 \ln \frac{2R}{d}}} \quad (4)$$

G_m is the shear modulus of the matrix, d is the fibril diameter and $2R$ is the inter-fibril spacing.

For a twisted assembly of the nanocomposite fibrils embedded in a resin matrix that we will call yarn composite, with fibril orientation of ϕ , The modulus of the yarn composite can be related to the modulus of CNT by equation (5) :

$$E_{\text{fibril}} = \eta_l E_{\text{cnt}} v_{\text{cnt}} \cos^4 \phi + E_m (1 - v_{\text{cnt}}) \quad (5)$$

By taking the packing density of CNT and fibrils into consideration, using the CNT properties shown in Table II., the tensile modulus of the composite fibril and

yarn can be plotted as a function of CNT and fibril orientation respectively in Figures 5a and 5b:

Table II CNT and Polymer Matrix Properties

CNT	
Elasticity, E_{cnt}	1 TPa
Length, l	1000 nm
Diameter, d	1 nm
Matrix	
Elasticity, E_m	3.5 GPa

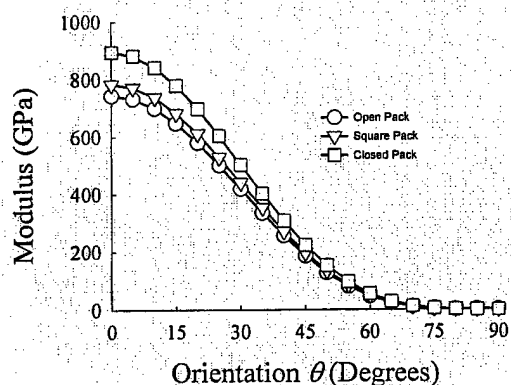


Figure 5a. Longitudinal modulus of the fibril as a function of orientation of the CNT

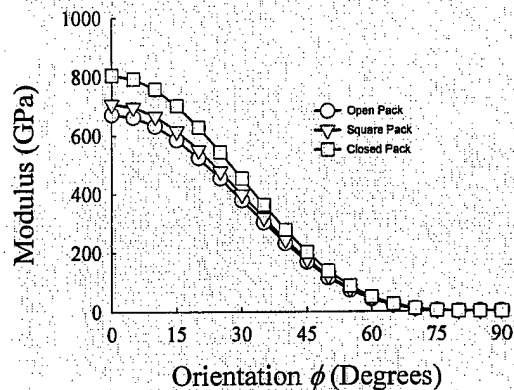


Figure 5b. Longitudinal modulus of the yarn composite as a function of orientation of the fibril

For a close packed CNT fibril, it can be seen in Figures 5a and 5b that the tensile moduli for the fibril and composite yarn are 895 and 807 GPa respectively. Assume a 60% fibril volume fraction as in most of the structural composites the moduli of the unidirectional composite and quasi isotropic composite consisting of the CNT fibrils are 538 and 203 GPa respectively. This agrees well with the prediction by Harris et.al. [6] showing a more than three fold increase in modulus compared to aluminum and high modulus carbon fiber reinforced composites. For a spunbonded mat with randomly oriented CNT with 30% fibril fraction, the estimated tensile modulus is 100 GPa!

FABRICATION OF CNTNC BY CO-ELECTROSPINNING

To demonstrate the co-electrospun CNTNC concept, SWNT bundles were synthesized by ablating a graphite target containing Ni/Co metal catalysts (0.3 atm% each) using a 1064nm Nd:YAG laser in a Ar-filled furnace at 1150C. The raw SWNT are shown in Figure 6a. The raw material was refluxed in 20% H₂O₂ solution at 100°C for 6 hours then filtered and rinsed well with methyl alcohol assisted by ultrasonication after the ultrasonication in the CS₂ and methyl alcohol 1:1 mixture for 2 hours. After well dried in the air, the sample was annealed in 6.3 * 10⁻⁶ Torr vacuum at 200°C for 4 hours and then at 1000°C for 1 hour. The purified material is shown in Figure 6b.

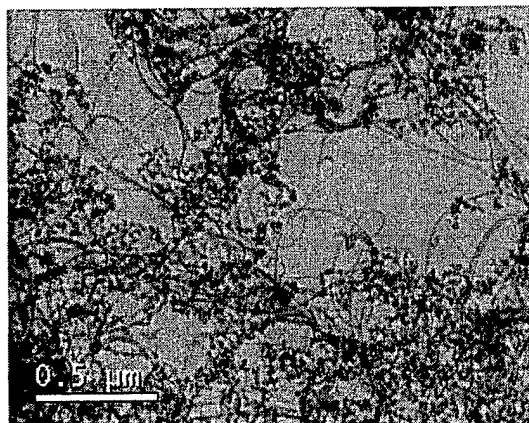


Figure 6a. Raw SWNT materials

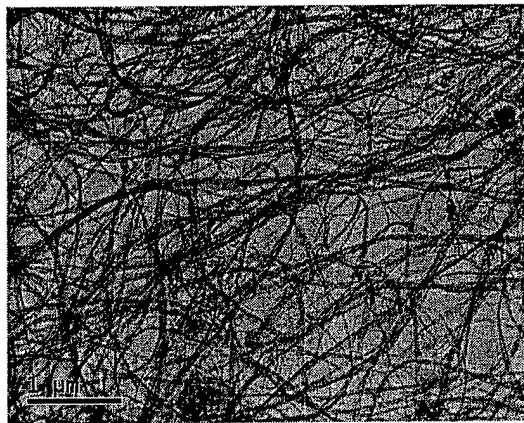


Figure 6b. Purified SWNT material

The CNT were dispersed in polyethylene oxide (PEO) with an appropriate surfactant so that the CNT are distributed uniformly in the polymer solution for subsequent formation of the CNT composite fibrils by the electrospinning process. The PEO/CNT systems were processed in two solvents, chloroform and water. A 95:5 mixtures by weight of PEO and CNT were mixed with 3% by weight solvent concentration of chloroform and water respectively.

Electrospinning for the PEO/CNT/Chloroform and PEO/CNT/water system were carried out with an electric field strength of 3.0 and 0.75 KV/cm. The nominal spinneret diameter was 1 mm. In the case of water base system, a 0.11 weight % of Polystyrene Sulfuric Acid was added to further disperse the CNT. The CNT fibrils are shown in Figures 7a and 7b using chloroform and water as solvent respectively. In Figures 8a the straight fibril and stretched coil fibrils are shown. Figure 8b is a close-up of the fibril showing the tendency of the CNT to cluster along the length of the fibril indicating that better dispersion of the CNT is required in order to produce fine fibrils with well aligned CNT.

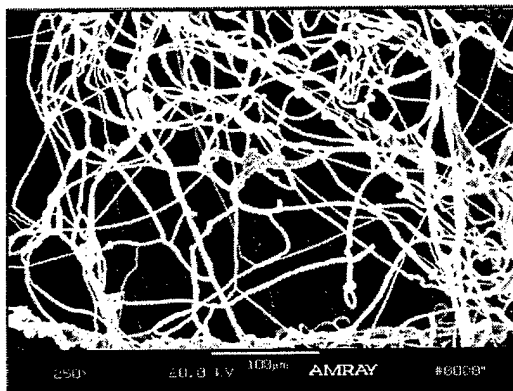


Figure 7a. Fibril mat of PEO co-spun with CNT from Chloroform solution

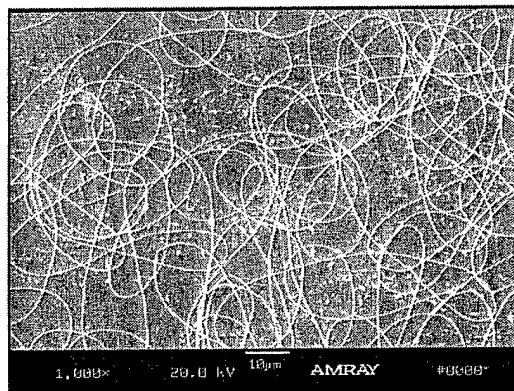


Figure 7b: Fibril mat of PEO co-spun with CNT from water solution 2,000x

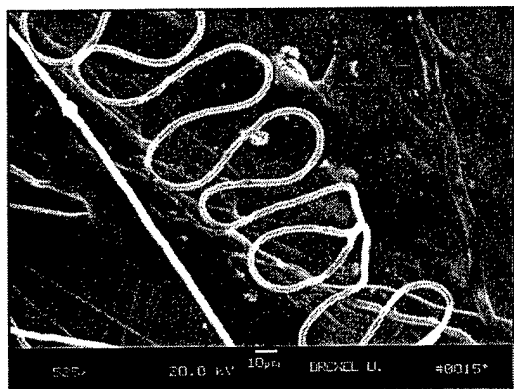


Figure 8a. Oriented and coil fibril of PEO co-spun with CNT (using Chloroform as solvent) 100x

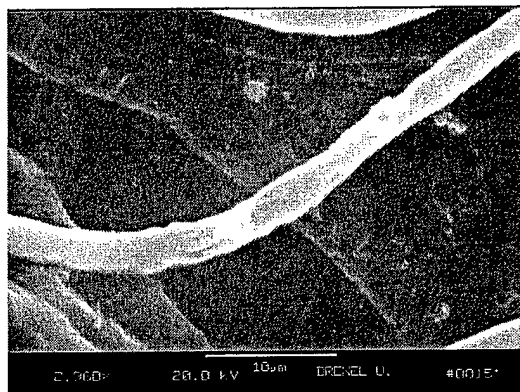


Figure 8b. Single fibril of PEO co-spun with CNT (using Chloroform as solvent) 2,960x showing clusters of CNT in the fibril

SUMMARY AND CONCLUSIONS

In order to assess the potential of CNT for structural composite applications, a method was proposed to convert CNT to continuous fibrils and fibrous assemblies using the electrospinning process. Preliminary experiments demonstrated the feasibility for the formation of composite CNT fibrils. It was also found that dispersion of CNT is essential for the formation of well-aligned CNT in nanoscale fibrils. These fibrils provide a critical material form to carry the CNT and facilitate the formation of macro composite structures. The level and the nature of CNT alignment need to be elucidated through TEM/AFM observations and spectra analysis. Mechanical testing of the nanofibril, nanofibril spunbonded mats and composite yarns will be carried out to assess the level of alignment and verify the predictions based on micromechanical computation.

A hierarchical fiber architecture based model was proposed to link CNT properties to higher order structures. This model predicted more than three-fold increase in modulus with CNT composites comparing to state of the art composites. This model not only facilitates the prediction of CNT composite structures but also provides a means to relate composite coupon properties to CNT properties.

It must be noted that the simple model that we employed in this study is based on traditional composite micro mechanics. Many of the unique features of the CNT such as the transverse properties; the interfacial characteristics; the unusually high elongation at break have not been considered. What is the failure behavior of the CNT composite? How does CNT react with metal, ceramic and carbon matrix? How does the "nano effect" of the CNT interact with the macro scale structures? Thus, there are plenty of challenging processing and analytical problems ahead as well as ample opportunities to uncover the exciting properties of CNT based composites.

ACKNOWLEDGEMENTS

This work is supported by the NASA NRA 99-OSS-05 program and by ARO under the MURI program. The assistance of Mitch Marmel in the preparation of the manuscript is greatly appreciated.

REFERENCES

- [1] S. Ijimi, Helical microtubules of graphitic carbon. *Nature*, 354:53-58, 1991.
- [2] M.M. Treacy, T.W. Ebbesen, and J.M. Gibson. *Nature*, 381:67-80, 1996.
- [3] E.W. Wang, P.E. Sheehan, and C.M. Lieber. Nanobeam mechanics: Elasticity, strength and toughness of nanorods and nanotubes. *Science*, 277(26):1971-1975, 1997.
- [4] J.P. Lu. Elastic properties of single and multilayered nanotubes. *Phys. Rev. Lett.* 1 79:1297, 1997
- [5] Leighton H. Peebles. *Carbon Fibers: Formation, Structure, and Properties*. CRC Press, Inc, Boca Raton, 1995.
- [6] C.E. Harris, J.H. Starnes, Jr., and M.J. Shuart, An Assessment of the State of the Art in the Design and Manufacturing of Large Composite Structures for Aerospace vehicles, NASA/TM-2001-210844, April 2001
- [7] A.C. Dillon, K.M. Jones, T.A. Belledahl, C.H. Kiang, D.S. Bethune, and M.J. Heben. Storage of hydrogen in single-walled carbon nanotubes. *Nature*, 386:377-379, 1997.
- [8] Y. Ye, C.C. Ahn, C. Witham, B. Fultz, J. Liu, A.G. Rinzier, D. Colbert, K.A. Smith, and R.E. Smalley. Hydrogen adsorption and cohesive energy of single walled carbon nanotubes. *Appl Phys. Lett.*, 74(16):2307-2309, 1999.
- [9] B. Gao, A. Kellinhammes, X.P. Tang, C. Bower, Y. Wu, and O. Zhou. Electrochemical intercalation of single walled carbon nanotubes with lithium. *Chem. Phys. Lett.* 307:153-157, 1999.
- [10] W.A. de Heer, A. Chatelain, and D. Ugarte. A carbon nanotube field-emission electron source. *Science*, 270:1171-1180, 1995.
- [11] W. Zhu, C. Bower, O. Zhou, G.P. Kochanski, and S. Jin. Very high current density from carbon nanotube field emitters. *Appl Phys. Lett.*, 75(6):873-875, 1999.
- [12] R. Saito, G. Dresselhaus and M.S. Dresselhaus, *Physical properties of Carbon Nanotubes*, Imperial College Press, 1998
- [13] O. Laurie, D.E. Cox, and H.D. Wagner. Bucking and collapse of embedded carbon nanotubes. *Appl Phys. Lett.*, 81(8):1638-1641, 1998.
- [14] C. Bower, R. Rosen, L. Jin, J. Han, and O. Zhou. Deformation of carbon nanotubes in nanotubular polymer composites. *Phys. Lett.*, 74(22):3317-3319, 1999.
- [15] L.S. Schadler, S.C. Giannaris, and P.M. Ajayan. *Appl Phys. Lett.*, 73:3842-3844, 1999.
- [16] T.G. Gutowski, ed., *Advanced Composites Manufacturing*, Wiley Interscience, 1997
- [17] L. Jin, C. Bower, and O. Zhou, Alignment of carbon nanotubes in a polymer matrix by mechanical stretching. *Appl. Phys. Lett.*, 73(9):1197-1199, 1998.
- [18] Structural anisotropy of magnetically aligned single wall carbon nanotube films, *Applied Physics Letters*, 77, 663, 2000
- [19] D. Reneker and I. Chun, Nanometre Diameter Fibres of Polymer, Produce by Electrospinning, *nanotechnology*, v. 7, pp. 216-233, 1996.
- [20] W. Han, F. K. Ko, R. Rosen and O. Zhou, Electrospinning of Continuous Fibers of Carbon Nanotube and Polymer Composites, *Proceedings, MRS Fall Meeting*, 2000
- [21] F. Ko, Processing of Preforms for Composites, in T.G. Gutowski, ed., *Advanced Composites Manufacturing*, Wiley Interscience, 1997
- [22] H.L. Cox, The elasticity and strength of paper and other fibrous materials, *Brit. J. Appl. Physics*, 3: 72-9, 1952.

Electrostatically-generated nanofibers of electronic polymers

A.G. MacDiarmid^{a*}, W.E. Jones, Jr.^a, I.D. Norris^a, J. Gao^a, A.T. Johnson, Jr.^b, N.J. Pinto^a,
J. Hone^b, B. Han^c, F.K. Ko^c, H. Okuzaki^a, M. Llaguno^b

^a Department of Chemistry, University of Pennsylvania, Philadelphia, PA 19104-6323 USA

^b Department of Physics, University of Pennsylvania, Philadelphia, PA 19104-6323 USA

^c Fibrous Materials Research Center, Drexel University, Philadelphia, PA 19104 USA

Abstract

Long nanofibers of conducting electronic polymers and their blends and also conventional polymers are conveniently fabricated in air by a non-mechanical electrostatic dispersion method. All fibers in a given preparation of certain polymers have diameters < 100 nm. Fibers of 100% doped polyaniline as well as its blends in polymers such as polystyrene and polyethylene oxide have been prepared. Current/voltage in addition to conductivity/temperature relationships of single fibers as small as 419 nm have been obtained. Polyacrylonitrile and polystyrene fibers can be easily and uniformly coated from aqueous solution with conducting polypyrrole or with gold by electroless deposition. Polyacrylonitrile fibers can be thermally converted to conducting carbon nanofibers.

Keywords: Solution processing, Scanning electron microscopy, Coatings, Polyaniline and derivatives, Polypyrrole and derivatives

1. Introduction

It is commonly accepted that the rapidly-expanding field of nano-materials is defined as one consisting of a substance or structure which exhibits at least one dimension of less than 100 nm (0.1 μm).[†] [1]

The objectives of the present study were: (i) to develop a method by which nanofibers (diameter < 100 nm) of organic polymers could be controllably and reproducibly fabricated such that in one given preparation, all fibers would have a diameter < 100 nm and (ii) to reproducibly and controllably fabricate, for the first time, nanofibers of pure electronic polymers (in their semiconducting and metallic regimes) and/or their blends in conventional organic polymers for the purpose of ascertaining their applicability in the fabrication of nano-electronic devices.

We have made substantial progress in achieving these objectives by using a relatively little known, simple, convenient and inexpensive "electrospinning" method first reported in a patent in 1934. [2] Since this date a few scattered papers using this technique have appeared in the

literature, the number of which has begun to substantially increase during the past ten years. [3-5]

We have previously reported [6] fabrication of the first conducting polymer fibers (diameter ~950 nm to 2,100 nm) of polyaniline doped with *d,l* camphorsulfonic acid (Pan.HCSA) as a blend in polyethylene oxide (PEO). We were surprised to find that an electronic polymer, such as polyaniline, which might have been expected to be more susceptible to degradation than most conventional organic polymers, survived, without observable chemical or physical change, following the 25,000 V electrospinning fabrication process in air at room temperature.

2. Experimental

The electrospinning technique for the fabrication of submicron to nanometer scale fibers involves a simple, rapid, inexpensive, electrostatic, non-mechanical method in which a polymer solution in a variety of different possible common solvents, including water, is placed in a hypodermic syringe or in a glass pipette, at a fixed distance (5-30 cm) from a metal cathode electrode such as aluminum foil. [3] The positive (anode) terminal of a

* Corresponding author. Tel. +215-898-8307; fax +215-898-8378;
email: macdiarm@sas.upenn.edu.

[†] For comparison, a human hair is ~ 50,000 nm.

variable high voltage transformer (Gamma High Voltage Research) capable of delivering 30,000 V is attached to the metal tip of the hypodermic syringe or to a copper wire inserted into the polymer solution in the glass pipette, the negative terminal being attached to the aluminum foil target electrode. The tip of the syringe can be placed vertically over the cathode or at any other convenient angle to it. When the voltage applied between the anode and cathode reaches a critical value, e.g. 14,000 V for polyacrylonitrile and a 20 cm separation, the charge overcomes the surface tension of the deformed drop of the suspended polymer solution formed on the tip of the syringe and a jet is produced. Since the polymer molecules all bear the same (positive) charge, they repel each other while traveling in air during a few milliseconds from the anode to cathode and become separated. [5] At the same time, evaporation of the solvent molecules occurs rapidly. Evaporation of solvent is also enhanced because the similarly-charged (positive) solvent molecules repel each other. Under appropriate conditions, dry, meters-long fibers accumulate on the surface of the cathode resulting in a non-woven mesh of nano- to micron diameter fibers.

3. Results and Discussion

3.1. Nanofiber Fabrication

Since the submicron fibers (500 -1,600 nm) obtained in our initial work (See Fig. 1) were not classifiable as true "nanofibers," our immediate objective was to break the "nanotechnology barrier" and to consistently and reproducibly fabricate true nanofibers (diameter <100 nm) of an organic polymer.

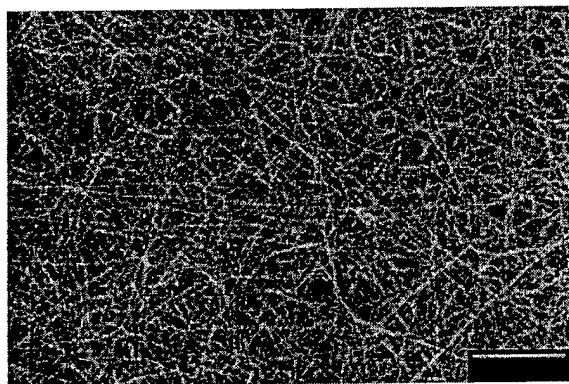


Figure 1. 50 wt% Nanofiber blend of PAn.HCSA fabricated from 2 wt% PAn.HCSA and 2 wt% PEO from chloroform solution at 25,000 V (anode/cathode separation, 25 cm). Scale bar: 100,000 nm. [6]

This was accomplished (see Fig. 2) using a 8 wt% solution of polystyrene (Mw 212,400; Aldrich Co.) in THF (glass pipette orifice: 1.2 mm) at a potential of 20,000 V between the anode and cathode which were separated by 30 cm. The fibers were collected as a mat on an aluminum

target and found by SEM to have diameter characteristics: average, 43.1 nm; maximum, 55.0 nm; minimum, 26.9 nm. Other studies involving polystyrene gave fibers whose diameters were consistently < 100 nm. For example, another sample of polystyrene had the following fiber diameter characteristics: average, 30.5 nm; maximum, 44.8 nm; minimum, 16.0 nm. It might be noted that these data represent a decrease (approximately two orders of magnitude) in fiber diameter as compared to those obtained in our earlier studies (Fig. 1). It might also be noted that the above 16 nm fiber is ~ 30 polystyrene molecules wide. Dimensions of this size will be expected to greatly affect the kinetics, as well as possibly the thermodynamics, of the polymer. It is also of interest to note that a 16 nm fiber such as the one mentioned above lies well within the ~ 4 - 30 nm diameter range of multi-walled carbon nanotubes.[8]

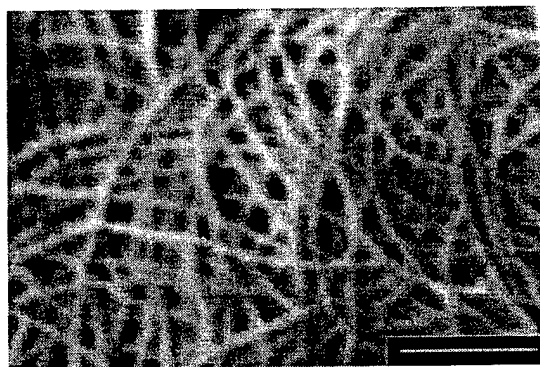


Figure 2. Electrospun fibers of polystyrene (see text). Scale bar: 1000 nm. The extended length of the fibers is clearly visible.[7]

3.2. Electronic Polymer Fibers

By using a previously observed method for producing polyaniline fibers [9] we have prepared highly conducting sulfuric acid-doped polyaniline fibers (average, 139 nm; maximum, 275 nm; minimum, 96nm) by placing a ~ 20 wt% solution of polyaniline (Versicon™, Allied Signal) in 98% sulfuric acid in a glass pipette with the tip ~ 3 cm above the surface of a copper cathode immersed in pure water at 5,000 V potential difference. The fibers collect in or on the surface of the water. The conductivity of a single fiber was ~ 0.1 S/cm, as expected since partial fiber dedoping occurred in the water cathode. The diameter and length of the fibers appear (Figure 3) to be sensitive to the nature of the polyaniline used. This is not necessarily surprising since, as is well known, "there are as many different types of polyaniline as there are people who make it!" No great difficulty is foreseen in producing fibers < 100 nm diameter.

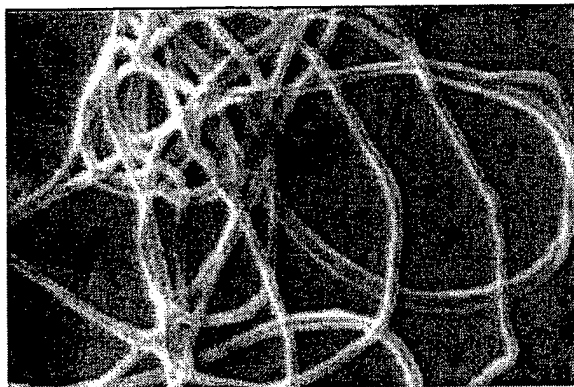


Figure 3. 100% polyaniline fiber with an average diameter of 139 nm.

It is relatively easy to prepare conducting blends of PAn.HCSA in a variety of different conventional polymers such as PEO, polystyrene, polyacrylonitrile, etc. For example, ~ 20 wt% blends of PAn.HCSA in polystyrene (Mw 114,200) are obtained by electrospinning a chloroform solution; fiber diameter characteristics: average, 85.8 nm; maximum, 100.0 nm; minimum 72.0 nm. These fibers are sufficiently electrically conductive that their SEMs may be recorded without the necessity of applying a gold coating.

Separate, individual nanofibers can be collected and examined if so desired. An appropriate substrate—glass slide, silicon wafer or loop of copper wire, etc.—is held between the anode and cathode at a position close to the cathode for a few seconds to collect individual fibers (see Fig. 4).



Figure 4. Polystyrene fibers collected on a bent copper wire (magnification 33x) and subsequently coated with a thin layer of polypyrrole by *in situ* deposition from aqueous solution. [13] Scale bar: 1 mm.

The fibers on the copper wires are in a good configuration for certain electrical studies.

Current/voltage (I/V) curves are given in Fig. 5 for a single 419 nm diameter fiber (Fiber 1) of a blend of 50 wt% PAn.HCSA and polyethylene oxide collected on a silicon wafer coated with a thin layer of SiO₂. Two gold electrodes separated by 60.3 μ m are deposited on the fiber

after its deposition on the substrate. The conductivity (two probe) of Fiber 1 (diameter ~ 600 nm) is ~ 10⁻¹ S/cm. The conductivity (two probe) of Fiber 2 (diameter ~ 419 nm) is ~ 10⁻¹ S/cm. Non-linear I/V curves may be obtained from some polyaniline samples, possibly caused by the presence

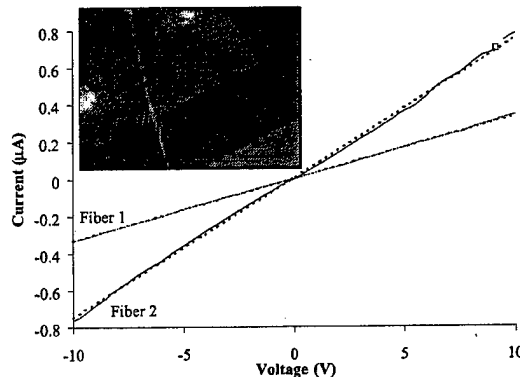


Figure 5. Current/voltage curves of 50 wt% PAn.HCSA/PEO blend nanofiber.

of defect sites induced by imperfections or impurities in the polyaniline. Such imperfections are expected to be more apparent in thin fibers since there are fewer molecular pathways by which charge carriers can by-pass the defect sites.

The (reversible) conductivity/temperature relationship between 295 K and 77 K for a single 1,320 nm fiber containing (72 wt% PAn.HCSA in PEO) spun from chloroform solution is given in Fig. 6. To minimize heating effects the applied voltage was held constant at 10 mV, at

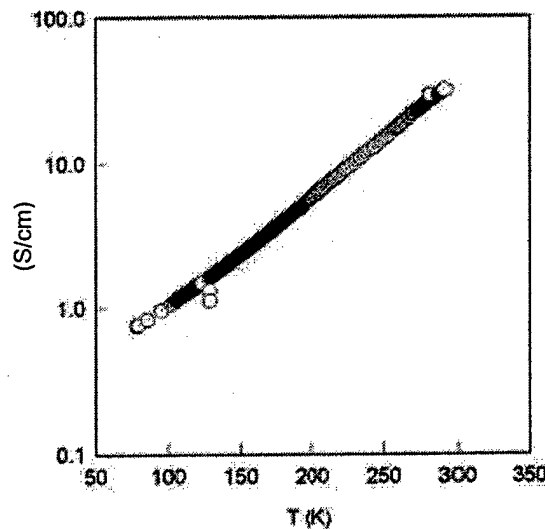


Figure 6. Conductivity/temperature relationship for a 72 wt% blend fiber of PAn.HCSA in PEO (see text).

which value the current is very small. The conductivity (~ 33 S/cm at 295 K) was unexpectedly large for a blend since the conductivity of a spun film of the pure polymer cast

from chloroform solution is only $\sim 10^{-1}$ S/cm. [11] This suggests there may be significant alignment of polymer chains in the fiber [12].

3.3 Nanofibers as Substrates

The large surface to volume ratio offered by nanofibers makes them excellent, potentially useful substrates for the fabrication of coaxial nanofibers consisting of superimposed layers of different materials. Catalysts and electronically active materials can be deposited by chemical, electrochemical, solvent, chemical vapor, or other means, for use in nanoelectronic junctions and devices.

We have found, for example, that polyacrylonitrile nanofibers can be easily and evenly coated with a 20-25 nm layer of conducting polypyrrole (Fig. 7) by immersion in an aqueous solution of polymerizing polypyrrole. [10,13] Analogously, we have found that electroless deposition of metals can also be performed. Polyacrylonitrile fibers, for example, can be evenly coated with gold by treatment with a solution of AuS_2O_3 and ascorbic acid. [14]

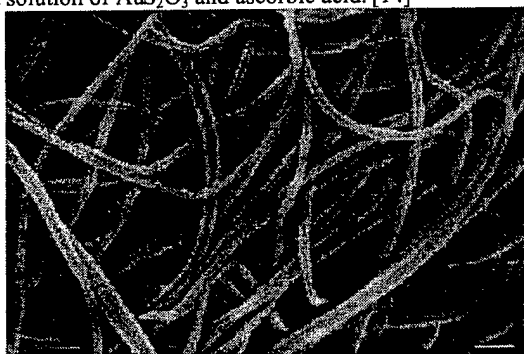


Figure 7. Conducting polypyrrole coated polyacrylonitrile nanofibers. Scale bar: 1000 nm.

3.4 Carbon Nanofibers

As previously reported [15] polyacrylonitrile fibers may be thermally converted to carbon nanofibers with some shrinkage. We have similarly converted a polyacrylonitrile fiber (diameter 750 nm) to a carbon fiber by first heating at 200°C in air for 20 minutes followed by heating at 800°C for 2 hours under nitrogen. A current/voltage curve was obtained for a 600 nm diameter carbon fiber. The controlled conversion of organic electrospun polymer fibers presents interesting opportunities for the fabrication of a variety of carbon nanofibers.

Summary

A new approach to molecular electronics – a general simple, inexpensive, method for controllably generating

electronic polymer fibers which are only a few molecules thick is presented as detailed below:

- (1) It is possible to consistently fabricate true nanofibers of an organic polymer electrostatically in which the diameters of *all* fibers in a given preparation are $< 100\text{nm}$ and hence fall well within the definition of a nanomaterial. Blends of conducting polyaniline in polystyrene which fall within this category have been produced.
- (2) Submicron fibers (down to 96 nm) of 100% doped polyaniline were consistently electrostatically generated.
- (3) In view of the above findings, it is confidently predicted that true nanofibers of both doped and non-doped electronic polymers can be fabricated such that all fibers in a given preparation have diameters $< 100\text{ nm}$.
- (4) The demonstrated fabrication of coaxial cladding of nanofibers with electronic polymers and metals presents the possibility of p/n junctions, Schottky barriers and the like in true nanoelectronic devices.

Acknowledgements

This work was financed jointly by the Office of Naval Research and the Army Research Office under the Multidisciplinary University Research Institute (MURI) program and the University of Pennsylvania Materials Science Laboratory (NSF Grant # DMR-9872689).

References

- [1] "Nanotechnology- A Revolution in the Making – Vision for R&D in the Next Decade," report of the Interagency Working Group on Nanoscience, Engineering, and Technology, March 10, 1999.
- [2] A. Formhals, US patent No. 1,975,504, 1934.
- [3] J. Doshi, D. H. Reneker, J. Electrostat. 35 (1999)
- [4] P. W. Gibson, H.L. Schreuder-Gibson, D. Riven, AIChE J. 45 (1999) 190.
- [5] D.H. Reneker, A. L. Yarin, H.Fong, S. Koombhongse, J. Appl. Phys. 87 (2000) 4531.
- [6] I.D. Norris, M.M. Shaker, F.K. Ko and A.G. MacDiarmid, Synthetic Metals, 114(2) (2000) 109.
- [7] Measurements of fiber diameter characteristics were completed directly on a high resolution SEM screen and have better accuracy than printed reproductions.
- [8] S. Iijima, Nature, 354, 56, 1991.
- [9] D.H. Reneker and I. Chun, Nanotechnology, 7(3) (1996) 216.
- [10] Z. Huang, P.-C. Wang, A.G. MacDiarmid, Y. Xia, and G. M. Whitesides, Langmuir, 13 (1997) 6480.
- [11] Y. Xia, A.G. MacDiarmid, A.J. Epstein, Macromolecules, 27 (1994) 7212.
- [12] A.G. MacDiarmid, Y. Min, J.M. Wiesinger, E.J. Oh, E.M. Scherr and A.J. Epstein, Synthetic Metals, 55 (1993) 753; S.J. Pomfret, P.N. Adams, N.P. Comfort, A.P. Monkman, Polymer, 41 (2000) 2265.
- [13] R.V. Gregory, W.C. Kimbrell and H.H. Kuhn, Synthetic Metals, 28(1-2) (1989) C823.
- [14] A.M. Sullivan and P.A. Kohl, J. Electrochem. Soc., 142(7) (1995) 2250.
- [15] I. Chun, D.H. Reneker, H. Fong, X. Fang, J. Deitzel, N.B. Tan K. Kearns J. Advanced Materials, 31 (1999) 36.

SECTION 2

**NORTH
CAROLINA
STATE
UNIVERSITY**

ARO Final Progress Report

Sam Hudson
NCSU

Advanced Polymers, Initiative 1.2 Core Filled Hollow Fibers and also Bioengineered Polymers, Initiative 1.3.

2.b.4 Statement of Problem

Init. 1.2 The objective of this project is to develop a class of smart fibers based on the concept of core filled hollow fibers. The mechanical, chemical and perhaps optical properties of the fiber might then be controllable at will, i.e. by application of an externally applied field.

Init. 1.3 The objective of this project is to evaluate the spinnability of silk-like fibrous proteins. Traditional wet spinning extrusion methods, along with methods such as shear precipitated pulps would be included.

2.b.5 Summary

1. Init. 1.2 Polypropylene and poly(ethylene terephthalate) (PET) have been blended together by others such as Cheung, Man Ken and David Chan, "Mechanical and Rheological Properties of Poly(ethylene terephthalate)/Polypropylene Blends," Polymer International, vol. 43, 1997, pp 281-287. However, the resulting polymer blends tended to phase separate, leading to decreased performance from fiber samples. The polymers were blended by simply feeding polymer chips together into an extruder. The resulting fibers had very little cohesion. In order to produce a more uniform blend, an additional step was added. The polypropylene and PET were blended in a bench-top extruder to form composite polymer chips. These chips were then extruded to form fibers. It was believed that this extra step would produce a fiber with a more uniform distribution of PET within the polypropylene. Another potential product of this technique would be to produce a fiber with a microporous network. For this to occur, the PET would be removed after the fiber is extruded. This is possible because the PET should blend with the polypropylene physically, but not chemically.

The PP/PET blends produced using the Atlas LME blender give a more consistent mixture than simply adding the polymers to the Killion extruder. The blend chips can then be fed to another extruder to produce a fiber. The blends of PET and PP formed separate networks, as shown by SEM photos and through experimental analysis. The thermal scans and dynamic mechanical analysis showed that these separate networks did not interact chemically. Any mixing which took place was totally physical. In compositions with 0-50% PET, the PP was the continuous phase, while blends with

greater than 50% PET had the PET as the continuous phase. The blend containing 40% PET gave the most favorable results. Since PET was the polymer that was to be extracted to form a porous network, a significant amount of PET had to be contained within the mixture in order to have the pores connect.

The major variables in producing a hollow fiber on the Killion were melt temperature, extruder RPM, and the pressure of the nitrogen feed gas. For the PET/PP blends, the melt temperature required depended on the amount of PET in the blend. As the percent PET increased, the temperature increased also. The optimal extruder screw speed was around 15 RPM. This speed forced an even flow of polymer through the tip of the extruder.

The extraction solution using NaOH and Vircon A-34 was the most effective at removing the PET from the hollow fiber structure. When the solution was heated to a temperature of 105°C, the solution efficiently attacked the fiber. The amount of time that the fiber sample was left in solution also effected the extraction. A second step to insure thorough removal of any residual terephthalic acid was to rinse the fiber sample with dioxane. The dioxane dissolved the terephthalic acid, leaving the PP network as the remaining structure. The solution cannot attack a solid fiber structure as efficiently as a hollow fiber because the solution can only attack the outer surface. The solution can dissolve the PET on the surface, but cannot penetrate the structure. In contrast, the solution can attack the hollow fiber from the inner and outer surfaces, leading to more efficient extraction of the PET. The SEM showed that the terephthalic acid was successfully removed from the fiber, leaving the center and the pores clear. Based on these results, rinsing any samples with dioxane after extraction seems to be a method to completely remove PET or any residual material from the fiber.

Init1.3 In the past few years, there have been increasing interests in the use of silk fibroin in biomedical applications and biotechnological fields. The reason for this increased interest is its excellent mechanical properties combined with flexibility, blood compatibility, and high oxygen permeability in the wet condition. To utilize this excellent material, it should be regenerated into desirable forms such as powder, film, fiber, or non-woven. Also, *Bombyx mori* silk fibroin may be considered as a model system for other semi-crystalline fiber forming proteins, becoming available through biotechnology (www.nexiabiotech.com).

Bombyx mori silk fibroin is known to be dissolved in neutral salt-alcohol systems without degradation of its molecular weight. Lithium bromide- or lithium thiocyanate-ethanol system and hexafluoroisopropanol (HFIP) have been widely used to dissolve silk fibroin. Mathur et al. studied the dissolution behavior of *Bombyx mori* silk fibroin using the calcium nitrate-methanol ($\text{Ca}(\text{NO}_3)_2\text{-MeOH}$) system and regenerated thin films were prepared from this solution and characterized by several analytical methods.

This paper reports a further study of *Bombyx mori* silk fibroin solution using the calcium nitrate-methanol system to regenerate fibroin into a fiber form. The dissolution of silk fibroin as related to the roles of salt, alcohol, and water; and coagulation of the fibroin solution are discussed. A compositional phase diagram was constructed at various concentrations of the solvent system. In the case of salt-alcohol systems, the remaining salt concentration after dialysis has always been a problem. However, there have been no

concerns about the amount of salt in the dialyzed fibroin solution. Atomic absorption analysis revealed that the calcium cations strongly interact with fibroin molecules in dialyzed fibroin solution. The diffusion coefficient of the coagulant, methanol, into fibroin dope solution was calculated using the Stoke-Einstein equation. The properties of the as-spun fiber were characterized by X-ray diffraction, differential scanning calorimeter (DSC), and scanning electron microscopy (SEM). Regenerated fibroin powders from undialyzed fibroin solution in several coagulants showed different conformations. The properties of both original and regenerated fibroin such as solubility in water and thermal behaviors using DSC were compared. X-ray diffractogram showed that the regeneration process decreased the crystallinity of regenerated fibroin fiber. Surface and cross sectional images showing viscous fingering phenomena of the regenerated fibroin fibers were captured by SEM.

2.b.6.d Manuscript Submitted

The Dissolution of *Bombyx mori* Silk Fibroin in the Calcium Nitrate Tetrahydrate-Methanol System and Wet Spinning of the Fibroin Solution. Sung-Won Ha, Young Hwan Park and Samuel M. Hudson
Submitted to Biomacromolecules

2.b.7 Participating Personnel

Prof. John A. Cuculo

Dr. Gang Wu

Tom Patterson (earned MS Tex. Chem. Degree NCSU 1999)

Sung Won Ha (earned MS Tex. Chem. Degree NCSU 2000)

Overall Summary of Accomplishments during the 6 Years For
Initiative 1.2 (Advanced Polymers & Fibers) in the ARO/MURI
Research Program "Functionally Tailored Textiles"

PI: Alan E. Tonelli, College of Textiles, NCState

Graduate students: Lei Huang, Jin Lu, and Francis Porbeni

Our research has progressed primarily along the front of induction of chain-extended crystalline morpholgy and formation of intimately mixed polymer blends. When PET, polycarbonate (PC), and nylon-6 were coalesced and consolidated from their inclusion compounds (ICs) formed with γ -cyclodextrin (CD), we found their structures, morphologies and even their conformations to be significantly modified in comparison to their solid samples formed from solution or the melt. Coalesced nylon-6 shows a dramatic increase in crystallinity while coalesced PC melts $\sim 15^\circ\text{C}$ higher than solution crystallized PC. PET coalesced from its γ -CD-IC rapidly crystallizes from the melt and never evidences normal amorphous behavior, such as a T_g or recrystallization upon heating a quenched melt. We are currently scaling-up the production of such coalesced polymer samples to explore their macroscopic physical characteristics. With the assistance of several undergraduate students, we have formed CD-ICs from solutions of 2 different polymers, which, after coalescence produce polymer-polymer blends with an enhanced miscibility of the blend constituents. Polycarbonate (PC)/PMMA and PC/PS blends coalesced from their common CD-ICs appear homogeneous by DSC, TGA, and FTIR measurements. In addition, heating both blends for several hours above their component T_g s did not result in phase separation/demixing. Thus we may have discovered a general means to obtain thermally stable intimate blends of normally incompatible polymers by simultaneous coalescence from their common CD-ICs. Most recently we have achieved intimately mixed PET/PEN blends by this means without recourse to inducing trans-esterification at high temperatures normally used to blend these aromatic polyesters.

We have also formed CD-ICs with biodegradable/bioabsorbable block copolymers, such as poly(ϵ -caprolactone) (PCL)-b-poly(L-lactic acid) (PLLA) and PCL-b-poly(R,S-3-hydroxybutyrate) (a-PHB), and have subsequently coalesced them from their CD-ICs by washing with hot water or by enzymatic degradation of CD with an amylase. In general, we find these CD-IC coalesced block copolymers to be significantly less phase separated than their solution cast samples, which results in a dramatic reduction in their crystallinities. As a consequence, we find the biodegradation of the coalesced block copolymers can be significantly enhanced and controlled, thereby suggesting their utility as agents for the controlled delivery of drugs or additives.

We have also formed high-melting crystalline CD-ICs with a variety of small molecules used as polymer additives, such as dyes, antibacterials, flame retardants, antistats, antifoulants, and spermicides. These additive-CD-ICs were melt-processed into polymer films and fibers, and this mode of additive delivery was tested for efficacy in several instances. In particular antibacterial films, fibers, and a cotton fabric laminated with several biodegradable/bioabsorbable polymers were achieved by means of CD-IC delivery. Also embedding a few weight % of a flame-retardant (FR)-CD-IC into PET film provided a significant improvement in flame protection in comparison to PET con-

taining a similar amount of the same FR padded-on from a bath and then baked into the PET film. Furthermore, because the FR does not directly contact the PET or the wearer of FR-CD-IC/PET, much more aggressive FRs, which might normally be toxic, can be safely delivered by the CD-IC route.

In general we expect such CD-IC processing of polymer films and fibers to significantly enhance the functionalities and capabilities of the uniforms worn by the 21st Century Warrior.

Recent Publications:

"Creation of Polymer Films with Novel Structures and Properties by Processing with Inclusion Compounds", L. Huang, M. Gerber, H. Taylor, J. Lu, E. Tapaszi, M. Wutkowski, M. Hill, F. N. Nunalee, A. Harvey, C. C. Rusa, F. Porbeni, E. Edeki, and A. E. Tonelli, ACS Symposium Series # 790, "Film Formation", T. Provder and M. Urban, Eds., Amer. Chem. Soc., Wash, DC, 2001, Chap. 14.

"Fundamental Studies of Crystalline Polymer-Cyclodextrin Inclusion Compounds: Formation Kinetics and Thermodynamics, Separation of Polymers by Chemical Type and Molecular Weight, and Observations of the Mobilities of the Included Polymer Chains" and "Formation of polymer-Polymer Composites and Delivery of Additives to Polymers via the Embedding and Coalescence of Crystalline Polymer- and Additive-Cyclodextrin Inclusion Compounds", C. C. Rusa, J. Lu, L. Huang, P. A. Mirau, and A. Tonelli, Proceedings of the 10th International Cyclodextrin Symposium (CD-2000), May 21-24, 2000, Ann Arbor, Mich., J. Szejtli, Ed., Mira Digital Publ. (314-776-6666), 2001.

"Formation of Polymer-Polymer Composites and Delivery of Additives to Polymers via the Embedding and Coalescence Of Crystalline Polymer- and Additive-Cyclodextrin Inclusion Compounds", C. C. Rusa, J. Lu, L. Huang, and A. E. Tonelli, "Cyclodextrin: From Basic Research to Market", Proceedings of the 10th International Cyclodextrin Symposium (CD-2000), May 21-24, 2000, Ann Arbor, Michigan, J. Szejtli, Ed., Mira Digital Publ. (314-776-6666), 2001.

"Chain Conformations and Dynamics of Crystalline Polymers as Observed in Their Inclusion compounds by Solid-State NMR", J. Lu, P. A. Mirau, and A. E. Tonelli Prog. Polym. Sci., 27, 357, 2002.

"Creation of Unique Polymer Materials by Processing with Inclusion Compounds", L. Huang, M. Gerber, H. Taylor, J. Lu, E. Tapaszi, M. Wutkowski, M. Hill, A. Harvey, C. C. Rusa, M. Wei, C. S. Lewis, and A. E. Tonelli, Macromol. Chem., Macromol. Sympos., in press, 2001.

"Polymer-Cyclodextrin Inclusion Compounds: Towards New Aspects of Their Inclusion Mechanism", Macromolecules, 34, 1318, 2001.

"Compatibilization of Polymers via Coalescence from their Common Inclusion Compounds with Cyclodextrins", M. Wei and A. E. Tonelli, Macromolecules, 34, 4061, 2001.

"Reorganization of the Structures and Morphologies of Bulk Polymers via Coalescence from their Polymer-Cyclodextrin Inclusion Compounds", M. Wei and A. E. Tonelli, J. Polym. Sci, Polym Phys. Ed., accepted, 40, xxxx, 2002.

"Inclusion Compounds Consisting of Host γ -Cyclodextrin and Poly(ethylene terephthalate) and Bisphenol-A Polycarbonate Guests: Formation and Characterization", T. A. Bullions, M. Wei, F. E. Porbeni, M. J. Gerber, J. Peet, M. Balik, and A. E. Tonelli, *Macromolecules*, 35, xxxx, 2002.

"Formation of and Coalescence from the Inclusion Complex of A Biodegradable Block Copolymer and α -Cyclodextrin", X. Shuai, F. E. Porbeni, M. Wei, I. D. Shin, and A. E. Tonelli, *Macromolecules*, 34, 7355, 2001.

"Formation of and Coalescence from the Inclusion Complex of A Biodegradable Block Copolymer 2: A Novel Way to Regulate the Biodegradation Behavior of Biodegradable Block Copolymers", X. Shuai, M. Wei, F. E. Porbeni, T. A. Bullions, and A. E. Tonelli, *Biomacromolecules*, 3, 201, 2002.

"Formation of Inclusion Complexes of Poly(3-hydroxybutyrate)s with Cyclodextrin 1: Immobilization of Atactic-Poly(R,S-3-hydroxybutyrate) and Miscibility Enhancement Between Poly(R,S-3-hydroxybutyrate) and Poly(ϵ -caprolactone)", X. Shuai, F. E. Porbeni, M. Wei, T. A. Bullions, and A. E. Tonelli, *Macromolecules*, 35, 7355, 2002.

"Inclusion Complex Formation between α , γ -Cyclodextrins and a Triblock Copolymer and the Cyclodextrin Type-Dependent Microphase Structures of Their Coalesced Samples", X. Shuai, F. E. Porbeni, M. Wei, T. A. Bullions, and A. E. Tonelli, *Macromolecules*, 35, xxxx, 2002.

Educational contributions:

Lei Huang, Jin Lu, and Francis Porbeni Ph.D. Candidates. Lei Huang and Jin Lu obtained their Ph.D.s in 1998 and 2001, respectively, and Francis Porbeni will defend his Ph.D. Thesis in Spring 2002. Lei Huang is doing research at Kimberly-Clark in Atlanta after a post-doc. At Emory, and Jin Lu will shortly join Rohm & Haas Research in Philadelphia after a post-doc. at U. of Penn. with Nobel laureate Alan McDairamid.

Mehgan Wutkowski, Efe Edeki, Chris Lewis, April Herndon, Kristen Jenkins, Michael Gerber, Chris Lewis, Dale Greeson, Elizabeth Tapaszi, A. Harvey, Brad Urban, and Mary Gruenhagen have all assisted as undergraduate researchers.

Hiedi Taylor, Miriam Hood, Marcus Hill and Walter Davis were Am. Chem. Soc. Project **SEED** High School Student researchers.

Drs. Cristian Rusa and Todd Bullions were Post-Doctorals who were partially funded by this ARO-MURI.

Prof. Xintao Shuai visiting Prof. from the Chinese Academy of Sciences.

ARO-MURI Collaborators

Dr. Peter Mirau - Bell Labs.-Lucent Technologies

Prof. Dan Shin - Fayetteville State University

Prof. S. Nojima - Japan Adv. Inst. of Science & Technology

On behalf of all those above and myself, I would like to express my deepest appreciation to ARO for supporting our research during the past 6 years. Thank you!

ARO-MURI Publications

1. Formation, Characterization, and Segmental Mobilities of Block Copolymers in Their Urea Inclusion Compound Crystals, N. Vasanthan, I. D. Shin, L. Huang, S. Nojima, and A. E. Tonelli, *Macromolecules*, 30, 3014, 1997.
2. Polymer-Polymer Composites Fabricated by the in situ Release and Coalescence of Polymer Chains From Their Inclusion Compounds with Urea Into a Carrier Polymer Phase L. Huang, N. Vasanthan, and A. E. Tonelli, *J. Appl. Polym. Sci.*, 64, 281, 1997.
3. Polymer Inclusion Compounds: Model Systems for Ordered Bulk Polymer Phases and Starting Materials for Fabricating Polymer-Polymer Molecular Composites, A. E. Tonelli, *Polymer International*, 43, 295, 1997.
4. Study of the Inclusion Compounds formed Between α -Cyclodextrin and High Molecular Weight Poly(ethylene oxide) and Poly(ϵ -caprolactone) L. Huang, E. Allen, and A. E. Tonelli, *Polymer*, 38, 4857, 1997.
5. Modeling Ordered Bulk Polymer Phases and Fabricating Polymer-Polymer Molecular Composites with Polymer Inclusion Compounds, L. Huang, E. J. Allen, and A. E. Tonelli, *Recent Research Developments in Macromolecular Research*, S. G. Pandalai, Ed., Research Signpost, Trivandrum, India, 1997, Vol. 2, p. 175.
6. Inclusion Compounds as a Means to Fabricate Controlled Release Materials, L. Huang and A. E. Tonelli, *ACS Symposium Series # 728, Intelligent Materials for Controlled Release Technologies*, S. M. Dinh, J. D. DeNuzzio and A. R. Comfort, Eds., ACS, Washington, D.C., 1999, Chap. 10.
7. Polymer Inclusion Compounds, L. Huang and A. E. Tonelli, *J. Macromol. Science, Revs. Macromol. Chem. and Phys.*, C38(4),

781, 1998.

8. Inclusion Compounds formed between Cyclodextrins and Nylon 6, L. Huang, E. Allen, and A. E. Tonelli, *Polymer*, 40, 3211, 1999.
9. NMR Observation of the Conformations and Motions of Polymers Confined to the Narrow Channels of Their Inclusion Compounds, D. I. Shin, L. Huang, and A. E. Tonelli, *Macromolecular Chemistry, Symposium Ed.*, 138, 21, 1999.
10. Formation of Antibiotic, Biodegradable/Bioabsorbable Polymer by Processing with Neomycin Sulfate and Its Inclusion Compound with β -Cyclodextrin, L. Huang, H. Taylor, M. Gerber, P. Orndorff, J. Horton, and A. E. Tonelli, *J. Appl. Polym. Sci.*, 74, 937, 1999.
11. Formation and Characterization of the Inclusion Compounds between Poly(e-caprolactone)-Poly(ethylene oxide)-Poly(e-caprolactone) Tri-block Copolymer and α - and γ -Cyclodextrins, J. Lu, I. Daniel Shin, S. Nojima, and A. E. Tonelli, *Polymer*, 41, 5871, 2000.
12. Formation of a Flame Retardant-Cyclodextrin Inclusion Compound and Its Application as a Flame Retardant for Poly(ethylene terephthalate), L. Huang, M. Gerber, J. Lu, and A. E. Tonelli, *Polym. Degrad. Stabil.*, 71, 279, 2001.
13. Formation of Antibiotic, Biodegradable Polymers by Processing with Irgasan DP300R (Trichlosan) and Its Inclusion Compound with β -Cyclodextrin, J. Lu, M. Hill, M. Hood, D. F. Greeson, Jr., J. R. Horton, P. E. Orndorff, A. S. Herndon, and A. E. Tonelli, *J. Appl. Polym. Sci.*, 82, 300, 2001.
14. Separation of Polymers by Molecular Weight Through Inclusion Compound Formation with Urea and α -Cyclodextrin Hosts, C. C. Rusa and A. E. Tonelli, *Macromolecules*, 33, 1813, 2000.
15. Polymer/Polymer Inclusion Compounds as a Novel Means to Obtaining a PLLA/PCL Intimately Compatible Blend, C. C. Rusa and A. E. Tonelli, 33, 5321, 2000.
16. Creation of Polymer Films with Novel Structures and Prop-

erties by processing with Inclusion Compounds, L. Huang, M. Gerber, H. Taylor, J. Lu, E. Tapazsi, M. Wutkowski, M. Hill, F. N. Nunalee, A. Harvey, C. C. Rusa, F. Porbeni, E. Edeki, and A. E. Tonelli, in ACS Symposium Series # 790, "Film Formation in Coatings: Mechanisms, Properties, and Morphology", T. Provder and M. Urban, Eds., Am. Chem. Soc., Wash., D.C., **2001**, Chap. 14.

17. Structure and Dynamics of Isolated Polymer Chains in Cyclodextrin Inclusion Compounds, A. E. Tonelli, J. Lu, I. D. Shin, and P. A. Mirau, PMSE Preprints (Am. Chem. Soc.), **82**, 163, **2000**.
18. Fundamental studies of Crystalline Polymer-Cyclodextrin Inclusion Compounds: Formation Kinetics and Thermodynamics, Separation of Polymers by Chemical Type and Molecular Weight, and Observations of the Mobilities of the Included Polymer Chains, J. Lu, P. A. Mirau, C. C. Rusa, and A. E. Tonelli, "Cyclodextrin: From Basic research to Market", Proceedings of the 10th International Cyclodextrin Symposium (CD-2000), May 21-24, 2000, Ann Arbor, Michigan, J. Szejtli, Ed., Mira Digital Publ. (314-776-6666), **2001**.
19. Formation of Polymer-Polymer Composites and Delivery of Additives to Polymers via the Embedding and Coalescence Of Crystalline Polymer- and Additive-Cyclodextrin Inclusion Compounds, C. C. Rusa, J. Lu, L. Huang, and A. E. Tonelli, "Cyclodextrin: From Basic Research to Market", Proceedings of the 10th International Cyclodextrin Symposium (CD-2000), May 21-24, 2000, Ann Arbor, Michigan, J. Szejtli, Ed., Mira Digital Publ. (314-776-6666), **2001**.
20. The Dynamics of Isolated Polycaprolactone Chains in Their Inclusion Complexes with Cyclodextrins, J. Lu, P. A. Mirau, And A. E. Tonelli, *Macromolecules*, **34**, 3276, **2001**.
21. Chain Conformations and Dynamics of Confined Polymers as Observed in Their Crystalline Inclusion Compounds by Solid State NMR, J. Lu, P. A. Mirau, and A. E. Tonelli, *Prog. Polym. Sci.*, **27**, 357, **2002**.
22. Creation of Unique Polymer Materials by Processing with Inclusion Compounds, L. Huang, M. Gerber, H. Taylor, J. Lu, E. Tapazsi, M. Wutkowski, M. Hill, A. Harvey, C. C. Rusa, M. Wei, C. S. Lewis, and A. E. Tonelli, *Macromol. Chem., Macromol. Sympos.*, **176**, 129, **2001**.

23. Formation and Characterization of the Inclusion Complexes Between Poly(dimethyl siloxanes) and Polyacrylonitrile with γ -CD, F. E. Porbeni, E. M. Edeki, I. D. Shin, and A. E. Tonelli, *Polymer*, 42(16), 6907, **2001**.
24. Molecular Motions in Supramolecular Complexes between Poly(ϵ -caprolactone)-Poly(ethylene oxide)-Poly(ϵ -caprolactone) and Cyclodextrins, J. Lu, P. A. Mirau, I. D. Shin, S. Nojima, and A. E. Tonelli, *Macromol. Chem. & Phys.*, 203, 71, **2001**.
25. Polymer-Cyclodextrin Inclusion Compounds: Towards New Aspects of Their inclusion Mechanism, C. C. Rusa, C. Luca, and A. E. Tonelli, *Macromolecules*, 34, 1318, **2001**.
26. Compatibilization of Polymers via Coalescence from their Common Inclusion Compounds with Cyclodextrins, M. Wei and A. E. Tonelli, *Macromolecules*, 34, 4061, **2001**.
27. Reorganization of the Structures and Morphologies of Bulk Polymers via Coalescence from their Polymer-Cyclodextrin Inclusion Compounds, T. A. Bullions, M. Wei, F. E. Porbeni, M. J. Gerber, J. Peet, M. Balik, and A. E. Tonelli, *J. Polym. Sci., Polym Phys. Ed.*, 40, xxxx, **2001**.
28. Formation of and Coalescence from the Inclusion Complex of A Biodegradable Block Copolymer and α -Cyclodextrin, X. Shuai, F. E. Porbeni, M. Wei, I. D. Shin, and A. E. Tonelli, *Macromolecules*, 34, 7355, **2001**.
29. NMR Studies of the Dynamics of Homo- and Block-Co-polymer Poly(ϵ -caprolactone) Chains in Their Inclusion compounds With α - and γ -CDs, J. Lu, P. A. Mirau, S. Nojima, and A. E. Tonelli, in "NMR of Polymers Symposium", H. N. Cheng and A. English, Eds., Am. Chem. Soc. Sympos. Ser.# XXX, Wash., DC, **2002**, Chap. YY.
30. Formation of and Coalescence from the Inclusion Complex of A Biodegradable Block Copolymer 2: A Novel Way to Regulate the Biodegradation Behavior of Biodegradable Block Copolymers, X. Shuai, M. Wei, F. E. Porbeni, T. A. Bullions, and A. E. Tonelli, *Biomacromolecules*, 3, 201, **2002**.

31. Formation of Inclusion Complexes of Poly(3-hydroxybutyrate)s with Cyclodextrin 1: Immobilization of Atactic-Poly(R,S-3-hydroxybutyrate) and Miscibility Enhancement Between Poly(R,S-3-hydroxybutyrate) and Poly(ϵ -caprolactone), X. Shuai, F. E. Porbeni, M. Wei, T. A. Bullions, And A. E. Tonelli, *Macromolecules*, 35, xxxx, 2002.
32. Inclusion Complex Formation between α,γ -Cyclodextrins and a Triblock Copolymer and the Cyclodextrin Type-Dependent Microphase Structures of Their Coalesced Samples), X. Shuai, F. E. Porbeni, M. Wei, T. A. Bullions, and A. E. Tonelli, *Macromolecules*, 35, xxxx, 2002.
33. Intimate Blend of Poly(ethylene terephthalate) and Poly(ethylene 2,6-naphthalate) via Formation with and Coalescence From Their Common Inclusion Compound with γ -Cyclodextrin, T. A. Bullions, E. M. Edeki, F. E. Porbeni, M. Wei, X. Shuai, and A. E. Tonelli, *J. Polym. Sci., Polym. Phys. Ed.*, YY, xxxx, 2002.
34. Biodegradable Polymers Enzymatically Coalesced from Their Cyclodextrin Inclusion Complexes, I. Melting Behavior and Isothermal Crystallization, M. Wei, X. Shuai, and A. E. Tonelli, *Macromolecules*, 35, xxxx, 2002.
35. Biodegradable Polymers Enzymatically Coalesced from Their Cyclodextrin Inclusion Complexes. II. Non-isothermal Crystallization, M. Wei, X. Shuai, and A. E. Tonelli, *Macromolecules*, YY, xxxx, 2002.

Functionally Tailored Textiles

3-D Fabric Structures through Meltblown Technology

Final Report
May 2002

Principal Investigators
Tushar K. Ghosh
Abdelfattah M. Seyam

Graduate Students
Raoul Farer, Paul Nguyen, Yogeshwar Velu, and Abhay Mohan

College of Textiles
North Carolina State University
Raleigh, NC 27695-8301

Abstract

The specific aim of this project is to demonstrate the feasibility of direct garment manufacturing using advanced nonwoven fabric manufacturing technologies. The technology can be used to produce low cost combat uniforms with effective barrier characteristics, using minimal joining. The technology being developed may be used to incorporate fibers, powders, or other appropriate additives into the garment systems. The additives may identify, measure, absorb, and/or deactivate chemical/biological agents. The technology may be further enhanced to manufacture garments with embedded sensors that will generate information on the nature and severity of the attack.

We designed and built a complete Robotic Fiber Assembly Control (RFAC) system and the meltblowing equipment necessary for the development and demonstration of the technology. The RFAC system, which is designed to manipulate the melt-blowing die, consists of a six axis industrial robot and an integrated external seventh axis to drive any desired three-dimensional (3D) mold mannequin.

Parametric studies evaluating effect of manufacturing conditions on polypropylene melt-blown webs through analysis of fiber orientation distribution, fiber diameter distributions, pore size distribution have been completed. Fiber flaring profiles exiting from the die were investigated to develop a manufacturing model for uniform fiber lay-down on mold structures. Several control algorithms were developed to deposit fibers on a 3D mold mannequin in order to control the uniformity of fiber distribution over the mold body. The control algorithms included 2D and 3D modeling with rotation speeds of the mold and die speed and orientation manipulation allowed for optimization of fiber lay-down on molds when using the mold drive in conjunction with the robotics system.

A Study to investigate and control the structure of the meltblown webs deposited on the mannequin is near completion. The study deals with varying the curvature and change in the surface speed of the collecting surface.

An investigative study regarding the manufacturing of electrospun structures under various conditions (Voltage, Polymer Concentration, and spinneret-to-receiver distance) is near completion. After successfully producing electrospun fibers from solution using polyester resins, an investigation to produce the fine polypropylene fibers from melt is being conducted.

Scientific Progress and Accomplishment

The RFAC system developed in this research to create molded garments, or garment parts, based on meltblowing technology is shown in Figures 1 and 2. The technology could be utilized to manufacture combat uniforms to protect against hostile environments (chemical, biological, etc.).

- a. *Review of State of the Art:* Extensive review of published literature and patents has been carried out to understand the current status of knowledge in this area. Detailed discussion of the state-of-the-art has been completed in form of a thesis and publications listed at the end of the report. The state of the art does not include a process comparable to the RFACS production technology developed in this research.

- b. *Installation of Laboratory Scale Melt Blowing Equipment:* The equipment consists of an extruder equipped with a 3 inch wide die, with very small jet openings, through which the fibers are extruded by means of two sheets of hot pressurized air converging from the top and bottom of the orifices. The die is mounted inside of a small holding cage, which is attached as an end-effector to the six axis robotics system. The robot is used to manipulate the die to control the spray pattern of the fibers exiting the die. Two flexible hoses are attached to the die one of which supplies hot pressurized air, the other supplies molten polymer. The fiber deposition on the mold is further controlled by moving the mold in conjunction with the die, using a 7th axis (Figures 1 and 2).

Numerous molds have been used to produce three-dimensional fabrics to demonstrate capabilities of fiber deposition by using this novel production technology. Some of the three-dimensional fabrics formed were limbs, torsos, gloves, facemasks, and a structure to encapsulate bullet/shrapnel proof materials.

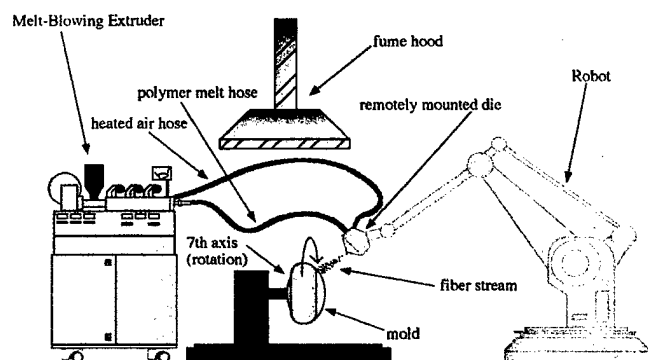


Figure 1 RFAC Set-Up Schematic.

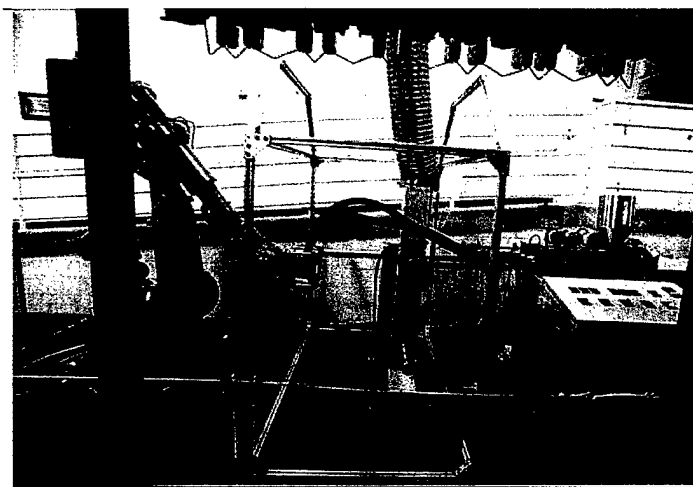


Figure 2 Photograph of RFAC Set-Up

- c. *Development of Mold Drive System:* In order to have better control of fiber deposition to form a 3-dimensional shape a mold drive system has been incorporated with the RFAC system and it is being used in conjunction with the six axis robotics system. This mold drive system has been constructed so that it easily allows for various structures to be mounted to, and removed from it, after 3D fabric formation (see Figure 3). Some of the mold structures used in conjunction with this drive system are collapsible, eliminating cutting steps to remove fabrics after forming, as well as subsequent re-seaming.

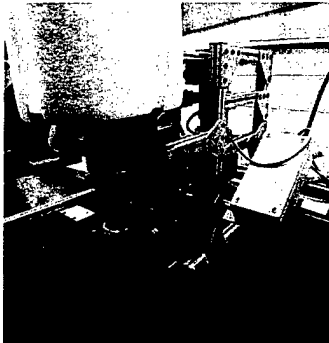


Figure 3 Seventh-Axis Support Structure Showing the Mold Mounted on the Lathe.

- d. *Development of Contour-Following Algorithm:* Study of different robotics control algorithms to achieve best contour-following on mold shapes has been conducted on the following systems:

1. Point-to-point programming
2. Distance/proximity sensing

1. Point-to-point programming is being used to control the robot movement according to manual measurements, which have been taken from mold objects.

2. Distance or proximity sensing provides an alternative approach to point-to-point programming. Through proper implementation of distance sensors the robot arm and melt-blowing die may be always automatically positioned at the same distance from a mold. Manipulating the robot directly using sensed distances can provide an online positioning approach to achieve contour-following on mold objects.

- e. *Investigation of basis weight uniformity:* A production algorithm for uniform basis weight control was developed. Contributions of the fiber flaring profile and robot motion was evaluated.

Fiber flaring profiles characterize the shape and size of the fiber approach stream at specific Die-to-Collector-Distance (DCD). These can be used to determine appropriate die movement depending on machine settings and DCDs used. Figure 4 shows a number of typical flaring profiles superimposed on each other. These profiles were determined using 0.35 bar air pressure and DCDs ranging from 2 to 34 cm. The profile in the center was taken at 2 cm DCD. Profiles below were taken at subsequently increasing DCDs.



Figure 4 Fiber Flaring Profile at 0.35 bar and DCD range of 2-34 cm.










The die, which is mounted on the end-effector of the robot sprays the fiber onto the mold mounted on the external seventh axis. Two models have been developed to control the movement of the die and the mold. The objective of the control models is to dispense a uniform fiber distribution onto the mannequin mold body. The quality of the fiber distribution is evaluated using a basis weight distribution, and expressing this distribution as a percent of coefficient of variation (CV%). The two models are:

- A 2D model which compensates for the die-to-collector-distance (DCD) position and height of the tool (melt-blowing die) on the mold.
- A 3D rule-based model which additionally adjusts the tool orientation such that it aligns the plane containing the row of die orifices parallel to the mold's forming surface in order to accommodate the curvature changes for a given mold.

In order to develop a simple rule-based control algorithm, a linear variable differential transducer (LVDT) was integrated into the system. The LVDT was mounted to the support frame structure of the external axis and a wheel was attached to the end of the displacement rod. The wheel of the LVDT was in direct contact with the surface of the mold. Thus the rotation of the mold causes the rod to have transnational displacements. The data from the LVDT was sent to the robot controller as voltage outputs ranging from -5 to +5 volts.

General geometric principles were used to establish four positions, or tool orientations, respective to an angular position of the mannequin mold. These positions were developed so that the row of polymer orifices spraying the meltblown fiber would be aligned approximately parallel to the surface of the continuously rotating mannequin. The control rules were established by using the data being gathered from the LVDT. We have adopted a qualitative approach with three curvatures (shallow, medium and deep curvatures) to correspond with the variation of the mold curvature that depends on which part of the torso the LVDT is on at any instant. Table 1 illustrates the control rules (tool orientation) along with the three qualitative curvatures adopted. Since the rate of change of displacement indicated which position of the torso was being measured (e.g. the curvature of the front part of the torso is shallow), the meltblowing die orientation would be adjusted accordingly.

Table 1: LVDT Control Rules

Torso	LVDT	Melt-Blowing Die
		
		
		

The basis weight distributions of the fabrics obtained from the 2D model, is shown in Figure 5. The CV values for the samples formed using the no-correction model (Figure 6) were eight percent higher than the CV values obtained using the linear correction. The two-layer structure of the fabric shows an improvement over the single layer structure of the fabric. The constraint in obtaining better uniformity in the center front and back regions is inherently related to the die orientation during the production of the fabric. Since, the die does not re-orient properly, in relation to the surface of the mannequin, fiber overshoot occurs. This results in more fiber accumulation in the center of the mannequin. The overshoot causes a large variation in the basis weight distribution on the side region. The rule-based control system developed will take into account the variation in the rotational speeds of the mannequin and also the position of the die in relation to the surface of the mannequin. Use of the rule-based control system produced a fabric with the lowest CV of 11% as can be seen in Figure 7.

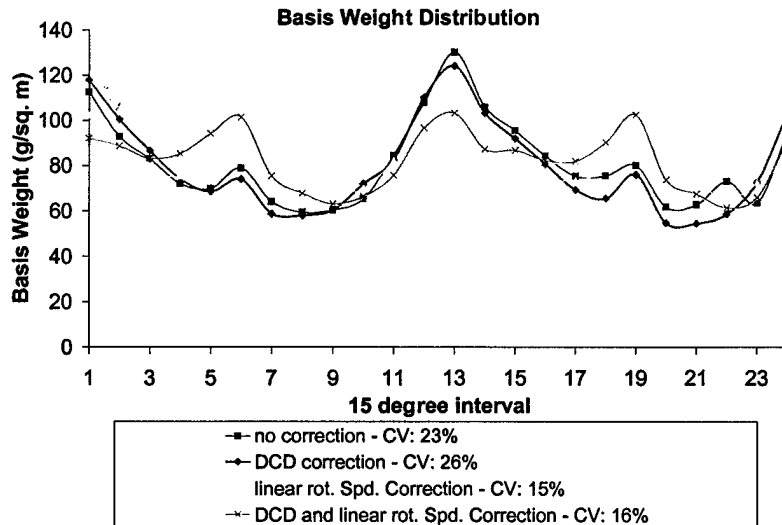


Figure 5: Two layer basis weight distribution using the 2D Model

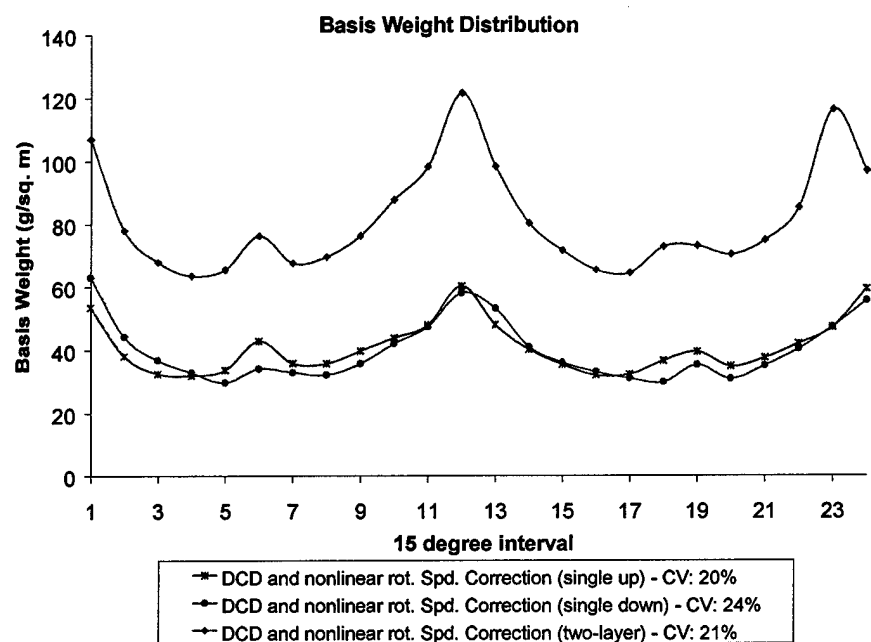


Figure 6: Single-Layer/Two-layer Basis-Weight Distribution using the 2D Model and Nonlinear Rotation Speeds

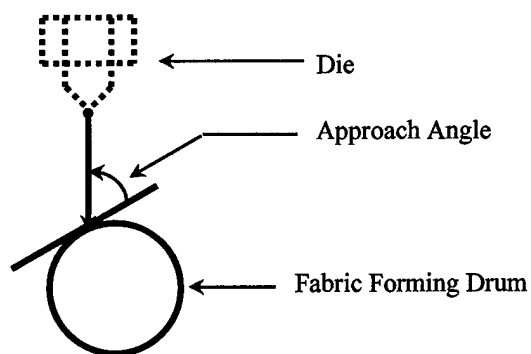


Figure 7: Rule-Based Control System – Basis weight Distribution

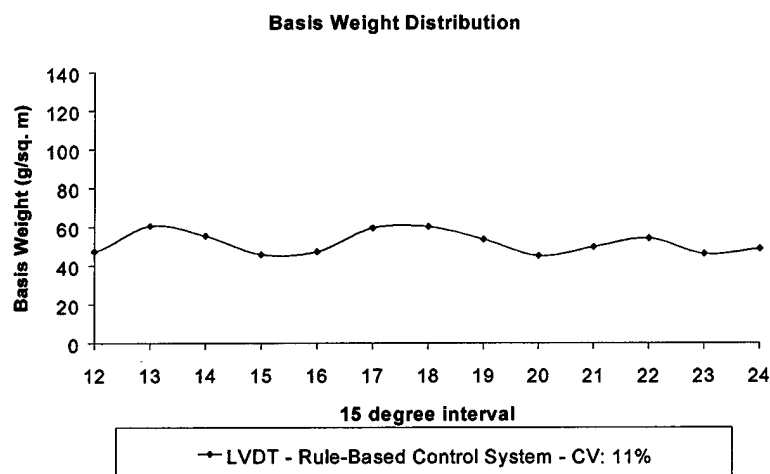


Figure 8: Fiber Stream Approach Angle Schematic

- f. *Parametric Studies:* The fiber web structure defined by the orientation distribution function (ODF) and fiber diameter distribution (FDD) governs the anisotropic nature of the mechanical and physical properties of the fabric. Hence, a series of parametric studies, evaluating the effect of process parameters on the ODF and FDD of the fabric was conducted. Light scattering and Image Analysis techniques were used to determine the ODF of the fabrics. The fabric is placed in the path of a laser beam and its image captured. A Fourier Transform (FT) analysis of the image was conducted to obtain the number of fibers aligned in the different directions. The different process parameters were varied and the effects studied. The fiber stream approach angle defined in Figure 8 was found to have a significant effect on the ODF of the fabric.

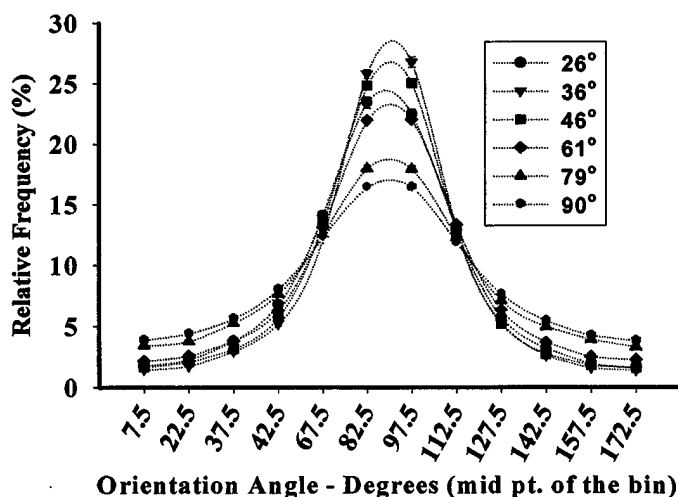


Figure 9: ODF for different Fiber Stream Approach Angle

The Fabric orientation along machine direction (MD) is shown to increase with reduced fiber approach-angle from 90° through 36°. At a 26° approach-angle setting the trend is shown to reverse and fabrics are less oriented along “MD”, as is shown in Figure 9. It was found that with increase in the attenuating air pressure and DCD, the fraction of fibers oriented in the MD decreased. The increase in the take-up speed of the fabric increased the fraction of fibers in the machine direction.

- g. *Investigation of meltblown fiber fineness (or fiber diameter distribution)*: Research has shown that more than 95% of the fiber diameters produced using the RFAC system to fall in the range of 0.8 to 20 microns. The fiber diameter distribution measurements were conducted on the SEM images of the samples. The images were analyzed using an Image Analysis Software. The diameter of the fiber is obtained by measuring the intensity difference between the central medial axis of the fiber and the edge of the fiber. The cumulative frequency distributions of the diameter, as a function of the processing parameters have been reported (Figures 10 to 12).

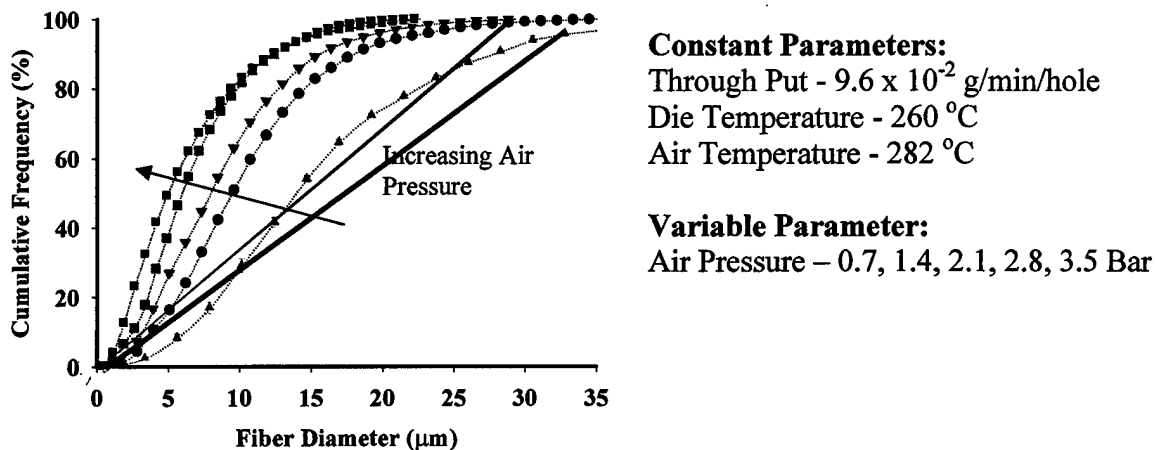


Figure 10: Influence of attenuating air pressure on the fiber diameter distribution

- Increase in attenuating air pressure decreases the fiber diameter distribution and produces finer fibers.
- Increase in polymer through put, increases the fiber diameter distribution

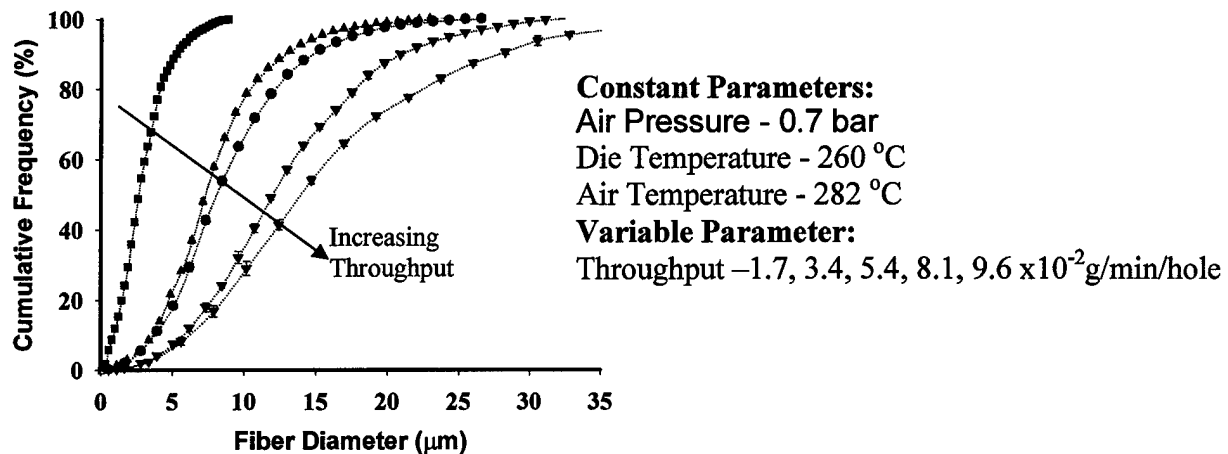


Figure 11: Influence of polymer throughput on the fiber diameter distribution

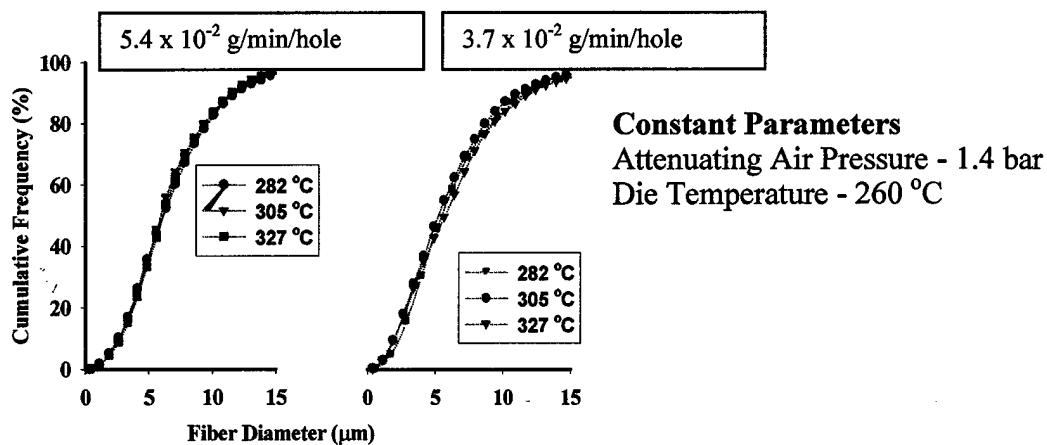


Figure 12: Influence of attenuating air temperature on the fiber diameter distribution

- Attenuating air temperature does not have any significant effect on the fiber diameter distribution

h. *Pore size measurement and its distribution:* The pore size and its distribution in a fabric structure is of prime importance in determining the transport properties of the fabric. The filtration efficiency, and hence the level of chemical/biological warfare protection, is directly related to the pore size and its distribution. Studies have been conducted to evaluate the effect of process parameters on the pore size and its distribution.

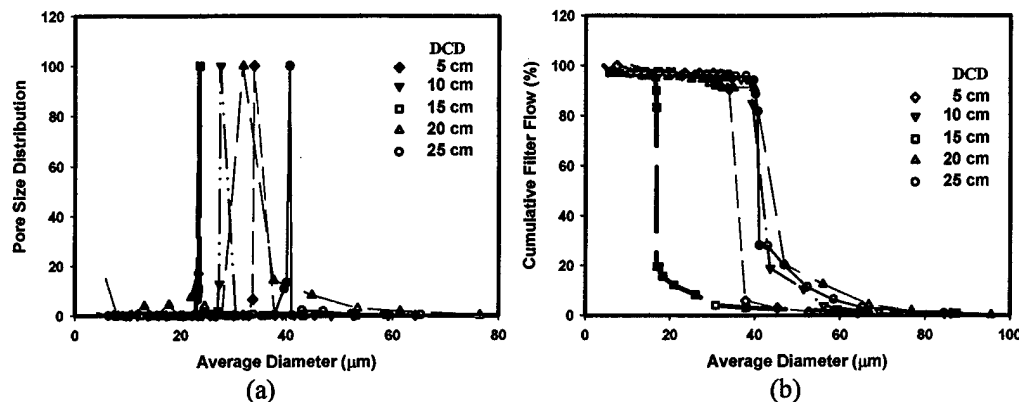


Figure 13: (a) Pore Size Distribution and (b) Cumulative Filter Flow (%) for MB PP fabrics for different Die to Collector Distances (Throughput: 3.7×10^{-2} g/min/hole, Attenuating Air Pressure: 1.4 bar, Number of Layers: 2, Take Up Speed: 6.09 m/min).

Increase in the die to collector (DCD) distance from 5 cm. to 15 cm. decreases the pore size but with further increase in DCD the pore size increases. At 15 cm. distance the web has a filtration efficiency greater than 95% (shown in Figure 13 (b)), and hence particles larger than 18 microns can be filtered. The filtration efficiency of the fabric is found to increase with an increase in the DCD.

An increase in the attenuating air pressure results in an increase in the velocity of forming air and hence an increase in the drag force exerted on the fiber and forms finer fibers. Finer fibers result in a higher surface area and increased cover leading to a decrease in the size of the pores formed in the web. Figures 14 (a) & (b) shows the pore size distribution and the filtration efficiency of the webs produced at different attenuating air pressures. Complementing the pore size distribution, the filtration efficiency increases with increasing attenuating air pressure. A higher percentage of finer pores increases the filtration efficiency of the web.

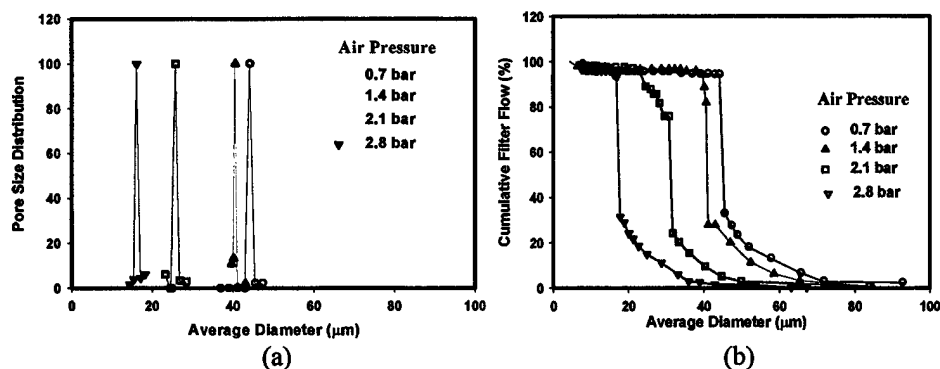


Figure 14: (a) Pore Size Distribution and (b) Cumulative Filter Flow (%) for MB PP fabrics for variation in attenuating air pressure (Throughput: 3.7×10^{-2} g/min/hole, DCD: 15 cm, Number of Layers: 2, Take Up Speed: 6.09 m/min).

- i. *Electrospinning of fibers from Solution:* The Electrospinning process is used to make fine fibers in the range of nano meters, which are also called nano fibers. The electrospinning system consists of two separate entities, a sprayer and a collecting device. The sprayer essentially consists of a glass spinneret, which holds the polymer solution. One of the metal electrodes from the high voltage supply is given to the solution, which serves as the positive terminal. A collector, which collects the fibers is given the other end of the electrode, which serves as the negative terminal. In this process, polymer solution is charged to a very high electrical potential. Because of the electric field, charge is induced on the liquid surface. The presence of potential difference between the two electrodes i.e., the mutual charge repulsion, causes a force opposite to the surface tension of the polymer solution. As the electric field increases, the hemispherical surface of the solution at the tip of the capillary tube extends to form a cone like structure, which is also known as the Taylor cone. As the intensity of the electric field is further increased the field reaches a critical point value at which the repulsive electric force overcomes the surface tension force. At this point a charged jet of the solution is ejected from the tip of the Taylor cone. So as the force acting on the polymer solution becomes greater than the surface tension, the charged droplet becomes unstable and a charged jet forms. As this charged jet moves in the air, the solvent evaporates, leaving behind a charged polymer fiber, which lays itself randomly on a collecting plate. So, fiber formation is due to the instability created by the repulsion between similar charges. Thus, continuous fibers are laid to form a fibrous web or nonwoven fabric.

Electrospinning experiments were carried out using PET or Poly (ethylene terephthalate) as the polymer. The solvent used to dissolve the PET was a 50:50 mixture of trifluoroacetic acid and dichloromethane (methylene chloride). The following are the three variable parameters that were investigated:

- The concentration of the polymer solution,
- The collecting distance of the fibers, and
- The electric voltage.

Experiments using PET were conducted to identify the optimum conditions of these three parameters using electrospinning system (Figure 15) built by our team at the College of Textiles, NCSU. No significant fibers were produced at 13% concentration of the polymer solution. This could be due to the lack of continuity in the solution molecules, and hence the lower limit on the concentration of the solution is 13%. At 28% there was no formation of fibers. The solution was dropping off as droplets. The reasons could be lower electric field and higher viscosity of the solution. From these experiments we have concluded that the concentration range for our set up to be 15% to 27%. As mentioned in literature, the electric field, the ratio of voltage and the collecting distance, should not be more than 0.9 kV/cm. Experiments were conducted to verify this range. Samples produced below or above this range had a variety of defects. Although the splaying of the fibers was random, innumerable shots were produced. Literature review and the experiments revealed that viscosity of the solution, the speed of the collecting surface (external drum, see Figure 15), the collecting distance, surface tension of the solution, net charge density and the electric field play an important role in the formation of shots. Considerable steps have been undertaken in the design and the experimental procedure to prevent the formation of shots and have been

successful in doing so. For example, 1) when the electric field reaches a critical value at which the repulsive force overcomes the surface tension force, charged jet of the solution is ejected from the tip of the Taylor cone. Since this jet is charged, its trajectory can be controlled by the electric field. 2) Higher viscosity favors formation of fibers without shots, higher net charge density not only favors formation of fibers without shots, but also favors the formation of thinner fibers. 3) Reduced surface tension favors formation of fibers without shots. 4) Smooth beveling has been done to the spinneret and the inner and outer diameter of the pipette has been reduced to about 0.3mm near the tip, 5) Changing the polymer concentration, 6) A new look to the collecting device to name a few of the other steps undertaken. Hence, for experimental setup, we concluded that the voltage should be in the range of 15 to 25kV and the collecting distance should be in the range of 17 to 30 cm to produce an electric field in the range of 0.65 to 1.15 kV / cm.

Properties under evaluation are:

- Physical characteristics of the fiber and web
- Diameter of the fiber
- Fiber diameter distribution
- Strength of fiber and web
- Fiber orientation distribution
- Surface morphology of the fibers and the web

The laboratory equipment, which was used to collect the fibers, had a number of shortcomings and had to be re-designed since the entire process has to be performed under a hood for obvious safety reasons. The fibers splayed from the spinneret, which was placed normal to the collecting surface. Due to several ambient factors, mainly the air velocity inside the hood, the fiber collection was difficult. Therefore samples were to be prepared from solution with the pipette splaying the fibers at an angle to the ground and hence a new design was made for the collector. The new system of collection of fibers included a drum with an external drive. As shown in figure 15 below, the collector is a PVC pipe cylindrical drum (8" in diameter and 14" in length), which is attached with a metal plate, a bush so as to complete the electrical connection. The cylinder is driven by an external source and, rotates clockwise and anti-clockwise at variable speeds. The entire setup is insulated and vertical position of the cylinder can be adjusted to change the distance from the spinneret as per requirements. The electrical connection is used as the negative terminal from the high voltage equipment. Hence the cylindrical drum serves as the negative terminal and aids in the splaying and collecting of fibers. Because of various limitations and constraints of the set-up and the environment, narrower values of the parameters have been used. The concentration of the solution was in the range of 21-27%, voltage in the range of 15-21 kV, and the collecting distance between 19-22 cm. Based on these parameters an experimental design was setup having four values of each parameter.

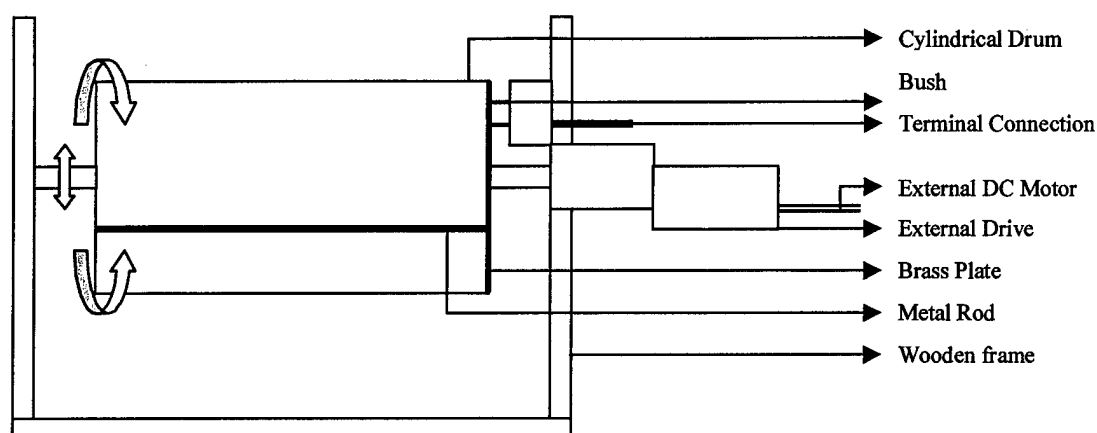


Figure 15: Collecting Device for Electrospinning from Solution

j. *Results of Fiber Diameter in electrospun fiberweb*: Analyses of the fibers included the capture of images using a Hitachi ESEM S-3200 in the environmental mode with voltage at 15 kV, air pressure of 40 to 80 Pa, working distance of 23 mm and integrating eight to sixteen picture frames. The images were analyzed using commercially available image analysis software NIH Image. The images were studied for the effect of the polymer concentration and electric field. Figure 16 shows the effect of the electric field on the diameter distribution of the fibers at four different concentrations of the polymer solution. As is expected, an increase in the electric field decreases the diameter of the fiber.

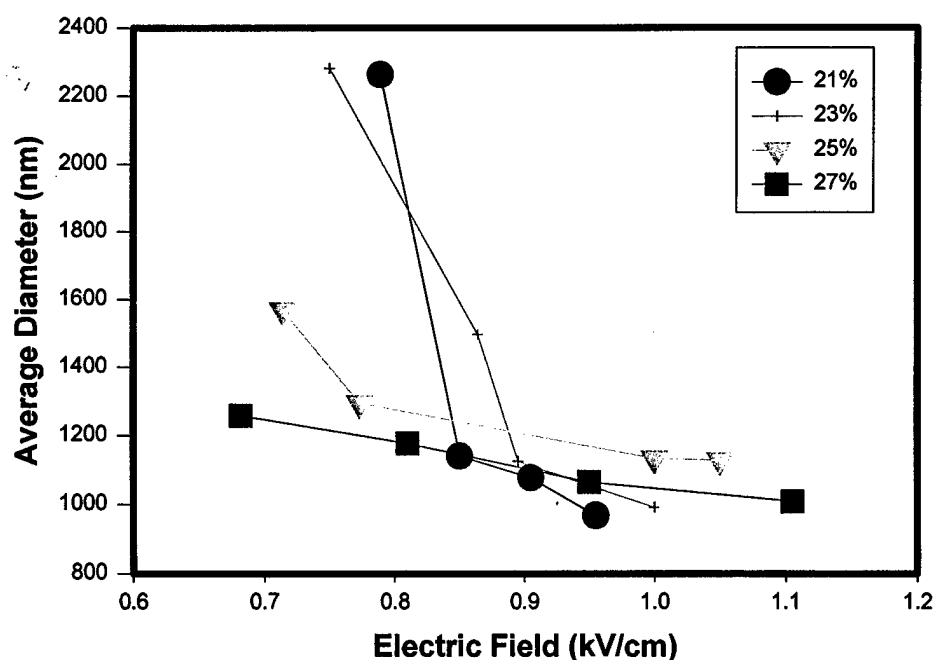


Figure16: Influence of electric field on the diameter distribution of electrospun fibers

It is evident from the graph that as we increase the electric field at all concentrations, the average diameter of the electrospun fibers decreases. From this figure, apart from the two points (21% concentration, 0.7890 kV/cm and 23% concentration, 0.7500 kV/cm), interaction between the concentration of the polymer solutions at different electric fields can be very clearly seen. In other words it can be said that, concentration is not affecting much to the average diameter of the fibers at the given electric fields. But, clearer conclusion can only be obtained by doing statistical analysis. It can also be noted that lower diameter fibers are obtained in the range of 0.85 kV/cm to 1.0 kV/cm, which agrees with results of previous work published. Figures 17-20 show the effect of the electric field at different polymer concentration on the diameter distribution of the fibers. Same comments on the fiber diameter distribution data can be made as those on the fiber diameter.

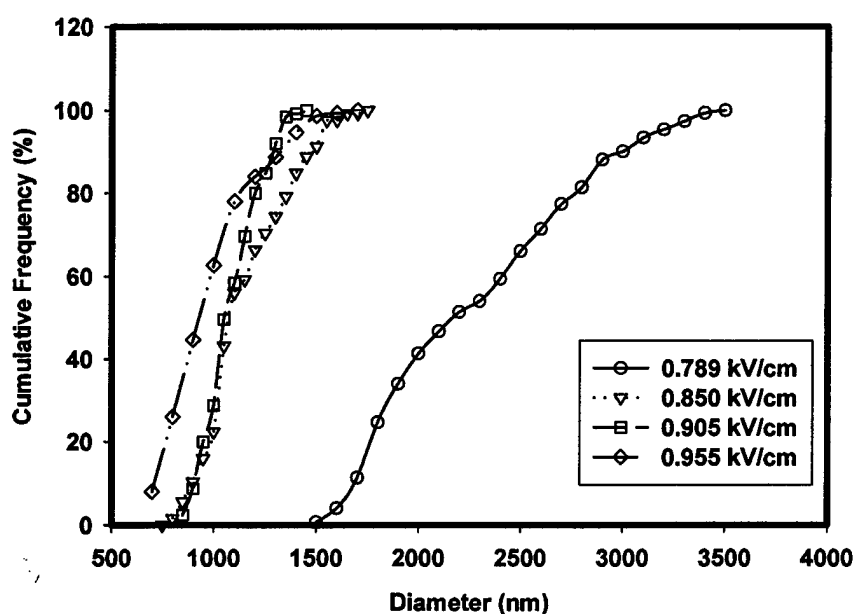


Figure 17: Effect of varying electric field on the diameter distribution of the fibers at a constant concentration of 21%

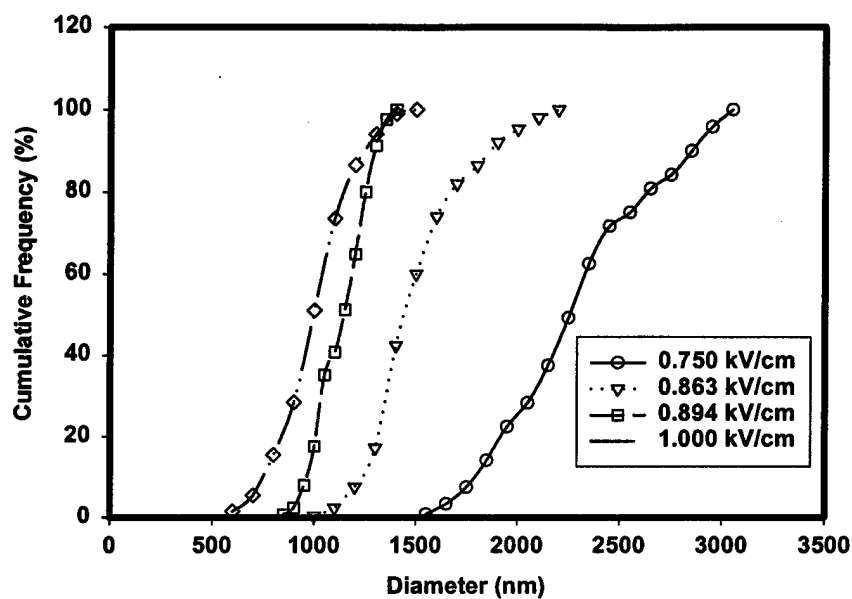


Figure 18: Effect of varying electric field on the diameter distribution of the fibers at a constant concentration of 23%

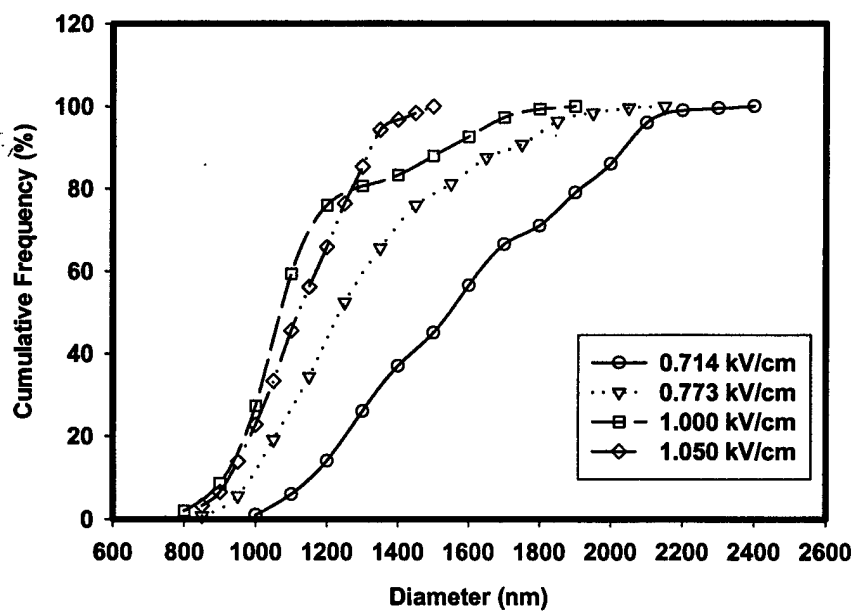


Figure 19: Effect of varying electric field on the diameter distribution of the fibers at a constant concentration of 25%

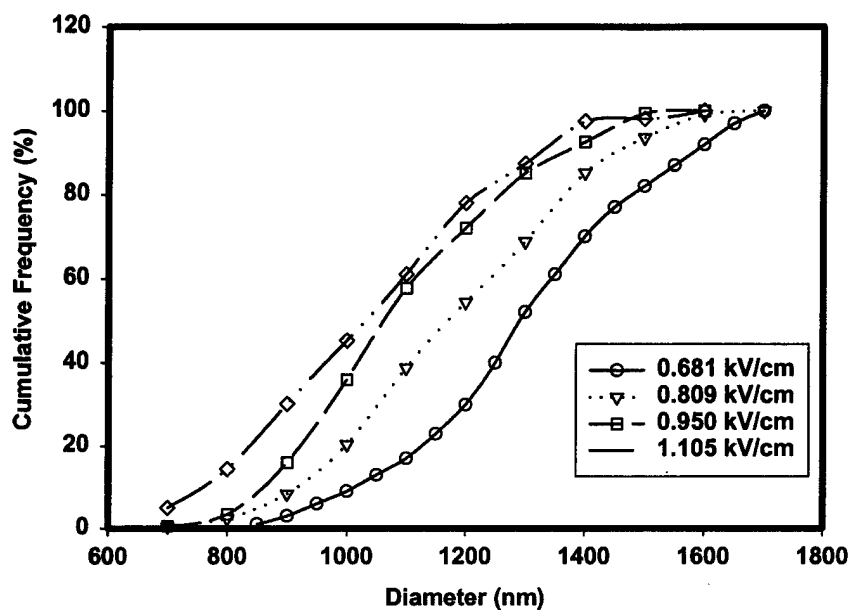


Figure 20: Effect of varying electric field on the diameter distribution of the fibers at a constant concentration of 27%

As the concentration of the solution changes the fiber diameter increases with increase in concentration. The diameter range is broadened (Figure 21). This behavior can be related to the fact that an increase in polymer concentration causes an increase in viscosity, which in turn causes the splay of thicker fibers.

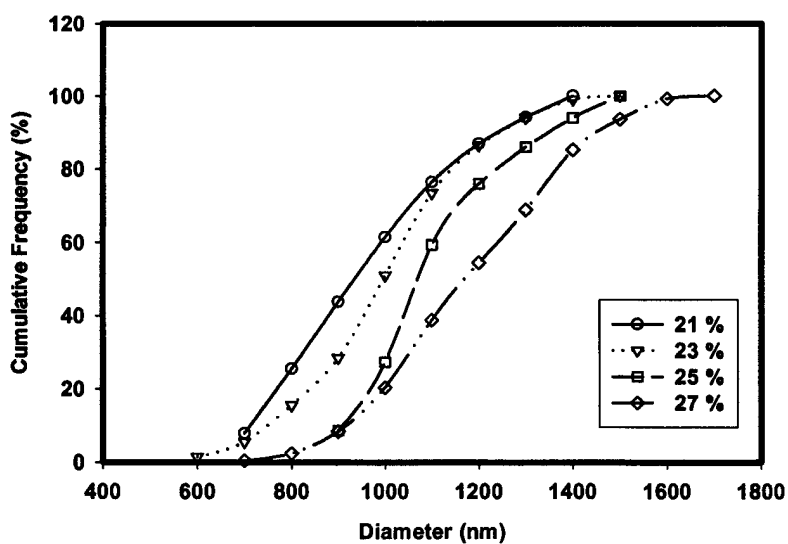


Figure 21: Effect of Concentration on the diameter distribution of fibers.

Future Plans

The electrospun webs that have been produced need to be characterized for the orientation distribution, pore size distribution and web strength.

Formation and characterization of composite structures of meltblown and electrospun webs will be conducted.

Investigation to control the structure of the meltblown webs deposited on the mannequin will be carried out.

Studies will be conducted by varying the curvature and change in the surface speed of the collecting surface.

A mannequin to meet the requirements of various curvatures of the collecting surface is being developed.

Publications

Theses:

Farer, R., Formation of 3D Meltblown Structures Using Robotic Control of Fiber Deposition, Ph.D. Thesis, NC State University, 1999.

Nguyen, P., Evaluation of Meltblown Nonwoven Fabric, M.S. Thesis, NC State University, 2000.

Mohan, A., Investigation of Electrospinning Process and Structures, M.S. Thesis, NC State University, Summer 2002 (Expected Date of Completion).

Velu, Y., Study of 3D Meltblown Structures, Ph.D. Thesis, NC State University, Summer 2002 (Expected Date of Completion).

Journals and Conference Proceedings:

Farer, R., Ghosh, T.K., Seyam, A.M., Grant, E., and Batra, S.K., Study of Meltblown Structures Formed by Robotic and Meltblowing Integrated System: Impact of Process Parameters on Fiber Orientation, Submitted to INJ.

Farer, R., Batra, S.K., Ghosh, T.K., Grant, E., and Seyam, A.M., Study of Meltblown Structures Formed by Robotic and Meltblowing Integrated System: Impact of Process Parameters on Fiber Diameter Distributions, Submitted to INJ.

Farer, R., Seyam, A.M., Ghosh, T.K., Batra, S.K., Grant, E., Lee, G., Formation of Shaped/Molded Structures by Integration of Meltblowing and Robotic Technologies, Accepted for Publication, Textile Research Journal.

Farer, R., Seyam, A.M., Ghosh, T.K., Grant, E., and Batra, S.K., Study of Meltblown Structures Formed by Robotic and Meltblowing Integrated System: Impact of Process Parameters on Fiber Orientation and Fiber Diameter Distribution, Accepted for Publication, Textile Research Journal.

Farer, R., Ghosh, T.K., Seyam, A.M., and Lee, G., Formation of Shaped/Molded Meltblowing Nonwoven Structures, Proceedings of the TI 82nd World Conference, Cairo, Egypt, March 2002.

Velu, Y., Ghosh, T., Seyam, A., Farer, R., New process for the Production of Three-dimensional Nonwoven Structures, Proceedings of the TECHTEXTIL-Symposium 2001, Frankfurt, April 23-26, 2001.

Farer, R., Grant, E., Ghosh, T. K., Seyam, A. M., and Lee, G. "A Rule-Based Robotic Control Approach to Melt-Blowing for Shaped Fabric Structures, Proceedings of the IEEE Conference on Circuits and Systems, Geneva, May 28-31, 2000.

Farer, R., Grant, E., Ghosh, T. K., Seyam, A. M., and Lee, G., On the Use of Robotics for Melt-Blowing to Form Shaped/Molded Fabric Structures, Proceedings of the IEEE Robotics and Automation Conference, San Francisco, April 24-28, 2000.

Presentations

Farer, R., Ghosh, T.K., Seyam, A.M., and Lee, G., Formation of Shaped/Molded Meltblowing Nonwoven Structures, the TI 82nd World Conference, Cairo, Egypt, March 2002.

Velu, Y., Ghosh, T.K., Seyam, A.M., Farer, R., New process for the Production of Three-dimensional Nonwoven Structures, the TECHTEXTIL-Symposium 2001, Frankfurt, April 23-26, 2001.

Farer, R., Grant, E., Ghosh, T. Seyam, A. M., and Lee, G. "A Rule-Based Robotic Control Approach to Melt-Blowing for Shaped Fabric Structures, IEEE Conference on Circuits and Systems, Geneva, May 2000.

Farer, R., Grant, E., Ghosh, T. Seyam, A. M., and Lee, G., On the Use of Robotics for Melt-Blowing to Form Shaped/Molded Fabric Structures, IEEE Robotics and Automation Conference, San Francisco, April 2000.

Farer, R., Ghosh, T.K., Grant, E., Seyam, A.M., and Batra, S.K., Formation of Molded Fabric Structures through Integration of Melt-Blowing and Robotics, the Techtextil Symposium, Atlanta, Georgia, March 2000.

Seyam, A. M., Ghosh, T. K., Batra, S. K., and Farer, R., Three-Dimensional Textile Structures through Meltblown/Robotic Technologies, Department of Textile Engineering, Seoul National University, Seoul & Department of Textile Engineering, Chungnam National University, S. Korea, June 22-23, 1999. (Invited)

Characterization of Meltspun Nanofibers

T. J. Little, and B. Pourdeyhimi with assistance of the following graduate students:

Weihua Shi, Kyeung Park, Beatrice Ruoth and Carol Gonzalez

College of Textiles, North Carolina State University

Raleigh, NC 27695-8301

Abstract and Objectives

The objective of this work was to characterize tensile properties of meltspun nanofibers. Nanofibers from meltspun bicomponent fibers were investigated to characterize their tensile properties by different methods. The methods were developed to predict the tensile properties of individual microfibers using the tensile data of the bicomponent and the cross sectional shape of bicomponent. The relationship between the tensile properties of individual microfibers and bicomponent was studied and mathematical models were developed to predict the properties of single fiber from those of bicomponent. Different testing technologies were applied and compared.

Introduction

The mechanical properties of textile fibers are probably their most important properties, contributing both to the behavior of fibers in processing and to the properties of the final product. The properties of a textile structure such as a yarn or a fabric depend on a

complex interrelation between fiber arrangement and fiber properties, so that, a knowledge of fiber properties is essential to an understanding of the properties of yarns and fabrics.

Data collection of single fiber strength is tedious, time consuming and cost-inefficient. The simplest and commonest way of providing information on fiber mechanical properties is to measure or estimate fiber strength by breaking a bundle of staple fibers. Fiber bundle strength is widely used in the wool industry and trade market. However, wool bundle strength does not give as much information as the results from single fiber testing, particularly for fibers with high variations in tensile behavior. Lijing et al [1] demonstrated the difference between ideal and actual fiber bundle strength profiles. Based on the results, they propose a method of obtaining "near ideal" bundle strength in practice and allude to the possibility of deriving the actual average single fiber strength without tedious single fiber strength measurements. They confirmed that fiber breaking load (P) is proportional to the fiber diameter squared (D^2). Preston [2] developed a method to measure the tensile properties of individual cotton fibers and to use the data from the method to study the relationships between the tensile properties of individual fibers and fiber bundles. Mathematical models were developed to predict bundle strength from individual fiber tensile properties. Analysis of the single fiber strength data suggests that the average single fiber breaking strength sets an upper limit for their fiber bundle strength.

Regarding the tensile properties of microfibers, it is generally known that microfibers have good tensile properties for their linear densities. M. V. Tsebrenko [3] found that there are the following distinctive properties of the complex threads consisting of microfibers:

- high strength and initial modulus,
- high elasticity contribute to exclusive softness,
- pleasant feel, coupling, capaciousness, and wool likeness without special textural procedures and
- high sorption of moisture, dyes and other substances.

Elasticity of microfibers can be 4 to 6 times greater than elasticity of the conventional fibers and has been explained as accumulation of considerable elastic deformations by the disperse phase polymer during the flow. The density of polymer in microfibers was found to be much higher than that in conventional fibers. M. Nishimura [4] showed that the strength of FOY microfiber is 4.8g/d. There is no data from measurements on single microfiber tests and the relationship between single microfiber and microfiber bundles. Therefore, for this research, it was necessary to study following:

- Developing a method to measure the tensile properties of bundle of microfibers and find out the relationships between the tensile properties of individual microfiber and fiber bundles. Mathematical models (linear regression analyses) can be developed to predict fiber strength from bundle strength.
- Differences in fiber strength according to the microfiber production methods.
 - From Island-in-the-Sea method, we can get a round cross section. From segment-pie, we get wedge-shaped or flat cross section. The segment-pie cross sectional shape can be easily separated into smaller fibers during processing.

- To examine the change of physical properties before and after extraction of the sea polymer.

There is a relationship between tensile properties and fiber structure. Through the parameters such as Young's modulus, yield strength, tensile strength, elongation at break, fiber structure and morphology can be explored.

Young's modulus \Rightarrow fiber orientation and molecular flexibility

Yield strength \Rightarrow shape of cross section

Tensile strength \Rightarrow draw ratio

The results can be confirmed by comparing the data of tensile strength and other methods for exploring molecular morphology such as X-ray diffraction.

[1] Lijing Wang and Xungai Wang, A Study of Wool's Tensile Strength in Early Stage Processing, *Textile Res.J.* 70(2),98-102(2000)

[2] Preston E. Sasser, Interpretations of Single Fiber, Bundle, and Yarn Tenacity Data, *Textile Res.J.* 61(11),681-690(1991)

[3] M.V.Tsebrenko, N.M.Rezanova, and I.A.Tsebrenko, Fiber-Forming Properties of Polymer Mixture Melts and Properties of Fibers on their Basis, *Polymer Engineering and Science*, 39(12), 2395-2402(1999)

[4] M.Nishimura, T.Hibino and K. Tsujimoto, A Microfiber of promise, *Textile Asia*, Dec.,54-67(1992)

Testing Methods

1. Wool

Fiber bundle strength is widely used in the wool industry and trade market. However, wool bundle strength does not give as much information as the results from single fiber testing, particularly for fibers with high variations in tensile behavior. Lijing et al demonstrated the difference between ideal and actual fiber bundle strength profiles. Based on the results, they propose a method of obtaining "near ideal" bundle strength in practice and allude to the possibility of deriving the actual average single fiber strength without tedious single fiber strength measurements. They confirmed that fiber breaking load (P) is proportional to the fiber diameter squared (D^2).

2. Cotton

Preston developed a method to measure the tensile properties of individual cotton fibers and to use the data from the method to study the relationships between the tensile properties of individual fibers and fiber bundles. Mathematical models were developed to predict bundle strength from individual fiber tensile properties. Analysis of the single fiber strength data suggests that the average single fiber breaking strength sets an upper limit for their fiber bundle strength.

3. Microfiber

Regarding the tensile properties of microfibers, it is generally known that microfibers have good tensile properties for their linear densities. M.V.Tsebrenko found

that there are the following distinctive properties of the complex threads consisting of microfibers:

- high strength and initial modulus,
- high elasticity and exclusive softness, pleasant feel, coupling, capaciousness, and wool likeness without special textural procedures,
- high sorption of moisture, dyes and other substances.

Elasticity of thread of microfibers is 4 to 6 times greater than elasticity of the conventional thread that can be explained by accumulation of considerable elastic deformations by the disperse phase polymer during the flow. Density of polymer in microfibers is much higher than that in conventional fibers. M. Nishimura showed that the strength of FOY microfiber is 4.8g/d.

3.1 Cantilever technique

Single fiber tenacity was measured using the cantilever technique. A cantilever consisting of a 30 μ m glass fiber was glued at one end onto a microscope slide and a 15 μ m nylon fiber was attached at the free end of the glass fiber. The electrospun test fiber (10mm) was glued with epoxy resin to the free end of the nylon fiber. A part of the same fiber was cut and deposited on a SEM specimen holder for diameter measurement using SEM. As the sample fiber was stretched, the deflection of the cantilever was measured under light microscopy using a calibrated eyepiece. A chart was used to convert deflection into actual values. The elongation to break of electrospun fibers was estimated using a caliper.

→ A typical 10mm length of electrospun PAN fiber, with diameter of 1.25 μ m (assuming a round cross-section, the corresponding denier is 0.014) exhibited failure at 0.4mm

deflection, or 41 mg of force. The resulting tenacity is 2.9 g/d. The mean elongation -at-break of the same fiber was 190% with a standard deviation of 16%.

3.2 Custom built stress-strain gauge

To measure nano-fiber properties, other researchers used a highly sensitive, rapid response stress-strain gauge. The gauge with a FORT 10 force transducer (of World Precision Instruments) and linear extension mechanism (Pen Motor Assembly of Hewlett Packard) were driven and recorded using Lab View on Macintosh. It had a time resolution of a few ms and a force resolution of 30 μ N. Using cyanoacrylate adhesive, a single thread was mounted on the upper and lower bar of gauge while taking care to avoid tensioning the thread (initial length 7mm).

Determination of longitudinal tensile property of microdenier fiber

1) The behavior of unidirectional composites

Unidirectional composite consists of parallel fibers embedded in a matrix. So it is assumed that microfibers embedded in a matrix are unidirectional composites.

Assuming that a perfect bonding exists between fibers and the matrix so that no slippage can occur at the interface and the strains experienced by the fiber (ϵ_f), matrix (ϵ_m), and composite (ϵ_c) are equal

$$\epsilon_f = \epsilon_m = \epsilon_c$$

The load (P_c) carried by the composite is shared between the fibers (P_f) and the matrix (P_m).

$$P_c = P_f + P_m$$

The loads may be written as follows in terms of stresses experienced by them and their corresponding cross-sectional areas.

$$\sigma_c = \sigma_f \frac{A_f}{A_c} + \sigma_m \frac{A_m}{A_c}$$

$$V_f = \frac{A_f}{A_c}, \quad V_m = \frac{A_m}{A_c}$$

$$\sigma_c = \sigma_f V_f + \sigma_m V_m$$

Where A_f, A_m, A_c are the cross-sectional area of fibers, matrix, and composite respectively.

By differentiating with respect to strain

$$\frac{d\sigma_c}{d\epsilon} = \frac{d\sigma_f}{d\epsilon} V_f + \frac{d\sigma_m}{d\epsilon} V_m$$

where represents the slope of the corresponding stress-strain diagrams at the given strain.

If the stress-strain curves of the materials are linear, the slopes are constants and can be replaced by the corresponding elastic modulus. Thus,

$$E_c = E_f V_f + E_m V_m$$

If $\sigma_m, \sigma_c, V_f, V_m, V_c$ can be measured, σ_f can be calculated.

Also with the composites made by different volume fraction of microfiber, simultaneous

equation can be established. By solving this, we can get the strength of an individual microfiber.

While deriving strength and stiffness of unidirectional composites, many simplifying assumptions regarding the physical variables of the system are made. It is very rare that all the assumptions are completely met in an actual situation. This results in deviations of composite properties from the derived equations. Followings are the factors influencing longitudinal strength and stiffness

- ① Disorientation of fibers
- ② Fibers of non-uniform strength
- ③ Discontinuous fibers
- ④ Interfacial conditions
- ⑤ Residual stresses

Many of these deviations may be small and may not require any correction. Corrections may be necessary in many other situations. Therefore it is necessary to know the variables in the microfibers matrix composite.

2) The relationship between the tensile properties of individual fibers and fiber bundles

It is possible to develop a method to measure the tensile properties of bundle of microfibers and to use the data from the method to study the relationships between the tensile properties of individual microfiber and fiber bundles. Mathematical models (linear regression

analyses) must be developed to predict fiber strength from bundle strength. The results of R-square can be different from the type of machine.

Generally the strength of a yarn (bundle) cannot be greater than the sum of the maximum strengths of its component fibers.

Characterization of Microfiber

1. Polymer

Polymer Types	Viscosity MFI	Melting Temp.
Poly (ethylene terephthalate)	IV=0.64	260
Poly (trimethylene terephthalate)	MFI=35	160
Nylon 6	IV=0.9	270
Poly (vinyl alcohol)	RV=3.2	255

2. Conjugate bicomponent

- PVA/PTT 300 Island-in-Sea
- PVA/PTT 600 Island-in-Sea
- Nylon6/PET 16 Segment-Pie

3. Linear Density Reduction

	Spinning Process	Ultra Fining Process
PTT/PVA Islands-in-Sea	Soluble Conjugate Bicomponent	Dissolving matrix (PVA) component - 100°C Water, 5hr

Nylon6/PET 16 Segment Pie	Separable Conjugate Bicomponent	Mechanical splitting
------------------------------	------------------------------------	----------------------

3. Linear Density

		Bicomponent	Microfiber
PVA/PTT IS	300(un-drawn)	14.48	0.021
	300(drawn)	6.86	0.01
	600(drawn)	12.21	0.013
PA6/PET 16 Segment Pie		7.75	0.48

<Results>

1. Tensile Properties of PTT/PVA Island in Sea Fiber

		Denier (d)	Elongation (%)	Tenacity (g/d)	Modulus (g/d)
300 (undrawn)	Bicomponent	14.5	228.9	1.0	-
	PTT microfiber	0.021	238.2	0.6	7.2
300 (drawn)	Bicomponent	6.9	56.0	3.4	18.8
	PTT microfiber	0.01	52.3	1.0	9.1
600 (drawn)	Bicomponent	12.2	41.2	2.1	18.0
	PTT microfiber	0.013	26.9	0.6	8.3

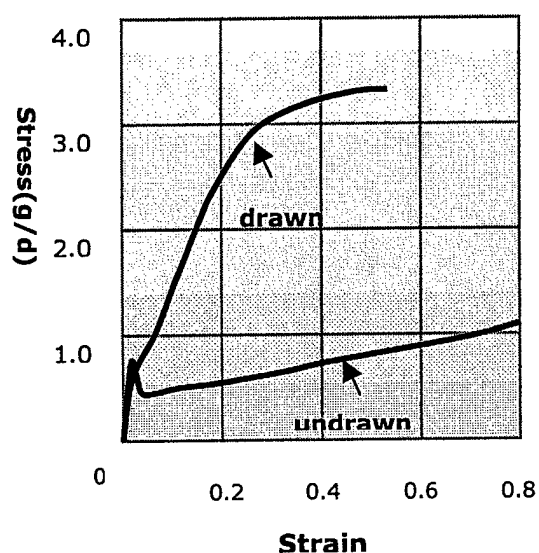


Figure. Stress-Strain curves of
300 Islands-in-Sea

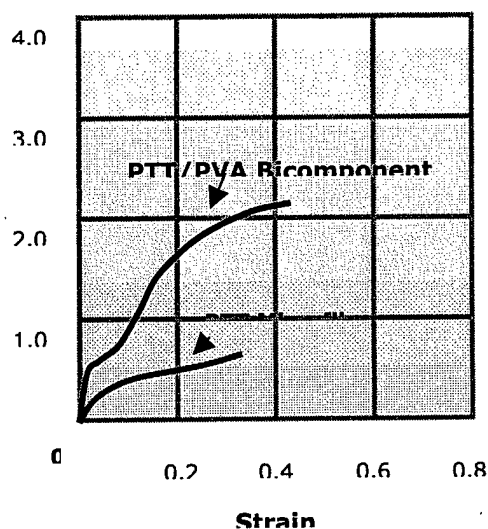


Figure. Stress-Strain curves of
600 Islands-in-Sea

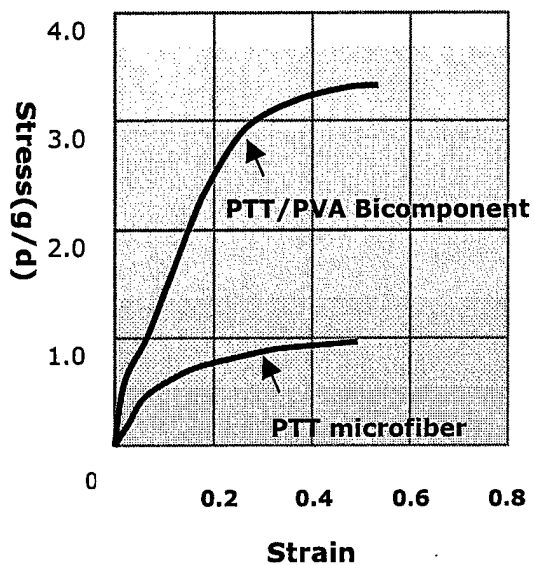


Figure. Stress-Strain curves of
300 Islands-in-Sea

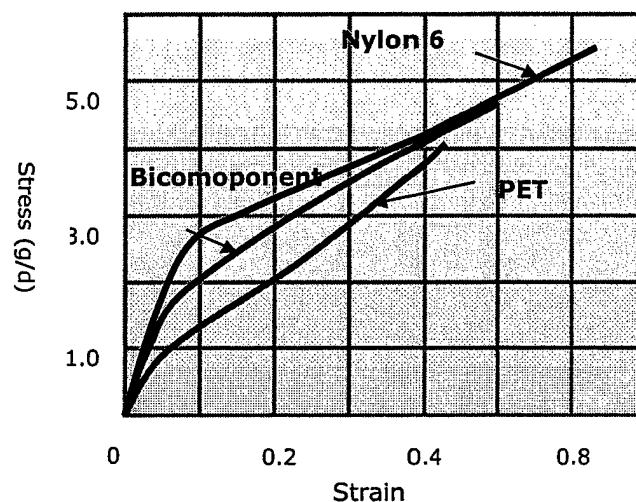


Figure Stress-strain curves of PA6/PET 16
Segment Pie Fiber

2. Tensile Properties of PA6/PET Segment Pie Fiber

	Bicomponent	Nylon 6	PET
Tenacity (g/d)	4.84	5.47	4.11
Elongation (%)	107.6	127.8	86.2
Modulus (g/d)	15.9	21.7	13.2

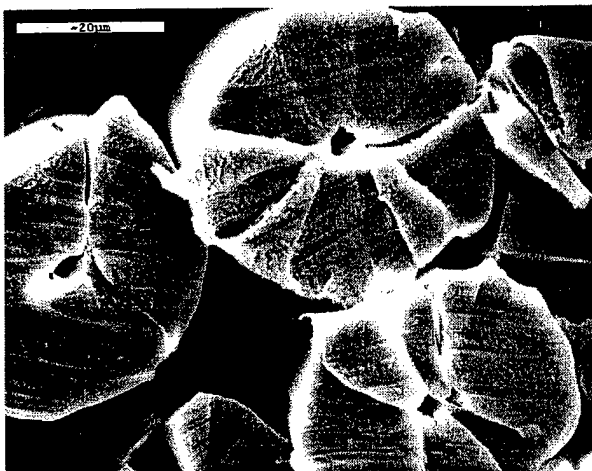
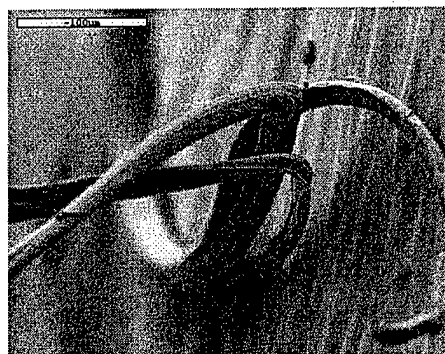
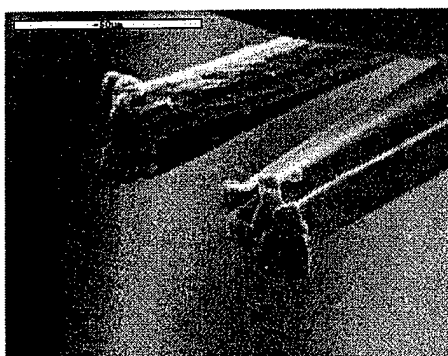


Figure The SEM micrograph of cross section of
PA6/PET 16 segment pie bicomponent fiber



The SEM micrograph of bicomponent
fractured end (PA6/PET 16 segment pie)



The SEM micrograph of bicomponent
fractured end (PTT/PVA 600 IS)



The SEM micrograph of bicomponent
fractured end (PTT/PVA 300 IS)

Analysis of tensile data of bicomponent fibers from different instrument

Tensile Testing

<Favimat>

- Load-extension measurement, Vibrational fineness measurement
- Maximum force: 200cN
- Force resolution : $\pm 0.0001\text{cN}$ (=0.0001g)
- Extension resolution : $\pm 0.1\mu\text{m}$

<Favimat Vs Instron>

Table. Input setup of Favimat and MTS

	load cell	test speed	pretension
Favimat	2.1N	24mm/min	0.8 cN/tex
MTS	1N	24mm/min	0.1 lb.

<Results>

		Linear density		Elongation		Tenacity		Modulus	
		Favimat	Length-weight measure	Favimat	Instron	Favimat	Instron	Favimat	Instron
PE/PET 600 Islands in Sea	Average	2.38	2.30	33.67	45.39	3.17	2.87	37.17	29.44
	CV(%)	(10.05)		(17.97)	(20.728)	(8.47)	(10.28)	(12.69)	(17.13)
PE/PET 900 Islands in Sea	Average	2.1	2.05	56.10	60.7	3.22	2.92		
	CV(%)	(7.04)		(23.96)	(30.97)	(7.76)	(14.44)		
PVA/PTT 600	Average	12.95	12.20	85.33	41.20	2.32	2.10		18.00
	CV(%)	(30.97)		(43.63)		(18.54)	(15.22)		
PVA/PTT 300	Average	6.15	6.90	27.83	56.00	3.26	3.40	45.23	18.80
	CV(%)	(15.06)		(19.8)		(14.61)		(8.65)	
PA/PET 16 Segment pie	Average	10.14	7.75	96.26	107.00	3.32	4.84		15.90
		(7.26)		(12.09)		(8.65)			

- 1) Favimat can measure tensile properties and linear density at once. So precise tenacity data can be obtained. (Testing time for one specimen is little longer in Favimat than in Instron)
- 2) Even Favimat used larger load cell, it measured the data more accurately.
- 3) CV of Favimat is less than that of Instron.
- 4) Instron calculates modulus automatically and underestimates the value. For favimat, the range should be set up before the test.

Table. Correlation between data from Favimat and MTS

	Elongation	Tenacity
Correlation coefficient	0.5435	0.7094

5) The tenacity data of Instron and Favimat are related each other. But for elongation, there is poor relationship between the data. It is caused by data of MTS. During mounting the specimen on the cardboard, certain amount of strain can be imposed to the specimen.

Influence of drawing parameters on structural properties of microfiber

Tensile Testing

<Favimat>

- Load-extension measurement, Vibrational fineness measurement
- Maximum force: 200cN, Force resolution : $\pm 0.0001\text{cN}$ (=0.0001g),
- Extension resolution : $\pm 0.1\mu\text{m}$

Table. Input setup of Favimat

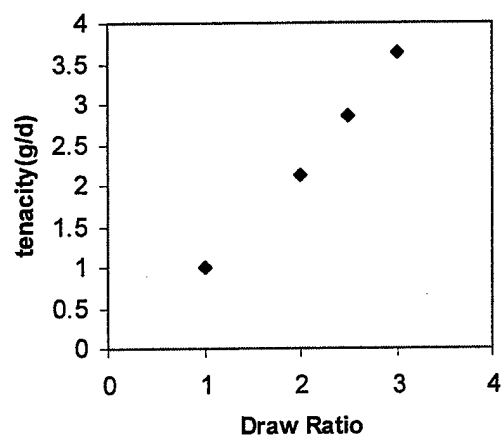
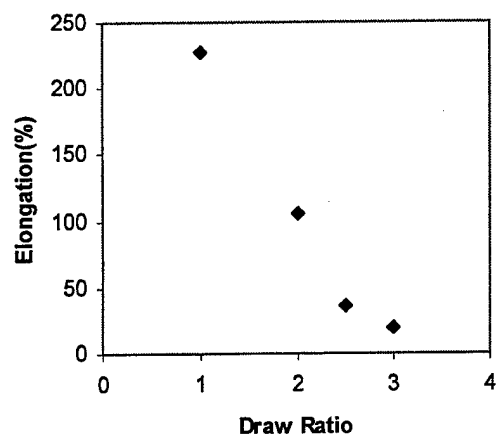
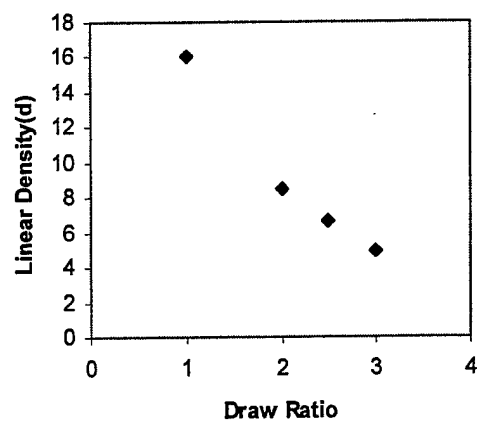
	load cell	test speed	pretension
Favimat	2.1N	24mm/min	0.8 cN/tex

Drawing

Yarns were drawn on a Stähle air-texturing machine. For studying the effect of draw ratio, four draw ratios namely 2, 2.5, 3, while the heating temperature was kept constant, 120°C.

<Results>

Draw ratio	count (denier)	elongation(%)	tenacity(g/d)	work to rupt.	Modulus(g/d)
1	16	228	1		
2.00	8.43	106.05	2.11	29.96	190.52
2.50	6.66	35.90	2.85	10.89	210.34
3.00	4.96	19.24	3.64	4.87	184.12



Tensile Properties of PA6/PET segment pie hollow fiber

<Testing method>

- Tensile testing on an Instron

The mechanical properties of the specimens were determined with an Instron tensile tester(model 1122) at a crosshead speed of 24mm/min. Samples will be prepared according to the ASTM D 3822-96. 0.5 N load cell and lever action grips were used.

- Linear Density

Measure the length-weight and calculate

PA/PET segment pie fiber

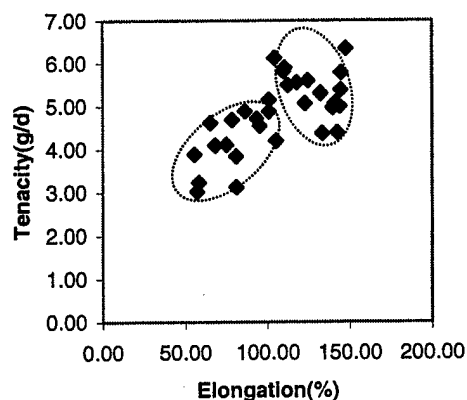
- Easy to separate - it consists of 8 PA microfibers and 8 PET microfibers and can be separated by stretching the fiber.
- Easy to determine the linear density by weighing fibers

	Filament(before separation)	Microfiber(after separation)
Denier	7.75	0.48

<Result>

Test of PA, PET microfibers -Number of samples: 36

	Break LOAD	%Strn @ BREAK	Modulus	Tenacity	Toughness
Average	2.30	107.63	15.91	4.84	3.15
Stdev.	0.39	29.56	6.29	0.839	1.16



⇒ Considering tenacity and elongation, data set can be divided to two groups, which are microfiber 1 and microfiber 2

		Microfiber 1	Microfiber 2
Tenacity(g/d)	Average	4.11	5.47
	Stdev.	0.60	0.41
Elongation(%)	Average	86.21	127.79
	Stdev.	25.39	15.88

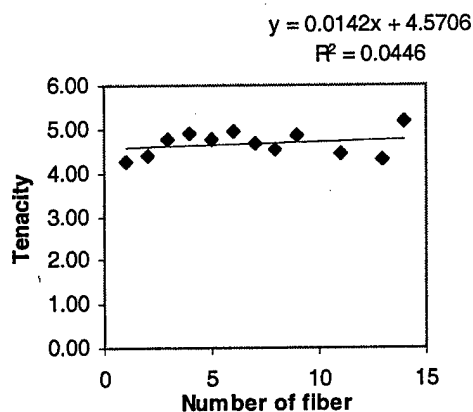
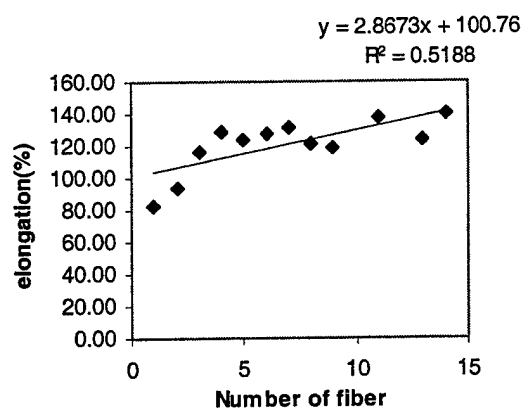
Each segment can be identified by its tensile property and identification of microfiber 1, and 2 can be achieved through staining or dissolving.

Elongation is higher than expected suggesting that the yarn is not fully drawn.

Fiber modulus data was difficult to attain under these testing conditions. Future work should consider measuring dynamic modulus and comparing with initial modulus data.

Test of various numbers of fibers (average of 6 or more)

Number of fiber	Elongation(%)	Tenacity
1	82.70	4.28
2	93.87	4.40
3	116.60	4.77
4	128.93	4.90
5	124.21	4.77
6	127.62	4.93



7	130.87	4.67
8	120.90	4.52
9	118.80	4.88
11	138.05	4.44
13	124.10	4.28
14	140.50	5.18

- As the number of fiber increases, elongation increases.
- As the number of fiber increases, there is no evident change in the tenacity

Test more samples to get a linear relationship between number of fiber and tensile property

Compare segment pie type and stripe type.

Recent Melt-extrusion Trials using PA6

A series of melt-extruded nanofibers were produced in Spring 2002 using PA6 (BASF) and PVA (Kuraray). All yarns produced were made using islands-in-the-sea approach and subsequently tested on a tensile tester using a single filament. Preparation of the specimens for tensile testing involved mounting the untreated islands-in-the-sea fiber between two plastic washers, immersing the ensemble in an aqueous ultrasonic bath of water and allowing the PVA to dissolve. The plastic washer was dried and mounted in the tensile tester before the outer edges were cut to enable testing of the bundle of "nanofibers". The tensile properties of the fibers produced are given in the table below. It will be noted that for Drawn Yarn (D) the tenacities ranged decreased slightly as the number of islands increased (5.61 for 300D to 4.80 for the 990D). These are well within the range of being "textile" fibers and they exhibit textile properties. This series of trials demonstrated conclusively that nano-fibers can be produced at commercial speeds via melt-extrusion methods. The design and building of the spin-pacs is a critical part of the process as well as the correct preparation of the polymers. It will also be noted that the 990D sample produced with an 80/20 ratio of pump throughputs showed a tenacity of 10.87g/d. This result is not consistent with the decreasing tenacity discussed above. Time did not permit a full exploration of this result in terms of actual denier produced since the denier per filament (0.59 denier) is estimated from the 80/20 ratio of polymer throughputs. There is also speculation that as fiber diameter decreases, there may be a change in the fiber morphology to a more crystalline fiber orientation resulting in increased tenacity. This result is included in this report to demonstrate that the islands-in-the-sea method of producing nano-fibers

can be exploited to further reduce fiber size and yield nano-fibers with acceptable properties.

Tensile Properties of PA6 nano-fibers

Yarn	Denier / filament	Pva/PA6 % Ratio		Tenacity Gm/denier	Std. Dev
300D	2.63/1.32	50/50		5.61	1.7
300UD	7.79/3.90	50/50		2.22	0.34
600D	2.70/1.35	50/50		5.48	0.76
600UD	8.15/4.08	50/50		3.12	0.74
990D	2.72/1.36	50/50		4.80	0.46
990UD	7.98/3.99	50/50		1.80	0.28
990D	2.93/0.59	80/20		10.87	1.38

List of Literature Review

1. Microfiber

- ▷ M.Nishimura, T.Hibino and K. Tsujimoto, A Microfiber of promise, Textile Asia, Dec.,54-67(1992)
- ▷ Ultrafine Microfibers, JTN, Nov.,49-57(1994)
- ▷ W.B.Achwai, Microfibers-characteristics,properties, and processing, Colurage, Aug.,35-36(1994)

2. Forming Microfiber

- ▷ M.V.Tsebrenko, A.V.Yudin and T.I.Ablazova, Mechanism of fibrillation in the flow of molten polymer mixtures, *Polymer*,17,831(1976)
- ▷ Kent G.Blizard and Conald G.Baird, The Morphology and Rheology of Polymer Blends Containing a Liquid Crystalline Copolyester, *Polym.Eng. Sci.* 27(9), 653(1987)
- ▷ H.E.H.Meijer, P.J.Lemstra and P.H.M Elemans, Structured Polymer Blends, *Makromol.Chem.Macromol.Symp.*,16,113(1988)
- ▷ Lloyd M.Robeson, Robert J. Axelrod, Menas S. Vratsanos, and Margaret R. Kittek, Microfiber Formation: Immiscible Polymer Blends Involving Thermoplastic Poly(vinyl alcohol) as an Extractable matrix, *J.Appl.Polym.Sci.*, 52,1837(1994)
- ▷ M.V.Tsebrenko,N.M.Rezanova, and I.A.Tsebrenko, Fiber-Forming Properties of Polymer Mixture Melts and Properties of Fibers on their Basis, *Polymer Engineering and Science*, 39(12), 2395-2402(1999)

3. Characterization of microfiber - Tensile Property

- ▷ Preston E. Sasser, Interpretations of Single Fiber, Bundle, and Yarn Tenacity Data, *Textile Res.J.* 61(11),681-690(1991)
- ▷ H.Brody, Synthetic fiber materials, Longman(1994)
- ▷ Lijing Wang and Xungai Wang, A Study of Wool's Tensile Strength in Early Stage Processing, *Textile Res.J.* 70(2),98-102(2000)
- ▷ Lijing Wang and Xungai Wang, Diameter and Strength Distribution of Merino Wool in

Early Stage Processing, *Textile Res.J.* 68(2),87-93(1998)

- ▷ Angelo J. Sabia, Modification of the Tactile and Physical Properties of Microfiber Fabric Blends with Silicone Polymers, *Textile Chemist and Colorist*, 27(9), 79-81(1995)
- ▷ J.Vlachopoulos, N.Hadijis and A.E.Hamielec, Influence of molecular weight on the tensile properties of nearly monodisperse polystyrenes,
- ▷ Nicole S.J.A.Gerrits, Roobert J. Young and Piet J. Lemstra, Tensile properties of biaxially drawn polyethylene, *Polymer*, 31(2), 231-236(1990)
- ▷ Tsuneo Sasuga, Naohiro Hayakawa, Kenzo Yoshida and Miyuki Hagiwara, Degradation in tensile properties of aromatic polymers by electron beam irradiation, *Polymer*, 26(7), 1039-1045(1985)
- ▷ Chang T.Kiang and John A. Cuculo, Influence of Polymer Characteristics and Melt-Spinning Conditions on the Production of Fine Denier Poly(Ethylene Terephthalate) Fibers. Part 3. Structure and Properties of Fine Denier As-spun PET Fibers, *Journal of Applied Polymer Science*, 46, 83-97(1992)
- ▷ S.K.Pal, R.S.Gandhi and V.K.Kothari, Influence of texturing parameters on structural properties of microfiber polyester yarns, *Chemical Fibers International*, 45, 418(1995)
- ▷ ASTM standard, D2524-91: Breaking Tenacity of Wool fibers, Flat Bundle Method, 1/8in. Gauge Length, D 1294-86: Breaking Tenacity, and Tensile Strength of Wool Fiber Bundles-1in. Gauge length, D 3822-96: Tensile Properties of Single Textile Fibers, Annual Book of ASTM Standards, V.07(02), 1999
- ▷ Zhenzhong Shao, Fritz Vollrath, The effect of solvents on the concentration and

mechanical properties of spider silk, *Polymer*, 40,1799(1999)

4. Processing with microfiber-Weaving fabrics and manufacturing apparel

- ▷ Sanjay Gupta, Polyester microfiber processing, *Textile Asia*, Jan., 53-56(1993)
- ▷ Making Up of Microfiber Fabrics, *Apparel International*, Jul./Aug.,21-23(1993)
- ▷ M.N.Chapatwala and R.S.Gandhi, Processing of Polyester microfibers fabrics-A New generation of fabrics, *Colourage*, Apr., 11-14(1992)
- ▷ Requirements for weaving microfiber yarns, *ITB Yarn and Fabric Forming*, 2,14-16(1994)
- ▷ Colleen Moynahan, Microfiber Solutions, *Apparel Industry Magazine*, May, 27-30(1992)

Nanostructures and Nanocomposites

The study of nanostructures is based largely on scrutiny of biological models which occur naturally on the nanoscale. Highly evolved, these systems are examples of self-assembly, self-maintenance and repair: desirable properties for functional microscopic structures. For instance, the immune system has been used to "create tools for recognition, assembly, and control of nanoscale fabrication."(1)

Magnetotactic bacteria navigate with the assistance of a magnetite nanocrystal assembly. The construction of this nanodevice is thought to date back two billion years on Earth, and is possibly similar to nanodevices found on Mars.(2)

A bacterial flagellar motor with a diameter of thirty nm rotates from 10,000 to 100,000 rpm.(3) Researchers are studying both the mechanisms through which to replicate the functionality of these structures and the creation of "hybrid biologic and non-biologic systems."(1) Because of their small size, nanofibers have the advantage of addressing issues on the molecular scale. Nano-Tex uses a nanofiber net over a synthetic yarn core to produce stain-resistant fabrics: liquid molecules cannot penetrate the textile structure, and remain beaded on the fabric surface.(4) However, this diminutive scale also results in production difficulties. It is not possible to produce individual or fully aligned fibers of specific dimensions; nanofiber generation often results in an entangled mass of randomly aligned fibers. Methods of production include: electrospinning, melt extrusion, and chemical vapor deposition. Lack of fiber alignment decreases overall potential strength of the composite, yet the uniform dispersion of the nanofibers produces a structure which is stronger than the matrix material alone.(5) While increased fiber content seems to improve composite strength, there is also a corresponding decrease in fiber alignment due to "fiber-fiber and fiber-wall interactions" among other factors.(6) Since composites generally require strength performance in a given direction, there are many techniques which attempt to direct fiber orientation into an application-specific form. One study has shown that "increasing the residence time of the composite flow through the die channel" during extrusion increased the degree of "fiber alignment along the preferred direction."(6) It is also easier to measure qualities such as tensile strength, strain and modulus using nanofiber composites, rather than nanofibers alone. Improved methods of production would enable carbon nanofibers to replace widely used glass fibers as polymer matrix composite-reinforcing fibers. Carbon fibers "offer higher strength and modulus, lower density, outstanding thermal and electrical conductivity" when compared to glass fibers, however they are also more expensive. (6)

Nanofiber Generation

Electrospinning: "In electrospinning, a polymer solution is suspended and stabilized by its surface tension. Charges are induced on the liquid droplet by an electric field. As the intensity of the field increases, the droplet elongates until a critical value at which the electrostatic force overcomes surface tension and a charged jet of the solution is ejected. As the jet travels, the solvent

evaporates, leaving behind a charged polymer fiber. Continuous fibers can be collected either in the form of non-woven fabric, or as aligned yarns...[the] ultra-large surface-volume ratio of these fiber mats is of great interest for reinforced composites, filtration, protective clothing, biomedical applications including wound dressing, and as supports for enzymes or catalysts.” (7)

* “It is widely assumed that when the critical potential $\phi(0^*)$ has been reached and any further increase will destroy the equilibrium, the liquid body acquires a conical shape referred to as the Taylor cone...[i]n the present work we show that the Taylor cone corresponds essentially to a specific self-similar solution, whereas there exist nonself-similar solutions which do not tend towards a Taylor cone. Thus, the Taylor cone does not represent a unique critical shape: there exists another shape, which is not self-similar.” (8)

* “In addition to round nanofibers, electrospinning a polymer solution can produce thin fibers with a variety of cross-sectional shapes. Branched fibers, flat ribbons, ribbons with other shapes, and fibers that were split longitudinally from other fibers were observed. The transverse dimensions of these asymmetric were typically 1 or 2 μm ...indicates that fluid mechanical effects, electrical charge carried with jet, and evaporation of solvent all contributed to the formation of the fibers.” (9)

Vapor Grown: “Carbon nanofibers are grown homogeneously on a large area of nickel-deposited sodalime glass substrate by thermal chemical vapor deposition of acetylene at 500 degrees C. The diameters of carbon nanofibers are uniformly distributed in the range between 50 and 60 nm.” (10)

Electrostatic Generation: “Long nanofibers of conducting electronic polymers and their blends and also conventional polymers are...fabricated in air by non-mechanical electrostatic dispersion method. All fibers...have diameters < 100 nm.” (11)

Possible Nanofiber Applications

* “[I]mproved electrolytes that heighten the efficacy and life span of rechargeable batteries... artificial skins and highly efficient hazard suits that...filter germs.” (1)

* “[S]olubilizing linear poly(ethylenimine)...and electrospinning the

solution... into a plurality of fibers; and crosslinking the fibers to render the fibers insoluble...making a fabric or membrane capable of protecting against attack by chemical warfare and nerve gases...the fibers provide multiple useful secondary amine sites for the nucleophilic decomposition of various chemical warfare agents such as mustard gases or fluorophosphate nerve gases such as sarin, soman, and tabun...electrospun fibers have a diameter from about 100 to 400 nm...also provides for gas and water permeability resulting in a more comfortable fabric...also allows for use in protective breathing apparatuses.” (2)

*”Use of...nanofibers, and other materials...are of particular interest to fuel cell developers as they provide such key properties as high conductivity, corrosion resistance, thermal stability, low creep, dimensional stability, and flame retardancy.” (3)

*”Carbon nanofibers...10-500 nm have been evaluated as novel electrode materials for electrochemical applications... they exhibit higher electrochemical capacitances (ca. 60 vs. 20 Fg(-1)) because the spaces between the fibers are readily penetrated by an electrolyte solution.” However, “when the spaces... are impregnated by an inert dielectric material, such as high-melting paraffin wax...the carbon nanofibers form a high-density composite electrode with good conductivity and low capacitance.” (4)

*From a Phase I SBIR (US Army): Development of “strong, lightweight helmets and other protective gear from metal oxide nanoparticle-reinforced polymer composites...[the] nanoparticles are very chemically active, [and it is theorized] that chemical bonding will occur between the polyesters at the ester group of the polymer and the hydroxyl group of the polymer. This is expected to create a strong cross-linking and a spatial redistribution that will increase the ability of the material to absorb shock and dissipate the energy during impact.” (5) *”Ten grams of nanofiber can stretch from the earth to the moon and back, 1300 times.” (1)

PROGRESS REPORT FOR April 2000 –May 2002

M.A. Zikry, Associate Professor. Mechanical and Aerospace Engineering

J.N. Baucom, Ph.D. Student, Mechanical and Aerospace Engineering

ABSTRACT

We have developed specialized dynamic experimental methodologies and numerical techniques for new woven composites that can be used for high strength and lightweight applications. We have developed new and innovative experimental techniques at high velocities (200-100 m/s) using powder guns and low velocities (1-5 m/s) using drop towers in conjunction with high speed photography and other diagnostics to determine how energy is absorbed, dissipated, and attenuated. We are using these techniques in conjunction with computational techniques to develop the framework for the design of new systems that are based on optimizing and accounting for fiber orientations, distributions, and volume fractions and matrix type as a function of failure modes, such as delamination, debonding, and matrix and fiber cracking in systems subjected to multi-axial dynamic loading conditions.

SUMMARY OF THE MOST IMPORTANT RESULTS

We have conducted dynamic experiments and numerical modeling for the following material systems to determine how failure and damage initiate and evolve:

- Benchmarking of 2D woven with 3D braided Kevlar and Spectra laminates with epoxy
- 3D braided and 2D Plain weave Kevlar fabrics
- Hybrid 2 layer systems comprised of oxide beads encased in epoxy (with Professor Ko)
- Carbon/epoxy 3D woven cellular polymer matrix composites (3DCPMC)

We are currently focusing on the 3DCPMC systems. In this system porosity is introduced in the matrix. This results in systems of low areal densities. We have found that if we can control the porosity to dissipate the impact, we may be able to design low

weight high strength systems that can *mitigate damage and resist damage*. However, the optimal fiber volume fractions for 3D systems and porosity distributions are yet to be determined. We are working with industrial partners to develop ideal processing techniques. We are also currently incorporating our experimental data into numerical codes so that we can obtain detailed information on how energy is dissipated, attenuated, and dispersed.

The experimental techniques have been based on determining wave speeds at impact and relating it to the absorbed and dissipated energy. Numerical techniques have utilized unit cells to determine how energy is dissipated as a function of impact speed.

MANUSCRIPTS

J.N. Baucom and M.A. Zikry (2001), Failure Modes in 2D and 3D Woven Composites, in *Failure Initiation and Evolution of Composite Systems*, ed.: A. Waas, AMD, ASME Press, New York, NY, 1-21.

J.N. Baucom, M.A. Zikry, Y. Qiu (2001), Porosity and Failure Evolution in 3D Failure Modes, ed.: Y. Rajapakse, AMD, ASME Press, New York, NY, 31-45.

G. Subhash, S. Sulibhavi, and M.A. Zikry (2001), Influence Of Strain Rate On The Uniaxial Compressive Behavior Of 2-D Braided Textile Composites, *Composites: Part A* Vol 32/11, pp 1583-1591.

Qiu, Y., Xu, W., Wang, Y., Zikry, M.A., Mohamed, M. (2001). Fabrication And Characterization Of Three-Dimensional Woven Carbon Preform Reinforced Cellular Matrix Composites. *Composites Science and Technology*, 2425-2435.

GRADUATE STUDENTS

J.N. Baucom, Ph.D will be completed 2/02

SECTION 3

THE UNIVERSITY OF AKRON

REPORT DOCUMENTATION PAGE

Form Approved
OMB NO. 0704-0188

Public Reporting burden for this collection of information is estimated to average 1 hour per response, including the time for reviewing instructions, searching existing data sources, gathering and maintaining the data needed, and completing and reviewing the collection of information. Send comment regarding this burden estimate or any other aspect of this collection of information, including suggestions for reducing this burden, to Washington Headquarters Services, Directorate for information Operations and Reports, 1215 Jefferson Davis Highway, Suite 1204, Arlington, VA 22202-4302, and to the Office of Management and Budget, Paperwork Reduction Project (0704-0188,) Washington, DC 20503.

1. AGENCY USE ONLY (Leave Blank)		2. REPORT DATE May 5, '02		3. REPORT TYPE AND DATES COVERED FINAL Feb., 1996 – May, 2002	
4. TITLE AND SUBTITLE Synthesis and Characterization of Novel Surfaces				5. FUNDING NUMBERS Grant No. DAAH04-96-1-0018 Proposal No. 35023-MS-MUR Subcontract to North Carolina State University	
6. AUTHOR(S) B. Zhao, D. Mulkey, S. Liou, R. Sedjo, S. Lewis, M. Baum, B. A. Granville, Mirous, S. Boyes and William J. Brittain					
7. PERFORMING ORGANIZATION NAME(S) AND ADDRESS(ES) The University of Akron Department of Polymer Science Akron, OH 44325-3909				8. PERFORMING ORGANIZATION REPORT NUMBER	
9. SPONSORING / MONITORING AGENCY NAME(S) AND ADDRESS(ES) U. S. Army Research Office P.O. Box 12211 Research Triangle Park, NC 27709-2211				10. SPONSORING / MONITORING AGENCY REPORT NUMBER	
11. SUPPLEMENTARY NOTES The views, opinions and/or findings contained in this report are those of the author(s) and should not be construed as an official Department of the Army position, policy or decision, unless so designated by other documentation.					
12 a. DISTRIBUTION / AVAILABILITY STATEMENT Approved for public release; distribution unlimited.				12 b. DISTRIBUTION CODE	
13. ABSTRACT (Maximum 200 words) Phenol-functionalized surfaces were prepared by the formation of phenol-terminated monolayers or by spin-casting phenol-functionalized polyphosphazenes. In collaborative work with ARCOVA using fluorescence-based detection, these phenol-functionalized thin films showed excellent sensitivity to DMMP (a nerve-agent simulant). Tethered diblock copolymers composed of styrene and acrylate monomers have been synthesized. The tethered diblock polymers exhibited reversible surface changes in response to solvent treatment. For Si/SiO ₂ //PS- <i>b</i> -PMMA, the advancing water contact angle increased from 75° (characteristic of PMMA) to 99° (characteristic of polystyrene) after treatment with methylcyclohexane. We attributed this contact angle change to reversible changes in the chemical composition at the polymer-air interface. We also prepared diblock brushes with the outer block composed of poly(dimethylaminoethyl methacrylate) or methyl acrylate. These diblock brush systems exhibited similar solvent-induced changes in surface composition. A tethered triblock copolymer has been synthesized by sequential monomer addition. Si/SiO ₂ //polystyrene- <i>b</i> -poly(methyl acrylate)- <i>b</i> -polystyrene and Si/SiO ₂ //PMA- <i>b</i> -PS- <i>b</i> -PMA were prepared by the "grafting from" method using atom transfer radical polymerization. Treatment of the triblock brushes with block-selective solvents caused reversible changes in the water contact angles and atomic force microscopy analysis.					
14. SUBJECT TERMS polyphosphazenes, phenol monolayers, polymer brush, ultrathin coatings				15. NUMBER OF PAGES 15	
				16. PRICE CODE	
17. SECURITY CLASSIFICATION OR REPORT UNCLASSIFIED		18. SECURITY CLASSIFICATION ON THIS PAGE UNCLASSIFIED		19. SECURITY CLASSIFICATION OF ABSTRACT UNCLASSIFIED	
				20. LIMITATION OF ABSTRACT UL	

NSN 7540-01-280-5500

Standard Form 298 (Rev.2-89)
Prescribed by ANSI Std. Z39-18
298-102

1.) LIST OF MANUSCRIPTS AND PAPERS PRESENTED

a.) Papers published in peer-reviewed journals

1. "Trichlorosilane Chemisorption on Surface-Modified Poly(tetrafluoroethylene)," Zhao, B.; Brittain, W. J.; Vogler, E. A. *Macromolecules* **1999**, 32, 796.
2. "Synthesis of Tethered Polystyrene-*block*-Poly(methyl methacrylate) Monolayer on a Silicate Substrate by Sequential Carbocationic Polymerization and Atom Transfer Radical Polymerization," Zhao, B.; Brittain, W. J. *J. Am. Chem. Soc.* **1999**, 121, 3557.
3. "Synthesis and Characterization of Phenol and *o*-Chlorophenol Terminated Monolayers," Zhao, B.; Mulkey, D.; Brittain, W. J.; Chen, Z.; Foster, M. D. *Langmuir*, **1999**, 15, 6856.
4. "Nanopatterned Films Formed by Treatment of PS-*b*-PMMA Brushes with Selective Solvents," Zhao, B.; Brittain, W. J.; Zhou, W.; Cheng, S. Z. D. *J. Am. Chem. Soc.* **2000**, 122, 2407.
5. "Synthesis of Tethered Polystyrene-*block*-Poly(methyl methacrylate) Brushes by Reverse Atom Transfer Radical Polymerization," Sedjo, R.; Mirous, B.; Brittain, W. J. *Macromolecules* **2000**, 33, 1492.
6. "Synthesis of Polystyrene Brushes on Silicate Substrates via Carbocationic Polymerization from Self-Assembled Monolayers," Zhao, B.; Brittain, W. J. *Macromolecules* **2000**, 33, 342.
7. "Synthesis, Characterization and Properties of Tethered Polystyrene-*b*-polyacrylate Brushes on Flat Silicate Substrates," Zhao, B.; Brittain, W. J. *Macromolecules* **2000**, 33, 8813.
8. "AFM Study of Tethered Polystyrene-*b*-poly(methyl methacrylate) and Polystyrene-*b*-poly(methyl acrylate) Brushes on Flat Silicate Substrates," Zhao, B.; Brittain, W. J.; Zhou, W.; Cheng, S. Z. D. *Macromolecules* **2000**, 33, 8821.
9. "Polymer Brushes: Surface-Immobilized Macromolecules," Zhao, B.; Brittain, W. J. *Prog. Polym. Sci.* **2000**, 25, 677.
10. "Synthesis of Polymer Brushes on Silicate Substrates via Reversible Addition Fragmentation Chain Transfer Technique," Baum, M.; Brittain, W. J. *Macromolecules* **2002**, 35, 610.
11. "Synthesis, Characterization and Properties of ABA Type Triblock Copolymer Brushes of Styrene and Methyl Acrylate Prepared by Atom Transfer Radical Polymerization," Boyes, S.; Brittain, W. J.; Weng, X.; Cheng, S. Z. D. *Macromolecules*, in press.

PARTICIPATING SCIENTIFIC PERSONNEL

Dr. William J. Brittain, Professor
Bin Zhao, Ph.D. Univ. Akron awarded 12/99
David Mulkey, M.S. Univ. Akron awarded 05/98
Stewart Lewis, M.S. Univ. Akron awarded 05/00
Marina Baum, Ph.D. Univ. Akron awarded 12/01
Randy Sedjo, Ph.D. Univ. Akron expected 08/02
Shing-Tza Liou, Ph.D. Univ. Akron expected 12/02
Anthony Granville, Ph.D. Candidate
Brian Mirous, Ph.D. Candidate
Dr. Stephen Boyes, Postdoctoral Research Associate

INVENTIONS

None

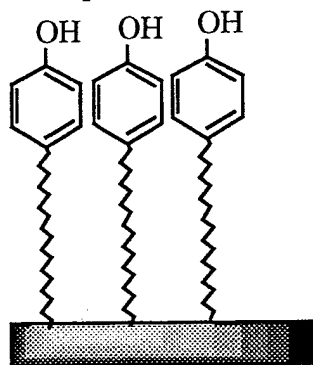
SCIENTIFIC PROGRESS AND ACCOMPLISHMENTS

Organic Thin Films Engineered for Nerve Agent Adsorption

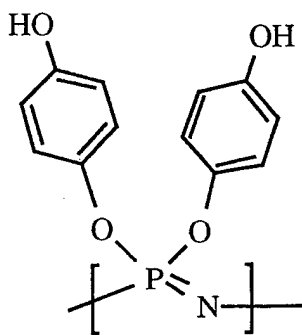
It has been demonstrated in the literature¹ that strong hydrogen-bonding materials interact strongly with organophosphorous esters (nerve agents GC and GB are organophosphorous esters). In particular phenol-functionalized polymers were proven useful as sorbent materials for dimethyl methylphosphonate (DMMP), a nerve agent simulant. We prepared thin, organic coatings containing phenol to strongly interact with organophosphorous chemical agents. Two systems have been synthesized with phenol groups: phenol-terminated self assembled monolayers (SAMs)² and phenol-substituted polyphosphazenes. Each system has distinct advantages. Because the SAMs are well-ordered thin films, the phenol groups are localized at the surface and thus, the interaction of the phenol with agents in the environment is maximized.³ The phenol-substituted polyphosphazenes have one of the highest functional group densities for a polymer.

Both systems have been used in coating applications. We were interested in three applications: (1) coatings for optical-based chemical agent sensors, (2) new filtration media for gas masks, and (3) surface modification of fabrics for permeation-selective clothing.

Considerable progress was made in the development of chemical agent sensors through a collaboration with the American Research Corporation of Virginia (ARCOVA). ARCOVA has developed an optical platform for chemical agent detection based on fluorescence changes in an adsorbent, thin film. We submitted samples of both the phenol-SAMs and phenol-functionalized polyphosphazenes for testing as absorbent layers in these optical sensors. Samples of the phenol-SAM demonstrated a 125 ppb sensitivity to DMMP. This promising result resulted in further optimization of the SAM. A phenol-functionalized polyphosphazene demonstrated a 24 ppb sensitivity to DMMP. These sensitivities surpass the best systems currently used by ARCOVA. However, the response times are ≈ 1 min which is several-fold slower than comparable systems.



phenol-terminated
monolayer



phenol functionalized polyphosphazene

The trichlorosilane chemistry used for phenol-SAMs has also been used to produce phenol-functionalized silica gel. Characterization by solid-state ^{13}C NMR confirmed the chemical structure. The high surface area of the silica gel makes it a potential substitute for current gas mask absorbent materials.

Surface modification of fabrics is also being pursued using the same coating chemistry. We have successfully modified poly(tetrafluoroethylene) (PTFE) by a multiple-step process: (1) chemical reduction of the PTFE, (2) oxidation to introduce hydroxyl groups, and (3) trichlorosilane deposition.⁴ The structure of the monolayers on PTFE was probed using FTIR, contact angles and X-ray photoelectron spectroscopy.

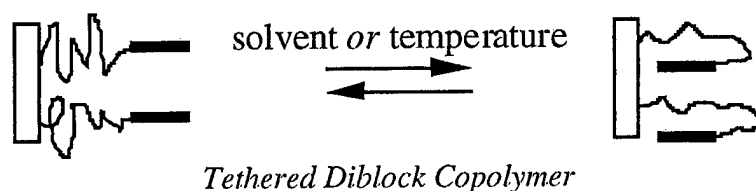
SURFACE-IMMOBILIZED BLOCK COPOLYMERS : POTENTIAL SMART SURFACES

An assembly of tethered polymer chains in mutual proximity are often called "polymer brushes." The study of well-defined polymer brushes is useful for understanding colloidal stabilization and other interfacial phenomena. The amount of theoretical work on polymer brushes equals or exceeds the amount of experimental

information available concerning properties and structure. Therefore, new developments in synthesis of polymer brushes is important.

*Diblock Brushes Composed of Si/SiO₂//PS-*b*-PMMA*

Tethered diblock copolymers composed of styrene and methyl methacrylate (MMA) were synthesized.⁵ The synthetic route involved the following sequence: 1) surface immobilization of 2-methoxy-2-(4-trichlorosilylphenyl)propane onto a silicate substrate, 2) carbocationic polymerization of styrene, and 3) atom-transfer radical polymerization of MMA. The thickness of the polystyrene layer was controlled by the conditions of the carbocationic polymerization (e.g., Lewis acid catalyst, time, and temperature). The progress of the polymerizations was monitored via FTIR and ellipsometry. The reaction of MMA with the polystyrene film presumably involved chloro-terminated polystyrene chains as initiators in accord with the analogous block copolymerization performed in solution. The samples of tethered diblock polymers exhibited reversible surface changes in response to solvent treatment. For a sample with a 26 nm polystyrene layer and a 9 nm PMMA layer, the advancing water contact angle increased from 75° (characteristic of PMMA) to 99° (characteristic of polystyrene) after treatment with methylcyclohexane; subsequent treatment with CH₂Cl₂ returned the contact angle to the original value of 75°. We attributed this contact angle change to reversible changes in the chemical composition at the polymer-air interface.



X-ray photoelectron spectroscopy (XPS) shows large compositional changes after treatment with CH₂Cl₂ and cyclohexane which are consistent with the contact angle observations. For a sample with 23 nm PS layer and 14 nm PMMA layer, AFM was used to study surface morphological changes.⁶ It was found the surface is relatively smooth with a roughness of 0.77 nm after CH₂Cl₂ treatment; treatment with cyclohexane at 35°C for 1 h increases the surface roughness to 1.79 nm. An irregular worm-like structure appeared on the surface. Nanopatterned film with well-defined morphology was formed if mixed solvents of CH₂Cl₂ and cyclohexane are used and the composition is gradually changed. The scale of the nanopattern can be controlled by the tethered block length.

*Synthesis of Tethered PS-*b*-polyacrylate Brushes on Flat Silicate Substrates.*

A carbocationic initiator was immobilized onto the silicate substrates by a self-assembly technique. Then surface initiated carbocationic polymerization of styrene produced tethered PS brushes followed by ATRP of an acrylate monomer to achieve diblock copolymer brushes. MMA, methyl acrylate (MA) and *N,N*-dimethylaminoethyl methacrylate (DMAEMA) were used in the synthesis of the second block.⁷

Previous FTIR-ATR study of surface-initiated carbocationic polymerization⁸ indicated that the initiator efficiency under typical polymerization conditions was low ($\approx 7\%$) and a sequential, second carbocationic polymerization involved both PS chain ends and immobilized initiators.⁸ To avoid the initiation from the immobilized cumyl methyl ether initiator in the synthesis of the second block, we used ATRP to synthesize the second block. Coca and Matyjaszewski⁹ successfully synthesized PS-*b*-PMMA copolymers in solution by carbocationic polymerization and ATRP. The chlorine-terminated PS chain end is an initiator for both carbocationic polymerization and ATRP. One advantage of ATRP is the larger number of available monomers for radical polymerization.

PS-*b*-PMMA Brushes. The FTIR-ATR spectrum (see Figure 1c) revealed that a strong peak appeared at 1732 cm⁻¹, which was assigned to the carbonyl stretching vibration of the ester group in PMMA. Based on ellipsometry, the film thickness in the dry state increased from 26 nm to 35 nm for a tethered PS brush that was subjected to ATRP with MMA. The thickness of the PMMA layer can be controlled by the concentration of free ATRP initiator in solution. Using this method, PMMA blocks with 3-25 nm thicknesses could be reproducibly

produced. The free initiator was 1-phenyl-1-chloroethane (PHECl), which has a similar structure to the chlorine-terminated PS chain ends. The FTIR-ATR spectra clearly indicate that the intensity of carbonyl peak increased with decreasing free initiator concentration in accord with our expectations.

Extension of Diblock Synthesis to PMA and PDMAEMA. Using the same strategy, PS-*b*-PMA brushes tethered on flat silicate substrates were successfully synthesized. ATRP was carried out on a 24 nm PS brush at 110 °C for 24 h with methyl 2-bromopropionate as the free initiator. After polymerization, the sample was extracted with THF or CH₂Cl₂ for 24 h. The FTIR-ATR spectrum displayed a strong carbonyl absorption peak at 1733 cm⁻¹ (Figure 2c); ellipsometry indicated that the film thickness increased 9 nm.

Many attempts have been made to synthesize block copolymers containing PDMAEMA in solution; well-defined PMMA-*b*-PDMAEMA and PMA-*b*-PDMAEMA copolymers with low polydispersities have been prepared by ATRP.¹⁰ PS-*b*-PDMAEMA has also been synthesized by ATRP, but the polymerization was not well controlled due to the relatively slow initiation from PS macroinitiator in comparison with the propagation rate of PDMAEMA. The reported polydispersity was 1.83. We attempted the synthesis of tethered PS-*b*-PDMAEMA by ATRP from PS brushes. The polymerization was allowed to proceed at 115°C for 9 h followed by THF extraction. The FTIR-ATR spectrum is shown in Figure 2d. Characteristic peaks of PDMAEMA such as the carbonyl peak located at 1729 cm⁻¹ and two symmetric stretching vibration absorptions of the methyl group in the N(CH₃)₂ moiety located at 2820 cm⁻¹ and 2769 cm⁻¹ were observed. Ellipsometry measurements indicated that the film thickness increased from 24 nm to 26.5 nm.

Tensiometry of Diblock Copolymer Brushes. We used water contact angles to probe the chemical nature of the outermost layer in our diblock copolymer brushes. The contact angles (Table 1) of the PS-*b*-PMMA brush ($\theta_a = 74^\circ$) and the PS-*b*-PMA brush ($\theta_a = 68^\circ$) after each brush was treated with CH₂Cl₂ (which is a good solvent for both blocks) indicate that the polyacrylate blocks are localized at the air interface because the contact angles are representative of spun-cast films of the corresponding homopolymers. When the PS-*b*-PDMAEMA brush was treated with H₂O/THF (1:1, v/v), advancing and receding contact angles of 63° and 44° observed (Table 1). Since PDMAEMA is a water soluble polymer, the contact angles should be closer to 0°. The possible reason for this difference is that the initiation efficiency in the polymerization of DMAEMA is lower; therefore, the topmost layer is composed of both PS and PDMAEMA chains. Another possibility may be due to the higher surface free energy of PDMAEMA relative to PS. When the sample was removed from the solvent, the PDMAEMA blocks may have aggregated and migrated into the bulk phase to avoid contact with air; the PS chains would remained localized at the air interface due to their lower surface energy.

We also used contact angles to study the influence of block-selective solvents on the copolymer brushes. In earlier work, we observed large changes in the contact angles of PS-*b*-PMMA brushes when the samples were treated with cyclohexane or CH₂Cl₂.⁵ Table 1 summarizes the results for the three diblock copolymer systems reported here.

Tethered PS-*b*-PMA brushes exhibited similar properties to tethered PS-*b*-PMMA brushes. Treatment with cyclohexane increased the advancing and receding contact angles to 98° and 74° (characteristic values for PS). Subsequent treatment with CH₂Cl₂ changed the contact angles back to their original values; these changes were reversible for many cycles of alternating solvent treatment. Tethered PS-*b*-PDMAEMA brushes also undergo self-reorganization in response to environmental changes. A mixed solvent of THF and water was chosen to treat the PS-*b*-PDMAEMA brushes. For a 30 nm PS-*b*-PDMAEMA brush with a 27 nm thick PS layer, the film exhibited an advancing contact angle of 63° and a receding contact angle of 44° after treatment in THF/H₂O (v/v = 1:1) for 60 min at elevated temperature. Treatment with cyclohexane at 35°C for 60 min increased the contact angles to 98° and 77°. These changes were also reversible.

The time-scale of the contact angle changes is dependent on the relative thicknesses of PS layer and polyacrylate layers. For a sample with 29 nm PS and 3 nm PMMA, reorganization of polymer chains occurred quickly upon immersion in cyclohexane at 35°C. The polymer brushes exhibited the characteristic contact angles of PS after treatment with cyclohexane in less than 20 min. For a sample with 28 nm PS and 22 nm PMMA, 40 min immersion in cyclohexane at 35°C resulted in an advancing contact angle of 93° and a receding contact angle of 74°. Longer immersion times (several h) are needed for this sample to achieve an advancing contact angle of

99°. For a sample with 11 nm PS and 18 nm PMMA, the highest advancing and receding contact angles which can be achieved after immersion in cyclohexane at 35°C for 3.5 h are 85° and 69°.

X-ray Photoelectron Spectroscopy of Diblock Copolymer Brushes. XPS was used to augment tensiometric data on the composition of diblock copolymer brushes at the air interface. After CH₂Cl₂ treatment of the PS-*b*-PMMA brush, 23.5% oxygen was observed; treatment with cyclohexane produced a sample that displayed only 7.8% oxygen. This large decrease in oxygen is consistent with the migration of PMMA blocks away from the air interface.

The surface compositions of a tethered PS-*b*-PMA brush with 24 nm PS and 6 nm PMA after treatment with CH₂Cl₂ and cyclohexane were recorded. The oxygen peak O_{1s} decreased significantly after treatment with cyclohexane. Calculations indicated that the PS content in the XPS probing region increased from 38.1% to 88.0% after immersion of this sample in cyclohexane at 35°C for 60 min. These results are consistent with the contact angle observations and are qualitatively similar to the PS-*b*-PMMA system. The XPS spectra of a 26.5 nm PS-*b*-PDMAEMA brush with 24 nm PS after treatment with THF/H₂O (v/v = 1:1) and cyclohexane were recorded. After treatment with cyclohexane, the oxygen content decreased from 8.8 % to 1.5 % in the XPS probing depth; the nitrogen content decreased from 2.2 % to nondetectable in the XPS spectrum.

Dynamic Properties of Tethered Diblock Copolymer Brushes. In bulk, diblock copolymers consisting of two homopolymer chains have a tendency to undergo microphase separation. A variety of phase morphologies ranging from spherical, hexagonal, lamellae to gyroid have been discovered and extensively studied. In tethered diblock copolymer brushes, the mobility of polymer chains is highly restricted because one end of the polymer chain is covalently connected to the solid surface. The chemically distinct nature of each block and fixation of one end of polymer chains to the surface underlies the unique behavior of polymer brushes. The different interactions of each block with solvents can force the tethered polymer chains to reorganize themselves to minimize the free energy, resulting in interfaces between copolymer brushes and air that exhibit different properties. This preferential interaction of one block with solvents has led to the theoretical prediction of nanopattern formation from tethered diblock copolymer brushes.¹¹

Experimentally, we have found that tethered diblock copolymer brushes exhibit interesting properties. The water contact angles of the films changed dramatically upon treatment with different solvents. XPS results are consistent with contact angle observations. Under appropriate conditions, a nanopattern can form from the tethered diblock copolymer brushes. Contact angles are very sensitive to the topmost surface composition changes (sensing depth is 0.5-1 nm); many factors such as surface roughness and chemical heterogeneity can have significant effects on the contact angle values. The changes in water contact angles are consistent with XPS spectra where an increasing contact angle (which we have interpreted in terms of PS localization at the air interface) is accompanied by a decrease in the O_{1s} peak in the XPS spectrum. Contact angles changes are dependent on the relative thicknesses of PS and PMMA layers. We have observed that ability of PS segments to localize at the air interface (as deduced by water contact angles) is dependent on the PMMA block thickness. Larger PMMA thicknesses are accompanied by smaller changes in water contact angles after the PS-*b*-PMMA brushes are immersed in cyclohexane (cyclohexane is a theta solvent for PS at 35°C).

Tethered PS-*b*-PMA brushes on flat silicate substrates exhibit similar properties to tethered PS-*b*-PMMA brushes (Table 1). After treatment with CH₂Cl₂, the advancing and receding contact angles are 68° and 55°. Treatment with cyclohexane increased the contact angles to 98° and 74°. These changes are reversible and the XPS spectra support this surface localization of different block segments. Tethered PS-*b*-PDMAEMA brushes also undergo reorganization in response to environmental changes (Table 1). Treatment with cyclohexane at 35°C for 60 min increased the contact angles to 98° and 77°. Subsequent treatment with in THF/H₂O (v/v = 1:1) for 60 min at elevated temperatures changed the contact angles back to their original value.

Reorganization Mechanism of Tethered Diblock Copolymer Brushes. For tethered PS-*b*-PMMA and PS-*b*-PMA, CH₂Cl₂ is a good solvent for PS, PMMA and PMA. When the sample is immersed in this solvent, the polymer chains are forced to stretch away from the interface to avoid contact with neighboring polymer chains. Removing the PS-*b*-PMMA brushes from CH₂Cl₂ condenses the polymer brushes and localizes PMMA blocks at the air interface. The T_g of PS and PMMA in the bulk state are both around 100 °C and there is little

difference in surface free energies of PS and PMMA. Therefore, The PMMA blocks remain at the air interface, which is supported by contact angle measurements and XPS results.

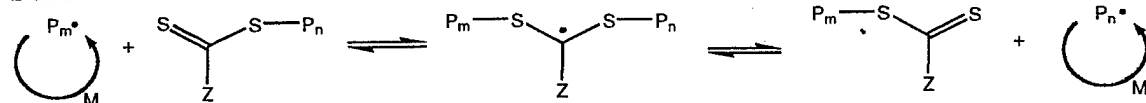
If the sample was immersed in the cyclohexane, we speculate that PMMA chains migrate from the solvent interface and form aggregates with neighboring PMMA blocks to avoid contact with solvent. Although PS blocks have a low mobility because of the covalent bond to the silicon wafer surface and to the PMMA block, they are miscible with cyclohexane and migrate to the solvent interface to form a shield around the PMMA aggregates. Based on earlier work that indicated a low ($\approx 7\%$) initiator efficiency, we believe that the PS chains are sparsely distributed on the surface (average occupied area $\approx 3 \text{ nm}^2$).⁸ This low grafting density should facilitate PS segment mobility during the reorganization process. If the PMMA layer is thick compared with PS layer, it would be difficult for PS chains to localize at the solvent interface and for PMMA to form aggregates which are shielded by PS chains. The thinner the PMMA layer, the easier it is for PS chains to move to the solvent interface. Similar to PS-*b*-PMMA brushes, when PS-*b*-PMA brushes are treated with cyclohexane, a reorganization takes place that localizes the PS segments at the air interface. Our impetus for comparing PMMA and PMA terminal blocks was to probe the effect of the Flory-Huggins parameter on the dynamics of diblock reorganization. The tensiometry and XPS results are similar for both systems in terms of the reversible localization of PS segments at the air interface. In a companion study to this report, we have observed significant differences in the nanomorphology of PS-*b*-PMMA vs. PS-*b*-PMA, as deduced by atomic force microscopy.¹²

For PS-*b*-PDMAEMA brushes, the mixed solvent of THF and water (1:1, v/v) is a good solvent for PDMAEMA but a poor solvent for PS chains. Therefore, PDMAEMA blocks have an extended conformation in this solvent, while PS chains remained collapsed. Removing the sample from the mixed solvent results in low advancing contact angles. We speculate that treatment with cyclohexane forces PDMAEMA blocks to aggregate with each other to minimize contact with solvent. The PS chains become swollen and form a shell around PDMAEMA. Consequently, the film exhibits the characteristic contact angles of PS. In all of three systems, the tethered diblock copolymer brushes reorganize themselves to achieve the lowest system free energy in response to the different solvent treatments.

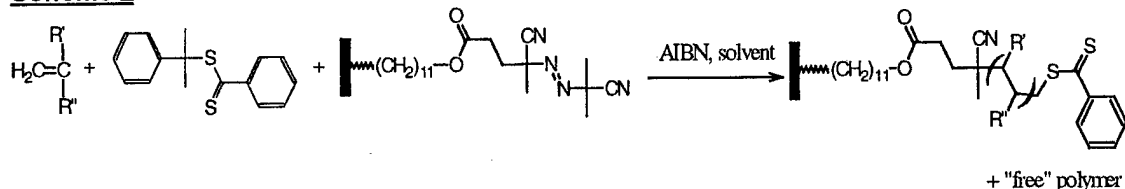
SYNTHESIS OF POLYMER BRUSHES BY REVERSIBLE ADDITION FRAGMENTATION CHAIN TRANSFER (RAFT)

The focus of this project is synthesis of polymer brushes utilizing the "grafting from" method and controlling the brush polymerization initiated by surface-immobilized azo-type initiator *via* the RAFT technique (Schemes 1 and 2).

Scheme 1



Scheme 2



Surface-initiated RAFT Polymerizations. Scheme 2 shows the general process of surface-initiated RAFT polymerizations using 2-phenylprop-2-yl dithiobenzoate as the chain transfer agent and a substrate-immobilized azo initiator. Homopolymer brushes of PMMA, poly(*N,N*-dimethylacrylamide) (PDMA), and PS were synthesized on silicon wafers (Table 2). For the surface-initiated RAFT polymerizations, we found that adding free initiator (AIBN concentrations ranging from 0.00368 M to 0.0147 M) was advantageous. The thickness of the polymer brushes was proportional to the amount of "free" initiator in the system. The polydispersity of the "free" polymer increased with increasing amount of "free" initiator. For CTA (chain transfer agent)/AIBN ratios 1/0.5 (for PS and PDMA) and 1/0.25 (for PMMA), reasonably thick films were prepared and the polydispersity of the "free" polymer was relatively narrow. Thermogravimetric analysis (TGA) was utilized to assess the amount of polymer brush on silica gel; up to 40% (w/w) polymer was grafted to the silica gel.

Sequential Surface-Initiated RAFT Polymerizations. To test the controlled behavior of the surface-initiated polymerizations, incremental monomer addition experiments were performed. The substrates were removed from the reaction mixture every several h, analyzed and placed into a fresh reaction mixture to resume brush growth. ATR-FTIR analysis confirms the stepwise growth of the immobilized PDMA and PS brushes. With each sequential monomer step, a gradual increase was observed for absorptions at 2930 (C-H) and 1645 (C=O) cm^{-1} for PDMA and absorptions at 2930 ($\text{sp}^3\text{C-H}$) and 3050 ($\text{sp}^2\text{C-H}$) for PS. A linear increase of the PDMA and PS brush thicknesses with number of sequential monomer addition was observed by ellipsometry as illustrated in Figure 3 for PDMA. A control experiment was performed with no RAFT chain transfer agent; no growth of the brush was observed after the first monomer addition.

Synthesis of Diblock Copolymer Brushes via RAFT. Si/SiO₂/PS-*b*-PDMA and Si/SiO₂/PDMA-*b*-PMMA diblock copolymer brushes were synthesized. A 10 nm thickness increase was observed in each case upon addition of the second monomer. This increase correlates with that expected for a polymer brush grown from a well defined initiator layer under the same reaction conditions.

The behavior of diblock copolymer brushes upon treatment with different solvent systems was observed in these films via tensiometry. The advancing water contact angles of a Si/SiO₂/PS-*b*-PDMA (where the PS block is adjacent to the silicate surface) brush increased from 42° to 65° upon treatment with methylcyclohexane at 35 °C for 1 h. Treatment of the same sample with THF/H₂O (1/1, v/v) at 35 °C for 1 h reversed the contact angle to the original value. The advancing water contact angle of the PS homopolymer brush prior to diblock formation was 78°. Normally, a PS overlayer exhibits an advancing contact angle of 100°. We attribute the lower contact angle for the PS brush made by RAFT to the dithioester terminal group. A control sample of dithioester groups was prepared for XPS by reacting the surface-immobilized azo-initiator with RAFT chain transfer agent in the absence of monomer; this sample displayed an advancing contact angle of 77°. In the case of the Si/SiO₂/PDMA-*b*-PMMA brush, the advancing water contact angle decreased from 66° to 58° after the sample was treated with THF/H₂O (1/1, v/v) at 35 °C for 1 h. Subsequent treatment with CH₂Cl₂ returned the contact angle to the original value. These contact angle changes were reproducible for several cycles of solvent treatment. The advancing contact angle of the PDMA homopolymer brush prior to diblock formation was 33°.

SYNTHESIS AND CHARACTERIZATION OF TETHERED TRIBLOCK COPOLYMER BRUSHES ON FLAT SILICATE SUBSTRATES

The synthesis of tethered triblock copolymer brushes of styrene and methyl acrylate on flat silicate substrates *via* a "grafting from" approach was accomplished by sequential monomer addition to surface-immobilized ATRP initiators.¹³ Si/SiO₂//PS-*b*-PMA-*b*-PS and Si/SiO₂//PMA-*b*-PS-*b*-PMA triblock copolymers were prepared. Preparation of the triblock copolymers involves immobilization of a bromo-isobutyrate ATRP initiator onto the silicate substrate by a self-assembly technique. The bromo-isobutyrate ATRP initiator used was (11-(2-bromo-2-methyl)propionyloxy)-undecyltrichlorosilane and was synthesised as described in literature.¹⁴ This initiator has been previously used to produce polymer brushes of both methyl methacrylate¹⁵ and styrene.¹⁴ The ATR-FTIR spectrum of the immobilized initiator shows peaks at 2925 cm⁻¹ and 2853 cm⁻¹, which are assigned to the C-H stretching and CH₂ stretching vibration respectively, and 1736 cm⁻¹ which is assigned to the carbonyl stretching vibration of the ester group.

The values in Table 3 outline the properties for each of the layers of the triblock copolymer brushes produced. Each of the values shown is representative of the outer layer only. The experimental molecular weight values shown in Table 3 are from the free polymer in solution and the calculated molecular weights are calculated from the overall conversion of monomer, which was determined by gravimetry. The good agreement between the experimental and calculated molecular weights, and the narrow molecular weight distributions, indicate that the solution polymerization in each case is a controlled polymerization. However, the thickness measurements in Table 3 suggest that the re-initiation efficiency decreased for the outer block in each case, as the thickness of the outer block was significantly lower than the first layer even though the same experimental conditions were used. This is believed to be due to radical-radical termination in preparation of the previous layers resulting in tethered chains that are unable to re-initiate. The contact angle for both the outer PS layer in the Si/SiO₂//PS-*b*-PMA-*b*-PS triblock brush and the middle PS layer in the Si/SiO₂//PMA-*b*-PS-*b*-PMA triblock brush were significantly lower than the characteristic contact angle for PS ($\theta_a \approx 99^\circ$). This is believed to be due to the presence of PMA at the surface in each of these cases.

The vast majority of literature on tethered polymer brushes is for homopolymer or diblock copolymer brushes; to the best of our knowledge there have been no previous reports on tethered triblock copolymer brushes. The preparation of triblock copolymers in solution using ATRP techniques has been previously reported.¹⁶ The ATR-FTIR spectra for the tethered Si/SiO₂//PMA-*b*-PS-*b*-PMA polymer brush confirmed the structure. The ATR-FTIR spectrum of the first PMA shows characteristic peaks at 2924 cm⁻¹ and 2852 cm⁻¹, for asymmetric CH₂ stretching and symmetric CH₂ stretching respectively, and also at 1734 cm⁻¹ for the C=O stretch. After reaction of the initial PMA layer with styrene, the ATR-FTIR spectrum showed the presence of peaks at 3026, 3060 and 3082 cm⁻¹, all attributed to aromatic C-H stretching vibrations. Further addition of PMA to form the triblock copolymer brush is confirmed by an increase in the intensity of the CH₂ peaks. Similar results and peak assignments were seen in the ATR-FTIR spectra for the Si/SiO₂//PS-*b*-PMA-*b*-PS triblock copolymer brush.

Solvent Treatment of Triblock Copolymer Brushes. Each of the triblock copolymer brushes were treated with a solvent that was a good solvent for the middle block but a non-solvent for the tethered and outer blocks. For the Si/SiO₂//PS-*b*-PMA-*b*-PS brush the solvent chosen was acetone and for the Si/SiO₂//PMA-*b*-PS-*b*-PMA brush the solvent was cyclohexane. After treatment with solvent the water contact angle of the brush was measured and then the process was repeated, these values are listed in Table 4. Contact angles are very sensitive to the topmost surface composition changes, with a sensing depth of approximately 0.5 – 1 nm, with many factors such as surface roughness and chemical heterogeneity having significant effects on contact angle values. The contact angles for the Si/SiO₂//PS-*b*-PMA-*b*-PS brush indicate that after the initial treatment with CH₂Cl₂, which is a good solvent for all blocks, the majority of the polymer localized at the air interface is PS. As mentioned previously, the deviation in this value from the characteristic water contact angle for PS is believed to be due to low initiation efficiency of the middle PMA block resulting in a thin outer PS layer and the presence of small amounts of PMA at the air interface. After treatment of the Si/SiO₂//PS-*b*-PMA-*b*-PS brush with acetone

the advancing and receding contact angles decreased to 74° and 56° respectively. These values are almost identical to the characteristic values for PMA. Subsequent treatment with CH₂Cl₂ changed the contact angles back to their original values. The switching of water contact angles was reversible for many cycles of alternating solvent treatment.

A similar response was seen for the Si/SiO₂//PMA-*b*-PS-*b*-PMA brush when it was treated with cyclohexane, although in this case treatment with CH₂Cl₂ resulted in the characteristic contact angle for PMA and treatment with cyclohexane resulted in close to the characteristic contact angle for PS. The deviation from the characteristic contact angle of PS in this case is believed to be due to the size of the triblock brush. As each of the blocks is approximately 20 nm long, rearrangement of the outer PMA layer to avoid contact with the non-solvent may be difficult due to steric hindrance and thus results in a small amount of PMA remaining at the air interface.

To further analyse the composition of the triblock copolymer brushes at the air interface after solvent treatment, XPS was used. The sampling depth of the XPS experiments is approximately 5 to 10 nm depending on the core level binding energy and takeoff angle. The molar contents of carbon and oxygen atoms after treatment with CH₂Cl₂ were 78.8 and 20.3 % respectively. After treatment with cyclohexane, the oxygen content decreased to 10.3 % and the carbon content increased to 89.2 %. In each case a small amount, approximately 0.5 %, of silicon could be detected. For the Si/SiO₂//PS-*b*-PMA-*b*-PS triblock copolymer brush, the molar contents of carbon and oxygen atoms after treatment with CH₂Cl₂ were 85.4 and 14.1 % respectively. After treatment with acetone, the oxygen content increased to 17.3 % and the carbon content decreased to 82.2 %. Again, approximately 0.5 % of silicon was detected in each case.

The XPS results confirm the observed water contact angle data on the composition of the triblock copolymer brushes at the air interface. The decrease in oxygen content of the Si/SiO₂//PMA-*b*-PS-*b*-PMA triblock brush, after treatment with cyclohexane, is consistent with the migration of the PMA blocks away from the air interface. However, as the oxygen content after cyclohexane treatment is still 10.3 %, a significant amount of PMA is still at or close to the air interface and as a result the water contact angle is below the characteristic value of PS. Whereas, with the Si/SiO₂//PS-*b*-PMA-*b*-PS triblock brush the oxygen content increases after treatment with acetone, as the PS blocks migrate away from the air interface. The high oxygen content of the Si/SiO₂//PS-*b*-PMA-*b*-PS brush after treatment with CH₂Cl₂, is believed to be due to a combination of the thin outer PS layer and incomplete re-initiation of the middle PMA block. This results in an observed water contact angle significantly lower than the characteristic value for PS.

AFM analysis of the treated brushes indicated that unusual nanomorphologies were formed when treated with a solvent that was a good solvent for the middle block but a non-solvent for the tethered and outer blocks. The observed nanomorphology is dependent upon the thickness of the blocks, the proximity of the chains to each other, and on the interaction parameter between the different components.

References

1. Chang, Y.; Noriyan, J.; Lloyd, D. R.; Barlow, J. W. *Polym. Eng. Sci.* **1987**, 27, 693.
2. Zhao, B.; Mulkey, D.; Brittain, W. J.; Chen, Z.; Foster, M. D. *Langmuir*, **1999**, 15, 6856.
3. Bertlsson, L.; Potje-Kamloth, K.; Liess, H.-D.; Engquist, I.; Liedberg, B. *J. Phys. Chem. B* **1998**, 102, 1260. Kepley, L. J.; Crooks, R. M.; Ricco, A. J. *Anal. Chem.* **1992**, 64, 3191.
4. Zhao, B.; Brittain, W. J.; Vogler, E. A. *Macromolecules* **1999**, 32, 796.
5. Zhao, B.; Brittain, W. J. *J. Am. Chem. Soc.* **1999**, 121, 3557.
6. Zhao, B.; Brittain, W. J.; Zhou, W.; Cheng, S. Z. D. *J. Am. Chem. Soc.* **2000**, 122, 2407.
7. Zhao, B.; Brittain, W. J. *Macromolecules* **2000**, 33, 8813.
8. Zhao, B.; Brittain, W. J. *Macromolecules* **2000**, 33, 342.
9. Coca, S.; Matyjaszewski, K. *Macromolecules* **1997**, 30, 2808.
10. Zhang, X.; Matyjaszewski, K. *Polym. Prepr. Am. Chem. Soc., Div. Polym. Chem.* **1998**, 39(2), 560.

11. Zhulina, E. B.; Singh, C.; Balazs, A. C. *Macromolecules* **1996**, *29*, 6338. Zhulina, E. B.; Singh, C.; Balazs, A. C. *Macromolecules* **1996**, *29*, 8254.
12. Zhao, B.; Brittain, W. J.; Zhou, W.; Cheng, S. Z. D. *Macromolecules* **2000**, *33*, 8821.
13. Boyes, S.; Brittain, W. J.; Weng, X.; Cheng, S. Z. D. *Macromolecules*, in press.
14. Matyjaszewski, K.; Miller, P. J.; Shukla, N.; Immaraporn, B.; Gelman, A.; Luokala, B. B.; Siclovan, T. M.; Kickelbick, G.; Vallant, T.; Hoffmann, H.; Pakula, T. *Macromolecules* **1999**, *32*, 8716.
15. Husseman, M.; Malmstrom, E. E.; McNamara, M.; Mate, M.; Mecerreyes, D.; Benoit, D. G.; Hedrick, J. L.; Mansky, P.; Huang, E.; Russell, T. P.; Hawker, C. J. *Macromolecules* **1999**, *32*, 1424.
16. Davis, K. A.; Matyjaszewski, K. *Macromolecules* **2000**, *33*, 4039. Davis, K. A.; Matyjaszewski, K. *Macromolecules* **2001**, *34*, 2101.

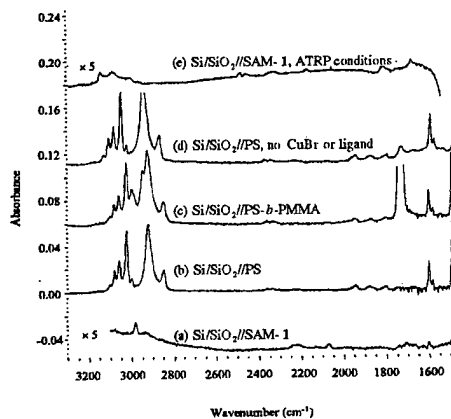


Figure 1. FTIR-ATR spectra of (a) Si/SiO₂//initiator-SAM; (b) Si/SiO₂//PS (tethered PS brush), film thickness = 26 nm; (c) Si/SiO₂//PS-*b*-PMMA (tethered PS-*b*-PMMA brush), film thickness = 35 nm; (d) Si/SiO₂//PS after attempted ATRP of MMA in the absence of CuBr and ligand; (e) Si/SiO₂// initiator-SAM after treatment with MMA under ATRP conditions.

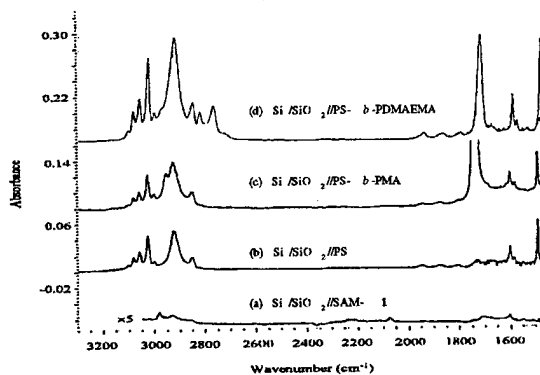


Figure 2. FTIR-ATR spectra of (a) Si/SiO₂//SAM-1; (b) Si/SiO₂//PS (tethered PS brush), film thickness = 24 nm; (c) Si/SiO₂//PS-*b*-PMA (tethered PS-*b*-PMA brush), film thickness = 33 nm; (d) Si/SiO₂//PS *b*-PDMAEMA (tethered PS-*b*- PDMAEMA brush), film thickness = 26.5 nm.

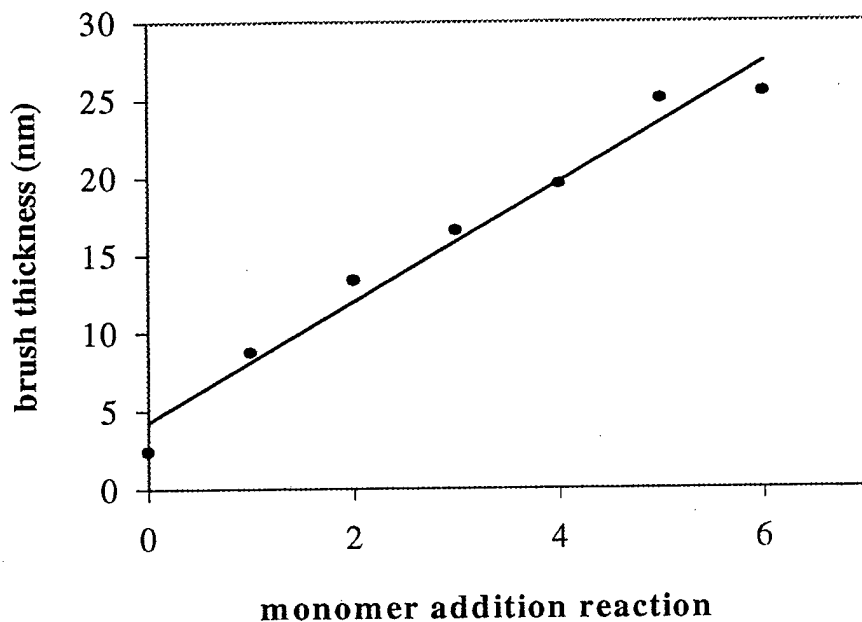


Figure 3. PDMA film thickness change with sequential monomer additions; thicknesses determined by ellipsometry.

Table 1. Water Contact Angles^a of PS-*b*-Polyacrylate Brushes

Sample Description	θ_a	θ_r
PS- <i>b</i> -PMMA after CH ₂ Cl ₂ treatment ^{b,c}	74	59
PS- <i>b</i> -PMMA after cyclohexane treatment ^{b,d}	99	78
PS- <i>b</i> -PMMA after second CH ₂ Cl ₂ treatment ^{b,c}	74	59
PS- <i>b</i> -PMMA after second cyclohexane treatment ^{b,d}	99	78
PS- <i>b</i> -PMA after CH ₂ Cl ₂ treatment ^{c,e}	68	55
PS- <i>b</i> -PMA after cyclohexane treatment ^{d,e}	98	74
PS- <i>b</i> -PMA after second CH ₂ Cl ₂ treatment ^{c,e}	69	55
PS- <i>b</i> -PDMAEMA after THF/H ₂ O treatment ^{f,g}	63	44
PS- <i>b</i> -PDMAEMA after cyclohexane treatment ^{f,h}	98	77
PS- <i>b</i> -PDMAEMA after second THF/H ₂ O treatment ^{f,g}	64	45

^a The standard deviation of contact angles < 2°. ^b PS layer thickness = 28 nm, PMMA layer thickness = 10.8 nm. ^c Immersion in CH₂Cl₂ at room temperature for 30-45 min. ^d Immersion in cyclohexane at 35°C for 30 min. ^e PS thickness = 24 nm, PMA thickness = 9 nm. ^f PS thickness = 27 nm, PDMAEMA thickness = 3 nm. ^g Immersion in THF/H₂O (1:1, v/v) at 35°C for 60 min. ^h Immersion in cyclohexane at 35°C for 60 min.

Table 2. Homopolymer Brushes Synthesized via RAFT on Silicon Wafers (CTA = chain transfer agent).

Brush	Solvent/T ^a (°C)	CTA/AIBN ratio	M_n calc. (g/mol) ^b	M_n exp "free" polymer (g/mol)	PDI of "free" polymer	% conv. ^c	Film thickness ^d (nm)
PMMA	benzene/60	1/0.5	18200	25400 ^e	1.72	86	28
PMMA	benzene/60	1/0.25	30700	21300 ^e	1.10	97	16
PDMA	toluene/90	1/0.5	21800	23000 ^e	1.42	100	11
PS	benzene/60	1/0.058	29200	800 ^f	1.25		7
PS	benzene/60	1/0.58	3900	3600 ^f	1.55	20	
PS	benzene/60	1/0.5	30900	36800 ^f	1.40	51	11

^a Reactions times were 12-24 h for PDMA and PMMA; times were 24-48 h for PS.^b M_n calc. = %monomer conversion x (monomer (g)/initiator (mol))^c % monomer conversion was determined by gravimetry.^d Film thicknesses were determined by ellipsometry with ± 3 nm instrument error.^e MW analysis was done by GPC with comparison to PMMA standards.^f MW analysis was done by GPC with comparison to PS standards.**Table 3.** Physical Properties of Triblock Copolymer Brushes

Layer	Water Contact Angle ^a		Thickness ^b (nm)	Molecular Weight (M_n) Calc. ^c	Expt. ^d	PDI
	θ_a	θ_r				
PS	97	87	20	13.2×10^3	10.5×10^3	1.10
PS- <i>b</i> -PMA	73	63	18	17.9×10^3	17.2×10^3	1.23
PS- <i>b</i> -PMA- <i>b</i> -PS	88	70	3	21.7×10^3	18.6×10^3	1.07
PMA	72	59	20	15.2×10^3	13.6×10^3	1.50
PMA- <i>b</i> -PS	87	72	23	21.8×10^3	18.7×10^3	1.08
PMA- <i>b</i> -PS- <i>b</i> -PMA	73	58	15	18.4×10^3	15.5×10^3	1.23

^a The standard deviation of contact angles was $< 2^\circ$. ^b Thickness determined by ellipsometry. ^c Calculated using the conversion determined from the free polymer. ^d Experimental molecular weight of the free polymer.**Table 4.** Contact Angles^a for Solvent Treatment of Triblock Copolymer Brushes

Solvent	PS- <i>b</i> -PMA- <i>b</i> -PS		PMA- <i>b</i> -PS- <i>b</i> -PMA	
	θ_a	θ_r	θ_a	θ_r
First CH ₂ Cl ₂	91	72	69	52
First Acetone / Cyclohexane ^b	74	56	90	72
Second CH ₂ Cl ₂	94	75	70	52
Second Acetone / Cyclohexane ^b	72	59	92	72

^a The standard deviation of contact angles was $< 2^\circ$. ^b PS-*b*-PMA-*b*-PS brush was treated with acetone and PMA-*b*-PS-*b*-PMA brush as treated with cyclohexane.

TECHNOLOGY TRANSFER

a.) Patent applications and/or awards

There were no patent applications.

b.) Individuals with whom the work was discussed. Individuals who have assisted with the work in some way as collaborators are marked as such.

Dr. Craig Hawker (IBM Almaden)

Professor Krys Matyjaszewski (Carnegie Mellon University)

Professor Erwin Vogler (Penn State Univ.) – collaborator

Professor Valdimir Tsukruk (Iowa State University) – collaborator

Professor Anna Balazs (Univ. of Pittsburgh)

Professor Stephen Z. D. Cheng (Univ. of Akron) – collaborator

Professor David Grainger (Colorado State University)

Dr. Barry Troughton (Lord Corp.)

Professor Tom McCarthy (Univ. of Mass.)

c.) Breakthroughs

We discovered phenol-based coatings that are extremely sensitive to DMMP. We also discovered nanopattern formation in tethered block copolymers.

d.) Leveraging of Army Funds

Related work has been funded by the National Science Foundation.

REPORT DOCUMENTATION PAGE

Form Approved
OMB NO. 0704-0188

Public Reporting burden for this collection of information is estimated to average 1 hour per response, including the time for reviewing instructions, searching existing data sources, gathering and maintaining the data needed, and completing and reviewing the collection of information. Send comment regarding this burden estimates or any other aspect of this collection of information, including suggestions for reducing this burden, to Washington Headquarters Services, Directorate for information Operations and Reports, 1215 Jefferson Davis Highway, Suite 1204, Arlington, VA 22202-4302, and to the Office of Management and Budget, Paperwork Reduction Project (0704-0188,) Washington, DC 20503.

1. AGENCY USE ONLY (Leave Blank)		2. REPORT DATE 5/31/02	3. REPORT TYPE AND DATES COVERED Final Jan. 1 '96 - May 15. '02
4. TITLE AND SUBTITLE Behavior of Ultrathin Coatings for Surface Modification and Novel Polymers for Sensing Environmental Changes		5. FUNDING NUMBERS Grant No. DAAH04-96-1-0018 Proposal No. 35023-MS-MUR Subcontract to North Carolina State University	
6. AUTHOR(S) Hyeonjae Kim and Mark D. Foster			
7. PERFORMING ORGANIZATION NAME(S) AND ADDRESS(ES) The University of Akron Department of Polymer Science Akron, OH 44325-3909		8. PERFORMING ORGANIZATION REPORT NUMBER	
9. SPONSORING / MONITORING AGENCY NAME(S) AND ADDRESS(ES) U. S. Army Research Office P.O. Box 12211 Research Triangle Park, NC 27709-2211		10. SPONSORING / MONITORING AGENCY REPORT NUMBER	
11. SUPPLEMENTARY NOTES The views, opinions and/or findings contained in this report are those of the author(s) and should not be construed as an official Department of the Army position, policy or decision, unless so designated by other documentation.			
12 a. DISTRIBUTION / AVAILABILITY STATEMENT Approved for public release; distribution unlimited.		12 b. DISTRIBUTION CODE	
13. ABSTRACT (Maximum 200 words) Work in Foster's research group contributed to the overall MURI objectives by characterizing behavior in thin surface coatings and novel polymer materials that could provide sensitivity to chemical agents. The first component of this effort was the leveraging of MURI equipment funds and manpower to acquire and startup four pieces of <i>sophisticated instrumentation for characterization</i> . The study of thin surface coatings and novel polymer materials can be subdivided into five project areas. <ol style="list-style-type: none"> 1.) Self-assembled monolayers for surface coatings and sensors 2.) Langmuir monolayers for surface coatings and sensors 3.) Novel poly(ferrocenylalkylsilane) materials that are responsive to environmental changes 4.) Grafted polymer layers for surface modification 5.) Behavior of polymer chains close to a surface The summary here focusses on results obtained from nanofibers of a poly(ferrocenylsilane) polymer, results from polymer brushes in the last year, and the behavior of polymer chains close to a surface.			
14. SUBJECT TERMS nanofiber, poly(ferrocenyldimethylsilane), polymer brush, interface, X-ray reflectometry confined polymers, ultrathin coatings			15. NUMBER OF PAGES 22
			16. PRICE CODE
17. SECURITY CLASSIFICATION OR REPORT UNCLASSIFIED	18. SECURITY CLASSIFICATION ON THIS PAGE UNCLASSIFIED	19. SECURITY CLASSIFICATION OF ABSTRACT UNCLASSIFIED	20. LIMITATION OF ABSTRACT UL

1.) LIST OF MANUSCRIPTS AND PAPERS PRESENTED

a.) Manuscripts submitted, but not published:

M.D. Foster, G. v. Krosigk, K. Ponomarenko, J. R  he, P. M  ller-Buschbaum, "Interface Correlations in Polymer Brushes," in revision.

b.) Papers published in peer-reviewed journals

1. E.J. Choi, M.D. Foster, "The Role of Specific Binding in Human Serum Albumin Adsorption to Self-Assembled Monolayers," *Langmuir* **18**, 557-561, 2002.
2. S. Petrash, T. Cregger, B. Zhao, J. Tremsina, M. D. Foster, W. J. Brittain, V. Sevastianov, C. F. Majkrzak, "Changes in Protein Adsorption on Self-Assembled Monolayers with Monolayer Order: Comparison of Human Serum Albumin and Human Gamma Globulin," *Langmuir*, **17** (24), 7645-7651, 2001.
3. Z. Chen, M.D. Foster, H. Fong, D.H. Reneker, R. Resendes, I. Manners, "Structure of Poly(ferrocenyldimethylsilane) in Electrospun Organometallic Nanofibers," *Macromolecules* **34**(18), 6164-6166, 2001. Published as a *Communication*.
4. K. Temple, J.A. Massey, Z. Chen, N. Vaidya, A. Berenbaum, M.D. Foster, I. Manners, "Living Anionic Ring-Opening Polymerization of Unsymmetrically Substituted Silicon-Bridged [1]Ferrocenophanes: A Route to Organometallic Block Copolymers with Amorphous Poly(ferrocenylsilane) Blocks," *Journal of Inorganic and Organometallic Polymers*, **9**, 189-198, 1999. (Actually submitted and appeared in 2000. Publication date is misleading.)
5. Yim, H.; Foster, M.D.; Engelking, J.; Menzel, H.; Ritcey, A.M. "Temperature dependent behavior of Langmuir monolayers of octadecyl substituted preformed polyimides," *Langmuir* **16**(25), 9792-9796, 2000.
6. I. Luzinov, D. Julthongpiput, A. Liebmman-Vinson, T. Cregger, M.D. Foster, V.V. Tsukruk, "Epoxy-Terminated Self-Assembled Monolayers: Molecular Glues for Polymer Layers," *Langmuir* **16**(2), 504-516, 2000.
7. B. Zhao, D. Mulkey, W.J. Brittain, Z. Chen, M.D. Foster, "Synthesis and Characterization of Phenol and *o*-Chlorophenol Terminated Monolayers," *Langmuir*, **15** (20), 6856-6861, 1999.
8. W. Li, N. Sheller, M.D. Foster, D. Balashis, I. Manners, J.-S. Lin, "Morphology and Ordering Behavior of a Poly(styrene)-*b*-poly(ferrocenyldimethylsilane) Diblock Copolymer," *Polymer* **41**, 719-724, 1999.
9. H. Yim, M.D. Foster, D. Balaishis, I. Manners, "Structural Study of Monolayers of Alkyl Side Chain Substituted Poly(ferrocenylsilane)," *Langmuir* **14**, 3921-3925, 1998.
10. H. Yim, M.D. Foster, K. McCreight, X. Jin, S.Z.D. Cheng, F.W. Harris, "Structural Study of monolayers of alkyl side chain substituted polyimides," *POLYMER*, **39**, 4675-4678, 1998.
11. H. Menzel, A. Heise, Hyun Yim, M.D. Foster, R.H. Wieringa, A.J. Schouten, "Factors Influencing the Layer Thickness of Poly-L-glutamates Grafted From Self-Assembled Monolayers", *ACS Symp. Ser. 695: Organic Thin Films: Structure and Applications*, Oxford University Press, Curtis W. Frank, ed., 1998, p. 131-141.
12. H. Menzel, A. Heise, H. Yim, M.D. Foster, R.H. Wieringa, A. J. Schouten, "Anbindung von Polymeren an Festk  rperoberfl  chen zur Erzielung einer speziellen Ausrichtung," *Gummi, Fasern, Kunstst.* **50**(4) 288-292, 1997.
13. H. Yim, H. Wu, M.D. Foster, S. Z.D. Cheng, F. W. Harris, "Ultrathin Polyimide Films from Preformed Polymers," *Langmuir* **12**, 3202-3205, 1997.
14. A. Heise, H. Menzel, H. Yim, M.D. Foster, R. H. Wieringa, A.J. Schouten, V. Erb, M. Stamm, "Grafting of Polypeptides on Solid Substrates by Initiation of N-Carboxyanhydride Polymerization by Amino Terminated Self Assembled Monolayers," *Langmuir*, **13**, 723-728, 1997.

c.) Papers published in non-peer-reviewed journals or in conference proceedings

1. E. J. Choi, M.D. Foster, C.F. Majkrzak, P. Witte, H. Menzel, "The Role of Hydrophobic Pockets in Human Serum Albumin Adsorption to Self-Assembled Monolayers," International Conference, Korea.

2. Z. Chen, N. Vaidya, T-H. Chang, M.D. Foster, R.P. Quirk, "Morphology and Ordering Behavior of a Novel Organometallic Diblock copolymer: Poly(isoprene)-*b*-Poly(ferrocenyldimethylsilane)," *Polym. Prepr., Am. Chem. Soc., Div. Polym. Chem.*, **41** (2), 2000.
 3. K. Temple, J.A. Massey, Z. Chen, M.D. Foster, M.A. Winnik, I. Manners, "Living Anionic Ring-Opening Polymerization of [1]-Methylphenylsilaferrocenophane: Solution and Solid State Morphology of Diblock Copolymers with Amorphous Poly(ferrocene) Blocks," *Polym. Prepr., Am. Chem. Soc., Div. Polym. Chem.*, **41** (1), 4-5, 2000.
 4. W. J. Brittain, L.M. Siewierski, S. Petrash, M.D. Foster, "Photoresponsive Monolayers Containing In-Chain Azobenzene," *Polym. Prepr., Am. Chem. Soc., Div. Polym. Chem.*, **39** (2), 264-265, 1998.
 5. N. Sheller, W. Li, M.D. Foster, D. Balaishis, I. Manners, L. Guo, R.P. Quirk, "Scanning Probe Microscopy of Surfaces of Novel Poly(styrene-ferrocenyldimethylsilane) Block Copolymers," *Polym. Prepr., Am. Chem. Soc., Div. Polym. Chem.*, **39** (2), 1204-1205, 1998.
 6. G.v. Krosigk, M. Foster, S. Cunis, R. Gehrke, R. Kranold, "A new set-up for grazing incidence X-ray diffraction measurements at BW4," HASYLAB Annual Report 1998 (This is a two page unrefereed report which will have wide circulation).
 7. M.D. Foster G.v. Krosigk, K. Ponomarenko, J. R  he, "Interface Correlations in Polymer Brushes," HASYLAB Annual Report 1998 (This is a two page unrefereed report which has had wide circulation).
- d.) Papers presented at meetings, but not published in conference proceedings
- M.D. Foster, "Novel Polymer Monolayers and Ultrathin Films," International Microsymposium on Polymer Physics, Guilin, China, November 25-29, 1997 - invited talk
- H. Yim, M.D. Foster, S. Z.D. Cheng, F. Harris, "Structure of Monolayers from Alkyl Side Chain Substituted Polyimides," LB8 The Eighth International Conference on Organized Molecular Films, Asilomar, California, August 24- 29, 1997
- M. D. Foster, " X-ray and Neutron Scattering Techniques for the Study of Polymer Organization at Interfaces," Canadian Society of Chemistry National Meeting, Windsor, Ontario, June 2, 1997.
- H. Yim, M.D. Foster, K. McCreight, X. Jin, S.Z.D. Cheng, and F.W. Harris, "Hairy-Rod Polyimide Polymers Confined At The Air-Water Interface," Materials Research Society Fall Meeting, Boston, Massachusetts, Nov. 3 - Dec. 5, 1997.

PARTICIPATING SCIENTIFIC PERSONNEL

Dr. Mark D. Foster, Professor
 Hyun Yim, Ph.D. 8/98
 Wei Li, M.S. 8/98
 Nina Sheller, Ph.D. 12/98
 Dr. Shijun Jia, Postdoctoral researcher
 Prof. Timothy Vierheller, Visiting Faculty Scientist
 Dr. Nitin Vaidya, Part-time postdoctoral researcher
 Zhihao Chen, Ph.D. 8/00
 Hyeonjae Kim, Ph.D. candidate

INVENTIONS

None

SCIENTIFIC PROGRESS AND ACCOMPLISHMENTS

Work in Foster's research group contributed to the overall MURI objectives by characterizing behavior in thin surface coatings and novel polymer materials that could provide sensitivity to chemical agents. The first component of this effort was the leveraging of MURI equipment funds and manpower to acquire and startup four pieces of *sophisticated instrumentation for characterization*. The actual study of thin surface coatings and novel polymer materials can be subdivided into five project areas.

- 1.) Self-assembled monolayers for surface coatings and sensors
- 2.) Langmuir monolayers for surface coatings and sensors
- 3.) Novel poly(ferrocenylalkylsilane) materials that are responsive to environmental changes
- 4.) Grafted polymer layers for surface modification
- 5.) Behavior of polymer chains close to a surface

The description below focusses on results obtained from the poly(ferrocenylsilane) polymers and polymer brushes in the last year.

Sophisticated instrumentation for characterization

First, a one-of-a-kind high intensity X-ray wide angle scattering facility with ultrafast two-dimensional detection and auxiliary equipment for the study of fibers under various conditions was developed with funds from the State of Ohio and made available for use in this project. Changes in electron spun fibers (from Prof. Reneker) with post spinning processing were investigated with this facility.

Secondly, a one-of-a-kind X-ray surface spectrometer for studying thin films and surfaces purchased with State of Ohio funds was brought on-line. The very first measurements were done on poly(ferrocenylsilane) ultrathin films. This device provides capabilities to investigate smart layers on the surface of water, to depth profile heavy metals and various chemicals in sensor layers, to determine lateral order in SAMs for chemical agent sensing and to investigate block copolymer smart material thin layers on solid substrates.

The third capability developed has been that for small angle X-ray scattering (SAXS). Substantial monies from other sources (U. Akron, State of Ohio) were leveraged with the MURI funds allocated for the upgrade of our SAXS capabilities, allowing us to purchase a new, custom designed instrument with focusing optics, position sensitive detector, and variable temperature sample stage. This new instrument is far better for studying the smart block copolymer materials than even the upgraded older instrument would have been.

The fourth acquisition of instrumentation, funded through the ARO Defense University Research Instrumentation Program (DURIP) competition provided two state-of-the-art scanning probe microscopes (SPMs) with a range of imaging modes. These have been used extensively already in studying SAM surfaces, Langmuir monolayers deposited on substrates, and the surfaces of the smart block copolymer materials. The SPMs offer the greatest opportunities for studying surface modifying layers on fibers.

Thin surface coatings and novel polymer materials

Self-assembled Monolayers for coatings

The first of four project areas was the characterization of functionalized self-assembled monolayers (SAMs) that could be used to modify fiber and other surfaces to provide sensitivity to the presence of chemical agents. Chemical sensors based on single component SAMs synthesized by Prof. Brittain were tested by the American Research Corporation and found to sense a simulant at the 150 ppb level. The structure of these SAMs was characterized by X-ray reflectometry¹.

Langmuir monolayers for coatings

Monomolecular coatings for modifying surfaces can also be created using the deposition of Langmuir monolayers and the study of such layers comprised a second project area. As the student was trained in the skills needed to study such systems, monolayers of derivatized polyimides^{2,3,4} were studied because they could be used to change the way in which molecules or subsequent coatings oriented on the surface.

Films made with novel polymers containing various poly(ferrocenylalkylsilane) polymers were of primary interest, however, since changes in the environment can cause redox changes in the polymer that lead to dimensional changes that could be used for actuation. Large dimensional changes in a monomolecular layer^{5a} in response to the presence of an oxidizing threat were studied in the first thrust of a two-pronged investigation of novel smart materials. Monolayers were created on the water surface using *side chain substituted poly(ferrocenylsilane)* polymers and subsequently transferred to solid substrates. Very strong changes in layer dimensions upon exposure to the oxidizing agent FeCl_3 were documented for films on water. Two further molecules which build more stable layers were designed on the basis of these results. One of these has been shown to undergo strong dimensional change upon exposure to the organophosphorous compound triphenylphosphine oxide.

Novel Poly(ferrocenylalkylsilane) Materials

Novel *poly(ferrocenyldimethylsilane)* (PFS) *block copolymers* synthesized by Prof. Quirk and Prof. Manners acted as smart materials as well. The PFS block copolymers showed dimensional changes and changes in crystallization behavior when exposed to oxidizing agents^{5b}. It should also be possible to make coatings from these materials which respond to the presence of electromagnetic radiation.

Structure of Poly(ferrocenyldimethylsilane) in Nanofibers

Poly(ferrocenyldimethylsilane) (PFS) can be incorporated into small fibers that could be used in textiles that respond to environmental stimuli. The crystal structure of this polymer in nanofibers can be studied by electron diffraction from a single fiber. Scanned digital images cannot successfully capture several of the diffraction spots of weaker intensity, so the pattern is reproduced by a hand drawing in Figure 1. This pattern can be reconciled reasonably with that expected for a monoclinic cell with $a = 14.2\text{\AA}$, $b = 6.03\text{\AA}$, $c = 13.9\text{\AA}$, and $\gamma = 95.1^\circ$ (Table 1). This represents a significant refinement from the structure proposed earlier by us. The diffraction features, their d-spacings, and assigned indices are given in Table 1, which also gives a comparison between the experimental d-spacings and those calculated for the proposed structure.

Table 1. Unit Cell Parameters

Unit Cell Parameters	
a (Å)	14.2
b (Å)	6.03
c (Å)	13.9
γ	95.1
Volume	1184
Relative Deviation	2.04E-2
Z	4
Density (g/cm ³)	1.35

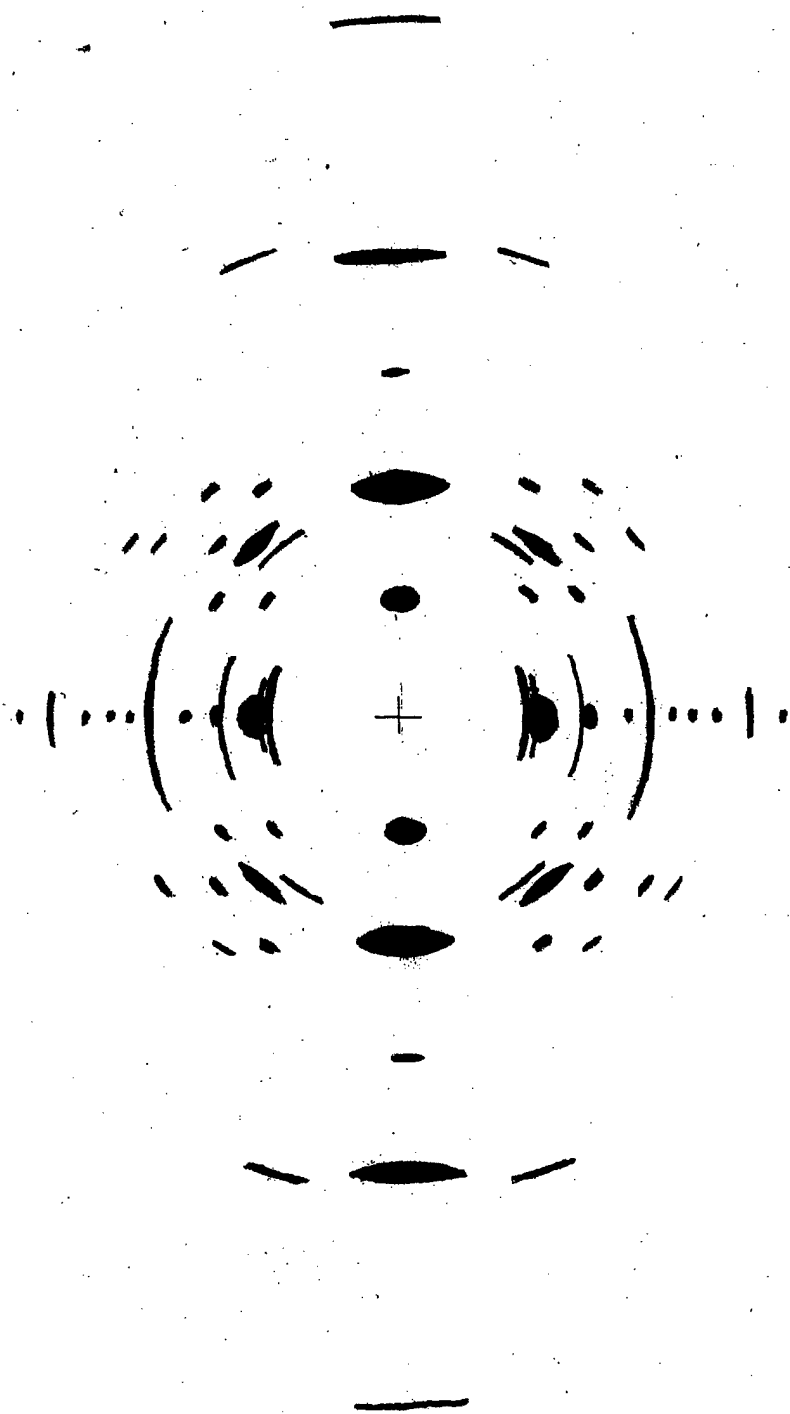


Figure 1. Electron diffraction pattern from a nanofiber of poly(ferrocenyldimethylsilane).

Table 2. Diffraction Features with Corresponding Indices and d-spacings

Layer	No.	(hkl)	d-experimental	d-calculated
0	(-1)	(200)	(7.13)	(7.08)
	2	010	5.99	6.01
	3	-110	5.83	5.71
		-210	4.47	4.80
	5	210	4.36	4.39
	6	400	3.54	3.54
		-410	3.33	3.18
	8	020	2.99	3.00
	9	120	2.79	2.89
	10	220	2.59	2.68
	12	420	2.12	2.20
1	missing			
2	21	002	6.90	6.94
	22	-112	4.54	4.41
	25	012	4.54	4.54
	23	212	3.72	3.71
	26	-212	3.75	3.94
3	11	013	3.87	3.66
	16	203	3.91	3.89
	12	113	3.61	3.50
	17	-113	3.63	3.59
	13	213	3.18	3.18
	18	-213	3.20	3.32
	14	-413	2.69	2.62
	19	403	2.72	2.81
4	6	004	3.51	3.47
	7	-114	3.01	2.96
	9	014	3.03	3.00
	8	-214	2.72	2.81
	10	214	2.70	2.72
6	5	006	2.33	2.31
8	2	008	1.75	1.75
	3	018	1.67	1.65
	4		1.68	1.67
12	1		1.16	1.16

Grafted polymer layers for surface modification

The fourth project area involved *modifying surfaces by the tethering of synthetic polymers* to surfaces covered with mixed SAMs. The resulting layers may sometimes be referred to as "polymer brushes." Tethering has been accomplished by grafting preformed polymers to tethering sites ("grafting to") and by polymerizing from initiation sites ("grafting from"). The first work was done with polypeptides grafted onto surfaces using both the "grafting to" and "grafting from" procedures^{6,7,8}. This established the feasibility for attaching to surfaces biological polymers which can be designed to have specific interactions with species in the environment. Another type of SAM for use in attaching polymer surface coatings was also investigated⁹. The further study of polymer brushes focussed on interface/interface correlations in a polymer brush used to modify a surface.

Interface/Interface Correlations in a Polymer Brush Used to Modify a Surface

Introduction: The deposition of a polymer brush (Figure 2)¹⁰ on a surface represents one means of modifying the behavior of a surface with regard to both its chemical nature and physical properties. Brushes have advantages over spun cast polymer films because they are monomolecular in thickness and are more robust since the chains are covalently tethered to the surface of the substrate. It is particularly of interest to understand how the surface of the brush may reflect the microroughness of the underlying substrate or if it is possible to completely decouple the roughness of the surface of the brush from that of the substrate. A constant local film thickness is desirable in coatings for protection from battlefield threats or for sensing. A local deviation in the film thickness can lead to the failure of the film. In practice such difficulties could be overcome by working with larger film thicknesses. However, progress towards miniaturized devices demands means of creating extremely thin coatings with controlled thicknesses and uniformity. On the other hand, for biomimetic applications it is of interest to achieve flexible coating surfaces that are decoupled from the underlying hard surface¹¹. For X-ray optics applications it is desirable to achieve both low interface roughness and vertical correlation, because roughness decreases specular reflectivity and correlated roughness generates additional diffuse scattering which degrades the resolution of X-ray mirrors¹².

Experimental studies of correlation between the interfaces of spun cast films of homopolymers have already appeared^{13,14}. Müller-Buschbaum and coworkers¹³ have shown that when a film is spun cast from polystyrene chains of molecular weight above the entanglement molecular weight, the polymer film surface microroughness is strongly correlated to that of the substrate. In this case the polymer film has dried into a nonequilibrium glassy state. This correlation may be subsequently erased when the polymer is heated above its glass transition temperature. At that temperature the surface becomes sufficiently mobile to rearrange. The film moves toward a state of lower overall free energy by adopting a surface with characteristics dictated by the interplay between the cost of increasing surface area and the tendency for the formation of thermally stimulated microscopic waves at the surface. The surface roughness will be decoupled from that of the substrate for a sufficiently thick film in the melt state. For a simple liquid the thermally excited waves are strongly damped for films thinner than about 100Å¹⁵ in agreement with a theory of Andelmann, Joanny, and Robbins¹⁶. The thickness of a spin coated polymer film required to avoid this coupling between the substrate and film surface has been considered by Li *et al.*¹⁴ and Müller-Buschbaum and coworkers¹⁷.

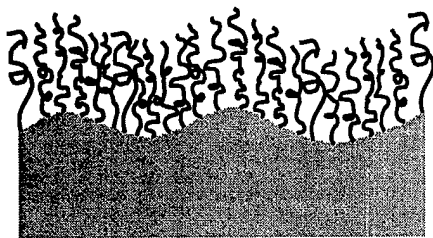


Figure. 2. Schematic of a strongly stretched brush.

In this study roughness correlation of PS brush films having different film thickness was probed using grazing incidence X-ray diffuse scattering. Two sets of brushes were prepared *via* the "grafting from" method. In one set, the thicknesses were varied by means of varying the grafting density at a fixed molecular weight. So the film quality was expected to change from that of a free chain film to that of a highly stretched brush film with increasing film thickness. In the other set, the thicknesses were varied by means of varying the molecular weight at a fixed grafting density. Two different types of states of the brush are of interest. First is the dry or collapsed state that exists in the absence of solvent. The brush may be either molten or glassy depending on its glass transition temperature. In the case that the brush is glassy when dry the details of the drying process play a key role in determining the surface structure. The second category of states encompasses various swollen states formed when solvent molecules penetrate the brush. For all but very small concentrations of solvent in the brush, the brush will typically be molten.

Experimental:

Preparation of PS brushes. Polymer brushes were created by the "grafting from" procedure in which an initiator layer was first immobilized on the substrate using a self-assembled monolayer and then the polymer chains were polymerized from the surface using free radical polymerization. A detailed description of the preparation and characterization of the surface-attached initiator monolayers has been presented elsewhere¹⁸. Briefly, the initiator was immobilized onto the silicon oxide at room temperature in toluene solution under dry argon atmosphere using triethyl amine as a catalyst. The concentration of the initiator was *ca.* 0.5 - 1.0 mmol/l. After completion of the immobilization reaction the substrates were rinsed with toluene and methanol (p. a. grade) to remove non-bound initiator and other by-products of the reaction. The polymerizations were carried out in toluene solvent at 60 °C under dry argon atmosphere. Several important characters and preparation conditions of the samples are summarized in Table 1.

Two strategies were used to control the thickness of polymer brush films. First, the thickness of the brush film was increased with increasing grafting density at a fixed molecular weight. Grafting density is a function of initiator decomposition rate, initiator efficiency, reaction temperature, and reaction time. To make the molecular weights the same throughout this series of samples the same concentrations of styrene monomer were used (50 volume %). Since all other polymerization parameters were the same except the reaction time, the grafting density was determined only by reaction time. The half distance between grafting sites is about one-fourth of the unperturbed radius of gyration for the lowest grafting sample. Samples are identified with codes beginning with "GD" and followed by a 4-digit number that indicates the thickness of the film in Angstroms. Second, the thickness of the brush film was increased with increasing molecular weight at a fixed grafting density. The molecular weight of the brush chains is a function of monomer concentration, reaction temperature, and reaction time. To make grafting densities the same throughout this series of samples, polymerizations were carried out for 5 hours for each of the samples. Because all other polymerization parameters were the same except the monomer concentration, the molecular weight was determined only by monomer concentration. These samples are identified with a code beginning with "MW" and followed by a 4-digit number that indicates the thickness of the film in Angstroms. To study the effect of physical state (collapsed or swollen), another PS brush sample of thickness *ca.* 172Å was prepared separately.

After polymerization had proceeded for the desired time, the samples were removed from the reaction mixtures, extracted with toluene for at least 12 hours to remove the physically adsorbed polymer chains, and dried in a vacuum for about 3 hours. Non-bound polymer generated during polymerization was isolated through precipitation from toluene solution into methanol and dried in vacuum for later GPC analysis.

Table 1. Characteristics of PS brush films

Sample	Thickness (Å)	Roughness (Å)	M _n (kg/mol)	Grafting density ^b (μmol/m ²)	Monomer concentration (vol %)	Polymerization time (hours)
1. Grafting density variation						
GD0057	57.1	5.9	709±17 ^a	0.011	50	0.5
GD0098	98.0	6.6		0.023	50	1
GD0198	198.1	4.6		0.044	50	2
GD0411	410.6	11.4		0.106	50	5
GD1070	1070.4	6.5		0.211	50	11
2. Molecular weight variation						
MW0059	58.8	7.3	380	0.106	8	5
MW0120	120.0	9.3	431		16	5
MW0275	275 ^c		462		20	5
MW0344	343.6	10.9	531		45	5
MW0951	950.6	30.3	798		80	5

^a Averaged over the samples that were prepared by varying grafting density.

^b Calculated from following relation, $\sigma = \sigma_0 f [1 - \exp(-k_d t)]$, where $\sigma_0 = 1.8 \mu\text{mol m}^{-2}$, initiator efficiency $f = 0.37$, initiator decomposition rate constant $k_d = 9.6 \times 10^{-6} \text{ s}^{-1}$, and t is polymerization time.

^c Directly calculated from the fringes of reflectivity curve.

X-ray Reflectometry. The thicknesses and roughnesses of the surfaces and interfaces of the dried brushes were measured using a rotating anode source (Rigaku, 18kW, Ultra X 18S) with Cu K α radiation ($\lambda = 1.54 \text{ \AA}$) by specular X-ray reflectivity. A focusing gold mirror, double-bounce Ge monochromator, and detector slits were used to collimate and monochromatize the incident beam. Longitudinal diffuse scans with an offset of $\theta_i = 0.057^\circ$ were also collected and subtracted from the measured reflectivities to get true specular reflectivities. The experimental curves were then fit with simulated reflectivity curves corresponding to a model sample structure. In the model the interfaces between the homogeneous layers are described by *tanh* refractive index profiles.

X-ray Off-Specular Detector Scan. Grazing incidence X-ray scattering is a useful tool to probe the structure of thin films¹⁹. Specular X-ray reflectivity reveals the density profile perpendicular to the surface, microroughnesses of the interfaces, and total film thickness of uniform films. However, it is only sensitive to the structure in the direction normal to the surface. The intensity scattered off-specular is sensitive to the lateral structure of rough interfaces. If the roughness profiles of different interfaces are partially or fully correlated with one another, the diffusely scattered intensity reveals maxima in reciprocal space, the so-called resonant diffuse scattering (RDS)²⁰. The intensity is concentrated into stripes. The distance between these stripes in the direction of wavevector transfer q_z is equal to $2\pi/D$, where D is the layer thickness. Scanning a step counting detector through various detector angles while staying in the plane of incidence corresponds to a parabolic trajectory in a reciprocal space map of q_x and q_z . This "detector scan" passes through the Yoneda peak and the specular ridge as well as the RDS stripes. So, the existence of additional modulation in scattered intensity besides the Yoneda peak and specular peak is an evidence of conformal roughness in a system.

The grazing incidence diffuse scattering was measured on the BW4 USAX beamline of the DORIS III storage ring at HASYLAB/DESY. Schematically, the experimental geometry is presented in Figure 3, where the incidence angle is denoted by θ_i and the detector angle with respect to the surface of the sample is denoted by θ_f . The selected wavelength was 1.38 \AA . The incidence angle was set to 1.194° and both the specular and diffuse scattering were captured on a two-dimensional detector placed at a distance of 2732 mm from the sample. The sample rested on a goniometer mounted in an evacuated beam path. With this goniometer the

sample surface could be aligned parallel to the beam and the incidence angle precisely varied for small angles. A measurement lasting three hours was required to attain the modest statistics seen here. For the present comparison there is no need to correct the data for background scattering. For the study of the effect of the physical state, diffuse scattering was measured for the brush both in the dry collapsed state and in the swollen state at nominal incident angles of 0.8, 1.0, 1.2, and 1.4 degrees.

The data of central interest were extracted from the two dimensional data set by taking a cut of the data about the plane of incidence for channels corresponding to positions varying upwards from the horizon of the sample, through the Yoneda and specular peaks and above. For each value of $\theta_i + \theta_f$ the intensities of three channels, corresponding to $\Delta q_y = 0.0021 \text{ \AA}^{-1}$ were averaged. A diffuse scattering curve arrived at in this way is shown in Figure 5.

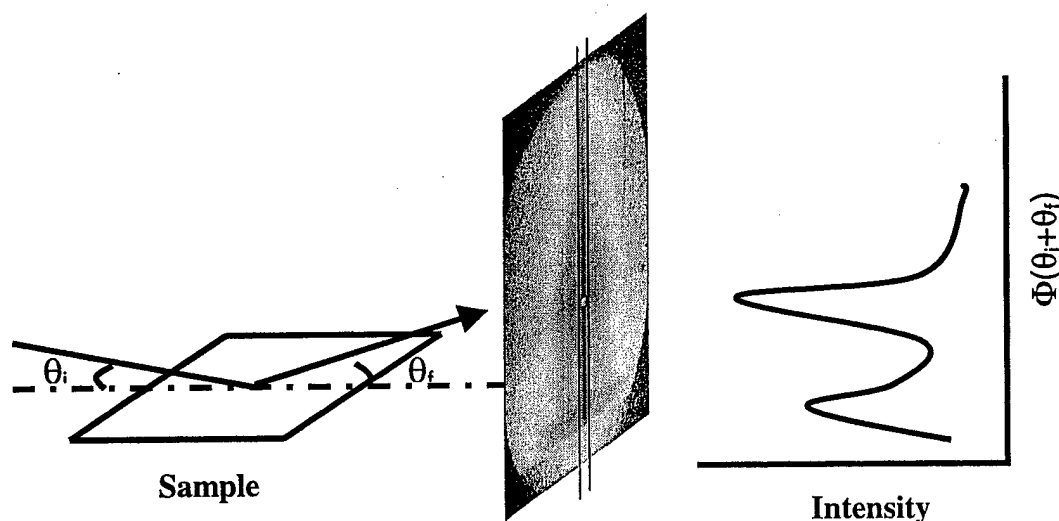


Figure 3. Geometry of the diffuse scattering experiment under grazing incidence. The plot at right shows the variation of intensity with $\theta_i + \theta_f$ within a rectangular cut corresponding to the shaded region shown on the plane of detection.

X-ray Off-Specular Longitudinal Scan. The longitudinal off-specular scattering was measured using a rotating anode X-ray source (Rigaku, 18kW Ultra X 18S) with Mo Ka radiation ($\lambda = 0.71 \text{ \AA}$). The detector angle with respect to the incident beam direction was offset 0.03° from that corresponding to the specular beam position. The longitudinal diffuse scattering scan is very similar to the specular reflectivity measurement and shows oscillations if cross-correlations between the two interfaces are present. In the special case of perfectly conformal roughness system, the oscillations in the diffuse scattering are in phase with the Kiessig fringes from the specular reflectivity scans. In contrast, if both surfaces are perfectly anticonformal, the diffuse scattering is out of phase with the specular reflectivity²¹.

Results and Discussion: Specular reflectivities measured with the laboratory rotating anode X-ray source are shown in Figure 4. Each curve is shifted in intensity by one order of magnitude with respect to the previous curve for clarity. Details of the structures of the brush films derived from the reflectivity results are summarized in Table 1. The thicknesses of the brush films increased linearly with increasing grafting density at a constant molecular weight and increasing molecular weight at fixed grafting density. The grafting densities

shown in the Table 1 are estimated values from the kinetics of initiation decomposition, initiation efficiency, and reaction time. Grafting density is shown to have little effect on the roughness of the brush film as does the molecular weight below a certain molecular weight around 7.1 kg/mol. However the roughness increased abruptly above that molecular weight.

Diffuse scattering at a fixed geometry was measured for the two sets of brush films and the results are shown in Figure 5. Overall scattering behaviors are pretty much same between two sets of samples. Two common scattering features were observed for all samples. One is the Yoneda peak at $\theta_f \approx 0.2^\circ$. This is due to the enhancement of the scattering intensity from the surface when the detector angle is equal to the critical angle for the substrate. These peaks are caused by a multiple scattering process so that they have purely dynamic nature. The other one is the strong specular peak at the value of $\theta_f \approx 1.194^\circ$.

The scattering patterns show three types of behavior that appear to correspond to three thickness regimes. First, the scattering from the brush films with thicknesses of about 58 Å revealed features characteristic of solid-like surfaces. Besides the Yoneda peak and specular peak no additional features were observed. The scattering intensity between the Yoneda and specular peaks did not change much with increasing detector angle. Second, the scattering from the brush films with thicknesses over 950 Å revealed features found for liquid-like surfaces. The scattering intensity increased around the specular peak. However, no oscillations were observed between the Yoneda and specular peaks. Finally, the samples with thicknesses between 98 Å and 410 Å revealed additional modulations between the Yoneda and specular peaks. If roughness profiles of the two interfaces in a sample are partially or fully correlated, the diffusely scattered intensity reveals maxima in reciprocal space, RDS, mentioned above.

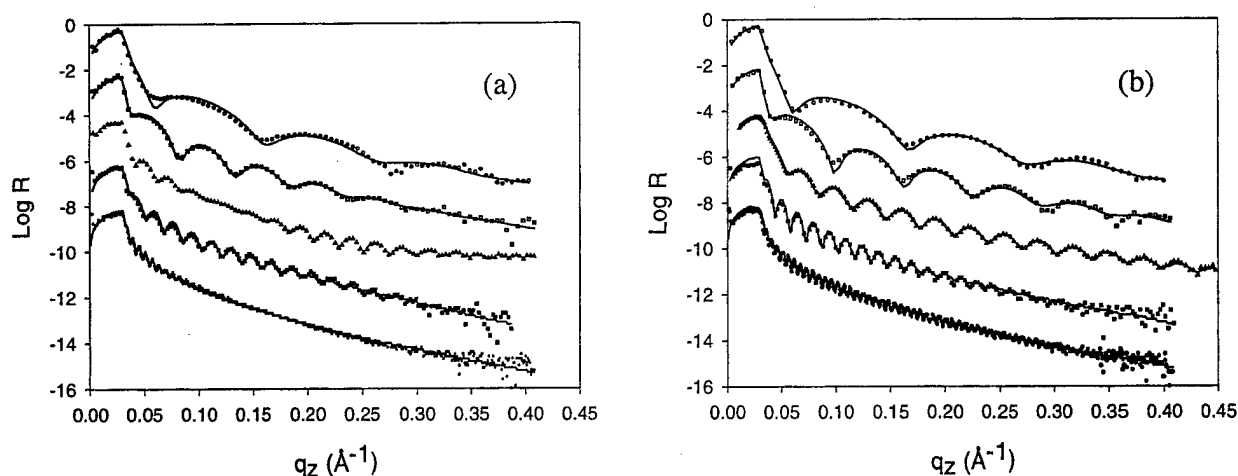


Figure 4. X-ray specular reflectivities with the model curves (—) for PS brushes prepared by means of varying molecular weight (a) and varying grafting density (b). Each curve is shifted in intensity by two orders of magnitude with respect to the previous curve for clarity. From top to bottom, each curve corresponds to MW059, MW120, MW275, MW344, and MW951 for (a) and GD0057, GD0098, GD0198, GD0411, and GD1070 for (b), respectively.

The observed difference ($\Delta\Phi$) between the minima of the modulations in our experiment is about half of that expected from conformal roughness. The amplitude of the oscillation decreases with increasing film thickness. A doubled frequency would generally be associated with waveguide behavior of the two interfaces in the layer structure²². To get a better understanding of the origin of these oscillations, longitudinal diffuse scattering was measured subsequently using a rotating anode source, and the results are shown in Figure 6. Specular and

longitudinal scans are plotted together on an arbitrary intensity basis to show the phase relations clearly. Because the experiments are still ongoing, the results are shown only for the samples with varying grafting density. The fringes from the longitudinal scans are in phase with the Kiessig fringes from the specular

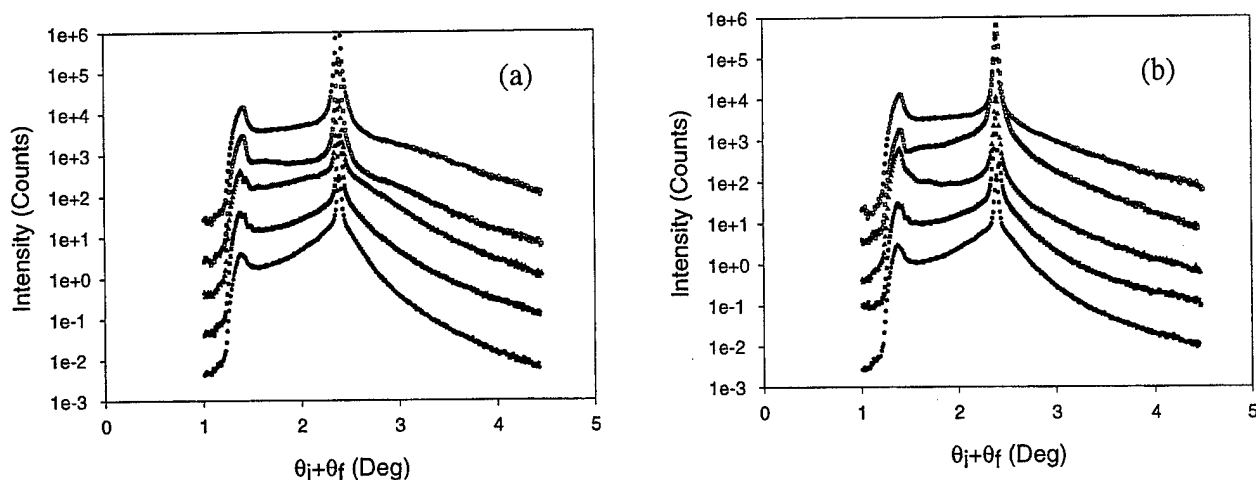


Figure 5. Detector scans for PS brushes prepared by means of varying molecular weight (a) and varying grafting density (b). Each curve is shifted in intensity by one order of magnitude with respect to the previous curve for clarity. From top to bottom, each curve corresponds to MW059, MW120, MW275, MW344, and MW951 for (a) and GD0057, GD0098, GD0198, GD0411, and GD1070 for (b), respectively.

reflectivity scans only for the samples with thicknesses less than 410 Å. So the surfaces of the PS brushes thinner than 410 Å have roughnesses conformal with that of the substrates. Additional oscillations observed at $\theta_i > \theta_f$ in the detector scans are due to the waveguide effect. The fact that there are no fringes at $\theta_i < \theta_f$ in this case as compared to those seen from spun-cast PS films²³ indicates that the interface/interface correlation is weaker for this particular dry collapsed brush than it is for spun-cast films.

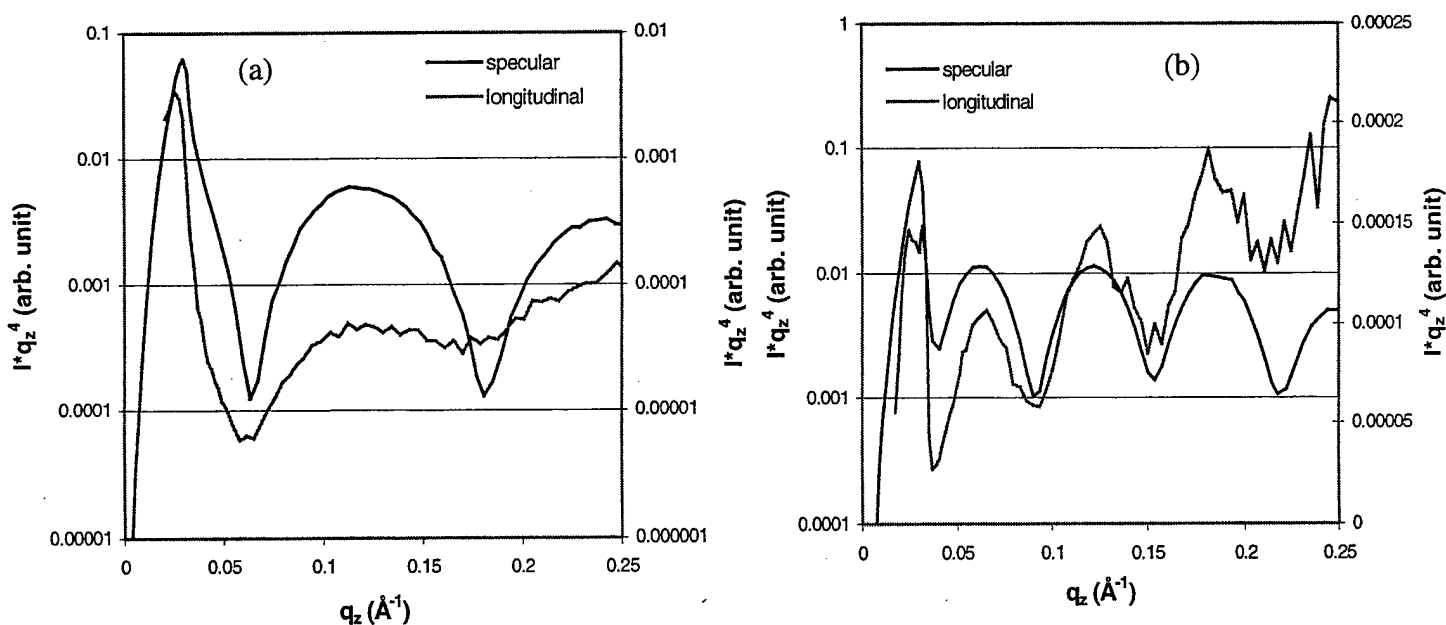


Figure 6. Comparison between specular and longitudinal scans for the grafting density varying samples. The fringes are in phase for the samples whose thicknesses are thinner than 410 Å. (a) GD0057, (b) GD0098.

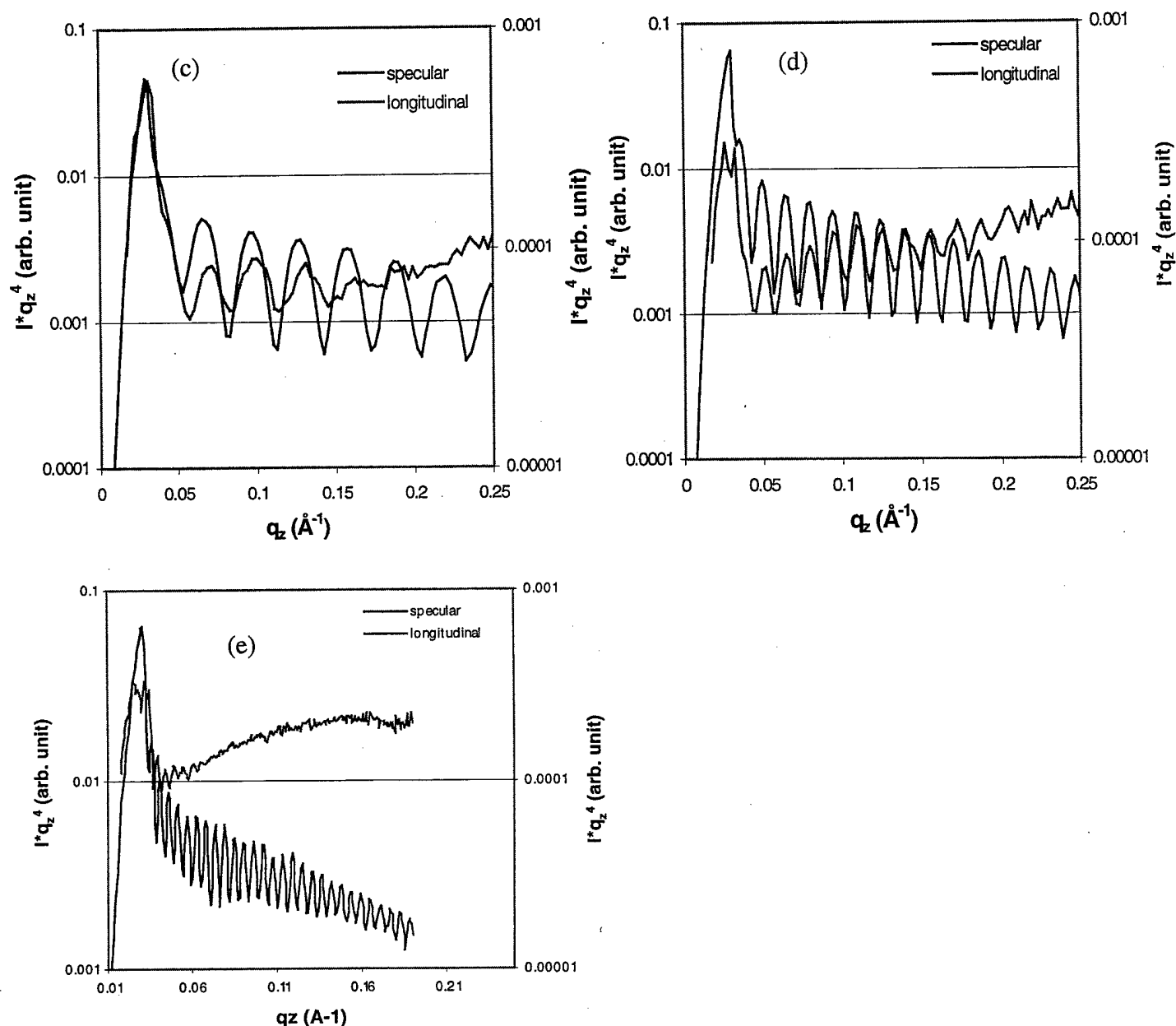


Figure 6. continued. Comparison between specular and longitudinal scans for the grafting density varying samples. The fringes are in phase for the samples whose thicknesses are thinner than 410 Å. (c) GD0198, (d) GD0411, (e) GD1070

This is the first time that either conformal roughness or waveguiding behavior have been reported for PS brush thin films. The underlying principles that govern these phenomena are not still understood.

Diffuse scattering was measured for the brush with overall thickness 172 Å in the dry collapsed state at nominal incident angles of 0.8, 1.0, 1.2, and 1.4 degrees. The scattering revealed correlation of the roughness of the brush surface with that of the substrate. Here, for sake of brevity, only the data obtained at a single incident angle close to 1° are shown in Figure 7. Once again the scattering curve for the collapsed brush shows three prominent features. First, the very strong intensity from the specular reflection is seen at a value of θ_i of about 1°. The full height of the specular peak is not resolved due to the limited dynamic range of the detector. However, for simply assessing the presence or absence of interface correlations the full shape of the peak from MURI Final Report

the specular reflection is not needed. The second feature is the Yoneda peak at $\delta \sim 0.22^\circ$. The broadening of the Yoneda peak for the swollen brush is real and may derive from two sources - scattering due to the small difference in electron densities between the polymer and solvent and inhomogeneities in the swelling of the brush. Finally, the fringes adjacent to the Yoneda peak. Such fringes appear in the diffuse scattering measured at all four incident angles. The spacings of the fringes are half of those that are expected to be in case of conformal roughnesses.

When a brush film is exposed to toluene vapor, it swells, and in the case of a sufficiently high grafting density^{24,25} this swelling can be substantial. Diffuse scattering patterns were collected from the brush in the swollen state at four incident angles, 0.8, 1.0, 1.2, and 1.4°. The scattering data for the particular case of ca. 1.0° incidence are shown in Figure 7. (The small difference in actual incident angle is inconsequential to the argument here.) While neither the scattering intensity for the dry brush nor the intensity for the swollen brush has been placed on an absolute intensity basis, the two have been normalized with respect to run time and therefore the intensities can be qualitatively compared. The diffuse scattering from the swollen brush is clearly stronger than that from the dry collapsed brush, even though the X-ray beam is attenuated somewhat by a path through the toluene vapor of greater than 5 cm. More to the point, however, is the observation that the fringes due to correlation have disappeared. No fringes were observed for any of the four different incident angles. Thus, swelling the brush is seen to destroy the wave guiding effect. However, it is not possible with this data alone to assert that swelling also destroys the correlation.

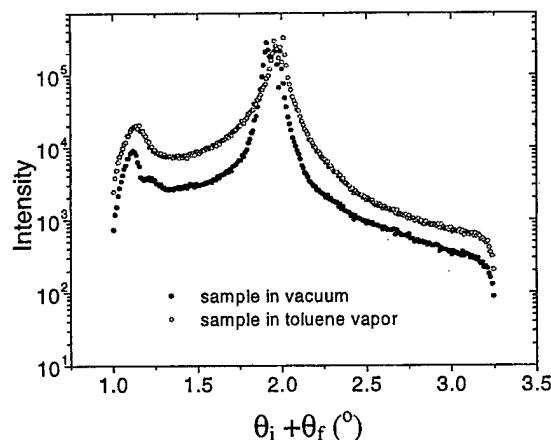


FIG. 7. Diffuse scattering patterns from a dry, collapsed polystyrene brush of thickness 172Å (filled dots) and from the same brush swollen in toluene vapor (open circles).

Behavior of a Polymer Chain Close to a Surface

The behavior of ultrathin coatings on fabrics and other surfaces depends importantly on the details of the structure of the layer immediately adjacent to the substrate, i.e. in the first few monomeric lengths from the substrate. Due to the small scale of this structure, it has not yet been successfully studied directly experimentally. We have undertaken to do this for ungrafted chains using X-ray reflectometry at a synchrotron source in collaboration with Dr. Sunni Sinha and other scientists at the Advanced Photon Source.

It is thought that in the case the chains are not grafted to the surface the density profile close to a substrate should be inhomogeneous, e.g. oscillatory, on the length scale of the diameter of the polymer chain. Molecular level variations in the layering of linear²⁶ and branched²⁷ polymer melts due to chain architecture have been

experimentally observed *indirectly* by force distance measurements with the surface forces apparatus done by Israelachvili and coworkers. Force measurements with linear polydimethylsiloxanes²⁶ show oscillations characteristic of layering, while those with melts of branched polybutadienes²⁷ show no oscillations. Layering in a confined space has also been studied by simulations²⁸. Experimental evidence for layering of *small molecules* at a solid/liquid interface obtained using X-ray reflectivity (XR) has recently been published for the case of a liquid film with a free surface²⁹ and an experimental report³⁰ records successful XR experiments to determine the layering of small molecules in a confined geometry where two solid/liquid interfaces are close together. In previous attempts by this group, in collaboration with Dr. M. Kent of Sandia National Lab, attempts to measure the structure close to the substrate failed due to difficulties with dewetting of the polymer film. Therefore, in the work done here we have adopted the approach and sample cell of the team of Sinha *et al.* to probe the layering of a *polymer* melt close to the interface.

Experimental: The first polymer studied was a low molecular weight polydimethylsiloxane (PDMS) polymer ($M_n = 1350$) with narrow molecular weight distribution ($M_w/M_n = 1.24$). This polymer was chosen because the results could be easily compared with results from surface forces apparatus measurements done by Israelachvili and coworkers²⁶. We have characterized the structure in polymer melts directly using X-ray reflectivity with a novel sample cell allowing study of the melt structure in a highly confined space. Experiments were run on the 1-ID beamtime at APS using an X-ray energy of 30 keV. A schematic of the beam line is shown in Figure 8 and a schematic of the sample cell shown in Figure 9. Key to the experiment is the ability to prepare a clean sample and also to create an ultrathin film between two surfaces by bringing the surfaces very close together while maintaining them parallel to one another. The sample cell surfaces were cleaned carefully and the polymer was filtered several times before being placed between the silicon substrates in a laminar flow hood sitting in a portable clean room. The silicon surfaces were brought together by means of three micrometers advanced using a torque wrench.

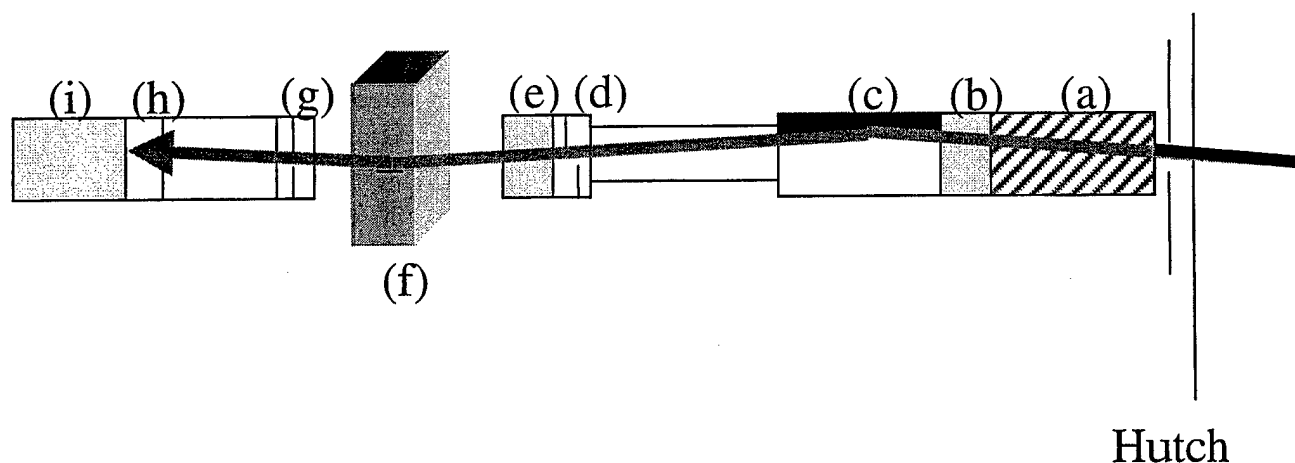
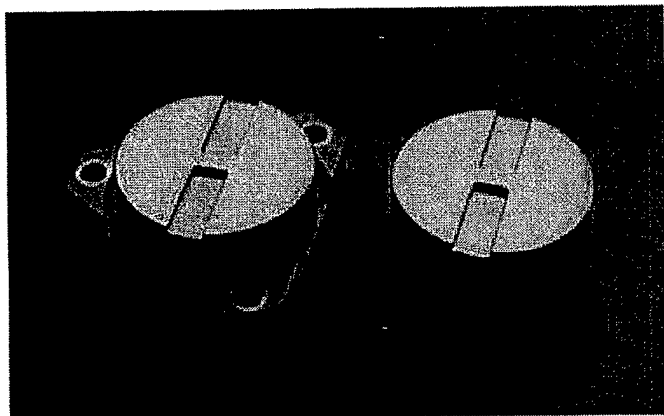
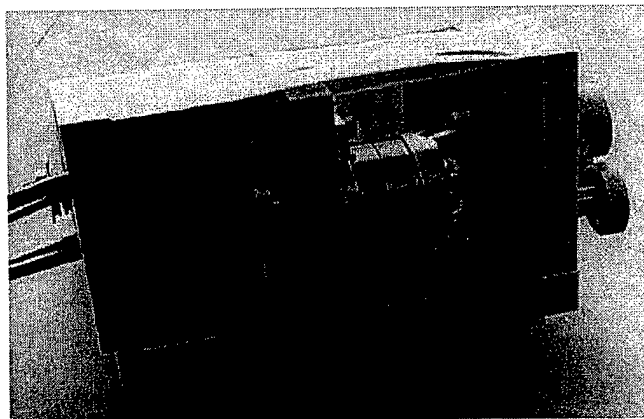


Figure 8. Beamline Setup: (a) attenuator, (b) monitor (ion chamber #1), (c) mirror, (d) J-J slit, (e) monitor (ion chamber #2), (f) sample cell, (g) guard slit, (h) detector slit, (i) detector (NaI scintillation detector)

(a) Silicon substrates



(b) sample cell



(c) beam path through the cell cross-section

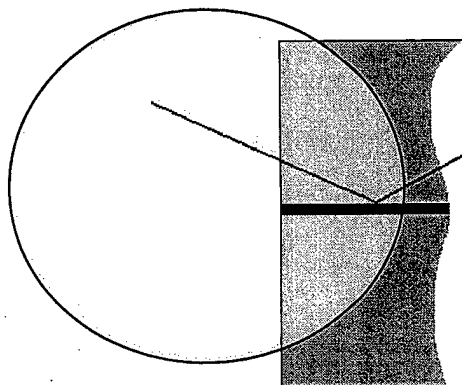
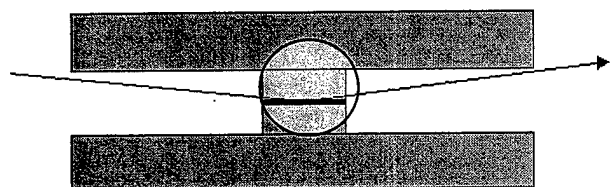


Figure 9. Schematic of the scattering cell for X-ray reflectivity from polymer in a confined film.

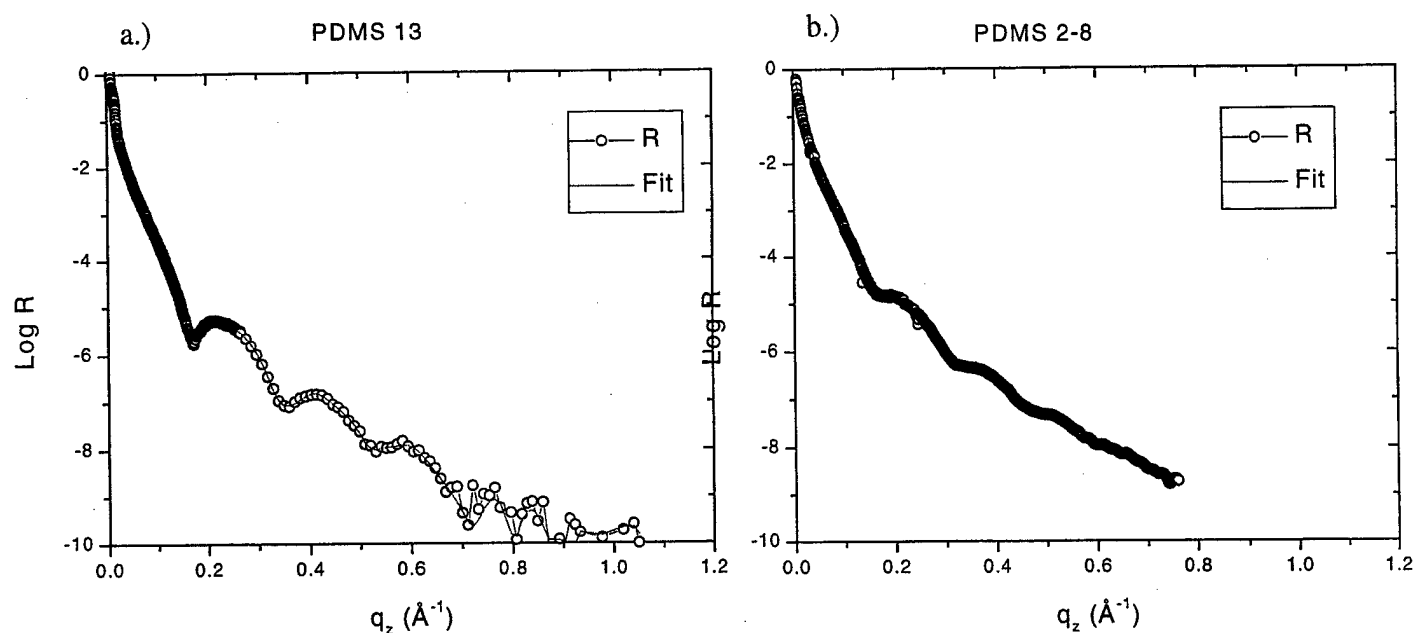


Figure 10. X-ray reflectivity curves for PDMS films confined between two silicon surfaces corresponding to approximate film thicknesses of a.) 37 Å and b.) 48 Å.

Results and Discussion: We were able to measure reflectivity from the confined film with the two surfaces at two clearly different film thicknesses. *This is the first measurement of its kind ever done for a polymer film.* The two reflectivity curves corresponding to these two cases are shown in Figure 10. From a simple hand calculation using the spacing between minima seen in the curves we can say that the films have thicknesses of about 37 Å and 48 Å, with the thicker film corresponding to the more tightly spaced fringes. These thicknesses are close to the values of surface-to-surface distance for which Horn and Israelachvili²⁶ saw jumps in their force-distance curve from the surface forces apparatus. These jumps, they surmised, were due to quantum changes in film thickness when a single layer of polymer molecules was squeezed out from between the two walls.

The X-ray reflectivity is sensitive to variations in electron density, which in turn vary with mass density and elemental composition. Here we capture these variations as expressed in the real part, δ , of the refractive index for X-rays. One profile of δ vs. depth corresponding to a reflectivity curve that represents the data well is shown in Figure 11. This profile suggests that the mass density within the film is asymmetric and that for some of the film the density is higher than that expected from the bulk. The value of δ expected for bulk PDMS at this wavelength is 2.36×10^{-7} . This analysis is still under discussion due to the very high density envisioned by the model and other possible models are being investigated. In particular, we are considering, with the aid of our collaborator, Mike Kent, the possibility that we may be able to fit the data using a model envisioning an oscillatory profile as expected from molecular simulations. Of one thing we are already certain. The data cannot be represented appropriately by assuming that the film has a uniform density across its thickness. It is also most likely that the density profile is asymmetric.

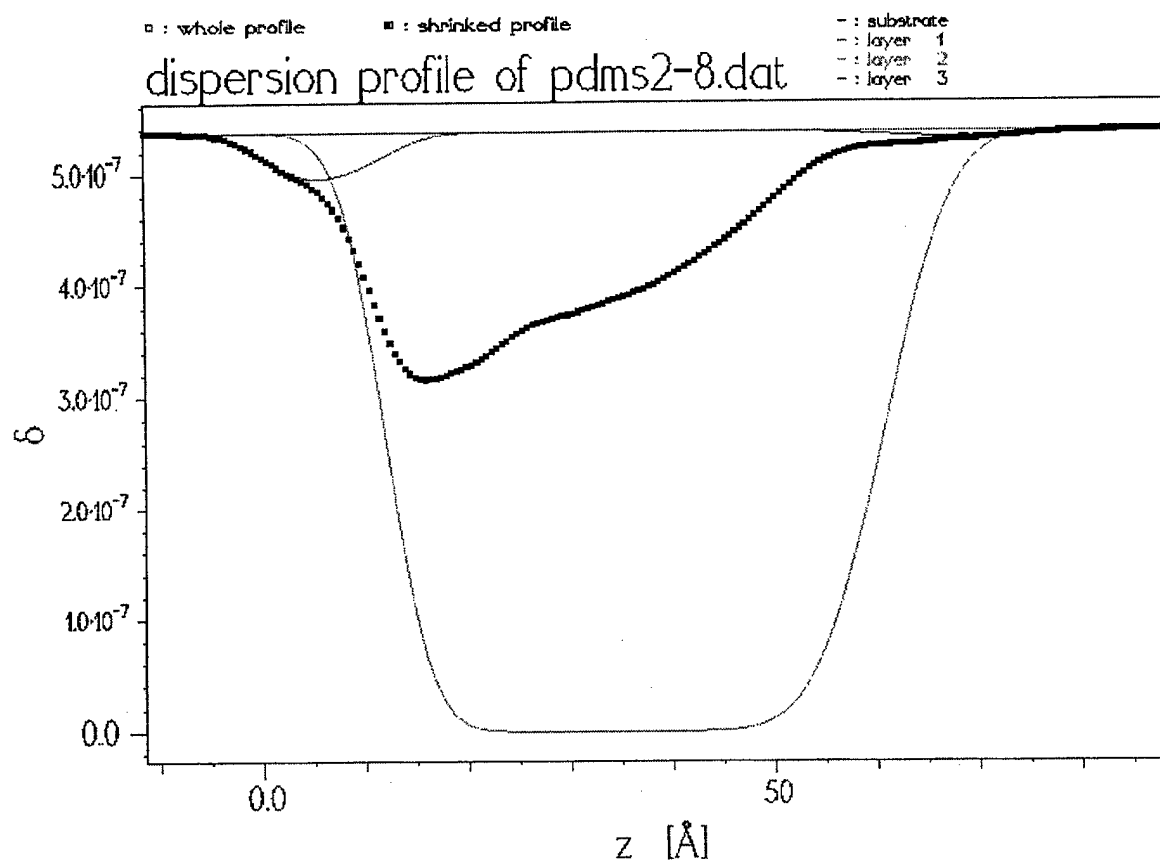


Figure 11. Candidate profile of the real part of the X-ray refractive index for the reflectivity curve (b) in Figure 10. The X-ray reflectivity calculated from this profile fits the data very well with a χ^2 parameter value of 0.087.

References

- [1] B. Zhao, D. Mulkey, W.J. Brittain, Z. Chen, M.D. Foster, *Langmuir* **15**, 6856, 1999.
- [2] H. Yim, H. Wu, M.D. Foster, S. Z.D. Cheng, F. W. Harris, *Langmuir* **12**, 3202, 1997.
- [3] H. Yim, M.D. Foster, K. McCreight, X. Jin, S.Z.D. Cheng, F.W. Harris, *POLYMER* **39**, 4675, 1998.
- [4] H. Yim, M.D. Foster, J. Engelking, H. Menzel, A.M. Ritcey, *Langmuir* **16**, 9792, 2000.
- [5a] H. Yim, M.D. Foster, D. Balaishis, I. Manners, *Langmuir* **14**, 3921, 1998.
- [5b] Z. Chen, Ph.D. Thesis, The University of Akron, 2000.
- [6] A. Heise, H. Menzel, H. Yim, M.D. Foster, R. H. Wieringa, A.J. Schouten, V. Erb, M. Stamm, *Langmuir* **13**, 723, 1997.
- [7] H. Menzel, A. Heise, H. Yim, M.D. Foster, R.H. Wieringa, A. J. Schouten *Gummi, Fasern, Kunstst.* **50**, 288, 1997.
- [8] H. Menzel, A. Heise, H. Yim, M.D. Foster, R.H. Wieringa, A.J. Schouten, *ACS Symp. Ser. 695: Organic Thin Films: Structure and Applications*, Oxford University Press, Curtis W. Frank, ed., 1998, p. 131.
- [9] I. Luzinov, D. Julthongpiput, A. Liebmann-Vinson, T. Cregger, M.D. Foster, V.V. Tsukruk, *Langmuir* **16**, 504, 2000.

- [10] B. Zhao, W. J. Brittain, *Prog. Polym. Sci.* **25**, 677, 2000.; J. R  he, W. Knoll, in *Supramolecular Polymers*, edited by A. Cifferri, (Marcel Dekker, New York, 2000) p. 565.
- [11] C. Heibel, S. Maus, W. Knoll, J. R  he, *Organic Thin Films, ACS Symp. Series* **695**, 104, 1998.
- [12] D. E. Savage, N. Schimke, Y. -H. Phang, M. G. Lagally, *J. Appl. Phys.* **71**, 3283, 1992.
- [13] P. M  ller-Buschbaum, J. Gutman, C. Lorenz, T. Schmitt, M. Stamm, *Macromolecules* **31**, 9265, 1998.
- [14] Z. Li, M. Tolan, T. H  hr, D. Kharas, S. Qu, J. Sokolov, M.H. Rafailovich, H. Lorenz, J.P. Kotthaus, J. Wang, S.K. Sinha, A. Gibaud, *Macromolecules* **31**, 1915, 1998.
- [15] I.M. Tidswell, T.A. Rabedeau, P.S. Pershan, S.D. Kosowsky, *Phys. Rev. Lett.* **66**, 2108, 1991.
- [16] D. Andelmann, J.-F. Joanny, M.O. Robbins, *Europhys. Lett.* **7**, 731, 1988.
- [17] P. M  ller-Buschbaum, J.S. Gutman, J. Kraus, H. Walter, M. Stamm, *Macromolecules* **33**, 569, 2000.
- [18] O. Prucker, J. R  he, *Macromolecules* **31**, 592, (1998); O. Prucker, J. R  he, *Langmuir* **14**, 6893, 1998.
- [19] M.D. Foster, *Crit. Rev. Anal. Chem.* **24**, 179, 1993.
- [20] V. Holy, T. Baumbach, *Phys. Rev. B* **49**, 10668, 1994.
- [21] K. Shin, Y. Pu, M. H. Rafailovich, J. Sokolov, O. H. Seeck, S. K. Sinha, M. Tolan, R. Kolb, *Macromolecules* **34**, 5620, 2001.
- [22] J. Dailland, A. Gibaud (ed.), *X-ray and Neutron Reflectivity: Principles and Applications* (Springer, 1999).
- [23] P. M  ller-Buschbaum, M. Stamm, *Macromolecules* **31**, 3686, 1998.
- [24] A. Domack, O. Prucker, J. R  he, D. Johannsman, *Phys. Rev. E* **56**, 1, 1997.
- [25] J. Habicht, M. Schmidt, J. R  he, D. Johannsman, *Langmuir* **15**, 2460, 1999.
- [26] R.G. Horn, J. N. Israelachvili, *Macromolecules* **21**, 2836, 1988.
- [27] J.N. Israelachvili, S.J. Kott, *J. Chem. Phys.* **88**, 7162, 1988.
- [28] P.A. Thompson, G.S. Grest and M.O. Robbins, *Phys. Rev. Lett.* **68**, 3448, 1992.; J.P. Gao, W.D. Luidtke and U. Landman, *J. Phys. Chem.* **B101**, 4013, 1997.; J.P. Gao et al., *Science* **270**, 605, 1995.
- [29] C.-J. Yu, A.G. Richter, A. Datta, M.K. Durbin and P. Dutta, *Phys. Rev. Lett.* **82**, 2326, 1999.
- [30] O.H. Seeck, I.D. Kaendler, D. Shu, H. Kim, D.R. Lee, M. Tolan, S.K. Sinha, "X-ray Reflectivity Studies of Confined Fluids, " Experimental Report, 2000.; H. Kim, O.H. Seeck, D.R. Lee, D. Shu, I.D. Kaendler, S.K. Sinha, "X-ray Scattering Studies of Confined Liquids," *Bull. Amer. Phys. Soc.* **45**(1), 999, 2000.

TECHNOLOGY TRANSFER

a.) Patent Applications and/or awards

There were no patent applications.

b.) Names and organization of individuals in government, academy, or industry to whom at least one year's report was sent and/or to whom this final report will be sent:

Dr. Michael Kent, Sandia National Lab
Dr. Ali Dhinojwala, The University of Akron
Dr. Charles F. Majkrzak, NIST
Prof. Jürgen Rühle, Max-Planck-Institute
Priv. Doz. Henning Menzel, University of Hannover
Dr. Doug Kiserow, ARO

c.) Individuals with whom some aspect of the work was discussed over the course of the project. Individuals who have assisted with the work in some way as collaborators are marked as such.

Dr. Michael Kent, Sandia National Laboratory, collaborator
Dr. Peter Mueller-Buschbaum, Technical University of Munich, collaborator
Dr. Ali Dhinojwala, The University of Akron, Dept. of Polymer Science
Prof. Jürgen Rühle, University of Freiburg, Germany, collaborator
Dr. Sunni Sinha, Argonne National Lab, collaborator
Prof. Dvora Perahia, Clemson University
Dr. Jin Wang, Argonne National Lab
Dr. Gebhard v. Krosigk, HASYLAB, collaborator
Prof. Ken Shull, Northwestern University
Priv. Doz. Henning Menzel, University of Hannover
Dr. Wendel Shuely, ERDEC
Dr. John Walker, Natick
Dr. Richard Shuford, ARL
Dr. Gary Hagenauer, ARL
Dr. Heidi Schroeder-Gibson, Natick
Dr. Nora Beck Tan, ARL
Prof. Christine Evans, U. Michigan
Dr. Peter Emanuel, CBDCOM/SCBRD-RT
Maj. Alan F. Weir, U.S. Army Medical Research, Institute of Chemical Defense
Prof. D. Grainger, Colorado
Prof. Anna Ritcey, University of Laval, Quebec, collaborator
Prof. Ian Manners, U. Toronto, collaborator
Dr. Richard Lareau, ARL Shady Grove Surface Analysis Center
Dr. Derek Demaree, ARL
Dr. Jim Hirvonen, ARL
Prof. Edwin Thomas, MIT

Army contractors

Dr. Richard M. Kopchik, The Catalyst Group
Dr. Jeffrey C. Andle, Biode (maker of prototype chemical sensor)

d.) Leveraging of Army funds

- Acquisition and setup of surface spectrometer. Capital cost from Ohio. Manpower for setup and cost of adaptation for MURI work from MURI funds.
- Acquisition of new small angle scattering spectrometer - bulk of cost from Ohio, matching from MURI
- The group of Sunni Sinha at Argonne National Laboratory has substantial funding for their work on confined fluids. We were very encouraged to be able to leverage the cell they have developed and the expertise they have in doing reflectivity of confined films.
- Prof. Jürgen Rühle, whose group synthesized the polymer brushes studied here, is funded by agencies in Germany.
- Prof. Ian Manners group synthesized poly(ferrocenylsilane) polymers. His research is funded by the Canadian government.

REPORT DOCUMENTATION PAGEForm Approved
OMB NO. 0704-

0188

Public Reporting burden for this collection of information is estimated to average 1 hour per response, including the time for reviewing instructions, searching existing data sources, gathering and maintaining the data needed, and completing and reviewing the collection of information. Send comment regarding this burden estimates or any other aspect of this collection of information, including suggestions for reducing this burden, to Washington Headquarters Services, Directorate for information Operations and Reports, 1215 Jefferson Davis Highway, Suite 1204, Arlington, VA 22202-4302, and to the Office of Management and Budget, Paperwork Reduction Project (0704-0188,) Washington, DC 20503.

1. AGENCY USE ONLY (Leave Blank)	2. REPORT DATE 5/31/02	3. REPORT TYPE AND DATES COVERED Final Jan. 1 '96 - May 15. '02
4. TITLE AND SUBTITLE New Materials and New Surface Grafting Procedures for Chemical Protection and Sensor Applications.		5. FUNDING NUMBERS Grant No. DAAH04-96-1-0018 Proposal No. 35023-MS-MUR Subcontract to North Carolina State University
6. AUTHOR(S) Roderic P. Quirk		
7. PERFORMING ORGANIZATION NAME(S) AND ADDRESS(ES) The University of Akron Department of Polymer Science Akron, OH 44325-3909		8. PERFORMING ORGANIZATION REPORT NUMBER
9. SPONSORING / MONITORING AGENCY NAME(S) AND ADDRESS(ES) U. S. Army Research Office P.O. Box 12211 Research Triangle Park, NC 27709-2211		10. SPONSORING / MONITORING AGENCY REPORT NUMBER
11. SUPPLEMENTARY NOTES The views, opinions and/or findings contained in this report are those of the author(s) and should not be construed as an official Department of the Army position, policy or decision, unless so designated by other documentation.		
12 a. DISTRIBUTION / AVAILABILITY STATEMENT Approved for public release; distribution unlimited.	12 b. DISTRIBUTION CODE	

13. ABSTRACT (Maximum 200 words)

The research completed by Professor Quirk's research group contributed to the overall MURI objectives by developing a wide range of new materials and new procedures for grafting these materials onto surfaces and fibers for use in chemical protection and sensor applications. The results from this research on new materials and new grafting methods can be subdivided into five project areas.

1.) Preparation of Well-defined, Thin Films by Anionic Grafting for Use in Chemical Protection and Sensor Applications.

2.) Synthesis and Characterization of Functionally-Tailored Poly(1,4-phenylenes) with Photoluminescent and Electroluminescent Properties, High Strength, and Fiber-forming Properties for Use as Smart Materials for Soldier's Apparel.

3.) Novel Poly(ferrocenylalkylsilane) Materials that are Responsive to Chemical and Environmental Changes for Use as Smart Materials for Soldier's Apparel.

4.) Development of Photochromic, Thermochromic and Mechanochromic Polyurethane Coatings for Fibers and Protective Battle Gear.

5.) Grafting Photoluminescent and Electroluminescent Poly(1,4-phenylenes) to Surfaces for Use as Smart Materials for Soldier's Apparel.

14. SUBJECT TERMS

thermochromic, mechanochromic, photochromic polyurethanes, polyphenylenes, photoluminescence, electroluminescence, smart materials, surface grafting nanofibers, poly(ferrocenyldimethylsilane), polymer brush.chemical sensors

15. NUMBER OF
PAGES
25

16. PRICE CODE

17. SECURITY
CLASSIFICATION
OR REPORT
UNCLASSIFIED

18. SECURITY
CLASSIFICATION
ON THIS PAGE
UNCLASSIFIED

19. SECURITY
CLASSIFICATION
OF ABSTRACT
UNCLASSIFIED

20. LIMITATION OF
ABSTRACT

UL

NSN 7540-01-280-5500

Standard

Form 298 (Rev.2-89)

Prescribed by ANSI Std. Z39-18

298-102

1.) LIST OF MANUSCRIPTS AND PAPERS PRESENTED

a.) Papers published in peer-reviewed journals

"Surface-Initiated Living Anionic Polymerization of Isoprene using a 1,1-Diphenylethylene Derivative and Functionalization with Ethylene Oxide", R. P. Quirk, R. T. Mathers, *Polym. Bull.*, 45/46, 471-477(2001).

b.) Manuscripts submitted, but not published:

1. "Anionic synthesis of Poly[(isoprene)-*block*-(ethylene oxide)] Block Copolymer Brushes Grafted to Silicon Wafers via a 1,1-Diphenylethylene Monolayer", R. P. Quirk, R. T. Mathers, *Macromolecules*, under revision.

c.) Manuscripts prepared and ready to be submitted to peer-reviewed journals.

1. "Anionic Polymerization of 1,3-Cyclohexadiene with High Stereoselectivity and the Formation of Crystalline Poly(1,2-cyclohexadiene) in Cyclohexane", R. P. Quirk, F. You, *to be submitted to Macromolecular Chemistry and Physics*.

b.) Papers published in non-peer-reviewed journals, preprints or in conference proceedings

1. "Surface Grafting to and from 1,1-Diphenylethylene Using a Surface-Bound Monolayer and Functionalization of the Living Chain Ends with Ethylene Oxide", R. P. Quirk and R. T. Mathers, *Polym. Mater. Sci. & Eng.*, **84**, 873-874.(2001).
2. "Surface Grafted Polyisoprene-*block*-ethylene oxide) Diblock Copolymer Brushes from a 1,1-Diphenylethylene Surface-bound Monolayer", *Polym. Mater.: Sci. & Eng.*, **85**, 198-199(2001).
3. Z. Chen, N. Vaidya, T-H. Chang, M.D. Foster, R.P. Quirk, "Morphology and Ordering Behavior of a Novel Organometallic Diblock copolymer: Poly(isoprene)-*b*-Poly(ferrocenyldimethylsilane)," *Polym. Prepr., Am. Chem. Soc., Div. Polym. Chem.*, **41** (2), 2000.
4. N. Sheller, W. Li, M.D. Foster, D. Balaishis, I. Manners, L. Guo, R.P. Quirk, "Scanning Probe Microscopy of Surfaces of Novel Poly(styrene-ferrocenyldimethylsilane) Block Copolymers," *Polym. Prepr., Am. Chem. Soc., Div. Polym. Chem.*, **39** (2), 1204-1205, 1998.
5. "Effect of Coligand on Regioselectivity of Poly(1,4-benzophenone) in Ni(0) Coupling Polymerization", R. P. Quirk and W. Yu, *Polym. Prep. (Am. Chem. Soc., Div. Polym. Chem.)*, **41**(1), 95-96 (2000).
6. "Synthesis and Characterization of Poly(2-Octoxycarbonyl-1,4-phenylene)-Based Functionally Tailored Polyphenylene Copolymers", R. P. Quirk and W. Yu, *Polym. Prep. (Am. Chem. Soc., Div. Polym. Chem.)*, **41**(1), 837-838. (2000).

c.) Ph.D. and M.S. dissertations.

1. "Synthesis and Characterization of Poly(2-octoxycarbonyl-1,4-phenylene) and Poly(2-benzoyl-1,4-phenylene) Homopolymers and Copolymers", Ph.D. thesis of Wenxin Yu, December, 2001.
2. "Anionic Synthesis of Diblock Copolymer Brushes and Functional Polymers", Ph.D. thesis of Robert T. Mathers, May, 2002.
3. "Synthesis and Characterization of organometallic Monomers and Polymers of 1,1'-Ferrocenyldimethylsilane", M.S. Thesis of Liping Guo, December, 1997.

d.) Papers presented at meetings without preprints.

1. "Synthesis and Properties of Polymers with Different Topologies", R. T. Mathers, 33rd Great Lakes/Central Regional Meeting of the American Chemical Society, Grand Rapids, Michigan, June 11, 2001.

PARTICIPATING SCIENTIFIC PERSONNEL

Dr. Roderic P. Quirk, Professor
 Robert T. Mathers, Ph.D., 5/02
 Wenxin Yu, Ph.D., 12/01
 Liping Guo, M.S., 12/97
 Dr. Qizhuo Zhuo, Postdoctoral research associate
 Dr. Shengqing Xu, Postdoctoral research associate
 Fengxiang You, PhD. candidate

INVENTIONS

None

SCIENTIFIC PROGRESS AND ACCOMPLISHMENTS

The research completed by Professor Quirk's research group contributed to the overall MURI objectives by developing a wide range of new materials and new procedures for grafting these materials onto surfaces and fibers for use in chemical protection and sensor applications. The results from this research on new materials and new grafting methods can be subdivided into five project areas.

- 1.) Preparation of Well-defined, Thin Films by Anionic Grafting for Use in Chemical Protection and Sensor Applications.
- 2.) Synthesis and Characterization of Functionally-Tailored Poly(1,4-phenylenes) with Photoluminescent and Electroluminescent Properties, High Strength, and Fiber-forming Properties for Use as Smart Materials for Soldier's Apparel.
- 3.) Novel Poly(ferrocenylalkylsilane) Materials that are Responsive to Chemical and Environmental Changes for Use as Smart Materials for Soldier's Apparel.
- 4.) Development of Photochromic, Thermochromic and Mechanochromic Polyurethane Coatings for Fibers and Protective Battle Gear.
- 5.) Grafting Photoluminescent and Electroluminescent Poly(1,4-phenylenes) to Surfaces for Use as Smart Materials for Soldier's Apparel.

Project 1.). Preparation of Well-defined, Thin Films by Anionic Grafting for Use in Chemical Protection and Sensor Applications.

A new methodology has been developed for grafting functional polymers onto fibers and surfaces based on 1,1-diphenylethylene chemistry¹⁻³. 1,1-Diphenylethylene units can serve as universal co-initiating groups for radical, anionic and cationic polymerizations. In addition, they can serve as living linking agents for coupling of living or functionalized polymer chains to the polymer surface.

Surface-bound monolayers of 1,1-diphenylethylene (DPE) on silica surfaces have been prepared and characterized by contact angle measurements, atomic force microscopy, X-ray reflectometry, X-ray photoelectron spectroscopy and ellipsometry. The utility of 1,1-diphenylethylene units for surface "grafting to" has been demonstrated by grafting both poly(styryl)lithium and poly(isoprenyl)lithium to the surface. The resulting polymer brushes were characterized by contact angle measurements, atomic force microscopy, X-ray reflectometry, X-ray photoelectron spectroscopy and ellipsometry. Work has continued to improve on the method of forming polymer brushes by reacting butyllithium with the DPE monolayer via "grafting from" procedures. Polystyrene, polyisoprene, ω -hydroxy-functionalized polyisoprene, ω -trifluoroethylsulfonfyl-functionalized polyisoprene and polyisoprene-*block*-poly(ethylene oxide) brushes have been prepared by this "grafting from" procedure. These polymer brushes have been characterized by contact angle measurements, atomic force microscopy, X-ray photoelectron spectroscopy and ellipsometry. These combined results show that the surface-bound DPE units are very useful to prepare hydrophobic or hydrophilic polymer brushes, block copolymer brushes that can change their surface properties depending upon the solvent or interface to which they are attached, and also chain-end functionalized polymer brushes for attachment of biological and chemical sensors.

Preparation of 1,1-diphenylethylene surface monolayers.

Self-assembled monolayers of 1,1-diphenylethylene groups were prepared by reaction of silyl chloride-functionalized 1,1-diphenylethylenes as shown in Scheme 1 and described in ref. 1. SAM-1 was prepared from DPE-SiCl (1) and SAM-2 was prepared from DPE-SiCl₃ (2). Contact angle measurements for these monolayers are shown in Table 1 and show the hydrocarbon nature of the surfaces after attachment of DPE groups. It is noteworthy that the advancing contact angle for a clean silicon wafer is 10°. X-ray reflectometry analysis was used to determine the thicknesses of both of these monolayers as shown in Table 1. Ellipsometry analysis indicated that the thickness of SAM-1 was 0.9 nm, in reasonably good agreement with the results from X-ray reflectometry. The increase in contact angle is consistent with deposition of a hydrocarbon monolayer on the surface. If the density of the monolayer is approximately 1g/cm³, then the number of DPE molecules on the

surface can be calculated using the estimated monolayer volume (from the ellipsometry thickness). Thus it was calculated that the surface contained approximately three DPE molecules/nm². The number of DPE molecules per unit area was also calculated from electron density calculations obtained from X-ray reflectometry measurements. The calculated number of DPE units on the surface from X-ray measurements corresponded to 2.4 DPE units/nm² for SAM-1 and to 2.6 DPE units/nm² for M-2, in good agreement with the results from ellipsometry. The surface roughness of this DPE monolayer was determined by AFM from multiple 1 x 1 μm² regions. The surface roughness for SAM-1 was 4 ± 1 Å which corresponds to a very uniform monolayer.

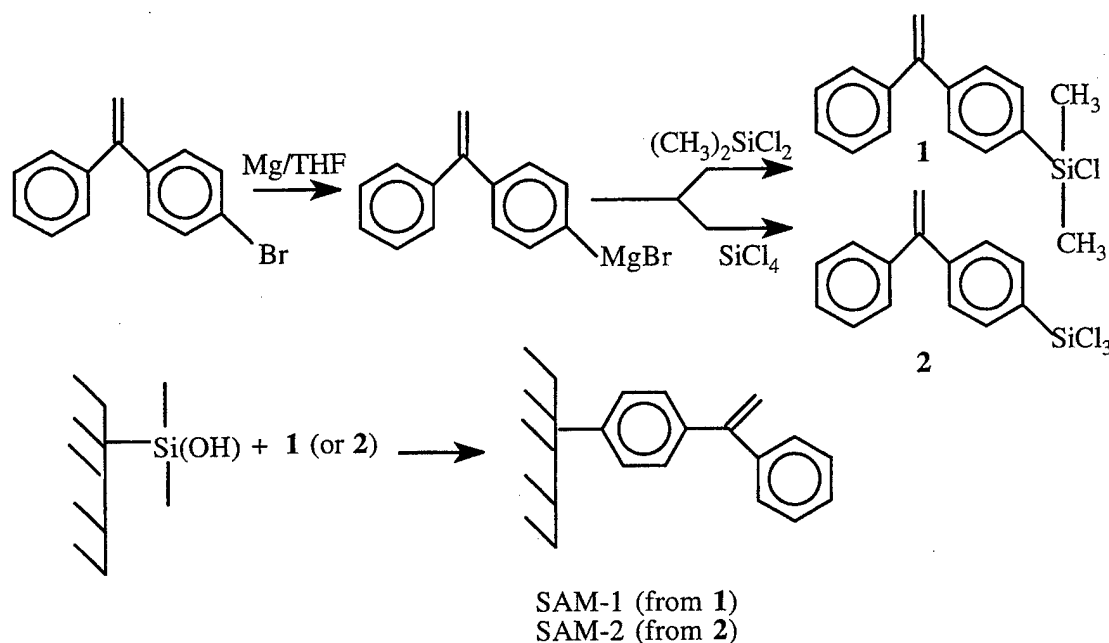
Table 1. Contact angle measurements and thicknesses for SAM-1 and SAM-2.

	SAM-1	SAM-2
Thickness (nm) ^a	0.72 ± 0.17	0.78 ± 0.17
θ _{adv} ^b	81 ± 3	66 ± 4
θ _{rec} ^b	72 ± 2	50 ± 4

^a measured by X-ray reflectometry

^b measured using a sessile drop

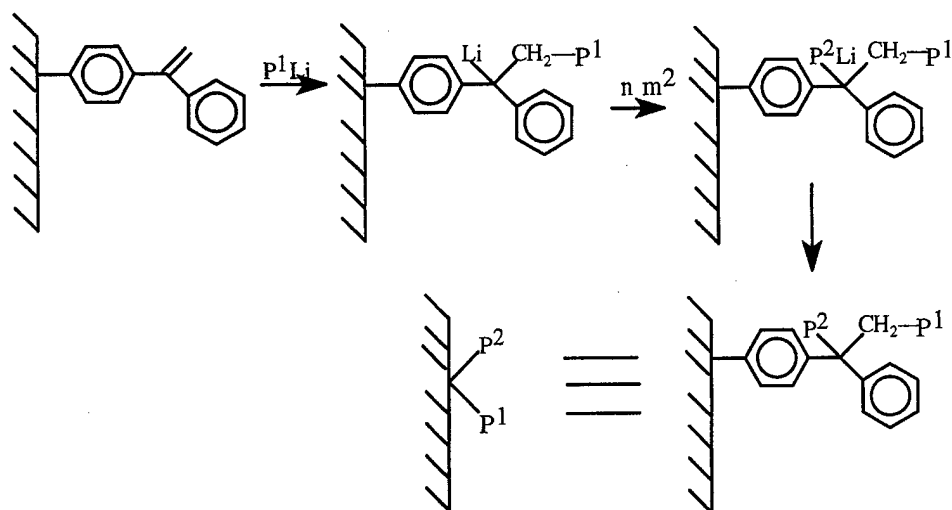
Scheme 1.



“Grafting to” reactions of Living Polymers to Self-Assembled Monolayers of DPE. As described previously, one of the unique features of the DPE grafting methodology is that it is applicable to both “grafting to” and “grafting from” procedures. Furthermore, it can be used for anionic, cationic or radical grafting because of the non-homopolymerizability of 1,1-diphenylethylene moieties and the fact that DPE units are very reactive with these types of reactive intermediates. Thus, although the “grafting to” methodology would be expected to generate lower density of polymer chains, the product of the grafting to reaction is itself a 1,1-diphenyl-alkyllithium species that can be used to generate a “grafting from” segment and thus generate an AB-type brush with two arms, joined at the surface, but incompatible as illustrated in Scheme 2. The reactivity of the surface-bound monomers of DPE with respect to linking reactions was investigated by addition of well-defined poly(styryl)lithium as shown in Scheme 2¹. The “grafting to” methodology has been demonstrated with both poly(styryl)lithium and with ω-[3-(*t*-butyldimethylsiloxy)propyl]poly(isoprenyl)lithium. “Grafting to” reactions of a higher molecular weight poly(styryl)lithium ($M_n = 20,000$ g/mol) have been carried to compare with previously reported results for a lower molecular weight PSLi lithium ($M_n = 1,000$ g/mol). Preliminary

characterization results indicate that the contact angles are comparable with those reported for grafting reactions in the literature ($\theta_{adv} = 86 \pm 2^\circ$ and $\theta_{rec} = 72 \pm 4^\circ$).

Scheme 2.

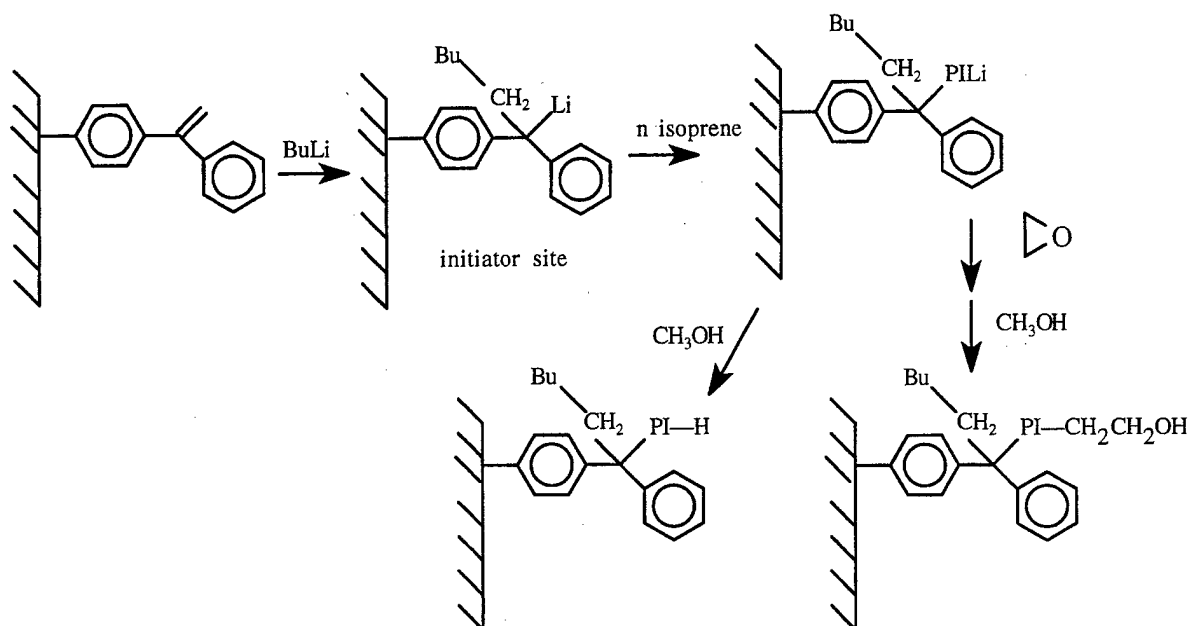


“Grafting from” reactions using Self-Assembled Monolayers of DPE. Since DPE units are universal co-initiators, they can be converted into surface-bound initiator sites by reaction with various initiators (anion, radical, cation). Initial studies utilized the reaction of an anionic initiator, butyllithium, as shown in Scheme 3¹. The factors that are unique with respect to this procedure compared to the literature on anionic surface grafting are the following:

1. *n*-Butyllithium was used to generate initiator sites by reaction with the surface-grafted DPE units. *sec*-Butyllithium is more reactive and could cleave Si-O-C bonds on the surface and remove the DPE units.
2. Excess *n*-butyllithium was used to react with impurities and also to convert any surface Si-OH groups into unreactive Si-OLi groups.
3. Initial experiments utilized cyclohexane rather than an ether such as tetrahydrofuran (THF) as solvent. It is known that alkylolithium compounds and polymeric organolithium compounds are not stable in solvents such as THF. Also preliminary results from anionic surface grafting using THF as solvent indicate that irregular grafting patterns are obtained.
4. Optimum procedures for production of thick polymer films and more rapid grafting rates utilized neat monomer (isoprene or styrene) rather than a dilute solution of the monomer.

Using these procedures, it was possible to generate very uniform films with low degrees of surface roughness and with film thicknesses ranging from 2-24 nm for styrene grafting and from 5-10 nm for isoprene grafting. It is noteworthy that the thicknesses of films formed by the “grafting to” procedure were only about 2 nm.

One of the advantages of living anionic polymerization is that the active chain ends retain their reactivity after all of the monomer has been consumed. Thus, polymer grafts with various functional groups at the chain end can be prepared by termination with different electrophilic functionalizing agents. As reported previously, termination with ethylene oxide was effected to obtain the corresponding hydroxyethylated chain end as shown in Scheme 3². The presence of the hydroxy-functionalized chain ends was demonstrated by contact angle measurements, EPS and FTIR spectroscopy. For example, the advancing contact angle decreased from $\theta_{adv} = 86 \pm 2^\circ$ for the polyisoprene graft to $\theta_{adv} = 47 \pm 3^\circ$ for the corresponding ω -hydroxypolyisoprene graft. The high functionality of the chain ends was also demonstrated by XPS atomic concentration measurements of carbon bonded to oxygen from the XPS carbon (1s) scans at 286.7 eV. The atomic concentration of carbon bonded to oxygen at 286.7 eV versus carbon bonded to carbon at 285 eV for the “grafting from” method to obtain hydroxyl-functionalized chain ends on a surface was three times larger than the analogous C_{1s} peak for the “grafting to” method to obtain hydroxyl-functionalized chain ends on a surface.

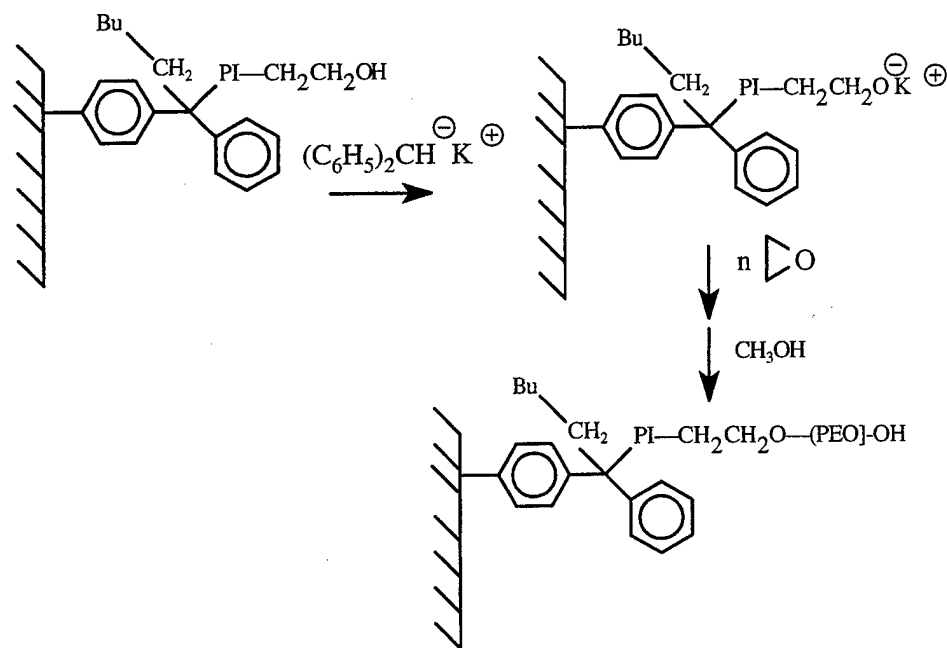


Scheme 3.

The hydroxy-functionalized polyisoprene brush prepared using the "grafting to" procedure used a protected hydroxy-functionalized initiator so that all of the polyisoprene chain ends had a hydroxyl group.

"Grafting from" reactions using Functionalized Polymer Brushes Prepared from Self-Assembled Monolayers of DPE. Synthesis of Polyisoprene-*block*-poly(ethylene oxide) Brushes. The utility of functionalized polymer brushes on surfaces was demonstrated by using the hydroxyl group of the hydroxy-functionalized polyisoprene brushes to initiate anionic polymerization of ethylene oxide as shown in Scheme 4. The resulting block copolymers were characterized by contact angle measurements, ellipsometry and by XPS measurements³.

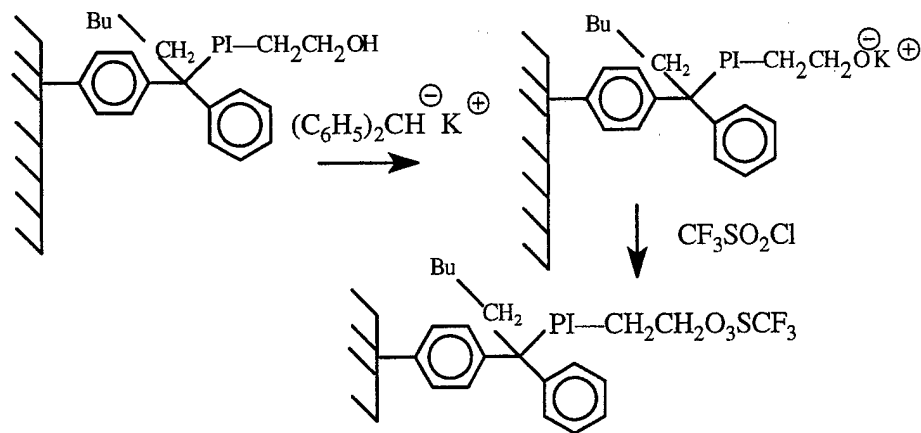
Scheme 4.



In order to demonstrate that the hydroxy groups are accessible to the diphenylmethyl potassium, this procedure was utilized to prepare the corresponding tresyl-functionalized chain ends as shown in Scheme 5. The fluorine (1s) XPS signal at 687 eV was detected after the functionalization reaction with tresyl chloride. The

underlying excess surface hydroxyl groups were protected by *t*-butyldiphenylsilyl chloride and control experiments determined the fluorine (1s) XPS signal at 687 eV only contained contributions from the reaction of the hydroxyl chain ends with tresyl chloride. The atomic concentration of fluorine relative to the number of carbon atoms in the polymer chain of known molecular weight ($M_n = 3000$ g/mol; from SEC) confirmed that all of the chain ends had reacted. The advancing contact angle increased as expected for conversion of a hydroxyl group to a trifluoromethyl group.

Scheme 5.



References for Project 1.).

1. "Surface-Initiated Living Anionic Polymerization of Isoprene using a 1,1-Diphenylethylene Derivative and Functionalization with Ethylene Oxide", R. P. Quirk, R. T. Mathers, *Polym. Bull.*, 45/46, 471-477(2001).
2. "Surface Grafting to and from 1,1-Diphenylethylene Using a Surface-Bound Monolayer and Functionalization of the Living Chain Ends with Ethylene Oxide", R. P. Quirk and R. T. Mathers, *Polym. Mater. Sci. & Eng.*, **84**, 873-874.(2001).
3. "Surface Grafted Polyisoprene-*block*-ethylene oxide) Diblock Copolymer Brushes from a 1,1-Diphenylethylene Surface-bound Monolayer", *Polym. Mater.: Sci. & Eng.*, **85**, 198-199(2001).

Project 2.). Synthesis and Characterization of Functionally-Tailored Poly(1,4-phenylenes) with Photoluminescent and Electroluminescent Properties, High Strength, and Fiber-forming Properties for Use as Smart Materials for Soldier's Apparel.

Poly (1,4) phenylenes with various substituents have been synthesized for use as smart materials for soldier's apparel.

- (1) The homopolymers and copolymers of octyl 2,5-dichlorobenzoate with 2,5-dichlorobenzophenone have been investigated for their photoluminescent properties. Pure poly(benzoyl-1,4-phenylene) exhibited an emission wavelength at 420 nm while pure poly(octoxycarbonyl-1,4-phenylene) exhibited an emission maximum at 385 nm which suggested that these polymers could be used for sensing or soldier identification because of the wavelength specificity of these polymers. The polymers have been spun into nanofibers that also exhibited photoluminescence of different colors depending on the specific polymer substrates. In addition, poly(octoxycarbonyl-1,4-phenylene) (POCP) shows liquid crystalline behavior. Textures were observed with a Nikon polarizing optical microscope. A crystalline peak was observed as DSC analysis of POP. Other alkyl 2,5-dichlorobenzoates (hexyl, decyl and dodecyl 2, 5-dichlorobenzoates) were synthesized and polymerized by Ni catalyst coupling polymerization.
- (2) Poly (benzoyl-1,4-phenylene)s (PBPs) with different microstructures were previously synthesized by nickel-mediated coupling of 2,5-dichlorobenzophenone in the presence of catalytic amounts of NiCl_2 , excess zinc, triphenylphosphine without 2,2'-dipyridine (PBP-A) or with 2,2'-dipyridine (PBP-B)¹. PBP-A and PBP-B samples with high modulus were prepared. PBP with a new microstructure (PBP-C) has been prepared as part of the MURI project. PBP-B showed a bright blue photoluminescence ($\lambda_{\text{max}}=440\text{nm}$) and electroluminescence, while PBP-A did not. Crystalline PBP-C has been synthesized in presence of the

ligand [1,2-bis-(diphenylphosphino)ethane]dichloronickel(II) (DPPE) and this polymer has been characterized by DSC and ^{13}C NMR. PBP-C was semi-crystalline as observed from DSC and X-ray characterization.

SYNTHESIS AND CHARACTERIZATION OF POLY(2-OCTOXYCARBONYL-1,4-PHENYLENE)-BASED FUNCTIONALLY TAILORED POLYPHENYLENE COPOLYMERS. Poly (alkoxycarbonyl phenylene)s with long alkoxy side groups are liquid crystalline, and some of them show amphotropism. Herein a series of poly (2-octoxycarbonyl-1, 4-phenylene) (POP) copolymers with PBP was synthesized and their photoluminescence was investigated.

Synthesis. Octyl 2, 5-dichlorobenzoate was synthesized by direct room temperature esterification. Syntheses of homopolymers and copolymers were accomplished by nickel catalyzed coupling of the aryl dichlorides by adjusting the comonomer feed ratio. Using a catalytic amount of anhydrous nickel salt, suitable coligands and an excess of high quality, activated zinc, an efficient polymerization of the aryl dichlorides was obtained. Low levels of nickel are beneficial if rapid formation of high molecular weight polymer is desired. The feed ratios and molecular weights are shown in Table 1. The copolymers and poly (2-octoxycarbonyl-1,4 phenylene) exhibited higher solubility than PBP homopolymer. The polymers are soluble in THF, chloroform, toluene and xylene.

Table 1. Characterization of Copolymers and Homopolymers of PBP and POP

Entry	Mole fraction of POP	M_n^a (g/mol)	M_w^a (g/mol)	T_g^b (°C)
a	X= 0.00	13,600	29,700	222
b	X= 0.14	7,220	10,500	161
c	X= 0.40	11,300	24,500	130
d	X= 1.0	17,200	24,200	92

^a Determined by SEC using light scattering or universal calibration method.

^b T_g was determined by DSC at heating rate of 10 °C/min under nitrogen flushing at 50 mL/min.

Thermal stability The homopolymers and copolymers exhibit high thermal stability. As shown in Figure 1, the TGA thermogram for copolymer b, Table 1, (X=0.14), exhibited less than 20% weight loss occurred at 600 °C in air or nitrogen. The first decomposition stage may be associated with scission of the side chains of octyl-2, 5-benzoate, the second stage with side chains of PBP, and third stage with main chain scission.

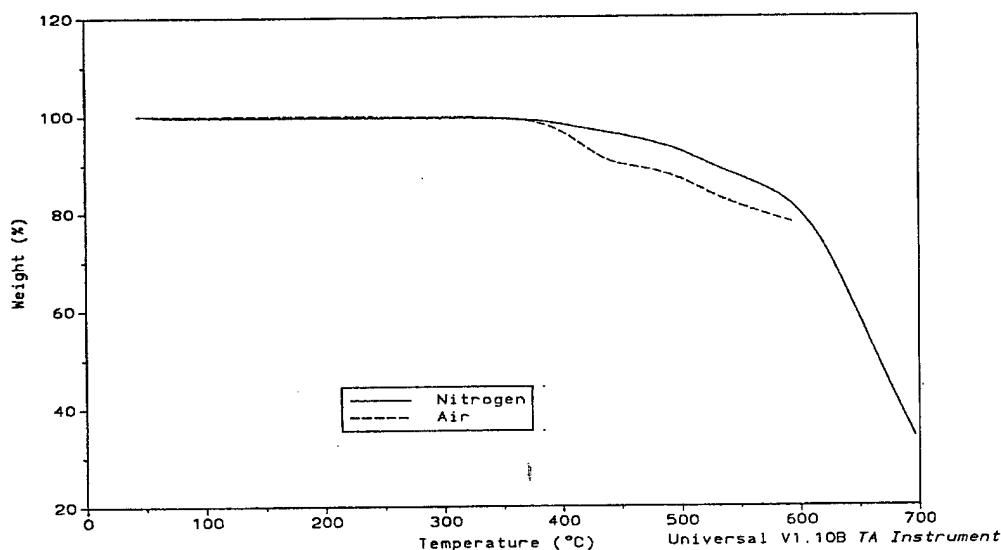


Figure 1 TGA thermogram for copolymer b, Table 1, (X=0.14)

Photoabsorption and photoluminescence The UV-vis spectra of the polymers with different comonomer ratios were obtained in chloroform. As shown in Figure 2, the λ_{max} of the long-wavelength absorption showed a red shift upon decreasing the ratio of POP to PBP. The long alkyl chain may lead to more twist of the aryl group along the main chain than does the side chain benzoyl group in PBP. It is concluded that the UV-vis absorptions of the polymers can be tailored by varying the molar ratio of POP/PBPPBP. It is concluded that the emission wavelength of the copolymers could be tuned by varying the ratio of comonomers.

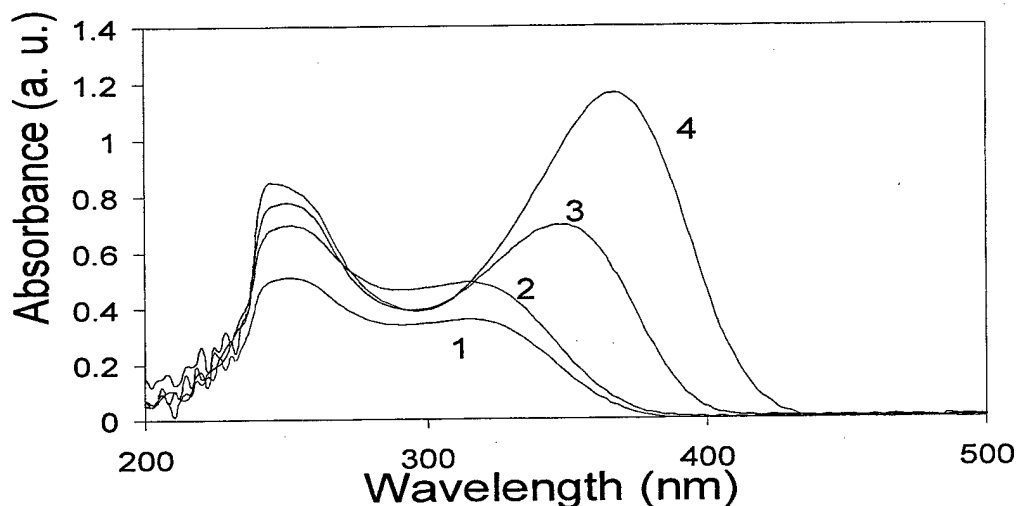


Figure 2. UV-vis absorption in chloroform. (1. POP, $X=1.0$; 2. POP: PBP= 2:3, $X=0.40$; 3. POP: PBP=1: 6.25, $X=0.14$; 4. PBP, $X=0$; see Table 1).

POLY[(2-OCTOXYCARBONYL) PHENYLENE]-BASED FUNCTIONALLY TAILORED ELECTROSPINNING NANOFIBERS.

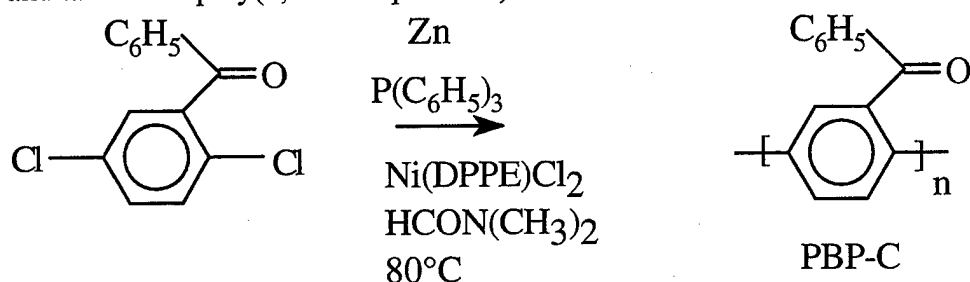
Electrospinning provides a way to produce polymer fibers with diameters in the nanometer range. In electrospinning, a polymer solution is held by its surface tension and the charge is induced to the liquid by an electric field. As the intensity of the electric field increases, the hemispherical surface of the solution elongates to form a conical shape known as the Taylor Cone. When the electric field reaches a critical value at which the electric forces overcome the surface tension forces, a charged jet of the solution is ejected from the tip of Taylor Cone. As the jet travels in air, the solvent evaporates, leaving behind a charged polymer fiber. Continuous fibers (usually in the form of non-woven fabric) can be collected. Electrospun fibers have unusually small diameters, ranging downward from typical textile fibers by as much as two orders of magnitude. The small diameter provides a large surface area to mass ratio, in the range from $10 \text{ m}^2/\text{g}$ to $1000 \text{ m}^2/\text{g}$. The research target was to synthesize polymers with good self-recognition function, and to use electrospinning to manufacture the material into the soldier's apparel.

Fiber Electrospinning. The electrospun poly(octoxycarbonyl phenylene) fibers had diameters around 800 nm. The fibers are birefringent when observed between crossed polarizers. The electrospun fibers were very easy to put into the apparel by simply using the cloth as the collector. The electrospun fibers can deposit on the surface of the cloth and form a very thin layer of poly(octoxycarbonyl phenylene) fabric. Such layer can emit violet blue, which presumably make self-recognition function realizable.

EFFECT OF COLIGAND ON REGIOSELECTIVITY OF POLY(1,4-BENZOPHENONE) IN Ni(0) COUPLING POLYMERIZATION.

PBP-B showed a bright blue photoluminescence and electroluminescence, while PBP-A did not. The microstructures of PBPs have been investigated by different methods. Herein crystalline PBP-C has been synthesized in presence of the ligand [1,2-bis (diphenyl-phosphino)ethane]dichloronickel(II) (DPPE) as shown in Scheme 1 and this polymer has been characterized by DSC and ^{13}C NMR. In addition, a molecular model for understanding the effects of coligands on

microstructure for PBPs has been developed. A new NMR method for distinguishing head-to-head, head-to-tail and tail-to-tail poly(2,5-benzophenone)s has been established based on model compound studies.



Scheme 1

Synthesis. Syntheses of PBP-A, PBP-B, PBP-C (Scheme 1), di-benzophenone and oligmeric benzophenones were accomplished by Colon's nickel coupling of aryl dichloride². In the ¹³C NMR spectra, a set of signals due to aromatic carbons and/or chlorobenzophenones occurred in the region from 120 -140 ppm, and signals due to the carbonyl carbons were observed in the region 196 -199 ppm.

Properties of PBP-C. PBP-A and PBP-B exhibit different properties when characterized by IR, UV-vis, ¹³C NMR spectra, and DSC analysis. As shown in Figure 3, PBP-A and PBP-C exhibit the same absorption maximum at 328 nm, while PBP-B has an absorption maximum at 360 nm. Meanwhile, PBP-B showed blue photoluminescence, whereas PBP-A and PBP-C did not, which suggests that PBP-B has a longer conjugation length in the polymer backbone compared with PBP-C and PBP-A. Interestingly, as shown in Figure 4, PBP-C shows an exothermic peak in its thermogram at 235 °C, while neither PBP-A nor PBP-B showed any observable melting endotherm or crystallization exotherm in their DSC traces. Furthermore, as shown in Figure 6, PBP-C shows only one sharp ¹³C NMR carbonyl resonance peak at 197.6 ppm, which suggests that PBP-C has higher regiochemical regularity in the placement of the lateral benzoyl groups along the polymer backbone. It was concluded PBP-C has a different microstructure than either PBP-A or PBP-B.

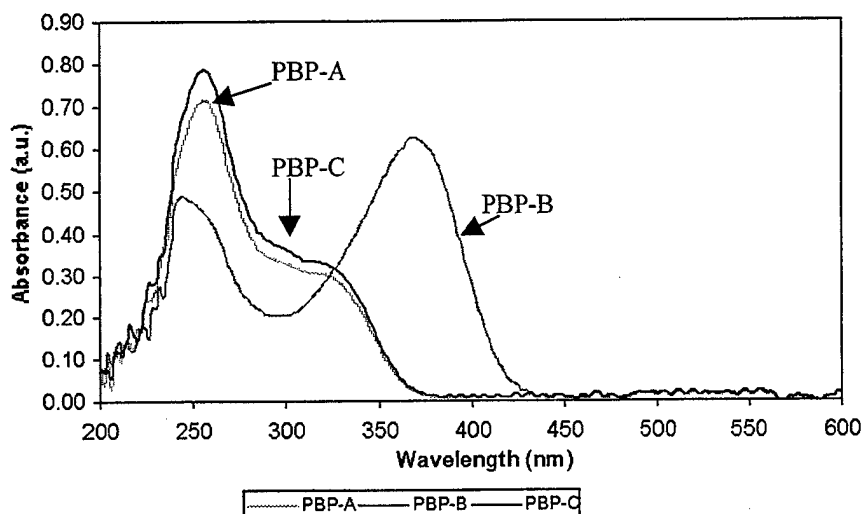


Figure 3. UV-vis absorption in chloroform. (PBP-A, PBP-B, PBP-C). (C=0.01 mg/mL)

Model for ¹³C NMR analysis of PBP. To elucidate the microstructure, bisbenzophenones with different substitution patterns were obtained by direct coupling of 2-chlorobenzophenones. H-H benzophenone dimer exhibited a carbonyl resonance at 197.5 ppm, and the corresponding resonance for the H-T benzophenone dimer occurred at 198.2 ppm, while the T-T benzophenone dimer exhibited a carbonyl resonance at 196.2 ppm. To simplify the peaks in the carbonyl region, oligmers PBP-A and PBP-B were synthesized by Ni(0) coupling of dichlorobenzophenone and end capping with monochlorobenzophenone. SEC results showed that the

number of repeat units of the oligomers was 4 to 5. Oligmer PBP-B shows a main carbonyl carbon peak at 198 ppm, while PBP-A exhibits six carbonyl carbon peaks in the region 196 ppm to 199 ppm. According to the proposed structural model above, oligmer PBP-B is assigned to be mostly head-to-tail, oligmer PBP-A is assigned a very random structure with H-H, H-T, and T-T units. Based on the spectra in Figure 3 and Figure 5, PBP-A is assigned a random structure and PBP-B is assigned to have more head-to-tail. This result is consistent with our previous work. PBP-C has only one sharp peak at 197.6 ppm, which is assigned exclusively to head-to-head units. Due to the fact that environment of the carbonyl group in the oligmers and polymers is more complicated than that in the dimers, peaks from H-H, H-T, T-T structural units may be further split in the corresponding oligmers and polymers.

References for Project 2.).

1. "Synthesis and Characterization of Poly(benzoyl-1,4-phenylene)s 2. Catalyst Coligand Effects on Polymer Properties", Y. Wang and R. P. Quirk, *Macromolecules*, **28**, 3495-3501, 1995.
2. I. Colon and D. R. Kelsey, *J. Org. Chem.*, **51**, 2627(1986).

Project 3.). Novel Poly(ferrocenylalkylsilane) Materials that are Responsive to Chemical and Environmental Changes for Use as Smart Materials for Soldier's Apparel.

The objective of this research was to investigate the synthesis and properties of polydialkylsilylferrocenes for chemical and biological detection and provide chameleon-like changes of color in response to the environment. Polydialkyl-silylferrocenes can exhibit the properties of plastics or elastomers depending upon the alkyl groups attached to silicon. In addition, the ferrocene moiety in the polymer is susceptible to oxidizing agents and can change color when subject to an electric field.

The following monomers were prepared: dimethylsilylferrocene and dihexylsilylferrocene, which form thermoplastic and elastomeric polymers, respectively. Each of these monomers can be polymerized by anionic, thermal and transition metal-catalyzed methods. In addition, block copolymers of dimethylsilylferrocene with both styrene and isoprene were investigated using anionic polymerization. The color of polydimethylsilylferrocene changes from yellow to blue upon treatment with ferric chloride; the color changes to brown upon treatment with hydrogen peroxide; and to black upon treatment with molecular iodine. In addition, these polymers appear to change size upon oxidation (see report of Professor Mark Foster). In order to investigate the ability to provide chemical detection using these polymers, a series of block copolymers were prepared in collaboration with Professor Foster and his coworkers. Conditions were found which provided controlled, living anionic polymerization and block polymerization of dimethylsilylferrocene. Both poly(styryl)lithium and poly(isoprenyl)lithium were prepared in benzene (> 90 % 1,4-microstructure) and then the block polymerization of dimethylsilylferrocene was effected in a mixture of benzene/tetrahydrofuran (50/50, vol/vol) at room temperature. These conditions were used to prepare both polystyrene-block-polydimethylsilylferrocene and polyisoprene-block-polydimethylsilylferrocene with well-defined structures (see following scheme).

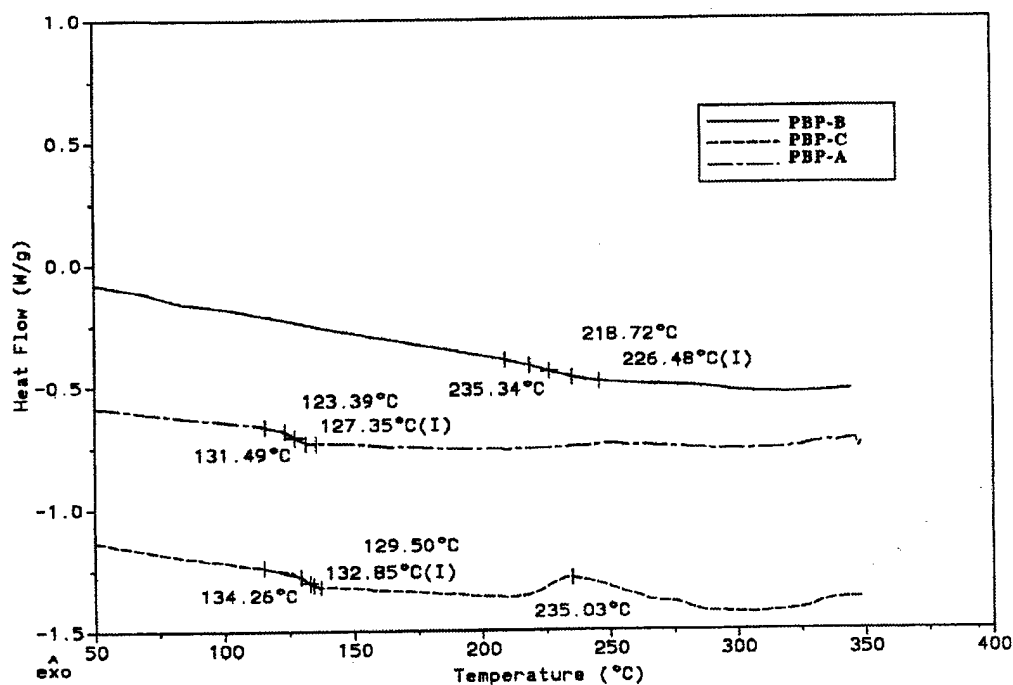


Figure 4. DSC thermograms. (--- PBP-A, — PBP-B, - - - PBP-C)

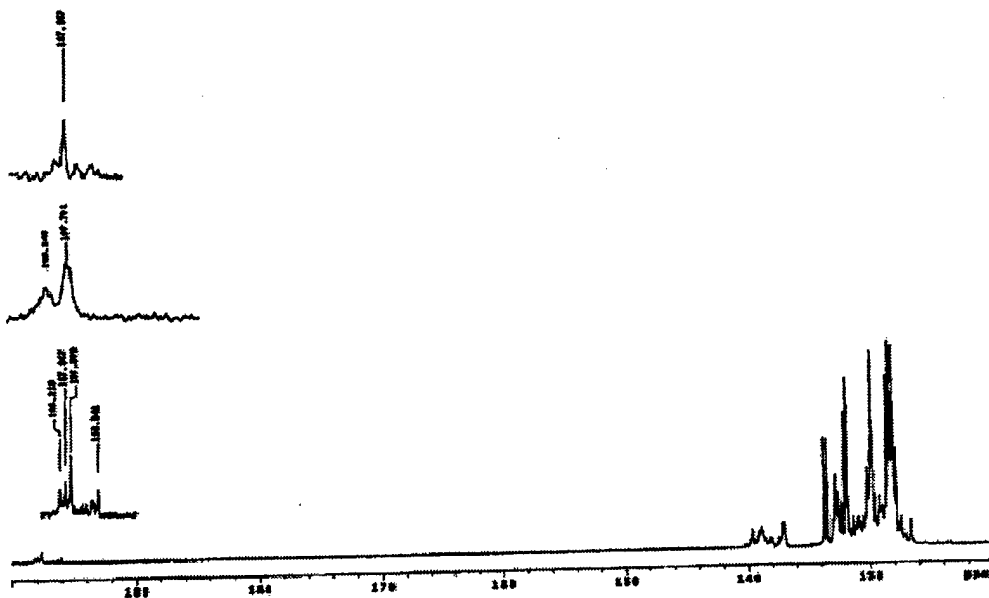
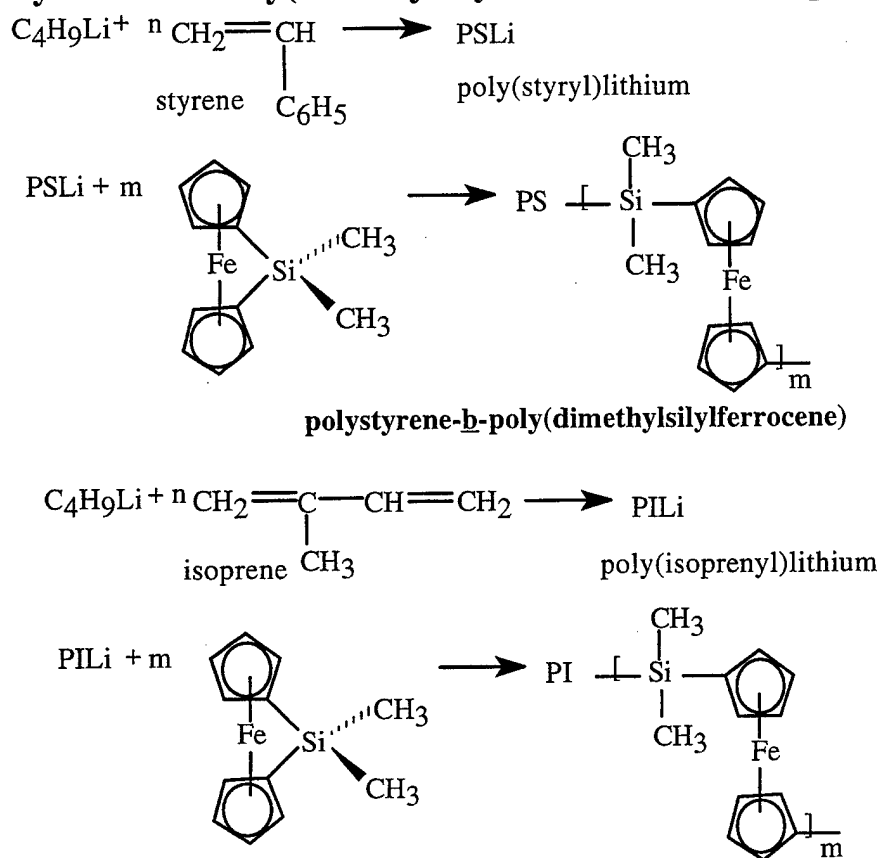


Figure 5. ^{13}C NMR spectra (From top to bottom: PBP-C; PBP-B; PBP-A).

The following polyisoprene-block-polydimethylsilylferrocene block copolymers have been prepared: 11,500-b-4,900 g/mol; 11,500-b-10,500 g/mol; and 7,300-b-12,700g/mol. The polyisoprene ($M_n = 11,500$)-block-polydimethylsilylferrocene ($M_n=4900$) exhibited a very narrow molecular weight distribution ($M_w/M_n = 1.01$). Phase separation was indicated by the observation of two DSC transitions at -60°C (T_g for polyisoprene) and at 140°C (T_m for polydimethylsilylferrocene). These samples have been given to Professor Foster for study as sensors via Langmuir-Blodgett films.

Synthesis of Poly(dimethylsilylferrocene) block copolymers.



Project 4.). Development of Photochromic, Thermochromic and Mechanochromic Polyurethane Coatings for Fibers and Protective Battle Gear.

Synthesis of Polyurethanes. A series of photochromic, thermochromic and mechanochromic polyurethanes were prepared. The elastomeric soft segments have been varied to optimize processing and physical properties for smart material applications. The elastomeric, telechelic, α,ω -dihydroxypolymers which have been investigated were α,ω -dihydroxypoly(tetramethylene oxide), α,ω -dihydroxypolybutadiene, α,ω -dihydroxypolyisoprene and hydrogenated α,ω -dihydroxypolyisoprene (α,ω -dihydroxypolyethylene-co-propylene).

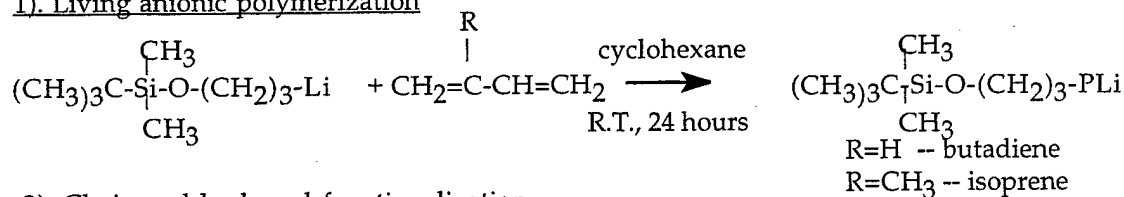
New methods have been developed to prepare well-defined α,ω -dihydroxypolybutadienes and α,ω -dihydroxypolyisoprenes with high chain-end functionality. These telechelic elastomers were prepared using living anionic polymerization with new alkyl lithium initiators containing protected hydroxyl functional groups as shown in Scheme 1¹⁻⁴. A series of seven α,ω -dihydroxypolyisoprenes ($M_n = 1400, 2200, 2400, 2700, 3250, 3800$ and 6200 g/mol) were prepared in large quantities (20-70g). It is important to note that these well-defined, functionalized polymeric diols have not been available previously for polyurethane synthesis.

The goal of synthesis of a thermo-oxidatively-stable elastomeric diols and their corresponding polyurethanes was also accomplished by developing efficient methods for the hydrogenation of protected α,ω -dihydroxypolyisoprenes as shown in Scheme 2. It was found that it was necessary to protect both of the hydroxyl groups as silyl ethers in order to obtain efficient hydrogenation (step 3 in Scheme 2). The optimum hydrogenation conditions are shown in Scheme 2. The resulting polymer has the structure of an alternating

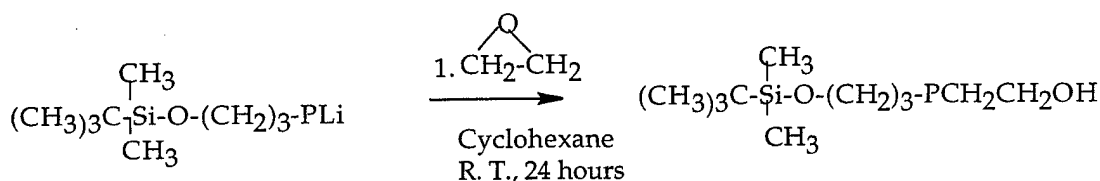
ethylene-propylene rubber after hydrogenation. Therefore, it should exhibit good elastomeric properties and the absence of double bonds increases the thermal and oxidative stability. It was anticipated that the resulting

Scheme 1. Synthesis of polybutadiene and polyisoprene diols with well-defined structures.

1). Living anionic polymerization

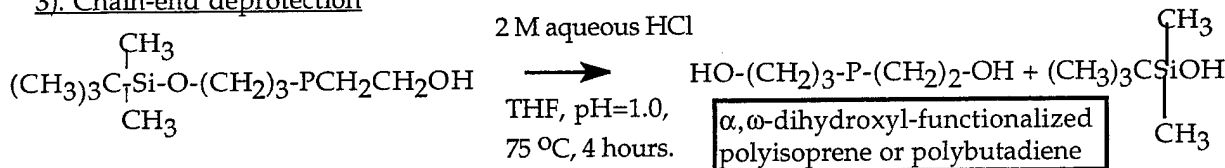


2). Chain-end hydroxyl functionalization



2. $\text{H}^+/\text{CH}_3\text{OH}$

3). Chain-end deprotection



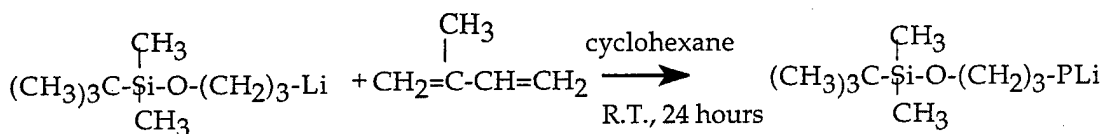
polyurethanes which would be formed from the hydrogenated polymeric diols would exhibit better ageing properties and also better resistance to chemicals. The efficient hydrogenation of all α,ω -dihydroxy-polyisoprenes was effected via the corresponding silyl ethers. All hydrogenated polymers were characterized by TLC, SEC, end-group titration and ^1H NMR. The ^1H NMR spectra after hydrogenation exhibited no peaks in the region $\delta = 4.8\text{--}5.5$ ppm, characteristic of the vinyl protons in polyisoprene.

The first step in the syntheses of segmented polyurethanes was the reaction of an elastomeric, polymer diol with two equivalents of aliphatic diisocyanate to form the corresponding polymeric diisocyanate as shown in Scheme 3. The same protocol was used for each of the different types of elastomeric diols. The diisocyanate of choice was 1,6-diisocyanatohexane (HDI), but 4,4'-methylene-bis(phenylisocyanate) (MDI) was also investigated. In the second step, the polymeric diisocyanate (Scheme 4) was chain extended by addition of a diacetylene diol as shown in Scheme 4. The diacetylene diols investigated were 2,4-hexadiyne-1,6-diol (HDD) and 5,7-dodecadiyne-1,12-diol (DDD).

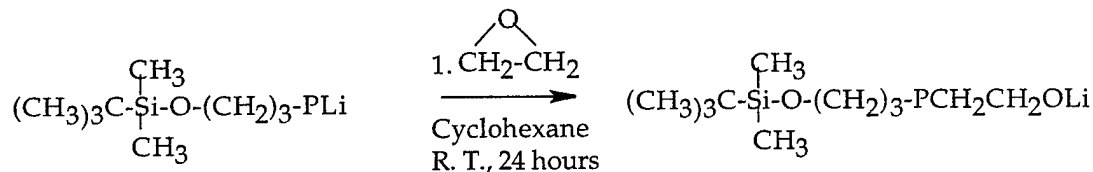
A comparison was made of the thermal properties of the different segmented polyurethanes (see Table 1). The polybutadiene-based polyurethane exhibited similar thermal stability to the traditional polyTHF-based polyurethane.

Scheme 2. Hydrogenation of polyisoprene diols by functionalization and protection.

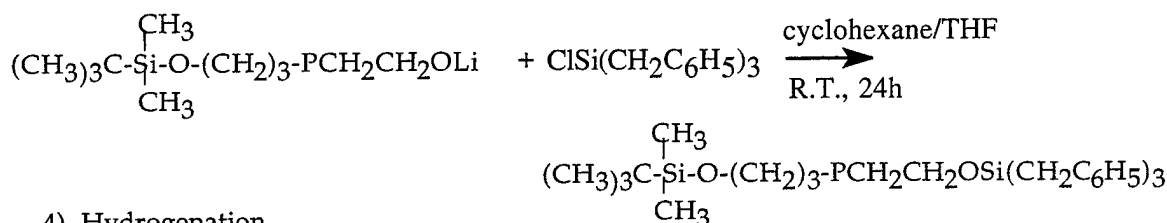
1). Living anionic polymerization



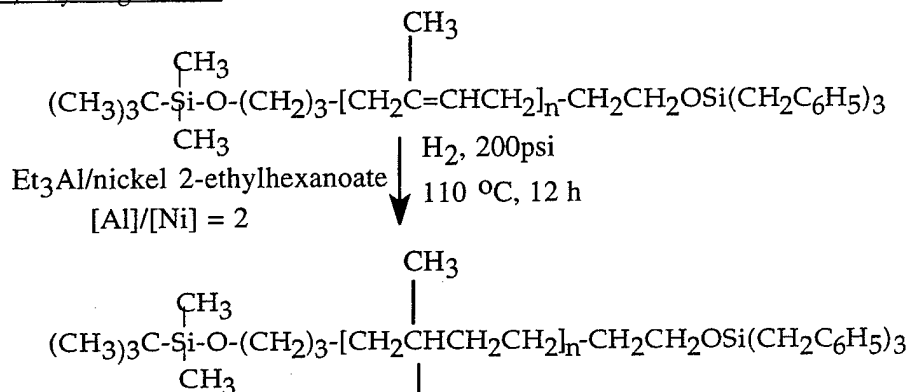
2). Chain-end hydroxyl functionalization



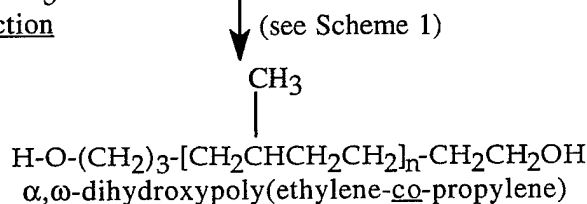
3) Chain-end protection



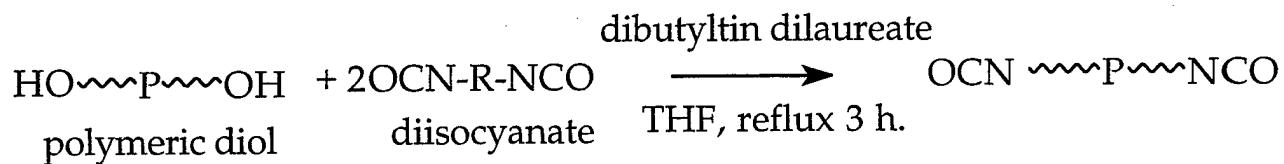
4). Hydrogenation



5). Deprotection



Scheme 3. Synthesis scheme for the diacetylene-containing segmented polyurethanes: Step I. prepolymer synthesis



P = polybutadiene, PB.

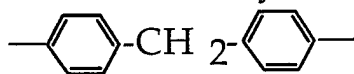
polyisoprene, PI.

polycaprolactone, PCL.

poly(tetramethylene glycol),

PTMG.

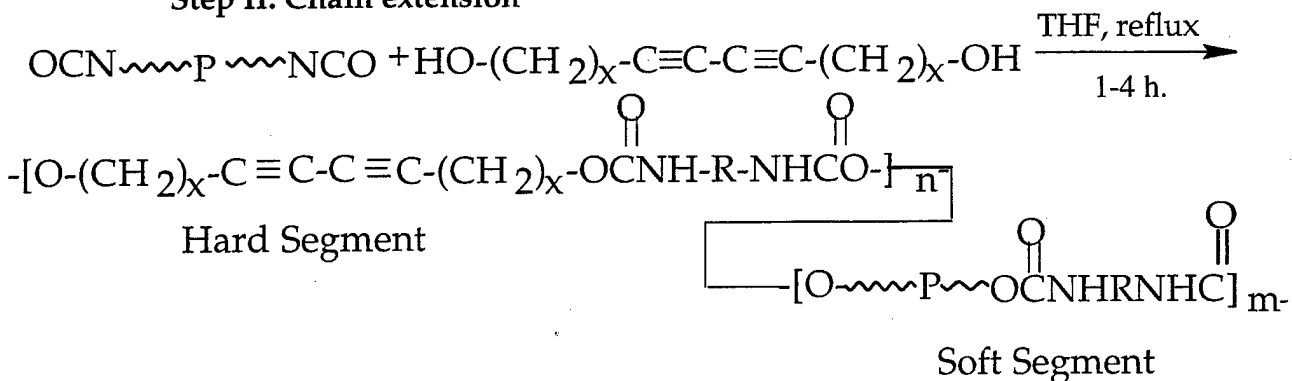
R = $-\text{CH}_2-\text{CH}_2-\text{CH}_2-\text{CH}_2-\text{CH}_2-\text{CH}_2-$
1,6-diisocyanatohexane, HDI



4,4'-methylenebis(phenyl isocyanate), MDI

Scheme 4 . Synthesis scheme for the diacetylene-containing segmented polyurethanes.

Step II. Chain extension



Segmented polyurethane with diacetylene functional group within the hard segment.

$x = 1$, chain extender is 3,5-hexadiyne-1,6-diol, HDD.

$x = 4$, chain extender is 5,7-dodecadiyne-1,12-diol, DDI

Table 1. TGA analysis of polyurethane samples.

Sample	Soft Segment	Hard Segment ^b	% Hard Segment	M _n (g/mol)	T5% weight loss, °C
PU-1	polybutadiene	MDI + HDD	30	30,000	311
PU-2	polyisoprene	HDI + DDD	26	23,800	268
PU-3	PTMG ^a	HDI + DDD	25	27,500	312
PU-4	PTMG ^a	HDI + DDD	25	84,600	313

^a poly(tetramethylene glycol)

^b MDI = 4,4'-methylenebis(phenylisocyanate); HDI = 1,6-diisocyanatohexane; HDD = 2,4-hexadiyne-1,6-diol; DDD = 5,7-dodecadiyne-1,12-diol.

By investigating various reaction conditions and by careful control of the stoichiometry, it was possible to prepare a series of higher molecular weight, segmented polyurethanes with different soft segment compositions (see Table 2). These polymers were prepared in large quantities so that comparative tensile properties could be measured. All of these samples exhibited photochromic, thermochromic and mechanochromic properties. The characterization data for these samples are listed in Table 2. The thermal and mechanical properties are listed in Table 3. The thermochromic and mechanochromic properties of the samples are listed in Table 4; all samples in Table 4 were irradiated with UV light for 1 minute. UV irradiation effected crosslinking of the diacetylene units (see Scheme 5). Samples of all segmented polyurethanes were submitted to Professor El-Sharif at Drexel for evaluation as smart material coatings in optical fiber detection systems.

Table 2. Characterization of high molecular weight polyurethane samples.

Sample	Soft Segment	Hard Segment ^b	% Hard Segment	M _n polymeric diol (g/mol)	M _w polyurethane (g/mol)
PU-HPI	hydrogenated polyisoprene	HDI + DDD	25	2200	64,000
PU-PI	polyisoprene	HDI + DDD	25	1400	73,000
PU-PTMG	PTMG ^a	HDI + DDD	25	2000	107,000

^a poly(tetramethylene glycol)^b HDI = 1,6-diisocyanatohexane; DDD = 5,7-dodecadiyne-1,12-diol.**Table 3.** Thermal and mechanical characterization of the high molecular weight, diacetylene-containing polyurethanes with different soft segments^a.

Sample	δ at break (MPa)	ε at break (%)	T 5% weight loss, °C
PU-HPI	11.58 (10.2)	615 (316)	295
PU-PI	18.9 (16.4)	624 (312)	286
PU-PTMG	20.8 (23.3)	795 (256)	282

^aThe first numbers refer the film properties before crosslinking. The numbers in parentheses are for samples after irradiation with UV light for 1 minute to effect crosslinking of the diacetylene units.**Table 4.** Thermochromic and mechanochromic properties of high molecular weight, diacetylene-containing polyurethane samples^a.

Sample	Thermochromic behavior	Mechanochromic behavior
PU-HPI	below 105 °C: reversible thermochromic behavior 65-105 °C : blue to pink to red > 105 °C : red to yellow	Exhibits reversible mechanochromism. The color of the film changes from blue to pink to light yellow with increasing strain.
PU-PI	below 140 °C: reversible thermochromic behavior 85-140 °C : blue to red > 140 °C : red to yellow	Exhibits reversible mechanochromism. The color of the film changes from blue to pink to light yellow with increasing strain.

PU-	below 135 °C: reversible thermochromic	Exhibits reversible mechanochromism. The
PTMG	behavior	color of the film changes from blue to light
	104-130 °C : blue to red	yellow after 200 % strain level.
	130-135 °C : red to yellow	

^aAll samples were irradiated with UV light for 1 minute to effect crosslinking of the diacetylene units.

These results were encouraging with respect to the goal of synthesizing thermo-oxidatively stable polyurethanes which exhibit good mechanical properties and are also photo-, mechano-, and thermochromic. It also suggests that these new elastomeric diols will be useful for toughening thermosets such as epoxies.

Several other approaches have been investigated to prepare environmentally responsive polymers, especially polymers which can change color at lower temperatures. Thus, a polyester was prepared from dodecanedioyl dichloride and 1,4-hexadiyne-1,6-diol. The resulting polymer exhibited photochromic behavior. In another effort to prepare polyurethanes which exhibit thermochromic behavior at lower temperatures, the chain extension of poly(tetramethylene glycol) with hexamethylenediisocyanate and 5,7-dodecadiyne was carried out in the presence of dibenzo-30-crown-10. Samples were prepared in THF and in toluene. Both polymers exhibited photochromic sensitivity and were thermochromic at a relatively low temperature (68°C) compared to the other polyurethanes investigated.

References for Project 4.).

1. "Recent Advances in Anionic Synthesis of Functionalized Elastomers Using Functionalized Alkylolithium Initiators", R. P. Quirk, S. Jang and J. Kim, *Rubber Reviews, Rubber Chemistry and Technology*, **69**, 444-461(1996).
2. "Anionic Synthesis of Hydroxyl-functionalized Polymers Using Protected, Functionalized Alkylolithium and Isoprenyllithium Initiators", Roderic P. Quirk, Sung H. Jang, Kwansoo Han, Huimin Yang, Brad Rix and Youngjoon Lee in *Functional Polymers; Modern Synthetic Methods and Novel Structures*, A. Patil, D. N. Schulz and B. Novak Eds., ACS Symposium Series no. 704, American Chemical Society, Washington, D. C., 1998, pp 71-84.
3. "Polymer Synthesis Using Functionalized Alkylolithium Initiators. Telechelic, Heterotelechelic and Functional Star-Branched Polymers", Roderic P. Quirk, Sung H. Jang, Huimin Yang and Youngjoon Lee, *Macromol. Symp* **132**, 281-291(1998).
4. "Anionic Synthesis of Hydroxyl-Functionalized Polymers Using Functionalized Initiators and Electrophilic Termination Reactions", R. P. Quirk, J.-J. Ma, G. Lizarraga, Q. Ge, H. Hasegawa, Y. K. Kim, S. H. Jang and Y. Lee, *Macromol. Symp.* **161**, 37-44(2000).

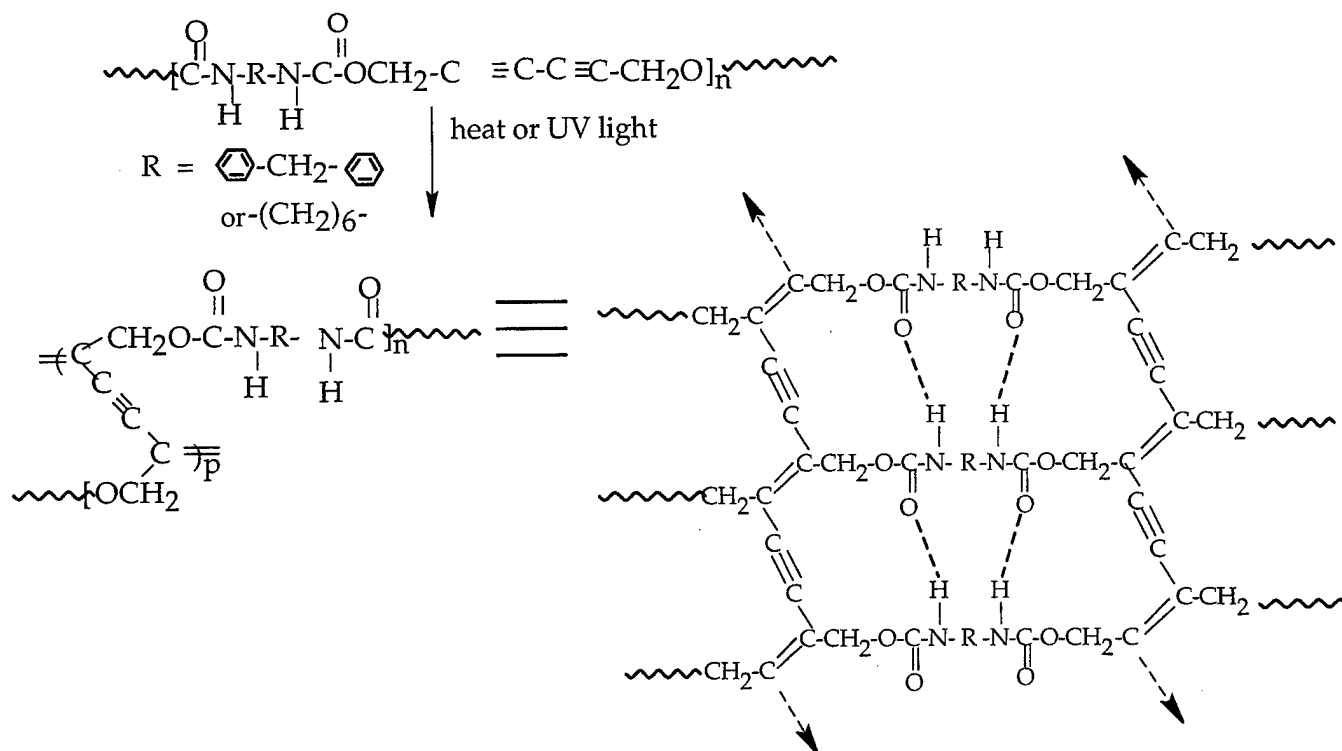
Project 5.). Grafting Photoluminescent and Electroluminescent Poly(1,4-phenylenes) to Surfaces for Use as Smart Materials for Soldier's Apparel.

One of the applications of surface-bound 1,1-diphenylethylene monolayers was the preparation of functionalized surfaces that can be used as chemical sensors. One type of sensor is a conducting polymer that can undergo detectable changes upon interaction with various types of chemicals. The goal was to generate polyphenylene brushes on silica surfaces indirectly using the "grafting from" approach. Toward this end, an investigation of the anionic polymerization of 1,3-cyclohexadiene was undertaken. Although the polymerization of 1,3-cyclohexadiene can be carried out using radical, cation, anion, Ziegler-type and transition metal type catalysts²²⁻²⁵, the best results with respect to conversion rate and molecular weight were obtained by anionic polymerization using organolithium compounds as initiators¹.

Aromatization of poly (1,3-cyclohexadiene) (PCHD) with 1,4-microstructure affords poly(*para*-phenylene (PPP). PPP has relatively low density, high mechanical strength, excellent thermal stability and

Scheme 5.

Step III. formation of conjugated poly(diacetylene) chain within the hard segment of polyurethane by solid-state, cross-polymerization of the diacetylene group.



remarkable chemical resistance which make it ideally suitable for use as a light weight high-performance engineering material. PPP possesses conductivity after doping and useful optical properties such as electroluminescence and photoluminescence which can be used in the light-emitting devices. Substituted PPP also gives liquid crystalline properties because of its rod-like structure³⁻⁷.

The first goal was to determine optimum conditions to obtain poly(1,3-cyclohexadiene) with the highest 1,4-microstructure. Solvent medium and polymerization mechanism strongly influence the microstructure of the polymers. Organolithium-initiated polymerization of 1,3-cyclohexadiene gives different microstructures depending on the polarity of solvent. In hydrocarbon solvent, 1,4-addition was predominant and in polar solvent such as THF, a mixture of 1,2 and 1,4 addition was obtained. In addition, cis or trans configurations with respect to the plane of the rings are expected². Francois et al prepared PS-PCHD and PMMA-PCHD block copolymers in cyclohexane using *sec*-butyllithium as initiator, converted them to PS-PPP and PMMA-PPP respectively and studied their interesting properties such as conductivity, photoluminescence and self-assemble morphology.⁸⁻¹⁴ The diblock copolymers, PS-PCHD and PMMA-PCHD, that they prepared had predominantly 1,4-microstructure. Natori et al studied the living properties of the polymerization of 1,3-cyclohexadiene in cyclohexane in the presence of TMEDA using *n*-butyllithium as initiator.¹⁵⁻¹⁶ Long et al synthesized the star PCHD using the method developed by Natori.¹⁷⁻¹⁸ The polymers that they obtained were a mixture of 1,2 and 1,4 microstructure. Mays et al prepared PCHD in benzene in the presence of DABCO using *sec*-butyllithium as initiator. They obtained a controlled polymerization and the microstructure was predominantly 1,4.¹⁹⁻²¹ Based on this background, the polymerization of 1,3-CHD was carried out in cyclohexane initiated by *sec*-butyllithium. After a few hours of reaction time, the solution started to become cloudy and some of the polymer precipitated out from the solution. After termination with methanol, a little more was precipitated out. The

precipitate was filtered and the solution was poured into methanol with BHT. So, two products were obtained, one was insoluble in the reaction solution and the other one was soluble in the reaction solution. About 10% of the insoluble polymer can be obtained. Three different calculated number molecular weight polymers, 3,000, 6,000 and 10,000 were investigated and they all gave both the soluble and insoluble products. These results are different from the organolithium initiated polymerization of 1,3-cyclohexadiene in the literature. To our knowledge, this phenomenon has not been reported previously in the literature. Two other polymerization conditions were carried out for comparison. One was using benzene as the solvent and the other is using cyclohexane as solvent but in the presence of DABCO. These two polymerizations gave totally soluble polymers.

High resolution 750 MHz ^1H NMR was used to determine to microstructure of the polymers obtained in benzene, in cyclohexane and DABCO, as well as the soluble and insoluble parts in cyclohexane. A representative spectrum for insoluble PCHD is showed in Figure 1. With respect to the determination of the amounts of 1,2 and 1,4-microstructure, there are two methods in the literature.²⁶ The first method (A) compared the olefinic integration with the allylic integration, and the second method (B) compared the allylic integration with the aliphatic integration. The amounts of cis and trans configurations were calculated by the ratio of the integration of the aliphatic peaks.² It was found that the insoluble polymer fraction had the highest 1,4-content (>99%) and the highest cis planomer content (76 %). It was concluded from the NMR studies that the PCHD obtained from the cyclohexane has higher stereoselectivity than those obtained in benzene or in cyclohexane with DABCO. It has higher amounts of both 1,4 content and cis configuration especially the insoluble polymer. The insoluble polymer from the solution is partially soluble in common organic solvents such as THF, toluene and soluble in CHCl_3 . It can be recrystallized from 1,2-dichloroethane. This polymer was characterized by X-ray powder diffraction, SEC, NMR and FT-IR

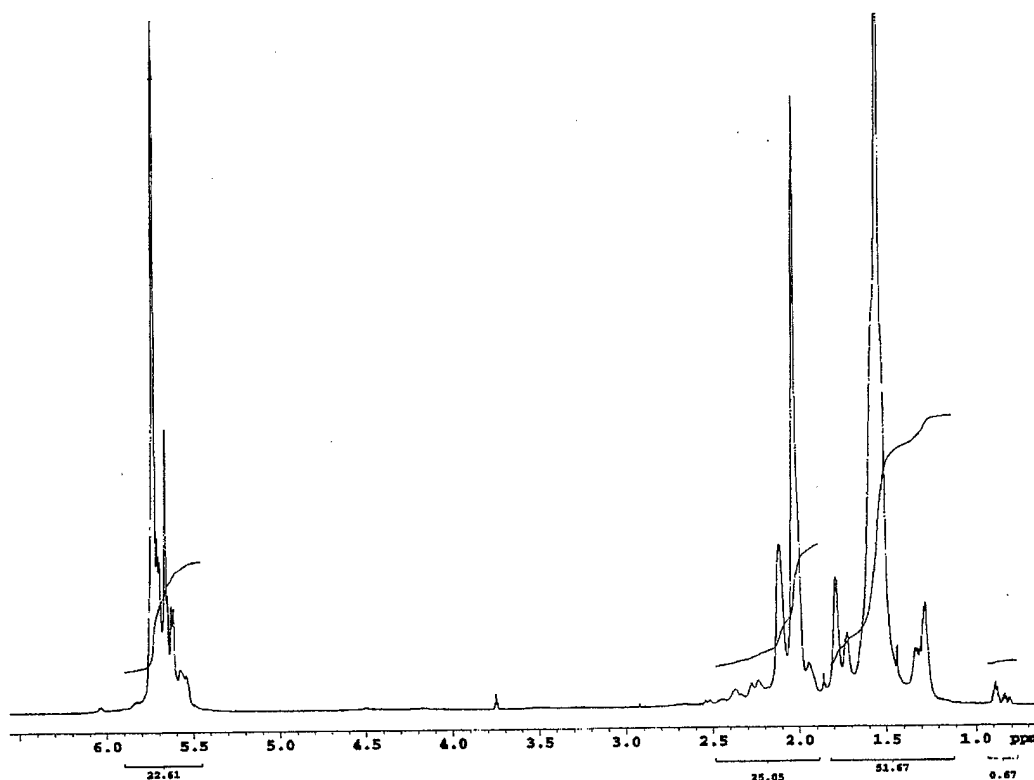


Figure 1 ^1H NMR Spectrum of Insoluble PCHD

The X-ray powder diffraction profile of the insoluble polymer with the calculated molecular weight of ~3000 showed three crystalline peaks, positioned at 2θ values of 16.95° , 19.7° and 22.35° which are very close the X-ray peaks obtained from the nickel catalyst polymerization. The X-ray powder diffraction profile of the insoluble polymer is shown in Figure 2. DCS analysis (Figure 3) showed an endothermic peak at 178°C in the second heating. It is concluded that although this polymer has a partially crystalline structure, the crystallinity is lower than the polymer obtained using the nickel catalyst²⁴. However the soluble polymer from cyclohexane has no crystalline character as deduced from DSC and X-ray analyses.

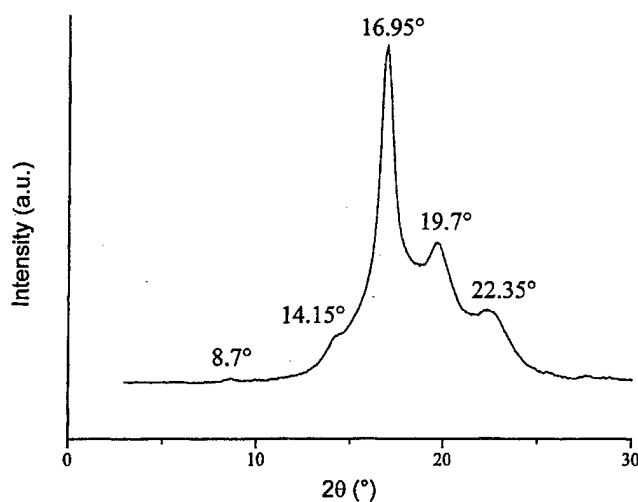


Figure 2. X-ray Powder Diffraction Profile of the Crystalline PCHD

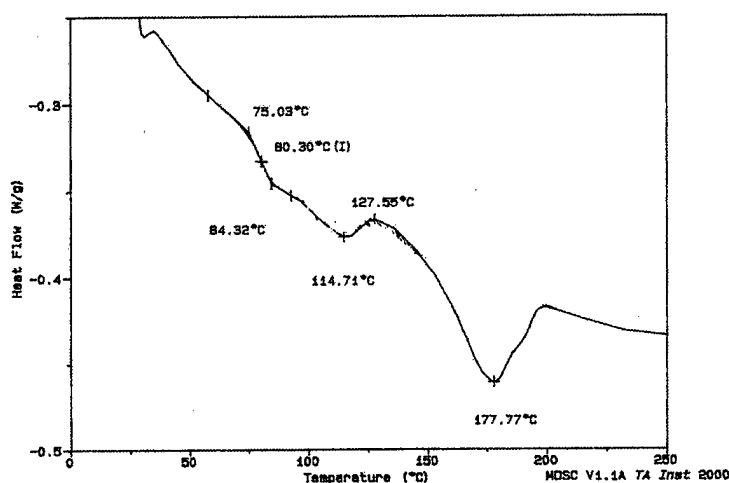


Figure 3. DCS for the Insoluble Polymer

The molecular weight of the polymer also plays a role with respect to crystalline character. Because of the chain transfer reaction of the polymerization, the obtained molecular weight is always lower than the calculated molecular weight. For example, with the calculated $M_n=3000$, molecular weight of about 2500 polymer was obtained, with the calculated $M_n=6000$, molecular weight of about 4500 polymer was obtained, and with the calculated $M_n=10000$, molecular weight of about 5500 polymer was obtained. Because of the limited solubility of the crystalline polymer in THF, the accurate determination of molecular weight was difficult to obtain. However, the crystalline polymer always had higher molecular

weight than the soluble polymer as deduced from the SEC chromatogram. The SEC spectrum for both the soluble and insoluble PCHD are showed in Figure 4. The curve on the left is for the crystalline PCHD. It was also concluded that the crystalline polymer had higher molecular weight than the soluble polymer as calculated from the ^1H NMR spectra of these polymers using the initiator residue as a quantitative marker.

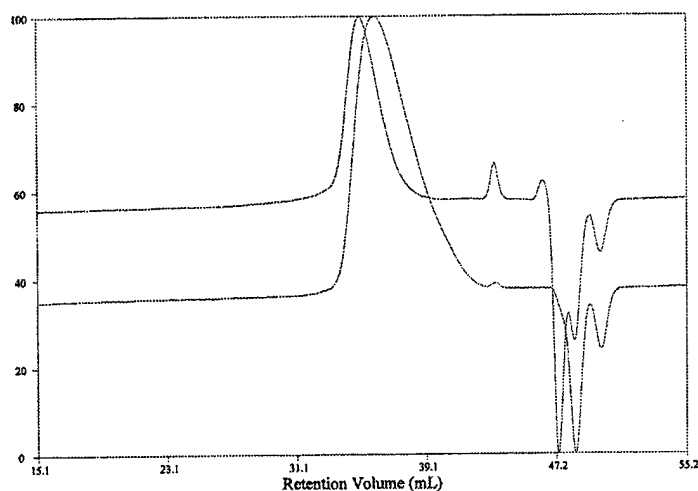


Figure 4 SEC Spectrum for Soluble and Insoluble PCHD

The insoluble polymers with a calculated number molecular weight of about 6,000 and 10,000 showed no crystalline peaks both in X-ray powder diffraction profile and DSC. This might be because the higher the molecular weight, the harder it is to crystallize.

The IR spectrum of the crystalline polymer is also different from the amorphous polymer. The spectrum of crystalline polymer showed strong sharp peaks at 907 and 733 cm^{-1} , but the amorphous polymer showed small peak at 909 and 728 cm^{-1} and it has an extra peak at 1066 cm^{-1} . The spectra are shown in Figures 5 and 6.

References for Project 6.).

1. Lefebvre, G.; Dawans, E.; *J. Polym. Sci.: Part A* **1964**, 2, 3277
2. Sharaby, Z.; Martan, M.; Jaseph-Grodzinski, J. *Macromolecules* **1982**, 15, 1167
3. Kovacic, P.; Jones, M. B. *Chem. Rev.* **1987**, 87, 357.
4. Schlüter A. D. In *Handbook of conducting polymers*; Skotheim, T. A.; Elsenbaumer R. L.; Reynolds J. R. Ed.; Marcel Dekker: New York, **1998**, Chapter 8.
5. Kraft, A.; Grimsdale, A. C.; Holmes, A. B. *Angew. Chem. Int. Ed. Eng.* **1998**, 37, 402.
6. McCarthy, T. F.; Witteler, H.; Pakula, T.; Wegner, G. *Macromolecules* **1995**, 28, 8350.
7. Kaeriyama, K.; Kouyama, S.; Sekita, M.; Nakayama, T.; Tsukahara, Y. *Macromol. Rapid Commun.* **1999**, 20, 50.
8. Zhong, X. F.; Francois, B. *Makromol. Chem., Rapid Commun.* **1988**, 8, 411
9. Zhong, X. F.; Francois, B. *Synth. Met.* **1989**, 29, E35.
10. Widawski, G.; Rawiso, M.; Francois, B. *Nature* **1994**, 369, 387.
11. Francois, B.; Pitois, O.; Francois J. *Adv. Mater.* **1995**, 7, 1041.
12. Romero, D. B. et al. *Solid State Commun.* **1995**, 95, 185.
13. Leclere, Ph.; Parente, V.; Bredas, J. L.; Francois, B.; Lazzaroni, R. *Chem. Mater.* **1998**, 10, 4010.
14. Mignard, E.; Tachon, C.; Francois, B. *Synth. Met.* **1999**, 102, 1246.

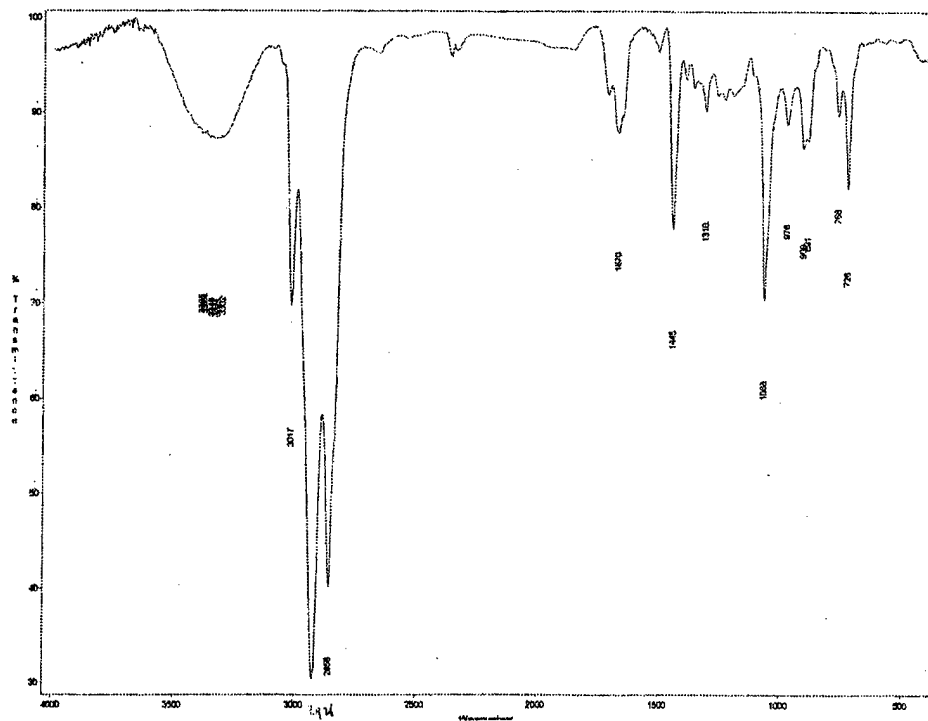


Figure 5. FT-IR Spectrum for amorphous fraction of PCHD.

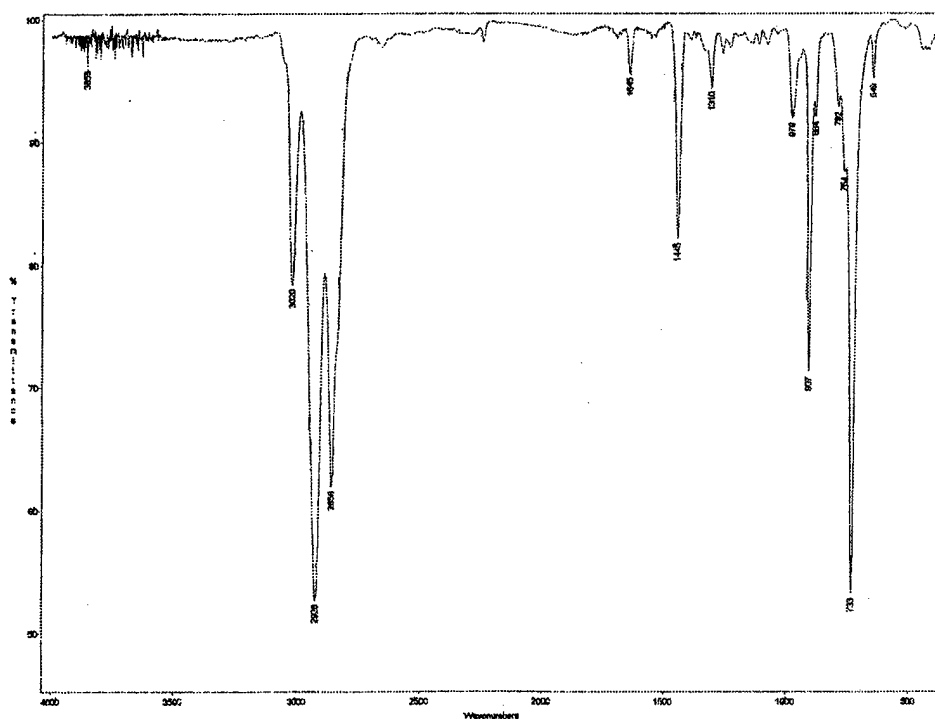


Figure 6. FT-IR Spectrum for crystalline fraction of PCHD.

15. Natori, I. *Macromolecules*, **1997**, *30*, 3696
16. Natori, I.; Inoue, S. *Macromolecules*, **1998**, *31*, 982.
17. Kara, S.; Pasquale, A. J.; Long, T. E. *Polym. Prepr. (Am. Chem. Soc. Div. Polym. Chem.)*. **2000**, *41*(1), 8
18. Williamson, D. T.; Brazhnik, K. P.; Elman, J. F.; Pasquale A. J.; Long, T. E. *Polym. Prepr. (Am. Chem. Soc. Div. Polym. Chem.)*. **2000**, *41*(2), 1544.
19. Hong, K.; Mays, J. W. *Macromolecules* **2001**, *34*, 782
20. Hong, K.; Wan, Y.; Mays, J. W. *Macromolecules* **2001**, *34*, 2482
21. Hong, K.; Mays, J. W. *Macromolecules* **2001**, *34*, 3540
22. Dolgoplosk, B. A.; Beilin, S. L.; Korshak, Y. V.; Chernenko, L. M.; Vardanyan, L. M.; Teterina, M. P. *Eur. Polym. J.* **1973**, *9*, 895
23. Po, R.; Santi, R.; Cardici, M. A. *J. Polym. Sci.: Part A: Polym. Chem.* **2000**, *38*, 3004
24. Lango, P.; Freda, C.; Ballesteros, O. R. D.; Grisi, F. *Macromol. Chem. Phys.* **2001**, *202*, 409
25. Tanimura, S.; Matsuoka, T.; Nakano, M.; Usuki, A. *J. Polym. Sci.; Part B: Polym. Phys.* **2001**, *39*, 973
26. Williamson, D. T.; Glass, T. E.; Long, T. E. *Macromolecules* **2001**, *34*, 6144

TECHNOLOGY TRANSFER

a.) Patent Applications and/or awards
There were no patent applications.

b.) Names and organization of individuals in government, academy, or industry to whom at least one year's report was sent and/or to whom this final report will be sent:

c.) Individuals with whom some aspect of the work was discussed over the course of the project. Individuals who have assisted with the work in some way as collaborators are marked as such.

Professor Mark Foster, University of Akron, collaborator

Professor Darrell Reneker, University of Akron, collaborator

Professor William Brittain, University of Akron, collaborator

Professor Mahmond El-Sherif, Drexel University, collaborator

Professor Lynn Penn, University of Kentucky.

Dr. Sergio Corona-Galvan, Dynasol Industries.

d.) Leveraging of Army funds

- Muri project has led to collaborative effort with Professor Lynn Penn in the Department of Materials Science and Engineering at the University of Kentucky. This has resulted in submission of an NSF proposal on tethering macromolecules to surfaces.

177 Anderson Hall

University of Kentucky

MURI/ARO FUNCTIONALLY TAILORED TEXTILES FINAL REPORT

1996 – 2001

Submitted January 15, 2002

Darrell H Reneker

The University of Akron

Textiles

1) Objectives

D. H. Reneker. 2001 MURI/ARO- FTT Final Report. dh@polymer.uakron.edu

A) Functionally Tailored Textiles

D. H. Reneker. 2001 MURI/ARO- FTT Final Report. dh@polymer.uakron.edu

Electrospinning technology is being developed to produce nanofibers of polymers that have potential uses in battle clothing. Samples are being prepared for laboratory scale testing of the properties of the resulting nanofibers.

B) Advanced Textile-Based Composite Materials

D. H. Reneker. 2001 MURI/ARO- FTT Final Report. dh@polymer.uakron.edu

Develop the science needed to produce nanofibers with remarkably high surface area per unit mass, for making composite textiles, protective clothing, and advanced fiber reinforced composites.

C) Bioengineered Polymers

D. H. Reneker. 2001 MURI/ARO- FTT Final Report. dh@polymer.uakron.edu

Develop the special scientific information needed for the production of nanofibers of biological polymers.

D) Textile Manufacturing

D. H. Reneker. 2001 MURI/ARO- FTT Final Report. dh@polymer.uakron.edu

Develop scientific basis of technology for handling nanofibers and for incorporation of nanofibers into textiles for protective clothing.

E) Fibers and Processing Protective Clothing

D. H. Reneker. 2001 MURI/ARO- FTT Final Report. dh@polymer.uakron.edu

Protection from chemical and biological warfare agents, at a useful level, can be provided by protective clothing. Fabrics with large surface area per unit mass can be designed to

absorb and hold or degrade these agents. Incorporation of nanofibers into protective clothing greatly increases the surface area of a garment, while at the same time creating pores that are small enough to prevent the passage of liquid droplets that do not wet the nanofiber. The pores are large enough to allow the passage of water vapor so that the protective garment is more comfortable than a material that is impervious to water vapor.

F) Textile Based Fabrics and Composites

D. H. Reneker. 2001 MURI/ARO- FTT Final Report. dh@polymer.uakron.edu

Incorporation of substances useful for detection of chemical and biological warfare agents into military clothing, using nanofibers.

This work is aimed at the incorporation, into clothing, of nanofibers made from polymers, which have promise as chemical sensors, or of nanofibers of other polymers that contain substances, which serve as sensors for particular chemicals. An array of nanofibers, with sensitivities to different chemical or bio warfare agents, could be added to a fabric.

G) Protective Clothing Fibers and Processing

D. H. Reneker. 2001 MURI/ARO- FTT Final Report. dh@polymer.uakron.edu

The objective of this work is to develop the technology of electrospinning of polymer nanofibers, to give designers options in the design and fabrication of battlefield clothing. The production of carbon nanofibers from polymer or pitch precursors is included.

2) Scientific Progress and Accomplishments

1996

A) Electrospinning

D. H. Reneker. 2001 MURI/ARO- FTT Final Report. dh@polymer.uakron.edu

Polymer fibers with diameters ranging downward from the five micron diameter of contemporary textile fibers to one hundredth of that diameter (.05 micron) can be produced by a process called electrospinning.

Electrospinning easily creates continuous polymer fibers with diameters in a range that is not readily available. Experimental quantities of thin fibers have been electrospun from many different polymers that are of potential use in this project.

In the electrospinning process, a high electrical potential applied to a liquid polymer melt or solution creates an electrical force, at the surface of the liquid, that is opposed by surface tension. This electrical force can be larger than the surface tension, making the shape of the surface unstable and causing a charged liquid jet to be ejected from the surface. The jet is solidified by solvent evaporation or cooling and collected as a fiber.

High extensional flow rates are present in the region where the jet leaves the liquid surface, and where the liquid is in the presence of a high electric field. After the jet leaves the surface, the stretching continues, as a result of the electrical charge on the surface of the jet.

The solidified fibers can be collected on a screen, a conducting surface, in a liquid, or on a winder. Many process parameters are experimentally accessible. By adjustment of experimentally accessible process parameters it is possible to make fibers that are coiled, folded, beaded, tapered, flattened, or otherwise variable along their length.

B) Creation of a multitude of jets

D. H. Reneker. 2001 MURI/ARO- FTT Final Report. dhrr@polymer.uakron.edu

There are many ways to create a large number of jets simultaneously. A separate pipette is not required for each jet. Many jets can be created from the open surface of a pool of liquid. We made a video record of multiple jets created from droplets of a viscous solution of polyethylene oxide. Over a dozen jets formed from droplets hanging from the rounded edge of a metal cylinder that was about 15 cm in diameter and had a thickness of about 2 mm. The electrical potential was applied to the entire cylinder. Each jet extended about 3 cm below the edge of the cylinder and then became fibers as they dried. The jets, which were separated by a few centimeters, repelled each other slightly, but the perturbations caused on one jet by its neighbor were small.

The video showed the easy creation of more than ten separate, well-behaved jets in one experimental setup, using only one high voltage power source. It appears that many more jets could be created simultaneously.

C) Observation of interference colors

D. H. Reneker. 2001 MURI/ARO- FTT Final Report. dhrr@polymer.uakron.edu

It is possible to create a jet which has a diameter of a few microns which elongates into diameters in the range of the wavelength of light, that is from around 600 nm to around 300 nm. With proper illumination of the jets it is possible to observe and photograph interference colors, which are similar to those observed in a bubble. We successfully videotaped a number of such jets. No color is seen from the region where the jets are smaller than the wavelength of light. The slightly larger jets are yellow, and the even larger jets there is a complicated succession of pastel orange, green, pink and purple colors. These colors help us to understand the stretching and drying processes that are involved in the creation of nanofibers by electrospinning.

D) Electrical measurements on the jets and spinning solutions

D. H. Reneker. 2001 MURI/ARO- FTT Final Report. dhrr@polymer.uakron.edu

The relationships between the potential of the jet and the current carried by the jet were measured. The current increases with voltage at a faster than linear rate. Mass flow rate, and charge density on the jet are being measured. The dielectric constant, dielectric loss factor, viscosity and other properties are being measured, since these parameters are needed in the development of physical and mathematical models of the electrospinning process.

E) Characteristics of nanofiber

D. H. Reneker. 2001 MURI/ARO- FTT Final Report. dhrr@polymer.uakron.edu

1. Electrospun nanofibers are:

D. H. Reneker. 2001 MURI/ARO- FTT Final Report. dh@polymer.uakron.edu

- A. very small in diameter, from one-half to one-hundredth the diameter of ordinary textile fibers.
- B. characterized by a very high surface area to volume ratio.
- C. electrically charged so they can be moved with electric fields.
- D. easy to spin from many kinds of polymer solutions or melts.
- E. readily form non-woven fabrics, yarns, and other aggregates.
- F. absorb as much as 40 times their weight of liquids.
- G. capable of floating in air for long times.
- H. PAN fibers, and mesophase pitch nanofibers, can be electrospun and carbonized.

2. The electrospinning process:

D. H. Reneker. 2001 MURI/ARO- FTT Final Report. dh@polymer.uakron.edu

- A. simple apparatus is used.
- B. electrospinning apparatus is portable so that fibers can be spun in the field or wherever they are needed.

E) Potential applications of electrospun nanofibers in battle clothing

D. H. Reneker. 2001 MURI/ARO- FTT Final Report. dh@polymer.uakron.edu

1. Camouflage and concealment

D. H. Reneker. 2001 MURI/ARO- FTT Final Report. dh@polymer.uakron.edu

Thin sheets scatter light very effectively. As drapes, thin sheets equilibrate quickly with the temperature of the air and screen the thermal signature of objects that are not at air temperature.

2. Friend or foe recognition

D. H. Reneker. 2001 MURI/ARO- FTT Final Report. dh@polymer.uakron.edu

Electrospun fibers bearing recognition materials can be applied over uniforms and used for identification.

3. Global positioning

D. H. Reneker. 2001 MURI/ARO- FTT Final Report. dh@polymer.uakron.edu

Fabrics of specialized design can be functional and comfortable in different environments, including hot, cold, wet, or dry.

4. Soldier comfort

D. H. Reneker. 2001 MURI/ARO- FTT Final Report. dh@polymer.uakron.edu

Fabrics containing nanofibers can be made to have very small pores, and to absorb or not absorb moisture.

5. Chemical/biological protection

D. H. Reneker. 2001 MURI/ARO- FTT Final Report. dh@polymer.uakron.edu

Nanofiber fabrics are materials with nanometer pores. These can, perhaps, be made small enough to stop some important biological warfare agents without adding much weight to the fabric, and still allowing small molecules such as air and water to pass through.

As a support, with unusually large surface area per unit mass, for chemicals that inactivate chemical/biological warfare agents.

6. Thermal protection

D. H. Reneker. 2001 MURI/ARO- FTT Final Report. dh@polymer.uakron.edu

Scatter thermal radiation. Produce a durable char upon exposure to high intensity thermal radiation.

7. Medical/Environmental protection

D. H. Reneker. 2001 MURI/ARO- FTT Final Report. dh@polymer.uakron.edu

Wound dressings to separate cells and molecules used by or secreted by the cells.

8. Body armor

D. H. Reneker. 2001 MURI/ARO- FTT Final Report. dh@polymer.uakron.edu

As a component of fibrous systems for stopping projectiles.

9. Eye protection

D. H. Reneker. 2001 MURI/ARO- FTT Final Report. dh@polymer.uakron.edu

Nanofibers, bearing photochromic functional groups, and imbedded in an index matching substance could scatter light very effectively when their color changed.

10. Electrospinning process parameters

D. H. Reneker. 2001 MURI/ARO- FTT Final Report. dh@polymer.uakron.edu

11. Nylon copolymers from formic acid solutions

D. H. Reneker. 2001 MURI/ARO- FTT Final Report. dh@polymer.uakron.edu

Measurements of process parameters, including the electrical current carried by the jet, and the mass flow rate, and the charge transported per unit mass of the solution were measured as a function of the distance between the tip and the collection screen for solutions of nylon 6 and a copolymer of nylon 6 and a polyimide. Measurements were made for two solutions, one with a viscosity around 100 centipoise and the other with a viscosity of around 1500 centipoise.

This experiment observes effects that occur as the electric field is varied in the flight region where the jet dries, and is stretched by the electric field during its flight toward the screen. Experiments in which the potential of the tip is varied are more sensitive to the processes that occur very close to the tip, such as acceleration, high extensional velocities, and the creation of multiple jets.

For short distances between the jet and the screen, a wet jet with a large diameter reached the screen. For longer distances, the jet became thinner, by stretching. The mass transfer rate decreased, and the charge transported per unit mass of solution also decreased at long distances.

12. Carbonized nanofibers

D. H. Reneker. 2001 MURI/ARO- FTT Final Report. dhrr@polymer.uakron.edu

Nanofibers of mesophase pitch were successfully electrospun from the melt. Fiber diameters ranged from around 5 microns to about 0.5 micron. The fibers were birefringent when drawn and the alignment persisted through the carbonization treatment. The fibers were stabilized by heating to around 230 °C in air and then carbonized at 1000 °C in nitrogen gas. Electron diffraction patterns, obtained from the thinnest fibers, showed that the graphitic planes were parallel to the axis of the fiber. Electrospun polyacrylonitrile nanofibers were also carbonized. The electron diffraction patterns from these fibers did not show much orientation of the graphite.

This work demonstrates that electrospinning is a new route to the production of oriented carbon fibers, which have small diameters, large surface area per unit mass, and are expected to have high thermal conductivity along the fiber.

The carbonized fibers provide new options in thermal management problems, particularly those with an inherently small scale, such as are encountered in electronics packaging. The thermal conductivity of carbonized fibers is larger than that of aluminum (273 w/[m K], at 300 °K).

The carbonized nanofibers are electrically conducting, flexible, and are expected to have a high capacity for absorption of molecules. Incorporation of a small quantity of carbonized nanofibers into a textile may provide a significant increase in the ability of the textile to absorb organic molecules from air or from liquids. The availability of carbonized nanofibers could lead to designs for gas masks that combine the functions of the canister and mask in one fabric-like structure.

Carbonized nanofibers with high strength and high stiffness are expected to be useful in composites because nanofibers can fit between, and reinforce, the matrix between ordinary 7 to 20 micron reinforcing fibers, particularly at critical locations where delamination or other kinds of cracking would otherwise occur.

We are scaling up our capability to produce carbonized nanofibers from mesophase pitch. Larger quantities are needed for measurement of the mechanical, thermal, and absorptive properties of the fibers so that their unique properties can be incorporated into new designs for battle clothing.

13. Nanofibers from biopolymers

D. H. Reneker. 2001 MURI/ARO- FTT Final Report. dhrr@polymer.uakron.edu

14. Natural silk and spider silk

D. H. Reneker. 2001 MURI/ARO- FTT Final Report. dh@polymer.uakron.edu

This section describes work performed at the University of Akron during visits by Dr. Heidi Schreuder-Gibson, who has since established an electrospinning laboratory at the Army Natick Laboratory.

Wet fibers of reconstituted silk were formed by electrospinning and collected onto glass microscope slides. The fibers tend to relax into droplets faster than the solvent, a mixture of water, alcohol and salts, such as calcium nitrate or lithium chloride, dries in air. Other solvents that evaporate faster, or other methods for removing the solvent, such as electrospinning the fiber into a non-solvent liquid that dilutes the solvent and precipitates the fiber rapidly may provide a route to reconstituted silk fibers.

Chitosan, in a 5% solution in water and acetic acid behaved in a similar way. Jets formed, but collapsed into droplets before the solvent evaporated. The chitosan is available in larger quantities, so it will be used to develop electrospinning procedures that are likely to be applicable to silk.

Fibers were spun from redissolved spider dragline silk, but the fibers were very weak, perhaps as a result of molecular weight degradation during the redissolving process. Attempts to spin spider silk dissolved in formic acid were unsuccessful because the silk formed a gel at room temperature instead of a normal solution. Perhaps heating the gel would convert it to a spinnable solution, but the limited amount of material available did not allow us to test this hypothesis.

A second attempt to spin cloned silk from Natick showed that although liquid jets could be formed, the silk molecules relaxed before they could be immobilized in a fiber. Fiber formation would be enhanced by obtaining a higher molecular weight polymer, increasing the concentration, and by using a more volatile solvent that would allow drying to occur faster than relaxation of the orientation of the molecules in a liquid jet.

Spider silk, resolubilized in a mixture of alcohol and a calcium salt, was successfully electrospun into short beaded fibers. The conditions for steady electrospinning were not found in the initial attempts, so that the spinning had to be started repeatedly by mechanically pulling a bit of material from the electrified tip. This produced a short length of fiber and then the process stopped.

Spider silk resolubilized in a mixture of alcohol and calcium nitrate, formed liquid jets in the electrospinning apparatus. The jets could be collected on a microscope slide, but the liquid jet dried slowly into relatively large diameter (several microns) fibers, which were not birefringent.

Heidi Schreuder Gibson sent us a sample of chitosan, which was studied at Natick in the 1980's. Chitosan is a naturally occurring biopolymer, and can be blended with

collagen or nylon 4. Chitosan with complexed copper reacted with chemical warfare agents when an 80% relative humidity was maintained. Chitosan, in a 5% solution in water and acetic acid behaved in a way similar to the resolubilized silk samples. Jets formed, but collapsed into droplets before the solvent evaporated. The chitosan is available in larger quantities, so it can be used to develop electrospinning procedures that are likely to also be applicable to silk.

15. Polylactide nanofibers

D. H. Reneker. 2001 MURI/ARO- FTT Final Report. dh@polymer.uakron.edu

A few nanofibers were electrospun from a sample of polylactide, supplied by Frank Ko of Drexel University, to demonstrate the feasibility of the process. Polylactides are used as biomaterials, such as sutures, that can be absorbed by the body as a wound heals. This work shows that electrospinning can be used to produce a non-woven fabric or yarn of polylactide fibers with diameters chosen to optimize the rate of bioabsorption.

16. Poly(benzimidazole) Nanofibers

D. H. Reneker. 2001 MURI/ARO- FTT Final Report. dh@polymer.uakron.edu

Poly(benzimidazole) nanofibers were electrospun from solution in dimethylacetamide (DMAc) and collected in the form of non-woven sheets. The sheets were washed to remove the solvent and treated in sulfuric acid to improve their strength. The sheets had a mass per unit area of around 0.1 mg/cm², and were strong. The nanofibers were also spun, by hand, into yarn.

Poly(benzimidazole) fibers were developed by Hoechst-Celanese for possible application as tire cord and other specialty fiber applications. Of particular relevance to this ARO-Functionally Tailored Textile (FTT) project is a report that regular textile fibers of PBI were investigated as a support for a copper catalyst to detoxify nerve gas, by researchers at the Natick laboratory.

Other uses considered for poly(benzimidazole) fibers are: Catalyst support that is stable in phosphoric acid; Filtration; Filament wound composites; Lacing for bundles of reinforcing fibers; Rigid objects made by hot pressing fiber sheets. Electrical conducting fibers can be made by impregnating the PBI fibers with copper.

A video of the experimental electrospinning for polybenzimidazole shows the presence of a relatively large corona discharge region and a relatively short jet length between the tip of the capillary bending region.

17. Molecular absorption onto nanofibers

D. H. Reneker. 2001 MURI/ARO- FTT Final Report. dh@polymer.uakron.edu

It is clear that electrospinning technology provides textile designers with a useful parameter, the diameter of the fiber, that has a large effect on the transport of air, water, and other molecules through a non-woven fabric made from nanofibers.

Samples of fabric made from nanofibers of polybenzimidazole and of polyacrylonitrile were tested, by Phil Gibson at the Army Natick Laboratory, for airflow resistance (air permeability) and for water vapor diffusion properties. The non-woven fabrics tested were from 50 to 100 microns thick, and made of many layers of 300 nm diameter fibers in a random pattern.

The high specific surface area of nanofibers makes it possible for a designer to incorporate several kinds of nanofibers, each of which absorbs a particular chemical warfare agent, into a fabric whose textile properties are not much different than those of the fabrics now used. This forms the basis for a uniform that protects against multiple threats.

The electrospun materials behave much like a microporous membrane, which has a high resistance to convective flow (low air permeability) and very low resistance to the diffusion of water vapor. Microporous membranes are films, of fluorocarbon or of other polymers, supported on a conventional fabric. Polytetrafluoroethylene microporous membrane wind barrier has a Darcy Flow Resistance value of 2×10^9 .

18. Air flow resistance

D. H. Reneker. 2001 MURI/ARO- FTT Final Report. dh@polymer.uakron.edu

The nanofiber fabrics have high resistance to convective flow (low air permeability), and have very low resistance to the diffusion of water vapor. The polybenzimidazole had a Darcy Flow Resistance (resistance to air flow) of $1.8 \times 10^9 \text{ m}^{-1}$. The polyacrylonitrile had a Darcy Flow Resistance of $2.2 \times 10^8 \text{ m}^{-1}$.

19. Water vapor diffusion

D. H. Reneker. 2001 MURI/ARO- FTT Final Report. dh@polymer.uakron.edu

The water vapor resistance of the polyacrylonitrile fabric was 40 s/m and of the polybenzimidazole was 10 s/m. The water vapor resistance increased very slightly as the humidity increased to a relative humidity of 0.8.

1997

A) Advanced Textile-Based Composite Materials

D. H. Reneker. 2001 MURI/ARO- FTT Final Report. dh@polymer.uakron.edu

A cooperative research program was established at the Army Research Laboratory, Aberdeen to characterize carbonized nanofibers made from mesophase pitch and from polyacrylonitrile. Environmental scanning electron microscopy, x-ray diffraction, optical tunneling microscopy, and neutron scattering are examples of characterization methods that may be used. Electron diffraction patterns from carbonized mesophase pitch nanofibers show that the graphitic planes extend along the axis of the fiber, and that the degree of

perfection and alignment is commensurate with that produced when mesophase pitch is spun into larger fibers using conventional spinning methods and then carbonized. At the invitation of Dr. Nora Beck Tan, Dr. Reneker visited and gave a talk in November. He helped them establish an electrospinning facility in their laboratory. Dr. Beck Tan and Dr. Joe Dietzel also visited the electrospinning laboratory at the University of Akron.

A high productivity process for spinning Mitsubishi AR mesophase pitch into nanofibers was developed. Batches of more than one gram of fibers with diameters ranging from 300 to 1000 nanometers are currently being produced.

Samples of carbonized nanofibers were supplied to the Edgewood Research, Development, and Engineering Center for evaluation for use in aerosol filtration, and for use as airborne obscurants.

Sheets of non-woven polyacrylonitrile fibers about 1 meter long and 0.2 meters wide were made. Some of the sheets were carbonized at 800 C. Sheets of the same size were made from polyester nanofibers. Sheets of polybenzimidazole, with a mass per unit area in the range from 15 to 50 grams per square meter were made from electrospun nanofibers with an average diameter of around 300 nanometers. Some of these sheets were supplied to Pall Corporation for testing as filters. The polybenzimidazole sheets were also used to increase the modulus and toughness of epoxy based composites, and to produce dramatic increases in the modulus of natural rubber and SBR rubber.

In a cooperative project with the University of Nebraska, which is partly supported by the National Science Foundation, thin sheets of these polybenzimidazole nanofibers were used to demonstrate a new concept for the reinforcement of interfaces between plies of a graphite/epoxy laminate. Substantial improvements in the resistance to the growth of interply cracks were obtained with the addition of only 2.5% of the nanofibers.

In another part of the University of Nebraska collaboration, we developed a mathematical model of the electrospinning process and obtained data needed to validate the model. Parameters measured include jet diameter, mass flow rate, fiber diameter, voltage, current, concentration, polymer molecular weight, and shape of the liquid surface from which the jet emerges. It is expected that this work will produce information that will lead to better understanding and control of the factors that influence the electrically driven bending instability of the jet.

We have obtained samples of mesophase pitch that was extracted, using a critical point solution method that was developed at Clemson University, in Professor Mark Thiess' laboratory. We are evaluating the spinnability of these samples. Initial efforts produced nanofibers, but processing parameters need to be optimized to increase the yield.

Samples of polyacrylonitrile nanofibers in nonwoven sheets were given to Dr. Mark Purdy of the BF Goodrich Corporation. He is interested in making carbon-carbon composites with carbon nanofibers.

Professor Reneker visited Dr. Heidi Schreuder-Gibson at the Army Natick Laboratory and gave a talk on nanofibers. She visited the University of Akron, and received samples of nonwoven nanofiber fabric for permeation testing at Natick. Strategies based on copolymers, for creating nanofibers with a high affinity for chemical warfare agents were discussed. He also visited Phil Gibson, who made measurements of the permeation of water and air through non-woven sheets of nanofibers during the first year of this project. He had discussions about electrospinning and possible applications of electrospun nanofibers with laboratory managers and other staff.

B) Bioengineered Polymers

D. H. Reneker. 2001 MURI/ARO- FTT Final Report. dh@polymer.uakron.edu

Electrospinning methods for making nanofibers from natural silk were discovered. The silk nanofibers are needed as samples that can be examined by transmission electron microscopy.

Nanofibers of DNA with diameters less than 100 nanometers were produced by electrospinning from a solution of DNA in a mixture of alcohol and water. Transmission electron micrographs of the DNA fibers were obtained and published.

C) Textile Manufacturing

D. H. Reneker. 2001 MURI/ARO- FTT Final Report. dh@polymer.uakron.edu

Ways to incorporate nanofibers into cloth made primarily from ordinary textile fibers were described. If about 10% of the mass of a textile yarn is converted into nanofibers and then incorporated into a fabric along with the remaining 90% of the textile fibers, the geometrical surface area of the resulting fabric can be increased about fourfold.

Nanofibers of polybenzimidazole were electrospun directly onto a conventional polyester sewing thread. The thread was pulled through the bending, looping and spiraling fibers without being twisted. Layers thick enough to prevent the color of the thread from showing were easy to obtain. The nanofibers resisted removal by rubbing, but were not tightly attached to the thread. Samples of the nanofiber-coated thread were supplied to Professor Frank Ko at Drexel University for possible use in weaving a small piece of fabric.

1998

A) Advanced Polymers and Fibers

D. H. Reneker. 2001 MURI/ARO- FTT Final Report. dh@polymer.uakron.edu

Cyclic oligomers of polycarbonate have been tested (collaboration with John Song, Natick Lab) as adhesives between ceramics and Kevlar composites. Although the cyclic oligomers wetted the pieces better, brittle failure was still observed. Currently, the cyclic oligomers are being tested for thermoplastic composites in antiballistic applications.

We have successfully performed a synthesis of poly(dichlorophosphazene) by a ring-opening polymerization of the cyclic trimer using a catalyst complex composed of boron

trichloride and triphenylphosphonate. The polymer was functionalized with 4-hydroxyanisole followed by deprotection to the phenol-functionalized polymer. We plan to send this polymer to the American Research Corporation for testing as an absorbent film in a nerve agent sensor. We are currently exploring the synthesis of water-soluble polyphosphazenes, which might be suitable for fiber treatment to impart both absorbent and fire-resistant characteristics.

Samples of carbonized mesophase pitch fibers, which had been treated in an inert atmosphere at 800 °C were delivered to Dave Tevault for measurements relative to its use in treatment of air used to ventilate the inside of tanks or ships. Joe Rehrmann, (410-671-5780) has begun surface area measurements based on the adsorption of a gas. A sample of these fibers was also given to Jeff Hale for evaluation as airborne obscurants.

A paper entitled "Carbon nanofibers from polyacrylonitrile and mesophase pitch" was prepared for presentation at a SAMPE meeting later this spring. This is a collaborative effort involving Nora Beck Tan and Joe Deitzel, at the U.S. Army Research Laboratory, Kristen Kearns at the Air Force Wright Laboratory, and Dr. Reneker's research group at the University of Akron.

A proposal for research that will lead toward the use of polymer and carbon nanofibers in a wide range of filter applications was prepared and submitted to the National Science Foundation.

The surface area per unit mass of a sample of graphitized nanofibers, made from mesophase pitch, was measured by Joe Rehrmann, ERDEC, Edgewood. He used the BET method, with nitrogen gas. The specific surface area was 3.3 square meters per gram. A parameter called "pore volume" was also determined from the data to have a value of 0.006 cc/gm, suggests a pore size of less than 2 nm. Rehrmann gave some typical values of specific surface area for materials that are of interest as air filters: Activated carbon, 1000; catalyst alumina, 100; carbon black, 80 to 100; and glass, less than 10. All these numbers are in units of square meters per gram. The value of 3.3 is commensurate with the geometrical specific surface area of fibers with a diameter of around 500 nanometers. The sample used in this measurement had a mass of 200 milligrams.

We have fabricated thin films containing phenol-functionalized polyphosphazene plus fluorophore on optical substrates. We will submit these novel polymer films for testing in nerve agent sensors.

B) Smart Materials

D. H. Reneker. 2001 MURI/ARO- FTT Final Report. dh@polymer.uakron.edu

Study of the poly(ferrocenylsilane) block copolymers has continued in order to establish more detail of the ordered structure and to investigate how the ordered structure may be optimized for using this material in smart applications. On one front, more information was gathered on the polymers bulk thermal behavior, particularly when cast as a film. A

film cast from THF is found to have a broad melting peak at about 111°C, indicating that some crystallinity forms during the process of casting, though the ordering by microphase separation during casting is poor. Annealing at 115°C perfects the crystals considerably, raising the melting temperature to 128°C. Samples annealed above 140°C and then quenched show no evidence of crystallinity, but have better microphase segregation.

The poly(ferrocenylsilane) block copolymers have also been studied in spun cast thin films (ca. 660, 790, and 1250 Å thick) and films made by simply casting a single drop of solution on a carbon film. Characterization has been done with X-ray reflectometry, TEM, electron diffraction, and scanning probe microscopy. For as-cast samples and samples annealed below 140°C no ordered domain structure can be seen with XR in spun cast films, indicating that the domains are not parallel to the surface. This is consistent with TEM from the single drop cast films, which show microphase separation with the domains standing "edge on" to the surface of the film. However, electron diffraction from crystals may be obtained from the single drop films, and this pattern improves with annealing at 115°C. Annealing above 140°C for one hour leads to considerable roughening of the spun cast film surface.

The thermochromic and mechanochromic properties of high molecular weight, diacetylene-containing polyurethane samples have been characterized. All of these segmented polyurethanes undergo rapid photochromism upon UV irradiation. The polyurethane with the hydrogenated polyisoprene soft segment undergoes reversible thermochromic changes from blue to pink to red in the temperature range of 65-105°C. It also exhibits reversible mechanochromism; the color changes from blue to pink to light yellow with increasing strain.

The polyurethane with the polyisoprene soft segment undergoes reversible thermochromic changes from blue to red in the temperature range of 85-140 °C. It also exhibits reversible mechanochromism; the color changes from blue to pink to light yellow with increasing strain. Synthesis of large samples of alpha, omega-dihydroxypolyisoprene are in progress for evaluation as impact improvement in reinforced epoxy systems such as helmets.

Work has continued toward the synthesis of elastomeric block copolymers with polysilylferrocenes to develop versatile chemical sensors with the ability to change colors or size/shape in response to chemical stimuli (collaborative work with M. Foster). We have prepared three polyisoprene-block-poly(dimethylsilylferrocene) block copolymers. Two polymers have polyisoprene block molecular weights of 11,500 g/mol ($M_w/M_n = 1.01$) and overall molecular weights of 16,400 ($M_w/M_n = 1.01$) and 22,000 g/mol (bimodal). A third block copolymer had a polyisoprene block molecular weight of 7,300 g/mol ($M_w/M_n = 1.09$) and overall molecular weight of 20,000 g/mol ($M_w/M_n = 1.26$). These samples have been given to Professor M. Foster.

After obtaining a stable monolayer from the new alkyl side chain derivatized polyferrocenylsilane, oxidized monolayers were transferred onto solid substrates to make multilayer films (2, 8, 12 layers). Transfer ratios for all layers were around 1.0(± 0.2) although the transfer ratios obtained during the down strokes were always higher than those

during the upstrokes. X-ray reflectometry measurements were carried out to characterize the multilayer films. Only one sample (8-layer film) could be studied in February because the instrument was shut down for the move into a new lab on the 10th floor. Preliminary analysis of this data suggests very weak ordering in the multilayer film.

The polyferrocenylsilane block copolymer has been studied further. TEM and electron diffraction measurements were done on a sample of PS-*b*-PFSiMe₂ annealed for one hour at 125°C and then for one hour at 140°C. Both temperatures are above the glass transition temperature of the polystyrene and 140°C is just above the melting temperature of the polyferrocenylsilane block. No lamellae due to microphase separation were observed and electron diffraction showed a broad ring at a spacing of 3.48Å. The texture of the sample appeared the same when annealed at 140°C as when annealed at 125°C. However, the contrast was enhanced for the sample annealed at the higher temperature. Also, TEM showed islands or holes on the surface of the sample annealed at 140°C. AFM measurements of as-cast films showed holes on the surface with heights of about 300Å.

It is now clear that the ordering behavior at temperatures below 127°C, the melting temperature of the poly(ferrocenyldimethylsilane) block, is dictated by the crystallization behavior of that block, while that above 127°C is dictated by the ordering behavior due to microphase segregation.

C) Textile Fibers and Processing

D. H. Reneker. 2001 MURI/ARO- FTT Final Report. dh@polymer.uakron.edu

Experiments were designed and used to gather a systematic set of data relevant to the behavior of an electrically driven jet of a polymer solution. This data is being used to create and validate a comprehensive theory of the behavior of electrically driven jets. The theory starts with Maxwell's equations for the electromagnetic fields and incorporates the partial differential equations for fluid mechanics. The resulting partial differential equations are solved with geometry and boundary values that are appropriate for electrically charged liquid jets. We are in the midst of this work, which has produced a predictive hypothesis about the maximum diameter of an electrically driven jet emerging from the surface of a liquid. This hypothesis is now being tested experimentally. The ARO funds are complemented by a NSF funded cooperative project shared with the University of Nebraska Lincoln.

We have obtained high-speed video photographs of the behavior of the electrospinning jets, using borrowed cameras. High frame rates and short exposure times have revealed important details of the processes. We are in the process of purchasing, with funds from the State of Ohio, a high-speed video camera system, which will be available for use on this project, and will help to resolve questions that emerge from our first observations. Discussions with experts on the use of Doppler radar techniques using visible laser light offer encouragement that we can utilize this method to directly observe the velocity of the larger, primary jets.

Ordinary video recordings, at a rate of 30 frames per second have also provided much valuable information. The initiation and stability of a jet moving upward from a droplet

sitting on the end of an inverted pipette has been photographed and correlated with a record of the electrical potential applied to the jet, and with the current carried by the jet. Of particular interest are instances in which several jets emerge from the droplet at the same time. When control of this phenomenon is achieved, the productivity of the apparatus is expected to be higher.

Protection from chemical and biological warfare agents, at a useful level, can be provided by protective clothing. Fabrics with large surface area per unit mass can be designed to absorb and hold or degrade these agents. Incorporation of nanofibers into protective clothing greatly increases the surface area of a garment, while at the same time creating pores that are small enough to prevent the passage of liquid droplets that do not wet the nanofiber. The pores are large enough to allow the passage of water vapor so that the protective garment is more comfortable than a material that is impervious to water vapor.

In this project, we are making nanofibers of various kinds of polymers available, and conducting research to optimize the processes by which polymer nanofibers are made. Control of the nanofiber diameter rests on the control of the mechanisms by which a jet of polymer liquid is divided into many smaller jets, which become nanofibers as they solidify. Flow measurements, electrical field parameters, dielectric relaxation, viscoelastic parameters, and molecular orientation by extensional flow are among the parameters which are being observed, and incorporated into a detailed model that can be used to improve the processes by which nanofibers are made. Nanofiber production is already being used in our laboratory and at the Army Natick Laboratory to produce small samples of nanofibers that can be characterized for their potential value in protective clothing. This capability is of importance for the early characterization of nanofibers produced from small samples of newly synthesized polymers, such as the ferrocenylsilanes being synthesized by Professor Quirk, and examined by Professor Foster.

D) Textile Manufacturing

D. H. Reneker. 2001 MURI/ARO- FTT Final Report. dlr@polymer.uakron.edu

An air vortex is being constructed and used for twisting the electrospun nanofibers from jet into a nanofiber yarn. The vortex is being designed with a large inlet orifice to collect the nanofibers at a level where the nanofibers are dry, and then, in a smaller diameter region of the vortex, twist the nanofibers into a yarn, which is collected on a screen or on a winder. The apparatus is being designed in cooperation with Frank Ko at Drexel University. The design is based on a discussion between Ko and Reneker on Wednesday, March 2, when Reneker visited Drexel University. Current experiments are producing short sections of loosely twisted nanofiber yarns.

A paper, "Nanofibers for Engineered Textiles", was presented at a meeting on Textiles Engineered for Performance, which is sponsored by UMIST, Manchester, England. UMIST is a leading center for research on textiles and textile fibers, and for the education of textile scientists and engineers. The paper described ways to incorporate nanofibers into textiles by replacing a textile fiber with a nanofiber yarn, by wrapping a layer of nanofibers around a textile fiber, and by wrapping a textile fiber yarn with layers of nanofibers. Conversion of 10 % of the mass of a fabric into nanofibers that are re-incorporated into the

fabric can increase the surface area per unit mass of the fabric by a factor of four, with no increase in the mass per unit area of the fabric. Uses of nanofiber fabrics in composites, as solar sails, and for reducing the thermal conductivity of air were discussed.

A number of textile and clothing designers attended the conference, and several expressed interests in the details of using nanofibers, for example, to improve the performance of specialty clothing for mountain climbing and other challenging sports.

A practical way to incorporate nanofibers into cloth for uses in tests is being developed. An air vortex is used to collect many nanofibers and twist them into a yarn. Short pieces of yarn, containing a number of nanofiber ranging from less than 100 to many thousands have been produced in an experimental vortex. It appears that it will also be possible to produce yarns that are a blend of ordinary textile fibers and nanofibers, with the nanofibers wrapped around the textile yarn. Such processes are being developed on a laboratory scale with the goal of creating enough fiber or yarn to weave small areas of cloth. At the same time, non-woven mats of nanofibers, which could be quilted or glued to an ordinary textile fabric, are being made and characterized. Frank Ko, at Drexel, is collaborating in this effort. The Army Research Office request for SBIR proposals to prepare sheets of nanofibers has attracted the attention of several small businesses, who are planning to submit proposals. We will serve as a consultant to one of the small businesses that applied, if they are successful.

A number of design changes are being incorporated into the air vortex is used to collect many nanofibers and twist them into a yarn. The new apparatus should make possible the extraction of the yarn from the vortex without getting it caught in strongly turbulent air are in progress. Short lengths of thread were successfully wrapped with nanofibers. Some of the modifications are intended to make this a continuous process.

E) Filtration

D. H. Reneker. 2001 MURI/ARO- FTT Final Report. dlr@polymer.uakron.edu

We have joined a consortium of filter manufacturers that was established by George Chase, in the Chemical Engineering Department of the University of Akron. This consortium is interested in the use of nanofibers in filters designed to coalesce small droplets. This effort provides a complementary point of view, which is expected to be helpful in the design of protective clothing that contains nanofibers

A consortium of filter manufacturers, for which we prepare nanofiber sheets for use as filter media, met in Akron. Samples of nylon nanofibers were provided to members of the consortium for testing in filter applications. This information should be relevant to the design of nanofiber layers that would prevent the passage of small droplets of chemical warfare agents, particularly those that are oil-like.

1999

A) Functionally Tailored Textiles

D. H. Reneker. 2001 MURI/ARO- FTT Final Report. dlr@polymer.uakron.edu

The discovery of the electrically driven bending instability in electrospinning jets and the development of a mathematical model of this phenomena resulted in a comprehensive paper, which that will be published in the Journal of Applied Physics in May 2000. The electrically charged, nearly straight jet of polymer fluid that is ejected from the liquid surface is unstable. The jet bends, developing a complex path, and becoming much thinner as it elongates in response to the electrical charge carried with the fluid. The mathematical model includes parameters that describe the viscoelastic behavior of a polymeric fluid. The three-dimensional paths of continuous jets were calculated, both in the nearly straight region where the instability grew slowly and in the region where the bending dominated the path of the jet. The model provided a good representation of the experimental data, particularly of the jet paths observed with a high-speed video camera. This work provides many insights that will lead to a much more sophisticated control of the electrospinning process.

Processes for making yarns from nanofibers were investigated. Methods involving an air vortex, and methods for twisting nanofibers collected on a liquid or solid surface were invented. This work was done in collaboration with Dr. Frank Ko, Drexel University, who is listed as co-inventor on an invention disclosure filed at the University of Akron. The production of continuous nanofiber yarns, with very high surface area per unit mass, was demonstrated. Such nanofibers yarns can be blended into a textile yarn. Larger diameter nanofiber yarns that could replace a thread line in a weaving process were also made. This provides a number of feasible options for incorporating nanofibers into textiles that can be used in protective clothing, for example.

Mesophase pitch nanofibers were produced using a new processing technology, which is the subject of a patent application. The molecules in these nanofibers were also well aligned along the fiber axis, and the orientation was retained during the stabilization, carbonization and graphitization. This process is of potential interest to the Army, for the production of air-borne obscurants, and in air filtration gas masks.

Other work on the electrospinning of styrene-butadiene-styrene triblock copolymer, which is an elastomeric material, is reported. Elastomeric sheets with good rubber-like properties were produced. This work resulted in the production of a nanofiber that contained only about 50 parallel molecules and which was decorated with beads 60 nanometers in diameter. The beginning of phase separation of the blocks was observed in transmission electron micrographs of the beads. This picture was selected for use on the cover of the current issues of the Journal of Polymer Science B: Physics, where the work is published.

The successful electrospinning of polymers chosen for their potential to neutralize chemical warfare agents was also demonstrated.

2000

A) Textile Based Fabrics and Composites

D. H. Reneker. 2001 MURI/ARO- FTT Final Report. dhrr@polymer.uakron.edu

Methods for making nanofibers of high performance nylon like fibers (MPI) were developed and the resulting nanofibers were characterized by electron diffraction and x-ray diffraction. Interactions of nanofibers and airborne, oily droplets, that could include simulants for chemical warfare agents, were investigated.

Wound Care

1) Objectives

D. H. Reneker. 2001 MURI/ARO- FTT Final Report. dh@polymer.uakron.edu

A) Wound Care Fibers and Processing

D. H. Reneker. 2001 MURI/ARO- FTT Final Report. dh@polymer.uakron.edu

New methods for incorporating nanofibers into yarns, for application of nanofibers for wound dressings were developed. Significant advances in the understanding of the electrospinning process that will result in a variety of process improvements were discovered and reported in the scientific literature.

A further objective is the use of electrospun nanofibers to protect wounds and to apply both disinfectants and therapeutic substances to wounds by directly electrospinning nanofibers onto the wounds. This work is done with Professor Dan Smith, of the Chemistry Department, University of Akron, and Heidi Schroeder Gibson of the Army Natick Laboratory.

2000

A) Wound Care Fibers and Processing

D. H. Reneker. 2001 MURI/ARO- FTT Final Report. dh@polymer.uakron.edu

Methods for electrospinning polymers and therapeutic substances from solutions in solvents, which can be applied to an open wound, were developed. Incorporation of proteins, spores, mixed polymers, living cells, and other substances or objects into nanofibers was accomplished. The resulting nanostructures within the fibers were characterized. On the experimental front, light diffraction methods were developed for the characterization of the diameter of fibers smaller than the wavelength of light. The resulting nanostructures within the fibers were characterized. Improved processes for making carbon nanofibers from mesophase pitch were developed. Electron microscopy and electron diffraction were used to characterize new, metal containing or metal coated polymer nanofibers. Our computer model of the electrospinning process was made "user friendly" by the addition of a graphical user interface. Methods for measuring the elongational relaxation time of columns of polymer fluid were developed and tested.

3) Research Team

D. H. Reneker. 2001 MURI/ARO- FTT Final Report. dh@polymer.uakron.edu

Professor Darrell H. Reneker

(PI)

Professor Frank Ko
Iksoo Chun
Sirina Putthanarat
Xiaoyan Fang
Dr. Hao Fong
Vesselin Velikov
Toprak Serhatkulu
Jong-sang Kim
Sureeporn Koombhongse
Han Xu
Woraphon Kataphinan
Wenxia Liu
Ratthapol Rangkupan
Prof. Zongquan Wu
Professor Alex Yarin
Dr. Dan Galehouse
Steven Roberts
Dale Ertley

(PI)
Postdoctoral Research Associate
Postdoctoral Research Associate
Postdoctoral Research Associate
Postdoctoral Research Associate
Research Associate
Research Associate
Ph. D. Candidate
Graduate Student
Graduate Student
Graduate Student
Graduate Student
Graduate Student
Visiting Scientist
Visiting Scientist
Visiting Scientist
Technician
Electronics Engineering Technician

4) List of Manuscripts Publications and Technical Reports (Abstract and first page of these articles in Section following invention disclosures)

D. H. Reneker. 2001 MURI/ARO- FTT Final Report. thr@polymer.uakron.edu

1. "Electrospinning Process and Applications of Electrospun Fibers," Jayesh Doshi and Darrell H. Reneker, *Journal of Electrostatics*; Vol. 35, pp. 151-160 (1995).
2. "Nanometer Diameter Fibers of Polymer, Produced by Electrospinning", Darrell H. Reneker and Iksoo Chun, *Nanotechnology*, Volume 7, pages 216-223, 1996.
3. "DNA Fibers by Electrospinning", Xioayan Fang and Darrell H. Reneker, *Journal of Macromolecular Science--Physics*, 1996, Volume B36, pages 169-173, 1997.
4. "Mechanical Properties of Composites Using Ultrafine Electrospun Fibers", Jong-sang Kim and Darrell H. Reneker, *Polymer Composites*, Feb. 1999, Vol. 20, No. 1. pages 124-131.
5. "Polybenzimidazole Nanofibers Produced by Electrospinning", Jong-sang Kim and Darrell H. Reneker, *Polymer Engineering and Science*, May 1999, Vol. 39 pages 849-854.
6. "Development of Laminated Composites with Electrospun Polymer Nanofiber Reinforcement of Interfaces", Yuris A. Dzenis, Darrell H. Reneker, S. Sergiyenko, and Jong-sang Kim, Submitted to *Composites: A. Manufacturing and Applied Science*, October 1997.
7. "Nanofibers for Engineered Textiles", Darrell H. Reneker, Proceedings of a conference on "Textiles Engineered for Performance," Manchester, England, 1998.

8. "Carbon Nanofibers from Polyacrylonitrile and Mesophase Pitch" Iksoo Chun, Darrell Reneker, Xiaoyan Fang, Hao Fong, Joe Deitzel, Nora Beck Tan, and Kristen Kearns, Proceedings of the 43rd International SAMPE Symposium, Anaheim, California, May 31-June 4, 1998. Published in, *Journal of Advanced Materials*, 1999, pages 36-37.
9. "Beaded Nanofibers Formed During Electrospinning", Hao Fong, Iksoo Chun, and Darrell Reneker, *Polymer*, Volume 40, 1999, pages 4585-4592.
10. "Elastomeric Nanofibers of Styrene-Butadiene-Styrene Tri-block Copolymer", Hao Fong, and Darrell Reneker, *Journal of Polymer Science, Polymer Physics Edition*, Volume 37, 1999, pages 3488-3493.
11. "Carbon Nanofibers" Hao Fong, Iksoo Chun, and Darrell Reneker, Proceedings of the 24th Biennial Conference on Carbon, Charleston, South Carolina, July 11-16, 1999
12. "Bending Instability of Electrically Charged Liquid Jets of Polymer Solutions in Electrospinning", Darrell H. Reneker, Alexander L. Yarin, Hao Fong and Sureeporn Koombhongse, *Journal of Applied Physics*, Volume 87, pages 4531 to 4547, May, 2000.
13. "Structure of Poly(ferrocenyldimethylsilane) in Electrospun Organometallic Nanofibers", Zhihao Chen, Mark D. Foster, Hao Fong, Darrell H. Reneker, Rui Resendes, Ian Manners, *Macromolecules* 34(18), 6164-6166, 2001.
14. "Electrospinning and the Formation of Nanofibers", Hao Fong and Darrell H. Reneker, Chapter 6 in *Structure Formation in Polymeric Fibers*, edited by David R. Salem and Martin V. Sussman, pages 225 to 246, published by Hanser, 2000.
15. "Structure and Morphology of Poly(Meta-phenylene isophthalamide) Nanofibers Produced by Electrospinning", Wenxia Liu, Zongquan Wu and Darrell H. Reneker, *Polymer Preprints* 2000, Vol. 41 (2), pages 1193-4.
16. "On Bending Instability in Electrospinning of Nanofibers", Alexander L. Yarin, Sureeporn Koombhongse, and Darrell H. Reneker, *Journal of Applied Physics*, Volume 89, pages 3018 to 3026, 2001.
17. "Taylor Cone and Jetting from Liquid Droplets in Electrospinning of Nanofibers", Alexander L. Yarin, Sureeporn Koombhongse, and Darrell H. Reneker, Volume 90, November 2001, pages 4836-4846.
18. "Motion of Droplets along thin fibers with temperature gradient", Alexander L. Yarin, Wenxia Liu, and Darrell H. Reneker, , Submitted to *Journal of Applied Physics*, June 6, 2001.

5) Publicity

D. H. Reneker. 2001 MURI/ARO- FTT Final Report. dh@polymer.uakron.edu

A news release about the goal of this project, better uniforms for soldiers, resulted in three television interviews by Professors Brittain and Reneker, who discussed work on sensors embedded in the uniform, that would detect threats such as chemical warfare agents, and the use of electrospun nanofibers to make clothing with selective absorbency and light weight. Work on synthesis of new polymers for uniforms and on the characterization of surfaces composed of thin layers of sensitive or reactive molecules was also described.

The Plain Dealer, the largest Cleveland newspaper, published a feature article entitled "Battle wear of the future" by Ulysses Torassa, which told about this project and mentioned the University of Akron, Drexel University and North Carolina University, on Monday, October 28, 1996.

The feature article, originally published in the Plain Dealer, entitled "Battle wear of the future", which told about this project and mentioned the three Universities involved, was picked up and distributed by the Newhouse News Service. At least two other newspapers have re-published the article.

The Times of London published a feature article on November 18, 1996, by Anjana Ahuja on fabrics woven from optical fibers, in which the uses of optical fibers being investigated in this project were mentioned.

BBC radio broadcast a telephone interview with Professor Reneker and others that centered around the use of optical fibers in fabrics.

6) Invention Disclosures

D. H. Reneker. 2001 MURI/ARO- FTT Final Report. dh@polymer.uakron.edu

University of Akron #	Title
329	Process of Production of Nanofibers from Spinnable Fluids Battelle, North Carolina State University
357	Electrospun Medical Dressings U.S. Army Research Office
369	Process for Making Yarn from Nanofibers, for Wrapping Nanofibers onto a Texture Fiber on a Textile Yarn, and for Incorporating Nanofibers into Braided, Woven or other Textiles
399	A Process and Apparatus for the Production of Mixtures of Nanofibers (Cylindrical Concentric Tube-Like Structure)
400	A Process and Apparatus for the Production of a Web of Nanofibers (Flat Plate-Like Structure)

The first page, including the abstract, of each of the above papers that resulted from this project are included on the following pages. These pages were scanned from the published versions of the articles, and are therefore not editable.

Reprinted from

Journal of

ELECTROSTATICS

Fundamentals, Applications and Hazards

Journal of Electrostatics 35 (1995) 151-160

Electrospinning Process and Applications of Electrospun Fibers

Jayesh Doshi and Darrell H. Reneker



Journal of Electrostatics 35 (1995) 151-160

Journal of
ELECTROSTATICS

Electrospinning Process and Applications of Electrospun Fibers

Jayesh Doshi and Darrell H. Reneker

The Maurice Morton Institute of Polymer Science, The University of Akron, Akron, Ohio 44325-3909, USA

Abstract

An electric field is used to create a charged jet of polymer solution. As this jet travels in air, the solvent evaporates leaving behind a charged fiber that can be electrically deflected or collected on a metal screen. Fibers with a variety of cross sectional shapes and sizes were produced from different polymers. The diameter of these fibers was in the range of 0.05 to 5 microns. This paper describes the electrospinning process, the processing conditions, fiber morphology, and some possible uses of electrospun fibers.

1. Introduction

Various industrial applications of the production of liquid jets in the presence of intense electric field have been investigated. Some of these applications are listed in the literature [1-4]. One such application is the electrospinning process to spin microdenier synthetic fibers from polymer solutions. The electrospinning process has previously been employed for over three decades in industries to produce various products [5-13]. The present study is an attempt to characterize the electrospinning process, and identify the process parameters governing it. In this paper, the initial results of the study have been described.

In the electrospinning process, a polymer solution held by its surface tension at the end of a capillary tube is subjected to an electric field. Charge is induced on the liquid surface by an electric field. Mutual charge repulsion causes a force directly opposite to the surface tension. As the intensity of the electric field is increased, the hemispherical surface of the solution at the tip of the capillary tube elongates to form

0304-3886/95/\$09.50 © 1995 - Elsevier Science B.V. All rights reserved.
S001-0304(95)00041-0

Nanometre diameter fibres of polymer, produced by electrospinning

Darrell H Reneker and Iksoo Chun

Maurice Morton Institute of Polymer Science, The University of Akron, Akron, OH 44325-3909, USA

Abstract. Electrospinning uses electrical forces to produce polymer fibres with nanometre-scale diameters. Electrospinning occurs when the electrical forces at the surface of a polymer solution or melt overcome the surface tension and cause an electrically charged jet to be ejected. When the jet dries or solidifies, an electrically charged fibre remains. This charged fibre can be directed or accelerated by electrical forces and then collected in sheets or other useful geometrical forms.

More than 20 polymers, including polyethylene oxide, nylon, polyimide, DNA, polyaramid, and polyaniline, have been electrospun in our laboratory. Most were spun from solution, although spinning from the melt in vacuum and air was also demonstrated. Electrospinning from polymer melts in a vacuum is advantageous because higher fields and higher temperatures can be used than in air.

1. Introduction to nanofibres

Electrospinning provides a straightforward way to produce long polymer fibres with diameters in the range of 40–2000 nm. Expected improvements in the technique of electrospinning from liquid crystal or other disentangled systems may produce even thinner fibres.

The smallest polymer fibre must contain one polymer molecule. A typical polymer molecule has a diameter of a few tenths of a nanometre. Perhaps the record for the thinnest fibre known can be claimed by the recent discovery [1] of a way to make a chain of single carbon atoms. Oligomers of polyethylene, which have a diameter of around 0.4 nm, have been observed in single-layer crystal-like arrays of extended chains [2]. The DNA double helix has two backbone chains, with a diameter of around 2.5 nm. Optical fluorescence microscopy produces images of DNA molecules in a solution, and makes it possible to observe fibre-like properties such as the extension and transport of single molecules through a solution in response to external forces [3, 4]. DNA chains can be spread on a substrate and observed by electron microscopy or scanning probe microscopy. Three collagen molecules twist around each other to form a triple helix fibre, and higher levels of organization of collagen occur to form tendons.

Synthetic fibres with diameters in the nanometre range have been overshadowed by the technological development of textile fibres during the past century. Polyoxymethylene polymerized in the solid state [5, 6] forms crystal fibres of parallel extended molecules with diameters in the nanometre range. Mechanical deformation of polymer crystals often produces fibres which are observed in electron micrographs of fracture surfaces, for example. Such fibres typically have diameters of a few tens of nanometres and lengths up to a few micrometres.

Many images of polymer nanofibres exist in the literature [7–10] that deals with polymer morphology, but in almost all cases the nanofibres were observed incidentally to other features of the polymer. The ordered arrangements of molecules in the crystals eliminate entanglements and make it possible to convert the folded or extended chains in the crystals into smooth fibres by mechanical drawing. A process called crazing [11, 12] which occurs in glassy polymers such as polystyrene, involves the creation of fibres a few tens of nanometres in diameter with lengths up to a few micrometres.

A 50 nm diameter polymer fibre has about 10 000 molecules crossing any section of the fibre. A typical polymer molecule in such a fibre has an extended length in the range of 1–100 μm . The degree to which such long molecules are actually extended in a nanofibre depends on the way the fibre is prepared, for example the temperature, the number of entanglements, the draw ratio, and other parameters. About 3% of the polymer molecules in a 50 nm diameter fibre are on the surface of the fibre, if each molecule has a diameter of about 0.5 nm.

Commercial processes for manufacture of non-woven fabrics, which involve the expansion of a foam until most of the polymer is converted to fibres, produce large quantities of fibres with diameters around 100 nm mixed with non-fibre particles of a polymer. Experimental melt-blowing processes produce fibres with diameters in the range of 1–50 μm [13, 14]. Particles of polytetrafluoroethylene from dispersion polymerization processes, that are pressed together, adhere to each other and small fibres are formed when the particles are pulled apart. Gentle scratching of the surface of moulded polytetrafluoroethylene with coarse sandpaper leaves many fibres with nanoscale diameters on the surface. A commercial process for making air filters by electrospinning has been described [15].

0957-4484/96/030216+08\$19.50 © 1996 IOP Publishing Ltd

DNA Fibers by Electrospinning

X. FANG and D. H. RENEKER*
Department of Polymer Science
The University of Akron
Akron, Ohio 44325-3909

ABSTRACT

Thin fibers of calf thymus Na-DNA were electrospun from aqueous solutions with concentrations from 0.3% to 1.5%. In electrospinning, a high voltage is used to create an electrically charged jet of liquid solution, which dries to leave a polymer fiber. The electrospun DNA fibers have diameters around 50 to 80 nm. The diameter of the electrospun fibers is an order of magnitude or more smaller than that of previously reported fibers. The DNA fibers were observed by optical microscopy, scanning electron microscopy, and transmission electron microscopy. Bead-like structures were observed on many of the fibers. During electrospinning a process called splaying causes the jet to split longitudinally into two smaller jets, which split again, repeatedly, until the very small diameter fibers are formed. The small-diameter fibers are transparent in ordinary 100 kV electron microscopes. Fibers can be spun from samples of DNA as small as 1 mg.

INTRODUCTION

Deoxyribonucleic acid, or DNA, is well known as the carrier of genetic information. Work in many laboratories on the structure of this polymer in the 1950s culminated in the establishment of the double helix model by Watson and Crick [1]. To obtain oriented samples of DNA, early workers prepared fibers from solution. A few examples are cited here. Wilkins et al. [2] made DNA fibers with diameters in the range of 50 to 100 μm by slowly drawing a gel of the polymer. Wyckoff [3] and Marvin [4] used a dry-spinning method to obtain oriented DNA fibers. Rupprecht [5] obtained oriented fibers of DNA by wet spinning plus mechanical drawing.

*E-mail: dhr@polymer.uakron.edu

Mechanical Properties of Composites Using Ultrafine Electrospun Fibers

JONG-SANG KIM* and DARRELL H. RENEKER

*The Institute of Polymer Science
The University of Akron
Akron, Ohio 44325-3909*

The objective of this research was to show the reinforcing effects of nanofibers in an epoxy matrix and in a rubber matrix using electrospun nanofibers of PBI (polybenzimidazole). The average diameter of the electrospun fibers was around 300 nanometers, which is less than one tenth the diameter and 1/100 the cross sectional area of ordinary reinforcing fibers. The ultrafine fibers provide a very high ratio of surface area to volume. The nanofibers toughened the brittle epoxy resin. The fracture toughness and the modulus of the nanofiber (15 wt%)-reinforced epoxy composite were both higher than for an epoxy composite made with PBI fibrils (17 wt%), which are whisker-like particles. In an elastomeric matrix, The Young's modulus and tear strength of the chopped nanofiber-reinforced styrene-butadiene rubber (SBR) were higher than those of the pure SBR. Micrographs of the fracture surfaces were obtained by scanning electron microscopy (SEM).

INTRODUCTION

Fiber-reinforced composite materials consist of fibers of high strength and modulus embedded in or bonded to a matrix with a distinct interface between fiber and matrix. Both fibers and matrix retain their physical and chemical identities. Composites have a combination of properties that cannot be achieved with either of the constituents acting alone.

Nanofibers are small enough to reinforce the regions of the matrix between primary reinforcing fibers. This work demonstrates, in mm scale samples, improvements from incorporation of nanofibers into the matrix, and indicates that nanofibers should be useful to produce improvement at important smaller scale places, for example, between plies of a prepreg.

Fiber-reinforced composite materials offer a combination of strength and modulus that are either comparable to or better than many traditional metallic materials. The strength to weight ratios and modulus to weight ratios of these composite materials are, because of their low specific gravity, markedly superior to those of metallic materials. In addition, fatigue strength to weight ratios as well as fatigue damage tolerances of many composite laminates are excellent. For these reasons, fiber-reinforced composites have emerged as a major class of structural materials and

are either used or being considered as substitutes for metals in many weight-critical components in aerospace, automotive, and other industries (1).

The influence of long fibers is so dramatic that composite materials containing long fibers are treated as a separate class of solid materials. Composites with particles or whiskers are likely to produce only modest improvements over the non-reinforced matrix materials. Therefore, the emphasis is on the long nanofibers. Nanofibers have a surface area per unit mass that is about 100 times larger than for the carbon or glass fibers that are ordinarily used for reinforcement. The aspect ratio of the nanofibers is high, even after the fibers are broken by the action of a rubber mill used to incorporate them into rubber at high temperature.

EXPERIMENTAL

An epoxy resin was chosen as a matrix in these experiments because epoxies are widely used in composites. Epoxies adhere well to a wide variety of fibers. The DGEBA epoxy resin used in this work is EPON 828 from the Shell Chemical Company, Houston. It was a liquid at room temperature. A tetrafunctional aromatic amine crosslinker was used, 4,4'-diaminophenyl sulfone (DDS). A vacuum was used to remove air so that resin was in good contact with the fibers.

The production of non-woven fabric sheets of PBI nanofibers was described by Kim and Reneker (2). The fibers were collected in sheets about 8 centimeters wide and 50 centimeters long, with a compressed thickness of a few tens of microns. The mass per unit

*School of Chemical Engineering & Technology
College of Engineering
Chonbuk National University
Chonju, 561-756 Republic of Korea

REPRINTED FROM POLYMER COMPOSITES, FEBRUARY 1999, Vol. 20, No. 1

Polybenzimidazole Nanofiber Produced by Electrospinning

JONG-SANG KIM* and DARRELL H. RENEKER

*The Institute of Polymer Science
The University of Akron
Akron, Ohio 44325*

Nanofibers of aromatic heterocyclic PBI (poly(2,2'(m-phenylene)-5,5' bibenzimidazole)) polymer were made by an electrospinning process. The diameter of the fibers was around 300 nanometers. A liquid jet of a polymer solution, formed when electrical force overcame surface tension, stretched and dried as the solvent evaporated. The resulting electrically charged nanofibers were attracted to and collected on a rotating cylinder covered with aluminum foil that was electrically grounded. The fibers were collected in non-woven sheets about 20 centimeters wide and 100 centimeters long, with a compressed thickness of a few tens of microns. The mass per unit area of the nonwoven sheets was 15 to 50 g/m². The nonwoven fabric of PBI nanofibers was treated with sulfuric acid, and then washed, dried and heated to improve its strength. Optical microscopy showed that the electrospun PBI nanofibers were birefringent. Other morphological features of these fibers were observed with scanning electron microscopy, transmission electron microscopy and atomic force microscopy.

INTRODUCTION

In 1934, Formhals (1-3) patented a process and an apparatus for the production of the polymer filaments using electrostatic force. An electric field was applied to a free surface of polymer solution, such as cellulose acetate. One electrode was placed into the spinning solution and the other electrode was attached to a moving collector. The liquid jets that were ejected dried and formed charged fibers. Small holes in a metal plate allowed the formation of several jets. The distance between the solution feeding device and the collecting device was variable. When the distance was short, spun fibers tended to stick to the collecting device as well as to each other, due to incomplete solvent evaporation.

The electrospinning process never became competitive with melt spinning, partly because the electrospun fibers were generally much smaller in diameter than the fibers that are used to make textiles. In 1977, Martin and co-workers (4) manufactured a mat of fibers by electrostatically spinning organic polymers. The mat could be used for wound dressings. Here the small diameter of the nanofibers fibers was advantageous. The mats of small fibers had small interstices between the fibers, and a high surface area per unit mass. If the dressing was formed from a wettable

polymer, blood or serum escaping from the wound tended to penetrate the dressing, but readily clotted, owing to the high surface area and small interstices. Such dressings were usually sufficiently porous to allow interchange of oxygen and water vapor between the atmosphere and the surface of the wound. These mat dressings could be combined with woven textile fiber mats that provided strength and other useful properties, or with materials having antiseptic or wound healing properties. In 1982, Bornat (5) described an electrostatic fiber spinning process that produced a tube of nanofibers on a rotating metal mandrel.

In 1995, Doshi and Reneker (6) described electrospinning conditions, fiber morphology, and some possible uses of electrospun fibers made from several polymers. In electrospinning, the polymer solution is charged to a high electrical potential that produces a high electric field at the surface of the liquid. When the electrical force per unit area equals the pressure of surface tension at the surface of the polymer solution, a charged droplet hanging at the end of the capillary tube is in equilibrium, assuming that no other pressures are present. Increasing the potential makes the charged drop unstable, and usually a charged jet forms to carry the charge away. The jets stretch and dry in flight into solid, electrically charged fibers and are finally collected on an electrically grounded screen.

*School of Chemical Engineering and Technology, College of Engineering, Chonbuk National University, Chonju, 561-756, Republic of Korea.

*Composites: A. Manufacturing
and Applied Science*

Development of laminated composites with electrospun polymer nanofiber reinforcement of interfaces

Y. A. Dzenis^{1*}, D.H. Reneker², S. Sergiyenko¹, J.-S. Kim²

¹Department of Engineering Mechanics, Center for Materials Research and
Analysis, University of Nebraska-Lincoln, Lincoln, NE 68588-0347, U.S.A.

²Maurice Morton Institute of Polymer Science, Department of Polymer Science,
University of Akron, Akron, OH 44325-3909, U.S.A.

ABSTRACT

A problem of delamination in advanced polymer laminated composites is addressed. A new concept of thin continuous polymer fiber reinforcement of interfaces is formulated. A novel electrospinning technology is used as a method to produce continuous polymer fibers of submicron diameters. Experimental proof-of-concept is performed on a graphite/epoxy composite. It is found that the addition of 2.5 mass% of polybenzimidazole nanofibers results in 130% improvement of the Mode II critical energy release rate and 15% improvement of the Mode I critical energy release rate. Mechanisms of interlaminar fracture in laminates with nanoreinforced interfaces are discussed.

*To whom correspondence should be addressed

Nanofibers for Engineered Textiles

Darrell H. Reneker

The University of Akron
Akron, Ohio 44325-3909, U.S.A.
dhr@polymer.uakron.edu

Abstract

Nanofibers have diameters ranging downward from 1000 nanometers (nm), which is one micron, to the diameter of a single polymer molecule, which is about 0.5 nm while textile fibers range in diameter from one to 100 microns. For typical polymers, the denier of nanofibers ranges from 10^{-7} to 10^{-3} . Nanofibers of many kinds of polymers can be produced easily by a process called electrospinning. Nanofibers are finding uses in filters, protective fabrics, advanced composites, enzyme support in bioreactors, agriculture, and other applications. The production, characterization, and the identification of the useful properties of polymer nanofibers, are described. The engineering of fibrous structures, which are thinner than the diameter of a typical textile fiber, is introduced.

Introduction to Properties and Uses of Nanofibers

The diameters of the nanofibers produced in our laboratory are often in the range of 300 to 500 nm, which is about equal to the wavelength of light. Nanofibers have a high surface area per unit mass, because of their small diameters. Textile fibers, with a diameter of 10 microns, have specific surface areas of around 700 square meters per kilogram, as calculated. Nanofibers with a diameter of 100 nm have specific surface areas 100 times greater, which is in the same range as that of carbon black particles.

Non-woven sheets of nanofibers are unusually smooth to the touch. They are effective filters for small particles. The resistance to flow of liquids and gases is relatively low. Air and water vapor permeation rates are high. Incorporation of nanofibers into fabrics for protective clothing, to absorb noxious substances while allowing air and water vapor to penetrate, is being investigated. Small amounts of nanofibers, at strategic places between crossed plies in laminated reinforced composites, can improve the crack resistance of the composite. Nanofibers are attractive candidates for the manufacture, in space, of large structures such as solar sails, reflectors, and large aperture, long focal length reflective mirrors for light and other electromagnetic waves. Nanofibers can be made with diameters smaller than the mean free path of molecules in air, and therefore can decrease the thermal conductivity of still air.

The Electrospinning Process

A high electric field at the surface of a polymer liquid produces forces that are opposed to surface tension. For most polymer solutions, at electric fields smaller than the electrical

Carbon Nanofibers from Polyacrylonitrile and Mesophase Pitch

Iksoo Chun, Darrell H. Reneker, Hao Fong, Xiaoyan Fang

Institute of Polymer Science, The University of Akron, Akron, OH

Joe Deitzel and Nora Beck Tan

U.S. Army Research Laboratory, Weapons and Materials Research Directorate,

Aberdeen Proving Ground, MD

Kristen Kearns

Department of The Air Force Wright Laboratory (AFMC), Wright-Patterson AFB, OH

Received 08/07/98; revised manuscript received 11/14/98

Abstract

Carbon nanofibers were produced from both polyacrylonitrile and mesophase pitch. Stabilization and carbonization processes were used to convert as-spun nanofibers to carbon fibers. The nanofibers are arbitrarily long, although a way to make nanofibers less than a millimeter long, with high aspect ratios, was found. The diameters of typical carbon nanofibers are in the range from 100 nanometer to a few microns. A log normal distribution provides a good representation of the measured distribution of diameters. The carbon nanofibers were observed by polarized optical microscopy, scanning electron microscopy, transmission electron microscopy, and wide angle x-ray diffraction. As-spun mesophase pitch fibers are transparent, red or orange in transmitted light, and birefringent. Electron diffraction patterns were obtained from individual carbon nanofibers. The interplane spacing of (002) planes of mesophase pitch based carbon nanofibers was measured using wide angle x-ray diffraction. Nanofibers provide a higher ratio of surface area to mass than carbon fibers ordinarily used in composites. Carbon nanofibers can be useful in filters, as a support for catalysts in high temperature reactions, in composites to improve mechanical properties, or for thermal management in semiconductor devices. Nanopores in carbon fibers were produced using nitrogen gas saturated with water vapor.

Introduction

Electrospinning is a method for making very small diameter fibers. An electric field provides the driving force. When an applied electric field overcomes the surface tension of a polymer solution or melt, an electrically charged jet is formed. The jet is pulled toward an electrically conducting collector held at an attractive potential. As the electrically charged jet is stretched by the electric field, its diameter decreases and the radial component of the electrical force increases. The single jet divides into two or more jets and each of the divided jets divides repeatedly. The "splayed" jets are collected as a form of nonwoven fabric on a metal screen, aluminum foil, woven cloth, or other surfaces.

The electrospinning process has been known for a long time. In the early 20th century, threads of molten sealing wax were produced using a high electric field.¹ Formhals patented a process

and an apparatus to make fine polymer fibers using high electric field in 1934² and other patents followed. In 1952, Vonnegut and Neubauer³ invented an electrostatic fountain and found when the spray of droplets was illuminated with a beam of parallel white light, colors were seen. Taylor⁴ studied the disintegration of water drops in an electric field. He demonstrated that a drop elongates and a cone which has semi angles close to 49.3° forms at each end. In 1971, Baumgarten⁵ produced acrylic microfibers, using electrical forces, with diameters in the range from 0.05 to 1.1 microns. He observed the relationships between fiber diameter, jet length, solution viscosity, solution feed rate, and surrounding gas. Larrondo and Manley⁶⁻⁸ made continuous fibers of polyethylene and polypropylene using electric fields as the driving force. The diameters of these polyolefin fibers depended on the electric field and were around 50 microns. Reneker and Srinivasan⁹ electrospun nanofibers

from a liquid crystal solution of poly(p-phenylene terephthalamide) in sulfuric acid. Reneker and Doshi¹⁰ used electrospinning to make fibers of water soluble poly (ethylene oxide) with diameters of 0.05 to 5 microns. Reneker and Chun¹¹ produced polyester nanofibers from solution, from the melt in air, and from the melt in vacuum. Reneker and Kim¹² made a nanofiber reinforced epoxy composite using a fabric composed of partially aligned nanofibers.

The carbon fibers now used, with diameters around 10 microns, are made from polyacrylonitrile and mesophase pitch. The acrylic polymer precursor used contains about 85 weight percent acrylonitrile¹³, with acrylic acid or methacrylic acid comonomers. Melt spinning is difficult since polyacrylonitrile degrades below its melting temperature, so solution spinning is used. The as-spun polyacrylonitrile fibers are heated in air to 200 to 400 °C, under tension, to stabilize them for treatment at higher

Beaded nanofibers formed during electrospinning

H. Fong, I. Chun, D.H. Reneker*

Maurice Morton Institute of Polymer Science, The University of Akron, Akron, OH 44325-3909, USA

Dedicated to Professor Ronald K. Eby on the occasion of his 70th birthday

Received 10 September 1998; received in revised form 6 October 1998; accepted 22 October 1998

Abstract

Electrospinning is a straightforward method to produce polymer fibers from polymer solutions, with diameters in the range of 100 nm. Electrospun fibers often have beads in regular arrays. The viscoelasticity of the solution, charge density carried by the jet, and the surface tension of the solution are the key factors that influence the formation of the beaded fibers. © 1999 Elsevier Science Ltd. All rights reserved.

Keywords: Electrospinning; Beaded nanofiber; Nanofiber

1. Introduction

It was known in the early 1900s that if molten sealing wax was electrified, solid fibers were ejected. Sealing wax is brittle, and no viable commercial development of this process for making fibers has resulted so far. Focus is now on the liquid jets created by electric fields, the distortion of liquid droplets in an electric field, the collapse of liquid jets into droplets, and the development of processes for electro-spraying paint and other liquids. In the past century, electrostatic spinning and related phenomena, such as aerosol spraying, atomization in the charged droplets and the formation of particles, have received attention [1–5]. Baumgarten [6], working at Dupont in the 1970s, published high speed photographs and other data describing the formation of fibers of an acrylic polymer by electrostatic spinning. Reneker [7–9] and co-workers characterized the electrospinning process and the physical properties of electrospun nanofibers.

Electrospun fibers often have beads as “by products”. The formation of beaded fibers has been observed widely [10]. The electrospun beaded fibers are related to the instability of the jet of polymer solution, which was studied by Yarin [11] and Entov [12]. They developed a mathematical model for the break-up of jets of polymer liquids, which did not include the effects of electric fields. In 1962, Magarvey and Outhouse [13] found that the break-up of water jets depended on the electrical current. The more

current the water jet carried, the less likely it was to form droplets. Huebner [14] also considered such electrical phenomena. Fang [8] electrospun beaded DNA nanofibers. Jaeger [15,16] reported beaded fibers spun from aqueous solutions of poly(ethylene oxide) (PEO). He found that the bead diameter and spacing were related to the fiber diameter: the thinner the fiber, the shorter the distance between the beads and the smaller the diameter of the beads.

Characterization of the formation of electrospun beaded nanofibers shows that solution viscosity, net charge density carried by the electrospinning jet and surface tension of the solution are the main factors. Higher viscosity favors formation of fibers without beads, higher net charge density not only favors formation of fibers without beads, but also favors the formation of thinner fibers. Surface tension drives towards the formation of beads, hence reduced surface tension favors the formation of fibers without beads.

Changing the polymer concentration can vary the solution viscosity. The surface tension coefficient depends on the polymer and solvent. For example, changing the ratio of ethanol to water can change the surface tension coefficient of the PEO solution. Net charge density carried by the jet in the electrospinning process is primarily affected by the applied electrostatic field and to a lesser extent by the conductivity of the solution. For example, the addition of NaCl to a PEO/water solution is observed to increase the net charge density carried by the spinning jet. The use of the quantity charge per unit volume (C/l) does not imply that the net charge density is distributed uniformly throughout the jet. When the jet shape is changing rapidly, most of the net charge is found to be near the surface. The net charge density on the jet can be reduced to a low value, by ions

* Corresponding author. Tel.: + 1-330-972-6949; fax: + 1-330-972-5290.

Elastomeric Nanofibers of Styrene-Butadiene-Styrene Triblock Copolymer

HAO FONG, DARRELL H. RENEKER

The Maurice Morton Institute of Polymer Science, The University of Akron, Akron, Ohio 44325-3909

Received 3 April 1999; revised 29 July 1999; accepted 4 August 1999

ABSTRACT: Nanofibers of a commercial styrene-butadiene-styrene triblock copolymer were electrospun from solution, and collected either as a nonwoven elastomeric fabric, or on a layer of graphite that was evaporated onto a glass microscope slide. The resulting nanofibers were elastic, birefringent, and most had diameters around 100 nm. A few thin, beaded fibers were found among the smooth nanofibers. The diameter of the fibers between the beads was as small as 3 nm. After staining with osmium tetroxide, the nanofibers were examined using transmission electron microscopy. Separated phases of styrene and butadiene blocks were observed. The single-phase domains were irregular in shape, but elongated along the axis of the fiber. Wide-angle X-ray diffraction patterns showed a weak indication of molecular orientation along the fiber axis, and the birefringence confirmed that such orientation was present. The single-phase domains grew larger in nanofibers that were held at room temperature ($\sim 25^\circ\text{C}$) for several days. Annealing at a temperature 70°C greatly accelerated the growth of the single-phase domains. The nanofibers softened and flattened on the evaporated graphite during annealing. © 1999 John Wiley & Sons, Inc. *J Polym Sci B: Polym Phys* 37: 3488–3493, 1999

Keywords: nanofiber; electrospinning; SBS; phase separation; polymer; copolymer; triblock; elastomer; electron microscopy

INTRODUCTION

As new technologies demand predictable performance of materials at all length scales between atoms and useful objects, it is necessary to control material properties that are associated with nanometer scale structures.^{1,2} Electrospinning provides a way to produce polymer fibers with diameters in the nanometer range.^{3,4}

Electrospinning occurs when the electrical forces at the surface of a polymer solution overcome the surface tension and cause an electrically charged jet of polymer solution to be ejected. Electrical forces also cause the jet to become thinner

as it travels. When the jet dries or solidifies, an electrically charged nanofiber remains.⁴

In the electrospinning process, solvent evaporation occurs on a millisecond time scale. The rapid removal of the solvent decreases the mobility of the polymer molecules and makes it more difficult for the polymer blocks to segregate into single phase domains. In this series of experiments, it is clear that the nanofibers, as they are formed, contain a nonequilibrium distribution of phase domains.

Electrospinning can produce fibers in the diameter range that overlaps textile fibers, but fibers with diameters ranging from 1000 nm downward are most interesting, because fibers with such small diameters are difficult to produce by conventional processes.⁵ Polymer nanofibers are transparent in an ordinary 100,000 electron volt transmission electron microscope. Nanofibers

Correspondence to: D. H. Reneker (E-mail: dhr@polymer.uakron.edu)

Journal of Polymer Science: Part B: Polymer Physics, Vol. 37, 3488–3493 (1999)
© 1999 John Wiley & Sons, Inc. CCC 0887-6266/99/243488-06

CARBON NANOFIBERS

Hao Fong, Iksoo Chun[†] and Darrell H. Reneker

Department of Polymer Science, The University of Akron, Akron, OH 44325-2909 USA

[†] Johnson & Johnson Corporate Biomaterials Center, Somerville, NJ 08876-0151 USA

Keywords: polyvinyl alcohol (PVA), pitch, polyacrylonitrile (PAN), electrospinning, nanofiber, carbon fiber.

INTRODUCTION

Electrospinning provides a straightforward way to make precursors [1] to a variety of carbon nanofibers that have diameters around 100 nm, and physical properties that range from highly crystalline, strong fibers to very porous, high surface area, brittle and poorly crystallized fibers. Carbon nanofibers, which were made from mesophase pitch, had structural features quite similar to those of conventional, larger diameter carbon fibers. Electrospun polyacrylonitrile (PAN) nanofibers were stabilized in air and carbonized in nitrogen at 800 °C, with no tension in the fibers [2]. PAN derived carbon nanofibers were subsequently heated in water vapor, which caused the formation of pores that were easily visible in electron micrographs.

Polyvinyl alcohol (PVA) is not a widely used precursor for making carbon fibers, because PVA is not easily stabilized. Recently, it was found that the presence of ammonium phosphate ($(\text{NH}_4)_2\text{HPO}_4$) greatly improved the stabilization process [3]. Here, the objective was to produce fibers with a very high ratio of surface area per unit mass. The resulting nanofibers have a porous structure on the scale of tens of nanometers, and they are brittle. Measurements of the BET surface area, morphology, microcrystallites, and process yield are in progress.

EXPERIMENTAL

The experimental procedures for making the PAN and mesophase pitch precursors were already reported [2]. Some of the PAN fibers were heated at 650° C, for one hour, in a nitrogen stream that contained water vapor. PVA nanofibers were electrospun from solutions. A concentration of $(\text{NH}_4)_2\text{HPO}_4$, equal to 2 % by weight of the PVA in the solution, was added to improve the coke formation and to form pores in the carbon nanofibers. The nanofibers of mesophase pitch, which is insoluble, were made from the melt by a different, undisclosed method.

MICROGRAPHIC OBSERVATIONS

Figure (1 A) shows two segments of the same carbonized pitch nanofiber which are similar, but the segment at the right contains an interesting kind of inclusion which was occasionally seen. The images show that the lamellar structure is oriented so that the axis of the fiber lies in the graphitic planes. The spacing between the lines on the surface of the nanofiber in Figure 1A is somewhat greater than the spacing between the graphitic planes. The diffraction pattern from this nanofiber is shown in Figure (1 B). The spacing of the (002) planes in the carbonized mesophase pitch nanofibers is the same as that observed in other carbon fibers. The height (along the arc) of the equatorial spots associated with the graphitic planes show that these planes have a waviness that is about the same as the waviness of the lines in Figure (1 A). The presence of other diffraction spots provides additional information about the structure.

Carbon nanofibers from PAN, and the corresponding water treated nanofibers are shown in a previous paper [2]. The PAN derived carbon nanofibers are smoother than the nanofibers from pitch, had a diameter of around 250 nm, and are relatively brittle. The water treated fibers had pores with diameters of a few tens of nm, that are easily noticed in the micrographs [2].

In the carbon nanofibers made from PVA, $(\text{NH}_4)_2\text{HPO}_4$ decomposes to ammonia which evaporates during the carbonization. This process produces a porous form of carbon fiber. The PVA derived carbon nanofibers are shown in Figure (2A). The nanofibers are strong enough to withstand the handling required to make samples for examination in the transmission electron microscope, but they break and crumble easily during ordinary handling. Figure [2B] shows a high magnification view of one nanofiber. Grains and pores on a scale ranging around ten nanometers are evident throughout the nanofiber. Figure [3C] shows the electron diffraction pattern from a typical PVA derived nanofiber. The diffraction pattern shows that the carbon grains in the nanofibers are very small and randomly oriented.

Bending instability of electrically charged liquid jets of polymer solutions in electrospinning

Darrell H. Reneker^{a)}

Department of Polymer Science, The University of Akron, Akron, Ohio 44325-3909

Alexander L. Yarin

Technion-Israel Institute of Technology, Haifa 32000, Israel

Hao Fong and Sureepom Koombhongse

Department of Polymer Science, The University of Akron, Akron, Ohio 44325-3909

(Received 20 September 1999; accepted for publication 25 January 2000)

Nanofibers of polymers were electrospun by creating an electrically charged jet of polymer solution at a pendent droplet. After the jet flowed away from the droplet in a nearly straight line, it bent into a complex path and other changes in shape occurred, during which electrical forces stretched and thinned it by very large ratios. After the solvent evaporated, birefringent nanofibers were left. In this article the reasons for the instability are analyzed and explained using a mathematical model. The rheological complexity of the polymer solution is included, which allows consideration of viscoelastic jets. It is shown that the longitudinal stress caused by the external electric field acting on the charge carried by the jet stabilized the straight jet for some distance. Then a lateral perturbation grew in response to the repulsive forces between adjacent elements of charge carried by the jet. The motion of segments of the jet grew rapidly into an electrically driven bending instability. The three-dimensional paths of continuous jets were calculated, both in the nearly straight region where the instability grew slowly and in the region where the bending dominated the path of the jet. The mathematical model provides a reasonable representation of the experimental data, particularly of the jet paths determined from high speed videographic observations. © 2000 American Institute of Physics. [S0021-8979(00)03609-4]

I. INTRODUCTION

Electrospinning is a straightforward and cost effective method to produce novel fibers with diameters in the range of from less than 3 nm to over 1 μm , which overlaps contemporary textile fiber technology. Polymer nanofibers are being used, or finding uses, in filtration, protective clothing, biomedical applications including wound dressings, drug delivery systems, the design of solar sails, light sails, and mirrors for use in space, the application of pesticides to plants, as structural elements in artificial organs, and in reinforced composites. Ceramic or carbon nanofibers made from polymeric precursors make it possible to expand the list of possible uses for nanofibers. The electrospinning process easily incorporates particles of materials such as pigments, carbon black particles, and many others into the nanofibers that are produced. Flexible fibers are needed on a scale commensurate with micro- or nanoelectrical, mechanical and optical systems. The use of Coulomb forces to fabricate polymer objects may lead to ways to make such fibers *in situ* for such devices.

Observations and a theoretical model of the electrospinning process are presented in this article. The theory accounts for the nonlinear effects that are characteristic of finite perturbations, as well as for the rheological behavior of viscoelastic liquids. The general reason for the bending in-

stability in electrospinning is discussed. The three-dimensional equations describing the dynamics of the bending of electrospun jets are derived and the calculated behavior is compared with experimental observations of jets.

A. History and patents

Interest in the behavior of thin liquid jets in electric fields dates back to the work of Rayleigh.¹ Later Zeleny² studied liquid jets in strong electric fields. Theoretical and experimental activities in this area in the last 30 years were revitalized by several important contributions by Taylor.³⁻⁶ He produced useful experimental evidence, and calculated the conical shape of the protrusion from which a jet sometimes leaves the surface of a liquid. Taylor also made the first attempt to calculate the growth rates of both varicose and bending perturbations of electrified liquid jets in the linear approximation when the perturbations are small. In his theoretical analysis, only inviscid fluids were considered.

The bending instability of thin, highly viscous jets moving in air, with no electrical forces, is a kindred phenomenon to that treated in the present work. The theory of the bending instability of uncharged jets was developed and described by Yarin and co-workers.⁷⁻¹⁰

Electrified jets of polymer solutions were investigated as routes to the manufacture of polymer nanofibers.¹¹⁻¹⁵ Since 1934, when a U.S. patent on electrospinning was issued to Formhals,¹⁶ over 30 U.S. patents have been issued.

^{a)}Electronic mail: dhr@polymer.uakron.edu

Structure of Poly(ferrocenyldimethylsilane) in Electrospun Nanofibers

Zhihao Chen, Mark D. Foster,* Wensheng Zhou, Hao Fong, and Darrell H. Reneker

Department of Polymer Science, The University of Akron, Akron, Ohio 44325

Rui Resendes and Ian Manners

Department of Chemistry, University of Toronto, 80 St. George Street, Toronto, Ontario M5S 3H6, Canada

Received November 2, 1999

Revised Manuscript Received August 21, 2000

Introduction. Poly(ferrocenylsilane) polymers, consisting of alternating ferrocene units and silicon atoms in the main chain, have novel redox, electrical, optical, chemical, and other characteristics.¹⁻³ Replacing the conventional condensation synthesis by ring-opening polymerization (ROP) of silicon-bridged ferrocenophane has made it possible to make well-defined, high molecular weight materials and to tailor their structure.⁴⁻⁶ These materials present scientific challenges both in characterizing their structure and in understanding how this structure can best be exploited in various applications.

Poly(ferrocenyldimethylsilane), $[-(fc-Si(CH_3)_2)]_n-$, where $fc = Fe(\eta-C_5H_4)_2$ is a recently discovered crystalline material. Single crystals obtained by precipitation from solution of the pentamer analogue, penta(ferrocenyldimethylsilane),⁷ have been characterized with wide-angle X-ray diffraction (WAXD). Those X-ray diffraction data displayed many sharp peaks,⁷ with the most intense corresponding to d spacings of 0.58, 0.63, and 0.66 nm. The investigators in that work proposed a triclinic crystal structure⁷ having the lattice parameter values $a = 1.176$ nm, $b = 1.185$ nm, $c = 1.251$ nm, $\alpha = 94.85^\circ$, $\beta = 114.15^\circ$, and $\gamma = 117.66^\circ$. Powder patterns of poly(ferrocenyldimethylsilane) (PFDMS) polymers⁸ (Figure 1) of several molecular weights have also been measured. The WAXD data showed the strongest peak at a d spacing of 0.637 nm. The authors ascribed that spacing to the distance between sets of planes containing the iron atoms since that element has a relatively high scattering length. Other peaks seen in the WAXD pattern from each polymer powder were associated with d spacings of 0.379, 0.445, and 1.106 nm.⁸

One form into which the poly(ferrocenylsilane) polymers could be processed to provide novel possibilities is that of nanofibers.^{9,10} Nanofibers created by electrospinning^{11,12} have very high surface area to mass ratios, e.g., 1000 m²/g for a fiber with a diameter of 50 nm. The smallest nanofibers¹³ with a diameter of only 3 nm have 50% of the molecules on the surface. They present a confined environment in which one might expect deviations in the structure from that characteristic of conventional fibers. Here electron diffraction from a segment of a single nanofiber has been used to characterize its crystalline structure, which is compared with what is known of the crystal structure in related samples. Unit cell parameters were determined using usual methods for analysis of X-ray fiber diffraction patterns.

Experimental Section. The poly(ferrocenyldimethylsilane) homopolymer used to create nanofibers was

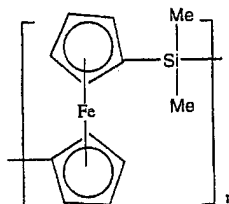


Figure 1. Chemical structure of poly(ferrocenyldimethylsilane).

prepared by Pt-catalyzed ROP in the presence of Et_3SiH^1 and had a molar mass, M_w , of 87 000 g/mol and polydispersity index of 1.3 as measured by gel permeation chromatography using universal calibration relative to polystyrene standards. The polymer powder was dissolved at room temperature in a mixture of 90 wt % tetrahydrofuran and 10 wt % dimethylformamide to create a viscous orange solution that contained 30 wt % polymer.

PFDMS nanofibers were created by electrospinning. The setup of the apparatus has been described elsewhere.¹² The solution was first transferred into a capillary pipet charged to a high electrical potential (160 μA at 30 kV). As the electrical potential was gradually increased, a liquid jet issued from the surface of the droplet and flew toward a grounded metal mesh collector. The solidified nanofibers were collected on a grid for study with transmission electron microscopy (TEM) or on a screen or cover glass for study by optical microscopy and scanning electron microscopy (SEM). A layer of evaporated carbon was deposited on the TEM sample grids to prevent the nanofibers from becoming charged by the electron beam.

A Nikon polarizing microscope was used to observe and photograph the nanofibers on cover glasses. The morphology of fibers and distribution of fiber sizes were observed using SEM. Smaller scale morphology was observed using a JEOL JEM-1200LX microscope operated at an accelerating voltage of 120 kV. Electron diffraction patterns were recorded on photographic film and scanned using a digital image scanner (Minolta Dimage Scan Multi Scanner).

Results and Discussion. The fibers studied ranged from around 100 to 1000 nm in diameter. When observing a collection of nanofibers with different diameters, using backscattered light (epi-illumination with white light) by optical microscopy, different interference colors were seen from fibers of different diameter. Birefringence characteristic of fibers with polymer molecules extended along the fiber axis was observed by rotating the fibers between crossed polarizers in an optical microscope.

A TEM negative image (150 000 \times) of a short segment of one nanofiber is shown in Figure 2. The variation in brightness across the fiber reveals that the beam is able to penetrate the fiber and that the distance traversed by the beam varies from the edge of the fiber to the middle. Figure 3a presents an electron diffraction pattern from the as-spun nanofiber shown in Figure 2 taken with the fiber axis perpendicular to the electron beam. The pattern is consistent with the notion that

David R. Salem (Editor)

Structure Formation in Polymeric Fibers

With Contributions from

N. Aminuddin, D.G. Baird, C.W.M. Bastiaansen, J. Blackwell,
S.Z.D. Cheng, B. Claus, J.A. Cuculo, H. Fong, M.W. Frey,
R.V. Gregory, F.W. Harris, J.W.S. Hearle, J.F. Kotter,
D.J. Johnson, R.K. Krishnaswamy, P.J. Lemstra, C.Y. Li, F. Li,
K.W. McCreight, N.S. Murthy, S. Raastog, D.H. Reneker,
D.R. Salem, J.M. Schultz, J.E. Spruiell, N.Vasanthan, Y. Yoon,
Q. Zhou

HANSER

Hanser Publishers, Munich

Hanser Gardner Publications, Inc., Cincinnati

6 Electrospinning and the Formation of Nanofibers

Hao Fong and Darrell H. Reneker
University of Akron, Akron, Ohio, USA

6.1 Introduction	225
6.2 Electrospinning Process	227
6.2.1 Jet Initiation and the Diameters of a Single Jet	228
6.2.2 Bending Instability and the Elongation of the Jet	229
6.2.3 Diameter of Nanofibers	233
6.2.4 Observations of Electrospinning of Polyethylene Oxide Solution: Length of the Straight Segment, Flow Rate of the Solution, Current, and Voltage	234
6.3 Nanofibers and their Unique Properties	236
6.3.1 Beaded Nanofibers	236
6.3.2 Electrospun Poly (<i>p</i> -phenylene terephthalamide)	237
6.3.3 Composites with Nanofiber Reinforcement	239
6.3.4 Elastomeric Poly(styrene-butadiene-styrene) Nanofibers, Phase Miscibility	240
6.3.5 Carbon Nanofibers	241
6.3.6 Nanofibers for Biomedical, Filtration, Agricultural, and Outer-Space Applications	244
6.4 Acknowledgements	245
6.5 References	245

6.1 Introduction

Electrospinning is a straightforward method that produces polymer nanofibers. When the electrical force at the surface of a polymer solution or polymer melt overcomes the surface tension, a charged jet is ejected. The jet extends in a straight line for a certain distance, and then bends and follows a looping and spiraling path. The electrical forces elongate the jet thousands or even millions of times and the jet becomes very thin. Ultimately the solvent evaporates, or the melt solidifies. The resulting, very long, nanofiber collects on an electrically grounded metal sheet, a winder or some other object, often in the form of a non-woven fabric.

The electrospinning process makes fibers with diameters in a range one or two orders of magnitude smaller than those of conventional textile fibers. The small diameter provides a large surface area to mass ratio, in the range from $10 \text{ m}^2/\text{g}$ (when the diameter is around 500 nm) to $1000 \text{ m}^2/\text{g}$ (when the fiber diameter is around 50 nm). The equipment required for electrospinning is simple and only a small amount of polymer sample is needed to produce nanofibers.

STRUCTURE AND MORPHOLOGY OF POLY(META-PHENYLENE ISOPHTHALAMIDE) NANOFIBERS PRODUCED BY ELECTROSPINNING

Wenxia Liu, Zongquan Wu and Darrell H. Reneker

Department of Polymer Science
The University of Akron
Akron, Ohio 44325-3909 USA

Introduction

Fibers of Poly(meta-phenylene isophthalamide) (MPD-I) were commercialized by the Dupont company under the trademark of Nomex®. The fiber is characterized by its thermal stability and flame resistance, which are attributed to the aramid groups and hydrogen bonds through acidic N-H groups [1]. Depending upon the type, MPD-I fibers are applicable to a wide variety of consumer and industrial uses, from protective clothing, upholstery and carpets to filter bags and honeycomb structures for airplane construction [2].

In this study, MPD-I nanofibers were prepared by electrospinning, a straightforward method to produce novel fibers with diameters in the range of from less than 3 nm to over 1 μm [3]. During the electrospinning process, a charged jet of polymer solution bent and elongated into spiraling loops [3]. This was observed by a high-speed, high-frame-rate video camera. These loops grew larger in diameter as the jet traveled and became thinner. After the solvent evaporated, nanofibers remained.

The morphological features and crystalline structure of MPD-I nanofibers were studied by scanning electron microscopy (SEM), transmission electron microscopy (TEM) and wide angle X-ray diffraction (WAXD).

Experimental

Nomex® fibers were obtained from the Dupont Company. The molecular weight was around 90,000 g/mole. The fibers were dissolved in N, N-dimethylacetamide (DMAc) containing 4% lithium chloride (LiCl) at 60 °C to form a homogeneous solution with 16% polymer concentration. The solution was filtered to remove any particles.

The experimental procedure used for electrospinning was similar to that described [4]. The voltage was in the range of 15 to 25 kilovolts. The applied electric field was around 10^4 V m^{-1} .

Results and Discussion

Figure 1 is a SEM micrograph showing a thin layer of electrospun MPD-I nanofibers on a conventional 9-micron diameter Nomex® textile fiber. The dramatic difference between the diameter of the electrospun fibers and that of the textile fiber is obvious. The nanofibers had a distribution in diameter ranging from 20 to 300 nm. Figure 2 is a TEM micrograph showing a web-like MPD-I nanofiber structure. The "web" was made of 20 nanometer diameter fibers. The connection of these fibers was caused by the contact of the fibers before the solvent totally evaporated. After the fibers dried in air, the web-like structure was solidified and remained among the other nanofibers.

Figure 3 (A) shows WAXD pattern of a yarn of as-spun MPD-I nanofibers. The diffuse equatorial spots indicate that the molecules were oriented to some extent, along the axis of the nanofibers. This orientation is also indicated by the optical birefringence of nanofibers. Figure 3 (B) shows the WAXD pattern of MPD-I yarn, after annealing at 320 °C for 4 minutes. The diffraction spots became much sharper, and other spots appeared, indicating that the as-spun fibers were in a metastable state. Thermal annealing improves crystallographic packing, since it allows cooperative picometer-scale molecular movements, which eliminate small irregular voids between molecules. The lattice spacings observed are 3.3, 3.7, 3.8, 4.4, 4.8 and 5.2 Å. These spacings are consistent with the triclinic crystal unit cell with dimensions of $a = 5.27 \text{ Å}$, $b = 5.25 \text{ Å}$, c (fiber axis) $= 11.3 \text{ Å}$, $\alpha =$

111.5° , $\beta = 111.4^\circ$ and $\gamma = 88.0^\circ$, proposed by Kakida et al. for MPD-I textile fibers [5]. The spots corresponding to (110), (011) and (101) planes have the strongest intensities, as is the case for MPD-I textile fibers.

Figure 4 is the electron diffraction pattern of an annealed MPD-I nanofiber annealed in the same way as the yarn. The diffraction spots from the (102) and (012) planes are weak and broad. The other spacings calculated from the stronger spots of the electron diffraction pattern are the same as those from the WAXD pattern of the yarn, demonstrating that the local structure of the nanofiber and the global structure of the yarn are the same.

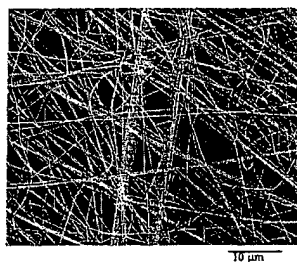


Figure 1. MPD-I nanofibers lying on a conventional MPD-I fiber, showing the relative diameters.

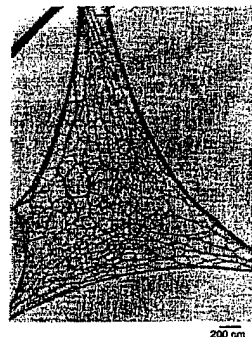
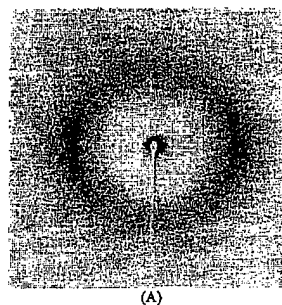


Figure 2. Web-like MPD-I nanofiber structure observed with a transmission electron microscope.



(A)

Bending instability in electrospinning of nanofibers

A. L. Yarin

Faculty of Mechanical Engineering, Technion, Haifa 32000, Israel

S. Koombhongse and D. H. Reneker^{a)}

Maurice Morton Institute of Polymer Science, Department of Polymer Science, The University of Akron, Akron, Ohio 44325-3909

(Received 17 July 2000; accepted for publication 23 October 2000)

A localized approximation was developed to calculate the bending electric force acting on an electrified polymer jet, which is a key element of the electrospinning process for manufacturing of nanofibers. Using this force, a far reaching analogy between the electrically driven bending instability and the aerodynamically driven instability was established. Continuous, quasi-one-dimensional, partial differential equations were derived and used to predict the growth rate of small electrically driven bending perturbations of a liquid column. A discretized form of these equations, that accounts for solvent evaporation and polymer solidification, was used to calculate the jet paths during the course of nonlinear bending instability leading to formation of large loops and resulting in nanofibers. The results of the calculations are compared to the experimental data acquired in the present work. Agreement of theory and experiment is discussed. © 2001 American Institute of Physics. [DOI: 10.1063/1.1333035]

I. INTRODUCTION

Electrospinning of polymer solutions and melts is a promising process for manufacturing fibers with cross-sectional diameters of about 10^2 nm.¹ Mechanics of this process deserve a special attention, since there is an urgent need for predictive tools to develop deeper understanding and optimization. As was shown in a recent publication of this group,² the bending instability of electrified polymer jets plays a central role in the electrospinning process. This relates the electromechanical aspects of the process to the pioneering studies of Taylor³ of the instabilities of electrified liquid jets of low-molecular mass Newtonian liquids. In particular, Taylor³ recognized that bending instability can occur, and derived a characteristic equation for small bending perturbations of an inviscid liquid column.

Discretized equations describing the dynamics of the bending instability of electrified jets of polymer solutions were proposed and solved in Ref. 2. In the present work we elucidate the relation of these equations to the quasi-one-dimensional partial differential equations of the dynamics of thin free liquid jets. The latter were proposed and used mainly in the studies of the aerodynamically driven bending instability of liquid jets moving in air with high enough speed.^{4,5} The main difference between the electrically and aerodynamically driven instabilities is in the nature of the destabilizing force. In Sec. II of the present work we introduce a localized approximation leading to a very simple expression for the bending force acting on the jet due to mutual Coulomb interactions. Using this force, in Sec. III we formulate the continuous quasi-one-dimensional partial differential equations of the dynamics of bending electrified jets. We

also show how these equations correspond to the discretized equations used in Ref. 2.

In Sec. IV we present the expressions for the growth rate and the wavelength of small electrically driven bending perturbations of an electrified liquid column. In Sec. V solvent evaporation and the related solidification processes are accounted for. Examples of calculations are shown, discussed and compared with experiment in Sec. VI. Conclusions are drawn in Sec. VII.

II. LOCALIZED APPROXIMATION

In the dynamics of thin vortices in fluids the localized-induction approximation is widely used to describe velocity induced at a given vortex element by the rest of the vortex line.⁶⁻¹⁰ A similar approach may be used to calculate the electric force imposed on a given element of an electrified jet by the rest of it. Consider an enlarged element of a curved jet shown in Fig. 1. We assume that the arc length ξ is reckoned along the jet axis from the central cross section of the element where $\xi=0$. We denote the coordinates reckoned along the normal and binormal by y and z , so that the radius vector of point A on the surface of the element $\mathbf{R}_{OA} = y\mathbf{n} + z\mathbf{b}$. The radius vector of point B at the jet axis close enough to the element considered is thus given by

$$\mathbf{R}_{OB} = \tau\xi + \frac{1}{2}|k_0|\xi^2\mathbf{n}, \quad (1)$$

where k_0 is the curvature of the jet axis at point O and τ is a unit tangent vector. Therefore

$$\mathbf{R}_{BA} = \mathbf{R}_{OA} - \mathbf{R}_{OB} = [y - \frac{1}{2}|k_0|\xi^2]\mathbf{n} + z\mathbf{b} - \tau\xi. \quad (2)$$

Denote the cross-sectional radius of the jet element by a , assume that charge is uniformly distributed over the jet surface with the surface density Δe , and denote the charge per

^{a)}Electronic mail: dhr@polymer.uakron.edu

Taylor cone and jetting from liquid droplets in electrospinning of nanofibers

A. L. Yarin

Faculty of Mechanical Engineering, Technion, Haifa 32000, Israel

S. Koombhongse and D. H. Reneker^{a)}

Maurice Morton Institute of Polymer Science, Department of Polymer Science, The University of Akron, Akron, Ohio 44325-3909

(Received 7 September 2000; accepted for publication 10 August 2001)

Sessile and pendant droplets of polymer solutions acquire stable shapes when they are electrically charged by applying an electrical potential difference between the droplet and a flat plate, if the potential is not too large. These stable shapes result only from equilibrium of the electric forces and surface tension in the cases of inviscid, Newtonian, and viscoelastic liquids. In liquids with a nonrelaxing elastic force, that force also affects the shapes. It is widely assumed that when the critical potential ϕ_{0*} has been reached and any further increase will destroy the equilibrium, the liquid body acquires a conical shape referred to as the Taylor cone, having a half angle of 49.3° . In the present work we show that the Taylor cone corresponds essentially to a specific self-similar solution, whereas there exist nonself-similar solutions which do not tend toward a Taylor cone. Thus, the Taylor cone does not represent a unique critical shape: there exists another shape, which is not self-similar. The experiments of the present work demonstrate that the observed half angles are much closer to the new shape. In this article a theory of stable shapes of droplets affected by an electric field is proposed and compared with data acquired in our experimental work on electrospinning of nanofibers from polymer solutions and melts. © 2001 American Institute of Physics. [DOI: 10.1063/1.1408260]

I. INTRODUCTION

Rayleigh¹ studied theoretically the stability of an isolated charged liquid droplet and predicted that it becomes unstable and fission takes place when the charge becomes sufficiently large compared to the stabilizing effect of the surface tension. Zeleny² tried to adapt this theory to the case of an electrified droplet losing its stability when jetting begins at its vertex. His theoretical results were corrected by Taylor³ in seminal work in which the spheroidal approximation of droplet shapes was proposed for the case of (i) a charged droplet sustained at a given potential Φ_0 relative to the ground, or (ii) an uncharged droplet in a given uniform field E .

Taylor showed that in case (i) a droplet raised to a potential Φ_0 could be sustained by surface tension in equilibrium with its own electric field provided the Rayleigh condition was satisfied, namely, at $\Phi_0(\pi R_0 \sigma)^{-1/2} < 4$, where R_0 is the volume-equivalent droplet radius, and σ is the surface tension coefficient. In spite of the fact that case (i) is quite similar to the situation in which a droplet is attached to an electrode mounted at some potential Φ_0 relative to the ground, the predictions of the spheroidal approximation do not agree with the experimental evidence. Instead, the theory predicted that, as Φ_0 increases and approaches the critical (Rayleigh) value, the stable shape becomes less and less prolate, tending toward a sphere, whereas in the experiment an increase in the potential results in more prolate droplets.

^{a)}Electronic mail: dhr@polymer.uakron.edu

Case (ii) corresponds to a droplet positioned inside a capacitor. As the strength of the field E increases, the droplet becomes more and more prolate until no shape is stable beyond some critical value E^* . This resembles the behavior recorded in Ref. 3 for droplets subjected to a higher and higher potential Φ_0 : they elongate to some extent, but then suddenly tend toward a cone-like shape. The boundary between the stable electrified droplets and those with a jet flowing from the tip lies somewhere near this potential. Taylor calculated the half angle at the tip of an infinite cone arising from an infinite liquid body. In Sec. II we calculate the half angle by a different method which brings out the self-similar nature of the Taylor cone, and state the assumptions involved in its calculation. Then, in Sec. III we consider a family of nonself-similar solutions for the hyperboloidal shapes of electrified liquid bodies in equilibrium with their own electric field due to surface tension forces. In Sec. IV we show that these solutions do not tend toward a self-similar solution corresponding to the family of the Taylor cone, and represent an alternative to the Taylor cone. Thus we conclude that another shape, one tending towards a sharper cone than that of Taylor, can precede the stability loss and the onset of jetting. In Sec. V we consider predictions of the hyperboloidal approximation in the case of bodies of elastic liquids. In Sec. VI experimental results are presented and compared with the theory. These results confirm the theoretical predictions of Sec. IV. A summary is presented in Sec. VII.

MOTION OF DROPLETS ALONG THIN FIBERS WITH TEMPERATURE GRADIENT

Alexander L. Yarin
Faculty of Mechanical Engineering
Technion, Haifa 32000, Israel

Wenxia Liu and Darrell H. Reneker
Maurice Morton Institute of Polymer Science,
The University of Akron,
Ohio 44325-3909, U.S.A.

Liquid n-decane, n-undecane, n-dodecane and n-hexadecane formed tiny symmetrical droplets on a partially wettable cylindrical fiber. When a temperature gradient was created along the fiber, the droplets began to move along the fiber toward the cold end. An explanation of the phenomenon is related to the thermocapillary motion. Other possible mechanisms were ruled out. The theoretical results and experimental data agree reasonably well.

I. INTRODUCTION

Small droplets deposited on a partially wettable cylindrical fiber are axisymmetric.¹ In the present experiments it was found that when a temperature gradient is created along a thin horizontal fiber, droplets begin to move toward the cold end. Motion of tiny droplets and bubbles driven by temperature gradients is typically related to the thermocapillary Marangoni convection.^{2,3} Thermal Marangoni effects result from surface tension changes, typically reduction of surface tension as temperature increases. In the experiments of Ref. 2, as well as in a number of works discussed in Ref. 3, it was shown that droplets and bubbles move toward the *hot end*. On the other hand, motion of thin liquid films toward the *cold end* demonstrated in Refs. 4. and 5 was also attributed to the thermocapillary Marangoni convection. The clue of this paradoxical contradiction is related, from our point of view, to the fact that in Refs. 2

Motion of droplets along thin fibers with temperature gradient,

Page 1 of 28

81

SECTION 4

**THE UNIVERSITY
OF
PENNSYLVANIA**

Sensors and Smart Fabrics

Subcontract between

North Carolina State University

and

University of Pennsylvania

Primary Sponsor: US Army Research Office

Primary Agreement No.: DAAH 04-96-1-0018

Final Report

Report Submitted by:*

Alan G. MacDiarmid
Department of Chemistry
University of Pennsylvania

Tel: 215-898-8307

Fax: 215-898-8378

e-mail: macdiarm@sas.upenn.edu

and

Wayne E. Jones Jr.
Department of Chemistry
State University of New York at Binghamton

Tel: 607-777-2421

Fax: 607-777-4478

e-mail: wjones@binghamton.edu

* Studies supported by the sub-contract were completed in collaboration with Dr. M. El-Sherif from Drexel University.

Abstract

During the three year duration of the sub-contract synthesis and development of thin film, conducting polymer-based optical sensors for detection of low-concentration molecular contaminants such as volatile nerve agents was achieved. Two conducting polymers were investigated, polyaniline (PANI) and polypyrrole (PPy). These polymers were prepared through chemical oxidation and the thin films were prepared using *in-situ* deposition techniques. In a parallel, complementary study, various $[\text{Cu}(\text{bpy})_x]^{2+}$ complexes were synthesized, characterized and incorporated into the polymer thin films to determine if their presence improved the optical sensing capability by decomposition of molecular analytes. Films were prepared on glass substrates and later on fiber optics in collaboration with Drexel University. In all cases, dimethyl methylphosphonate (DMMP) and diisopropyl fluorophosphonate (DFP) were used as nerve agent mimics and the electromagnetic response was monitored between 280nm – 1100nm. The largest reproducible switch (40%) was observed with PPy in the presence of DMMP. The overall result of these studies is very encouraging for the combination of these chemosensitive materials with integrated fiber optic assemblies. In addition, eight different graduate and undergraduate students and two post-doctoral fellows received training in this important area of scientific development.

Introduction and Background

The development of a garment based soldier platform to provide chemical and physical analysis of the battlefield environment represents an exciting interdisciplinary challenge. This team of investigators has been developing the integration of recent advances in conducting polymers with state of the art fiber optic signal processing and detection. The key is the application of organic conducting polymers to the surface of optical fibers in order to monitor changes in the optical response of these sensors to antagonist gases.

Conducting polymers represent an exciting class of inorganic and organic polymer materials, which have recently become highly investigated for use in sensor applications.¹ These polymers, that are typically conjugated, can be "doped" either chemically or electrochemically from the insulating state through the semiconducting state to the metallic state.² They can also be de-doped through these states, reversibly in many cases. During the doping/de-doping process many physical and chemical properties are modulated including the electronic, optical, and magnetic characteristics. In most electronic polymers doping (de-doping) occurs by partial oxidation (reduction) of the π backbone system of the polymer.³ A number of these polymers are also found to be stable under ambient conditions including polypyrrole, polyaniline, and more recently the polybenzothiophenes. For example, treatment of the polymer with vapors or solutions of oxidizing (reducing) agents can readily accomplish doping (de-doping). Polyaniline represents a unique case in these systems in that doping can *also* take place simply by protonation of the "emeraldine" (EB) oxidation state of the polymer by vapors or solutions of

acids. De-doping occurs equally simply from deprotonation by vapors or solutions of bases. Thus, conducting polymers are likely to be highly sensitive to a variety of properties common to chemical warfare agents.

A number of groups have investigated the response of the conductivity (resistivity) in these conjugated polymers in the presence of analytes.¹ While this has been, and continues to be effective, it is the *changes* in the optical properties *rather than conductivity* at which this research is specifically directed in order to exploit the advantages of fiber optics for the purpose of sensing chemical warfare agents. The use of changes in such properties has never previously been investigated for this purpose, though several groups have begun investigating fluorescence responses in conjugated polymers.⁴

One challenge to the combination of conducting polymers with fiberoptics is the adhesion of the polymer to the glass substrate at the interfaces. A number of studies have taken advantage of the solubility of these materials to spin coat a thin layer of polymer onto glass substrates. We have extended this technique to deposit a spin-coated film on an exposed section of the fiber optic filament. Recently, we have also been investigating the *in situ* deposition of conducting polymers on treated and untreated glass slides.⁵ This technique provides a number of advantages over spin coating for the investigations described here including uniform thin films, control of the fiber polymer interface, and ease of assembly.

Copper Bipyridine Complexes and Nerve Agents. In the past year we have shifted part of our focus on fiber optics to the incorporation of transition metal complexes of copper. A great deal of work on nerve agent simulants has lead to significant improvements in the area of decontamination in a number of different settings. Methods for decontamination include metal ion catalytic hydrolysis, enzymatic decontamination and biodegradation, and catalytic oxidation. It must be noted that in light of the extensive research devoted to nerve agent simulants, differences in the degradation of the actual nerve agent (rate, extent, mechanism, etc.) must be anticipated and accounted for³⁶. Of great interest for this current research is the metal ion catalytic hydrolysis, specifically in the presence of copper(II) 2,2' bipyridine (bpy) complexes. As can be expected, structural information regarding these complexes is of critical importance before an understanding of the hydrolysis mechanism can be achieved.

The synthetic procedure for generating these Cu(II) bpy complexes is a straightforward reflux of stoichiometric amounts of reactants in a purified, deoxygenated methanol solvent³⁷. Noack and Gordon were the first researchers to attempt a rigorous structure elucidation study via electron paramagnetic spectroscopy (EPR)³⁸. Probing the lone pair electrons in the central core Cu atom allows researchers to detect differences not only in the gross structure of the complex (i.e. number of bpy ligands complexed) but also in subtle differences in conformation of these ligands. Initial research by Noack and Gordon in the late 1960's indicated that the inner sphere of the mono- or bis(bpy) Cu(II) complex included water. They also were able to differentiate between the *cis* and *trans* isomers of the bis(bpy) complex via small differences in the coupling of the lone pair electrons on the central copper atom. Further solid state EPR work by Marov et.al. confirmed the structures elucidated by the Noack and Gordon ground breaking research³⁹. Very recent research on the configuration of these complexes offer insights into the actual structure of the molecule³⁷. In the bis(bpy) complex, the bpy ligands were shown to be non-planar, which the authors attribute to a steric interference between the 3,3' hydrogen atoms on

the adjacent ligands that prevents them from existing in the same plane. This same group also proposed structures of the $[\text{Cu}(\text{bpy})_2]^{2+}$ complex in various solutions: tetragonal in water, square pyramidal in a water-ethanol solution, and trigonal bipyramid in pure ethanol.

In the early 1970s, a dissenting opinion of the true structure of the bis(bpy) complex was offered by Dr. Walker and his associates⁴⁰. The analysis of the EPR data they generated indicated that instead of the bis(bpy) complex providing a new EPR signal, it was actually a superposition of the spectra obtained for the mono- and tris(bpy) complex. This idea led them to hypothesize that the bis(bpy) complex did not exist, and that due to thermodynamic considerations actually disproportionated into the mono- and tris(bpy) complexes. Current crystal data exists providing that the bis(bpy) complex is actually present, however this debate was quite active for more than two decades.

It is well established that nerve agents are difficult to oxidize or reduce, which makes the hydrolysis of these agents difficult to detect directly⁴¹. This situation required the development of indirect sensing methods based on either conductivity or enzymatic reactivity. In the case of Sarin and Soman gas or their simulants DMMP and DFP, the base molecule contains a fluorine atom (Figure 1). Therefore, if a reagent were able to evolve fluoride ion, the presence and



Figure 1. Structures of Nerve Agent Mimics.

ultimately the concentration of that ion could be measured using an ion-selective electrode. A great deal of research has centered around the catalytic ability of the $[\text{Cu}(\text{bpy})_x]^{2+}$ complexes to hydrolyze nerve agents and their simulants^{41,42,43}. Research by Xie, et.al. showed a drastic reduction in potential (vs. Ag/AgCl electrode) when a solution of a particular nerve agent mimic of Sarin (diisopropyl fluorophosphonate, DFP) was treated with a sample of a $[\text{Cu}(\text{bpy})_x]^{2+}$ complex⁴¹. Reaction rates of the hydrolysis of various nerve agent mimics in the presence of certain $[\text{Cu}(\text{bpy})_x]^{2+}$ complexes shows a tremendous increase in reaction rate, with reports as high as 1600 times greater⁴². Kinetics studies show that the rate of reaction is first order with respect to the quantity of the unreacted nerve agent simulant in the reaction mixture. In a more detailed look at the hydrolytic rate of various $[\text{Cu}(\text{bpy})_x]^{2+}$ complexes ($x=1, 2, 3$), there seems to be some consensus that the mono(bpy) complex ($x=1$) has the greatest catalytic activity^{41,42}. In this complex, EPR data seems to indicate that there are a number of water molecules bound to the central Cu atom. The working hypothesis for the mechanism of this hydrolysis reaction is that one of the water molecules is displaced by one of the oxygen atoms on the nerve agent simulant where it is degraded, and the copper complex is then regenerated^{41,42,43,44}. Other nerve agent mimics were exposed to various copper bpy complexes with similar results⁴⁴.

Plan of Attack

The focus of the research presented in the following sections outlines work conducted on synthesizing and developing an optical sensor created by the coupling of the unique actions of conducting polymers and the catalytic nature of the $[\text{Cu}(\text{bpy})_x]^{2+}$ complexes. Using *in-situ* deposition techniques, thin films of the conducting polymers polyaniline and polypyrrole were synthesized either with or without the $[\text{Cu}(\text{bpy})_x]^{2+}$ complex incorporated into the polymer matrix. These films were then exposed to two different nerve agent mimics (diisopropyl fluorophosphonate, DFP, and dimethyl methylphosphonate, DMMP) and their optical response to these vapors was measured. Pre- and post-exposure UV/Vis spectra were taken to determine if there was an increase or decrease in absorption across the entire wavelength range (300nm – 1100nm). An extension to this sensing project was undertaken as a result of the collaboration with the University of Pennsylvania and Drexel University. This arm of the project investigated the ability of an etched fiber optic, coated with a conducting polymer (*in-situ* deposition), to detect the presence of the above mentioned nerve agent simulants via an increase or decrease in power across the etched portion of the fiber. Another extension included the chemistry behind the $[\text{Cu}(\text{bpy})_x]^{2+}$ complexes, especially their structure elucidation.

Characterization techniques for the conducting polymer films (before and after exposure to nerve agent simulants) centered on the UV/Vis and infrared spectra as benchmarked against various literature sources^{45,46,47}. Energy dispersive spectroscopy (EDS) was used to determine if the $[\text{Cu}(\text{bpy})_x]^{2+}$ complex in the polymer matrix was evenly distributed throughout the *in-situ* deposited polymer film. Electron paramagnetic resonance (EPR) spectroscopy and X-ray diffraction (XRD) were employed to elucidate the structure of the $[\text{Cu}(\text{bpy})_x]^{2+}$ complexes used. Optical microscope techniques confirmed the etching procedure for the fiber optics, and a monochromatic laser and power measurements were used to characterize any change associated with the *in-situ* deposited fiber optic in the presence of the nerve agent mimics DFP and DMMP, Figure 1.

Experimental Techniques Developed

A. Preparation of $[\text{Cu}(\text{bpy})_2(\text{NO}_3)](\text{NO}_3)$

$\text{Cu}(\text{NO}_3)_2 \cdot 2.5\text{H}_2\text{O}$ (Aldrich Chemical) and bipyridine (Aldrich Chemical) were used as received from the supplier. 0.256g (1.1mmol) of $\text{Cu}(\text{NO}_3)_2 \cdot 2.5\text{H}_2\text{O}$, along with 0.343g (2.2mmol) bipyridine, were added to 50mL methanol (Fischer Scientific, used as received) in a 100mL round bottom flask. The reaction mixture was purged with N_2 and left to reflux for approximately 20 hours under continuous mixing. The reaction mixture was reduced in volume by half (rotoevaporation) and left for >3 days to crystallize. Crystals were clear blue with rod-like geometry. Elemental – Theoretical: 48.0% C, 3.2% H, 16.8% N; Actual: 47.6% C, 3.1% H, 16.6% N.

B. Preparation of $[\text{Cu}(\text{bpy})(\text{NO}_3)_2]$

$\text{Cu}(\text{NO}_3)_2 \cdot 2.5\text{H}_2\text{O}$ (Aldrich Chemical) and bipyridine were used as received from the supplier. Similar reflux process (conditions and duration) as previously described, however reactant ratios were altered: 0.256g (1.1mmol) of $\text{Cu}(\text{NO}_3)_2 \cdot 2.5\text{H}_2\text{O}$ and 0.172g (1.1mmol) bipyridine. Crystals were clear blue with rod-like geometry. Elemental – Theoretical: 34.9% C, 2.3% H, 16.3% N; Actual: 35.0% C, 2.2% H, 16.2% N.

C. Preparation of $[\text{Cu}(\text{bpy})_2\text{Cl}_2]$

$\text{CuCl}_2 \cdot 2\text{H}_2\text{O}$ (Fischer Scientific) and bipyridine were used as received from the supplier. Similar reflux process (conditions and duration) as previously described, however reactant were altered: 0.170g (1.1mmol) of $\text{CuCl}_2 \cdot 2\text{H}_2\text{O}$, along with 0.343g (2.2mmol) bipyridine. Crystals appeared to be very small, opaque, light blue with cubic geometry. Elemental – Theoretical: 34.9% C, 2.3% H, 16.3% N; Actual: 35.0% C, 2.2% H, 16.2% N.

D. Infrared Spectroscopic Characterization of $[\text{Cu}(\text{bpy})_2]^{2+}$ Complexes

Infrared spectroscopy (IR) was one of the primary characterization techniques used for these complexes. IR scans were performed on a Nicolet 20SXC FTIR Spectrometer using KBr pellets (KBr from Aldrich Chemical, stored in dessicator and used as received) pressed with a lab-scale Carver Press (Model C) using flat-faced, polished stainless steel tooling.

E. Single Crystal X-Ray Diffraction Characterization of $[\text{Cu}(\text{bpy})_2]^{2+}$ Complexes

Obtaining accurate information regarding the true molecular structure was of utmost importance during this research project. Single crystals were produced from these reaction mixtures, and X-Ray diffraction (XRD) was performed (Bruker AXS, Inc. – hardware and software) by the Institute for Materials Research, Binghamton University (Binghamton, NY).

The XRD experiments done for this study were performed at two different temperatures: room temperature (approximately 293K) and low temperature (77K), at an X-ray wavelength of 0.71073Å. The reason for the low temperature experiments was to prevent any transformation of the crystal structure that was withdrawn from the reaction mixture prior to capture of relevant XRD data.

F. Preparation of Hydrophilic Slides

A solution was prepared of 100mL concentrated H_2SO_4 and 50mL 30% H_2O_2 (Piranha Solution) under constant mixing. The glass slides were immersed (as received from manufacturer) into the solution and allowed to soak for at least 1 hour. After removing the slides from the Piranha Solution, each slide was rinsed with DI water and dried with a stream of N_2 . These cleaned slides were placed in a dessicator (under vacuum) until needed.

G. Preparation of Hydrophobic Slides

A 0.5% (v/v) solution of octadecyl trichlorosilane (OTS, Aldrich Chemical, used as received) in hexanes (Aldrich Chemical, used as received) was prepared by adding 0.5mL OTS to 100mL hexanes under constant mixing. The slides were removed from the solution after 30s immersion, and dried under a stream of room temperature N_2 . These functionalized slides were placed in a dessicator under vacuum until needed.

H. Preparation of Etched Fiber Optics (Drexel University, Philadelphia, PA)

Fiber optics (Corning, Inc.) were used as received from the manufacturer. A section of approximately 30cm was isolated from the bulk roll. A small section of the fiber (approximately 5cm) was immersed in hydrofluoric acid, HF, (48% aqueous, Aldrich Chemical) for 80-90 minutes. This treatment of the fiber removes the cladding from the fiber and exposes the core. This etched portion of the fiber is subsequently coated with a conducting polymer and tested.

I. Preparation of In-Situ Deposited Polypyrrole Films on Functionalized Glass Slides or Etched Fiber Optics

Pyrrole (Aldrich Chemical) was distilled under vacuum and stored under nitrogen. The oxidant solution was prepared by adding 3.5g FeCl_3 (J.T. Baker, used as received) to 100mL of DI water and allowed to dissolve under constant stirring until a clear orange solution was obtained. To this solution 1mL of 1M HCl was added as dopant for the polymerization reaction. In a separate beaker, 0.6mL pyrrole monomer was added to 100mL of DI water and allowed to mix until the pyrrole was incorporated into solution. Glass slides (hydrophilic or hydrophobic)

and/or etched fiber optics were immersed in the FeCl_3 solution, after which the pyrrole solution was added. Time was started when the last drop of monomer solution was added to the reaction vessel. Slides/fibers were removed at different time intervals, ranging from 2 minutes to 15 minutes. Once the slides/fibers were removed from the reaction mixture, they were immersed in a DI water bath to remove any aggregates of polypyrrole that may have adhered to the slide/fiber surface. After >10 minutes of soaking, the slides/fibers were rinsed under a stream of DI water to further clean the slide/fiber surface. After this rinsing process was complete, each slide/fiber was dried with a stream of N_2 and then placed in a dessicator (under vacuum) for further drying and storage until needed.

J. Preparation of *In-Situ* Deposited Polyaniline Films on Functionalized Glass Slides or Etched Fiber Optics

Aniline (Aldrich Chemical) was distilled under vacuum and stored under nitrogen. The oxidant solution was prepared by adding 1.45g $(\text{NH}_4)_2\text{S}_2\text{O}_8$ (Aldrich Chemical, used as received, stored in refrigerator under nitrogen) to 100mL of 1M HCl in a volumetric flask. In a separate 100mL volumetric flask, 2.0mL freshly distilled aniline was added to 1M HCl. A 50mL aliquot of the oxidant solution was pipetted from the volumetric flask and added to a clean 150mL beaker under constant stirring. Slides and/or etched fibers were added to this beaker. Another pipet was used to obtain a 50mL sample of the aniline solution. This solution was added to the oxidant solution to initiate the reaction. Timing started as soon as the last drop of aniline was added to the reaction vessel. The remaining aniline solution (50mL) was added to a 100mL beaker. As the slides/fibers were removed from the reaction vessel, they were immersed in the beaker containing the remainder of the aniline solution under constant stirring to remove any polymer aggregates that may have adhered to the surface of the slide/fiber, as well as remove any pernigraniline that may have deposited. The slides/fibers were then dried under a stream of N_2 and placed in a dessicator (under vacuum) to await later use.

K. Spin Coated Deposition

Polyaniline (emeraldine base - EB) was synthesized by following our published method.[6] A 1.0% (w/v) solution was made by dissolving 0.1 gram of emeraldine base powder slowly in 10ml N-methylpyrrolidinone (NMP) solvent with stirring. The dark blue solution was stirred for ~20 hours before it was filtered through a $0.45\mu\text{m}$ filter. A 3.0% (w/v) solution was made in the same way, i.e., 0.3 gram EB powder in 10ml NMP solvent followed by filtration. A 5.0% (w/v) solution was made in the same way, i.e., 0.5 gram EB powder in 10ml NMP solvent followed by filtration.

L. Ultraviolet/Visible Spectroscopy Characterization of Thin Films

The ultraviolet/visible (UV/Vis) spectroscopic analysis was conducted on a Perkin Elmer Spectroscope (scan rate of 4 nm/sec). UV/Vis is a very good characterization tool for substances that are colored. The absorption corresponds to electronic transitions within the molecule that occur within the ultraviolet to visible region of the electromagnetic radiation spectrum. Both polyaniline (green to dark blue) and polypyrrole (pale gray to light brown) are colored, and thus can be characterized by UV/Vis spectroscopy. Polyaniline has a characteristic maximum absorbance at approximately 366nm, as well as a free carrier tail for the emeraldine salt form (green). Polypyrrole has maxima at approximately 466nm, as well as a free carrier tail.

M. Energy Dispersive Spectroscopy Characterization of $[\text{Cu}(\text{bpy})_2]^{2+}$ Dispersed in Thin Polymer Film

Energy dispersive spectroscopy (EDS) was conducted on an Electroscan Model 2020 (accelerating potential=20 kV, current = 10nA, PGT IMIX System with a thin window, PRISM, detector).

Results and Discussion

A. Optical and Conductivity Changes upon Exposure to Acidic/basic Vapors

Films prepared in this manner on glass slides could readily be evaluated by spectroscopy. Shown in Figure 1 is the difference in UV-vis-NIR absorption observed after exposure to acid (HCl) or base (NH₃) vapors for 30 seconds. It should be noted that the UV/Vis spectra showed a very large change in intensity of wavelengths beyond 1300nm. This indicated that light sources at these wavelengths may also give a very large change in light intensity.

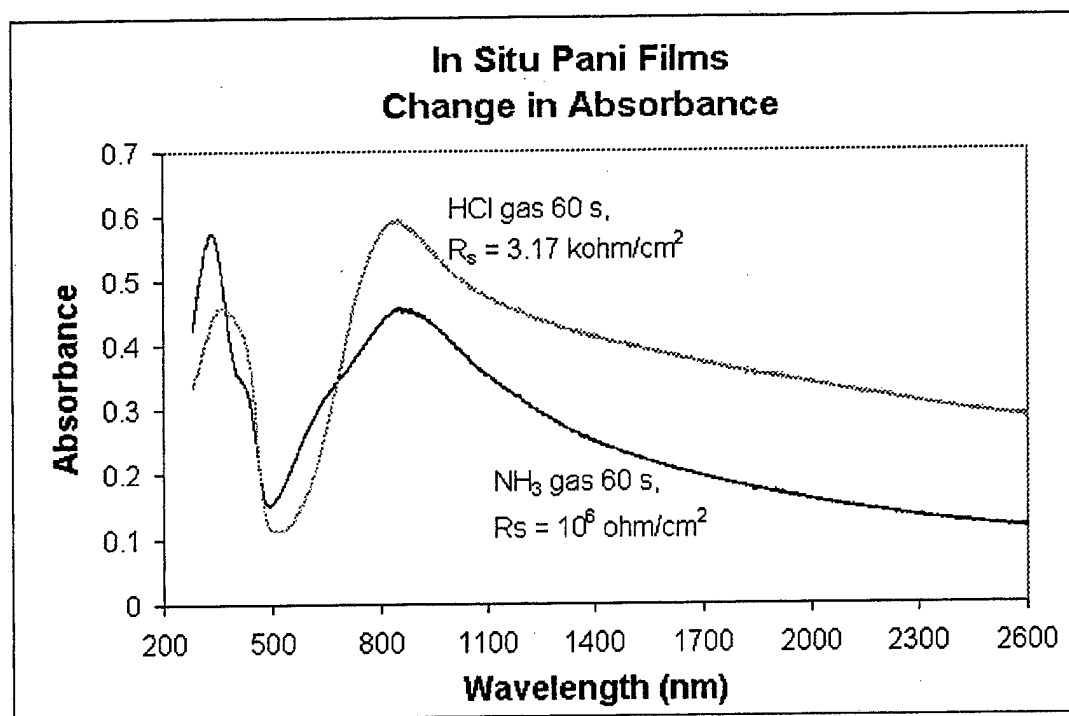
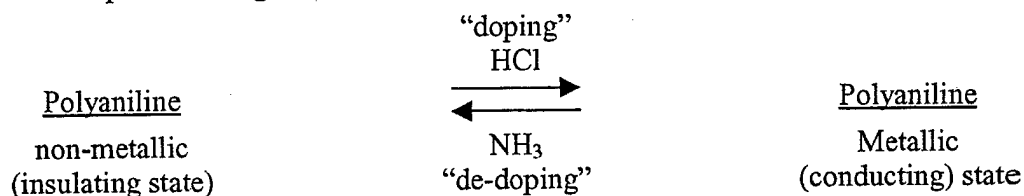


Figure 1. Changes of in situ deposited polyaniline induced by acid (HCl) or base (NH₃) vapor.

The observed spectral changes above are consistent with the processes:



B. Time Response of Films to Acid/Base Vapors

As shown in Figure 2 there is a range of different spectra observed for the glass slides as a function of the elapsed time following the initial exposure to the vapor. The optical response of the *in situ* deposited films on glass was very rapid. Preliminary conductivity measurements also suggest that the change in conductivity was rapid, but that following ammonia exposure, when the film was left in air, there was a slow reformation of the acid form. It is important to note the three isosbestic points in this data which indicate that this is a reversible process involving two components interchanging, consistent with the equilibrium described above.

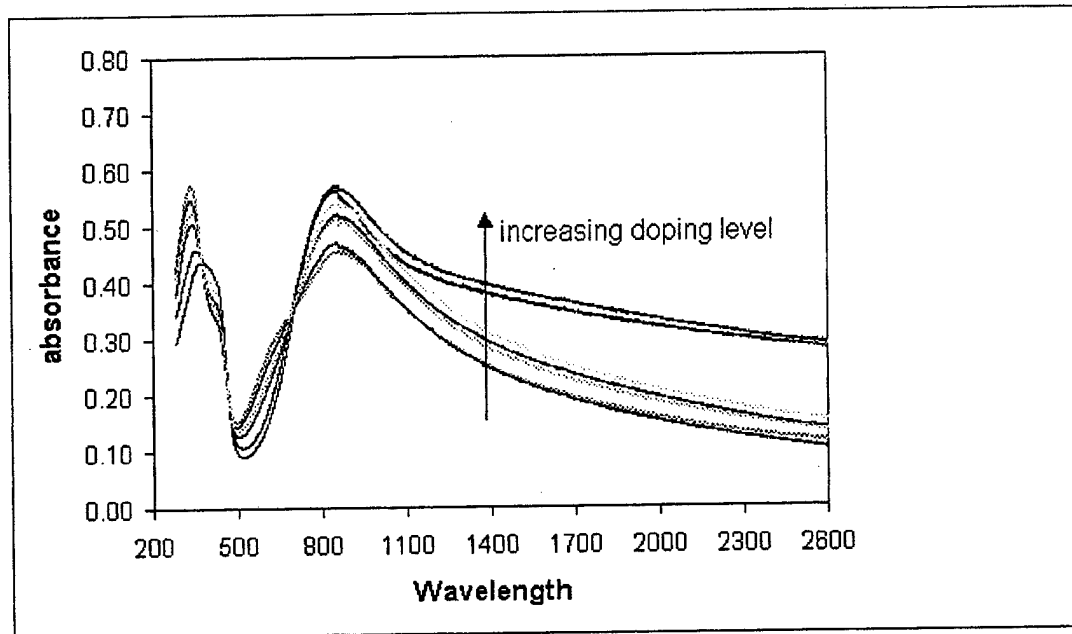


Figure 2. Change in absorption induced under varying doping levels for *in situ* polyaniline.

In order to determine the amount of time necessary for both the complete optical conversion of the thin film and the time required for recovery, we monitored the UV-vis-NIR as a function of time following exposure of the sample to acid or base vapor. The result is shown in Figure 3 when monitoring at 2000 nm near the maximum difference in absorption.

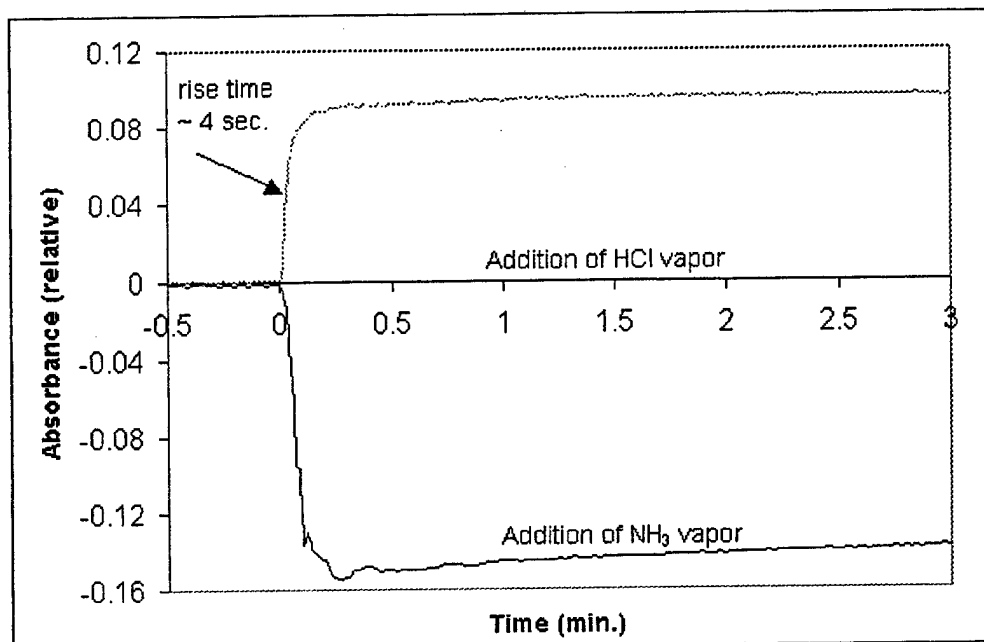


Figure 3. Time resolved absorption following exposure to acid or base vapors.

This initial change in absorbance for either the acid (a) or base (b) is very rapid occurring in ~ 4 seconds. The acid form of the polymer is stable and does not change once formed. The base form of the polymer slowly decomposes to the acid form by loss of ammonia, presumably from the NH_4Cl product of the acid base reaction. This occurs over the course of 1-2 hours. The first 20 minutes of this re-doping process are shown in figure 4. Note that a significant portion of the change occurs within the 10-20 seconds necessary to transfer the sample to the spectrometer.

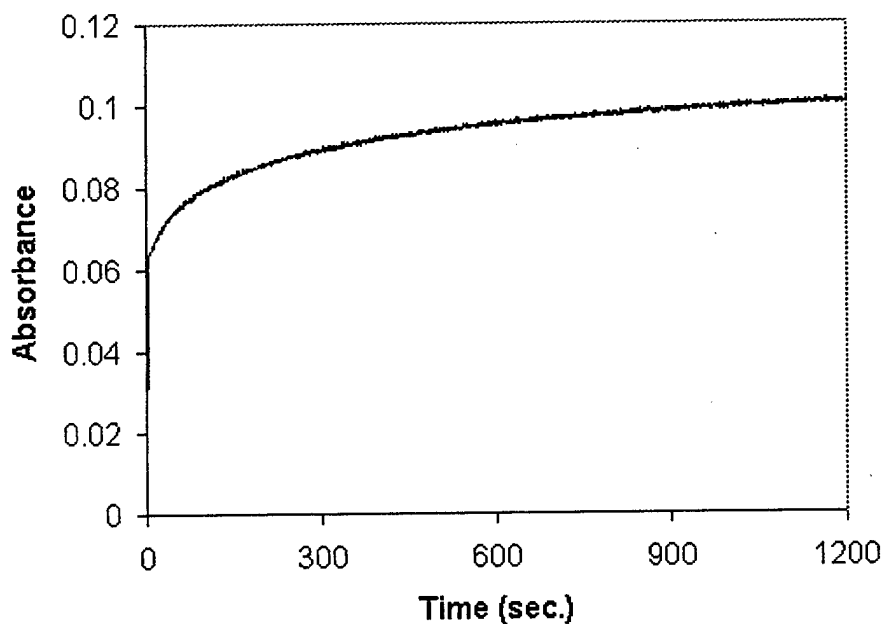


Figure 4. Absorbance change of thin film de-doped with NH_3 and allowed to stand in air.

The kinetics of this increase in absorption is complex. Initial attempts to fit the decay were unsuccessful. The data did not fit first or second order kinetic processes.

C. Optical Response to Oxidizing/Reducing Agents

Polyaniline, as mentioned above responds optically to changes in acidity as well as changes in oxidation state.[2] In order to evaluate *in situ* deposited films in oxidizing or reducing environments a sample was exposed to the highly corrosive chemical agent hydrazine (N_2H_4) which is highly reducing and capable of converting the emeraldine form of the polymer to the leucoemeraldine base. There was an observable loss of color from the film immediately upon exposure to hydrazine vapor consistent with the spectra shown in Figure 5. This change in absorption was stable on a time scale of hours with only minor changes in the absorption spectrum.

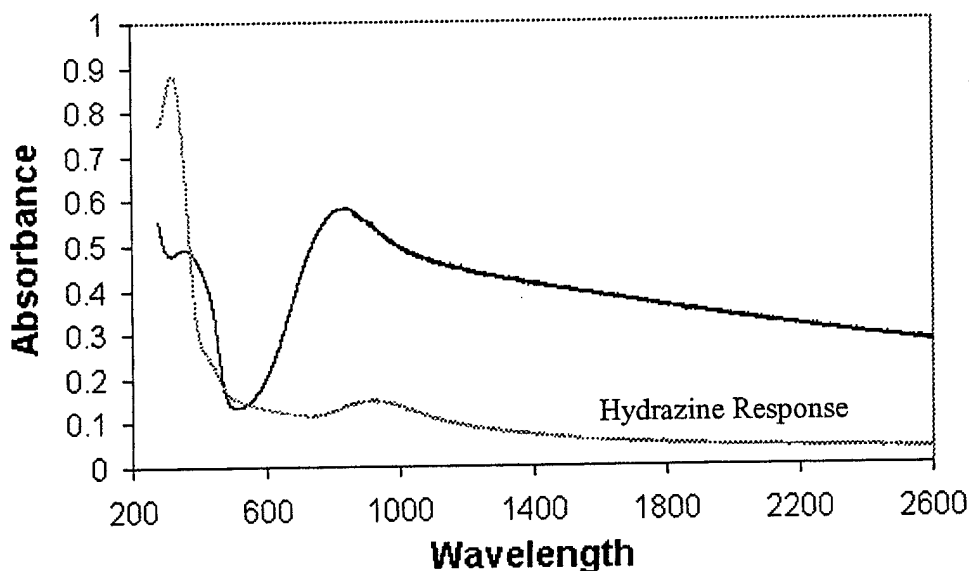


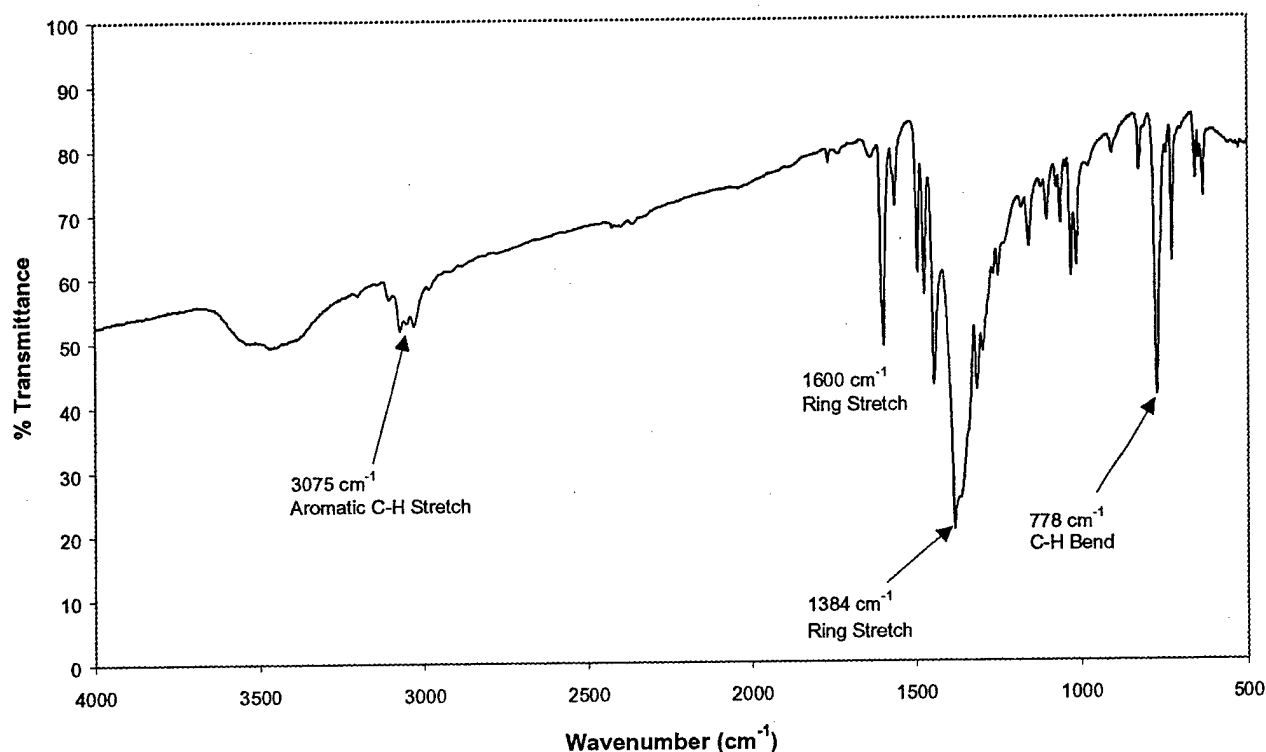
Figure 5. Change in absorption of an in situ deposited polyaniline film in response to hydrazine (N_2H_4) vapor.

The reduced polymer could be partially re-generated by exposure to hydrogen peroxide vapor as an oxidizing agent. The result showed that the change in absorption was ~90% reversible after washing with liquid hydrogen peroxide and acid (HCl).

D. Infrared Spectroscopy of $[\text{Cu}(\text{bpy})_x]^{2+}$ Complexes

This figure shows the typical IR scans for one of the copper bisbipyridine complexes. Relevant features of these spectra for each complex are as follows: $[\text{Cu}(\text{bpy})_2\text{Cl}_2]$ - 769cm^{-1} (C-H bend), 1385cm^{-1} (Ring Stretch), 3053cm^{-1} (Aromatic C-H Stretch); $[\text{Cu}(\text{bpy})_2(\text{NO}_3)](\text{NO}_3)$ - 778cm^{-1} (C-H bend), 1384cm^{-1} (Ring Stretch), 3075cm^{-1} (Aromatic C-H Stretch); $[\text{Cu}(\text{bpy})_2\text{SO}_4]$ - 778cm^{-1} (C-H bend), 1384cm^{-1} (Ring Stretch), 3075cm^{-1} (Aromatic C-H Stretch). The blue shift in the C-H bend and stretch seems to be a function of the electronegativity of the ligand

IR Spectra - $[\text{Cu}(\text{bpy})_2(\text{NO}_3)](\text{NO}_3)$



bound to the central Cu atom. As the electronegativity of the charged ligand increases ($\text{Cl}^- < \text{NO}_3^- < \text{SO}_4^{2-}$), the Cu-ion bond may increase in strength, which in turn may reduce the strength of the Cu-bpy bond. The weaker the Cu-bpy bond is, the stronger the C-H bonds are in the bipyridine system. This phenomenon manifests itself in the higher energy C-H bend and stretch observed in the IR spectra for these complexes.

E. Energy Dispersive Spectroscopy Characterization of $[\text{Cu}(\text{bpy})_2]^{2+}$ Dispersed in Thin Polymer Film

Energy dispersive spectroscopy (EDS) was used to characterize the uniformity of the $[\text{Cu}(\text{bpy})_2]^{2+}$ complexes as they were dispersed in the conducting polymer films. There are a number of different detection schemes that can be used in electron microscopy. Detection of secondary electrons, electrons ejected from the sample atoms upon irradiation by the electron beam, offers the best depth of field and resolution from an imaging perspective, but does not

indicate composition of the sample. Also available for detection are backscattered electrons, electrons from the incident beam that have been scattered back out of the sample. Resolution from detecting backscattered electrons is less than that from the analysis of secondary electrons. However, the energy of the backscattered electrons is a function of the atomic number of the atoms in the sample, with higher atomic number producing higher energy backscattered electrons. These images are more difficult to interpret, but can offer important information about sample composition.

EDS works in the same fashion as the previously mentioned techniques, except that emitted X-rays are the signal that is detected. As incident electrons impinge on the sample, some core electrons may be ejected by collisions with the primary electron beam. As electrons from higher shells transition to fill this "hole", the energy released by this process is an X-ray photon. It is this radiation that is detected in EDS. Because the energy differences between shells are well defined and specific to each element, the energy of the X-ray is characteristic of the emitting atom. An X-ray spectrometer collects these X-rays and plots the number of X-ray photons emitted versus energy. The image produced by the X-ray signal is usually much poorer than traditional SEM images. The reason for this poor image is due to the fact that X-rays travel through a sample further, thereby generating a large volume of interaction and poor spatial resolution. An X-ray map is normally generated, which shows the spatial distribution of the corresponding element. By tracking the characteristic energy for the Cu nucleus, the distribution of the complexes can be mapped over the entire surface of the polymer film. Areas of high and low concentration at the surface can be discovered and changes to the deposition technique can be made as necessary.

EDS was run on 5% (w/w) $[\text{Cu}(\text{bpy})_2(\text{NO}_3)](\text{NO}_3)$ in both an *in-situ* deposited polyaniline matrix on glass substrates. The images generated by the researchers in the Geology Department indicated that there was a homogeneous distribution of copper within the polymer matrix, however the signal was weak. There are a number of different explanations for this data. First, the concentration of the copper ions, and thus the copper complex, was extremely low on the surface. This may indicate that the copper complexes preferentially incorporate themselves into the bulk of the polymer matrix rather than the surface. Another possibility is that the copper complexes, during the *in-situ* deposition process, were not incorporated into the polymer matrix whatsoever – rather it remained in solution and was not incorporated during the reaction process. Third, this may be an indicator that the mass percent of copper complex used in the reaction mixture (1-3%) may be too low to be observed in the matrix, and ultimately too low to enhance the optical switching of the conducting polymer thin film.

C. Single Crystal X-Ray Diffraction Study of $[\text{Cu}(\text{bpy})_2]^{2+}$ Salts

Single crystal X-ray diffraction (XRD) is the most conclusive technique for structure elucidation available in the field of analytical chemistry. In this study, determination of the exact structure of the inner sphere coordination of these $[\text{Cu}(\text{bpy})_2]^{2+}$ complexes was critical to the understanding of their catalytic activity in the hydrolysis of the nerve agent mimics. Previous literature reports^{49,50} indicated that the inner sphere of these catalytic copper bipyridine complexes included water bound to the copper ion via a coordinate covalent bond, and that these water molecules serve as the active center for the catalysis of nerve agent hydrolysis. No XRD data has been reported previously on these catalytic complexes, and these experiments were critical in testing this hypothesis.

It became apparent early on that the solvent would have a significant impact on the crystalline structure of these complexes. In the case of the nitrate system, the $[\text{Cu}(\text{bpy})(\text{NO}_3)_2]$ produced only one structure (Figure 3, left), and was stable in air, with no change being seen over a 24-hour period. However, the $[\text{Cu}(\text{bpy})_2(\text{NO}_3)](\text{NO}_3)$ produced two distinct crystalline structures depending on whether the solvent, methanol, was present or absent. This particular crystal (light blue, usually twinned) was unstable in air, in that the solvent evolved from the crystal lattice within 6 hours of its removal from the reaction mixture. Figure 3 (right) shows the crystal structure of the complex prior to the evolution of methanol from the lattice. It is evident that there are three bidentate ligands (two bipyridine, one nitrate) coordinated to a central octahedral Cu atom.

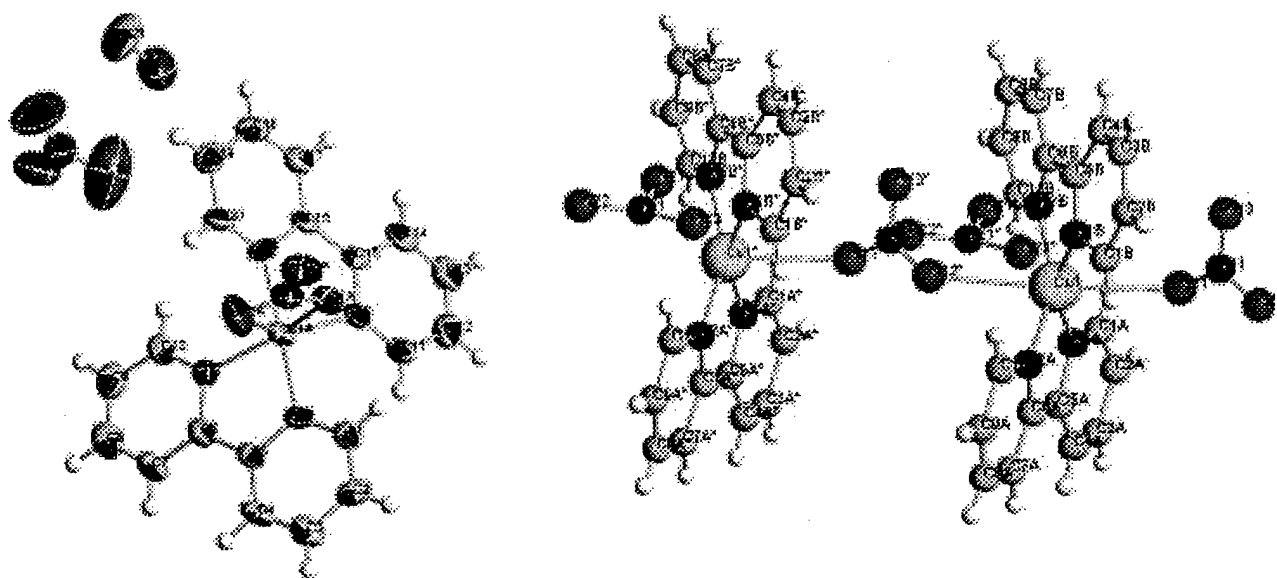


Figure 3. X-Ray crystal structures of different forms of the $\text{Cu}(\text{bpy})_x(\text{H}_2\text{O})_y$ complex (see text).

Upon the evolution of the solvent, the crystalline structure transformed into a 1-dimensional, quasi-polymeric, columnar structure with the nitrate ions serving as bridging ligands between the octahedral Cu atoms. Due to steric hindrance, the bpy ligands lie in a staggered configuration and occupy the equatorial positions of the octahedral field ("propeller" configuration). The bidentate nitrate ion bridges adjacent Cu atoms by binding one of its oxygen atoms to one Cu atom, and another oxygen atom to a different Cu atom. When methanol is present in the crystal lattice, the non-coordinated oxygen atom on the nitrate ion is exposed to enable hydrogen bonding to occur with the polar, protic solvent molecules, thus stabilizing the structure. Without the solvent molecules, hydrogen bonding cannot occur with the non-coordinated oxygen atom on the nitrate ligand. One hypothesis for this phenomenon is that the nitrate configures itself so as to minimize the exposure of non-coordinated oxygen atoms, which now have nowhere to hydrogen bond, to lower the energy of the crystalline system. The most efficient way to achieve this goal is to transform itself into the 1-dimensional, quasi-polymeric crystal structure discovered by the XRD analysis. This new finding may define the need to devise a new catalytic degradation mechanism for certain nerve agent mimics.

D. Optical Response of Conducting Polymer Films to Dimethyl methylphosphonate (DMMP) and Diisopropyl fluorophosphonate (DFP)

The use of conducting polymers as sensors has been widely reported in the literature^{1,2,20,21}. It has also been demonstrated that certain $[\text{Cu}(\text{bpy})_2]^{2+}$ complexes play a critical role in hydrolyzing nerve agents and their mimics.⁴¹ The focus of this portion of the project was to investigate whether or not the incorporation of certain $[\text{Cu}(\text{bpy})_x]^{2+}$ complexes would initiate or enhance a switch in the optical properties of the conducting polymer matrices in the presence of a basis set of nerve agent mimics. The specific nerve agent mimics studied in this project were dimethyl methylphosphonate (DMMP), a simulant of the nerve agent Sarin, and diisopropyl fluorophosphonate (DFP), a mimic of the nerve agent Soman.

The hydrolysis products of the DMMP include an ionized phosphonate backbone along with a methanol residue, while those for DFP include not only the ionized phosphonate backbone, but also fluoride ion. In both cases, the ionic products of the hydrolysis would be expected to yield a change in the electronic structure of the conducting polymer. This would provide for two effects on light propagation through the fiber: change in absorption of the evanescent field and change in the refractive index of the polymer relative to the fiber optic core. An additional potential advantage of using DFP is that the evolution of the fluoride ion upon hydrolysis may etch the glass surface, providing additional change in the refractive index.

Initial experiments centered on polyaniline (PANi) films. As stated previously, polyaniline is unique among the many different conducting polymers in that it can reversibly switch between its conducting (emeraldine salt, ES) and insulating (emeraldine base, EB) forms as a function of exposure to acid or base vapors. In these experiments, *in-situ* deposited polyaniline films on glass slides were exposed to vapors of either dimethyl methylphosphonate (DMMP) or diisopropyl fluorophosphonate (DFP) for 60 seconds. Immediately following this exposure, a UV/Vis spectra was taken to measure the effects of the vapor on the absorbance characteristics of the film. As seen from the characteristic spectra shown in Figure 4, there is a rather small, reproducible optical switch when *in-situ* deposited PANi films deposited over 20 minutes are exposed to DMMP. Exposure to DFP, regardless of deposition times (5, 10, 15 minutes) showed no change from baseline.

Incorporation of 5% (w/w) $[\text{Cu}(\text{bpy})_2(\text{NO}_3)](\text{NO}_3)$ into the PANi matrix through co-deposition did not result in an enhancement of the optical switch of this conducting polymer in the presence of either DMMP or DFP. This result indicates that there is no change in the nature of the electronic transitions in the PANi polymer in the presence of the Cu complex. It also points to the conclusion that if the $[\text{Cu}(\text{bpy})_2(\text{NO}_3)](\text{NO}_3)$ is indeed hydrolyzing the DMMP and DFP while in the PANi matrix, the degradation products from this reaction cause no change in the electron transitions present in the PANi film, nor a change in the refractive index of the substrate. It can also be concluded from this result that the degradation products of the hydrolysis of the either DMMP or DFP do not absorb light in the range of 280nm – 1100nm.

UV/Vis - PANi (20 Minutes) and DMMP

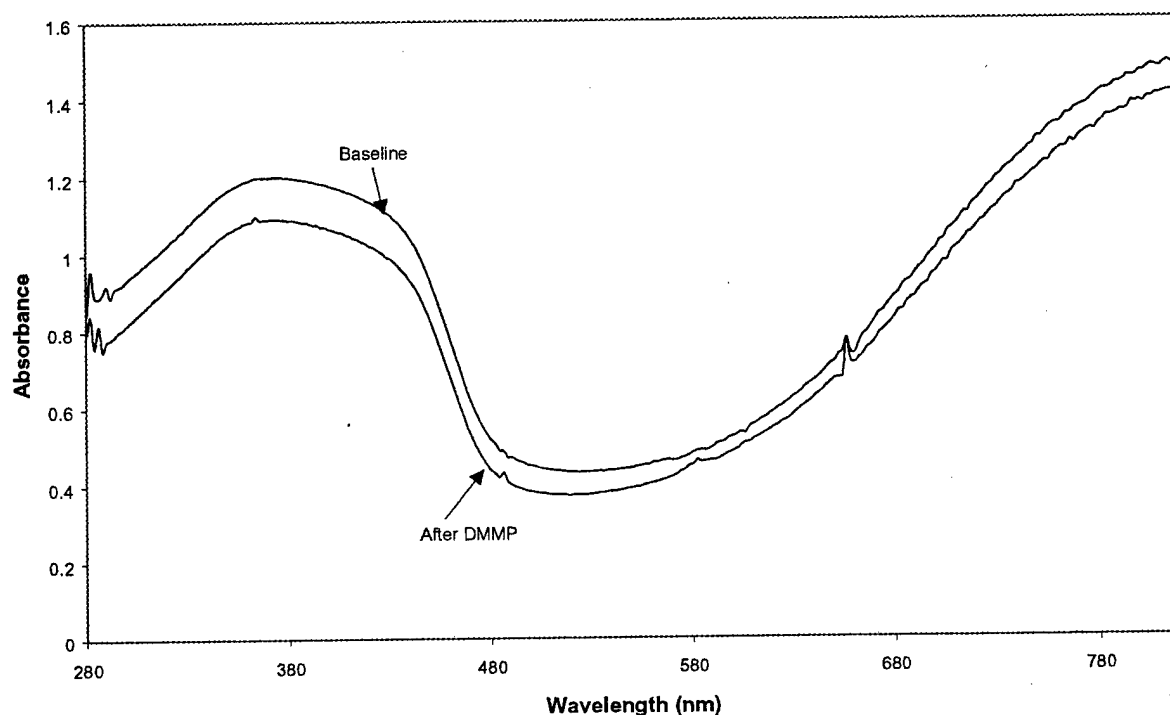


Figure 4: Representative UV/Vis Spectra of PANi Film Exposed to DMMP Vapor.

The next experiments conducted involved the exposure of *in-situ* deposited polypyrrole to the nerve agent mimics, DMMP and DFP. The initial investigation involved *in-situ* deposited films of polypyrrole on glass substrates using deposition times of 5, 10 and 15 minutes. Baseline scans demonstrated a time-dependent UV/Vis response of the growing films consistent with an increase in film thickness with deposition time. This result was consistent with previously reported *in-situ* deposition experiments.^{17, 21}

Exposure of the pure polypyrrole films to DMMP shows a marked switch at all deposition time intervals on both hydrophobic and hydrophilic surfaces. The optimum result was achieved with the 15-minute deposition sample on a hydrophobic glass surface **which achieved over 40% reduction** in the UV/Vis absorbance following exposure, Figure 5. The downward shift in the UV/Vis spectra is nearly uniform throughout the entire range of wavelengths. This observation could be explained in a number of different ways. The fact that the λ_{max} values did not change upon exposure to DMMP indicates that the charge carriers present in these films (polarons) did not change, or pair, to form a different class of charge carriers (bipolarons)¹. The uniform decrease in absorption could be a surface morphology difference upon the interaction of the PPy film with the DMMP vapor. It has previously been shown that interaction of conducting polymers with many gaseous analytes causes film swelling and subsequent changes in conductivity.²⁰ Another possibility is the fact that the DMMP vapor may have partially reduced the PPy film at the surface, causing a decrease in conductivity and hence a reduction in the

absorption in the UV/Vis region. One argument against this reasoning is that upon reduction, the λ_{max} values tend to shift due to the fact that different charge carriers normally take over as the polymer is oxidized or reduced¹. There is only an insignificant switch when the copper(II) bipyridine complexes are incorporated into the PPy matrix.

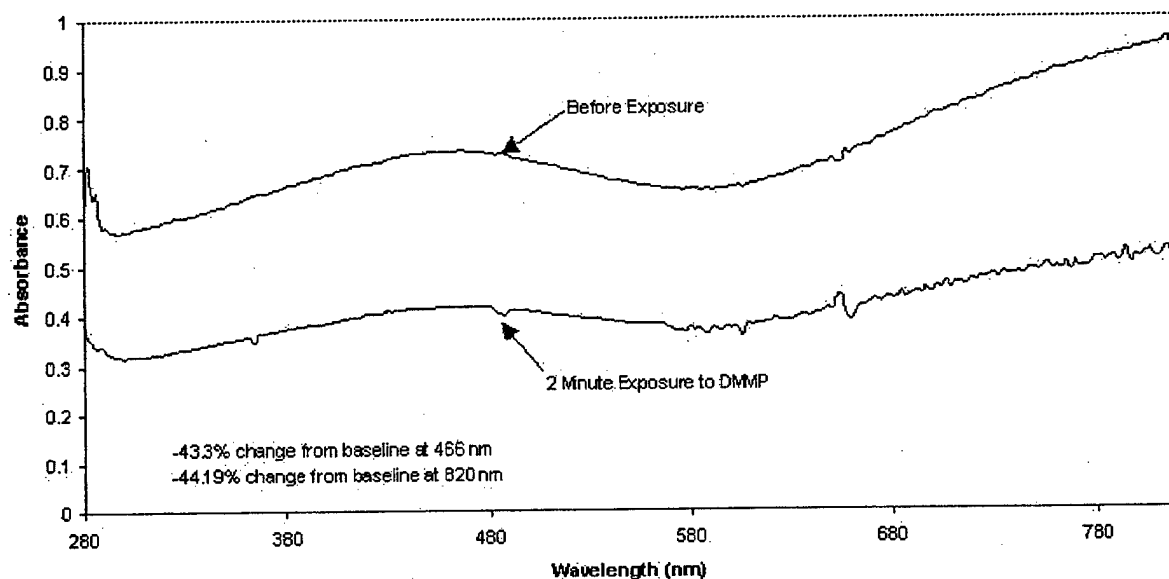


Figure 5: Representative UV/Vis Spectra of PPy Films on Hydrophobic Surfaces Exposed to DMMP.

Incorporation of the $[\text{Cu}(\text{bpy})_2(\text{NO}_3)](\text{NO}_3)$ complex into the *in-situ* deposited PPy film showed no change whatsoever from the baseline UV/Vis scan when exposed to DMMP. This result was noteworthy since the pure polypyrrole film had shown significant response. In this case, it appears that the addition of the catalytic copper complex resulted in a loss of the DMMP which was responsible for the initial shift. Since the DMMP is known to hydrolyze upon interaction with the copper complex, we conclude that the degradation products do not interact with the polymer film in a manner that changes the absorption or refractive index of the film. Thus, the catalyst decontaminates the film, which in turn reduces, or nullifies, the UV/Vis optical switching capability of the $\text{PPy}/[\text{Cu}(\text{bpy})_2(\text{NO}_3)](\text{NO}_3)$ system.

Exposure of the PPy films to DFP was also examined and the optical response of the polymer film in the UV/Vis region was monitored. In both cases (with or without $[\text{Cu}(\text{bpy})_2(\text{NO}_3)](\text{NO}_3)$ complex), there was no significant change from baseline in the UV/Vis spectra. As stated before, this can be explained in a couple of different ways: (1) the DFP did not hydrolyze in the presence of the $[\text{Cu}(\text{bpy})_2(\text{NO}_3)](\text{NO}_3)$ complex and therefore did not change the optical properties of the film; (2) the degradation products of the DFP upon reaction with $[\text{Cu}(\text{bpy})_2(\text{NO}_3)](\text{NO}_3)$ did not change the optical properties of the film, Figure 6. In an additional study, spin cast films of polypyrrole and $[\text{Cu}(\text{bpy})_2(\text{NO}_3)](\text{NO}_3)$ were found to have no significant optical change with exposure to DFP.

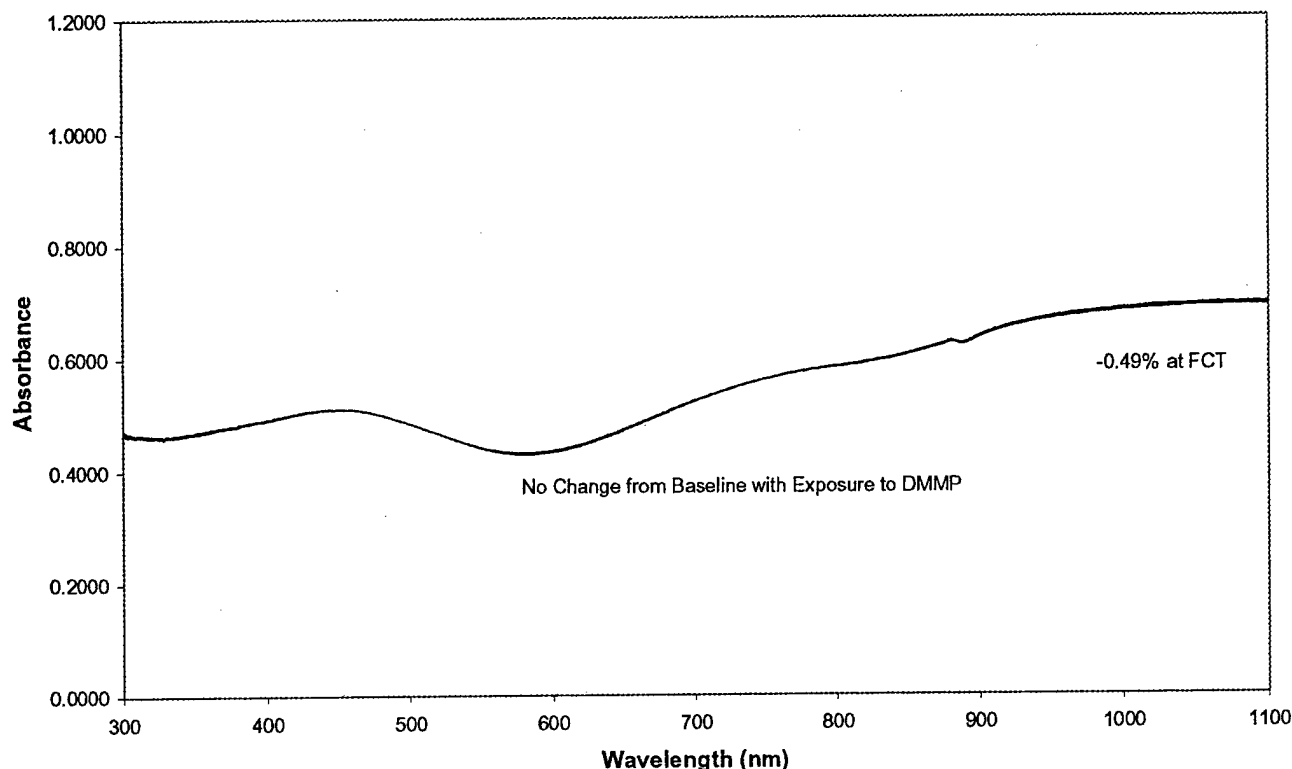


Figure 6: Representative UV/Vis Spectrum of PPy + [Cu(bpy)₂(NO₃)](NO₃) Films Exposed to DMMP

E. Electrical Response of Conducting Polymer Films

Conductivity experiments were conducted on a multitude of PANi and PPy thin films of different deposition times. The purpose of these experiments was to ensure that the films being studied in this project were similar in their properties to those published in the literature. The data generated on the unexposed polymer films were in agreement with published data.

F. Surface Morphology Response of CP Films to DMMP and DFP

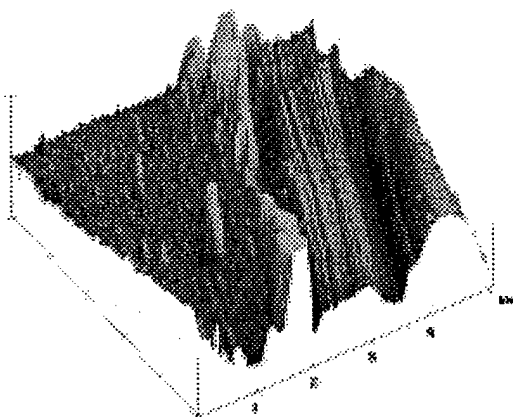
Atomic force microscope (AFM) data was generated to test the hypothesis that a surface morphology change was the major reason for the decrease in UV/Vis absorbance of PPy when exposed to DMMP. Contact-mode AFM studies were conducted and the surfaces mapped are summarized in Figure 7. It is evident that the differences in height measurements (before and after the DMMP exposure) cannot be definitively accounted for by the previously stated hypothesis. There is no clear change in morphology (i.e. from rough to smooth) as a result of the exposure of the thin films to the nerve agent mimic vapor. The average height for the unexposed

sample was 50-100 nm, while after DMMP vapor exposure the average height was still in the 50-100 nm range.

Recent research has indicated that a potential reason for the decrease in UV/Vis absorbance is a change in morphology of the polymer film³². This study was a contact-mode AFM study which showed differences in average height and surface roughness between the unexposed and exposed PPy thin films. There are a number of potential explanations for the data generated in this study. Exposure time to the nerve agent mimic was not clearly delineated in the above literature. Longer exposure time of these films could allow more of the nerve agent mimic to permeate and diffuse through the polymer film and ultimately change the morphology of the film. Also running the AFM in the contact-mode may provide more consistent height and roughness data, minimizing the affects of the variability in the microscope (reduce S/N ratio). These data should not completely preclude this hypothesis as a possible explanation for the change in optical absorbance. Further studies need to be conducted to definitively confirm or deny this hypothesis as a reasonable and reliable explanation of this optical switch.

Unexposed

Exposed

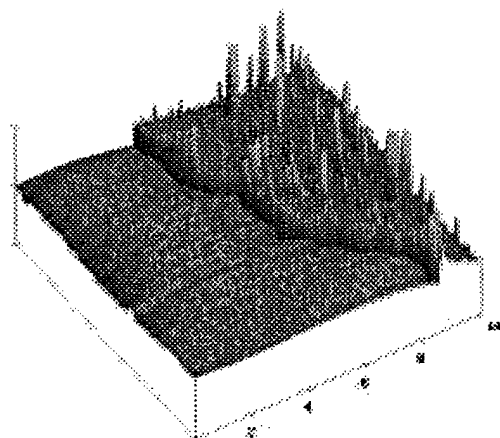


4min Polypyrrole on Hydrophilic
Hydrophilic Glass Substrate

(Exposed)

data scale: 100nm

Cross Section: ~ 64nm



4min Polypyrrole on
Glass Substrate

data scale: 100nm

Cross Section: ~ 150nm

Figure 7: Atomic Force Microscopy Data on PPy Films Before and After DMMP Exposure

Conclusion

The continuing search for a rapid, sensitive sensing material for the detection of nerve agents has lead to the development of a conducting polymer based sensor. By exploring the application of polyaniline and polypyrrole based materials, we have demonstrated reproducible

switching in the optical properties of thin films operating in the visible region of the spectrum. The optimum result was achieved for polypyrrole on hydrophobic surfaces where a ~ 40% change in absorbance was observed. Application of the decontamination agent $\text{Cu}(\text{bpy})_x$ lead to no significant increase in the optical response of these new materials. It was hypothesized that this was the result of a smaller response between the degradation products and the conducting polymer thin films than the pure agent. Morphology studies before and after exposure to DMMP or DFP did not suggest a significant change in film thickness as the cause for the optical changes. More work will be necessary to identify the specific interaction which yields this exciting result.

References

1. a) J. Feng and A. G. MacDiarmid, *Synth. Met.*, **1999**, *102*, 1304. b) M. Josowicz, J. Janata, *Anal. Chem.*, **1986**, *58*, 514. c) Kanatzidis, M.G., *Chemical & Engineering News*, December 3, 1990.
2. Schmeiber, D., Appel, G., Bohme, O., Heller, T., Mikalo, R., Hoffmann, P., Batchelor, D., *Sensors and Actuators B*, **70** (2000), 131-138.
3. A. Malinauskas, *Polymer*, **42** (2001), 3957-3972.
4. a) T. Swager, *Acc. Chem. Res.*, 1998, **31**, 201. b) G.S. Kanner, Vardeny, Z.V., Lanzani, G., Zheng, L.X., *Synthetic Metals*, **116** (2001), 71-73.
5. Jiang, B., Yang, S.W., Bailey, S.L., Hermans, L.G., Niver, R.A., Bolcar, M.A., Jones, Jr., W.E., *Coordination Chemistry Reviews*, **171** (1998), 365-386.
6. a) A. G. MacDiarmid, J.-C. Chiang, A. F. Richter, N. L. D. Somasiri and A. J. Epstein, "Polyaniline: Synthesis and Characterization of the Emeraldine Oxidation State by Elemental Analysis," *Conducting Polymers*, eds. L. Alcacer, Reidel Publishing: Dordrecht, Holland, 1987, 105. b) Sherman, B.C., Euler, W.B., Force, R.B., *Journal of Chemical Education*, Volume 71, Number 4, April 1994.
7. MacDiarmid, A.G., Chiang, J.-C., Richter, A.F., Somasiri, N.L.D., Epstein, A.J., "Polyaniline: Synthesis and Characterization of the Emeraldine Oxidation State by Elemental Analysis", *Conducting Polymers*, Luis Alcacer, Editor, p. 105.
8. Xia, Y., Wiesinger, J., MacDiarmid, A.G., Epstein, A.J., *Chemistry of Materials*, 1995, **7**, 443-445.
9. Ray, A., Asturias, G.E., Kershner, D.L., Richter, A.F., MacDiarmid, A.G., Epstein, A.J., *Synthetic Metals*, **29** (1989), E141-E150.
10. Focke, W.W., Wnek, G.E., Wei, Y., *Journal of Physical Chemistry*, 1987, **91**, 5813-5818.
11. Manohar, S.K., MacDiarmid, A.G., Epstein, A.J., *Synthetic Metals*, **41-43** (1991) 711-714.
12. Kulsewicz-Bajer, I., Pron, A., Abramowicz, J., Jeandey, C., Oddou, J.-L., Sobczak, J.W., *Chemistry of Materials*, 1999, **11**, 552-556.
13. Wang, Z.H., Scherr, E.M., MacDiarmid, A.G., Epstein, A.J., *Physical Review B*, Volume 45, Number 8, 15 February 1992-II.
14. Misurkin, I.A., Zhuraleva, T.S., Geskin, V.M., Gulbinas, V., Pakalnis, S., Butvilos, V., *Physical Review B*, Volume 49, Number 11, 15 March 1994-I.
15. Jeon, D., Kim, M.C., Gallagher, M.C., Willis, R.F., *Science*, Vol. 256, 19 June 1992.
16. Pinto, N.J., Torres, C.M., Kahol, P.K., McCormick, B.J., *Journal of Applied Physics*, **79** (11), 1 June 1996.
17. Chiang, J.-C., MacDiarmid, A.G., *Synthetic Metals*, **13** (1986), 193-205.
18. Wang, Y., Rubner, M.F., *Synthetic Metals*, **47** (1992), 255-266.
19. Wu, C.-G., Chen, J.-Y., *Chemistry of Materials*, Volume 9, Number 2, February 1997.
20. Jin, Z., Su, Y., Duan, Y., *Sensors and Actuators B*, **72** (2001), 75-79.
21. MacDiarmid, A.G., Norris, I.D., Jones, Jr., W.E. El-Shariff, M.A., Yuan, J., Han, B., Ko, F.K., *Synthetic Metals*, 2001, **119**, 27.
22. Joo, J., Lee, J.K., Baeck, J.S., Kim, K.H., Oh, E.J., Epstein, J., *Synthetic Metals*, **117** (2001), 45-51.

23. Skaarup, S., West, K., Gunaratne, L.M.W.K., Vidanapathirana, K.P., Careem, M.A., *Solid State Ionics*, 136-137 (2000), 577-582.
24. Mikat, J., Orgzall, I., Hochheimer, H.D., *Synthetic Metals*, 116 (2001), 167-170
25. Avlyanov, J.K., Kuhn, H.H., Josefowicz, J.Y., MacDiarmid, A.G., *Synthetic Metals*, 84 (1997), 153-154.
26. Sakkopoulos, S., Vitoratos, E., Dalas, E., *Synthetic Metals*, 92 (1998), 63-67.
27. Huang, Z., Wang, P.-C., Feng, J., MacDiarmid, A.G., Xia, Y., Whitesides, G.M., *Synthetic Metals*, 85 (1997), 1375-1376.
28. Ram, M.K., Adami, M., Faraci, P., Nicolini, C., *Polymer*, 41 (2000), 7499-7509
29. Huang, Z., Wang, P.-C., MacDiarmid, A.G., Xia, Y., Whitesides, G., *Langmuir*, 1997, 13, 6480 – 6484.
30. Wang, P.-C., Huang, Z., MacDiarmid, A.G., *Synthetic Metals*, 101 (1990) 852-853.
31. van de Leur, R.H.M., van der Waal, A., *Synthetic Metals*, 102 (1999), 1330-1331.
32. Hosseini, S., Entezami, A.A., *Iranian Polymer Journal*, Volume 8 (3), July 1999, 205-213.
33. de Souza, J.E.G., Neto, B.B., dos Santos, F.L., de Melo, C.P., Santos, M.S., Ludermir, T.B., *Synthetic Metals*, 102 (1999), 1296-1299.
34. Collins, G.E., Buckley, L.J., *Synthetic Metals*, 78 (1996), 93-101.
35. Gregory, R.V., Kimbrell, W.C., Kuhn, H.H., *Synthetic Metals*, 28 (1989), C823-C835.
36. Yang, Y.-C., Baker, J.A., Ward, J.R., *Chemical Reviews*, 1992, 92, 1729-1743.
37. Garribba, E., Micera, G., Sanna, D., Strinna-Erre, L., *Inorganica Chimica Acta*, 299 (2000), 253-261.
38. Noack, M., Gordon, G., *The Journal of Chemical Physics*, Volume 48, Number 6, 15 March 1968.
39. Marov, I.N., Belyaeva, V.K., Smirnova, E.B., Dolmanova, I.F., *Inorganic Chemistry*, Volume 17, Number 6, 1978.
40. Walker, F.A., Sigel, H., *Inorganic Chemistry*, Volume 11, Number 5, 1972, 1162-1164.
41. Xie, Y., Popov, B.N., *Analytical Chemistry*, 2000, 72, 2075-2079.
42. Morrow, J.R., Trogler, W.C., *Inorganic Chemistry*, 1989, 28, 2330-2333.
43. Beaudry, W.T., Wagner, G.W., Ward, J.R., *Journal of Molecular Catalysis*, 93 (1994), 221-231.
44. Tesfai, T.M., Sheinker, V.N., Mitchell, M.B., *The Journal of Physical Chemistry B*, Volume 102, Number 38, September 17, 1998.
45. Boyer, M.-I., Quillard, S., Rebourt, E., Louran, G., Buisson, J.P., Monkman, A., Lefrant, S., *Journal of Physical Chemistry B*, 1998, 102, 7382-7392.
46. Harada, I., Furukawa, Y., Ueda, F., *Synthetic Metals*, 29 (1989), E303-E312.
47. Ohira, M., Sakai, T., Takeuchi, M., Kobayashi, Y., Tsuji, M., *Synthetic Metals*, 18 (1987), 347-352.
48. Drago, R.S., "Physical Methods for Chemists", Second Edition (1992), Surfside Scientific Publishers.
49. Wagner-Jauregg, T; Hackley, B.E., Jr.; Lies, T.A.; Owens, O.O.; Proper, R.; *J. Am. Chem. Soc.* 1955, 77, 922-929.
50. Courtney, R.C.; Gustafson, R.L., Westerback, S.J.; Hyytiainen, H.; Chaberek, S.C., Jr.; Martell, A.E., *J. Am. Chem. Soc.*, 1957, 79, 3030-3036.